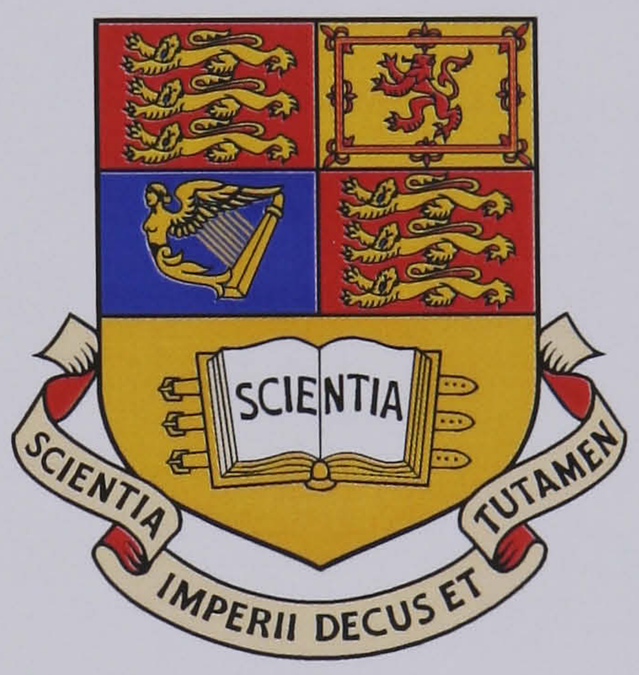
A Computational Study of Helicopter Coaxial Rotor Aerodynamics and Performance

by

Hyo Won Kim



Department of Aeronautics
Imperial College London
Prince Consort Road
London SW7 2BY

This thesis is submitted for the degree of Doctor of Philosophy of the University of London

2008

Abstract

Recently, a resurgence of interest in the coaxial rotor helicopter configuration has been prompted by its potential to achieve higher thrusts and higher forward speeds than has traditionally been possible with conventional single-rotor platforms. Accurate prediction of the performance of such systems is extremely difficult because of the strong aerodynamic interaction between the upper and lower rotors. The Vorticity Transport Model (VTM) is a comprehensive rotorcraft analysis code based on the solution of the time dependent Navier-Stokes equation in vorticity-velocity form. The high resolution of the wake modelling technique used in the VTM makes it particularly well suited to capturing the complex pattern of interacting vortical structures within the wake of coaxial systems. This dissertation demonstrates that the VTM is able to capture accurately the highly interactive aerodynamic environment associated with coaxial rotor systems. The aerodynamic performance and acoustic characteristics of a coaxial rotor are contrasted with those of an equivalent single rotor. The coaxial rotor is shown to consume less induced power than the single rotor and the aerodynamic origin of the differences in the performance are highlighted. Increasing the flapwise stiffness of the coaxial system reduces its induced power consumption further. Additional savings in power can be achieved, particularly at high speeds, if the system is augmented in thrust using an auxiliary device. Aerodynamic interactions between the sub-components of a thrust-compounded helicopter with a rigid coaxial rotor are identified as the sources of acoustic focusing and unsteady loading on the aircraft. These results suggest that state-of-the-art numerical models such as the VTM may have developed to the point where they can lend useful insights into the detailed aerodynamic characteristics of modern, complex helicopter configurations.

Acknowledgements

First and foremost, I would like to thank Professor Richard Brown for his unparallelled guidance and support throughout this research. I have thoroughly enjoyed my research experience and have been continuously inspired by his enthusiasm and breadth of knowledge.

I would also like to thank Mr. John Perry, former Chief Aerodynamicist at Westland Helicopters (Ltd.), for his interest and support for this research. The work presented in Chapter six was a collaborative project where Dr. Adam Kenyon (a former colleague who is now with Red Bull Racing) and Dr. Karthikeyan Duraisamy (University of Glasgow) assisted with the analysis of the fuselage aerodynamics and the acoustics respectively. Further collaboration with Dr. Duraisamy has culminated in Chapter five. Dr. Kenyon has also assisted in proof reading this dissertation and I am thankful for his diligence.

This research has been made financially possible by several sponsors. I am grateful for the care and support from Mr. Ki Youn Kim and Dr. Ruth Van Hoogstraten-Brown. I am also grateful for the generous support from the Royal Aeronautical Society in the form of a Centennial Scholarship Award and also for the scholarship from the University of Glasgow during my time there as a visiting researcher.

The Aerospace Speaker's Travel Grant from the Royal Aeronautical Society and the Conference Travel Award from the Korean Scientists and Engineers Association in the UK have allowed me to attend international conferences to present elements of this research and I am very grateful for these opportunities.

Finally, I would like to thank my family, friends, and both past and present members of the Rotor Aeromechanics Laboratory for their advice and support.

To the love of my mother, Soo Jung Lee,
and in memory of my grandfather, Ki Youn Kim (1932–2008).

I declare that, except where explicitly stated, the work contained in this dissertation is my own.



Signed HYO WON KIM

Date 26 SEPT. 2008

Contents

Abstract 1

Acknowledgements 2

Dedication 3

Declaration 4

Table of Contents 5

List of Figures 8

List of Tables 20

Nomenclature 21

1 Introduction 27

1.1 Synopsis 32

1.2 Publications 33

2 Model Description 35

2.1 Introduction 35

2.2 Governing Equations 36

2.3 Vorticity Transport Model 37

2.4 Numerical Implementation 38

2.4.1 Discretisation of the Governing Equations 39

2.4.2 Grid Structure 40

2.4.3 Arrangement of Flow Variables 42

2.4.4 Vorticity Advection 43
2.4.5 Evaluation of Velocity Field 45
2.5 Blade Aerodynamics 51
2.6 Structural Dynamics 53
2.7 Rotor Trim Control 57
2.8 Rotor Aeroacoustics 58
2.9 Fuselage Aerodynamics 60
2.10 Summary 62

3 Performance Comparison of Conventional and Coaxial Rotors 63
3.1 Introduction 63
3.2 Model Validation 64
3.2.1 Power Comparisons 71
3.3 Hover 74
3.3.1 Wake Geometry in Hover 77
3.3.2 Hover Performance 81
3.4 Steady Forward Flight 87
3.4.1 Forward Flight Performance 88
3.4.2 Wake Geometry in Forward Flight 89
3.5 Manoeuvring Flight 96
3.5.1 Turn Performance 98
3.5.2 Wake Geometry in a Steady Turn 101
3.6 Aerodynamic Origin of Power Differences 104
3.7 Summary 107

4 Effect of Rotor Stiffness on Coaxial Rotor Aerodynamics 108
4.1 Introduction 108
4.2 Rotor Model 111
4.2.1 Rotor Stiffness 111
4.2.2 Trim Model 112
4.3 The Effect of Trim Strategy on Performance 116
4.3.1 The Importance of Accurate Trim 124
4.4 The Effect of Stiffness on Performance 127

4.4.1 Rotor Power Consumption 130
4.4.2 Rotor Wake Geometry 137
4.4.3 Rotor Vibration 142
4.5 Summary 149

5 Aeroacoustics of Coaxial Rotors **151**
5.1 Introduction 151
5.2 Rotor Setup 153
5.3 Acoustic Analysis of Conventional Coaxial Rotor 154
5.3.1 Overall Noise Characteristics 155
5.3.2 BVI Noise Characteristics 157
5.3.3 Far-Field Noise 163
5.3.4 Implications of Minor Design Changes 166
5.4 Effect of Rotor Stiffness on Acoustic Characteristics 167
5.4.1 Consequences for BVI Noise 168
5.4.2 Consequences for Far-Field Noise 178
5.5 Summary 181

6 Compound Coaxial Helicopter **183**
6.1 Introduction 183
6.2 Description of Simulated Configuration 186
6.2.1 Main Rotor System 186
6.2.2 Auxiliary Propulsor 188
6.2.3 Fuselage Geometry 189
6.2.4 Trim Methodology 190
6.3 Aircraft Performance 192
6.4 Wake Structure 194
6.5 Aerodynamic Interaction Between Sub-components 202
6.5.1 Rotor-Rotor Interaction 202
6.5.2 Rotor-Propulsor Interaction 207
6.5.3 Rotor-Tailplane Interaction 210
6.6 Interdependencies in the Interactional Aerodynamics 213
6.6.1 Flight Condition of Interest 213

6.6.2 Categorisation of Interactions 215
6.6.3 Main Coaxial Rotor 216
6.6.4 Propulsor 223
6.6.5 Fuselage 226
6.7 Interactional Aeroacoustics 228
6.8 Summary 234

7 Conclusions **236**

References **248**

List of Figures

1.1 *Kamov Ka-32 coaxial rotor helicopter. The tip vortices from the rotor blades are visualised by natural condensation. (Courtesy of Dany Gaulé and Airliners.net.)* 28

1.2 *Examples of modern coaxial rotor helicopters. (Courtesy of 1000aircraft-photos.com and Airliners.net.)* 29

2.1 *Schematic illustration showing adaptive grid generation and destruction, tracking the regions where vorticity is present within the flow [29].* . . . 40

2.2 *Nested grid structure where the resolution decreases with increasing distance from the rotor hub [29].* 41

2.3 *Overlapping of the grid level boundaries provides both second order accuracy and monotonicity; shaded cells represent overlap region. Adapted from Brown and Line [29]* 42

2.4 *Staggered arrangement (left) and cell-centred arrangement (right) for flow variables.* 43

2.5 *Stencil for calculation of inter-cell fluxes of vorticity. Adapted from Toro [37]* 43

2.6 *Comparison of velocity fields generated by Biot-Savart and Rosenhead-Moore kernels. Adapted from Brown and Line [29]* 46

2.7 *Interaction between source and target clusters using the multipole method to evaluate velocity field. Adapted from Brown and Line [29]* 47

2.8 *Categorisation of the velocity-inducing clusters in to the near-field (light grey), intermediate field (dark grey), and far field (white) of cluster i.* . . 49

2.9 *Evaluation of velocity field by refinement through hierarchical decomposition.* 50

2.10 *Representation of blade aerodynamics and inner wake model.* 52
2.11 *Simplified representation of blade dynamics of an articulated rotor.* . . . 54
2.12 *Schematic showing axis convention for forces and moments. (Fuselage included for clarity.)* 57

3.1 *Power vs. Thrust: VTM simulations compared to Harrington's experimental data.* 66
3.2 *Comparison of VTM computed profile power against experimental estimates.* 67
3.3 *Variation of sectional profile drag coefficient with angle of attack as used in VTM simulations.* 69
3.4 *Power vs. Thrust: VTM simulations compared to Harrington's experimental data.* 70
3.5 *Overall power consumption in steady level flight ($C_T = 0.0048$).* 70
3.6 *Power constituents in hover, as a function of overall thrust coefficient.* . 72
3.7 *Thrust sharing between the upper and lower rotors of the coaxial system in hover, as a function of overall thrust coefficient.* 72
3.8 *Power constituents in forward flight, as a function of advance ratio (overall $C_T = 0.0048$).* 73
3.9 *Thrust sharing between the upper and lower rotors of the coaxial system in forward flight, as a function of advance ratio (overall $C_T = 0.0048$).* . 73
3.10 *Collective pitch required to trim to given thrust coefficient (using $C_D{}'$ profile drag model throughout).* 75
3.11 *Power vs. Thrust: comparison after normalising by rotor solidity.* 76
3.12 *Power vs. Thrust: comparison between rotors with identical solidity and blade properties.* 76
3.13 *Wake structure in hover ($C_T = 0.0025$).* 78
3.14 *Correlation of relative tip vortex trajectories against Landgrebe's empirical model for the rotors in isolation ($C_T = 0.0048$).* 79
3.15 *Spanwise inflow distribution experienced by a single blade during one revolution when in hover (Harrington's rotor, $C_T = 0.0048$).* 80
3.16 *Radial distribution of various parameters: top and bottom rotors of coaxial system compared (overall $C_T = 0.0050$).* 83

3.17 *Radial distribution of various parameters: top rotor of coaxial system ($C_T = 0.0028$) compared to the isolated rotor at the same collective pitch setting ($C_T = 0.0030$).* 84
3.18 *Radial distribution of various parameters: coaxial system (upper and lower rotors averaged) compared to the equivalent conventional rotor at the same thrust coefficient ($C_T = 0.0050$).* 85
3.19 *Overall power and its constituents in hover.* 87
3.20 *Overall power and its constituents in steady level flight ($C_T = 0.0048$).* . . 89
3.21 *Wake structure of coaxial rotor (left) and equivalent single rotor (right) in forward flight ($\mu = 0.12$).* 90
3.22 *Wake geometry in steady, level flight. (Left: coaxial rotor. Right: equivalent single rotor.)* 91
3.23 *Internal wake structure in steady, level flight. (Left: coaxial rotor. Right: equivalent single rotor.)* 92
3.24 *Spanwise inflow variation experienced by a single blade during one revolution at various advance ratios. (Far left: upper rotor of coaxial system. Left: lower rotor of coaxial system. Right: equivalent single rotor.)* . . . 93
3.25 *Spanwise variation of lift coefficient experienced by a single blade during one revolution at advance ratio $\mu = 0.24$.* 94
3.26 *Control angles required for trim in steady level flight.* 95
3.27 *Vertical clearance between the blade tips of the coaxial rotor in steady, level flight. (Azimuth defined with respect to the lower rotor.)* 95
3.28 *Wake of a coaxial rotor in a coordinated, level, left-hand turn at load factor 1.50. (Top: Top view. Bottom: Front view)* 97
3.29 *Total power required by coaxial and equivalent systems in a level, wind-up turn.* 98
3.30 *Total power and its constituents in a level, wind-up turn (with high frequency oscillations removed).* 99
3.31 *Control angles required in a level, wind-up turn.* 100
3.32 *Evolution of the vertical clearance between the blade tips of the coaxial rotor during a wind-up turn. (Azimuth defined with respect to the lower rotor.)* 100

3.33 *Spanwise inflow variation experienced by a single blade during one revolution in a level turn at various load factors. (Far left: upper rotor of coaxial system. Left: lower rotor of coaxial system. Right: equivalent single rotor.)* 102

3.34 *Wake geometry in a coordinated, level turn (front view). Left: coaxial rotor. Right: equivalent rotor.* 103

3.35 *Wake geometry in a coordinated, level turn (side view). Left: coaxial rotor. Right: equivalent rotor.* 103

3.36 *Spanwise induced power variation experienced by a single blade during one revolution in a level turn at various load factors. (Far left: coaxial system averaged over the two rotors. Left: equivalent single rotor system. Right: difference between equivalent single rotor system and averaged coaxial system — averaged coaxial system subtracted from equivalent single rotor system.)* 105

4.1 *The Sikorsky XH-59A Advancing Blade Concept helicopter.* 110

4.2 *The effect of trim strategy on overall power consumption ($\mu = 0.12$ and $C_T = 0.0048$) Percentage figures indicate relative increase or decrease with respect to trim method 1.* 118

4.3 *Distribution of blade loading on the upper and lower rotors of the rigid coaxial system at advance ratio $\mu = 0.12$. Trim methods 1 to 4 compared.* 119

4.4 *Distribution of induced power consumption on the upper and lower rotors of the rigid coaxial system at advance ratio $\mu = 0.12$. Trim methods 1 to 4 compared.* 120

4.5 *Distribution of profile power consumption on the upper and lower rotors of the rigid coaxial system at advance ratio $\mu = 0.12$. Trim methods 1 to 4 compared.* 121

4.6 *Total power consumed in forward flight. Static VTM computations for Harrington's rotor in steady level flight compared with VTM computation of accelerated level flight.* 124

4.7 *Total power consumed by the coaxial system in forward flight. Rigid and teetering rotors compared.* 125

4.8 *Thrust and propulsive forces, C_T and C_{Fx}, produced by the coaxial system in forward flight. Rigid and teetering rotors compared.* 126
4.9 *The effect of rotor stiffness on overall power consumption ($C_T = 0.0048$, various flight speeds). Percentage figures indicate relative increase or decrease with respect to the rigid rotor.* 128
4.10 *Inflow distribution at advance ratio $\mu = 0.12$, $C_T = 0.0048$. Articulated and rigid rotors compared.* 129
4.11 *Effect of rotor stiffness on the distribution of induced power consumption on the upper and lower rotors of the coaxial system at advance ratio $\mu = 0.12$.* 131
4.12 *Effect of rotor stiffness on the distribution of profile power consumption on the upper and lower rotors of the coaxial system at advance ratio $\mu = 0.12$.* 132
4.13 *Effect of rotor stiffness on the distribution of induced power consumption on the upper and lower rotors of the coaxial system at advance ratio $\mu = 0.24$.* 133
4.14 *Effect of rotor stiffness on the distribution of profile power consumption on the upper and lower rotors of the coaxial system at advance ratio $\mu = 0.24$.* 134
4.15 *Effect of rotor stiffness on the distribution of induced power consumption on the upper and lower rotors of the coaxial system at advance ratio $\mu = 0.36$.* 135
4.16 *Effect of rotor stiffness on the distribution of profile power consumption on the upper and lower rotors of the coaxial system at advance ratio $\mu = 0.36$.* 136
4.17 *Circulation distribution on upper and lower rotors at advance ratio $\mu = 0.12$ and thrust coefficient $C_T = 0.0048$. Articulated and rigid rotors compared.* 138
4.18 *Rotor wakes generated by the coaxial system in forward flight at advance ratio $\mu = 0.12$. (Varying stiffness including teetering configuration). The wake generated by the upper rotor is coloured a darker shade than the wake from the lower rotor.* 139

4.19 *Super-vortex formation on the coaxial rotor at advance ratio* $\mu = 0.12$. *Rigid and articulated configurations compared.* 140
4.20 *Rotor wakes generated by the coaxial system in forward flight at advance ratio* $\mu = 0.24$. *The wake generated by the upper rotor is coloured a darker shade than the wake from the lower rotor.* 141
4.21 *Rotor wakes generated by the stiff coaxial system in high-speed forward flight at advance ratio* $\mu = 0.36$. *The wake generated by the upper rotor is coloured a darker shade than the wake from the lower rotor. Rotor discs plotted for clarity.* 141
4.22 *Effect of rotor stiffness on unsteady aerodynamic forcing of the coaxial system at advance ratio* $\mu = 0.12$, *thrust coefficient* $C_T = 0.0048$. *(Mean component removed.)* 143
4.23 *Unsteady aerodynamic forcing of the rigid coaxial system. Contributions from upper and lower rotors to overall forcing compared at various forward speeds. (Mean component removed.)* 145
4.24 *Unsteady aerodynamic forcing of the rigid coaxial system with alternative blade phasing (*90° *offset compared to that from Figure 1.23). Contributions from upper and lower rotors to overall forcing compared at various forward speeds. (Mean component removed.)* 147
4.25 *Comparison of BVI patterns for different phasing. BVI visualised by high gradients of inflow using line contours. (Left: original phasing. Right: alternative phasing.)* 148

5.1 *Overall SPL in decibels in steady level flight at advance ratio* $\mu = 0.12$. . 155
5.2 *A time history of acoustic pressure over one rotor revolution one rotor radius below the tip of the rotor disc at* $\psi = 0^\circ$ *(labelled 'T') for advance ratio* $\mu = 0.12$. 156
5.3 *Frequency spectrum of sound pressure level one rotor radius below the tip of the rotor disc at* $\psi = 0^\circ$ *(labelled 'T') for advance ratio* $\mu = 0.12$. *The vertical dashed line represents the fundamental blade passage frequency.* 156
5.4 *BVI sound pressure levels (5–40*N_{bt}*/rev) in decibels at advance ratio* $\mu =$ 0.12. 157

5.5 *BVI sound pressure levels (5–40N_{bt}/rev) in decibels for individual rotors in coaxial configuration at advance ratio* $\mu = 0.12$. 158

5.6 *Time history of acoustic pressure at the BVI hot spot, marked 'B' in Figures 5.4 and 5.9, for coaxial rotor.* 159

5.7 *Acoustic source density (loading noise,* Pa/m^2*) on lower rotor of coaxial system as evaluated at the BVI hot spot. Also shown as a white line is the locus of sources corresponding to observer time* $t = 0.036$ *s in (a) and* $t = 0.049$ *s in (b).* 159

5.8 *Tip vortex structure of coaxial rotor at advance ratio* $\mu = 0.12$ *showing inter-rotor BVI via parallel impingement.* 160

5.9 *BVI sound pressure levels (5–40N_{bt}/rev) in decibels at advance ratio* $\mu = 0.24$. 161

5.10 *A rotor blade of the equivalent single rotor at advance ratio* $\mu = 0.24$ *interacting with tip vortex from preceding blade at* $\psi \approx 170°$. *Trailed vorticity generated by this blade is shaded dark to highlight secondary trailing vorticity generated by this interaction.* 162

5.11 *Parallel inter-rotor BVI where the tip vortex structure from upper rotor of coaxial system impinges on advancing blade of lower rotor at* $\mu = 0.24$. 163

5.12 *Maximum OASPL and BVISPL in decibels at* $M_{tip} = 0.42$ *on a hemispherical observer surface of radius* $2R$*, centred on the rotor hub.* 164

5.13 *BVISPL in decibels for coaxial rotor on a hemispherical surface of radius* $2R$ *centered on the hub of the lower rotor. (Left: isometric view. Right: top view.)* 165

5.14 *BVI sound pressure levels (5–40N_{bt}/rev) in decibels for coaxial rotor with design changes at advance ratio* $\mu = 0.12$. 167

5.15 *BVI pattern for different flapwise stiffnesses visualised by high gradients of inflow using line contours at advance ratios* $\mu = 0.12$ *(left) and* $\mu = 0.24$ *(right).* 169

5.16 *BVI sound pressure levels (5–40N_{bt}/rev) in decibels (left) and time history of acoustic pressure over one rotor revolution (right) at BVI hot spot on the advancing side of the lower rotor for advance ratio* $\mu = 0.12$. . . . 170

5.17 *Comparison between the teetering and stiffened configurations of the principal inter-rotor BVI on the advancing side of the lower rotor at advance ratio* $\mu = 0.12$. 171

5.18 *Acoustic source density (loading noise,* Pa/m^2*) on lower rotor of coaxial system as evaluated at the BVI hot spot directly below advancing side of lower rotor for advance ratio* $\mu = 0.12$*. Also shown as a white line is the locus of sources corresponding to observer time* $t = 0.037$ *s.* 172

5.19 *Time history of acoustic pressure over one rotor revolution at BVI hot spot below the rear of the rotor disc for advance ratio* $\mu = 0.12$. 173

5.20 *Acoustic source density (loading noise,* Pa/m^2*) on lower rotor of coaxial system as evaluated at the BVI hot spot below the rear of rotor disc for advance ratio* $\mu = 0.12$*. Also shown as a white line is the locus of sources corresponding to observer time* $t = 0.154$ *s.* 174

5.21 *BVI sound pressure levels (5–40*N_{bt}*/rev) in decibels (left) and time history of acoustic pressure over one rotor revolution at BVI hot spot marked 'B' (right) for advance ratio* $\mu = 0.24$. 175

5.22 *Acoustic source density (loading noise,* Pa/m^2*) on lower rotor of coaxial system as evaluated at the BVI hot spot for advance ratio* $\mu = 0.24$*. Also shown as a white line is the locus of sources corresponding to observer time* $t = 0.051$ *s in (a) and* $t = 0.049$ *s in (b).* 176

5.23 *Comparison of the principal inter-rotor BVI on the advancing side of the lower rotor between the configurations with various stiffnesses at advance ratio* $\mu = 0.24$. 177

5.24 *BVISPL in decibels for various stiffnesses of coaxial rotor system on a hemispherical surface of radius* $2R$ *centred on the hub of the lower rotor at advance ratio* $\mu = 0.12$*. (Left: isometric view. Right: top view.)* . . . 179

5.25 *Loading noise BVISPL in decibels for various stiffnesses of coaxial rotor system on a hemispherical surface of radius* $2R$ *centred on the hub of the lower rotor at advance ratio* $\mu = 0.24$*. (Left: isometric view. Right: top view.)* 180

5.26 *Comparison of maximum OASPL and BVISPL of total noise and those from loading noise in decibels on a hemispherical observer surface of radius $2R$, centred on the rotor hub for various stiffnesses.* 181

6.1 *Sikorsky's X2 technology demonstrator. (Images courtesy of Ashish Bagai, Sikorsky Aircraft Corporation.)* 185

6.2 *Generic thrust-compounded hingeless coaxial configuration.* 187

6.3 *Partition of the propulsive force between the main rotor and propulsor as a function of forward speed.* 192

6.4 *Partition between the main rotor and propulsor of the power required by the vehicle as a function of forward speed.* 193

6.5 *Partition between the main rotor, propulsor and tailplane of the pitching moment required to trim the vehicle as a function of forward speed.* 194

6.6 *Visualisation of the wake structure of the full configuration in steady forward flight at various advance ratios. Wakes from the different elements of the configuration coloured in separate shades of grey. (Left: top view. Right: bottom view.)* 195

6.7 *Trajectories of the tip vortices of the main rotors and propulsor. (Each plot is a composite showing the points of intersection of individual vortices with the longitudinal plane through the fuselage centreline at various times during a single main rotor revolution.)* 196

6.8 *Visualisation of the wake structure of the configuration, showing the distortion of the tip vortices around the fuselage and tailplane at advance ratio $\mu = 0.05$.* 197

6.9 *Visualisation of the wake structure of the configuration: view from above at advance ratio $\mu = 0.05$ showing the incipient formation of supervortices in the wake of the main rotor and the interaction-induced skewing of the propulsor wake.* 198

6.10 *Visualisation of the wake structure of the configuration, showing the distortion of the flow around the tail at advance ratio $\mu = 0.10$. (Propulsor wake not visualised for clarity.)* 199

6.11 *Visualisation of the wake structure of the configuration, showing the distortion of the flow around the tail at advance ratio* $\mu = 0.15$. *View from below the port side of the aircraft. (Propulsor wake not visualised for clarity.)* 200

6.12 *Visualisation of the wake structure of the configuration, showing the close passage of the root vortex from the lower rotor over the empennage at advance ratio* $\mu = 0.30$. *(Propulsor wake not visualised for clarity.)* . . . 201

6.13 *Inflow distribution over the main rotor discs, showing the strong interaction between the upper and lower rotors at all forward speeds. (Left: upper rotor. Right: lower rotor.)* 203

6.14 *Temporal variation in the thrust produced and power consumed by the coaxial system over one revolution.* 204

6.15 *Temporal variation in the thrust produced and power consumed by the upper and lower rotors of the coaxial system over one revolution at advance ratio* $\mu = 0.15$. 205

6.16 *Distribution of blade loading and power consumption over the upper and lower rotors of the coaxial system at advance ratio* $\mu = 0.15$. *(Left: upper rotor. Right: lower rotor.)* 206

6.17 *Temporal variation in propulsor thrust and power over one main rotor revolution.* 207

6.18 *Distribution of the blade loading coefficient over the propulsor disc, as seen from behind the helicopter. (Left: mean loading. Right: RMS fluctuation in loading.) Note that different scales are used in each plot.* . . . 208

6.19 *Time-dependent pressure signals on the upper surface of the tailplane at advance ratio* $\mu = 0.10$. *(Mean removed.)* 211

6.20 *Time-dependent pressure signals on the upper surface of the tailplane at advance ratio* $\mu = 0.15$. *(Mean removed.)* 211

6.21 *Time-dependent pressure signals on the upper surface of the tailplane at advance ratio* $\mu = 0.30$. *(Mean removed.)* 212

6.22 *Visualisation of the wake structure of the full configuration in steady forward flight at advance ratio* $\mu = 0.15$. *(Wakes from the different elements of the configuration coloured in separate shades of grey.)* 214

6.23 *Schematic summarising the various aerodynamic interactions between the various components of the simulated configuration. (Interactions represented by arrows.)* 216
6.24 *Distribution of inflow, $-v_i/R_c\Omega_c$, over the main rotor discs, showing the strong interaction between the upper and lower rotors at advance ratio $\mu = 0.15$. (Left: upper rotor. Right: lower rotor.)* 217
6.25 *Trajectories of the tip vortices of the main rotors and propulsor at advance ratio $\mu = 0.15$ showing the points of intersection of individual vortices with the longitudinal plane through the fuselage centreline at various times during a single main rotor revolution.* 218
6.26 *Distribution of blade loading over the main rotor discs at advance ratio $\mu = 0.15$. (Left: upper rotor. Right: lower rotor.)* 219
6.27 *Distribution of power coefficient over the main rotor discs at advance ratio $\mu = 0.15$. (Left: upper rotor. Right: lower rotor.)* 220
6.28 *Temporal variation in the thrust produced by the upper and lower rotors of the coaxial system over one revolution at advance ratio $\mu = 0.15$.* 221
6.29 *Temporal variation in the power consumed by the upper and lower rotors of the coaxial system over one revolution at advance ratio $\mu = 0.15$.* 221
6.30 *Comparison of the thrust generated, and power consumed, by the propulsor when operated in isolation and when operated as part of the helicopter configuration at advance ratio $\mu = 0.15$.* 222
6.31 *Comparison of propulsor wake geometry, when operated in isolation and when operated as part of the helicopter configuration at advance ratio $\mu = 0.15$, visualised as contours of vorticity magnitude on a vertical plane through the centreline of the fuselage.* 223
6.32 *Distribution of blade loading coefficient over the propulsor disc, as seen from behind the helicopter at advance ratio $\mu = 0.15$. (Left: mean loading. Right: RMS fluctuation in loading.) Note that different scales are used for the mean and RMS loading.* 224
6.33 *Temporal variation in the thrust produced and power consumed by the propulsor over one main rotor revolution at advance ratio $\mu = 0.15$.* 225

6.34 *Pressure variation along the top centreline of the fuselage at advance ratio* $\mu = 0.15$. *(Mean signal represented by curves, root-mean-square amplitude of fluctuating signal represented by error bars.)* 226

6.35 *Pressure distribution along the top centreline of the fuselage as a function of time (main rotor azimuth) at advance ratio* $\mu = 0.15$. *Mean component of signal removed.* 227

6.36 *Overall sound pressure level (in decibels) produced by the main rotor and propulsor on a plane parallel to the ground, one rotor radius below the hub of the lower main rotor at advance ratio* $\mu = 0.15$. *(Rotor positions marked by dashed lines.)* 229

6.37 *Overall sound pressure level (in decibels) produced by the propulsor on a plane parallel to the ground, one rotor radius below the hub of the lower main rotor when operated in isolation at advance ratio* $\mu = 0.15$. *(Rotor positions marked by dashed lines.)* 230

6.38 *Contribution from the propulsor to the sound pressure level (in decibels) produced by the full helicopter configuration on a plane parallel to the ground, one rotor radius below the hub of the lower main rotor at advance ratio* $\mu = 0.15$. *(Rotor positions marked by dashed lines.)* 231

6.39 *Contribution from the main rotor to the sound pressure level (in decibels) produced by the helicopter configuration on a plane parallel to the ground, one rotor radius below the hub of the lower main rotor at advance ratio* $\mu = 0.15$. *(Rotor positions marked by dashed lines.)* 232

6.40 *Contribution from the main rotor to the sound pressure level (in decibels) in the BVI frequency range produced by the helicopter configuration on a plane parallel to the ground, one rotor radius below the hub of the lower main rotor at advance ratio* $\mu = 0.15$. *(Rotor positions marked by dashed lines.)* 233

6.41 *Time-history of acoustic pressure at the locations of maximum sound pressure level, marked 'T' in Figure 6.36.* 234

List of Tables

3.1 *Summary of rotor properties* 65

4.1 *Summary of cyclic control strategies (L: linked to other rotor; O: trimmed to net moments; X: held fixed; I: trimmed to individual rotor moments.)* 117

5.1 *Summary of rotor dimensions* 154

6.1 *Main rotor and propulsor geometries* 188

6.2 *Fuselage geometry* 189

6.3 *Simulated flight conditions and corresponding trim targets* 191

Nomenclature

Helicopter System

A	rotor disc area, πR^2
c	blade chord
C_D	sectional profile drag, scaled by $\frac{1}{2}\rho(R\Omega)^2 c$
	or fuselage drag, scaled by $\rho A(R\Omega)^2$
C_L	sectional lift, scaled by $\frac{1}{2}\rho(R\Omega)^2 c$
C_M	sectional moment, scaled by $\frac{1}{2}\rho(R\Omega)^2 c^2$
	or rotor moment, scaled by $\rho A(R\Omega)^2 R$
C_F	rotor force, scaled by $\rho A(R\Omega)^2$
C_P	rotor power, scaled by $\rho A(R\Omega)^2 R$
C_T	rotor thrust, scaled by $\rho A(R\Omega)^2$
C_W	helicopter weight, scaled by $\rho A(R\Omega)^2$
C_X	propulsor force, scaled by $\rho A(R\Omega)^2$
FM	figure of merit, $C_T^{3/2}/(\sqrt{2}C_Q)$
h_z	tip separation between upper and lower rotors
I_β	(flapwise) blade moment of inertia
K	drag model coefficients
K_β	flap spring stiffness
M	Mach number
N, N_b	number of blades on rotor
n	load factor
R	rotor radius
r	radial position, scaled by R

Re	Reynolds number
u	local velocity
v_i	induced velocity
z	rotor axial coordinate
α	aerofoil incidence
α_s	rotor shaft tilt
Γ	circulation
γ	rotor bank angle / lateral shaft inclination
	or blade Lock number
θ	blade pitch angle
θ_0	collective pitch
θ_{1s}	longitudinal cyclic pitch
θ_{1c}	lateral cyclic pitch
μ	rotor advance ratio (rotor speed, scaled by $R\Omega$)
ν	relative natural flap frequency
σ	rotor solidity, blade area divided by rotor disc area
Ω	rotor rotational speed
ψ	azimuthal location, zero at rear of disc, positive anticlockwise
	or wake age

Subscripts/superscripts

c	coaxial system
i	induced component
l	lower rotor of coaxial system
p	profile component
t	propulsor
u	upper rotor of coaxial system
x, y, z	orthogonal components

Fluid Dynamic Model

F	intercell vorticity flux
N	number of grid cells
p	pressure in the flow
S	vorticity source
TV	total variation
m	number of sub-divided time steps
t	time
u	flow velocity
u_b	flow velocity relative to blade
V	cell volume
W	weighting function
Δt	time step
Δx	cell width
ρ	flow density
ν	kinematic viscosity of the flow
	or Courant number
ω	vorticity
ω_b	bound vorticity
ζ	limiting function

Fast Multipole Method

a_k	k^{th} Taylor coefficient of K_δ
K	Biot-Savart kernel
K_δ	regularised Biot-Savart Kernel
m_k	k^{th} moment of vorticity
δ	kernel smoothing parameter

Structural Dynamics

D	dissipation
$\mathcal{L}$	Lagrangian of the system
Q	non-conservative force
q	generalised coordinates
T	kinetic energy
U	potential energy
W	work

Control Algorithm

c	trim switch parameter
F	vector of overall forces and moments
F^*	vector of target forces and moments
$\overline{F}$	time average of the forces and moments
K	trim coupling matrix
k	trim constant
θ	array of control inputs

Acoustic Model

a_0	speed of sound
F	force vector
p'	acoustic pressure
p_L	acoustic pressure due to loading
r	observer distance from source
t	observer time
τ	acoustic source time

Fuselage Model

A	matrix of influence coefficients
C_D	fuselage drag coefficient
l	fuselage half-length
$\mathbf{n}$	unit vector normal to panel
N	number of fuselage panels
U_∞	freestream velocity
w	wake-induced velocity
Γ	matrix of vortex loop strengths
ϕ	velocity potential

Mathematical Notation

$a \cdot b$	scalar product of a and b
$a \times b$	vector product of a and b
$A \in B$	member A of B

Abbreviations

ABC	Advancing Blade Concept
BVI	blade vortex interaction
BVISPL	blade vortex interaction SPL (mid frequency 5–40/rev) (dB)
CFD	Computational Fluid Dynamics
CFL	Courant-Friedrichs-Lewy
FMM	Fast Multipole Method
OASPL	overall SPL (dB)
RMS	root mean square
SPL	sound pressure level (dB)
TVD	Total Variation Diminishing
VTM	Vorticity Transport Model
WAF	Weighted Average Flux

Chapter 1

Introduction

A recent resurgence of interest in the coaxial rotor configuration has been prompted by its potential to meet modern requirements for helicopters with increased speed and load carrying capabilities. The obvious advantage of a coaxial rotor over a conventional main rotor – tail rotor configuration is the elimination of the need for a tail rotor as the required torque balance is achieved inherently within the contra-rotating main rotor system. This appealing advantage of contra-rotating twin coaxial rotors prompted some of the early rotorcraft pioneers, including Igor Sikorsky, to attempt to exploit the configuration, yet the single main rotor – tail rotor configuration remains the prevailing platform for most military and civil helicopters of today.

There has been significant research interest in the characteristics of coaxial rotor aerodynamics in several countries including Russia, the US, the UK and Japan [1]. As a matter of fact, Russia remains the only country to mass produce coaxial helicopters to date. A series of coaxial helicopters produced by the Kamov company has been used mostly by the Russian Navy* as their compact airframe (since a large tail boom to accommodate a tail rotor is not required) is well suited for shipboard operations. The lack of a tail rotor has an added advantage as all the available power can be used to produce useful lift while maintaining a torque balance. Coaxial helicopters thus typically have high thrust-to-weight ratios and are often used for heavy-lift applications.

Kamov company's Ka-27 [2] is one such example. The Ka-27 was developed for the purpose of ferrying and anti-submarine warfare. Later variants were used in various

*The Kamov company, when first formed in 1945, was a naval design bureau.

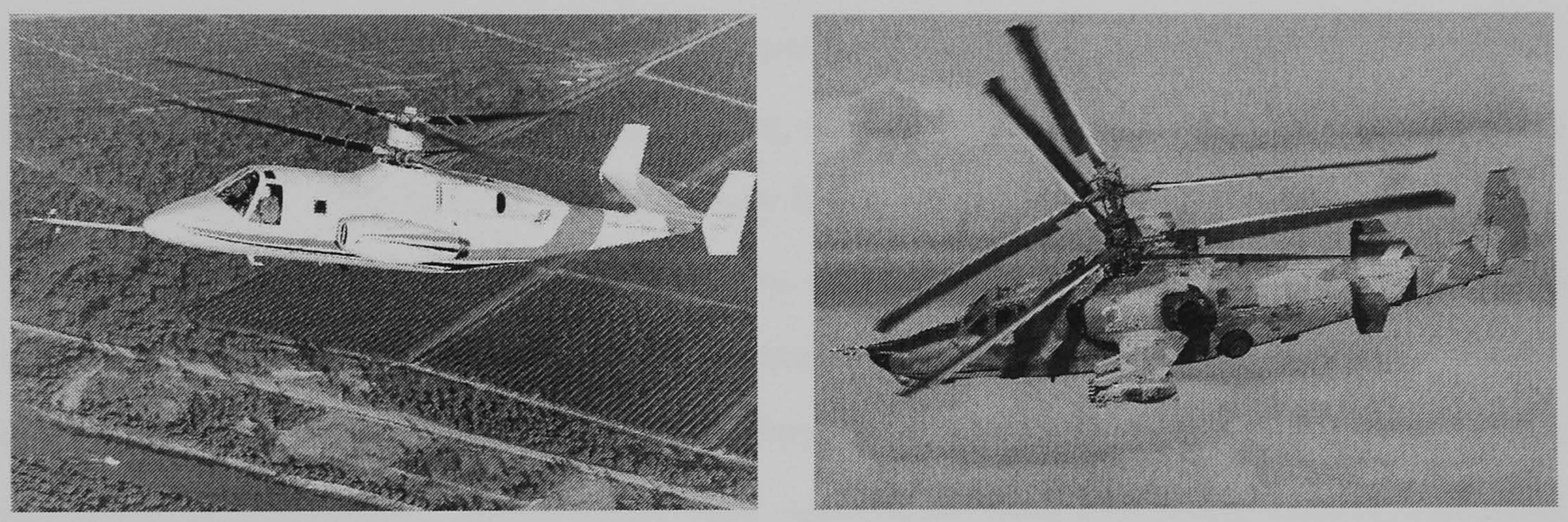
other types of missions ranging from search and rescue, assault transport, to surface surveillance. The civil version, designated Ka-32, also took advantage of its heavy-lift capability as a fire fighting helicopter, civil transport, and also as a flying crane (see Figure 1.1).



Figure 1.1: *Kamov Ka-32 coaxial rotor helicopter. The tip vortices from the rotor blades are visualised by natural condensation. (Courtesy of Dany Gaulé and Airliners.net.)*

Proponents of coaxial rotor helicopters have claimed that higher levels of manoeuvrability can be achieved than with conventional systems because of several practical engineering advantages of the coaxial configuration. For instance, the increased control moments because of the length of the rotor mast that is required for adequate rotor separation, and the low moments of inertia of the compact airframe result in greater control authority than with conventional systems [3]. To accommodate the ability to control a coaxial rotor system with a sufficient number of degrees of freedom requires a complex arrangement of control linkages and swashplates between the hubs of the two contra-rotating rotors. Coaxial rotor systems are thus mechanically more complex

than single rotor systems. Because the hubs of almost all coaxial systems are conventionally articulated, under the conditions where large flapping is induced, for instance in high speed forward flight or in manoeuvre, there is a possibility of collision between the blades of the upper and lower rotors. While it is tempting to increase the separation distance between the hubs of the upper and lower rotors to avoid blade collision, the increased drag of the elongated rotor mast is a distinctly undesirable penalty in forward flight. In hover, or in low speed flight, the inherent symmetry of the coaxial configuration makes it more stable than the single rotor configuration with a tail rotor. For this reason, coaxial configurations are becoming increasingly popular as a passively stable platform for modern, indoor flying toys [4]. Anikin [3] describes some of the aerodynamic advantages and disadvantages of a coaxial rotor in more detail.



(a) Sikorsky XH-59A (or S-69) Advancing Blade Concept (Courtesy of Johan Visschedijk, 1000aircraftphotos.com.)

(b) Kamov Ka-50 "Black Shark" (or Hokum A) attack helicopter (Copyright by Sergey Riabsev, Airliners.net.)

Figure 1.2: *Examples of modern coaxial rotor helicopters. (Courtesy of 1000aircraftphotos.com and Airliners.net.)*

Some highly innovative designs, such as Sikorsky Aircraft Corporation's XH-59A (also known as the S-69) Advancing Blade Concept and Kamov company's Ka-50 light attack helicopter, have attempted to exploit the coaxial configuration to obtain improved performance in parts of the flight envelope (see Figure 1.2). It is worth bearing in mind, though, that the forward flight performance of conventionally articulated coaxial rotors, such as that of the Ka-50, is limited by the same physical effects, such as retreating blade stall and compressibility effects on the tip of the advancing blade, that

are associated with a single main rotor configuration. The philosophy behind the Advancing Blade Concept (ABC) used in the XH-59A is to use rigid, or highly stiffened, rotors to allow the advancing blades of the upper and lower rotors to exploit the high dynamic pressure arising from the increased relative speed of the oncoming flow [5]. The advancing blades are thus able to generate significantly higher lift than those of a traditional single rotor and the resulting lateral imbalance in loading is compensated by the other rotor of the coaxial system. The XH-59A never entered production because of its several shortcomings in its performance although the ABC-type [6], rigid coaxial concept is being revisited by Sikorsky in the form of their thrust-compounded X2 technology demonstrator [7].

In those practical coaxial configurations where the performance fell short of expectations, the shortcomings in the practical implementation of the coaxial concept could be traced back, in many cases, to deficiencies in modelling or understanding the specific details of the interaction between the rotors, and the effect of the wake on the behaviour of the system — especially under unsteady flight conditions.

Modelling of the rotor aerodynamics in the light of predicting the performance of helicopter systems has been of great interest to the rotorcraft community. Indeed, the key to understanding the overall performance of a helicopter is in understanding the rotor aerodynamics, particularly that associated with the many interactions that occur within the system. A large body of previous research, summarised by Coleman [1], reviews the current body of work on the performance and wake characteristics of coaxial rotors by eminent authors such as Saito and Azuma [8], Andrew [9], Zimmer [10], Harrington [11], and Dingeldein [12]. More recently, Leishman has developed expressions for the figure of merit (FM) of coaxial rotors using momentum theory for an ideal coaxial rotor [13]. Metric quantities such as the figure of merit provide a comparison of the hovering efficiency relative to the ideal performance but care is required to ensure equal effective disc loading to yield an unbiased comparison. However, a common deficit in simple methods of performance analysis is their inability to capture, to the required level of fidelity, the detailed aerodynamic interactions that occur between the upper and lower rotors of the coaxial configuration. In recent years, though, computational tools have developed to the extent where the highly interactive and non-linear wake flows generated by the two rotors of the coaxial configuration can be modelled with a much

greater degree of confidence than has been possible in the past [14, 15].

Computational Fluid Dynamic (CFD) models solve numerically the discretised governing equations of fluid flow and perhaps offer the most rigorous approach to analysing the fluid mechanics of rotor-related flows since the underlying physics are encapsulated within the governing equations themselves. The limitations of any numerical scheme, however, must be evaluated carefully in order to select an appropriate technique before a given problem is investigated. In the helicopter context, the strong helicoidal vortices generated by the rotor blades persist within the flow and significantly influence the aerodynamics of the entire system. Of course, for coaxial rotors, this feature is exacerbated since the two individual rotors interact closely and produce even more complex vortical pattern in the wake of the system than for a conventional single rotor system. The accuracy of any numerical scheme is highly dependent on the resolution of these vortical structures. Conventional CFD schemes that solve the Navier-Stokes equations in terms of the primitive variables, i.e. pressure and velocity, are at a distinct disadvantage as the numerical diffusion of vorticity generally leads to premature dissipation of these vortical structures. This issue can be addressed, to an extent, by increasing the grid density to minimise the effects of numerical dissipation but the computation then runs the risk of becoming prohibitively expensive. While reduced-order models such as the free wake method offer greatly improved computational efficiency, such models are unable to resolve the subtle features of the vortical wake and thus their consequences of subtle changes in the wake, for instance those induced by small changes in the geometry of the system, on the performance of the rotor system.

Alternative methods based on the solution of the Navier-Stokes equations in vorticity-velocity form, such as Brown's Vorticity Transport Model (VTM), are capable of preserving the vortical structures in the wake of a rotor for very long times and are thus well suited to the modelling of the interactions between the vortices generated by the sub-components of a helicopter system and the sub-components themselves. In future, hybrid methods that utilise the primitive variable Navier-Stokes approach for modelling the aerodynamics of lifting solid surfaces, such as the rotor blades, and a wake model based on the vorticity transport approach may offer the greatest benefits to the rotorcraft community because of their potential to combine the advantages of both approaches [16, 17].

This dissertation will show how a high-resolution wake capturing technique can be used to model effectively the highly interactive aerodynamic environment of coaxial rotors, allowing a better understanding of their inherent aerodynamic characteristics than has been possible up to now.

1.1 Synopsis

The structure of the thesis is arranged as follows. Chapter 2 presents a comprehensive description of the theory of rotorcraft aerodynamics and its numerical implementation within a computational methodology, known as the Vorticity Transport Model (VTM), that will be used throughout the remainder of the dissertation.

In Chapter 3, the aerodynamics of a conventionally hinged coaxial rotor is discussed in terms of its performance, wake geometry and rotor loading. The discussion highlights some of the deficiencies in the method of comparison between coaxial and single rotor systems that has been adopted in the open literature and addresses this deficiency by constructing an aerodynamic equivalence between the coaxial and single rotor systems in order to compare their performance. A comparison of the performance of the two types of rotor system is carried out in hover, in steady forward flight, and in a level turn.

In Chapter 4, the effects of flapwise stiffness on the performance of the coaxial system are investigated. The stiffness is modelled using springs of varying strength, applied across the flapping hinges of the rotors. A unique feature of the coaxial configuration is that significant flapwise stiffness can be introduced while still maintaining an overall balance in the roll moment of the system in forward flight. The effects of rotor stiffness on the performance of the system, in terms of the power consumed by the rotor, are discussed in terms of the distribution of loads on the rotors and the resultant geometry of the wake.

In Chapter 5, the aeroacoustic characteristics of coaxial rotors are examined. Firstly, the acoustic characteristics of a conventionally articulated coaxial rotor is compared to those of an equivalent single rotor both in terms of near- and far-field radiation of noise. Secondly, the effects of flapwise stiffness on the acoustic signature of coaxial rotors is investigated. In particular, the mechanisms of radiation of noise from the blades of the

lower rotor as a result of their interaction with the wake produced by the blades of the upper rotor, are discussed in detail.

In Chapter 6, an analysis of the interactional aerodynamics associated with a full, but generic, compounded coaxial helicopter is presented. The configuration that is studied in this chapter features a coaxial main rotor system, augmented in thrust by an auxiliary propulsive device, with a fuselage that features a large horizontal tailplane. The configuration does not represent a particular aircraft but has been chosen based on current interest in platforms with this configuration as a potential solution to meet modern requirements for increased performance. The aerodynamic interactions between the sub-components of the proposed aircraft, at various forward flight speeds, are discussed in detail. The aerodynamics of the full configuration is then compared, at one forward flight speed, to various combinations of its sub-components in order to reveal the origins of the aerodynamic interactions within the system.

Finally, in Chapter 7 the dissertation concludes with a summary of the all the chapters and some suggestions for future work.

1.2 Publications

Several components of this dissertation have been published during the course of the research.

In May 2006, a paper contrasting the performance of coaxial and conventional single rotors was presented at the 62nd Annual Forum of the American Helicopter Society in Phoenix, Arizona [18]. This work was then extended and two further papers on the subject have been accepted for publication in the Journal of the American Helicopter Society [19, 20]. The first paper [19] describes the basis on which a fair comparison of performance can be made when considering coaxial and conventional single rotor systems. The second paper [20] uses the approach developed in the first paper to compare the performance of a coaxial rotor to that of an aerodynamically equivalent single rotor system. The differences between the computed wake structures and the resultant changes in the loading distributions on the rotor discs are used to explain some of the differences in the performance of the two systems.

An acoustic comparison of coaxial and equivalent single rotor systems was presented

in a paper at the 64th Annual Forum of the American Helicopter Society in Montréal, Canada [21]. Both the near-field and far-field characteristics of the radiated noise from the two types of rotors were considered and the principal sources of blade vortex interaction noise were identified.

In October 2007, the effects of flapwise stiffness on the performance of the coaxial rotor were discussed in a paper presented at the International Forum on Rotorcraft Multidisciplinary Technology, organised jointly by the American Helicopter Society and the Korean Society for Aeronautical and Space Sciences, held in Seoul, Korea [22]. Reductions in the power required by the stiffened coaxial systems were related to a redistribution in the rotor loading due to the introduction of rotor stiffness. This paper was awarded a Korean Aerospace Industries (Ltd.) Aerospace Paper Award at the Seoul Airshow in 2007.

Elements from Chapter 6 were presented at two conferences. In January 2008, a paper was presented at the American Helicopter Society Aeromechanics Specialists' Meeting held in San Francisco, California, where some of the interactional aerodynamics associated with a generic, thrust-compounded coaxial helicopter over a range of flight speeds was identified [23]. A detailed study of the origins of these interactions was presented for one particular flight speed in another paper at the 9th International Powered Lift Conference in London [24]. This paper was recognised as the Best Paper in Conference and has recently been accepted for publication in the Aeronautical Journal [25]. Preliminary results of this work were referred to by Professor J. Gordon Leishman in his latest book, *"The Helicopter — Thinking Forward, Looking Back"* [26], as an example of a modern computational analysis of the interactional aerodynamic problems of a full helicopter system.

Finally, in August 2008, a paper providing an overview of the research described within this thesis was presented at the EU-Korea Conference on Science and Technology in Heidelberg, Germany [27].

Chapter 2

Model Description

2.1 Introduction

The flow of air in the vicinity of a helicopter is highly unsteady even when the helicopter is subjected to an ostensibly steady flight condition. Due to the highly interactive nature of the vorticity produced by a system of rotor blades, when generating the required forces to attain a given flight condition, the resulting flow field is extremely complex. In turn, the performance of the rotor system is strongly influenced by the interaction between the rotor itself and the surrounding flow field. In the case of a coaxial rotor, the degree of complexity of the interaction is escalated further by the presence of the second rotor which operates within close proximity to the other rotor. For this reason, accurate modelling of the temporal and spatial evolution of the vortical wake structures produced by the helicopter rotors is of the utmost importance in predicting the overall performance of the rotorcraft.

Existing theoretical approaches, such as momentum theory and blade element theory, with suitable empirical corrections that are relevant to the problem at hand, can provide an approximate performance calculation to a reasonable accuracy. However, the significance of unmodelled physics in such calculations cannot be discounted and any detailed investigation into the problem of helicopter aerodynamics and performance requires a more rigorous approach. Computational Fluid Dynamics (CFD) provides one such approach where the discretised flow field is described from first principles. However, the vast majority of existing CFD methods originate from the fixed wing community

and use primitive variables, i.e. pressure and velocity, to describe the flow. As a result, vorticity, which is the primary flow variable in the context of rotor wake modelling, is not explicitly conserved. Due to the numerical diffusion of vorticity associated with the primitive variable approach, preservation of the vortical structures in the rotor wake becomes a distinct problem.

An alternative approach to the conventional CFD methods described above is to re-cast the governing equations in terms of time-dependent fields of vorticity and velocity. This allows explicit conservation of vorticity in the flow and, thus, has the potential to preserve the vortical structures in the wake of the rotor. The ability to resolve vortical flows is indeed essential in order to accurately capture the evolution of the wake, and hence the performance of the rotor system. The computational results presented in this dissertation are simulated exclusively using such a technique and this chapter elaborates on the theoretical basis as well as the numerical implementation of such an approach.

2.2 Governing Equations

The Navier-Stokes equations that describe the flow of fluid can be derived by applying Newton's second law to a small element of moving fluid. In primitive variable form, the equations of motion of the fluid can be written as

$$\frac{\partial}{\partial t}u + u \cdot \nabla u = -\frac{1}{\rho}\nabla p + \nu \nabla^2 u \tag{2.1}$$

if it is assumed that the flow is incompressible so that, by continuity,

$$\nabla \cdot u = 0\,. \tag{2.2}$$

The assumption of incompressibility, in the context of helicopter aerodynamics, is reasonably well justified except at the tips of the rotating blades where, due to the increased relative speed in forward flight, the effects of compressibility can become significant. Nonetheless, as far as the evolution of the flow away from the immediate vicinity of the blades is concerned, the incompressibility assumption can be held valid as long as the effects of compressibility on the sectional aerodynamic properties of the rotor blades can be accounted for. A methodology for achieving this will be described later in Section 2.5.

By taking the curl of Equation 2.1, the Navier-Stokes equations can be re-formulated

into the vorticity-velocity form

$$\frac{\partial}{\partial t}\omega + u \cdot \nabla\omega - \omega \cdot \nabla u = \nu\nabla^2\omega\,. \tag{2.3}$$

Equation 2.3 is known as the vorticity transport equation. The vorticity, ω, defined as $\omega = \nabla \times u$, thus becomes an explicitly conserved variable that evolves under the influence of the velocity field, u. Retaining the assumption that the flow is incompressible everywhere except in the immediate vicinity of the blades, the velocity field in the region of the rotor wake is divergence-free and thus the velocity field is uniquely defined by the vorticity field. The relationship between the velocity and the vorticity is given by the Biot-Savart equation

$$\nabla^2 u = -\nabla \times \omega\,. \tag{2.4}$$

Because helicopters operate typically at high Reynolds numbers, it may be assumed that the flow within the wake of the rotor is inviscid. The effects of viscous forces are thus assumed to be limited to within the boundary layers of solid surfaces. The viscous term on the right hand side of Equation 2.3 therefore becomes zero everywhere except in the boundary layer region, which may be assumed to be thin for high Reynolds number flows. Since the generation of vorticity from lifting components such as the rotor blades and the fuselage under the action of viscosity must be accounted for, the viscous term in Equation 2.3 may be replaced with a source term, S, to represent local sources of vorticity within the boundary layer of solid surfaces. The vorticity transport equation can therefore be simplified as

$$\frac{\partial}{\partial t}\omega + u \cdot \nabla\omega - \omega \cdot \nabla u = S\,. \tag{2.5}$$

2.3 Vorticity Transport Model

The Vorticity Transport Model (VTM), developed by Brown [28] and extended by Brown and Line [29], is a comprehensive code for simulating the aeromechanics of rotorcraft. The VTM is based on a finite volume, time-dependent computational solution of the Navier-Stokes equations written in vorticity-velocity form (the vorticity transport equation, Equation 2.3) on a Cartesian adaptive grid that encloses the rotorcraft. The particular formulation of the VTM presents a number of advantages over conventional primitive variable CFD methods.

Firstly, the problem of vorticity preservation that is associated with numerical diffusion is addressed by allowing vorticity to be an explicitly conserved flow variable using the vorticity-velocity formulation. A Total Variable Diminishing (TVD) scheme, employed to advect numerically the vorticity distribution, is particularly effective in preventing spatial smearing of the vorticity due to numerical diffusion. Thus, the compact vortical structures in the wake remain intact for many rotor revolutions. The long-range aerodynamic interactions that are produced by wake effects, therefore, generally tend to be well represented using such an approach.

Secondly, an adaptive grid system can be used by the method to follow the evolution of the wake. This can be done by generating computational cells where vorticity is present and destroying the cells once the vorticity moves elsewhere. The computational domain is thus effectively boundary-free, and significant memory savings are achieved using this procedure. In the VTM, computational efficiency is enhanced further by using a series of nested computational grids to capture the wake. The cells within the outer grids are arranged to be coarser than those closer to the rotor. This helps to reduce the overall cell count during a computation whilst still maintaining a highly resolved flow field near the rotor.

The model is thus suitable for solving a wide range of rotorcraft related problems and, indeed, the VTM has been used previously to investigate many such problems. The applications of the VTM include the derivation of linearised models for flight mechanics [30], the study of the fluid mechanics of the vortex ring state [31, 32], rotorcraft encounters with aircraft wakes [33, 34], and the influence of ground effect on rotor performance [35, 36]. All results presented in this dissertation are produced using the VTM unless otherwise stated.

2.4 Numerical Implementation

In this section, the numerical techniques implemented within the VTM to solve the discretised governing equations (presented in Section 2.2) and to evolve the solution in time are discussed in detail.

2.4.1 Discretisation of the Governing Equations

The governing equations introduced in Equation 2.3 are solved in an Eulerian frame of reference on a structured grid that is discretised into a number of cubic computational cells (for further details, see Section 2.4.2). The vorticity field obtained by Equation 2.3 is evolved through time in discrete time steps of duration Δt such that the time $t = n\Delta t$ at the n^{th} step where $n \in \mathbb{N}$.

Defining q as any flow variable, the operators

$$[q]^n = \int_V q(x, n\Delta t)\ dV \tag{2.6}$$

and

$$[q]^n_{\Delta t} = \int_n^{n+1} [q]^n\ dt \tag{2.7}$$

denote the spatial and temporal integration of $q(x,t)$ over the cell volume, V, and the duration of a time step, Δt, respectively. Using these integration operators, the vorticity transport equation (Equation 2.3) can be written in discrete form as

$$[\omega]^{n+1} - [\omega]^n = [\omega \cdot \nabla u]^n_{\Delta t} - [u \cdot \nabla \omega]^n_{\Delta t} + [\nu \nabla^2 u]^n_{\Delta t} + [S]^n_{\Delta t}\,. \tag{2.8}$$

Each operator can be approximated in terms of the local flow variables, vorticity and velocity, and the solution is then evolved through time. The numerical methods that are used to approximate all the operators are explicit in time with the exception of the vorticity source.

At the beginning of each time step, the velocity field is evaluated from the vorticity in the domain. In other words, at the beginning of the n^{th} time step, $t = n\Delta t$, the velocity $u^n = u\left([\omega]^n\right)$ is calculated by inverting Equation 2.4. The vorticity field at time $t = (n+1)\Delta t$ is then constructed by evaluating the integration operators in Equation 2.8 sequentially using an operator splitting approach as follows:

$$\begin{aligned}
[\omega]^* &= [\omega]^n + [S]^n_{\Delta t} \\
[\omega]^{**} &= [\omega]^* + [\omega \cdot \nabla u]^n_{\Delta t} \\
[\omega]^{***} &= [\omega]^{**} - [u \cdot \nabla \omega]^n_{\Delta t} \\
[\omega]^{n+1} &= [\omega]^{***} + [\nu \nabla^2 u]^n_{\Delta t}
\end{aligned} \tag{2.9}$$

The source term operator, $[S]^n_{\Delta t}$, which accounts for the aerodynamics of rotor blades and lifting surfaces (if there are any) is described in detail in Section 2.5. The stretching

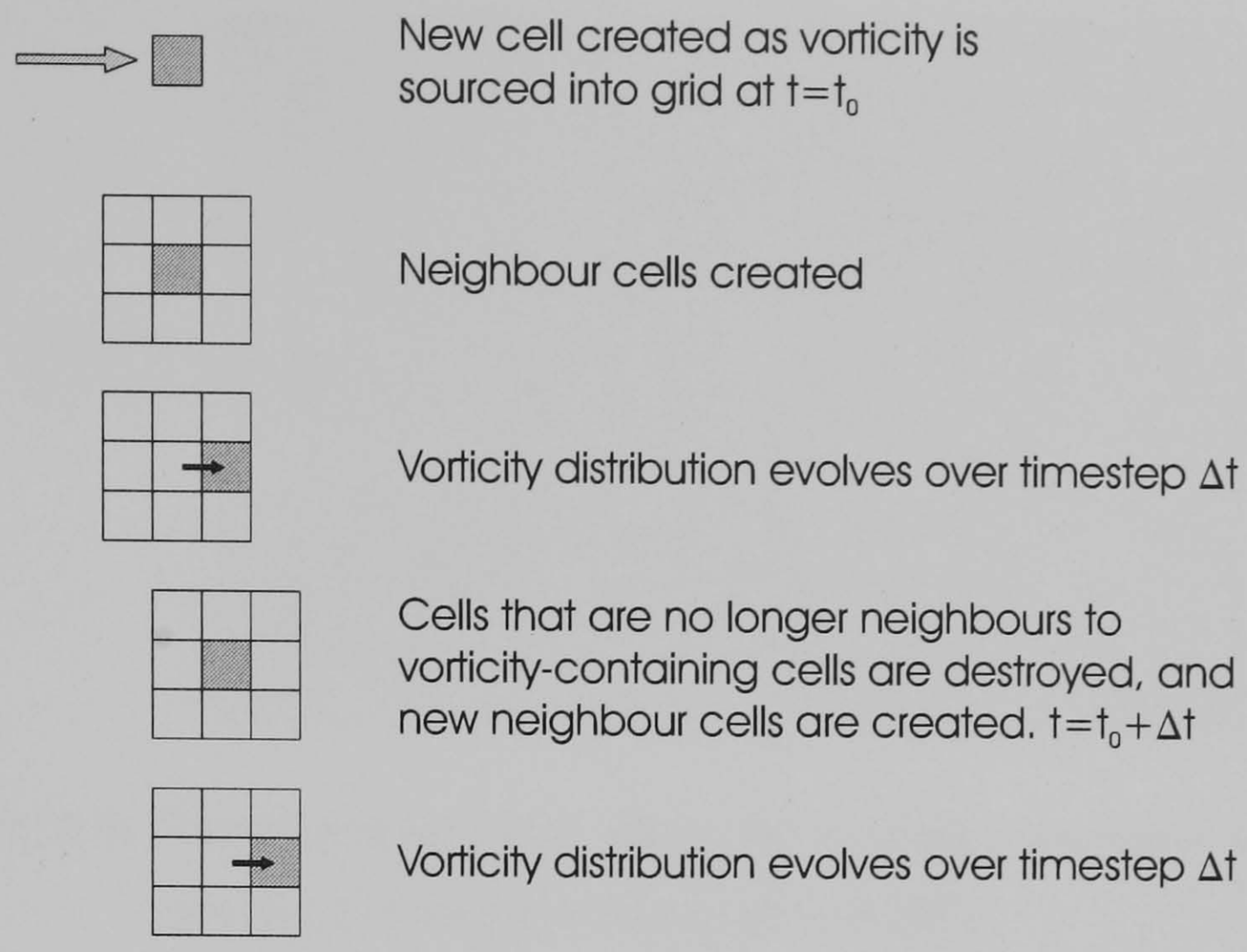


Figure 2.1: *Schematic illustration showing adaptive grid generation and destruction, tracking the regions where vorticity is present within the flow [29].*

operator, $[\omega \cdot \nabla u]^n_{\Delta t}$, is evaluated using Runge-Kutta integration while the advection operator, $[u \cdot \nabla \omega]^n_{\Delta t}$, is calculated using Toro's Weighted Average Flux (WAF) scheme [37]. The details of the WAF method are described in Section 2.4.4. The viscous diffusion operator, $[\nu \nabla^2 u]^n_{\Delta t}$, is neglected under the assumption stated in Section 2.1 and is included here for completeness only. The operator splitting approach has been shown to be second order accurate provided that each operator is approximated to at least second order accuracy [38].

2.4.2 Grid Structure

The VTM uses an adaptive grid system to follow the evolution of the vortical rotor wake. The three-dimensional computational domain is discretised in to a series of cubic cells founded on an underlying virtual Cartesian stencil or framework. Within the framework, the cells can be created or destroyed, as shown schematically in Figure 2.1, hence allowing a variable number of cells to track the evolution of vorticity in the flow in a semi-Lagrangian manner. In actual fact, the cells are fixed in space and hence the VTM is strictly an Eulerian solver. The nature of the adaptive grid system allows the entire flow-field around the helicopter to be captured without the need to truncate the

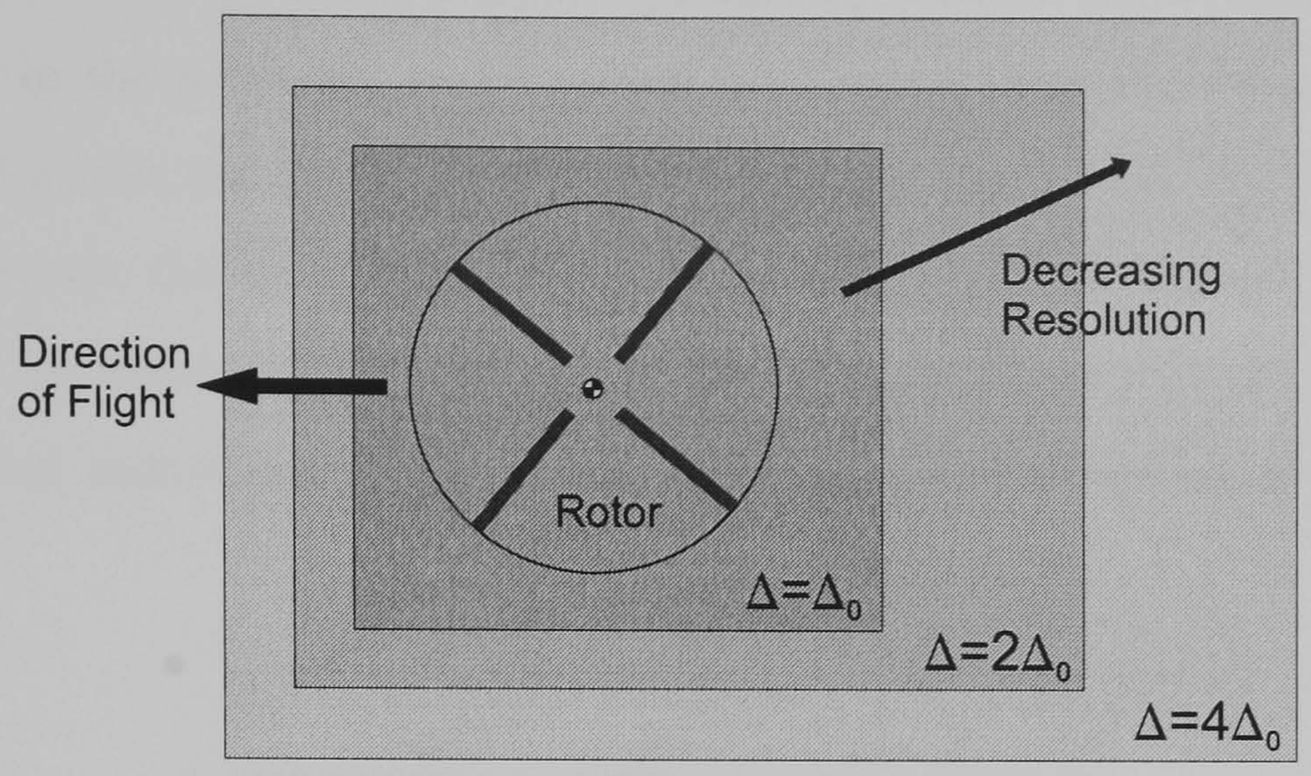


Figure 2.2: *Nested grid structure where the resolution decreases with increasing distance from the rotor hub [29].*

rotor wake arbitrarily and thus to impose an explicit far-field boundary condition on either the vorticity or the velocity. In fact, the spatial extent of the flow field that can be captured is largely governed by the computational memory that is available. Significant memory savings are achieved by using a series of nested grid levels within the stencil. These levels are arranged so that the cell sizes double from one grid level to the next as the distance from the rotor increases (see illustration in Figure 2.2). In this way, the overall cell count, and hence the memory requirement of any computation, is reduced significantly compared to if the fine grid structure was maintained throughout.

The nested grid structure offers an added advantage when evaluating the advection operator. In order to advance the solution of the explicitly discretised scheme in a stable fashion, the Courant-Friedrichs-Lewy (CFL) condition, in terms of the local velocity, u, and local grid resolution, Δx, should be satisfied such that

$$\left|\frac{u\Delta t}{\Delta x}\right| \leq 1\,. \tag{2.10}$$

As the length of the cells, Δx, doubles when moving from one nested grid level to the next, the flow in i^{th} grid level can be evolved at a time step of approximately $2^i\Delta t$ while maintaining a similar CFL condition provided that the rest of the flow conditions remain largely unchanged. The advantage of this arrangement is that the computational effort is focused on the highly resolved region in the finest grid level closest to the rotor.

Numerical implementation of the nested grid structure requires an effective procedure for advecting vorticity within the cells from one level of the hierarchy across to

the next. This is done by using a set of overlapping cells at the boundary of any two adjacent levels of the hierarchy (see Figure 2.3). The vorticity flux on the coarser grid is extrapolated across the overlapping region from that calculated within the finer grid region. In this way, the accuracy of the solution across different spatial and temporal resolutions can be maintained by conserving the vorticity flux across the boundary. The second-order and monotonic properties of the WAF scheme are also preserved in this way.

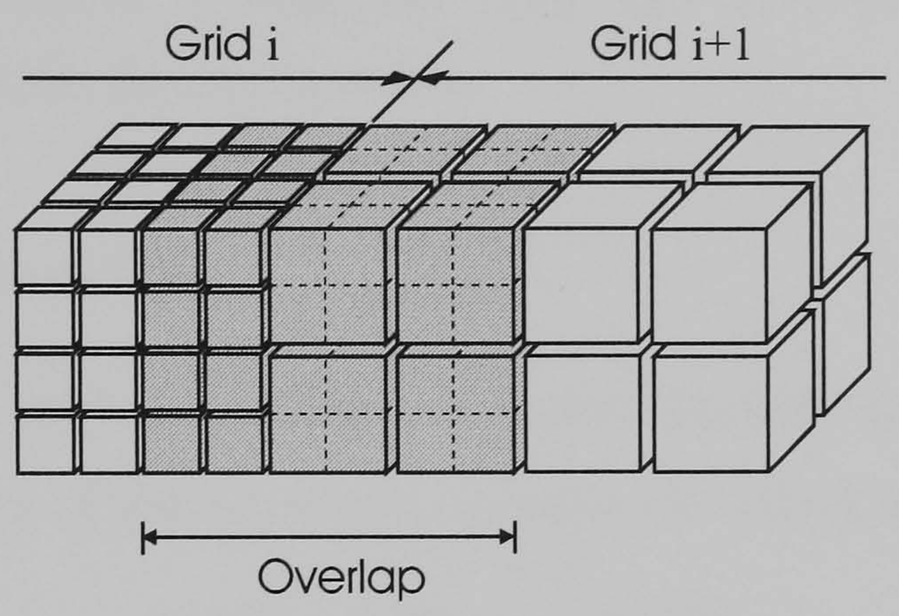


Figure 2.3: *Overlapping of the grid level boundaries provides both second order accuracy and monotonicity; shaded cells represent overlap region. Adapted from Brown and Line [29]*

2.4.3 Arrangement of Flow Variables

The WAF scheme that is used to evaluate the advection operator, presented in Equation 2.9, requires the velocity normal to each cell face in order to evaluate the inter-cell vorticity fluxes. The staggered arrangement of flow variables, introduced by Harlow and Welsh [39], is used to provide this information readily without the need to interpolate from the cell centres of the neighbouring cells as in the case of the collocated arrangement shown in Figure 2.4. In addition, the cell-centred approach is known to be prone to spurious oscillations in the velocity and vorticity fields arising from the error associated in the interpolation procedure. The staggered approach is also known to yield better performance as far as preserving the solenoidal property of the flow ($\nabla \cdot u$ and $\nabla \cdot \omega$) is concerned and hence offers improved accuracy over the cell-centred approach.

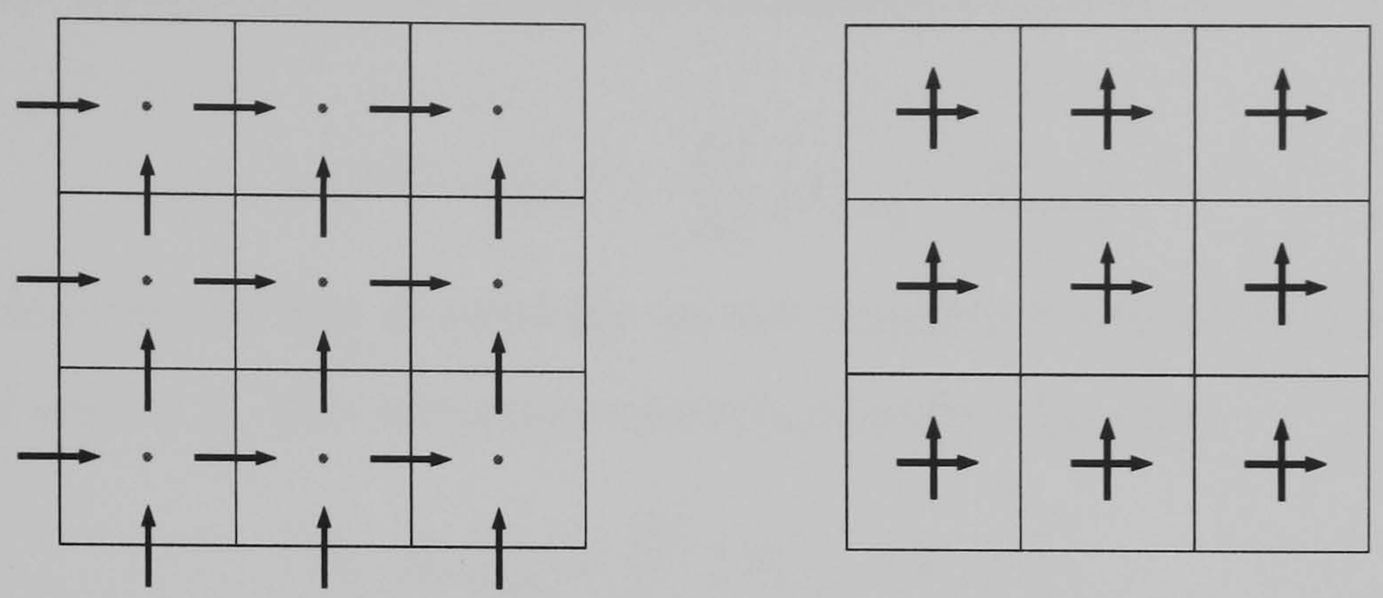


Figure 2.4: *Staggered arrangement (left) and cell-centred arrangement (right) for flow variables.*

2.4.4 Vorticity Advection

The vorticity contained within the flow is advected through the computational domain according to the solution of the advection operator described in Equation 2.9 as

$$[\omega]^{***} = [\omega]^{**} - [u \cdot \nabla\omega]^{n}_{\Delta t} \,. \tag{2.11}$$

The advection operator is evaluated using Toro's Weighted Average Flux (WAF) method. This method is based on the use of a second-order accurate, one-dimensional Riemann solver for hyperbolic conservation laws [37]. The ability of the WAF method to capture discontinuous solutions, such as shock waves in compressible gas dynamics [40], makes it ideally suited for resolving the steep vorticity gradients that occur within rotor wakes.

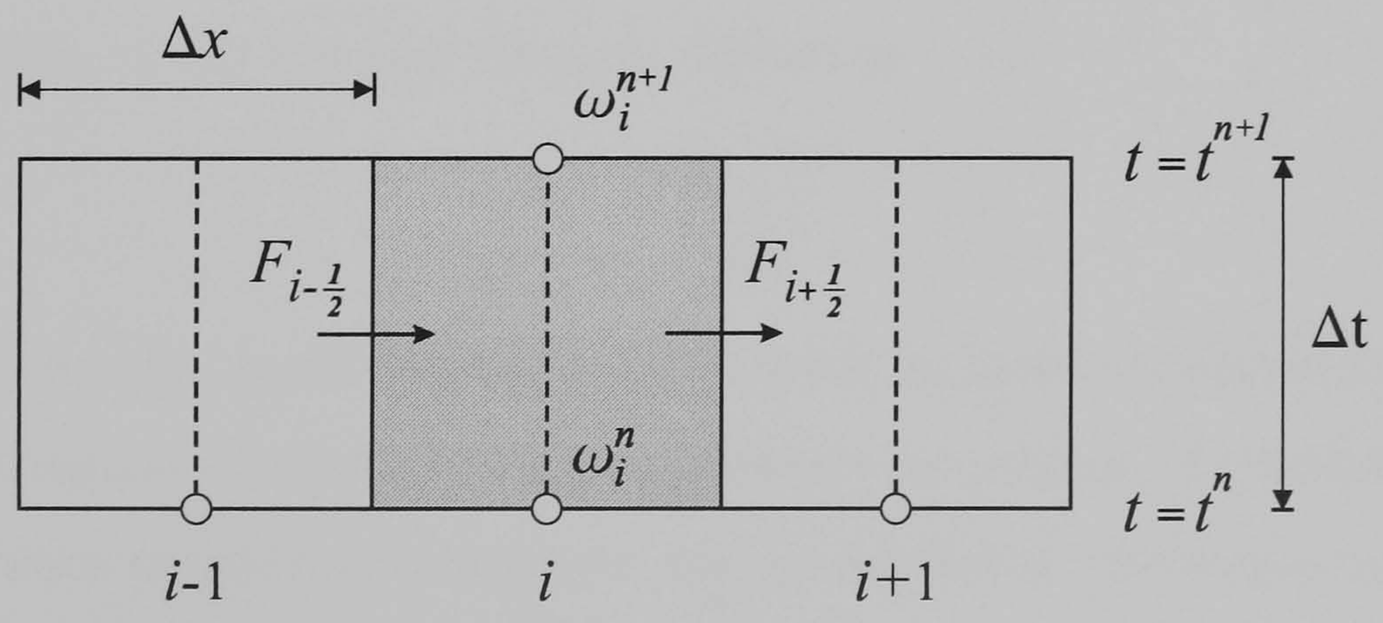


Figure 2.5: *Stencil for calculation of inter-cell fluxes of vorticity. Adapted from Toro [37]*

The three-dimensional advection operator in Equation 2.11 can be decomposed into three one-dimensional equations using the spatial-operator splitting technique proposed

by Strang [41]. Integrating each of the one-dimensional equations over the cell volume thus yields

$$[\omega_i]^{n+1} = [\omega_i]^n - \frac{\Delta t}{\Delta x}\left(F_{i+\frac{1}{2}} - F_{i-\frac{1}{2}}\right) \tag{2.12}$$

where $F_{i+\frac{1}{2}}$ denotes the flux of vorticity on the interface between the cells i and $i+1$ as shown in Figure 2.5. The advection operator therefore becomes

$$[u \cdot \nabla\omega]^n_{\Delta t} = \frac{\Delta t}{\Delta x}\left(F_{i+\frac{1}{2}} - F_{i-\frac{1}{2}}\right) . \tag{2.13}$$

The inter-cell fluxes are divided into two partial fluxes, each of which are assigned a weighting function such that

$$F_{i+\frac{1}{2}} = W_1 F^{(1)}_{i+\frac{1}{2}} + W_2 F^{(2)}_{i+\frac{1}{2}} \tag{2.14}$$

where the partial fluxes are given by

$$\begin{aligned} F^{(1)}_{i+\frac{1}{2}} &= u^n_{i+\frac{1}{2}}[\omega_i]^n \\ F^{(2)}_{i+\frac{1}{2}} &= u^n_{i+\frac{1}{2}}[\omega_{i+1}]^n \end{aligned}$$

The weighting functions that indicate the spatial extent of the wave front between x_i and x_{i+1} at time $t = t^n + \Delta t/2$, are

$$\begin{aligned} W_1 &= \frac{1}{2}(1+\nu) \\ W_2 &= \frac{1}{2}(1-\nu) \end{aligned}$$

where ν is the local cell Courant number, defined as

$$\nu = \frac{u^n_{i+\frac{1}{2}}\Delta t}{\Delta x} \tag{2.15}$$

The WAF method, being a second-order scheme, is, however, susceptible to spurious oscillations in regions where high vorticity gradients are present. A suitable flux limiting function, or wave amplification function, can be applied to the weighting functions to ensure that the scheme is Total Variation Diminishing (TVD), thus eliminating the oscillations. The total variation, $TV^n(\omega) = TV([\omega^n])$, of the discrete vorticity field is defined as

$$TV^n(\omega) = \sum_{i=-\infty}^{\infty} \left|[\omega^n_{i+1}] - [\omega^n_i]\right| \tag{2.16}$$

and for the scheme to be fully TVD the limiter functions must be chosen to ensure that

$$TV^{n+1}(\omega) \leq TV^{n}(\omega)\,. \tag{2.17}$$

Incorporating the limiting function $\zeta = \zeta\left(r^n_{i+\frac{1}{2}}, \nu\right)$, the weighting functions can be re-written as

$$\begin{aligned} W_1 &= \frac{1}{2}(1+\zeta\nu) \\ W_2 &= \frac{1}{2}(1-\zeta\nu) \end{aligned}$$

where r^n is the vorticity distribution ratio

$$r^n_{i+\frac{1}{2}} = \frac{\omega^n_i - \omega^n_{i-1}}{\omega^n_{i+1} - \omega^n_i}\,. \tag{2.18}$$

A number of flux limiting functions that satisfy Equation 2.17, including a SUPERA-type flux limiter similar to that which is used in the VTM, are derived by Toro [37].

2.4.5 Evaluation of Velocity Field

The flow velocities on the faces of cells that contain vorticity are required at the beginning of each computational time step in order for the vorticity transport equation (Equation 2.8) to be advanced in time. While the irrotational component of the velocity field is simply the freestream velocity in the given context, the rotational, or solenoidal, component is coupled to the vorticity field via the Biot-Savart relationship (shown in Equation 2.4 in its differential form). This may be expressed in integral form as

$$u(x) = \int_V K(x,y) \times \omega(y)\; dy \tag{2.19}$$

where K is the Biot-Savart kernel

$$K(x,y) = -\frac{1}{4\pi}\frac{(x-y)}{|x-y|^3}\,. \tag{2.20}$$

Equations 2.19 and 2.20 together yield an exact solution to the Biot-Savart relationship. The Biot-Savart kernel, however, may contain singularities which lead to unphysical velocities at the core of the vortex. These singularities in the induced velocity field can be removed by regularising the Biot-Savart kernel. This process essentially transforms a vortex singularity into a distribution of vorticity over a small but finite region of space.

The regularised Biot-Savart kernel used in the VTM is the Rosenhead-Moore kernel,

$$K_\delta(x,y) = -\frac{1}{4\pi}\frac{(x-y)}{(|x-y|^2+\delta^2)^{3/2}}\,, \tag{2.21}$$

hence the vorticity-induced velocity field is approximated by

$$u(x) \approx \int_V K_\delta(x,y) \times \omega(y)\; dy\,. \tag{2.22}$$

The Rosenhead-Moore kernel accounts for the fact that the computational cells contain a uniform distribution of vorticity rather than a vortex singularity. Setting the artificial smoothing parameter δ to zero reduces the Rosenhead-Moore kernel (Equation 2.21) back to the singular Biot-Savart kernel (Equation 2.20). The value of the artificial smoothing parameter, δ, is chosen such that the maximum velocity due to the vorticity contained within a cell of width Δx occurs on the faces of the cell. The velocity fields generated by the Biot-Savart and Rosenhead-Moore kernels are compared in Figure 2.6.

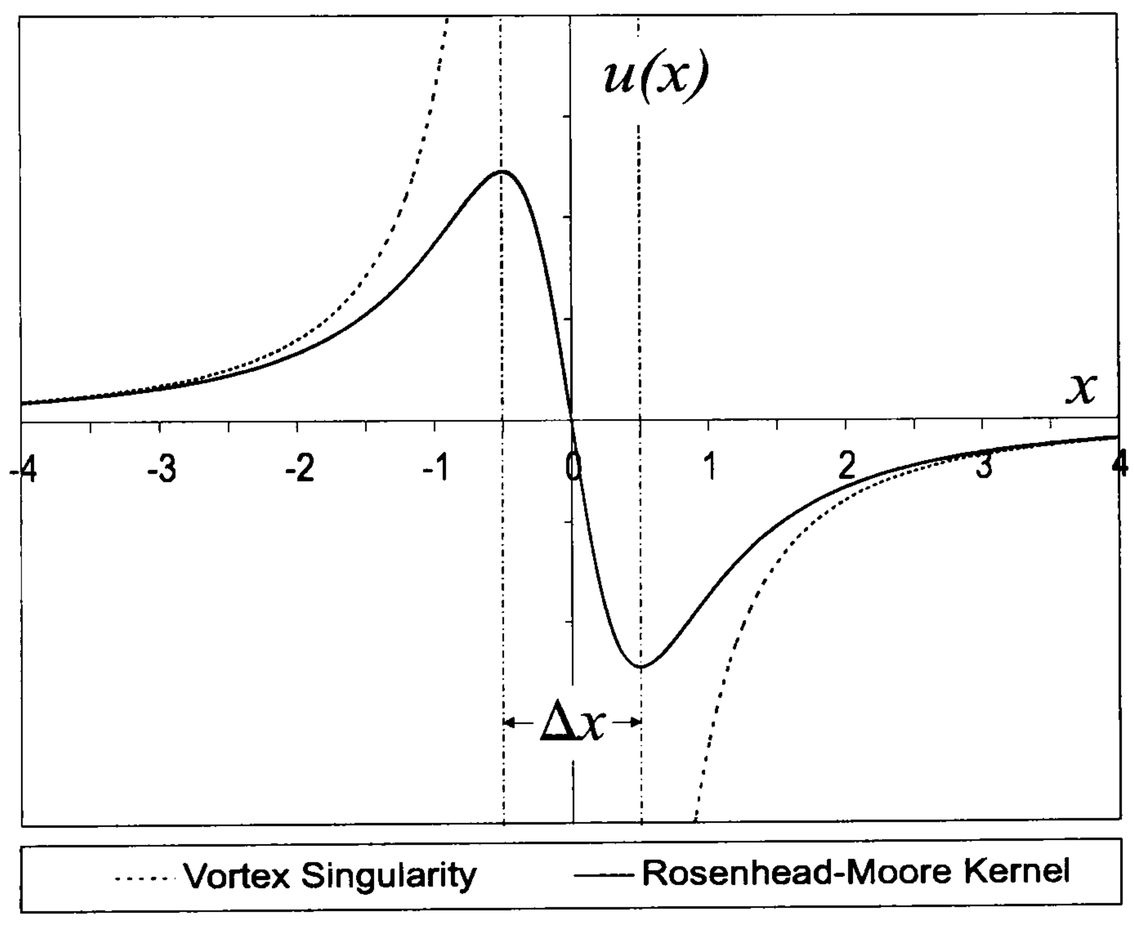


Figure 2.6: *Comparison of velocity fields generated by Biot-Savart and Rosenhead-Moore kernels. Adapted from Brown and Line [29]*

The approximation of the velocity field according to Equation 2.22 requires a summation over all computational cells within the discretised domain. Therefore, the velocity induced at $\mathbf{x}$ by the vorticity, $[\omega_i]$, contained within cell i, which is centred at $\mathbf{y_c}$, from N computational cells is

$$\mathbf{u}(\mathbf{x}) \approx \sum_{i=1}^{N} K_\delta(\mathbf{x},\mathbf{y_c}) \times [\omega_i]\,. \tag{2.23}$$

This is an N-body problem resulting in N^2 Biot-Savart interactions between the vorticity-containing cells, and the computational cost of the direct summation is $\mathcal{O}(N^2)$. This computational cost can quickly become prohibitive as the number of cells becomes large. In the VTM, the cost of the velocity calculation is reduced to $\mathcal{O}(N)$ by employing the Cartesian fast multipole method. This is a specific implementation of the fast multipole method (FMM) that exploits the underlying rectangular topology of the Cartesian grid structure. Fast multipole methods allow pairwise interactions between discrete elements to be evaluated efficiently by taking into account the diminishing influence of the interacting elements on each other with increasing distance between them. This is done by grouping the cells to form a number of clusters so that the long-range interaction due to the cells within the cluster can be described as a single interaction rather than a series of individual interactions. This is shown schematically in Figure 2.7.

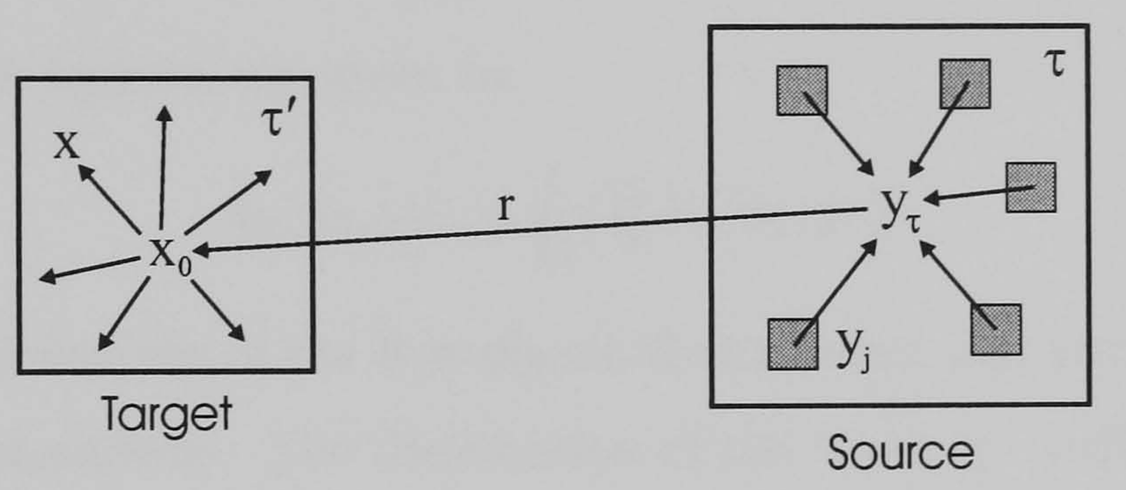


Figure 2.7: *Interaction between source and target clusters using the multipole method to evaluate velocity field. Adapted from Brown and Line [29]*

Consider a cluster, τ, with vorticity-weighted centre at $\mathbf{y}_\tau$, formed by grouping a number of cells, N_τ, with centres at $\mathbf{y}_j$. The velocity induced by cluster τ at another cluster, τ', centred at $\mathbf{x}_0$ and separated by distance r from $\mathbf{y}_\tau$, can be deduced from Equation 2.23 as

$$\mathbf{u}(\mathbf{x}_0) \approx \sum_{j \in \tau} K_\delta(\mathbf{x}_0, \mathbf{y}_j) \times [\omega_j] \,. \tag{2.24}$$

The Cartesian implementation allows such interactions to be expanded as a Taylor series

about the centre of the source cluster, $\mathbf{y}_\tau$, so that

$$\begin{aligned}\mathbf{u}(\mathbf{x}_0) &\approx \sum_{j\in\tau} K_\delta(\mathbf{x}_0, \mathbf{y}_j + (\mathbf{y}_j - \mathbf{y}_\tau)) \times [\omega_j] \\ &\approx \sum_{j\in\tau}\sum_{\mathbf{k}}^{\infty} \frac{1}{\mathbf{k}!} D_{\mathbf{y}}^{\mathbf{k}} K_\delta(\mathbf{x}_0, \mathbf{y}_j)(\mathbf{y}_j - \mathbf{y}_\tau)^{\mathbf{k}} \times [\omega_j] \qquad (2.25)\end{aligned}$$

where the order of the expansion, $\mathbf{k}$, is a vector, $\mathbf{k} = (k_1, k_2, k_3)$, and the subscripts 1, 2, and 3 refer to the three Cartesian directions. Hence it follows that $D_{\mathbf{y}}^{\mathbf{k}} = \partial/\partial y_1^{k1}\, \partial/\partial y_2^{k2}\, \partial/\partial y_3^{k3}$, $\mathbf{k}! = k_1!\, k_2!\, k_3!$, and $\mathbf{x}^{\mathbf{k}} = x_1^{k1}\, x_2^{k2}\, x_3^{k3}$ for $k_i \geq 0$. The result of the summation can then be approximated by truncating the series in Equation 2.25. The number of terms retained after truncation of the series determines the accuracy of the calculation. Truncating Equation 2.25 after the $\mathbf{p}^{\text{th}}$ term yields

$$\mathbf{u}(\mathbf{x}_0) \approx \sum_{\mathbf{k}=0}^{\mathbf{p}} \mathbf{a}_{\mathbf{k}}(\mathbf{x}_0, \mathbf{y}_\tau) \times \mathbf{m}_{\mathbf{k}}(\tau) \qquad (2.26)$$

where the multipole tensors, $\mathbf{a}_{\mathbf{k}}$, given by

$$\mathbf{a}_{\mathbf{k}}(\mathbf{x}_0, \mathbf{y}_\tau) = \frac{1}{\mathbf{k}!} D_{\mathbf{y}}^{\mathbf{k}} K_\delta(\mathbf{x}_0, \mathbf{y}_\tau) \qquad (2.27)$$

are the weighted derivatives of the Rosenhead-Moore kernel and are functions solely of the range of the interaction. The distribution of the vorticity within the cluster τ is described by the moment

$$\mathbf{m}_{\mathbf{k}}(\tau) = \sum_{j\in\tau} (\mathbf{y}_j - \mathbf{y}_\tau)^{\mathbf{k}} [\omega_j] \qquad (2.28)$$

which is independent of the range of interaction. The velocity at the centroid $\mathbf{x}_0$ of the target cluster τ', that is induced by the vorticity contained within the source cluster τ, can thus be evaluated directly from Equation 2.26. The velocities at other cell locations within the target cluster τ' can be expanded again by a Taylor series about the cluster centroid $\mathbf{x}_0$. This requires the spatial derivative of the velocity at this location. Differentiating Equation 2.26 with respect to $\mathbf{x}_0$ gives the spatial derivative

$$D_{\mathbf{x}}^{\mathbf{n}} \mathbf{u}(\mathbf{x}_0) = (-1)^{\mathbf{n}} \sum_{\mathbf{k}=\mathbf{n}}^{\mathbf{p}} \frac{\mathbf{k}!}{(\mathbf{k}-\mathbf{n})!}\, \mathbf{a}_{\mathbf{k}}(\mathbf{x}_0, \mathbf{y}_\tau) \times \mathbf{m}_{\mathbf{k}-\mathbf{n}}(\tau)\,. \qquad (2.29)$$

A Taylor expansion may be used to extrapolate from the velocity at location, $\mathbf{x}_0$, to the velocity at a nearby point, $\mathbf{x}$, in the target cluster such that

$$\mathbf{u}(\mathbf{x}) \approx \mathbf{u}(\mathbf{x}_0) + \sum_{\mathbf{k}=1}^{\mathbf{p}} \frac{1}{\mathbf{k}!}\, D_{\mathbf{x}}^{\mathbf{k}} \mathbf{u}(\mathbf{x}_0)(\mathbf{x} - \mathbf{x}_0)^{\mathbf{k}}\,. \qquad (2.30)$$

The derivatives of the velocities at the location $\mathbf{x}$ can also be obtained in a similar manner to yield

$$D_{\mathbf{x}}^{\mathbf{n}}\mathbf{u}(\mathbf{x}) \approx D_{\mathbf{x}}^{\mathbf{n}}\mathbf{u}(\mathbf{x}_0) + \sum_{\mathbf{k}=\mathbf{n}+1}^{\mathbf{p}} \frac{1}{\mathbf{k}-\mathbf{n}!} D_{\mathbf{x}}^{\mathbf{k}}\mathbf{u}(\mathbf{x}_0)(\mathbf{x}-\mathbf{x}_0)^{\mathbf{k}-\mathbf{n}}\,. \tag{2.31}$$

The efficiency of the FMM algorithm is exploited by implementing an octree data structure within the VTM. The octree structure decomposes the computational domain hierarchically such that eight individual child clusters are grouped to form a parent cluster. At the lowest level of hierarchy, each individual cell itself is a cluster and the grouping procedure continues to the highest level of hierarchy where the entire solution domain is contained in a single cluster. Such an arrangement of the data structure offers an added advantage in terms of managing efficiently the adaptive grid system described in Section 2.4.2 as the computational cells within the adaptive grid can be arranged to follow a similar hierarchical structure.

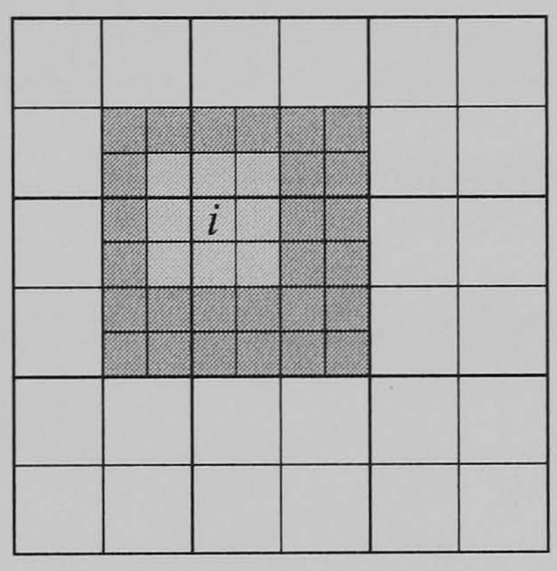


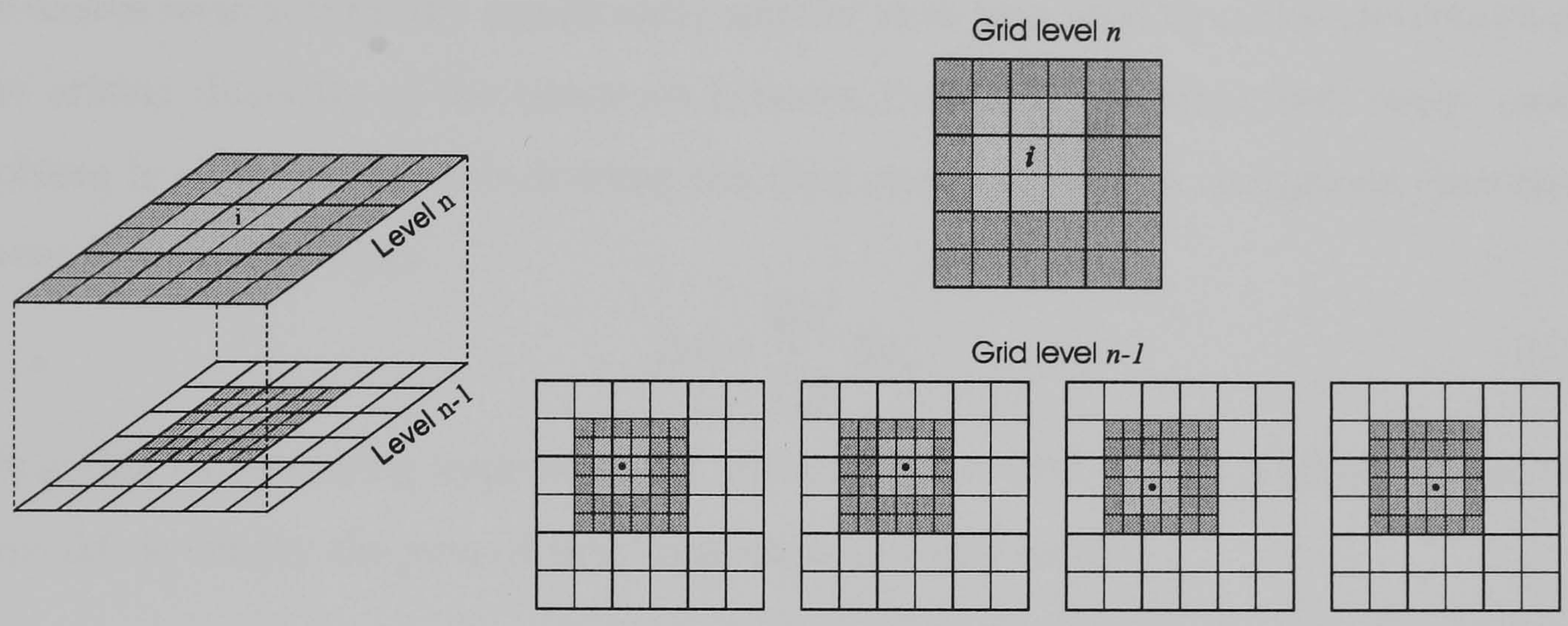
Figure 2.8: *Categorisation of the velocity-inducing clusters in to the near-field (light grey), intermediate field (dark grey), and far field (white) of cluster i.*

To evaluate the velocity field according to Equation 2.24, the FMM performs an upward sweep through the octree structure, calculating the moments of vorticity as described in Equation 2.28. The moments of each parent cluster τ can be written as a binomial sum of the moments of its child clusters $\bar{\tau}$ so that

$$\mathbf{m_k}(\tau) = \sum_{\bar{\tau}\in\tau}\sum_{\mathbf{n}=0}^{\mathbf{k}} \binom{\mathbf{k}}{\mathbf{n}} (\mathbf{y}_{\bar{\tau}} - \mathbf{y}_{\tau})^{\mathbf{k}}\, \mathbf{m_{k-n}}(\bar{\tau})\,. \tag{2.32}$$

The velocity field is calculated in a subsequent downward sweep of the octree. The influence of the distributed vorticity on the velocity at a given cluster i can be categorised according to the increasing range of the Biot-Savart interaction as the near-field,

intermediate-field, and far-field contributions. The near-field contributions are from all the adjoining clusters surrounding cluster i. The intermediate-field is defined within the next hierarchical level as the set of parent clusters neighbouring the particular parent cluster containing i, hence the intermediate-field contributions originate from the child clusters within these regional bounds. All other clusters are classed as far-field (see Figure 2.8 for two-dimensional representation of this categorisation).



(a) Hierarchical concept [29] (b) Hierarchical decomposition of velocity refinement

Figure 2.9: *Evaluation of velocity field by refinement through hierarchical decomposition.*

The similarity in geometry between different hierarchical levels allows the velocity field to be refined recursively as the FMM sweeps down the octree. Assuming that the far-field components of the velocity are known at cluster i on level n of the octree hierarchy, since the far-field velocity is inherited from the parent cluster of i (i.e. from level $n+1$), the contribution from the intermediate-field components can be evaluated from the cluster-cluster interactions associated with cluster i. Equation 2.30 allows the far- and intermediate-field contributions to the velocity at cluster i to be transferred down the hierarchy to the child clusters of i on level $n-1$. The contribution from the near-field is thus accounted for as the FMM moves down one level of the hierarchy. The description presented is aided by Figure 2.9 illustrating the procedure in two dimensions for clarity. At the lowest level of the hierarchy, the near-field contributions are calculated directly from the Biot-Savart relationship described by Equation 2.23.

2.5 Blade Aerodynamics

The vorticity generated by solid surfaces immersed within the flow is represented by the source term, S, in Equation 2.5. The source term operator, $[S]^n_{\Delta t}$, in Equation 2.8 thus accounts for the aerodynamics of the rotor blade. The computational time interval required to capture the unsteady aerodynamics and the associated high-frequency structural dynamics of the rotor blade while maintaining the accuracy and stability of the source term is typically significantly smaller than that used to evolve the rotor wake. The arising disparity of the timescale between the 'inner' (source) and 'outer' (wake) problem is addressed by sub-dividing the time step, Δt, into m contiguous time steps, where $m \in \mathbb{N}$, such that

$$\Delta t = \sum_{i=0}^{m-1} \Delta t_i \,. \tag{2.33}$$

Using this sub-stepping approach, the vorticity generated during a single global time step, Δt, is simply the sum of that from each sub-step so that

$$[S]^n_{\Delta t} = \sum_{i=0}^{m-1} [S]^{n+i/m}_{\Delta t_i} \,. \tag{2.34}$$

In the present implementation of the VTM, the aerodynamics of a rotor blade are modelled using a lifting-line approach based upon Weissinger's L-method [42]. The method, as an extension to the traditional Prandtl lifting-line theory, provides an efficient alternative to the lifting surface panel method (referred to as the F-method) for the analysis of wings with arbitrary sweep. As shown in Figure 2.10, the blade span is discretised into a series of individual panels that each represent a segment of the blade. A discrete bound vortex is placed at the quarter chord point of each panel. The strength of the bound vortex, ω_b, is determined by the condition that the component of the local flow velocity, u_b, normal to the panel is zero at the collocation point located at the three-quarter chord of the same panel. As a vortex in an inviscid fluid cannot have a discontinuity, the series of bound vortices are arranged to form a part of a system of bound horseshoe vortices. Furthermore, since vorticity is conserved within an inviscid fluid, any changes in the bound circulation must be accompanied by an equal and opposite circulation being shed into the wake. Therefore, as the blade sweeps through the flow domain during each subdivided, inner time step, a vortex panel consisting of shed and trailed components of vorticity is formed at the separation line which is fixed at

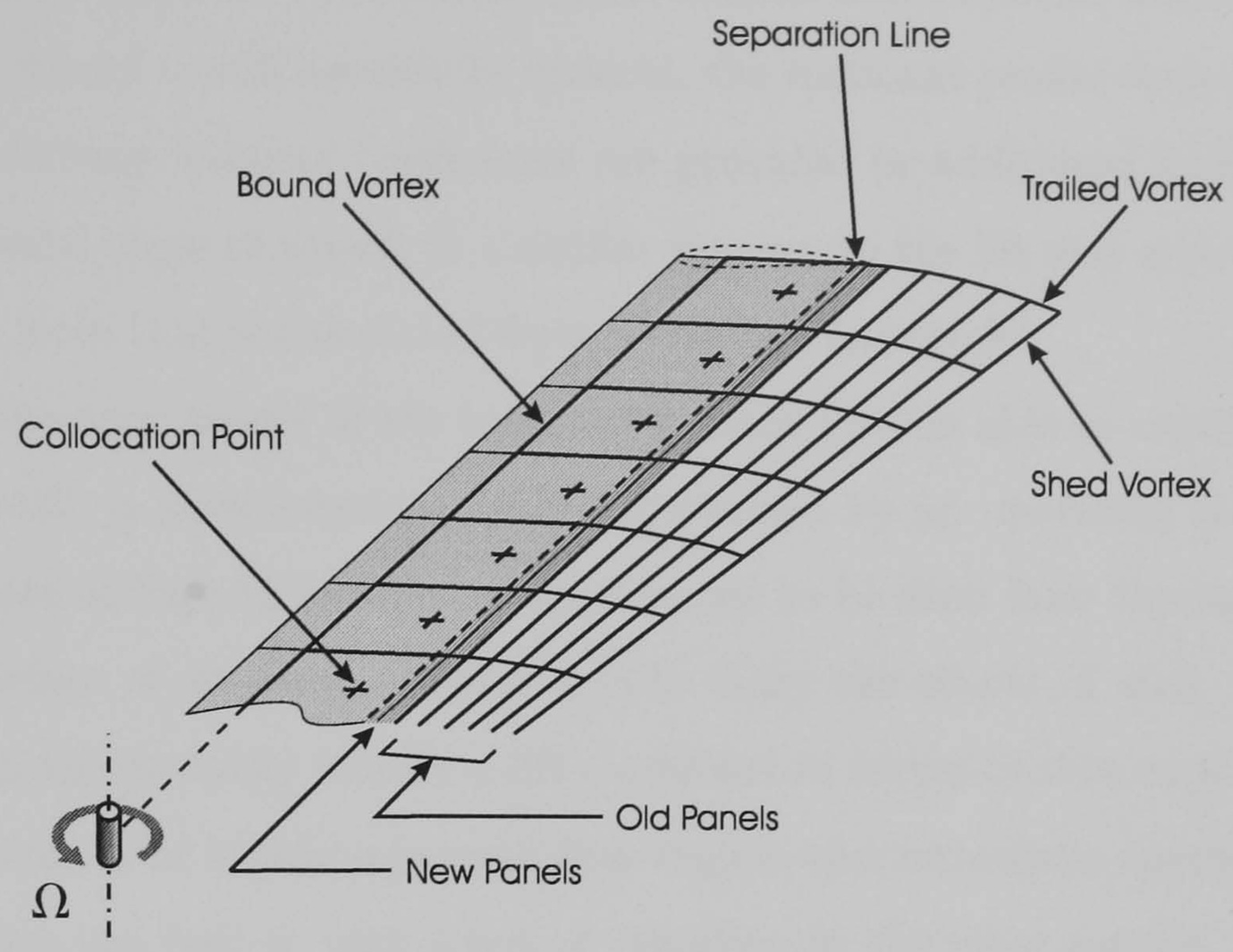


Figure 2.10: *Representation of blade aerodynamics and inner wake model.*

the trailing edge of the blade. In essence, the source term, S, therefore expresses the temporal and spatial gradients of vorticity entering the computational grid as

$$S = -\frac{d}{dt}\omega_b + u_b \nabla \cdot \omega_b \tag{2.35}$$

where the first and second terms represent the shed and trailed vorticity respectively. The process continues, forming a lattice structure within the inner wake which is then convected freely by the local flow velocity. The vortex panels at the rear end of the lattice structure are interpolated and deposited into the computational grid once the panels reach a pre-specified age, measured in terms of inner time steps.

The Weissinger-L approach predicts the lift-curve slope for a panel with infinite span to be exactly 2π. In practice, however, a typical aerofoil section of a rotor blade is likely to cycle through the full 360° range of angle of attack hence the non-linear variation of lift that occurs in regions of high angles of attack, stall and reverse flow must be accounted for in the model. This is done by applying a modified boundary condition of zero velocity normal to the panel on a set of aerodynamic stations along the length of each blade. The modification, which scales the strength of bound circulation, ω_b, enforces the two-dimensional aerodynamic characteristics of the rotor blade sections that are specified in a look-up table of the form $C_L(\alpha, M, Re)$ (for the coefficient of lift,

for instance) as a function of incidence, Mach number and Reynolds number. Since this aerodynamic model is still essentially inviscid, the sectional profile drag coefficients as well as the pitching moment coefficients are provided in additional look-up tables as functions of local angle of attack in a similar manner to the lift and added to the local aerodynamic force that is calculated from the lifting line model.

The aerodynamic model of the rotor blade must also be able to capture the effects of dynamic stall, a phenomenon readily experienced by an operating rotor blade. A rapid pitch rate at high incidences causes a vortex to be shed from the leading edge on the upper surface of an aerofoil which acts to delay the effects of stall, thus allowing the aerofoil to momentarily sustain a lift coefficient in excess of that experienced under static conditions. The highly separated flow regime also introduces significant pitching moments which can lead to high levels of vibration in the rotor system. In the VTM, the description of the dynamic stall behaviour of the aerofoil is based on the models of Beddoes [43, 44, 45] and Boeing-Vertol [46, 47] in which a first-order time delay, applied to an effective lift-curve slope, postpones the loss of lift beyond the static stall incidence. Despite the simplicity of the model, it has been shown to capture well the primary loading features that are induced by dynamic stall.

2.6 Structural Dynamics

The typical rotor system found in today's helicopters employs a complex arrangement of linkages, hinges, springs and dampers. There exists a variety of rotor hub configurations ranging from a relatively simple teetering two-bladed configuration through a more complex, articulated configuration to a semi-rigid system with elastomeric bearings. The particular arrangement of the components of the rotor system differ from helicopter to helicopter with consequent effects on the dynamic behaviour of the entire rotor system. Subtle changes such as the reordering of the flap-lag-feather hinges along the length of the root attachment of the rotor blades can have significant effect on the dynamics of the rotor by altering the coupling between the degrees of freedom of the blades. Given the wide variety of parameters that is required to describe a given system, and the variability from one system to another, accurate modelling of the dynamics of a rotor system poses a significant challenge. The coupling between the rotor and fuselage

dynamics adds a further complication to the problem at hand.

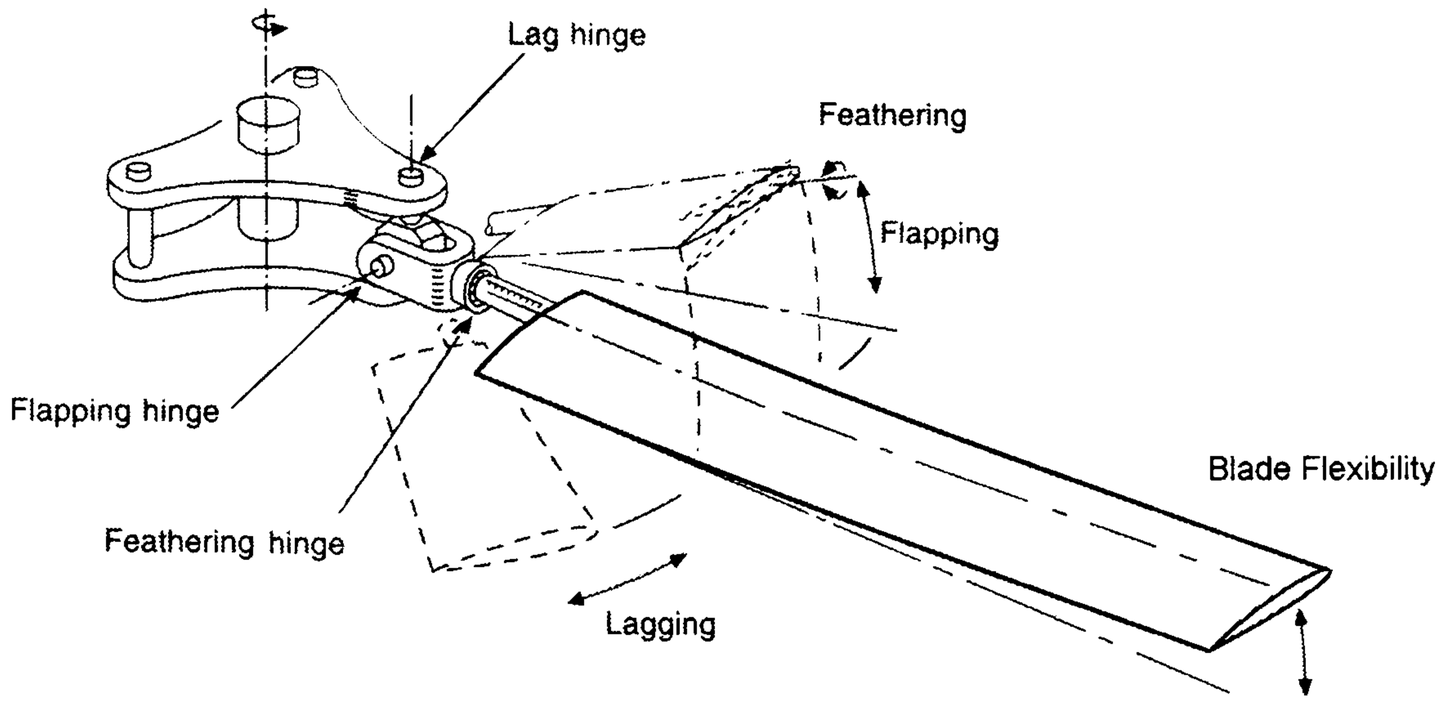


Figure 2.11: *Simplified representation of blade dynamics of an articulated rotor.*

In the VTM, a reduced representation of the rotor system is adopted in order to limit the complexity and the computational cost of the structural dynamic model. As illustrated schematically in Figure 2.11, for the example of an articulated rotor, some components of the rotor hub such as control linkages and swash plates are ignored completely for simplicity, while other components are simplified. The rotor blades, which may be either rigid or flexible, are free to move about a number of hinges placed near the attachment of the blades to the hub. A number of idealised springs and dampers may also be added to the hinges. This arrangement can be used to mimic other types of rotor hubs such as teetering or semi-rigid configurations by sensible and selective choice of stiffness and damping parameters. Although the VTM is capable of capturing the dynamic coupling between the rotor and fuselage, in all results presented within this dissertation, the rotor hub is assumed, for simplicity, to remain fixed relative to the prescribed trajectory of the helicopter.

A generalised approach, derived from Lagrangian dynamics, is adopted to model the structural dynamics of the rotor in the VTM. A multi-body Lagrangian approach allows the dynamics of the rotor system to be computed without the need to derive the equations of motion for each different rotor system that might be modelled. For a system with n degrees of freedom, n generalised coordinates, $q = (q_1, q_2, \cdots, q_n, t)$, and

their time derivatives, $\dot{q} = dq/dt$, are used to describe the energies of the system:

$$\begin{aligned} \text{Kinetic Energy} &= T(q, \dot{q}) \\ \text{Potential Energy} &= U(q, \dot{q}) \\ \text{Dissipation} &= D(q, \dot{q}) \\ \text{Work} &= W(q, \dot{q})\,. \end{aligned} \tag{2.36}$$

For a rigid blade, the generalised coordinates consist of the azimuthal angle of the blade, together with flap, lag, and feathering angles. In the case of a flexible blade, additional coordinates to account for the bending and torsional degrees of freedom must be introduced.

The Euler-Lagrange equation, which can be derived from Hamilton's principle, is solved to describe the structural dynamics of the rotor system. Hamilton's principle states that the line integral along the trajectory between fixed end-points t_1 and t_2 of the dynamical system has a stationary value such that the action does not vary with respect to any deformations in the trajectory. In other words, in terms of the kinetic energy of the system and the work done on the system,

$$\int_{t_1}^{t_2} (\delta T + \delta W)\ dt = 0\,. \tag{2.37}$$

The work done on the system may be decomposed into that done by the conservative and non-conservative forces. The former may be written as the gradient of the scalar potential energy and the latter in terms of the work done by the aerodynamic forces, Q_i, such that,

$$\delta W = -\delta U + \sum_{i=1}^{n} Q_i \delta q_i\,. \tag{2.38}$$

Equation 2.37 can thus be expanded as

$$\int_{t_1}^{t_2} \delta(T - U) + \sum_{i=1}^{n} Q_i \delta q_i\ dt = 0 \tag{2.39}$$

such that the Euler-Lagrange equation in the absence of dissipation is

$$\frac{d}{dt}\left(\frac{\partial \mathcal{L}}{\partial \dot{q}}\right) - \frac{\partial \mathcal{L}}{\partial q} = Q \tag{2.40}$$

where $\mathcal{L}$ is the conventional Lagrangian of the dynamical system defined as $\mathcal{L} = T - U$.

The dynamical system is, however, inherently dissipative due to the presence of damping within the system. The modified Lagrangian of the system at time t is thus

defined by introducing the Rayleigh dissipation function, D, to account for damping so that

$$\mathcal{L}^* = T - U + \int_{t_0}^{t_0+\Delta t} D_t \, dt \tag{2.41}$$

where $D_t = \partial D/\partial t$ is the rate of dissipation in the system at time t, and t_0 is the time at which the system is initialised so that $\Delta t = t - t_0$.

Hamilton's principle of minimisation of action applied to the modified Lagrangian (Equation 2.41) yields the Euler-Lagrange equation including dissipation terms

$$\frac{d}{dt}\left(\frac{\partial \mathcal{L}}{\partial \dot{q}}\right) - \frac{\partial \mathcal{L}}{\partial q} + \frac{\partial D_t}{\partial \dot{q}} - \int_{t_0}^{t_0+\Delta t} \frac{\partial D_t}{\partial q} \, dt = Q \tag{2.42}$$

The first term of Equation 2.42 can be expanded as

$$\frac{d}{dt}\left(\frac{\partial \mathcal{L}}{\partial \dot{q}}\right) = \frac{\partial^2 \mathcal{L}}{\partial \dot{q}_i \partial q_j} \, \dot{q}_j + \frac{\partial^2 \mathcal{L}}{\partial \dot{q}_i \partial \dot{q}_j} \, \ddot{q}_j \tag{2.43}$$

allowing the Euler-Lagrange equations to be expressed in terms of the generalised coordinates and their time derivatives as

$$\frac{\partial^2 \mathcal{L}}{\partial \dot{q}_i \partial \dot{q}_j} \, \ddot{q}_j + \frac{\partial^2 \mathcal{L}}{\partial \dot{q}_i \partial q_j} \, \dot{q}_j - \frac{\partial \mathcal{L}}{\partial q_i} + \frac{\partial D_t}{\partial \dot{q}_i} - \int_{t_0}^{t_0+\Delta t} \frac{\partial D_t}{\partial q_i} \, dt = Q_i \, . \tag{2.44}$$

Once the derivatives and the integral of the dissipation term are evaluated numerically using a central difference perturbation analysis, the acceleration of the generalised coordinate, $\ddot{q}$, can be found by directly solving the above expression. The structural dynamics of the rotor system are then evolved in time using Euler integration to evaluate the generalised coordinates at the next computational time step as

$$\begin{aligned} q^{n+1} &= q^n + \dot{q}^n \Delta t \\ \dot{q}^{n+1} &= \dot{q}^n + \ddot{q}^n \Delta t \, . \end{aligned} \tag{2.45}$$

The Lagrangian approach presented here is capable of handling the complex and highly non-linear nature of the rotor dynamics. The generality that is inherent in the formalism makes it ideally suited to modelling a variety of rotor systems with very different mechanical arrangements. The velocity arising from the rigid-body motion of the rotor blades that is calculated from the dynamics of the rotor system is added to the local velocity at the bound vortex location, u_b (in Equation 2.35), which is used in determining the strength of the bound vortex as described in Section 2.5. The dynamics of the rotor system are therefore coupled to the aerodynamics of the rotor blades via the source term, S.

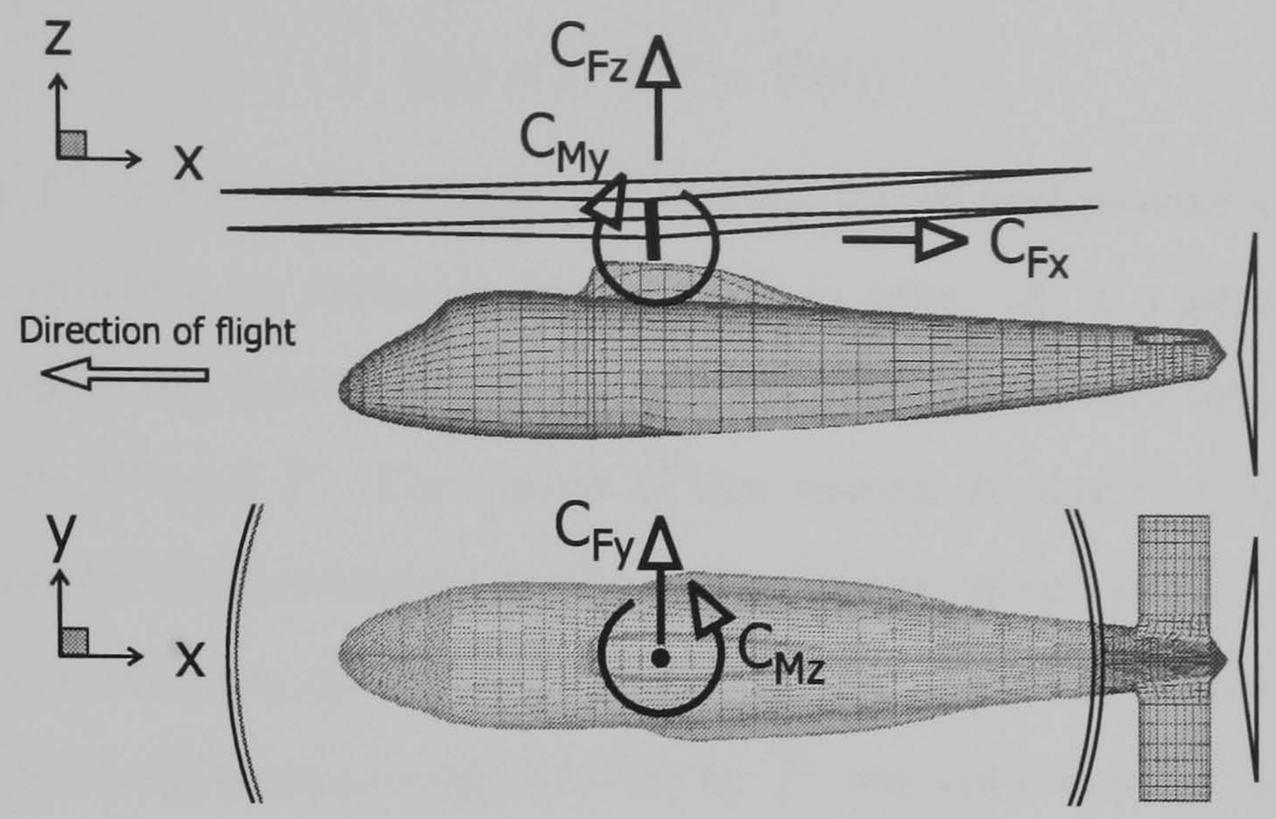


Figure 2.12: *Schematic showing axis convention for forces and moments. (Fuselage included for clarity.)*

2.7 Rotor Trim Control

The forces and moments generated by a rotor system can be altered by means of appropriate control inputs to the rotor in order to maintain the loads (or the attitude) of the rotor in a trimmed state for a given flight trajectory. The trim algorithm implemented in the VTM sets the rates of change of the rotor controls to be proportional to the difference between the current values and the prescribed target values of the components of an array of forces and moments that have been chosen to represent the loads on the vehicle in the given flight condition. The resulting scheme is thus a simple first-order dynamical system.

An array F, consisting of the orthogonal components of the overall forces and moments, is defined as

$$F = [\, C_{Fx}, C_{Fy}, C_{Fz}, C_{Mx}, C_{My}, C_{Mz} \,] \,. \tag{2.46}$$

The forces and moments are applied by the rotor system to some suitable reference point on the airframe (for instance the centre of gravity of the aircraft or the base of the rotor mast). For the axis convention adopted throughout this dissertation, refer to Figure 2.12. Given the control vector, θ, comprising available control inputs for the given rotor configuration, the generalised trim algorithm used in the VTM can be

written as

$$\dot{\theta}(t) = K\ (F^* - F(t)) \tag{2.47}$$

where the array F^* contains the components of the forces and moments that the rotors are required to produce to maintain the aircraft in trim. K is a prescribed coupling matrix that governs the rate at which each of the controls should respond to any discrepancy between F^* and F. The values of the matrix K should thus be selected to represent the control characteristics of the rotor system under study. A more detailed account of the construction of the coupling matrix K is presented in subsequent chapters. Denoting the long-term average of $F(t)$ by $\overline{F}$, the system is considered to be in a condition of trim when

$$\overline{F} = F^* \,. \tag{2.48}$$

The trim algorithm, therefore, works essentially as a simplistic pilot model that constantly adjusts the controls throughout the simulation in an attempt to meet the prescribed target loads on the vehicle. The same procedure can be used to define the trim condition of the vehicle in any given unsteady flight condition. The target forces and moments, F^*, need simply to be chosen in such cases, appropriately to yield the required acceleration of the aircraft.

2.8 Rotor Aeroacoustics

The radiated acoustic signature of the simulated rotor system is calculated by solving the Ffowcs Williams-Hawkings equation [48]. This equation is essentially the Navier-Stokes equations rearranged in the form of a wave equation using an acoustic analogy. Neglecting the terms due to quadrupole sources that are associated with non-linear acoustics (this requires that the Mach numbers in the flow are subcritical), the acoustic pressure, p', at a point x at time t can be written as

$$\begin{aligned} p'(x,t) \;=\; & \frac{1}{4\pi}\frac{\partial}{\partial t}\iint_S \left[\frac{\rho v_n}{r(1-M_r)}\right]_\tau dS + \frac{1}{4\pi a_0}\frac{\partial}{\partial t}\iint_S \left[\frac{F_r}{r(1-M_r)}\right]_\tau dS \\ & + \frac{1}{4\pi}\iint_S \left[\frac{F_r}{r^2(1-M_r)}\right]_\tau dS \end{aligned} \tag{2.49}$$

where a_0 is the speed of sound, and r is the distance between the point x and the acoustic source. F_r is the component of force on the fluid on the surface S of the source in the direction of the observer such that $F_r = F \cdot r$. Similarly, M_r is the Mach number

at which the source is moving relative to the observer such that $M_r = M \cdot r$. The source time τ, known as the *retarded time*, is the time at which the sound wave is emitted from the source relative to the observer time t. The concept of the retarded time thus accounts for the fact that a finite length of time is required for the acoustic waves to reach the observer point from location of the source where it was emitted.

The first term of Equation 2.49 represents what is known as the thickness noise. This term accounts for the pressure change that is induced by a moving rotor blade of finite thickness as it displaces the fluid at the perturbation velocity v_n normal to its surface. The second and the third terms, which collectively represent the loading noise, correspond to a far-field and a near-field contribution respectively. Notice that the far-field contribution of the loading noise is dependent on the time rate of change of the pressure on the blade. In the compact source limit*, this term is directly related to the time rate of change of lift on the blade. It is thus clear that the highly impulsive change in the lift generated by a blade encountering a vortex will have a significant impact on the acoustic signature.

The blade surface in the aerodynamic model is represented by a series of panels as described in Section 2.5. The aerodynamic force contributed by each panel is then used to construct a point acoustic source located at the collocation point of the panel. The sound that is radiated by each of these sources is then integrated to represent the loading noise that is produced by the blades. Although the aerodynamic effects of the thickness of the blade are introduced through a look-up table of airfoil characteristics, the lifting line model within the VTM otherwise assumes an infinitesimally thin blade. The thickness noise (the first term in Equation 2.49) is thus modelled independently using a source-sink pair attached to each blade panel [49]. The instantaneous acoustic pressure due solely to the loading contribution, $p_L(t)$, at a given observer location due to a discrete point force F moving at Mach number M, is thus given by

$$p_L(t) = \frac{1}{4\pi a_0}\left[\frac{\partial}{\partial t}\left(\frac{F_r}{r(1-M_r)}\right) + \frac{a_0 F_r}{r^2(1-M_r)}\right]_\tau . \tag{2.50}$$

The integration of Equation 2.50 is implemented numerically using the Farassat-1A formulation in which the source time derivatives are transformed to observer time deriva-

*An acoustic source is said to be compact if the size of the body is small relative to the wavelength of the sound wave that the body generates. The body can then be approximated as a point source.

tives [50, 51].

The VTM is particularly well suited to resolving the wake-induced interactions between the twin main rotors in the coaxial configuration, and hence the sources of acoustic radiation within the system. The coupled VTM-acoustic methodology has been used previously to predict the acoustics of the HART II rotor [52], where good agreement between the computed pressure time histories and sound pressure levels was demonstrated against measured data for three representative flight conditions involving strong BVIs [53]. Thus the method is expected to provide accurate measure of the acoustic properties of the rotor systems discussed in this dissertation.

2.9 Fuselage Aerodynamics

To model the presence of a fuselage, the fuselage surface is discretised into a system of N quadrilateral panels. Each panel edge is represented as a vortex filament of constant strength Γ_i, with the filaments on each panel i thus forming a closed loop of vorticity. The velocity at any panel centroid is then given by the sum of the influences from all vortex filaments on the body together with the velocity w that is induced by any other vorticity within the flow and the freestream component of velocity, U_∞. A boundary condition of zero through-flow is enforced simultaneously at the centroids of all panels so that

$$(U_\infty + w)_i \cdot \mathbf{n}_i + \sum_{j=1}^{N} A_{ij}\Gamma_j = 0 \tag{2.51}$$

where $\mathbf{n}_i$ is the unit vector normal to panel i. This linear equation is solved at each computational time step to obtain the matrix of vortex loop strengths, Γ. The influence matrix, A, accounts for the velocity induced on each panel by every other panel, and is thus of size N by N. The fact that the fuselage is closed provides an additional, but implicit, constraint on the relationship between the panel strengths, by requiring that they should sum to zero, that results in A being singular. In the VTM, the vortex loop strengths are thus evaluated using an approximation to the inverse of A that is obtained using Singular Value Decomposition. A considerable saving in computational effort is achieved by assuming the fuselage to be rigid. This is because the matrix of influence coefficients does not then change with time, allowing the inversion of A to be performed prior to the simulation.

The pressure on the fuselage surface is calculated from the unsteady Bernoulli equation

$$\frac{p - p_\infty}{\frac{1}{2}\rho} = U_\infty^2 - \mid \mathbf{u} \mid^2 - 2\frac{\partial \phi}{\partial t} \,. \tag{2.52}$$

In the VTM, the change in panel strengths with time as well as the disturbance to the velocity potential due to the convection of vortices within the wake are accounted for when evaluating the unsteady potential term $\partial\phi/\partial t$. Similarly, the contribution from all the vorticity in the computational domain, as well as a near-field correction term that accounts for the self-influence of the vorticity on each panel by assuming it to be distributed as an equivalent vortex sheet, is accounted for when evaluating the velocity $\mathbf{u}$ on the surface of the fuselage.

Lift generation by the fuselage is modelled in the VTM by applying the Kutta condition along pre-specified separation lines on the surface of the fuselage. The Kutta condition is satisfied by ensuring that the net circulation around the separation line is zero, and this is enforced in the VTM by releasing into the wake an amount of vorticity that is equal in strength to the difference between the strengths of the panels on either side of the separation line. This vorticity, created as a consequence of the generation of lift on the body, is sourced into the computational grid, where it feeds back into the loading produced on the system. The circulatory contribution to the unsteady aerodynamic characteristics of any lifting surface in the flow is thus fully represented. Note though that the viscous wakes of any bodies immersed within the flow are not accounted for at present.

Elements of this model have been used before to investigate the aerodynamic interactions experienced by a generic helicopter configuration [54], and the procedure described above has been shown to produce very good agreement with experimental results for the mean and time-dependent variation of inflow through the rotor, the position of the vortices within the rotor wake as they approach the surface of the fuselage, and both the mean and time-variation of the pressure fields that are induced on the surface of the fuselage by these vortical structures.

2.10 Summary

The VTM is a comprehensive code tailored for the aeromechanical analysis of rotorcraft systems. The governing equations are cast into vorticity-velocity form to address the problem of numerical diffusion by explicitly conserving vorticity. The vorticity transport equation is solved using a finite volume TVD scheme which is particularly well suited to preserving the compactness of the vortical structures in the rotor wake for long periods of time. In the context of coaxial rotor aerodynamics, this property of the VTM enables the long-range aerodynamic interactions between the twin main rotors and other geometrically well-separated components of the aircraft to be captured and resolved in detail. The generation of vorticity by lifting elements such as the rotor blades or fuselage appendages is accounted for by treating these components as sources of vorticity. The aerodynamics of the rotor blades are modelled using an extension of the Weissinger-L version of lifting-line theory in conjunction with a look-up table for the two-dimensional aerodynamic characteristics of the blade sections. The acoustic field is determined using the Ffowcs Williams-Hawkings equation. The aerodynamics of the fuselage are modelled using a vortex panel approach in which the condition of zero through-flow is satisfied at the centroid of each panel. Lift generation by the fuselage is modelled by applying the Kutta condition along pre-specified separation lines on its surface. The viscous wake of the fuselage is not accounted for, however. The dynamics of the rotor system are captured using a Lagrangian approach. The equations of motion for the blades, as forced by the aerodynamic loading along their span, are derived by numerical differentiation of a pre-specified non-linear Lagrangian for the particular system being modelled. No small-angle approximations are involved in this approach and the coupled flap-lag-feather dynamics of each of the blades are fully represented. The generality of the Lagrangian approach allows configurations as complex as that of a coaxial rotor to be accommodated easily.

Chapter 3

Performance Comparison of Conventional and Coaxial Rotors

3.1 Introduction

Recent developments in the rotorcraft world, led by Sikorsky Aircraft Corporation's announcement of their X2 demonstrator and the development of several UAV prototypes, indicate a resurgence of interest in the coaxial rotor configuration as a technological solution to operational requirements for increased helicopter forward speed, manoeuvrability and load-carrying ability.

The coaxial concept is not new, of course. Although Russia has historically been the world's largest developer and user of coaxial rotor helicopters, and an extensive body of research has been produced in that country, the US, UK, Germany and Japan have also pursued research into the coaxial rotor configuration [1]. Some highly innovative designs, such as Sikorsky's S-69 Advancing Blade Concept (XH-59A), and Kamov's Ka-50 attack helicopter, have attempted to exploit the coaxial configuration to obtain improved performance in parts of the flight envelope.

In several cases, however, the performance of practical coaxial configurations fell short of expectations, and this led to a temporary hiatus in the development of the concept. In many such cases the shortcomings in the practical implementation of the coaxial concept could be traced back to deficiencies in modelling or understanding the specific details of the interaction between the rotors, and the effect of the wake on the

behaviour of the system — especially under unsteady flight conditions. In recent years, though, computational tools have developed to the extent where the highly interactive and non-linear wake flows generated by the two rotors of the coaxial configuration can be modelled with a much greater degree of confidence than has been possible in the past.

The aim of this chapter is to quantify, through numerical simulation, the differences in performance between coaxial and conventional rotor systems, both featuring articulated hubs, in steady flight and during manoeuvres, and, in particular, to examine the effect of the differences in the structure and development of their wakes on the performance of the two types of rotor system. The aerodynamic environment of any of the blades of a conventional rotor is strongly influenced by close interactions not only with its own wake but also with the wakes that are generated by the other blades of the rotor. The aerodynamic environment of the rotor blades in a coaxial rotor configuration is further complicated by interactions with the wakes that are generated by the blades on the opposing rotor of the system. Given the relatively long-range nature of these interactions, the numerical modelling of coaxial systems has always posed a significant challenge. This is because adequate resolution of the loading on the blades, hence rotor performance, requires the strength and geometry of the wake of the rotor to be correctly captured and retained for the significant amount of time during which it has an influence on the loading on the system. Adequate resolution of the inter-rotor interactions that characterise the coaxial rotor system has proved to be beyond the capabilities of most current, conventional numerical methods because of the prohibitively large computational resources that are required to prevent premature dissipation of the wake. In this vein, calculations using the VTM are used in this chapter to expose some of the subtle differences between the wake structures generated by conventional and coaxial rotor systems that lie at the root of the differences in their performance.

3.2 Model Validation

A very useful benchmark against which the performance of computational models can be evaluated exists in the form of Harrington's experimental study of coaxial rotor performance in hover [11]. An interesting feature of Harrington's work was that he compared

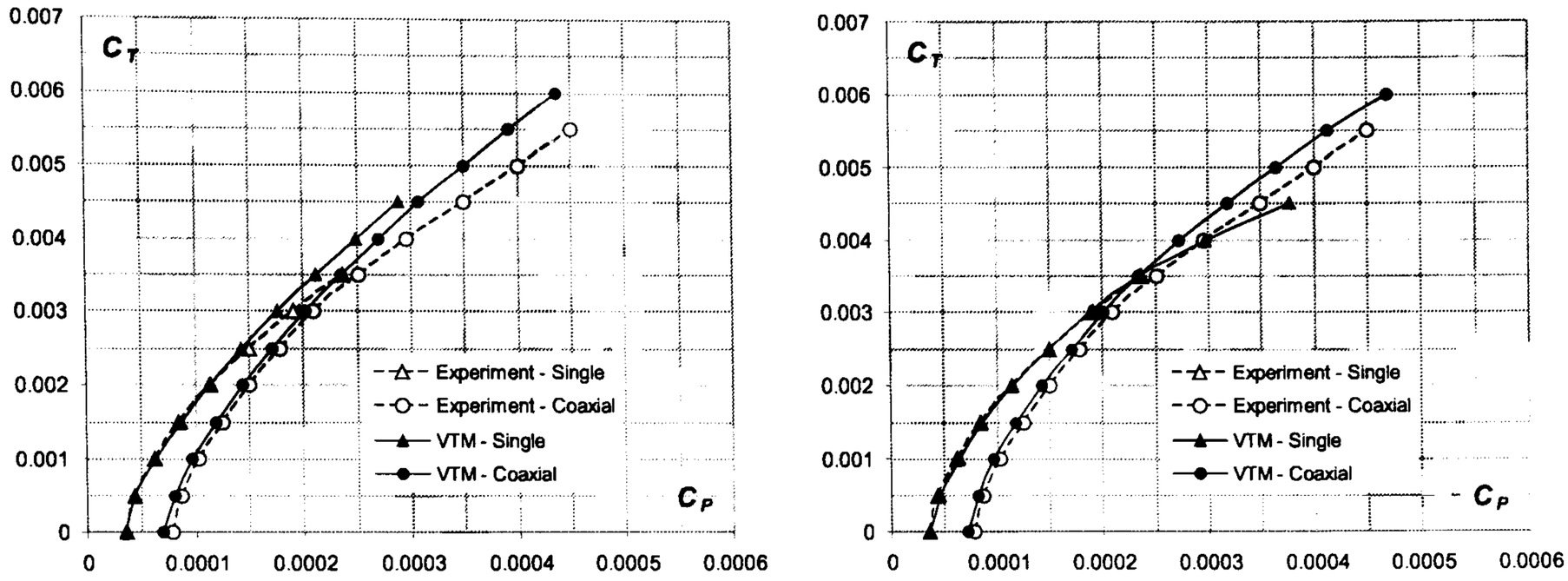
the performance of his coaxial rotor against the performance of a conventional single rotor — actually one of the two rotors from his coaxial configuration — allowing the data to be used to assess the ability of computational methods, particularly those that have proved adequate for conventional rotors, to represent the more highly-interactive aerodynamic environment of the coaxial rotor.

Table 3.1: *Summary of rotor properties*

Rotor radius	R
Number of rotors	2
Blades per rotor	2
Rotor separation	$0.190R$
Root cutout	$0.133R$
Solidity	0.054
Twist	None
Flap hinge offset	0 (Teetering)
Chord (Tapered)	$0.076R$-$0.029R$ (Linear)
Thickness (Tapered)	$0.023R$-$0.003R$ (Non-linear)
Airfoil sections	NACA-00xx series
Lock number	4.3 (Estimated)

Two different coaxial rotor configurations were tested in Harrington's original study; in this chapter the ability of the VTM to predict the performance of coaxial systems is assessed by comparing numerical results against experimental data for the system referred to as 'rotor 1' in Ref. 11. This system consisted of two, contra-rotating, two-bladed teetering rotors, separated by $0.19R$ along a shared rotational axis, which were operated at a tip Reynolds number of about 1×10^6. The blades were untwisted and had linear taper. A significant complication, from a modelling perspective, was introduced by allowing the blades to change thickness in a non-linear way along the span of the blade. Although the blade sections were based on the symmetric NACA 4-digit profile, this feature resulted in non-standard airfoil sections, for which measured aerodynamic information is unavailable, on most parts of the blade. The details of this rotor are summarised in Table 3.1.

In the absence of drag data for the airfoil sections, Harrington's experiment was



(a) *Using C_D profile drag model* (b) *Using $C_D{}'$ profile drag model*

Figure 3.1: *Power vs. Thrust: VTM simulations compared to Harrington's experimental data.*

replicated using a number of rather simple profile drag models within the VTM. Initially the profile drag was simply assumed to be independent of angle of attack so that

$$C_D(\alpha) = K_0 \ . \tag{3.1}$$

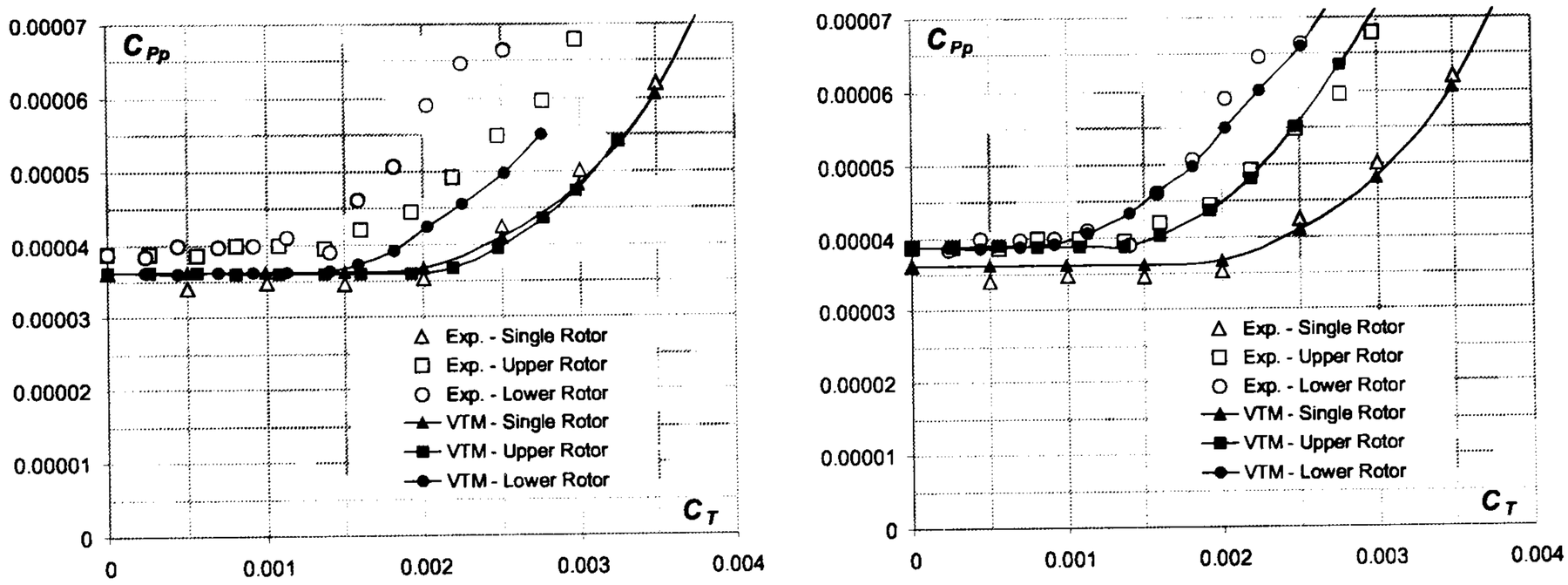
The same drag model was used everywhere along the blade regardless of its sectional profile; the value $K_0 = 0.0115$ was selected to reproduce the experimentally-measured torque on Harrington's isolated single rotor at zero thrust.

Figure 3.1(a) shows a comparison between Harrington's experimental data and VTM calculations of power versus thrust using this profile drag model, and, as is to be expected, reveals a significant discrepancy in the predicted power consumption of both the coaxial and single isolated rotors, especially at high C_T where airfoil stall and the associated increase in drag becomes significant. Figure 3.1(b) shows a comparison between experimentally measured power versus thrust and the VTM results calculated using a somewhat more sophisticated profile drag model that represents the drag rise due to blade stall at high angle of attack in a more realistic fashion. Compared to the earlier model, this second profile drag model simply modifies the post-stall behaviour of the airfoil sections by switching to a non-linear variation of drag at high angle of attack, as shown in Figure 3.3. More specifically,

$$C_D{}'(\alpha) = \max \ [\ K_0 \ , \ K_1 - K_2 \cos 2\alpha \ ] \tag{3.2}$$

where α is the local angle of attack of the blade section. The coefficients $K_1 = 0.49$ and $K_2 = 0.49$ were selected to give the best fit between VTM predictions and the measured performance of Harrington's isolated single rotor.

As shown in Figure 3.1(b), very good agreement between experiment and simulations for the isolated rotor is indeed obtained using this drag model, but the power consumed by the coaxial rotor is still significantly underpredicted at high C_T. In addition, it might have been expected that, at zero thrust, the power consumed by the coaxial system would have been exactly twice that of the isolated rotor, given that the blades of the rotors were not twisted. The VTM suggests that this is indeed the case, but the experimental data reveals Harrington's coaxial system to have had a slightly higher power consumption at zero C_T.



(a) Using $C_D{}'$ drag model throughout

(b) using $C_D{}''$ drag model for coaxial and $C_D{}'$ drag model for single rotor

Figure 3.2: *Comparison of VTM computed profile power against experimental estimates.*

These discrepancies are revealed more clearly in Figure 3.2(a), where the profile component of power consumed by the isolated rotor and each constituent rotor of the coaxial system is plotted against its own thrust, rather than against the overall thrust produced by the rotor system. In this figure, predicted values are compared against experimental estimates that were obtained by subtracting the computed induced component from the measured total power of the system, and, in the case of the coaxial rotor, enforcing the condition that at trim each rotor should consume the same overall

power. As can be seen, the results calculated by the VTM for the single isolated rotor using the more sophisticated drag model agree very closely with the experimental estimates of the profile power for this system. The calculations suggest, however, that the upper rotor of the coaxial system should have a nearly identical variation of profile power with thrust to that of the single isolated rotor, whereas the experimental data reveal the upper rotor of Harrington's coaxial system to have had a significantly higher profile power consumption than his isolated rotor. In both cases, the profile power consumption of both upper and lower rotors is very similar at low thrust, but as thrust is increased, the profile power consumption of the lower rotor becomes significantly greater than that of the upper rotor.

The simulations thus suggest, as far as profile power is concerned, that the upper rotor of the coaxial system operates as if it were effectively in isolation, while only the performance of the lower rotor is affected significantly by the presence of a second rotor. If the interaction between the two rotors is dominated by the behaviour of the wake of the system, then this behaviour is to be expected. As will be shown in the following sections, a significant proportion of the lower rotor is immersed in the wake of the upper rotor, whereas the upper rotor is affected most directly by its own wake and only indirectly by the presence of the wake of the lower rotor. Any wake-induced interactional effects (on profile power as well as more obviously on induced power) should thus be far more pronounced on the lower rotor than on the upper and, indeed, should become more obvious as the thrust of the system is increased.

The observed discrepancy between the experimental data for the profile power consumption of the isolated rotor and the coaxial rotor can be reconciled fairly easily with this notion of the effect of aerodynamic interactions within the system, though, if a slight difference between the profile drag characteristics of the two rotor systems is allowed for. By re-writing the sectional profile drag model for the coaxial system in slightly more general form as

$$C_D''(\alpha) = \max\ [\ K_0''\ ,\ K_1 - K_2 \cos 2(\alpha + \alpha_{mod})\ ] \tag{3.3}$$

to allow the zero-lift drag coefficient (i.e. K_0'') to be increased by 7.15% and the stall angle of the airfoil to be reduced by α_{mod}=1.75 degrees (see Figure 3.3) then a significantly better match between calculations and the experimentally-determined profile power of the coaxial system is achieved, as is shown in Figure 3.2(b). This small

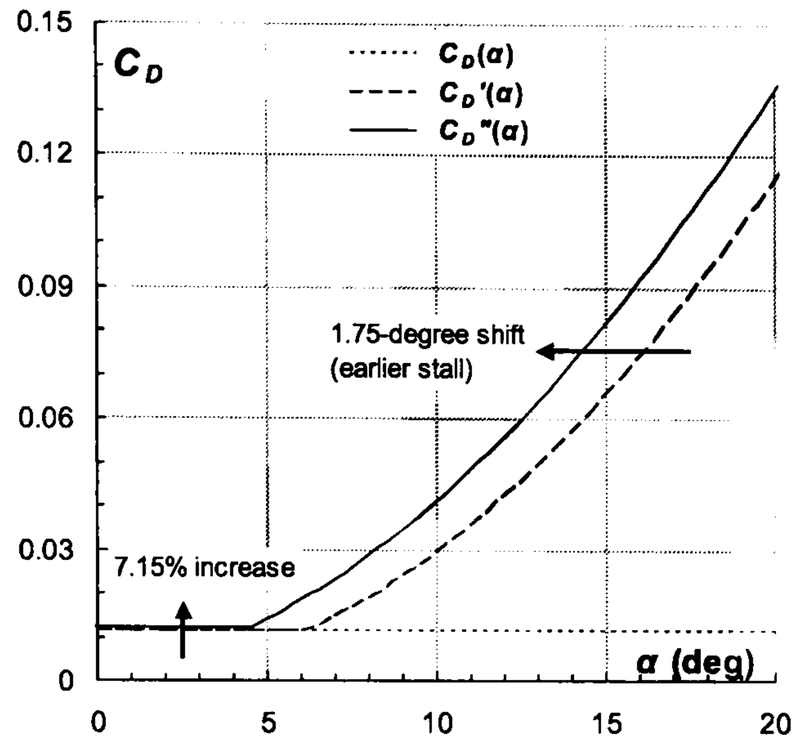


Figure 3.3: *Variation of sectional profile drag coefficient with angle of attack as used in VTM simulations.*

change in the drag model translates into a very much improved agreement between the VTM predictions and Harrington's experimental data for the overall power consumption of the coaxial system, as shown in Figure 3.4. Even bearing in mind the relatively low tip Reynolds number of the experimental system, and the likelihood thus that the sectional drag would be sensitive to the precise conditions on the rotor blade [55], it seems a little glib to attribute the modification to the drag polar that is required to achieve a good match with the experimental data for the coaxial rotor simply to some small discrepancy in Reynolds number between the experiments conducted on the isolated single rotor and on the coaxial rotor (such as might arise from imperfect control of the rotor speed, for instance). This many years after Harrington's experiments were conducted, the exact reason for this rather curious discrepancy can only be guessed at, but a purely viscous, or non-circulatory interaction between the two rotors of the coaxial system that is beyond the present capabilities of the VTM to resolve cannot be discounted [56, 57].

Turning next to the ability of the VTM to capture the performance of coaxial rotors in forward flight, this aspect of the performance of the model can be assessed rather neatly by comparing predictions against wind-tunnel data from Dingeldein's 1954 investigation of the performance of various coaxial rotor configurations [12]. The advantage of using this data set is that one of the rotors used in Dingeldein's study was geometri-

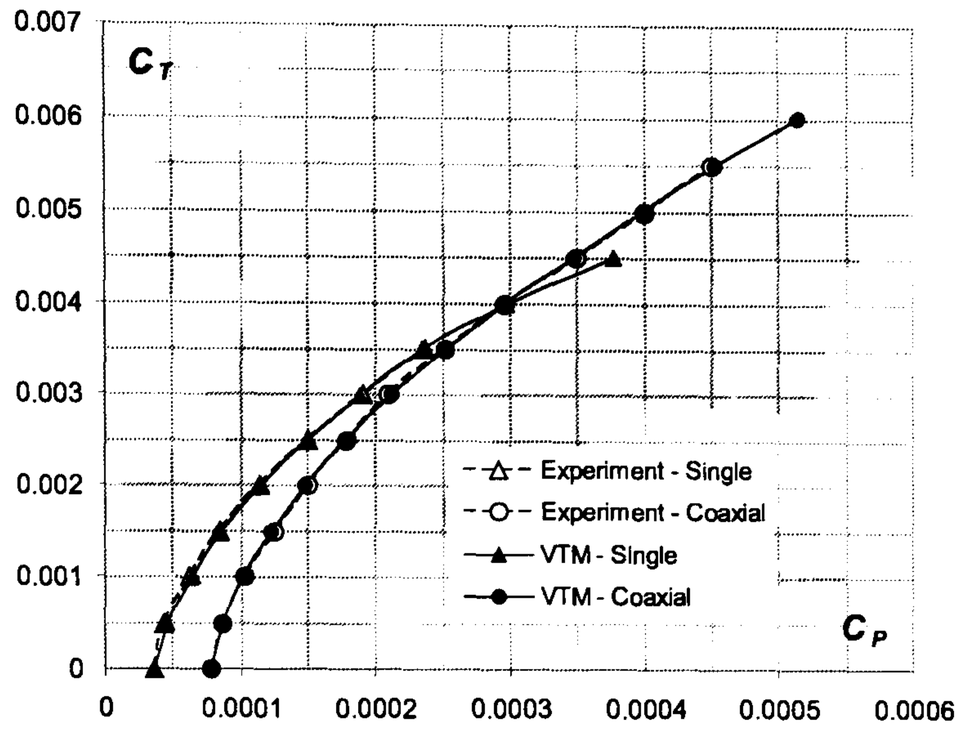


Figure 3.4: *Power vs. Thrust: VTM simulations compared to Harrington's experimental data.*

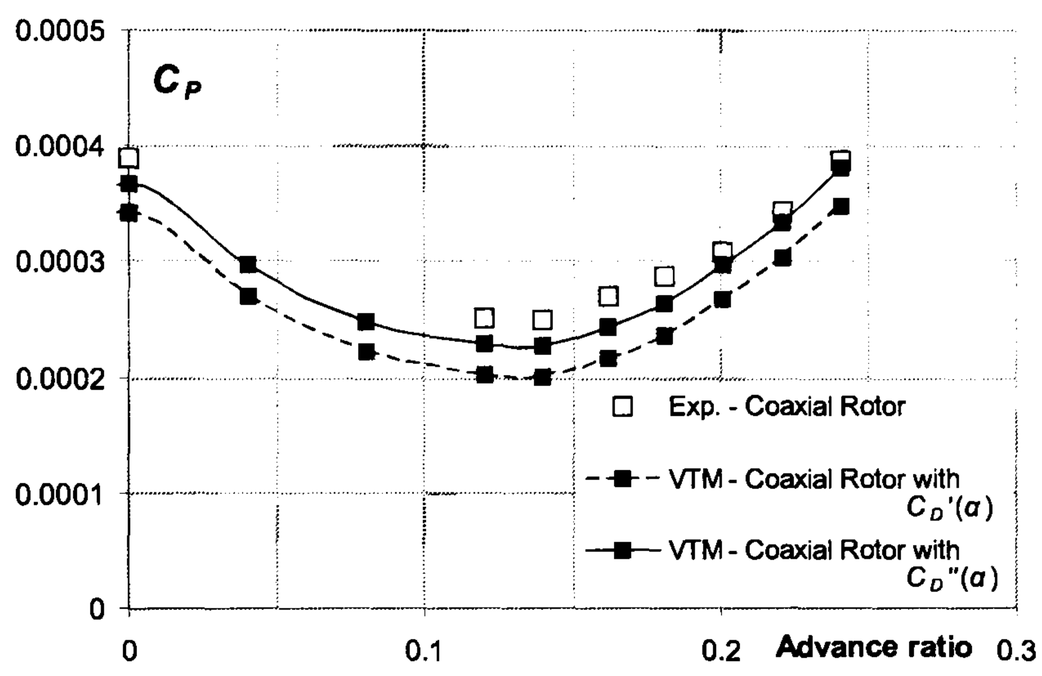


Figure 3.5: *Overall power consumption in steady level flight ($C_T = 0.0048$).*

cally identical to Harrington's 'rotor 1', and hence comparison with this data provides a logical extension to the validation of the VTM in hover that was presented above.

VTM simulations of Dingeldein's coaxial rotor were conducted over a range of forward flight speeds. To represent the effects of fuselage parasite drag on the trim state of the experimental system, the forward tilt of the rotor was adjusted to produce sufficient forward force to overcome the drag corresponding to a fuselage equivalent flat plate area of 0.02 times the rotor disc area. This effect was replicated in the simulations by trimming the rotor to the required force using collective pitch, aligning the shaft with

the required thrust vector, and trimming out residual lateral and longitudinal forces using suitable cyclic pitch input. The simple, mechanical linkages between the upper and lower rotors of Dingeldein's coaxial system were reproduced in the simulation by applying equal cyclic pitch inputs to both upper and lower rotors. As in the experiment, differential collective pitch was used in the simulations to trim the rotor to zero net yawing moment.

Figure 3.5 shows a comparison between VTM simulations and Dingeldein's measurements of power consumption against advance ratio, with the rotor trimmed to a thrust coefficient of 0.0048 throughout. Calculations using the $C_D{}'$ and the $C_D{}''$ profile drag models both underestimate slightly the experimental measurements of power, but the trend of the data is well matched by the VTM predictions over the entire speed range that was simulated. It is worth noting though that Dingeldein's and Harrington's measurements on ostensibly the same rotor system of the power required to hover at $C_T = 0.0048$ are not consistent. It is thus plausible that another small adjustment to the profile drag model, along similar lines to that which was required in the hover simulations described earlier, would be all that would be required to yield very close agreement between experimental and simulated results, but the apparent variability in the profile drag characteristics of the blades between tests is a distinct frustration to comprehensive validation of numerical predictions.

3.2.1 Power Comparisons

A major advantage of a computational analysis compared to an experimentally-based study is that the numerically-calculated power consumption of a rotor can be easily separated into its parasite, profile and induced constituents. With a conventional rotor, any uncertainty in performance that might arise from uncertainty in the profile drag characteristics of the rotor blades can thus be confined to the resultant uncertainty in the profile power consumption of the system without influencing the argument regarding the other constituents of the rotor power. This is because the torque produced by the rotor for any given thrust is cancelled by independent, external means (e.g. by the tail rotor). For a coaxial rotor the situation is slightly more complicated: any uncertainty in the profile power consumed by the rotor stands the risk of translating directly into a similar uncertainty in the induced power because of the additional requirement that,

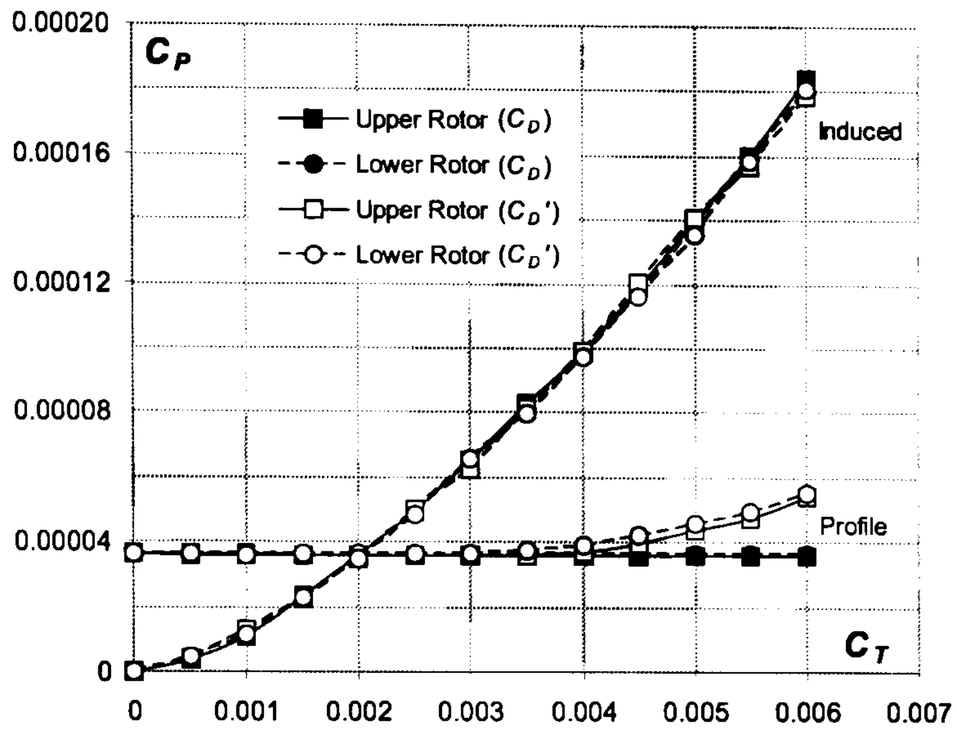


Figure 3.6: *Power constituents in hover, as a function of overall thrust coefficient.*

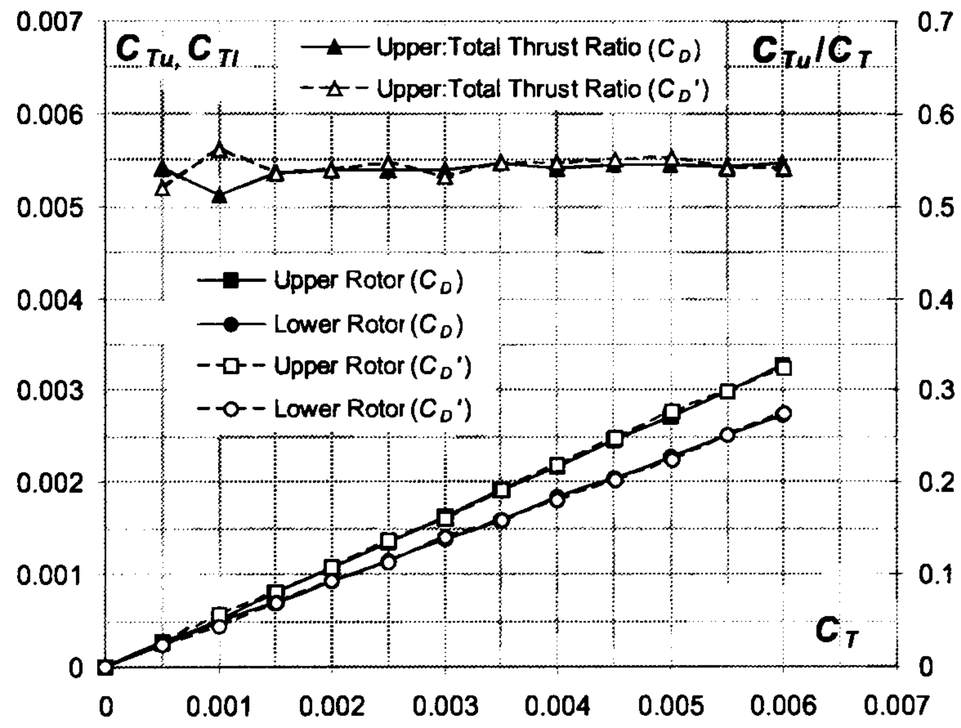


Figure 3.7: *Thrust sharing between the upper and lower rotors of the coaxial system in hover, as a function of overall thrust coefficient.*

for trim at any given overall thrust, both rotors must generate the same net torque. Thus, in reaching any generally-valid conclusions regarding the relative performance of coaxial and conventional rotor systems, as is attempted in this chapter, extreme care must be taken to ensure the robustness of any results to the particular profile drag characteristics of the systems being compared. This is despite the fact that in both types of rotor system the primary effect of the wake is on the induced power.

Figure 3.6 shows the VTM-predicted partition of power between the upper and

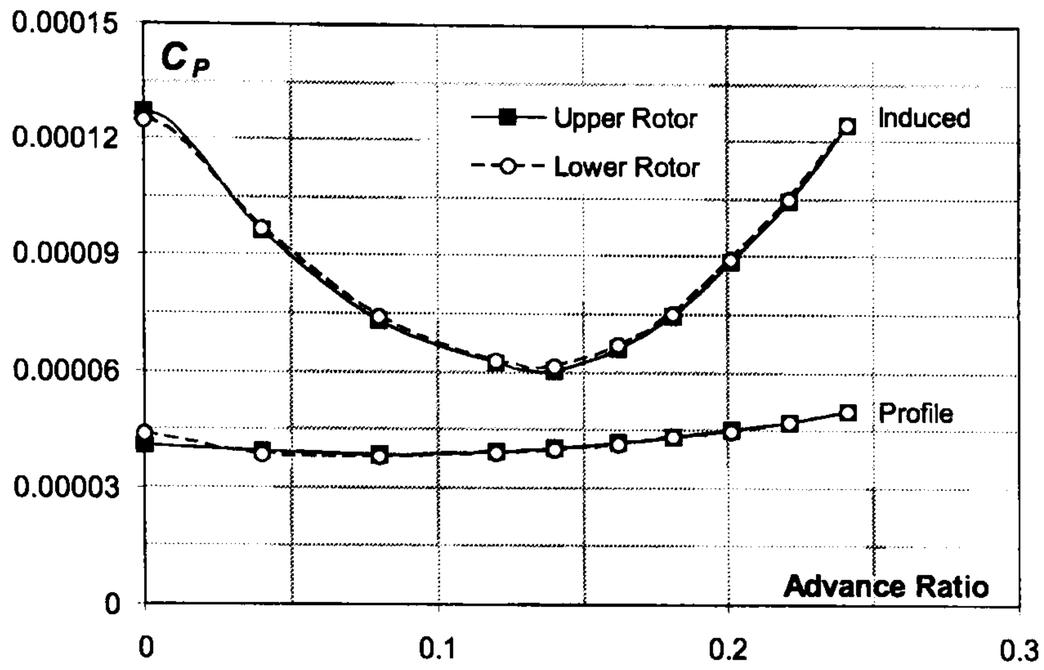


Figure 3.8: *Power constituents in forward flight, as a function of advance ratio (overall* $C_T = 0.0048$*).*

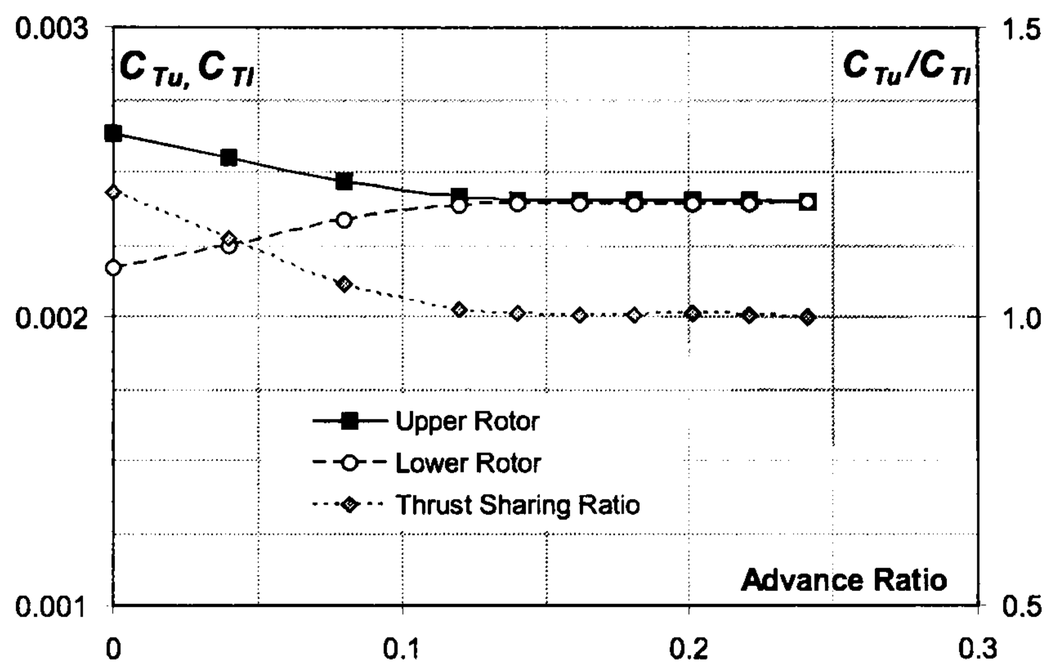


Figure 3.9: *Thrust sharing between the upper and lower rotors of the coaxial system in forward flight, as a function of advance ratio (overall* $C_T = 0.0048$*).*

lower rotors, separated into profile and induced constituents as a function of overall thrust coefficient, that results from satisfying the trim condition of zero net torque on Harrington's coaxial rotor. Figure 3.7 shows the associated partition of thrust between the upper and lower rotors that is required to generate overall torque balance within the system. Similar results are presented in Figures 3.8 and 3.9 for Dingeldein's rotor in forward flight, as a function of advance ratio. The sensitivity of the trim state to the profile drag characteristics of the blades can be judged by contrasting the results of the

calculations presented in these figures using the simple, constant C_D model and the more representative $C_D{}'$ profile drag model. Even though the two models produce distinctly different predictions of the profile power consumption of the rotor, particularly at high thrust coefficient, the figures show that, regardless of the profile drag characteristics of the blades, the profile power differential between the upper and lower rotors that results from trimming the system amounts to a very small percentage of the overall power consumed by each individual rotor and has almost negligible effect on the partition of thrust between the upper and lower rotors. It is hopefully not too great an extrapolation from the limited results presented here to suggest, thus, that a comparison between coaxial and conventional rotors, at least in terms of induced power consumption, can indeed be conducted without undue obscuration by the link between induced and profile power that results from the method that is used to trim the coaxial system.

3.3 Hover

The power required by a rotorcraft for a given lifting capacity is determined, in many cases, by the hover performance of its rotor system. For a coaxial rotor, trim of the yawing moment is achieved by matching the torque of the upper and lower rotors via differential collective pitch input so that the net torque about the shared rotor axis is zero. It has long been a point of contention whether or not this arrangement is more efficient than the more conventional main rotor – tail rotor configuration, where typically the tail rotor consumes an additional 5 to 10% of the main rotor power to maintain overall yaw moment equilibrium in steady hover [55].

When comparing the performance of a coaxial rotor configuration to that of a conventional rotor system, care must be taken to ensure appropriate equivalence between the two systems. Various aspects of the relative performance of the two systems can be made more (or less) apparent depending on whether the comparison is performed at equal disc loading or equal thrust coefficient, for instance. Figure 3.1(b) may be interpreted, at face value, to suggest that the single rotor is more efficient than the coaxial rotor at low thrust but less efficient at higher thrust. This is obviously the case, but somewhat obscures the point that Harrington's single rotor is relatively limited in lifting capability by rotor stall compared to the coaxial rotor simply because it has half the

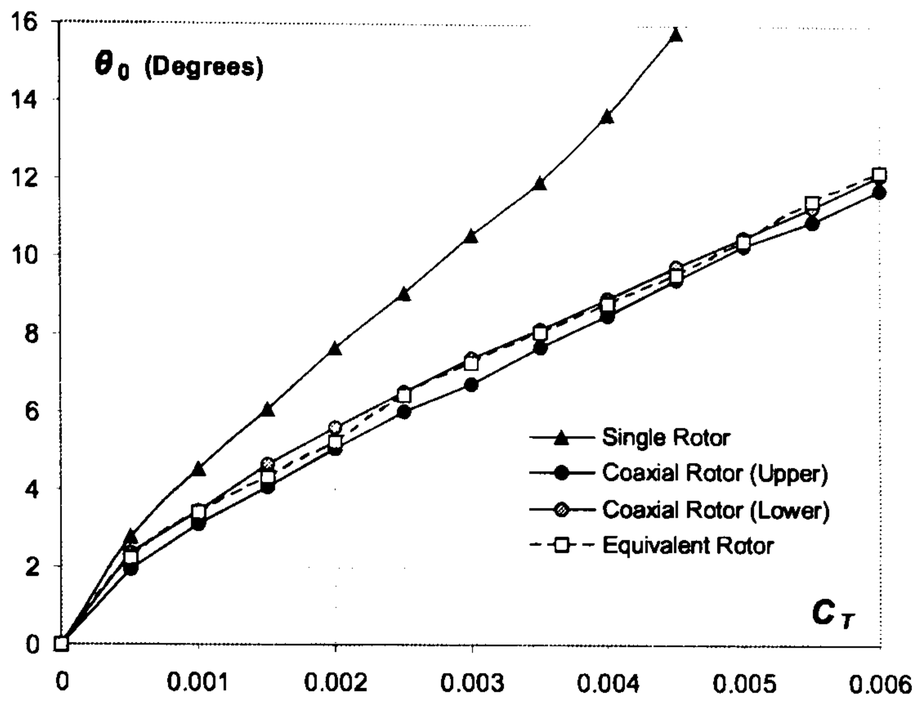


Figure 3.10: *Collective pitch required to trim to given thrust coefficient (using $C_D{}'$ profile drag model throughout).*

blade area of the coaxial rotor. This is shown more clearly in Figure 3.10 where, compared to the coaxial rotor, the rapid divergence in the collective pitch required to trim the single rotor is indicative of a sharp decline in the VTM-predicted lifting capability of the rotor beyond a C_T of approximately 0.003. The pitfalls of this form of comparison lie essentially in the unmatched solidities of the two systems [9]. It is tempting to try to avoid this problem by normalising C_T and C_P by the rotor solidity. Figure 3.11 shows the data from Figure 3.1(b) re-scaled in this manner, and it appears to reveal that, per blade, the single rotor is more efficient than the coaxial rotor throughout the tested range of thrust coefficients. For the comparison between the two configurations to be wholly consistent, though, it seems most reasonable to compare the performance of the coaxial rotor against a conventional system that has as similar geometry to the coaxial rotor as possible so that differences in performance can be attributed properly to the fundamental differences in configuration between the two types of rotor system. Such a comparison is presented in Figure 3.12. In this figure, VTM predictions of the performance of Harrington's two-bladed coaxial rotor are compared against predictions of the performance of a four-bladed, conventional (i.e. planar, co-rotating) rotor configuration with blades that have the same geometry and aerodynamic properties as the blades of the coaxial rotor. This approach yields a comparison between rotors that have the same solidity and hence very similar lifting performance, as indicated in Figure 3.10 by the similarity in the collective pitch required by the two rotors to trim to a given

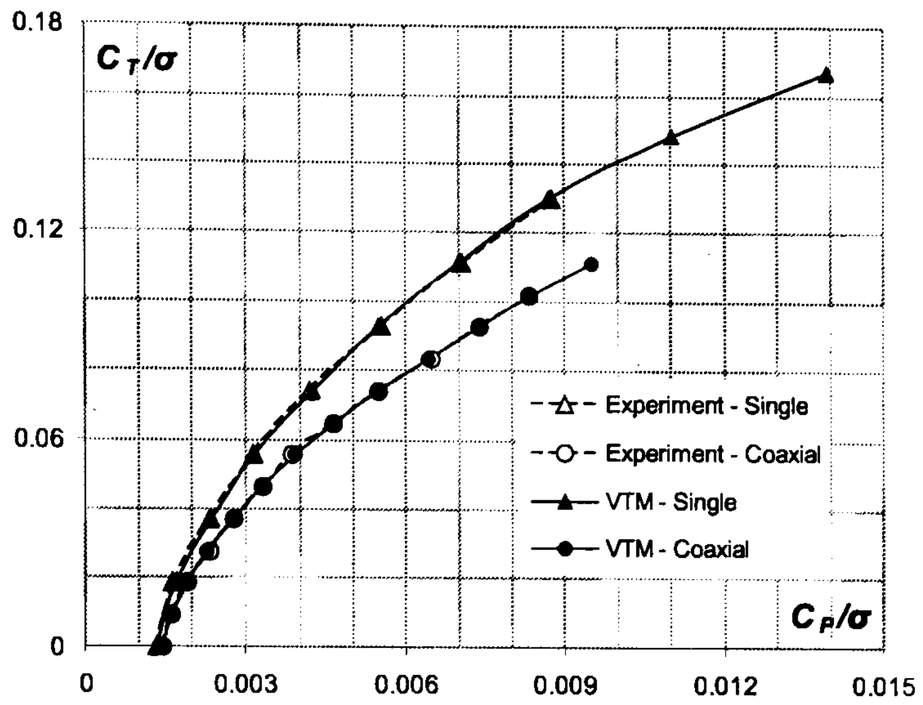


Figure 3.11: *Power vs. Thrust: comparison after normalising by rotor solidity.*

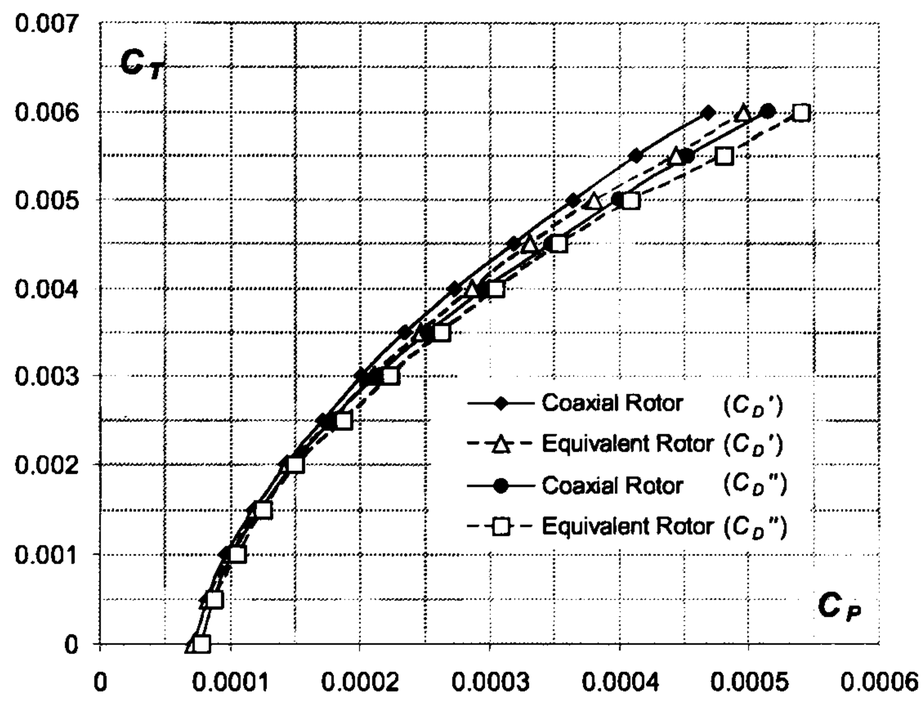


Figure 3.12: *Power vs. Thrust: comparison between rotors with identical solidity and blade properties.*

thrust coefficient. Since this form of comparison exposes most clearly the configuration-dependent effects on performance that are the prime focus of this work, it will be used exclusively throughout the remainder of this dissertation.

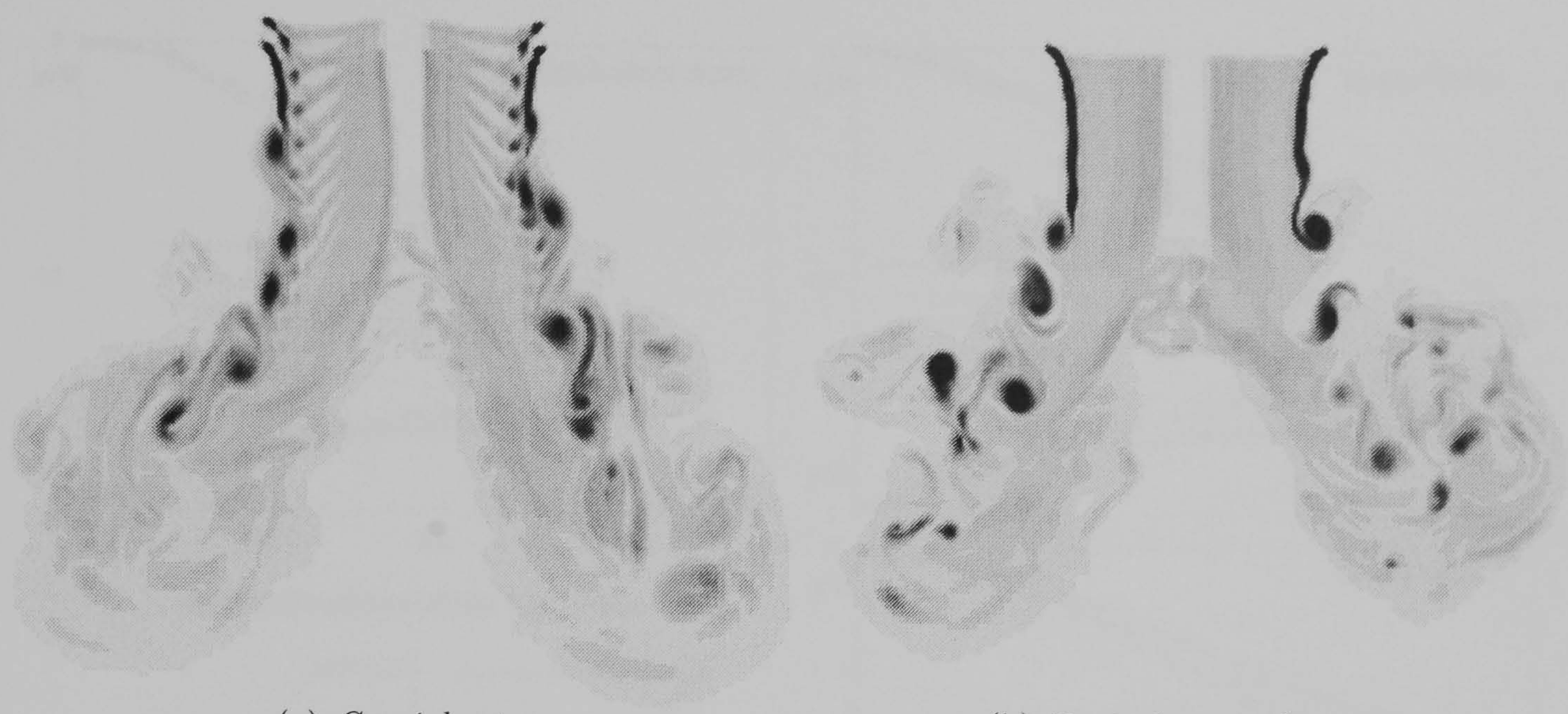
Presentation of the data in the form of Figure 3.12 shows the equivalent conventional rotor to consume increasingly more power than the coaxial rotor as thrust coefficient is increased, but also that the difference in performance between the two rotor systems is of similar order to the uncertainty in their profile power consumption. The data

thus raises significant doubt as to whether an absolute and general quantification of the merits of conventional rotors relative to coaxial systems in terms of *overall* power consumption is possible. This is because the rather small differences in performance that are seen between the two systems implies that the blade aerodynamic properties under the precise operating conditions of the systems being compared may have significant impact on their relative merits*. The discussion of rotor perfomance in the remainder of the chapter will thus largely be confined to the induced power characteristics of the coaxial rotor where, as demonstrated in the previous section, some degree of absolute quantification does appear to be justified.

3.3.1 Wake Geometry in Hover

The differences in performance between coaxial and conventional rotors must manifest themselves in the geometry of the wake of the system. In Figure 3.13, VTM-generated contour maps of vorticity strength on a vertical slice through the centre of the wake show the global differences between the geometry of the wake of Harrington's coaxial rotor and that of the equivalent four-bladed conventional rotor. Near to the rotors, the images show the orderly downstream procession of the tip vortices and their associated inner wake sheets, the obvious difference between the two systems being the double-tube structure formed by the tip vortices of the coaxial rotor. In both cases, the orderly helicoidal structure of the wake is disrupted, roughly a rotor radius below the rotor plane, as the individual tip vortices coalesce into larger vortical structures. In the case of the coaxial rotor, the tip vortices from both the upper and the lower rotors interact during this process to form a single sequence of coalesced vortical structures. As originally observed by Landgrebe [58] in his study of the geometry of the wakes of hovering rotors, the formation of these large structures effectively marks the end of the contraction of the wake and, in fact, the beginning of an expansion in the diameter of

*If the variability in the results presented here can indeed be attributed to Reynolds number related effects on the blades, then it is worth bearing in mind that this variability would, in all likelihood, become less marked the greater the Reynolds number of the system, since it is known that the sensitivity of sectional drag to Reynolds number is most marked at lower values of this parameter. This should have interesting consequences for the relative merit of the two types of rotor system when one considers the range of Reynolds numbers that current vehicles (from UAVs to full-scale aircraft) might be designed to operate.



(a) *Coaxial rotor* (b) *Equivalent single rotor*

Figure 3.13: *Wake structure in hover ($C_T = 0.0025$).*

the wake as these structures continue to convect downstream of the rotor. Eventually these structures are themselves torn apart, through their own mutual interaction, to form the extensive field of highly disordered, low-level vorticity in the far-wake that is seen in both images.

Figure 3.14 compares VTM calculations of the contraction and axial convection rate of the tip vortices generated by Harrington's coaxial rotor system in hover with that of the equivalent conventional rotor, and thus provides a somewhat more quantitative comparison of the differences in wake structure between the two rotor systems. ψ is the wake age in terms of relative blade azimuth since generation of the tip vortex. The finite resolution of the flow domain yields an estimated error in the calculated positions of the tip vortices of approximately 1/40 of the rotor radius. Langrebe's empirical correlations of wake geometry [58] for isolated rotors operating at the same thrust coefficient as the various individual rotors of the conventional and coaxial systems are also plotted to allow the differences between the wakes that are generated by the two systems to be assessed more clearly.

The agreement between Landgrebe's correlation and the VTM-predicted tip-vortex trajectory for the equivalent single rotor is extremely close, providing good faith in the accuracy of the numerical simulations. For the coaxial system, it is immediately obvious that the axial convection rate of the tip vortices that are generated by the upper rotor is

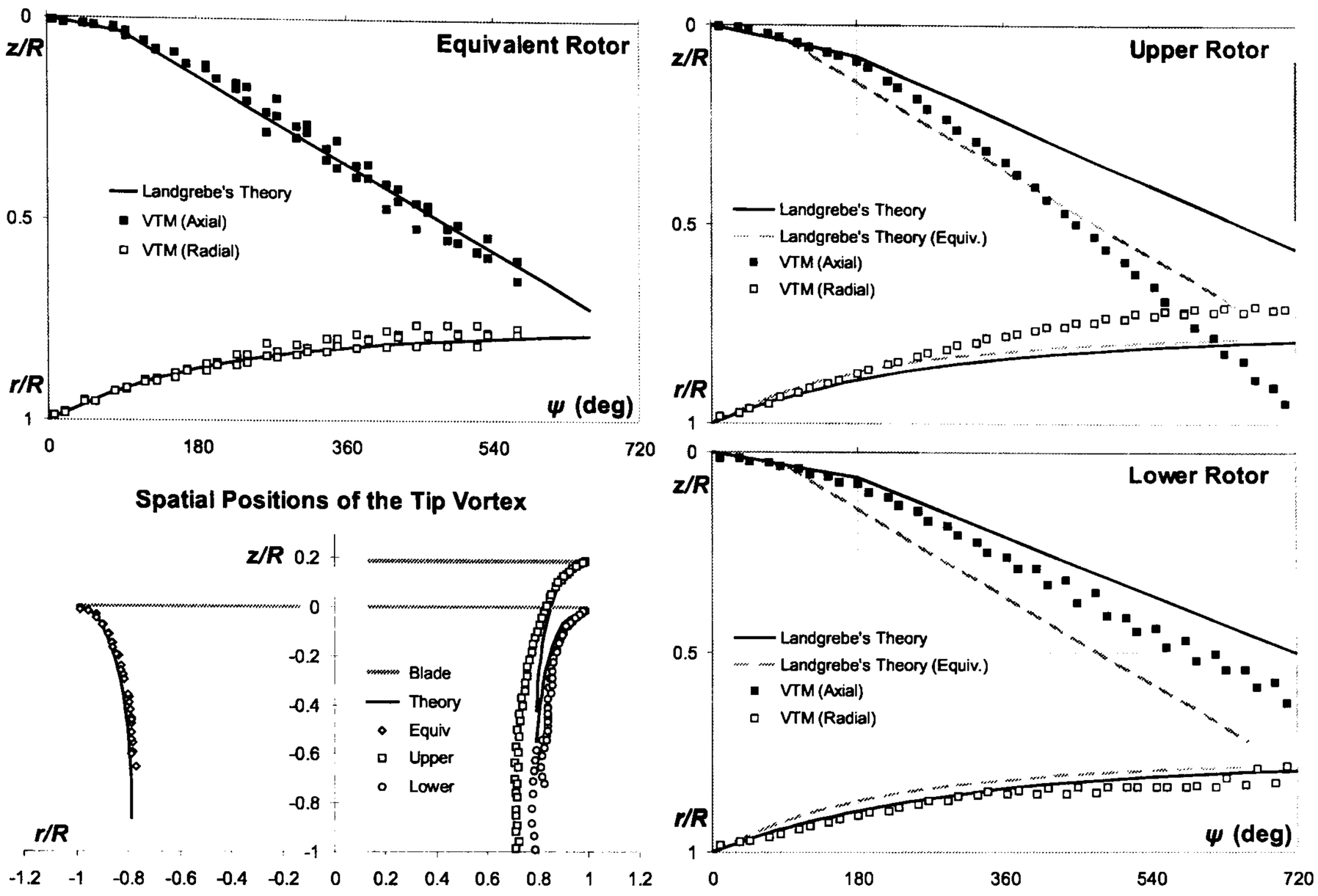
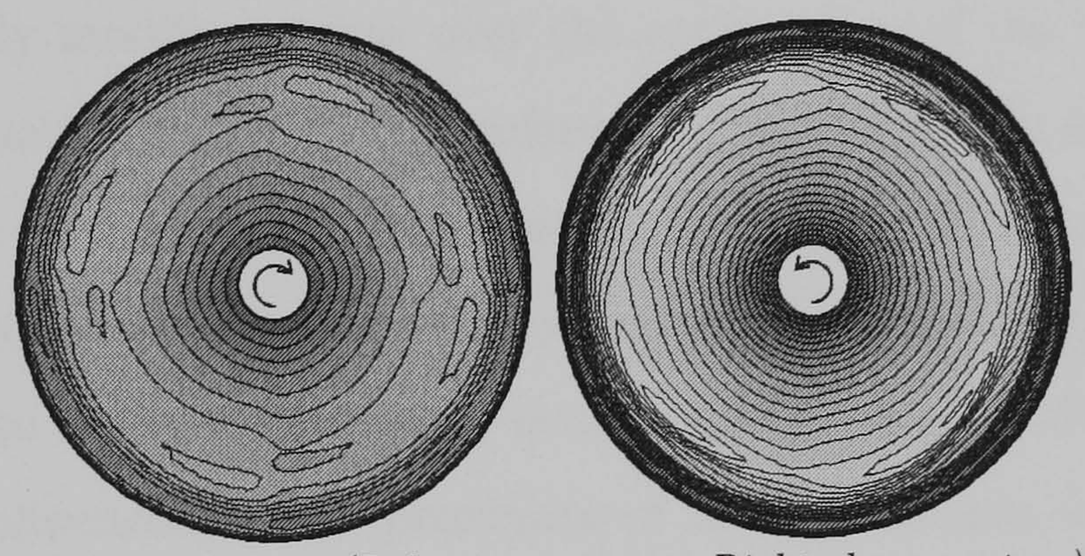


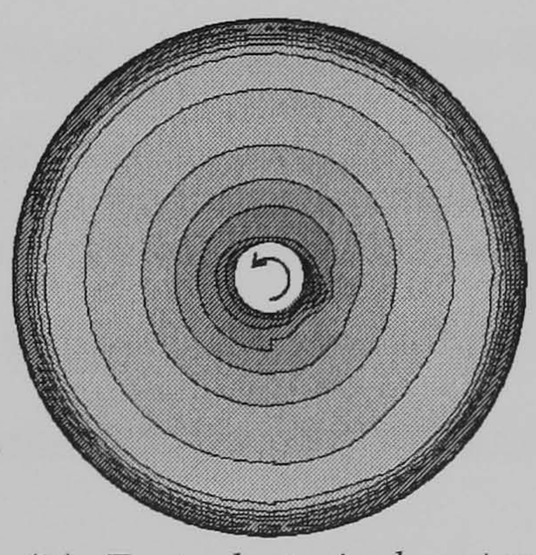
Figure 3.14: *Correlation of relative tip vortex trajectories against Landgrebe's empirical model for the rotors in isolation (C_T = 0.0048).*

greater, and, conversely, for the lower rotor, is smaller, than the axial convection rate of the tip vortices of the equivalent conventional rotor. This observation is consistent with the expected effect of the interaction between the wake structures that are generated by the two rotors of the coaxial system, whereby the convection rate of the vortices from the upper rotor is enhanced by their passage through the region of downwash that is generated by the wake of the lower rotor, and, vice versa, the convection rate of the vortices from the lower rotor is reduced by virtue of their passage through the region of retarded flow lying just outside the wake-tube of the upper rotor. Note though, that the axial descent rate of the tip vortices of both rotors of the coaxial system is increased compared to the rate at which the vortices convect when the rotors operate in isolation, as might be expected as a result of the increased overall thrust, and hence rate of transfer of momentum into the wake, of the combined rotor system. The rate of radial contraction of the tip vortices that are generated by the upper rotor of the

coaxial system is markedly increased compared to that of both the same rotor when operated in isolation and the equivalent conventional rotor. At first glance, the rate of contraction of the tip vortices of the lower rotor, especially when measured in terms of wake age, appears to be largely unaffected by the incorporation of the upper rotor into the coaxial system. However, bearing in mind that the rate of axial convection of the tip vortices from the lower rotor is higher than when operated in isolation, the contraction of the wake tube that is generated by this rotor is seen to be actually slightly less than that expected from an isolated operation. In this context, the relative geometries of the resultant wake tubes of the coaxial and conventional systems are visualised more clearly in the diagram at bottom left in Figure 3.14. Again, these changes in geometry are consistent with the expected form of the mutual interaction between the vortex systems that are generated by the two rotors of the coaxial system.



(a) *Coaxial rotor (Left: upper rotor. Right: lower rotor.)*



(b) *Equivalent single rotor*

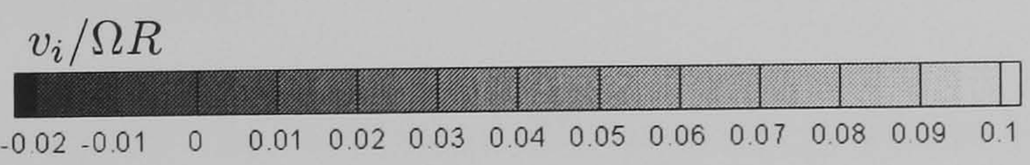


Figure 3.15: *Spanwise inflow distribution experienced by a single blade during one revolution when in hover (Harrington's rotor,* $C_T = 0.0048$*).*

It should be noted that the VTM provides a fully unsteady computation even when only the trimmed state of the rotor is of interest. Figure 3.15 shows the unsteadiness of the aerodynamic environment that is experienced by the blades of the rotors when in hover. The individual plots show the radial distribution of inflow that is experienced by a single blade, during a single rotor revolution, as a polar function of blade azimuth. A sharp peak in inflow on the lower rotor of the coaxial system, induced by the nearby passage of the tip vortices from the upper rotor, is clearly visible at a radius of approximately $0.75R$. The very obvious four-per-revolution character of this inter-rotor blade-vortex interaction is a consequence of the $2N$-per-revolution geometric periodicity of the system. The upper rotor shows a far more benign variation of inflow along the blade span because this interaction is absent. A weaker, secondary, blade overpressure-type interaction results from the direct influence of the bound vorticity of the blades of the top rotor on those of the bottom, and vice versa, and is visible on both rotors as a ridge of slightly modified inflow over the entire span of the blade at 0, 90, 180 and 270 degrees azimuth (i.e. when the reference blade passes by one of the blades on the adjacent rotor). In comparison, the bottom plot, for a blade on the isolated, four-bladed equivalent rotor, shows none of these effects to be present, and the resultant inflow distribution to be relatively steady except near the tips of the blades, where the inflow is strongly influenced by the proximity of the tip vortices that are trailed from the preceding blades of the same rotor. The fluctuation in the inflow is associated with a small variability in the trajectory of these vortices that seems to be induced by the unsteadiness in the wake further downstream as the individual tip vortices coalesce to form the larger, less coherent structures described earlier. A similar, but much weaker, fluctuation in the inflow is predicted near the root of the blade where the effects of a similar unsteadiness in the location of the root vortices is most strongly felt.

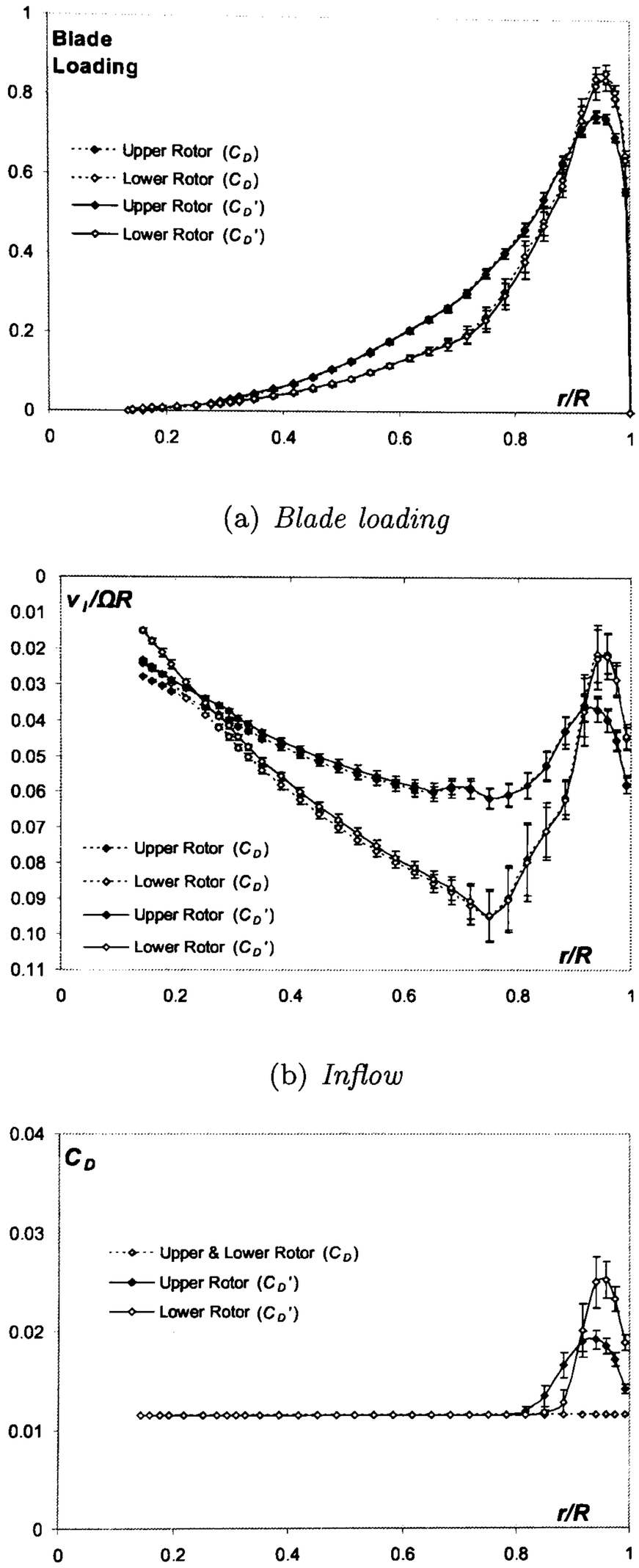
3.3.2 Hover Performance

Figures 3.16 – 3.18 compare the computed distribution of blade loading, inflow, profile drag and sectional power loading along the blades of Harrington's isolated two-bladed rotor, the upper and lower rotors of his coaxial system, and the equivalent four-bladed conventional system to show in detail how aerodynamic interaction between wake and blades subtly modifies the performance of each of the rotor systems. The error bars in

the figures represent the variability in the data over a single rotor revolution even when the rotor is ostensibly in a trimmed flight condition.

Calculations are presented for a representative overall thrust coefficient of 0.005. At this operating condition, the lower rotor is required to generate a thrust coefficient of 0.0022 and the upper rotor a thrust coefficient of 0.0028 to satisfy the zero-torque trim condition when using both C_D and $C_D{}'$ drag model. This operating condition is at a significantly higher thrust than that at which the power predictions obtained using the $C_D{}'$ profile drag model diverge from those obtained using the C_D drag model. Besides the obvious but expected differences in computed profile power, the predictions of the spanwise variations of the other aerodynamic properties of the rotors show very little sensitivity to the drag model that was used. It seems unlikely that this insensitivity is merely a fortuitous consequence of the form of the drag models used in the simulations presented here, supporting the assertion made earlier that the relative performance of coaxial and conventional rotor systems, at least in terms of lift-induced effects, can be compared independently of the profile drag characteristics of the blades.

Figures 3.16(a) – 3.16(f) compare the upper and lower rotors of the coaxial configuration and expose the effect of aerodynamic interactions between the two rotors on the performance of the system. Figure 3.16(b) shows strong distortion of the radial inflow variation along the lower rotor of the coaxial system compared to that along the upper rotor where the distribution of inflow is qualitatively (and quantitatively) not very different from that of one of the rotors of the coaxial configuration tested in isolation at very similar thrust coefficient (Figure 3.17(b)). The difference in loading near the tip of the isolated single rotor, compared to the top rotor of the coaxial system, is entirely consistent with the difference in the tip vortex trajectories of the two systems, as shown earlier, that yields an increased separation between vortex and blade — and hence a reduced effect on the loading on the top rotor of the coaxial system compared to the same rotor when tested in isolation. The distortion of the inflow at the lower rotor, compared to the relatively smooth radial variation on the upper rotor, is a somewhat more direct wake interference effect — the kink in the profile at $r/R \approx 0.75$ matches very closely the position of the intersection between the blades of the lower rotor and the mean trajectory of the tip vortices from the upper rotor. It is interesting that the inflow distribution predicted by the VTM differs quite considerably from the discontin-



(a) *Blade loading*

(b) *Inflow*

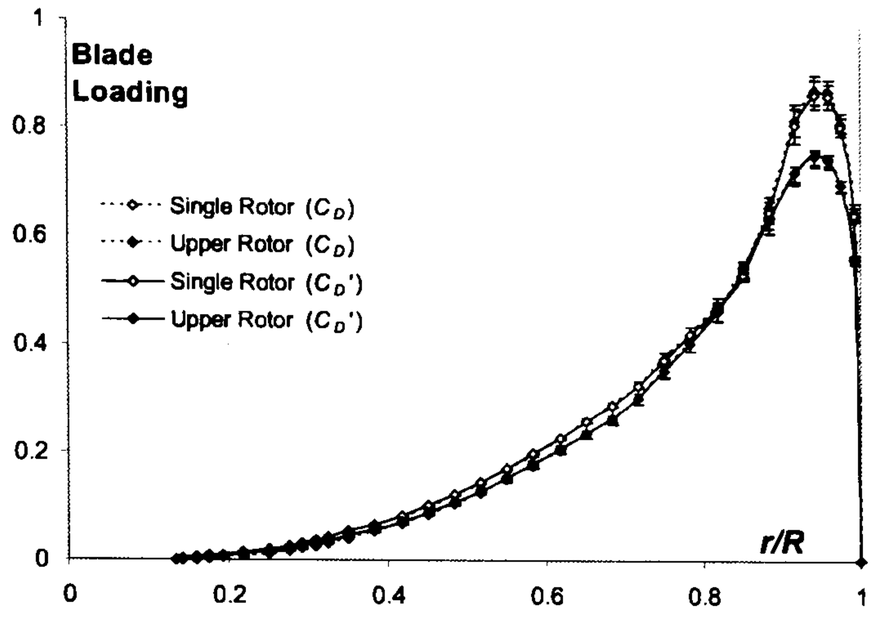
(c) *Profile drag*

(d) *Induced power*

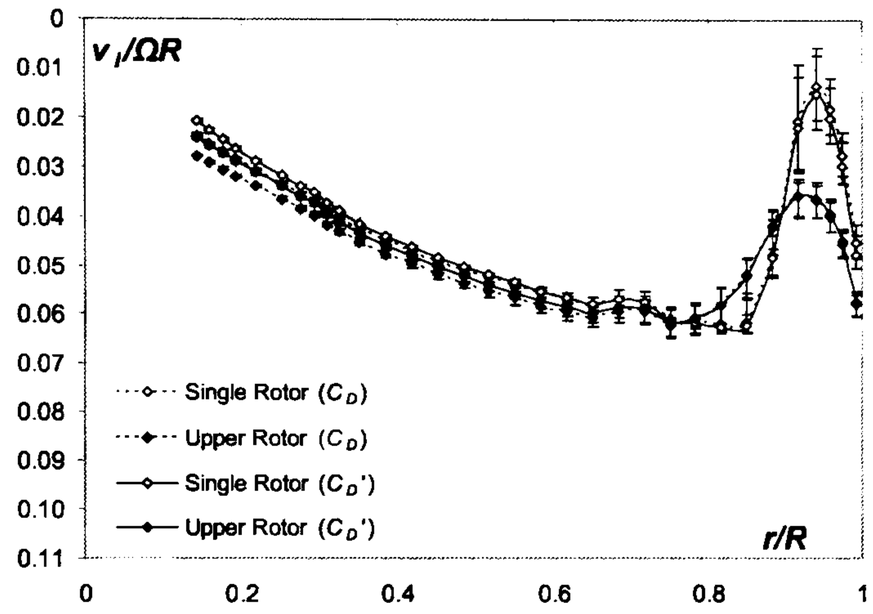
(e) *Profile power*

(f) *Total power*

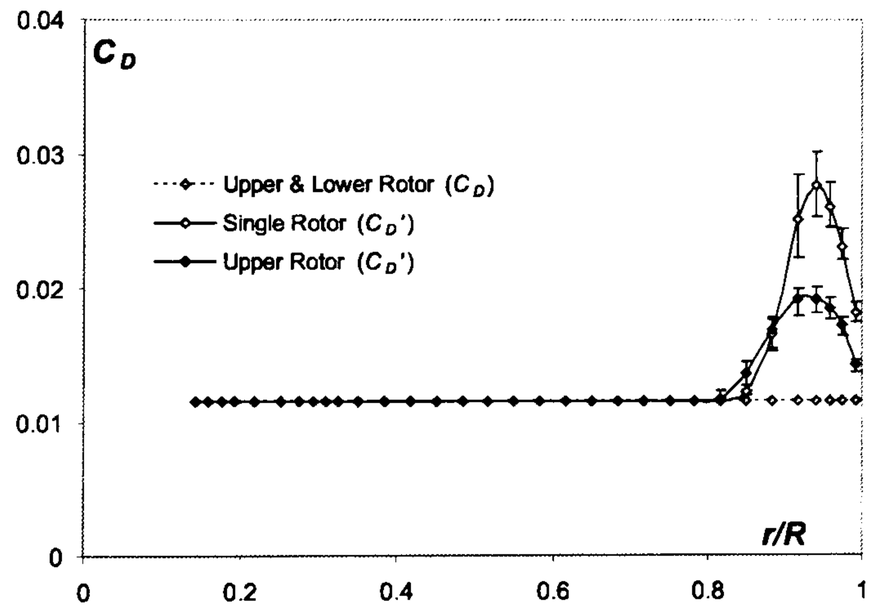
Figure 3.16: *Radial distribution of various parameters: top and bottom rotors of coaxial system compared (overall* $C_T = 0.0050$*).*



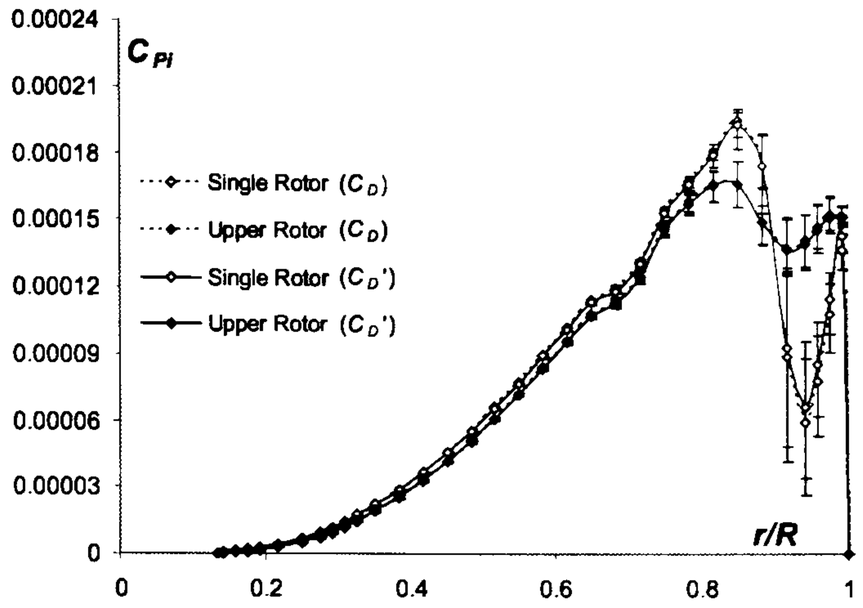
(a) *Blade loading*



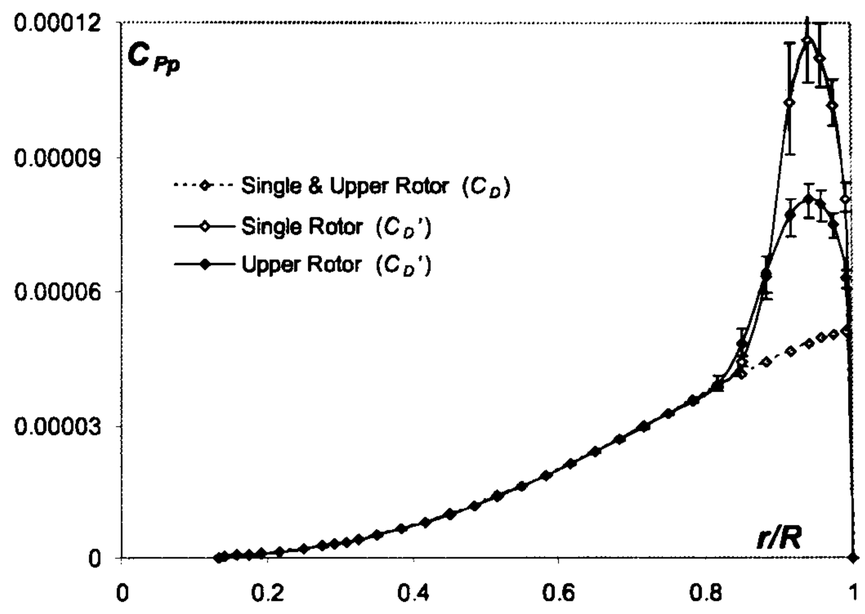
(b) *Inflow*



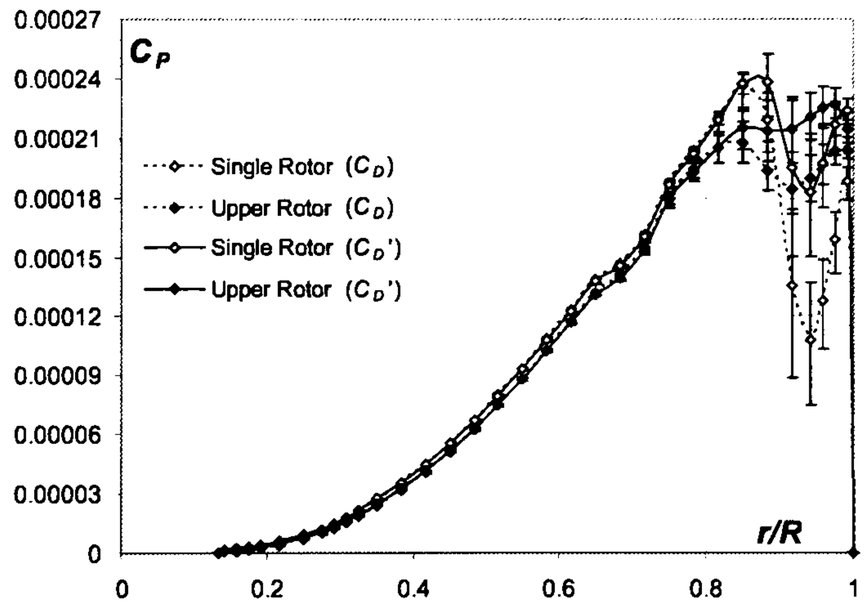
(c) *Profile drag*



(d) *Induced power*

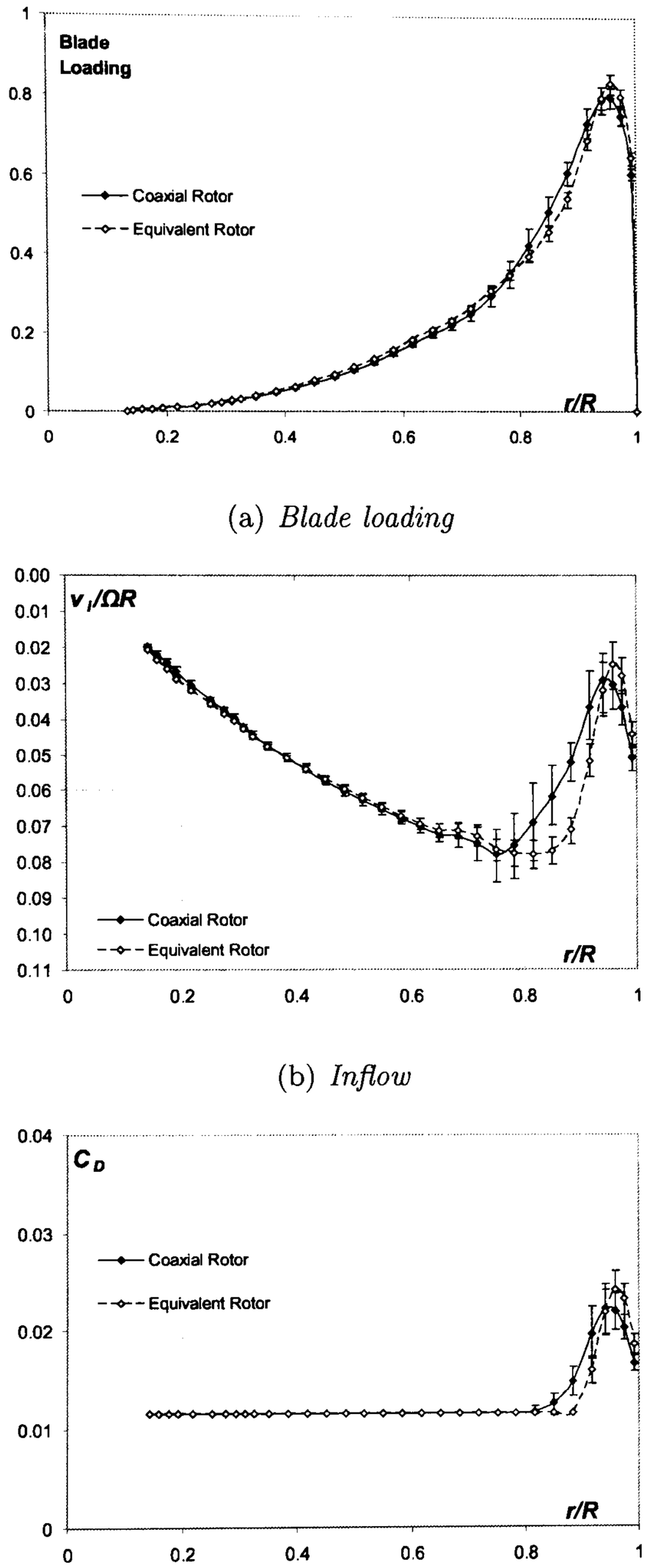


(e) *Profile power*



(f) *Total power*

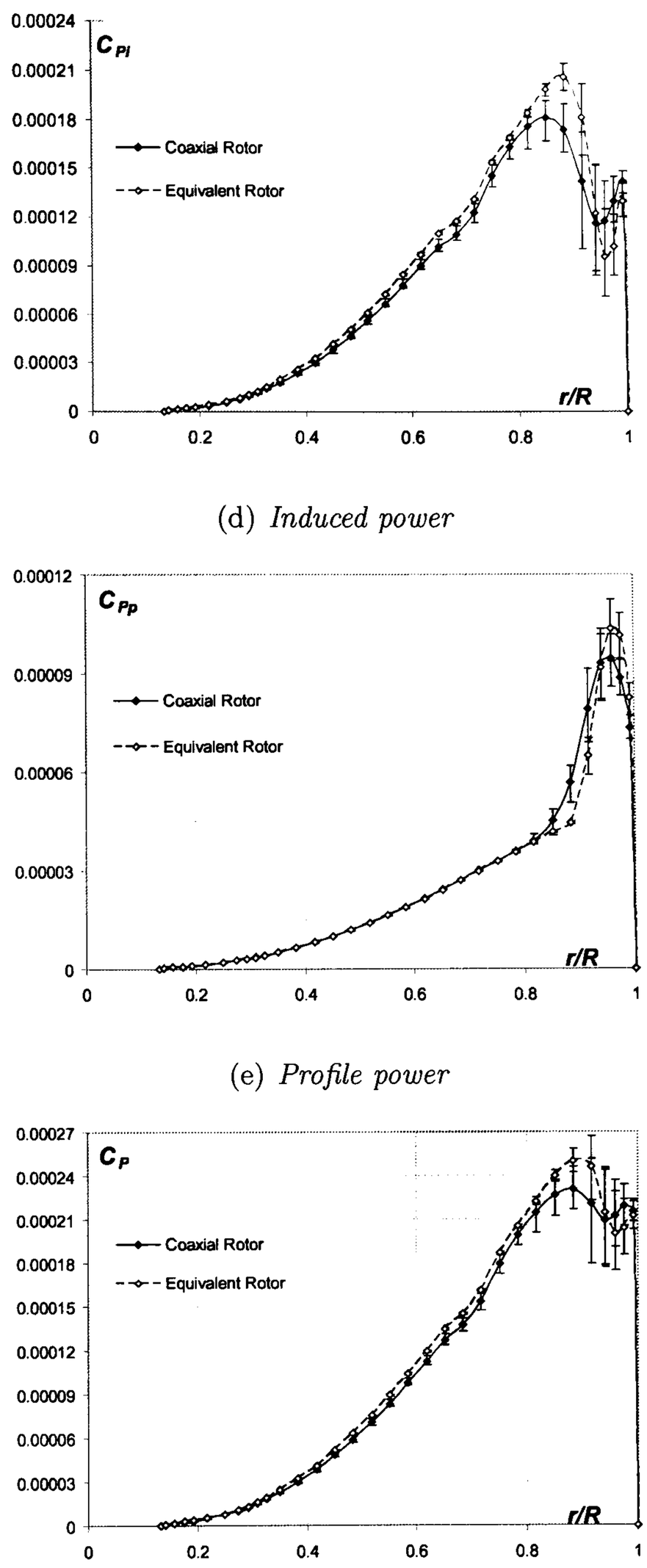
Figure 3.17: *Radial distribution of various parameters: top rotor of coaxial system ($C_T = 0.0028$) compared to the isolated rotor at the same collective pitch setting ($C_T = 0.0030$).*



(a) *Blade loading*

(b) *Inflow*

(c) *Profile drag*



(d) *Induced power*

(e) *Profile power*

(f) *Total power*

Figure 3.18: *Radial distribution of various parameters: coaxial system (upper and lower rotors averaged) compared to the equivalent conventional rotor at the same thrust coefficient* ($C_T = 0.0050$).

uous inflow profile assumed by momentum theory [55] or that predicted by some simpler free wake models that do not contain a representation of the inboard vortex sheet.

Figures 3.17(a) – 3.17(f) compare VTM predictions of the properties of the top rotor of Harrington's configuration when tested as part of the coaxial system and when tested in isolation at the same collective pitch setting. Together with Figures 3.16(a) – 3.16(f), these plots allow the behaviour of each of the two rotors of the coaxial system to be compared against the behaviour of a geometrically identical rotor when operated in isolation. Figure 3.17(b) shows the characteristic sharp peak in the inflow distribution outboard on the rotor that results from the interaction between the blade and its tip vortex. Figure 3.14 shows the separation between the tip vortex and the blade to be somewhat greater for the rotor when part of the coaxial system than when operated in isolation, and the associated reduction in the strength of the interaction explains why this feature of the inflow distribution broadens and reduces in amplitude quite considerably when the rotor is operated as part of the coaxial system. As shown in Figure 3.17(d), this change in the inflow distribution reduces considerably the peak sectional induced power consumption of the rotor when operated as part of the coaxial system rather than in isolation, but at the expense of an almost complete elimination of the sharp reduction in power consumption at the very tip of the blade. Comparing Figures 3.16(d) and 3.17(d) reveals this effect to be subtly present on the lower rotor too, but in this case the influence of the increased pitch of the tip vortices is counteracted to some extent by the full immersion of this rotor in the wake of the coaxial system.

Finally, Figures 3.18(a) – 3.18(f) (obtained by averaging the data for the upper and lower rotors of the coaxial system) compare the composite performance of Harrington's coaxial rotor against the performance of the equivalent, conventional, four-bladed rotor, and thus enable a direct assessment of the relative benefits of the two systems. Given the demonstrated insensitivity of predictions to the profile drag model that was used, only results obtained using the $C_D{}'$ model are shown. The composite results of the various effects shown in the previous figures on the overall performance of the coaxial system relative to the equivalent conventional rotor are seen clearly in this set of figures. The spanwise variation of blade aerodynamic properties for both rotor configurations is very similar inboard on the blades — significant differences are largely confined to the outer 20% of the blade span where the differences in tip vortex geometry have the

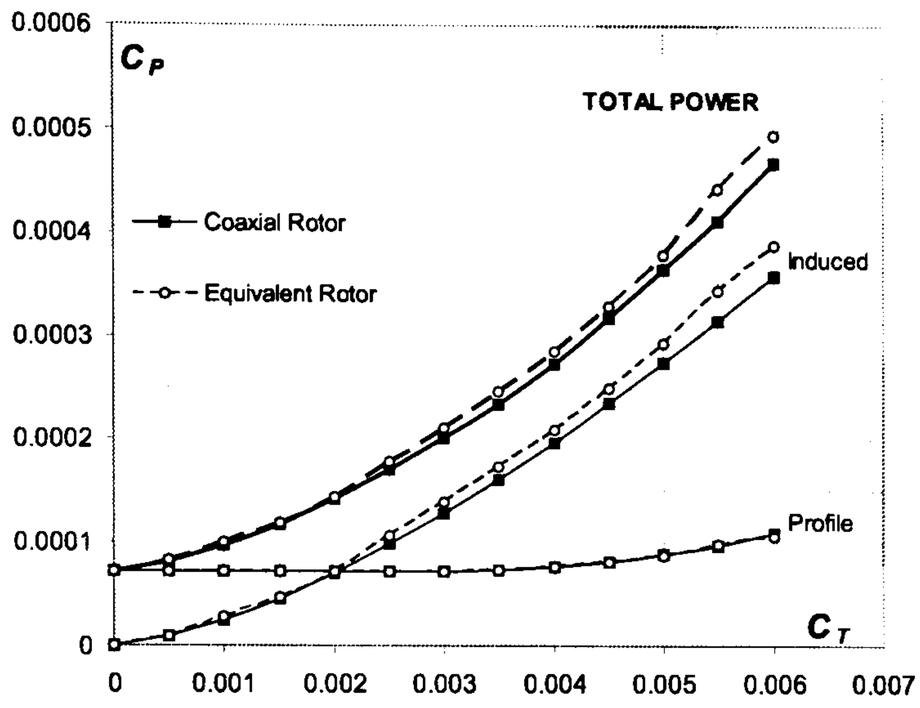


Figure 3.19: *Overall power and its constituents in hover.*

strongest effect on the distribution of aerodynamic loads on both upper and lower rotors. Most significant is the contribution of the interaction between the wake and blades, principally of the upper rotor, to a marked reduction in the induced power consumed between about 80% and 95% of the blade span of the coaxial system compared to the equivalent conventional system. This effect is the major contributor to the clear advantage, revealed in Figure 3.19, that the coaxial system possesses over the equivalent conventional system in terms of its induced power consumption.

3.4 Steady Forward Flight

In level flight, cyclic pitch inputs are used to tilt the rotor tip-path plane, and hence to provide the forward component of the thrust required to overcome the drag of the system. For trimmed flight (with zero net angular acceleration) the moment generated by the aerodynamic forces on the right-hand side of the rotor system needs, at least in the time-averaged sense, to balance that generated by the left-hand side of the system. The poor lifting efficiency of the retreating side of the disc compared to the advancing side implies that the performance of conventional rotors is often limited by the onset of blade stall on the retreating side of the rotor disc at some forward speed. In contra-rotating coaxial systems with rigid rotor hubs, the aerodynamic load distributions on the left and right hand sides of upper and lower rotors can be made to counteract each other's deficiencies and thus to act together to create an overall load balance between

the left and right-hand sides of the system [59]. If the coaxial rotor has an articulated hub, however, as modelled here†, then the rotor flaps, in much the same manner as it does for a single rotor, to create a balance in the aerodynamic loads on each individual rotor. The natural tendency for the tip-path plane to tilt towards the advancing side on both top and bottom rotors cannot be counteracted if the cyclic control of the two rotors is mechanically interconnected, as it usually is in most practical implementations of the coaxial system. Thus, the possibility that the blades on the lower rotor might strike those on the upper rotor at some critical forward speed limits the minimum separation between the rotors of a coaxial system. Similarly, backwards tilt of one of the rotors following blade stall on the retreating side of one of the rotors carries with it the risk of blade strike either at the front or rear of the system depending on which rotor stalls first. The following section of the chapter investigates the effect of the rotor wake geometry, and the resultant interaction between the rotors, on the relative performance of coaxial and equivalent conventional rotors in steady, level flight.

3.4.1 Forward Flight Performance

Figure 3.20 shows the VTM-predicted variation with advance ratio of the various components of the power required by Dingeldein's coaxial rotor and its equivalent four-bladed conventional rotor. This form of presentation of the data shows the profile contribution to the power required by both systems to be almost identical at all forward flight speeds. The figure thus suggests that the difference in power consumption between the coaxial and equivalent systems is almost solely due to a reduction in the induced power required by the coaxial rotor compared to that required by the equivalent system. This effect is indeed seen for all advance ratios, but the major effect is in the pre-transitional regime ($\mu < 0.1$) where, for instance, a reduction of approximately 14% in the induced power required by the coaxial rotor, compared to the equivalent rotor, is predicted at an advance ratio $\mu = 0.08$. At higher advance ratios, the induced power consumption of both rotor systems converges to a very similar value.

---

†Those systems with significant hub stiffness, such as Sikorsky's ABC concept, are analysed in Chapter 4.

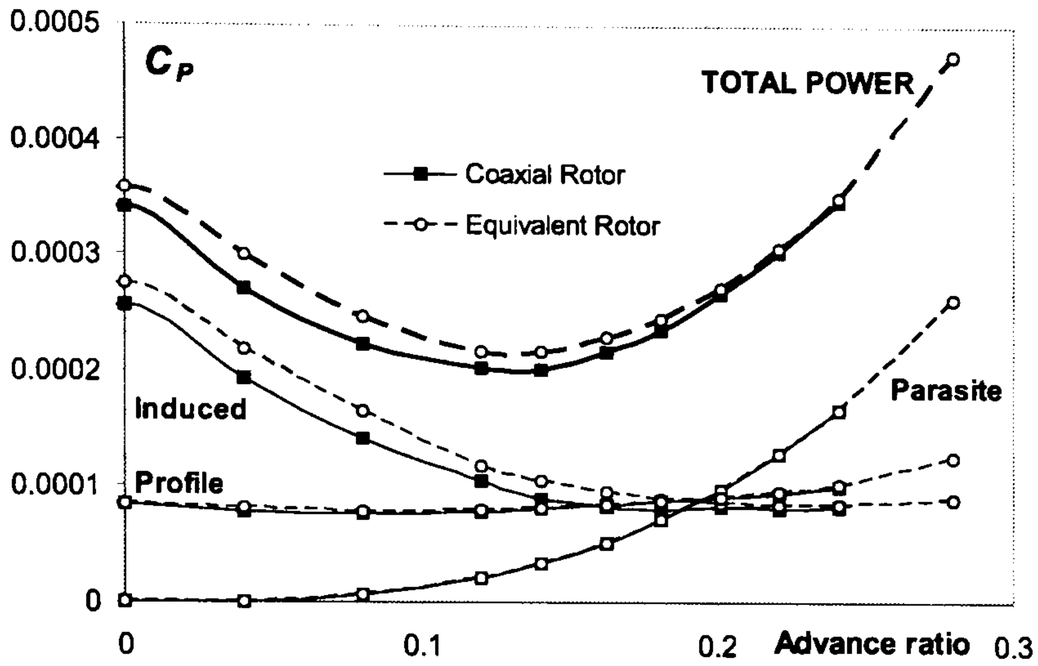
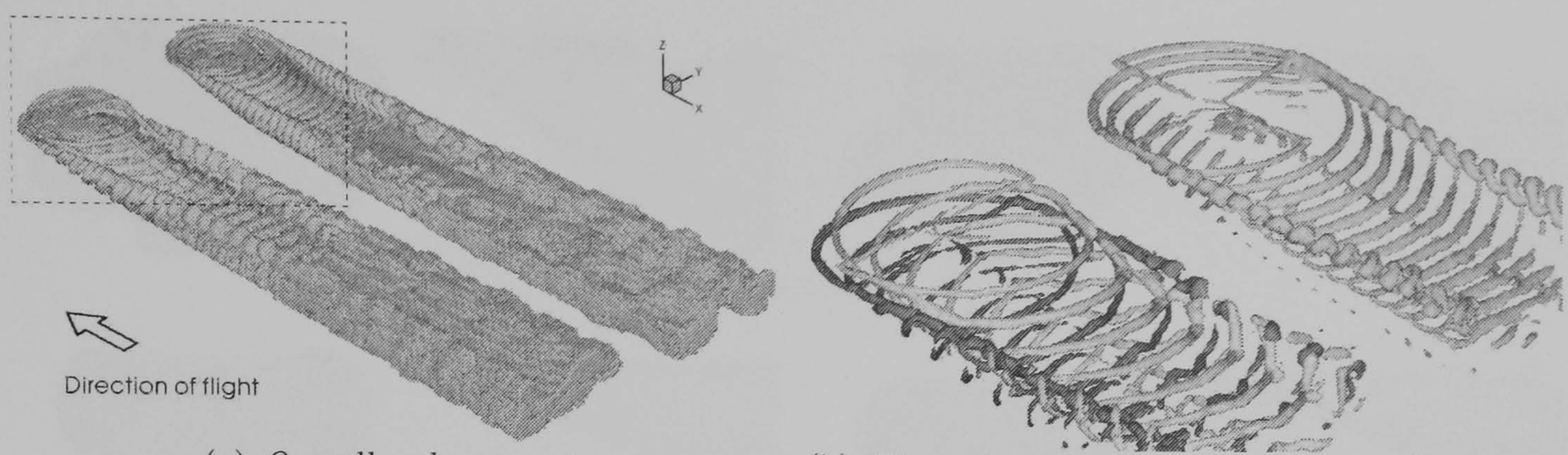


Figure 3.20: *Overall power and its constituents in steady level flight (C_T = 0.0048).*

3.4.2 Wake Geometry in Forward Flight

Figure 3.21 compares the basic features of the overall wake structures generated by Dingeldein's coaxial rotor and its equivalent four-bladed conventional rotor. In this figure, the VTM-computed wake, generated by the coaxial rotor at an advance ratio of 0.12 and a thrust coefficient of 0.0048, is visualised by plotting a surface in the flow on which the vorticity has constant strength. This figure illustrates well the use of nested grids within the VTM — the rotor diameter is resolved across eighty computational cells by the grid in which it is contained, but this cell size is doubled, then doubled again, downstream to reduce the resolution of the wake far from the rotor (where the wake has less direct influence on rotor performance) and hence to keep the computational requirements of the simulation within reasonable limits.

Figure 3.21(a) represents a surface of low enough vorticity magnitude to reveal the overall geometry of the wakes of the two systems. The gross features of the far wakes of both configurations are superficially very similar at this advance ratio: both wakes clearly show the helicoidal individual blade vortices to roll up to form a pair of large 'super-vortices' some distance downstream of the rotor disc. Figure 3.21(b) focuses on the flow near to the rotor, and represents a surface of high enough vorticity strength to expose the detailed geometry of the tip vortices of the rotors. This figure reveals the presence of interactional aerodynamic features in the coaxial system that are not found on the conventional rotor. In particular, the complex manner in which the tip



(a) *Overall wake geometry*

(b) *Tip vortex geometry (coaxial rotor: lower rotor vortices shaded darker than upper)*

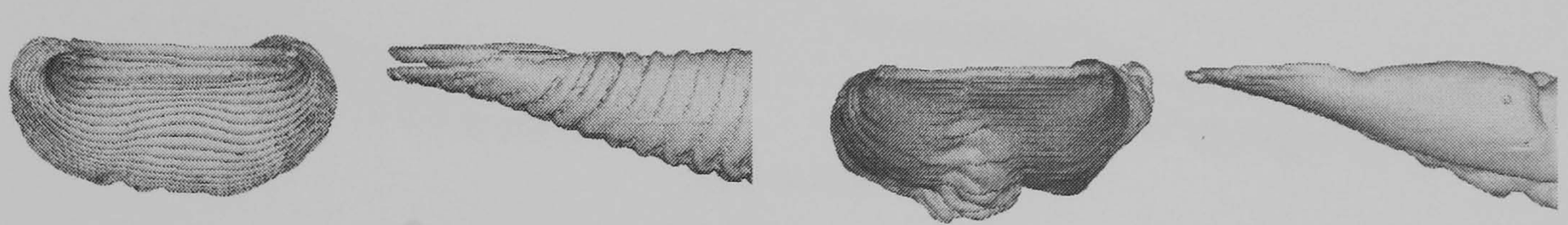
Figure 3.21: *Wake structure of coaxial rotor (left) and equivalent single rotor (right) in forward flight ($\mu = 0.12$).*

vortices from the upper and lower rotors interweave in the gap between the two rotors leads to a complicated pattern of inter-rotor blade-vortex interactions (BVIs) that are obviously not encountered with the conventional system. The tip vortex dynamics during the formation of the super-vortices of the coaxial system is also considerably more complicated than for the conventional rotor. The individual tip vortices from the upper and lower rotors are seen to wind around each other, at least at this advance ratio, to form a single pair of super-vortices rather than, as might be imagined, forming two distinct structures, one for each rotor.

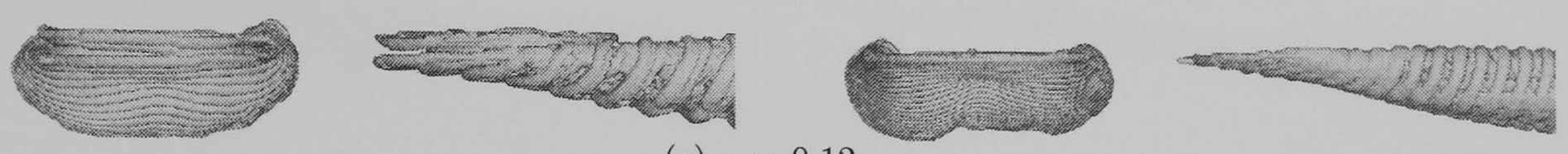
Figures 3.22 and 3.23 show the development of the wake downstream of the two different rotor systems at various forward speeds. Figure 3.22 shows the overall geometry of the wake, visualised by plotting a surface in the flow on which the vorticity has constant strength, while Figure 3.23 reveals the internal structure of the wake by showing a series of contour plots of vorticity magnitude on a longitudinal slice, containing the rotor shaft, through the wake of the system. At all advance ratios, the wake skew angles for the coaxial system and the equivalent single rotor are comparable, and the figure shows the transition of the wakes of both systems from their tubular, skewed but still essentially hover-like structure at low advance ratio, to a flattened, aeroplane-like geometry at higher advance ratio. This transition is counteracted at high advance ratio, to some extent, by the forward tilt of the rotor that acts to maintain the tubular structure of the wake. At low advance ratio the wake does not roll up to form the stable, well-structured super-vortices seen at higher forward speeds. Instead, the individual



(a) $\mu = 0.04$



(b) $\mu = 0.08$



(c) $\mu = 0.12$

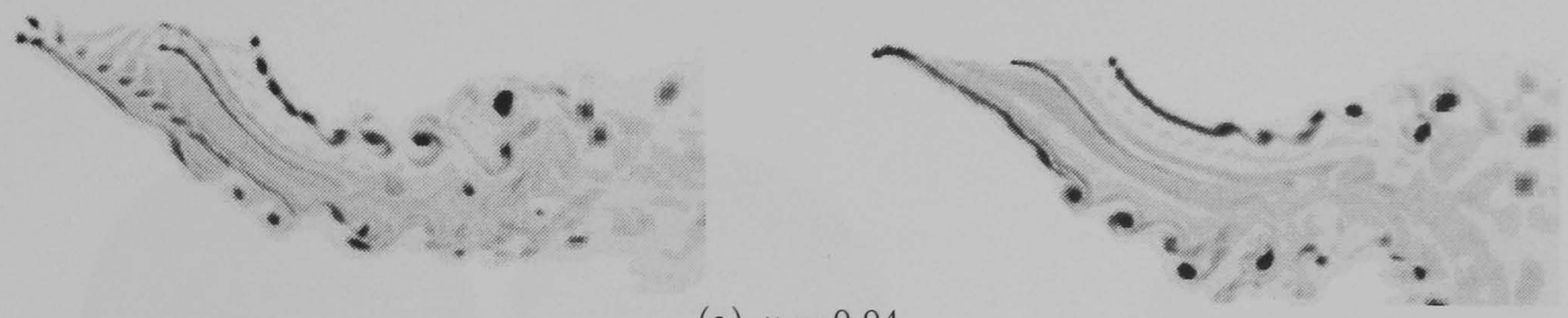


(d) $\mu = 0.24$

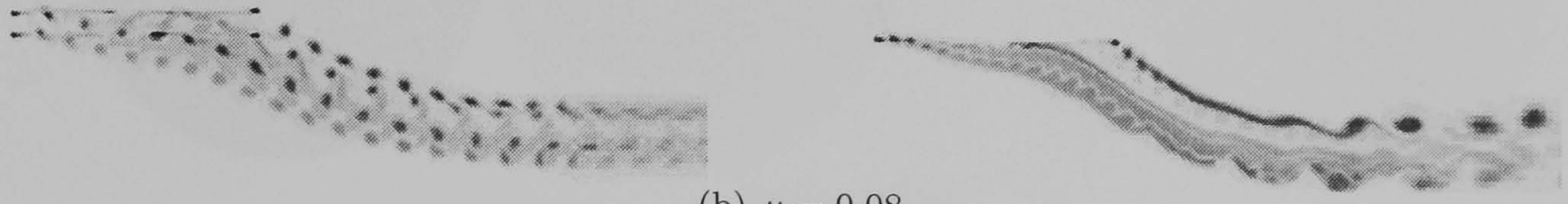
Figure 3.22: *Wake geometry in steady, level flight. (Left: coaxial rotor. Right: equivalent single rotor.)*

wakes from each of the blades interact in an unsteady process that involves the co-orbiting and eventual pairing of nearby tip vortices to form larger vortical structures further downstream in the wake, in much the same fashion as in hover. Interestingly, the coaxial rotor appears to produce a more structured wake downstream of the system than the equivalent conventional rotor does at the same advance ratio. This is particularly noticeable at forward speeds below $\mu = 0.08$. In Refs. 60 and 61, it was argued that the rate of development of perturbations to the ordered, helicoidal structure of the wake should be greater the more closely spaced the individual vortices within the wake. Even though both rotors have the same overall number of blades, the advantage, in terms of wake stability, of the coaxial rotor in producing two, albeit closely-spaced, streams of tip vortices with effectively twice the spacing between vortices of the equivalent rotor, is clearly evident. Whether this effect turns out to have a significant practical benefit, for instance in terms of its influence on tail-shake or other types of rotor-fuselage interference, remains to be shown.

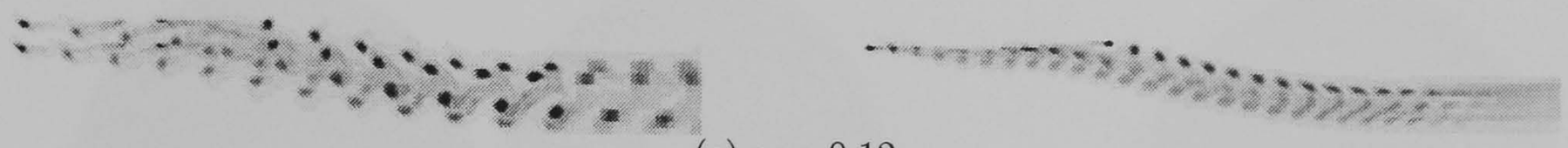
Figure 3.24 illustrates the corresponding changes in character of the interaction



(a) $\mu = 0.04$



(b) $\mu = 0.08$



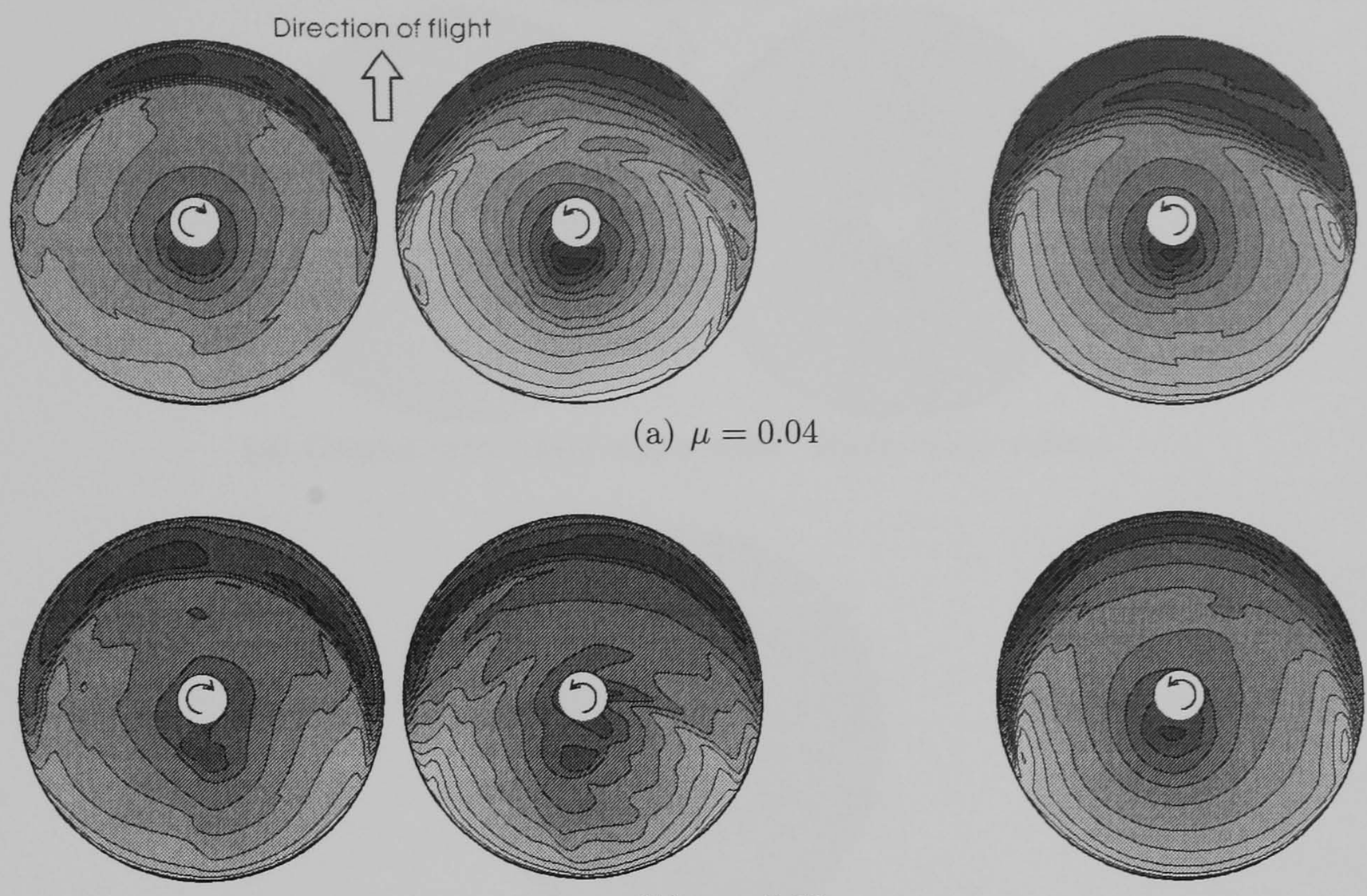
(c) $\mu = 0.12$



(d) $\mu = 0.24$

Figure 3.23: *Internal wake structure in steady, level flight. (Left: coaxial rotor. Right: equivalent single rotor.)*

between the upper and lower rotors of the coaxial system as the forward speed of the rotor is increased. In this sequence of diagrams, the spanwise distribution of inflow experienced by a single blade, during a single rotor revolution, is plotted as a polar function of blade azimuth. Figure 3.15 showed the almost axially symmetric distribution of inflow on both rotors when in hover, but this symmetry is destroyed in forward flight as a result of the skew of the rotor wake. At the lowest forward speeds, a prominent ridge is created in the inflow experienced by the blades of both the upper and the lower rotor as they traverse the forward half of their respective discs. This, and a series of weaker ridges further aft on the disc, results from intra-rotor BVI where the blades interact with the tip vortices trailed from blades on the same rotor. These features weaken as the forward speed of the system is increased and the rotors tilt forward to provide an increasing propulsive component of thrust. Figure 3.23 shows that the tip vortices from the upper rotor pass through the plane of the lower rotor at all forward speeds. The interaction of these vortices with the lower rotor is seen in Figure 3.24 as a second series of ridges in the inflow on the advancing side and rear of the lower disc



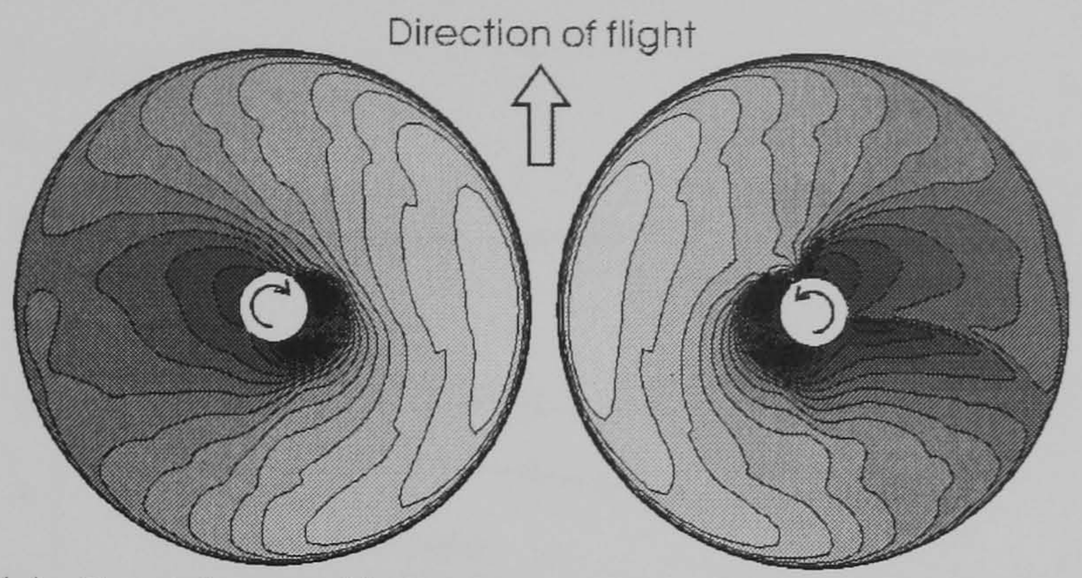
(a) $\mu = 0.04$

(b) $\mu = 0.08$

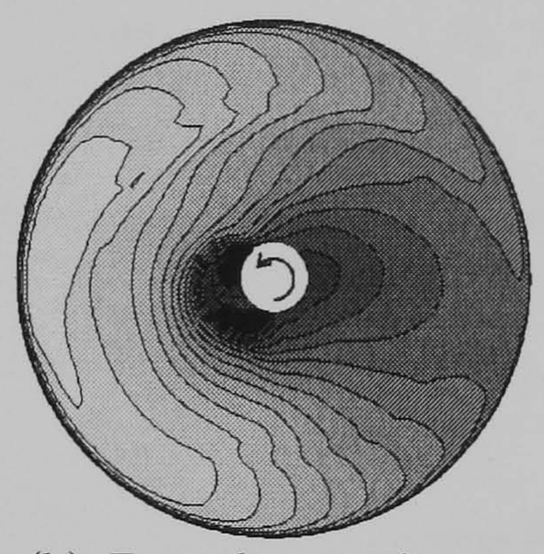
(c) $\mu = 0.12$

(d) $\mu = 0.24$

Figure 3.24: *Spanwise inflow variation experienced by a single blade during one revolution at various advance ratios. (Far left: upper rotor of coaxial system. Left: lower rotor of coaxial system. Right: equivalent single rotor.)*



(a) *Coaxial rotor (Left: upper rotor. Right: lower rotor.)*



(b) *Equivalent single rotor*

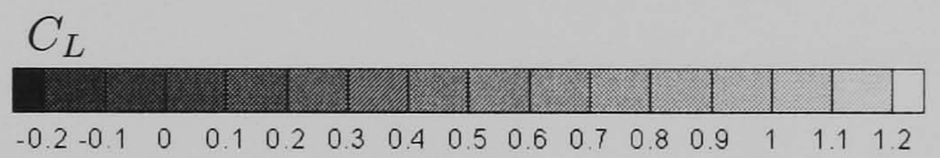


Figure 3.25: *Spanwise variation of lift coefficient experienced by a single blade during one revolution at advance ratio* $\mu = 0.24$.

that are interdigitated with the intra-rotor BVIs. Compared to the intra-rotor BVIs, these inter-rotor BVIs are persistent, and, as forward speed is increased, the primary inter-rotor BVI becomes the predominant feature of the inflow on the advancing side of the lower rotor.

Figure 3.25 shows how the inflow at high advance ratio results in a load distribution on the bottom rotor that, apart from some features on the advancing side, bears a more than superficial resemblance to the mirror image of the loading on the top rotor. This figure thus illustrates well how each individual rotor of a coaxial system with articulated hubs maintains its own individual load balance through blade flapping. The effect of forward speed on the control inputs that are required to trim the rotor are shown in Figure 3.26, while the adverse consequences of mechanical interlink between the cyclic controls of the two rotors are revealed in Figure 3.27. In this figure the separation between the tips of the blades of the upper and lower rotors is plotted against

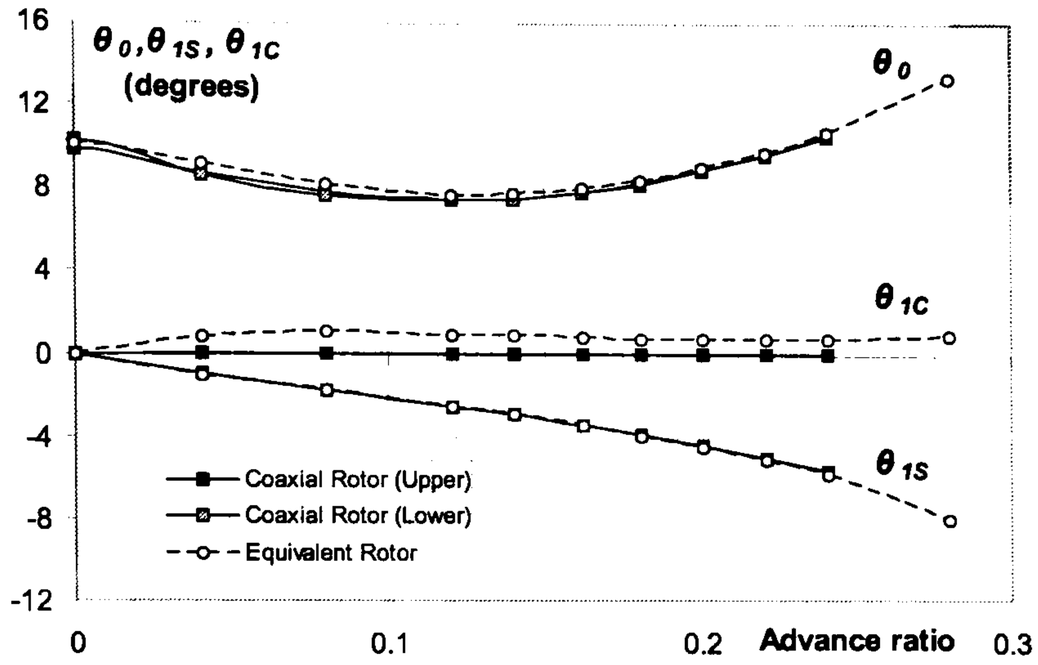


Figure 3.26: *Control angles required for trim in steady level flight.*

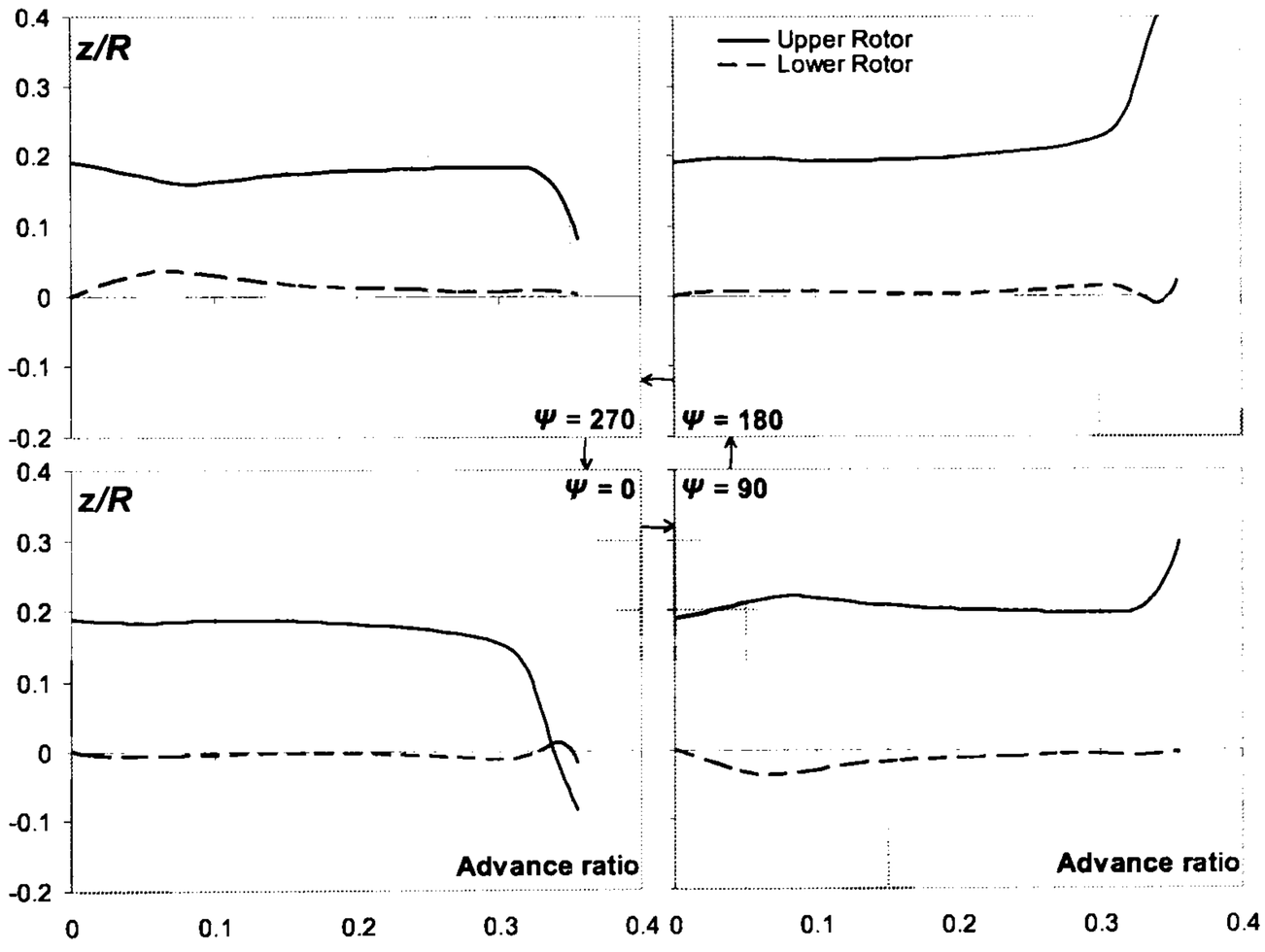


Figure 3.27: *Vertical clearance between the blade tips of the coaxial rotor in steady, level flight. (Azimuth defined with respect to the lower rotor.)*

advance ratio at each of the four azimuthal positions (with respect to the lower rotor) at which blade strike might possibly occur in a twin, two-bladed coaxial system (i.e. those azimuths at which the blades from the lower rotor pass directly underneath the blades of the upper rotor). Recalling that the separation between the upper and lower hubs is

$0.19R$, the tip clearance at the front and back of the rotor remains more or less constant throughout the flight envelope. The mechanical interlink between the two rotors does not allow independent control of the lateral cyclic inputs to the rotors, though, and the resultant lateral flapping towards the advancing side of both rotors reduces significantly the vertical separation between the two rotors at 270° azimuth (defined with respect to the lower rotor). This effect is particularly marked at pre-transitional advance ratios, although, for the rotor as operated, there was never any danger of blade-strike. Similar variations of blade clearance with advance ratio are observed in flight tests of full-scale coaxial systems with articulated rotors and mechanical cyclic interlink [3]. Note that the computational results extend to forward speeds beyond the maximum advance ratio that was tested in Dingeldein's experiments. The onset of blade stall on the retreating sides of both discs results in extreme longitudinal blade flapping. In this case a sudden reduction in clearance between the rotors at high advance ratio is precipitated by the dynamics of the upper rotor which stalls earlier and more abruptly than the lower rotor yielding the definite possibility of blade strike at the back of the rotor beyond an advance ratio of approximately 0.33.

3.5 Manoeuvring Flight

Proponents of the coaxial rotor system claim that higher levels of manoeuvrability can be achieved than with conventional systems (see Chapter 1). This section of the chapter explores the relative advantages and disadvantages of the coaxial rotor configuration over the equivalent single rotor in manoeuvring flight that arise from the particular aerodynamic characteristics of the system. VTM calculations of the performance of a coaxial system in a coordinated turn are presented and compared against similar calculations of the performance of an equivalent conventional rotor with equal solidity and the same number and design of blades as the coaxial system. For consistency with the earlier analysis presented in Sections 3.3 and 3.4, Harrington and Dingeldein's twin, two-bladed coaxial rotor was used as the basis for comparison.

In addition to the forward component of force required to overcome the fuselage parasite drag, in a trimmed, coordinated, level turn, the rotor is required to produce a lateral force to provide the necessary centripetal acceleration. For a rotor with no hinge

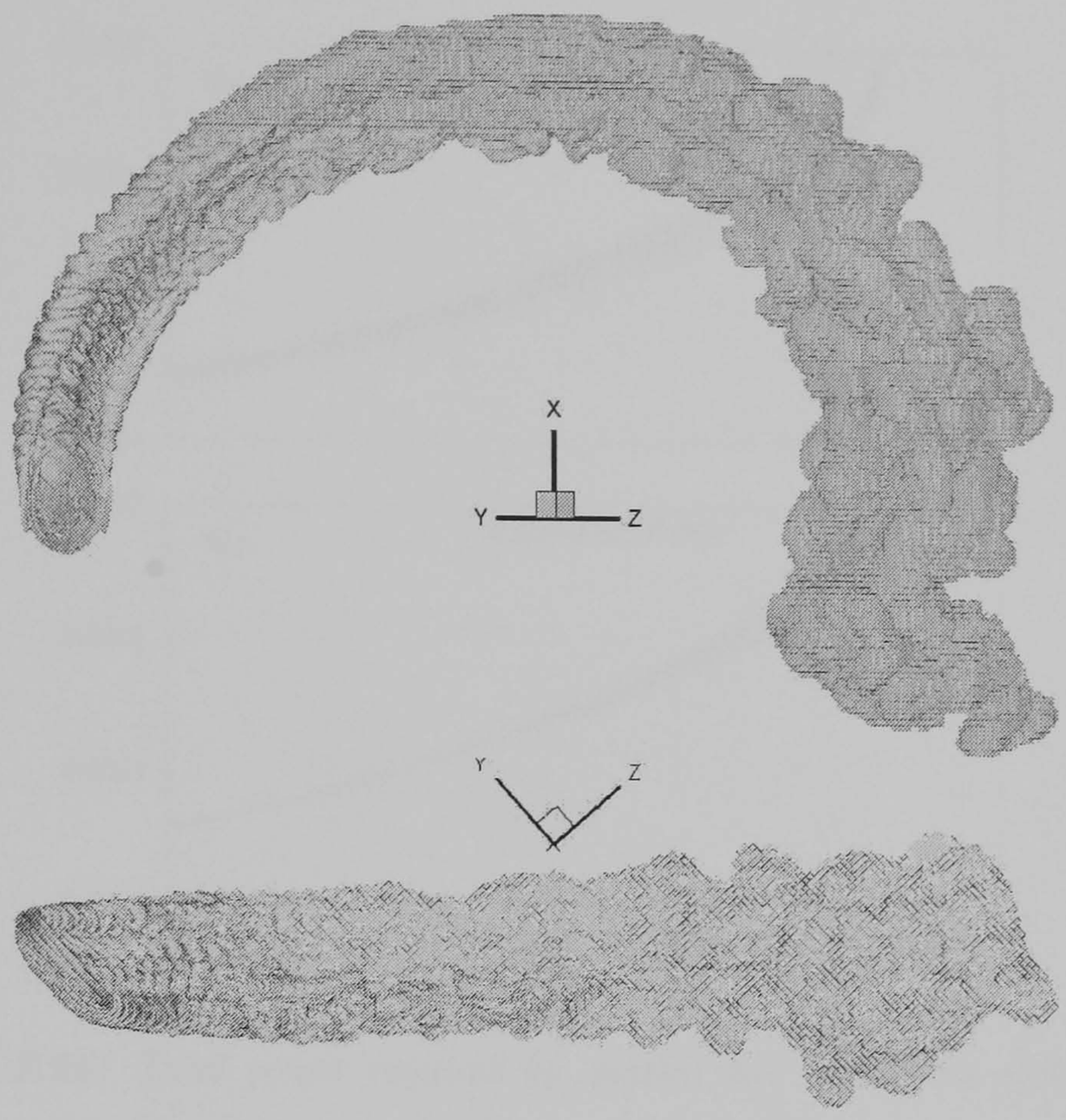


Figure 3.28: *Wake of a coaxial rotor in a coordinated, level, left-hand turn at load factor 1.50. (Top: Top view. Bottom: Front view)*

offset, the equilibrium lateral shaft inclination $\gamma = \cos^{-1}\left(\frac{1}{n}\right)$, to first approximation, where the load factor n is defined as the ratio of the rotor thrust required during the manoeuvre to the rotor thrust during steady level flight. In a coordinated turn, there is no lateral component of the rotor thrust with respect to the rotor shaft axes, and the force required to accelerate the rotor in the turn comes solely from the lateral inclination of the rotor disc.

As an example, for a steady level turn with $n = 1.5$ and $\mu = 0.12$, the required lateral shaft inclination is 48.2° and the radius of the resulting turn is approximately $7R$. The wake structure generated by the coaxial rotor in a such turn (with $C_T = 0.0072$ when $n = 1.50$) is shown in Figure 3.28 — the rotor, in a steep left-hand bank, can be seen on the left-hand side of the image. The distortion to the wake geometry as a result of the manoeuvre is clearly evident.

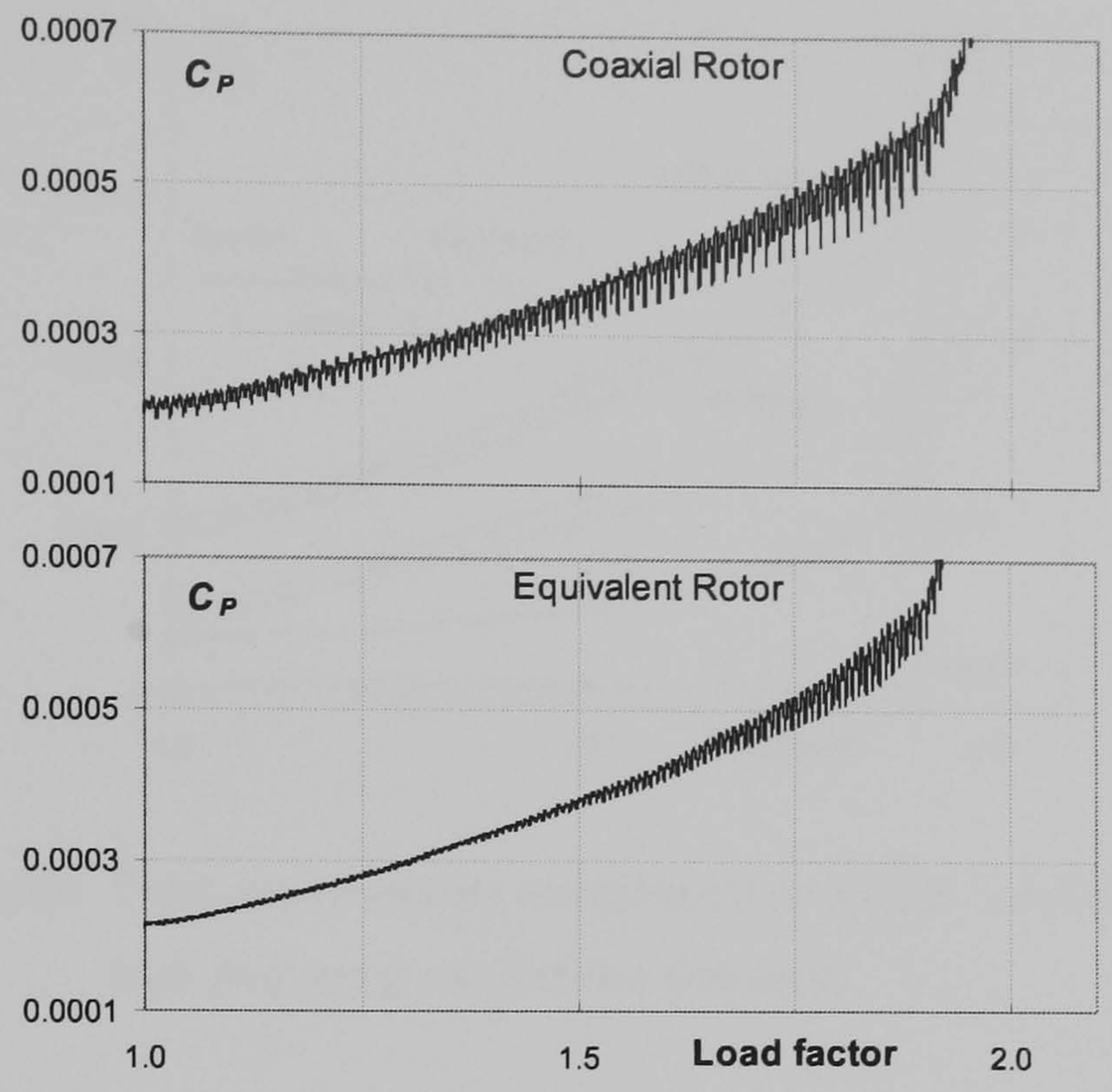


Figure 3.29: *Total power required by coaxial and equivalent systems in a level, wind-up turn.*

3.5.1 Turn Performance

Significant savings in computational time can be achieved by calculating the turn performance of a rotor system in a simulation of the real-world dynamic manoeuvre known as a 'wind-up turn'. In this manoeuvre, the load factor on the rotor is increased steadily with time, rather than being held constant. If the rate of increase of the load factor on the system is kept small enough, then the results should be the same as those obtained in a series of individual tests in turns at constant load factor. Figure 3.29 shows the variation of the VTM-predicted power consumption with increasing load factor, for both the coaxial system and its equivalent conventional rotor, in a coordinated, level wind-up turn to the left. The advance ratio was held constant at 0.12 throughout the simulation and the thrust was set so that, in steady level flight, $C_T = 0.0048$. As in the forward flight simulations of the coaxial rotor, a simple mechanical cyclic control system was modelled by applying the same cyclic control inputs to both rotors and using differential

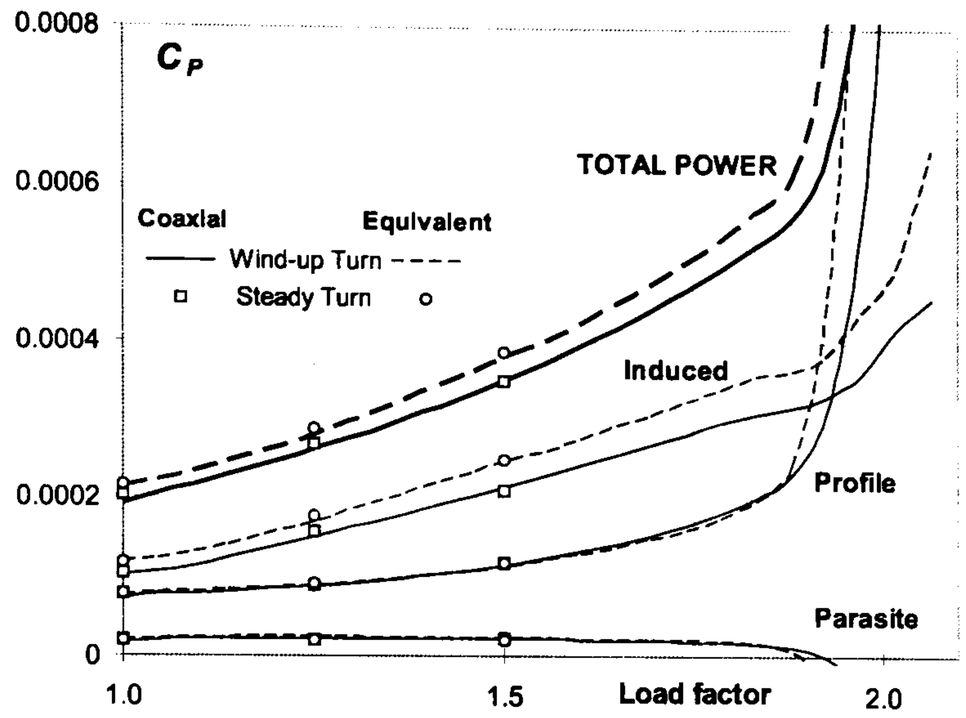


Figure 3.30: *Total power and its constituents in a level, wind-up turn (with high frequency oscillations removed).*

collective to give zero net yawing moment about its shaft[‡].

Figure 3.29 shows the unfiltered time-history of the overall power consumed by both rotor systems during the wind-up turn. Figure 3.30 shows a breakdown of the power into parasite, profile and induced components after filtering to remove all harmonics in the unsteady data at greater than the blade passing frequency. Results from simulations of steady turns at $n = 1.25$ and $n = 1.5$ are also shown to confirm the independence of the results of the unsteady simulation from the effects of the rate of increase of the load factor on the rotor. Although all the data presented here are for a left-hand turn, simulations of steady performance in the equivalent right-hand turn, most interestingly, show a slight increase in power requirement (of about 1.5% for the coaxial rotor and 2.1% for the equivalent system at a load factor of 1.5). The divergence in power that is seen at a load factor of approximately 1.7 is principally confined to the profile component of the power consumption of both rotors, and indicates the onset of blade stall. The slightly earlier rise in the profile power consumption of the conventional rotor suggests that the coaxial system possesses a small (approximately 0.1g) advantage over the equivalent conventional rotor in terms of absolute maximum manoeuvre performance, but the limitations of the model used for the profile drag of the rotor sections need to be

[‡]This is, of course, somewhat of an approximation, since, for instance, it yields a constant-rate turn only in the absence of fuselage aerodynamic moments.

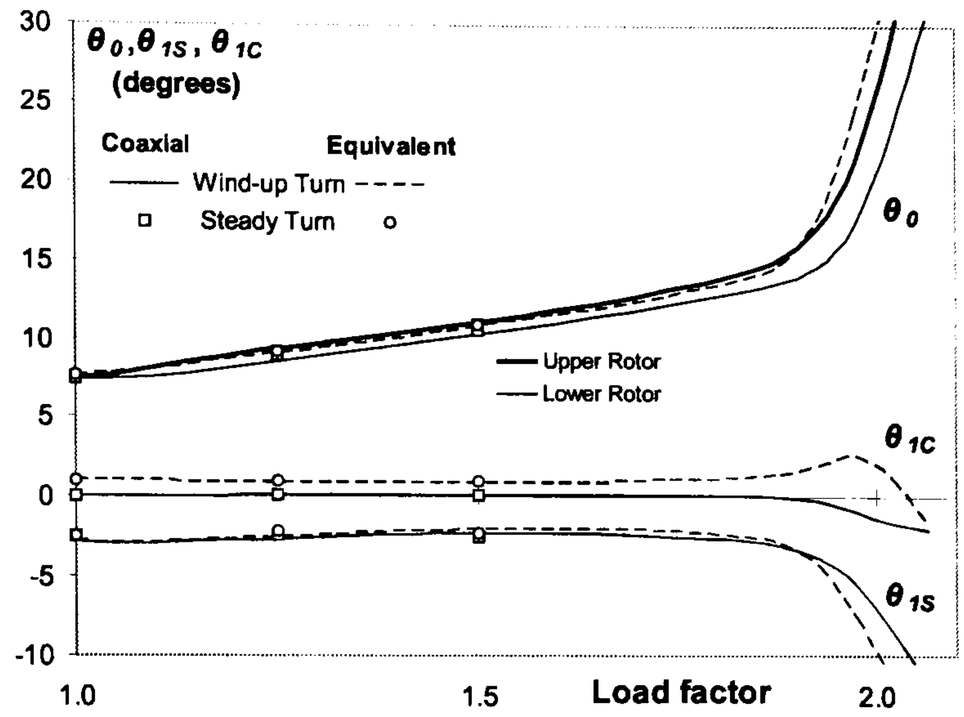


Figure 3.31: *Control angles required in a level, wind-up turn.*

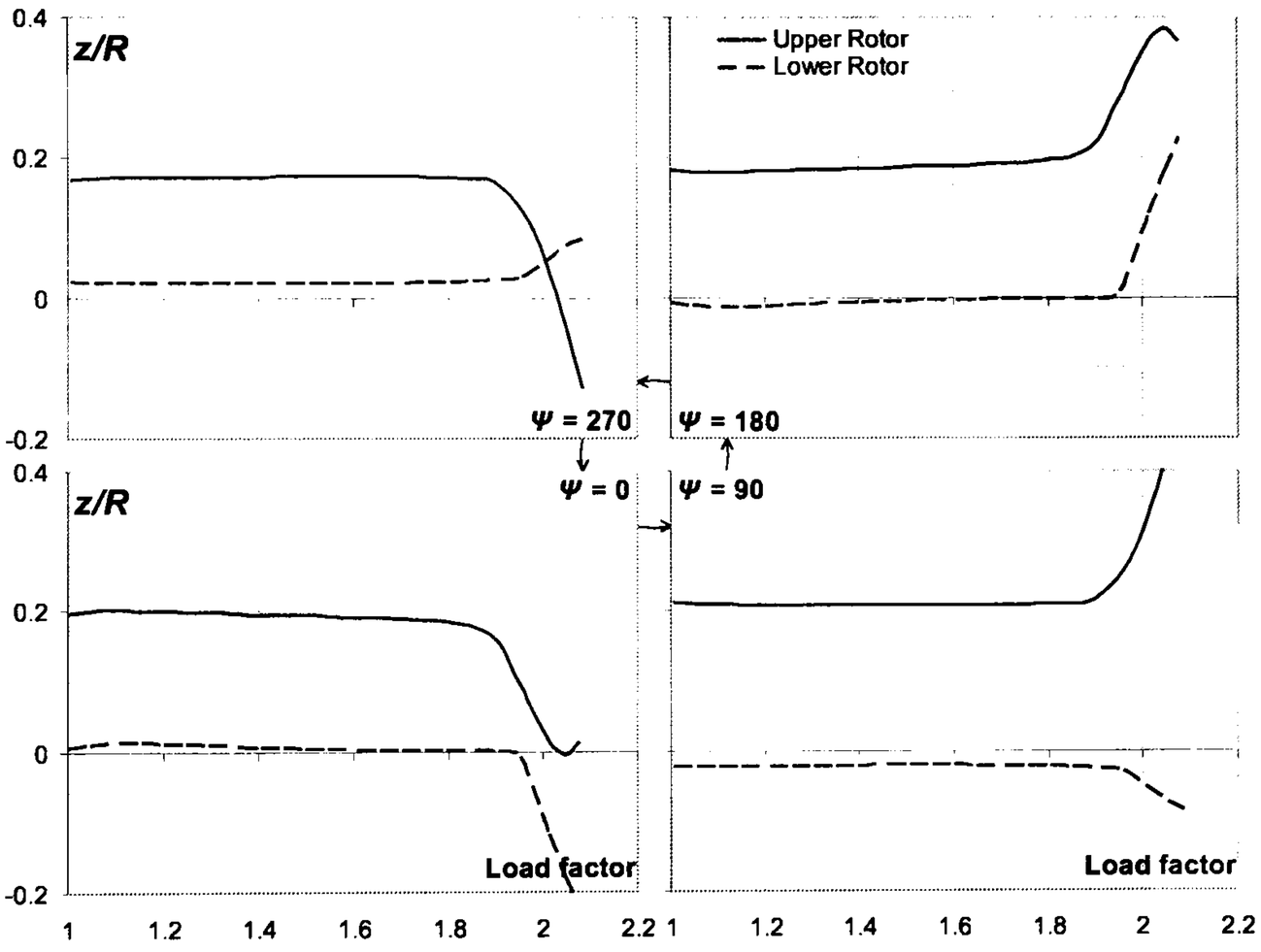


Figure 3.32: *Evolution of the vertical clearance between the blade tips of the coaxial rotor during a wind-up turn. (Azimuth defined with respect to the lower rotor.)*

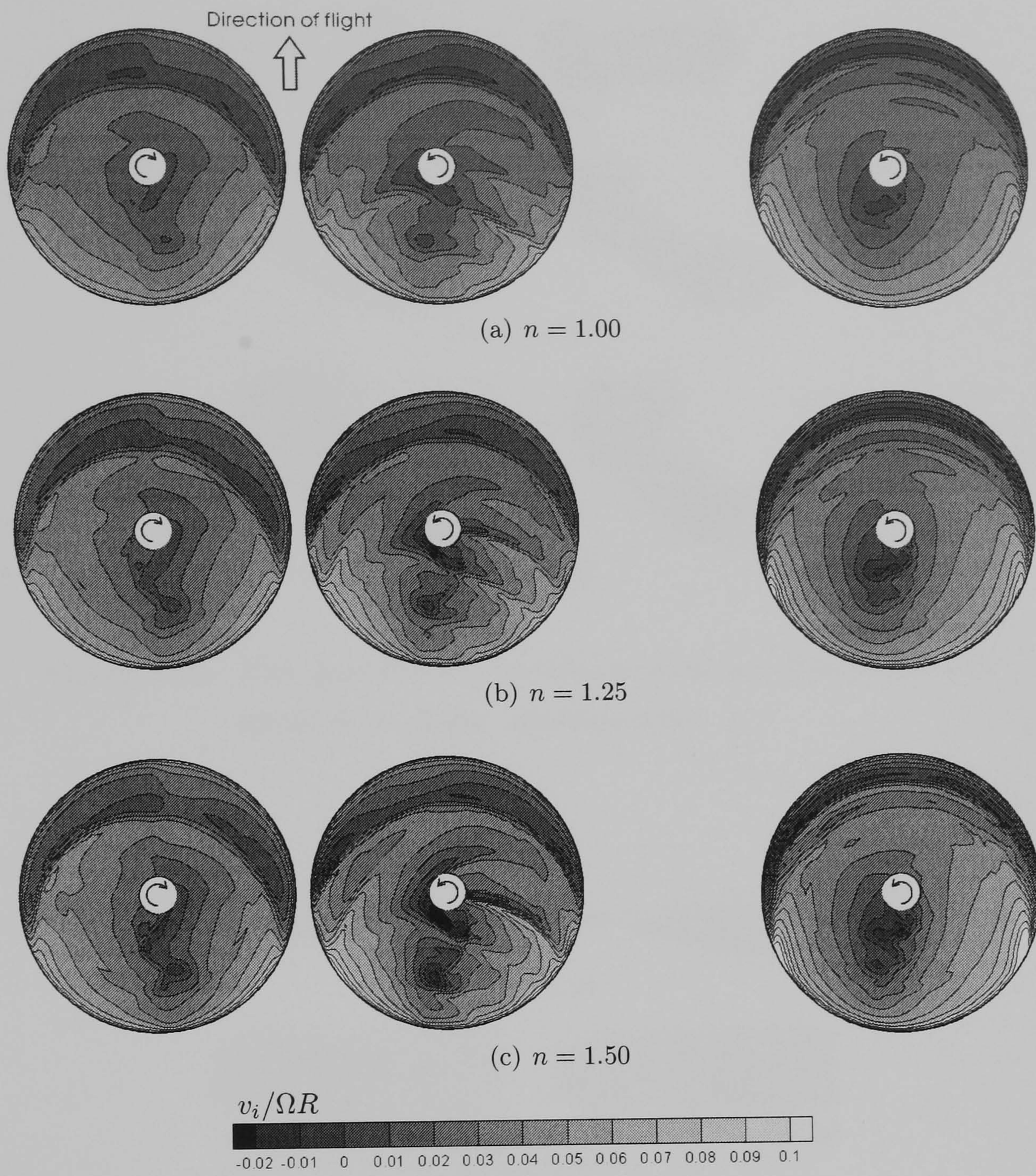
borne in mind before any generalisations can be made to the real world in this respect. On the other hand, the simulations also show a consistent advantage of the coaxial configuration over the conventional system in terms of the power required for the turn

(of approximately 8% compared to the conventional system) at all pre-stall load factors. The almost complete confinement of this effect to the *induced* power predictions of the model suggests that this benefit may indeed be realised in the real-world system. Comparison of the unfiltered response of the two systems, as shown in Figure 3.29, suggests, though, that the improved performance of the coaxial system may come at the cost of significantly higher rotor vibration. A detailed analysis of the high-frequency dynamics of the system is beyond the scope of the present work, however.

The predicted variation of the control inputs with load factor is shown in Figure 3.31. As in the level, forward flight simulations, the principal difference in the control inputs between the two rotor configurations is revealed to be in the lateral cyclic pitch required to trim the systems in the turn. Figure 3.32 shows the clearance between the rotors during the wind-up turn to be fairly independent of load factor, up until the onset of stall, beyond which the separation between the rotors decreases rapidly and blade-strike becomes a distinct possibility. Unlike in the forward flight case, where stall-induced blade strike occurred at the rear of the rotor, the modification of the loading distribution on the rotors at stall due to the angular velocity of the system in conjunction with the dynamics of the rotor in the accelerated reference frame of the turn, drives the position of initial blade strike to the left of the rotor (remembering that the results presented in this section are for simulations of a left-hand turn).

3.5.2 Wake Geometry in a Steady Turn

Figure 3.33 contrasts the development of the inflow distribution on the coaxial system with the conventional rotor as the load factor in the turn is increased. These diagrams, as in the forward flight comparisons, show the spanwise variation of inflow experienced by one of the blades of the rotor during a single revolution and are best interpreted in conjunction with Figures 3.34 and 3.35, which contrast the geometries of the wakes of the two systems. To represent properly the effects of a steady turn on the curvature of the wake, the images in these figures are all taken from the simulations of steady left-hand turns at constant load factor, rather than from the simulation of the wind-up turn. If anything, the diagrams reveal the rather subtle nature of the shifts in loading distribution that accompany any change in load factor. On the conventional rotor, a slight increase in blade-wake interaction at both 70° and 290° azimuth accompanies the



(a) $n = 1.00$

(b) $n = 1.25$

(c) $n = 1.50$

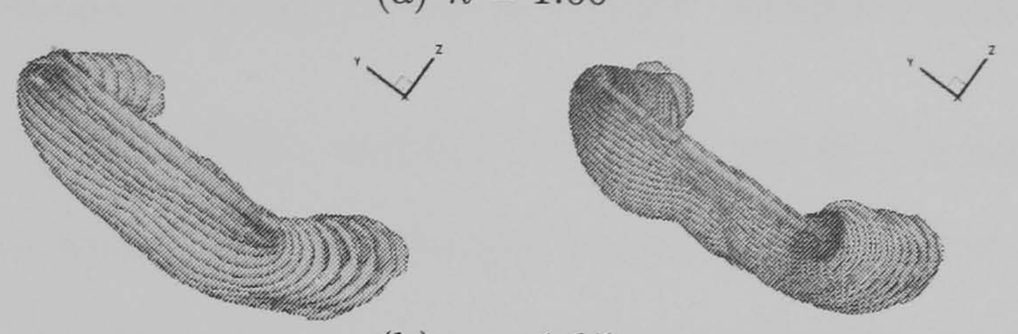
$v_i/\Omega R$

Figure 3.33: *Spanwise inflow variation experienced by a single blade during one revolution in a level turn at various load factors. (Far left: upper rotor of coaxial system. Left: lower rotor of coaxial system. Right: equivalent single rotor.)*

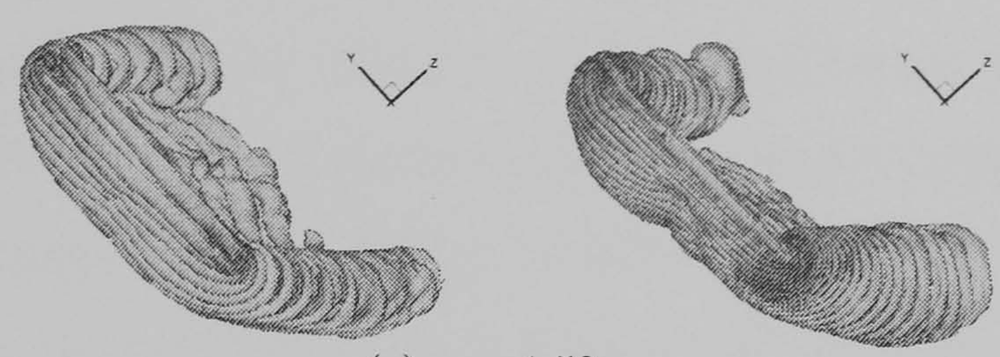
lifting of the trajectory of the super-vortices relative to the disc plane as the curvature of the wake increases with load factor. As the load factor on the coaxial rotor is increased, the rearward of the two inter-rotor BVIs on the advancing side of the lower rotor decreases in strength relative to the forward BVI, and the influence of the root vortices on the loading on the rear of both rotors increases. At the same time, another inter-rotor



(a) $n = 1.00$

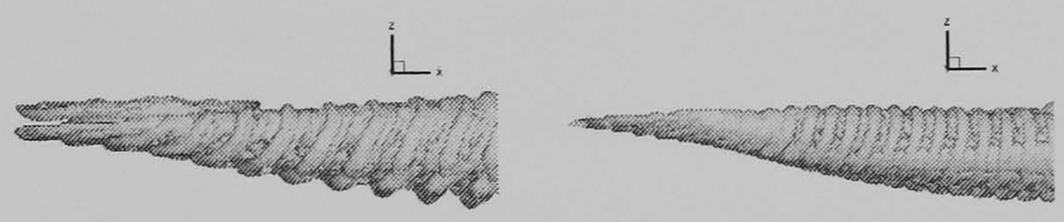


(b) $n = 1.25$

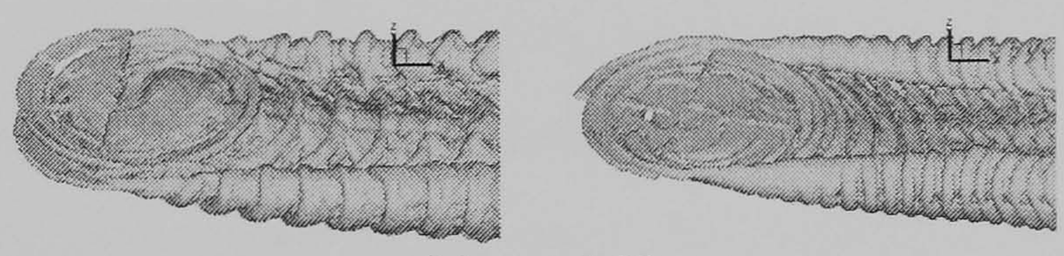


(c) $n = 1.50$

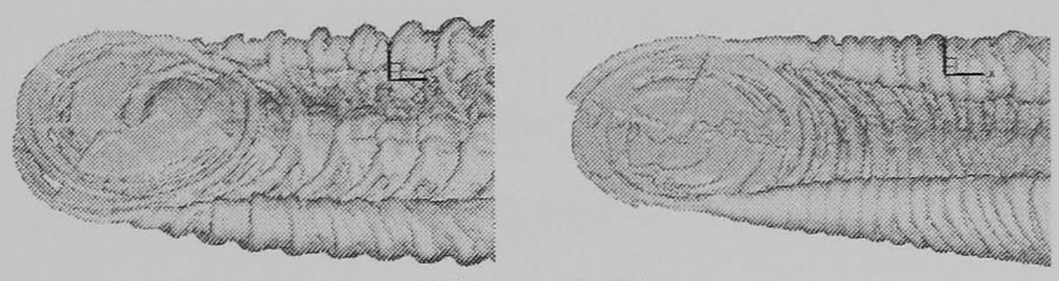
Figure 3.34: *Wake geometry in a coordinated, level turn (front view). Left: coaxial rotor. Right: equivalent rotor.*



(a) $n = 1.00$



(b) $n = 1.25$



(c) $n = 1.50$

Figure 3.35: *Wake geometry in a coordinated, level turn (side view). Left: coaxial rotor. Right: equivalent rotor.*

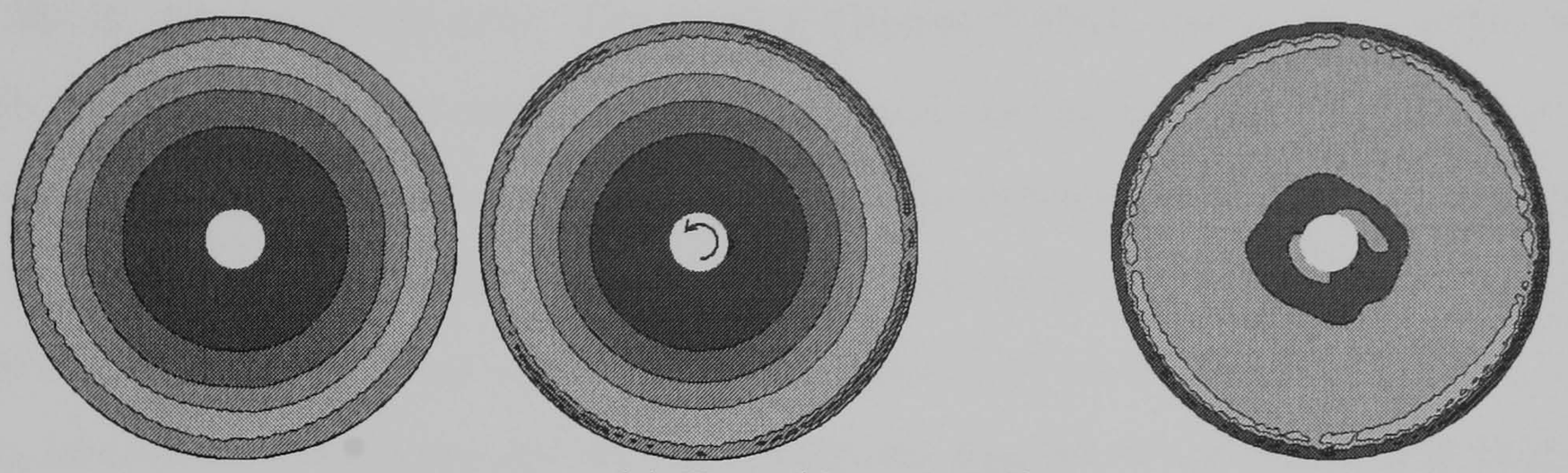
BVI on the retreating side of the lower rotor just aft of the primary intra-rotor BVI becomes steadily more prominent. Little obvious change in the geometry of the wake accompanies these changes in the pattern of BVIs on the rotors, but the lifting of the

wake into the plane of the rotors as a result of the curved trajectory of the system is clearly apparent in Figures 3.34 and 3.35.

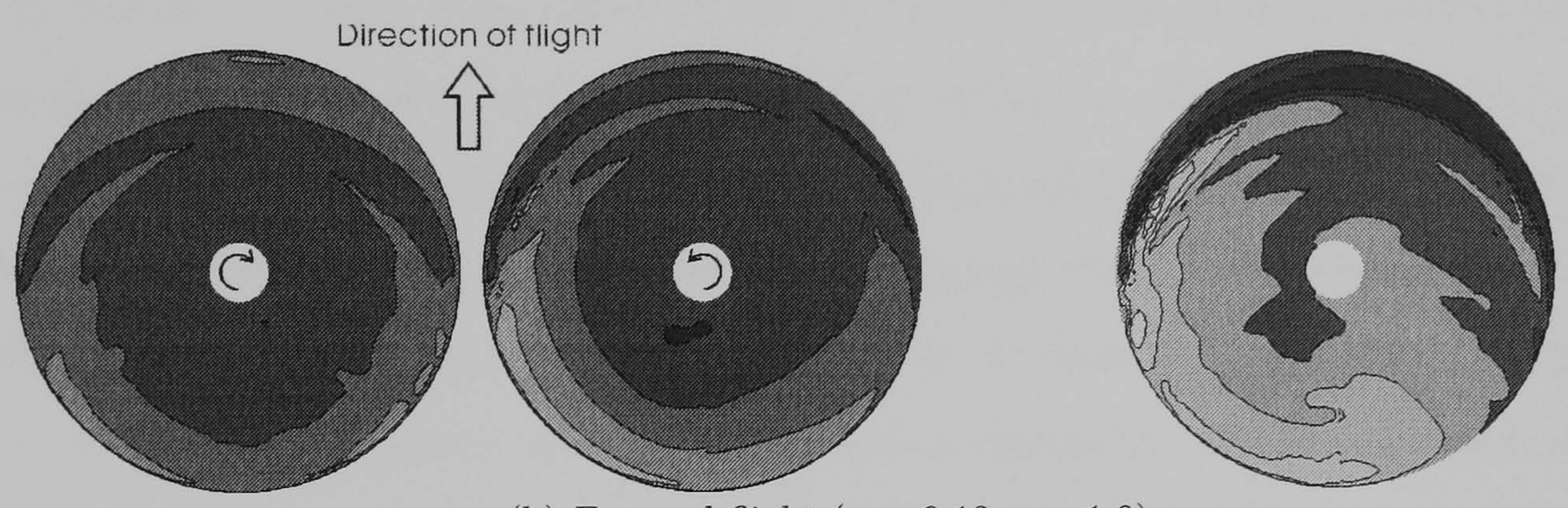
3.6 Aerodynamic Origin of Power Differences

The analysis of hover, forward flight and level turns shows the benefit of the coaxial rotor to lie in its reduced consumption of induced power compared to the equivalent single rotor. Much insight into the relative performance of the two systems can be obtained by localising this benefit to specific features of the aerodynamic loading on the rotors. Figure 3.36 uses the VTM-predicted spanwise distribution of sectional induced power on the rotor blades to achieve this aim. In the far left-hand images, the sectional induced power distribution on a second type of coaxial-equivalent rotor (that essentially neglects the vertical separation between the rotors) is defined by averaging the contributions (at the same azimuth, defined with respect to the lower rotor) to the sectional induced power from blades on the upper and lower rotors of the coaxial system. This composite distribution can be contrasted with the radial variation of sectional induced power on the equivalent single rotor (defined as in Section 3.3) shown in the middle images. The difference between the distributions of sectional induced power on these two, differently-defined equivalent rotors is shown at right, and provides a measure of the relative performance of the coaxial and conventional equivalent systems that is localised to specific features in the aerodynamic loading distribution on the two rotors. Light regions of the figures correspond to parts of the rotor disc where the coaxial rotor consumes less power than the conventional system and vice versa. As is to be expected from the relatively small difference in power consumption between the two systems, the features in the aerodynamic loading that yield the differences in overall induced power consumption are relatively subtle.

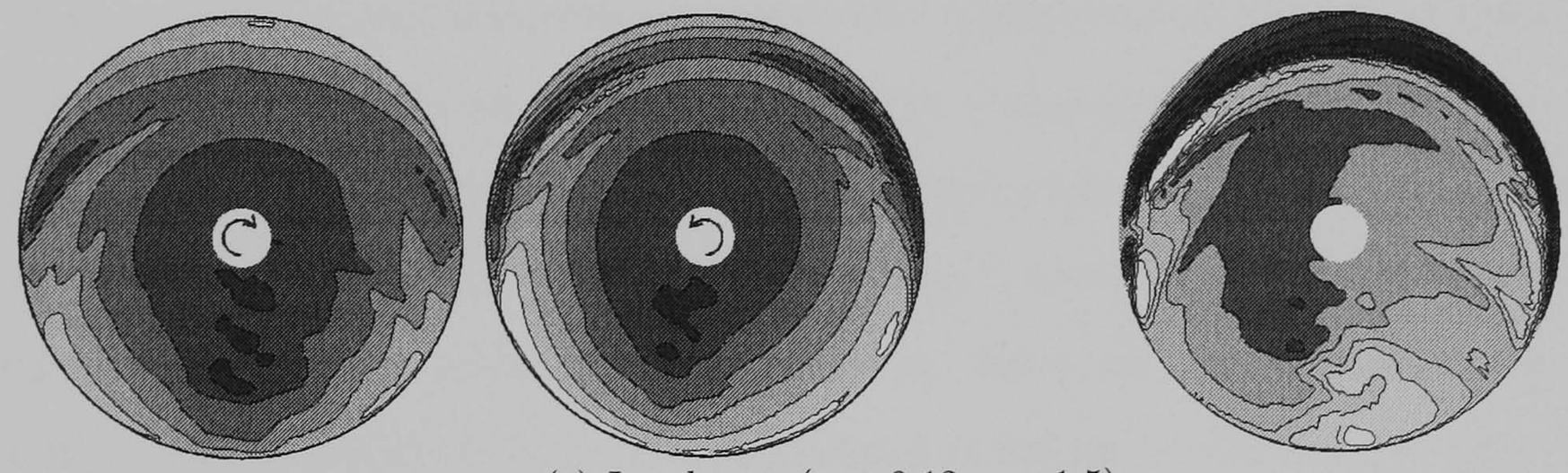
It appears that the relative merits of the two systems are closely tied to the position and strength of the various BVIs on the disc plane. In hover, the equivalent rotor benefits compared to the coaxial system from the slight reduction in induced power that is associated with a small reduction in the downwash that is induced on the very outboard part of the disc by a slightly stronger tip-vortex interaction. A similar reduction inboard is associated with a similar difference in the character of the interaction of the blades



(a) Hover ($C_T = 0.0048$)



(b) Forward flight ($\mu = 0.12, n = 1.0$)



(c) Level turn ($\mu = 0.12, n = 1.5$)



(Legend scaled by 10^4)

Figure 3.36: *Spanwise induced power variation experienced by a single blade during one revolution in a level turn at various load factors. (Far left: coaxial system averaged over the two rotors. Left: equivalent single rotor system. Right: difference between equivalent single rotor system and averaged coaxial system — averaged coaxial system subtracted from equivalent single rotor system.)*

with the root vortex. These benefits are outweighed on the whole, though, by the presence of a relatively broad band of lower induced power consumption just inboard of the tip of the coaxial system. Comparing Figures 3.17(d) and 3.18(d) shows that this effect results from a favourable re-distribution of the loading slightly inboard of the tip of the upper rotor, and is most likely due to the amelioration of the blade-vortex interaction on this rotor as a result of the increased axial convection rate of the tip vortices of the coaxial system compared to the equivalent rotor.

The inter-rotor BVIs that are such a prominent feature of the inflow distributions shown in Figure 3.24 have little effect on the relative apportionment of induced power between the two systems in forward flight since they primarily affect the loading inboard on the rotor where their contribution to the power required by the system is somewhat diminished. The conventional rotor gains some advantage over the coaxial system from the reduced inflow just upwind of the primary BVI on the forward part of the rotor disc, but this advantage is negated by the greater lateral symmetry of the composite load distribution on the rear of the coaxial system. This symmetry results in lower induced power than is given by the interaction between the highly-loaded retreating blade and the developing super-vortex on the left edge of the conventional rotor. Inboard, the power advantage is shared almost equally between the coaxial system and the equivalent single rotor, the conventional rotor generally having a lower power requirement than the coaxial system on its advancing side, and vice versa on the retreating side. In turning flight, the situation is more strongly biased in favour of the coaxial rotor. The conventional rotor still shows the strong positive effect of the upwash just forward of the strong BVI on the front of the disc, but the positive effects of the series of inter-rotor BVIs on the right hand side of the lower rotor, the influence of the root vortex on the loading on the rear of both rotors of the coaxial system, and the growing drag penalty on the conventional rotor of the increased downwash to the rear of the intra-rotor BVI and downwind of the interaction with the super-vortex on the retreating side, all conspire to reduce the overall induced power consumption of the coaxial system relative to the equivalent rotor.

3.7 Summary

The performance of an articulated coaxial rotor in hover, in steady forward flight, and in level, coordinated turns is contrasted with that of an equivalent, articulated, conventional rotor with the same overall solidity, number of blades and blade aerodynamic properties. The VTM is used to calculate the profile, induced and parasite contributions to the overall power consumed by the two systems, and the highly resolved representation of the rotor wake that is produced by the model is used to relate the observed differences in the performance of the two systems to the structures of their respective wakes. In all flight conditions, all else being equal, the coaxial system requires less induced power than the conventional system. In hover, the conventional rotor consumes increasingly more induced power than the coaxial rotor as thrust is increased. In forward flight, the relative advantage of the coaxial configuration in terms of its power consumption is particularly evident at pre-transitional advance ratios. In turning flight, the benefits of the coaxial rotor are seen at all load factors. The beneficial properties of the coaxial rotor in forward flight and manoeuvre, as far as induced power is concerned, are a subtle effect of rotor-wake interaction, and result principally from differences between the two types of rotor in the character and strength of the localised interaction between the developing super-vortices and the highly-loaded blade-tips at the lateral extremities of the rotor. In hover, the increased axial convection rate of the tip vortices appears to result in a favourable re-distribution of the loading slightly inboard of the tip of the upper rotor of the coaxial system. Validation of numerical predictions against experimental data suggests though that the merits of the coaxial system relative to the equivalent, conventional rotor in terms of overall power consumption may be obscured if the profile drag of the blades is overtly sensitive to operating condition, as for instance might possibly be the case at low Reynolds number.

Chapter 4

Effect of Rotor Stiffness on Coaxial Rotor Aerodynamics

4.1 Introduction

In terms of efficiency and practicality, helicopters with a coaxial rotor configuration are regarded in many quarters as viable competitors to those with a more conventional main rotor – tail rotor design [1]. Although there are many secondary arguments for and against the two types of system, the prime advantage of the coaxial rotor arises from the fact that it provides its own inherent anti-torque mechanism, thus eliminating the tail rotor that is required in the conventional system to achieve yawing moment balance. The tail rotor in a conventional helicopter consumes typically 5 to 10% of the main rotor power without making any significant contribution to the load-carrying capability of the aircraft [55]. In addition, the coaxial rotor consumes intrinsically less induced power in hover, in forward flight and during manoeuvres than an isolated equivalent single rotor of the same solidity and blade geometry (see Chapter 3), and thus is very attractive compared to conventional systems when viewed simply on the basis of power loading.

With a traditional articulated coaxial system, however, the cyclic controls to the upper and lower rotors are linked mechanically. The resultant lateral flapping, in opposition to each other, of the contra-rotating upper and lower rotors reduces the clearance between the two rotors as forward speed or load factor is increased. Unlike in a con-

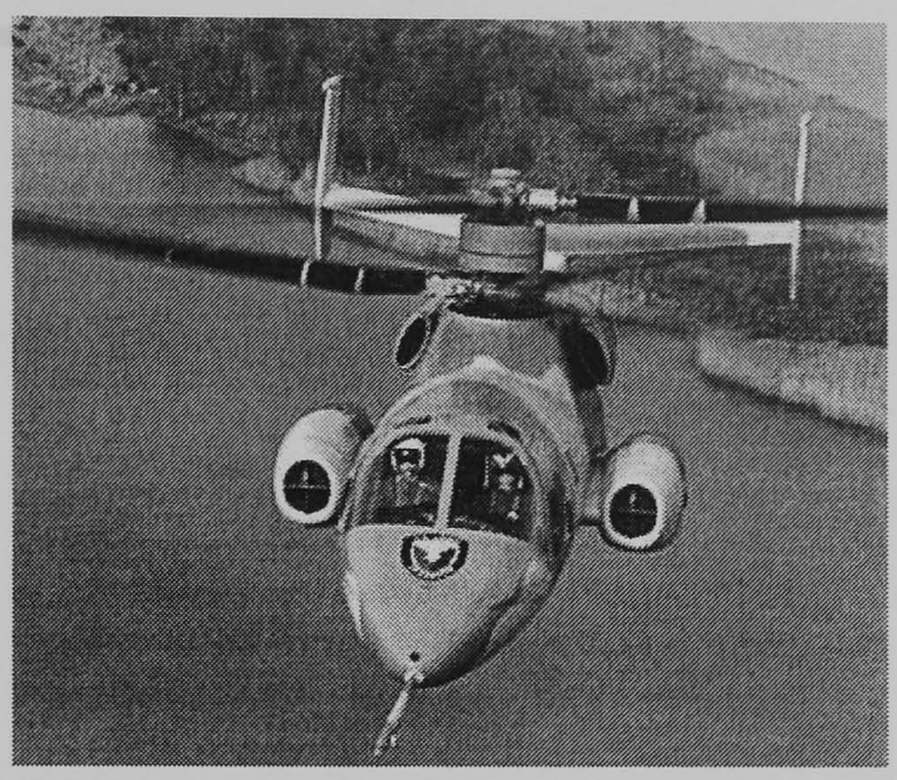
ventional configuration, aerodynamic stall is then non-benign in the sense that the associated aeromechanics of the blades can result in a very rapid reduction in the clearance between the rotors. The possibility that the blades of the two rotors might collide has to be counteracted either by placing strictly-observed limits on the flight envelope of the vehicle or by separating the rotors physically by adopting a tall rotor mast [62]. This can impose a very large penalty on the coaxial system in terms of the parasite power that is consumed by the vehicle in forward flight.

The Sikorsky XH-59A Advancing Blade Concept (ABC) helicopter (see Figure 4.1) attempted to exploit the inherent advantage of the coaxial configuration in terms of power consumption while circumventing this basic aeromechanical deficiency of the system [63]. The ABC system was unique in that its rotors each had a stiff, hingeless hub rather than the articulated design that is characteristic of all other full-scale coaxial helicopters. Flapping and lagging of the blades of the ABC system still occurred through the usual combination of the flexure of the blade root joint and the structural deformation of the blades themselves. Yet the increased stiffness of the rotor system allowed the aircraft to be flown with significant regions of stall on the retreating sides of both upper and lower rotors while still maintaining sufficient rotor clearance [59]. This was even though the separation between the rotor hubs was very small by comparison to other designs [59, 63]. Unfortunately, the resultant benefits in terms of overall power consumption were offset by a rather heavy transmission system, and the high stiffness of the rotor system resulted in some unsatisfactory dynamic characteristics including very high levels of rotor-induced vibration at high forward speed. Although the XH-59A did not reach production, part of the technology has been resurrected in Sikorsky's new thrust-compounded coaxial X2 Technology demonstrator.

A key complicating issue in the design of an efficient coaxial helicopter is the strong interaction between the method used to trim the helicopter and the resultant power consumption of the system. This coupling arises because, in the absence of an auxiliary trimming device such as a tail rotor, the rotor must be constrained to produce the propulsive force in such a way that the associated moments that it produces remain in balance. Prediction of the actual performance of the trimmed coaxial system is made particularly difficult by the very strong aerodynamic coupling between the two rotors, the effects of which have traditionally proved very difficult to model accurately.



(a) The first prototype without auxiliary propulsion (1973)



(b) The thrust-compounded second prototype with two Pratt & Whitney J60-P-3A turbojet engines (1977)

Figure 4.1: *The Sikorsky XH-59A Advancing Blade Concept helicopter.*

The coaxial system offers the interesting possibility, however, that the extra degrees of freedom inherent in its rotor configuration might allow one of several different control strategies to be adopted in trimming the system, and that one or the other of these strategies might offer improved overall performance of the system compared to the remainder.

This chapter investigates how the strategy that is used to trim the rotors can be used in conjunction with rotor stiffness to modify, in some cases favourably, the performance of a coaxial rotor system, specifically when the performance of the system is measured in terms of its power consumption. Although this topic has been addressed in the past, most notably during the development of the Sikorsky XH-59A, recent advances in high-fidelity rotor wake modelling, particularly of the highly interactive flow field that is

characteristic of the wake of the twin rotors of the coaxial system, have produced new insights into how sensitive the loading on the rotors is to the type of trim strategy that is adopted. It is shown in this chapter how the trim strategy can be used in conjunction with rotor stiffness to induce a relatively small re-distribution in the loading on the system, and how this re-distribution, particularly in the vicinity of the blade-wake interactions on the rotor discs, might manifest as a significant change in the overall performance of the coaxial system. Finally, the timewise variation of the aerodynamic forcing of the system is examined to yield some additional insights into the vibrational characteristics of stiff coaxial rotors.

4.2 Rotor Model

The geometric characteristics of the rotor adopted in this study are based on the two-bladed, teetering coaxial configuration (as in Chapter 3) that was used by Harrington to measure the performance of coaxial rotors in hovering flight [11], and by Dingeldein [12] in his measurements of performance in steady level flight. Note that this rotor has a rather low solidity ($\sigma = 0.054$ compared to, say, the ABC rotor which had a solidity of 0.127) and thus its lifting capability and high-speed performance is relatively deficient compared to more modern coaxial systems. The advantage of using this configuration, though, is that a database of good-quality experimental data exists for its performance, against which the results of the simulations presented in this chapter can be verified. The properties of Harrington's rotor were given in detail in Chapter 3.

4.2.1 Rotor Stiffness

From a dynamic point of view, rotors such as Sikorsky's ABC system fall somewhere in between the two limiting ideal cases of a freely articulated but rigid-bladed rotor and a completely rigid rotor with infinite stiffness. To simplify the comparison between the various cases presented in this work, and to avoid the details of mode shapes, mass distribution and other similar effects on the dynamics of the rotors from obscuring the fundamental aerodynamics that underpin the behaviour of the system, the effects of rotor flapwise stiffness are introduced very simply into the aerodynamic calculation by representing the rotors of the coaxial systems using rigid blades, articulated in flap,

together with a suitable flap spring. The teetering hinge of Harrington's rotor is simply replaced with individual flapping hinges for each blade (with zero offset from the rotor shaft). Each flapping hinge is then stiffened by the addition of a spring.

To gain a useful insight into how semi-rigid coaxial rotor performance is modified by the effects of rotor stiffness, data for a range of flap spring stiffnesses are contrasted. The range of practically-relevant spring stiffnesses can be determined quite simply by matching the natural frequency of flapping of the articulated system together with flap springs to the first harmonic flapping frequency of the flexible rotor blades of the representative full-scale system. Basing the study on the properties of the Sikorsky XH-59A suggests that a range of natural frequencies between 1Ω and 2Ω should be considered since the natural frequency of the first flapping mode of the ABC rotor was approximately 1.5-per-revolution when operated at high rotational speed and close to 2.0-per-revolution when the rotor was slowed down for operation at high forward speed [63, 64]. These frequencies are significantly higher than the fundamental flap frequencies associated with most conventional articulated or semi-rigid rotor designs, suggesting that considerable additional insight into the behaviour of this class of rotor system can be obtained by extending the range of systems studied to include the rotor with rigid hinges and thus infinite flap frequency. The philosophy adopted in this chapter will thus be to use this rigid rotor as the baseline case to which results for rotors with lesser stiffness will be compared. Results for the articulated rotor (i.e. with natural flapping frequency of 1Ω) will also be presented, where relevant as a point of reference, since the behaviour of this type of rotor is likely to be the most familiar to the readers of this work.

4.2.2 Trim Model

In the present study, given controls $\theta^u = [\theta^u_0, \theta^u_{1s}, \theta^u_{1c}]$ and $\theta^l = [\theta^l_0, \theta^l_{1s}, \theta^l_{1c}]$ for the upper and lower rotors respectively, the generalised trim algorithm used in the VTM can be written as

$$\left[\dot{\theta}^u(t), \dot{\theta}^l(t) \right] = K \ (F^* - F(t)) \tag{4.1}$$

where the array F^* contains the components of the forces and moments that the rotors are required to produce to maintain the aircraft in trim as described in Section 2.7 of Chapter 2. K is thus a prescribed 6×6 coupling matrix that governs the rate at which

each of the controls should respond to any discrepancy between F^* and F.

Denoting the long-term average of $F(t)$ by $\overline{F}$, the system is considered to be in a condition of trim when

$$\overline{F} = F^* = [-(C_D - C_X), 0, C_W, 0, 0, 0] \tag{4.2}$$

or, in other words, when, in the mean, the horizontal force C_{Fx} produced by the rotor matches the fuselage drag C_D less any augmentation C_X to the primary rotor system that is provided by an auxiliary propulsive device, the vertical force C_{Fz} matches the assumed weight of the helicopter C_W, the lateral force C_{Fy} produced by the rotor is zero and there is zero average net moment produced by the rotor about the airframe reference point. Throughout this study, this reference point is taken to be the centre of the hub of the lower rotor. Imposition of this set of trim conditions on the system yields a reasonably realistic assessment of the performance of the coaxial system under representative flight conditions. The limitations of the approach adopted here should nevertheless be borne in mind. In particular, the results presented in this chapter may not be directly transferable to full-scale practice if the fuselage of the helicopter produces significant pitching and rolling moments of its own.

In all simulations presented in this chapter, the forward component of force, C_{Fx}, required to overcome the fuselage drag was provided by suitable forward tilt of the rotor shaft. As in Dingeldein's experimental study [12], the variation of fuselage drag with forward speed was based on a representative equivalent flat plate area for the fuselage of 0.020 times the rotor area. The auxiliary propulsive device was assumed to provide no assistance to the primary rotor system below an advance ratio of 0.30. At higher forward speeds it was assumed to provide sufficient force to counteract fully the drag acting on the fuselage. The resultant of the force components C_{Fx} and C_{Fz} was set equal to 0.0048 throughout to allow the simulated data to be compared directly against Dingeldein's experimental measurements. Note that, as a simplifying measure, the lateral force produced by the rotor was not trimmed in the present calculations.

The control problem of driving the remaining components of the forces and moments produced by the rotor system into trim in a stable and robust fashion can be simplified by decomposing the matrix K so that the response of the collective and cyclic controls to the loads produced by the rotor system is decoupled. Let $K = K_1 + K_0$, then define

the cyclic coupling matrix

$$K_1 = \begin{bmatrix} 0 & 0 & 0 & 0 & 0 & 0 \\ 0 & 0 & 0 & k^u_{sx} & k^u_{sy} & 0 \\ 0 & 0 & 0 & k^u_{cx} & k^u_{cy} & 0 \\ 0 & 0 & 0 & 0 & 0 & 0 \\ 0 & 0 & 0 & k^l_{sx} & k^l_{sy} & 0 \\ 0 & 0 & 0 & k^l_{cx} & k^l_{cy} & 0 \end{bmatrix} \tag{4.3}$$

so that, through Equation 4.1, the cyclic controls respond directly to the pitching and rolling moments produced about the airframe reference point.

A simple dynamic analysis shows that the time-averaged pitching and rolling moments produced by a rotor are directly proportional to the first-harmonic flapping of the system [65]. The stiffness of the rotor system changes the phase delay of the flapping response to the cyclic control inputs and thus influences the choice of the elements of the cyclic coupling matrix. The flapping response of the blades is phase shifted with respect to the feathering of the blades by an azimuth angle $\Delta\psi$ that decreases as the stiffness of the system is increased [66]. Symbolically, if $\beta(\psi) \sim \theta(\psi - \Delta\psi)$ then a simple, linear analysis of the effects of hinge stiffness on the flapping dynamics of a rigid, articulated blade with no hinge offset [65] gives the phase delay (with the system in hover) as

$$\Delta\psi = 90^\circ - \tan^{-1}\left(\frac{\nu^2 - 1}{\gamma/8}\right) \tag{4.4}$$

where $\gamma = \rho a c R^4 / I_\beta$ is the Lock number of the rotor. The non-dimensional natural flapping frequency of the blade, ν, is given by

$$\nu^2 = 1 + \frac{K_\beta}{I_\beta \Omega^2} \tag{4.5}$$

where K_β is the hinge stiffness. These results suggest that an effective choice for the coupling constants in K_1 should be

$$\begin{bmatrix} k^i_{sx} & k^i_{sy} \\ k^i_{cx} & k^i_{cy} \end{bmatrix} = c^i k \begin{bmatrix} \cos(\Delta\psi) & \sin(\Delta\psi) \\ -\sin(\Delta\psi) & \cos(\Delta\psi) \end{bmatrix} \tag{4.6}$$

where $i \in \{u, l\}$ and k is a suitable constant. For later convenience, $c^u, c^l \in \{0, 1\}$ are switching parameters that allow the individual cyclic controls of each rotor to be isolated from the loads produced on the system, if needs be, when devising a suitable

trim strategy for the system. Thus, for all the simulations of articulated rotors presented in this work (i.e. those with $K_\beta = 0$ and thus $\Delta\psi = 90°$), the coupling constants were

$$\begin{bmatrix} k^i_{sx} & k^i_{sy} \\ k^i_{cx} & k^i_{cy} \end{bmatrix} = c^i k \begin{bmatrix} 0 & 1 \\ -1 & 0 \end{bmatrix} . \tag{4.7}$$

Implicit in this analysis though is the assumption that the aerodynamic forces produced on the rotor blade are in phase with the applied feathering. In forward flight, this assumption is tenuous at best. Further analysis shows the phase shift of the flapping of the blades with respect to their feathering to be a separate function of the forward speed of the helicopter for the sine and cosine components of the cyclic pitch [65]. Direct use of Equation 4.4 to set the cyclic coupling constants via Equation 4.6 yields highly oscillatory behaviour of the controls for rotors with finite stiffness, especially as the forward speed of the system is increased. Throughout the calculations presented here, the cyclic coupling constants for the rotors with high but finite flap hinge stiffness were thus set using the phase shift that applies in the limiting case of an infinitely stiff rotor (the rigid rotor defined earlier) i.e. the phase shift that is obtained from Equation 4.4 when $\nu \to \infty$ and hence $\Delta\psi \to 0°$:

$$\begin{bmatrix} k^i_{sx} & k^i_{sy} \\ k^i_{cx} & k^i_{cy} \end{bmatrix} = c^i k \begin{bmatrix} 1 & 0 \\ 0 & 1 \end{bmatrix} . \tag{4.8}$$

This choice of coupling constants allowed the pitching and rolling moments C_{My} and C_{Mx} on the airframe to be driven to their specified trim values by the cyclic pitch inputs to the rotors under all flight conditions.

If the collective coupling matrix is subsequently defined as

$$K_0 = \begin{bmatrix} 0 & 0 & k^u_{0z} & 0 & 0 & 0 \\ 0 & 0 & 0 & 0 & 0 & 0 \\ 0 & 0 & 0 & 0 & 0 & 0 \\ 0 & 0 & 0 & 0 & 0 & k^l_{0z} \\ 0 & 0 & 0 & 0 & 0 & 0 \\ 0 & 0 & 0 & 0 & 0 & 0 \end{bmatrix} \tag{4.9}$$

then Equation 4.1 contains the pair of ordinary differential equations

$$\begin{aligned} \dot{\theta}^u_0 &= k^u_{0z}(C^*_{Fz} - C_{Fz}) \\ \dot{\theta}^l_0 &= k^l_{0z}(C^*_{Mz} - C_{Mz}) \end{aligned} \tag{4.10}$$

no matter what the values of the elements of the cyclic coupling matrix K_1 as defined in Equation 4.3. At first glance the collective pitch controls for the upper and lower rotors appear to be driven independently by this system of equations. Note, though, that C_{Fz} and C_{Mz} are components of the overall loads generated by the rotor system, and hence are affected by the collective pitch settings of both rotors. The control routine thus forces the collective pitch inputs to the upper and lower rotors to respond differentially so that the system is driven to the required trim conditions on both the overall vertical force and the yaw moment acting on the system.

4.3 The Effect of Trim Strategy on Performance

By selecting various combinations for the switching parameters c^u and c^l in the cyclic coupling matrix, various trim strategies can be devised through which the pitching and rolling moments of the coaxial system can be trimmed using cyclic pitch inputs to the upper and lower rotors. The four different trim strategies that can be adopted are summarised in Table 4.1. In trim method 1, the same cyclic pitch inputs are applied to both rotors. This corresponds to the usual case with an articulated coaxial system where the swashplates of the upper and lower rotors are linked mechanically, and is achieved in the simulations by setting the switching parameters $(c^u, c^l) = (1, 1)$ in Equation 4.6. The pitching and rolling moments required to trim the system are produced by both rotors, but are shared between the rotors in a way that is inherently not controllable and is dependent instead on the intrinsic aerodynamics of the system. Alternatively, the cyclic pitch of only one of the two rotors can be adjusted to trim the pitching and rolling moments on the rotor while the cyclic pitch input to the other rotor is held fixed at zero. This approach may be beneficial under certain flight conditions because aerodynamic interference between the two rotors of the coaxial system may lead to one rotor being more efficient than the other in producing the non-uniform disc loading that is required to trim the pitching and yawing moments that are produced by the overall rotor system. This philosophy yields trim method 2 (with $(c^u, c^l) = (1, 0)$) and trim method 3 (with $(c^u, c^l) = (0, 1)$) for cyclic inputs only to the upper and to the lower rotor respectively. Strategies 1-3 are all capable of being implemented in practice since trim is achieved once conditions on the overall loads on the airframe are satisfied,

Table 4.1: *Summary of cyclic control strategies (L: linked to other rotor; O: trimmed to net moments; X: held fixed; I: trimmed to individual rotor moments.)*

Trim method	Upper rotor cyclic	Lower rotor cyclic
1	L	O
2	O	X
3	X	O
4	I	I

and thus can be verified by observations of the state of the vehicle with respect to the inertial frame of reference. Although not as easily achievable in practice since it requires being able to measure the moments that are produced independently by each rotor (and hence requires measurements of loads that are reacted internally within the system), a fourth trim method results from applying independent cyclic pitch input to each rotor in such a way that the global trim condition on the moments produced by the system are satisfied by trimming independently the pitching and rolling moments produced by each individual rotor to zero.

Figure 4.2 compares the power consumption of the rigid coaxial rotor when trimmed using each of these strategies. Data is presented for the rotor in forward flight at an advance ratio $\mu = 0.12$. Relative to trim method 1, all other strategies yield a distinct increase in the power consumed by the rotor. Method 2, for instance, yields a moderate increase in the overall power required by the system of about 1.6%, although with the benefit of a slight reduction in induced power consumption, while method 4 results in a rather extreme 7.7% penalty in overall power consumed. The effect of trim strategy in modifying the aerodynamic load distribution on the system and hence its power consumption is shown in Figures 4.3-4.5. Figure 4.3 compares the loading distribution along the length of the blades on the upper and lower rotors of the coaxial system, as a function of their azimuth, that is obtained using each trim method. The resultant distributions of local induced power and profile power consumption over the rotor discs are shown in similar format in Figures 4.4 and 4.5.

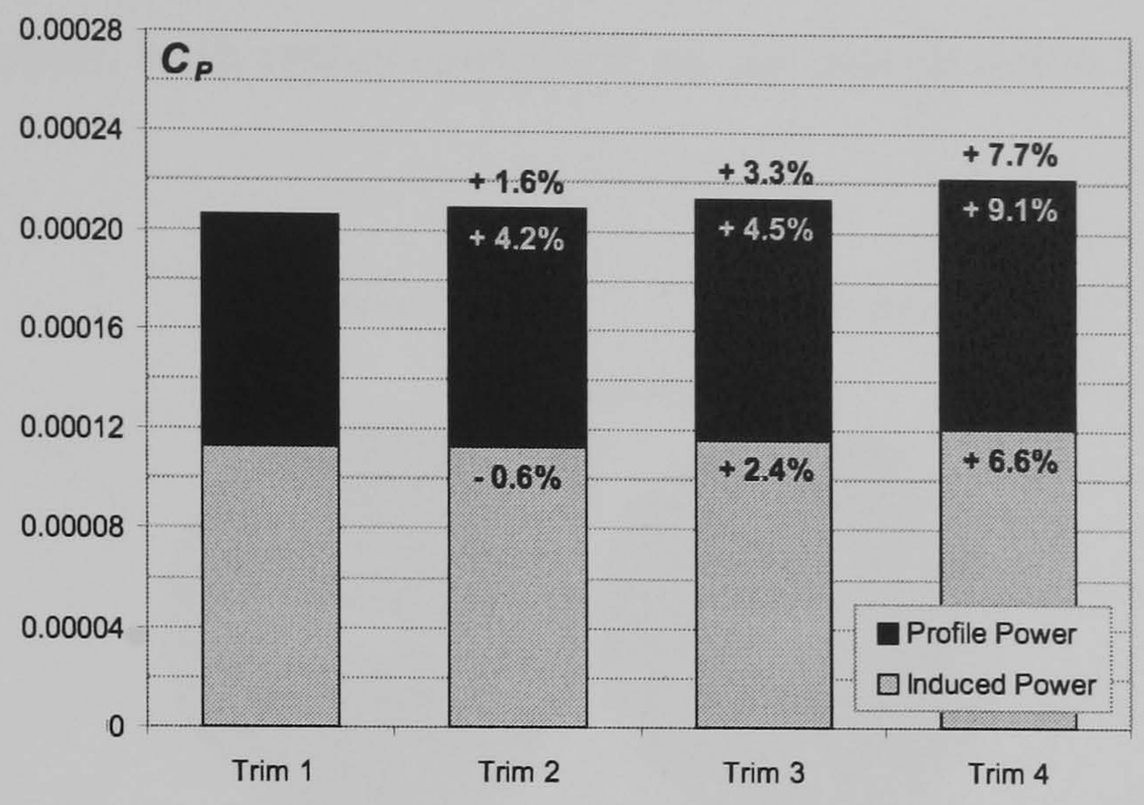
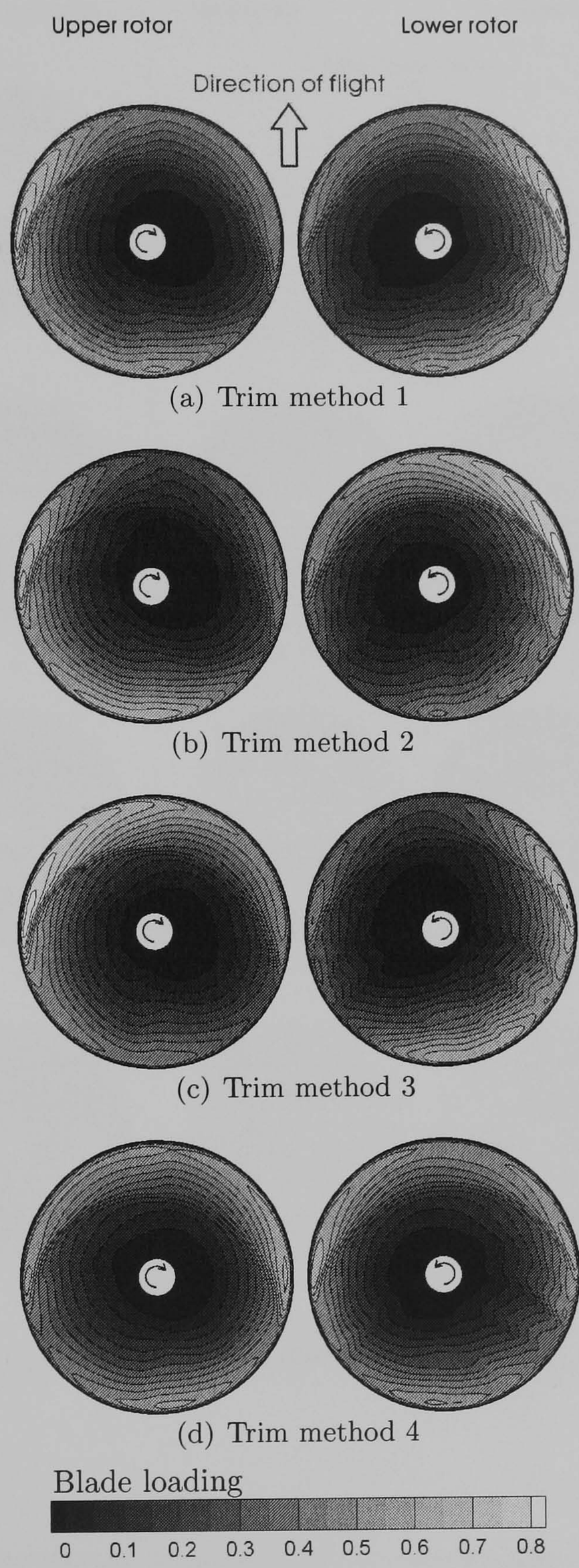


Figure 4.2: *The effect of trim strategy on overall power consumption ($\mu = 0.12$ and $C_T = 0.0048$) Percentage figures indicate relative increase or decrease with respect to trim method 1.*

In all cases, the aerodynamic environment of the rotors is characterised by fairly high loading and hence power consumption near the tips of the blades, with significantly lower loading and power consumption on the inboard parts of the rotor disc. This basic pattern is heavily disrupted, though, by the modifying effect of interactions between the blades and individual tip vortices (BVIs) that generate a series of localised ridges across which the loading varies rapidly. These interacting vortices either originate from blades on the same rotor (resulting in 'intra-rotor' BVIs) or, in the case of the lower rotor, also from the blades of the upper rotor (resulting in 'inter-rotor' BVIs). Although Figures 4.3-4.5 show clear differences in the distribution of loading and power consumption on the rotor discs in response to a change in the trim strategy, it is by no means obvious from the data presented which particular aerodynamic influences are responsible for the associated differences in overall rotor power consumption. Thus, in Figures 4.4 and 4.5, a series of additional plots are presented that show the result of subtracting the localised power distribution that is obtained using each trim method from the equivalent power distribution that is obtained using trim method 1. Thus, treating the distribution of power consumption that is obtained using trim method 1 as the baseline, these plots localise the increments of power that are obtained using the alternate trim methods to specific features in the load distribution on the rotor discs. At the far right of the

figures, the power increments that result on the upper and lower rotors are summed to show how, as a system, both rotors contribute to the overall power consumption of the coaxial rotor.



(a) Trim method 1

(b) Trim method 2

(c) Trim method 3

(d) Trim method 4

Figure 4.3: *Distribution of blade loading on the upper and lower rotors of the rigid coaxial system at advance ratio* $\mu = 0.12$. *Trim methods 1 to 4 compared.*

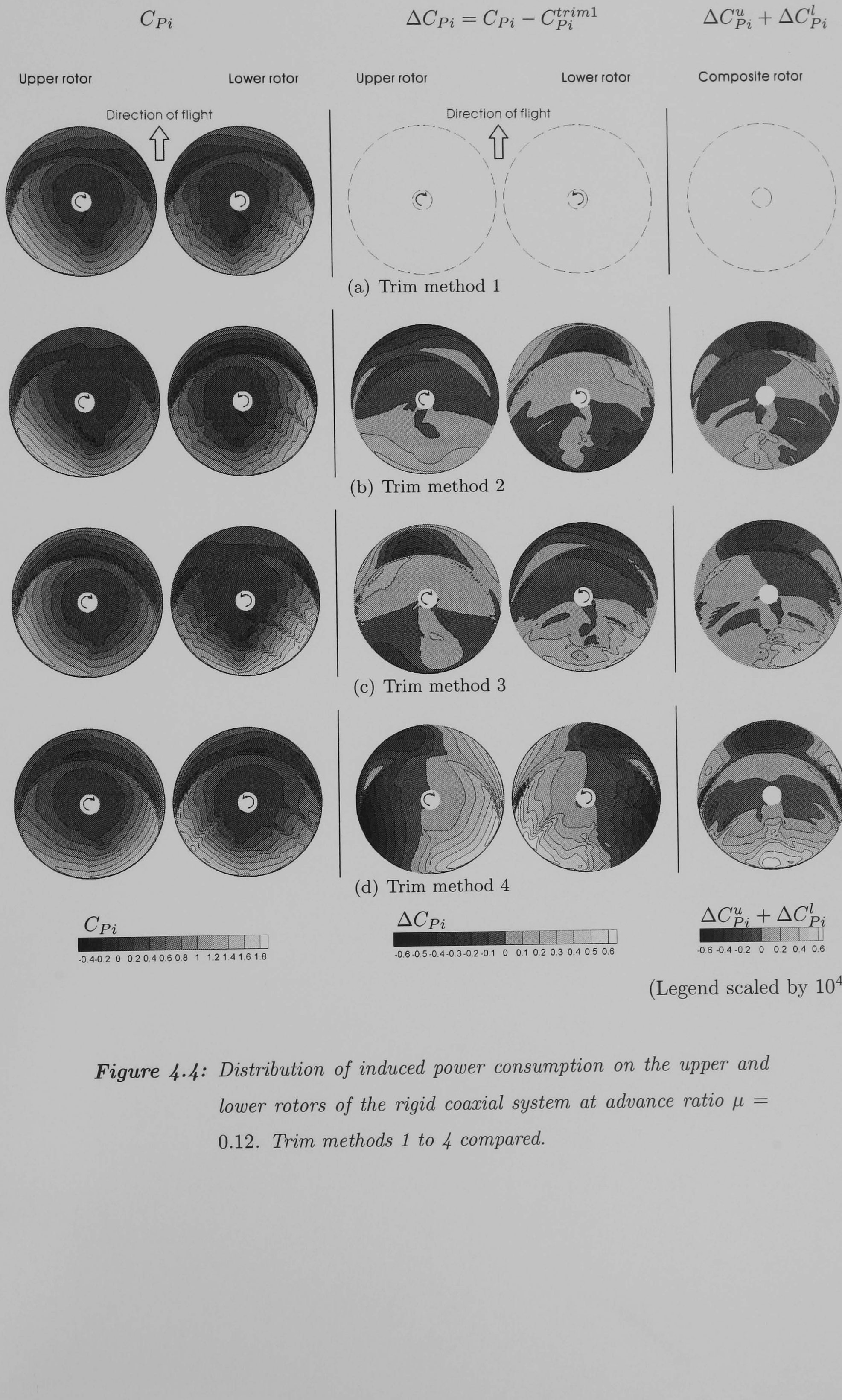


Figure 4.4: *Distribution of induced power consumption on the upper and lower rotors of the rigid coaxial system at advance ratio* $\mu = 0.12$. *Trim methods 1 to 4 compared.*

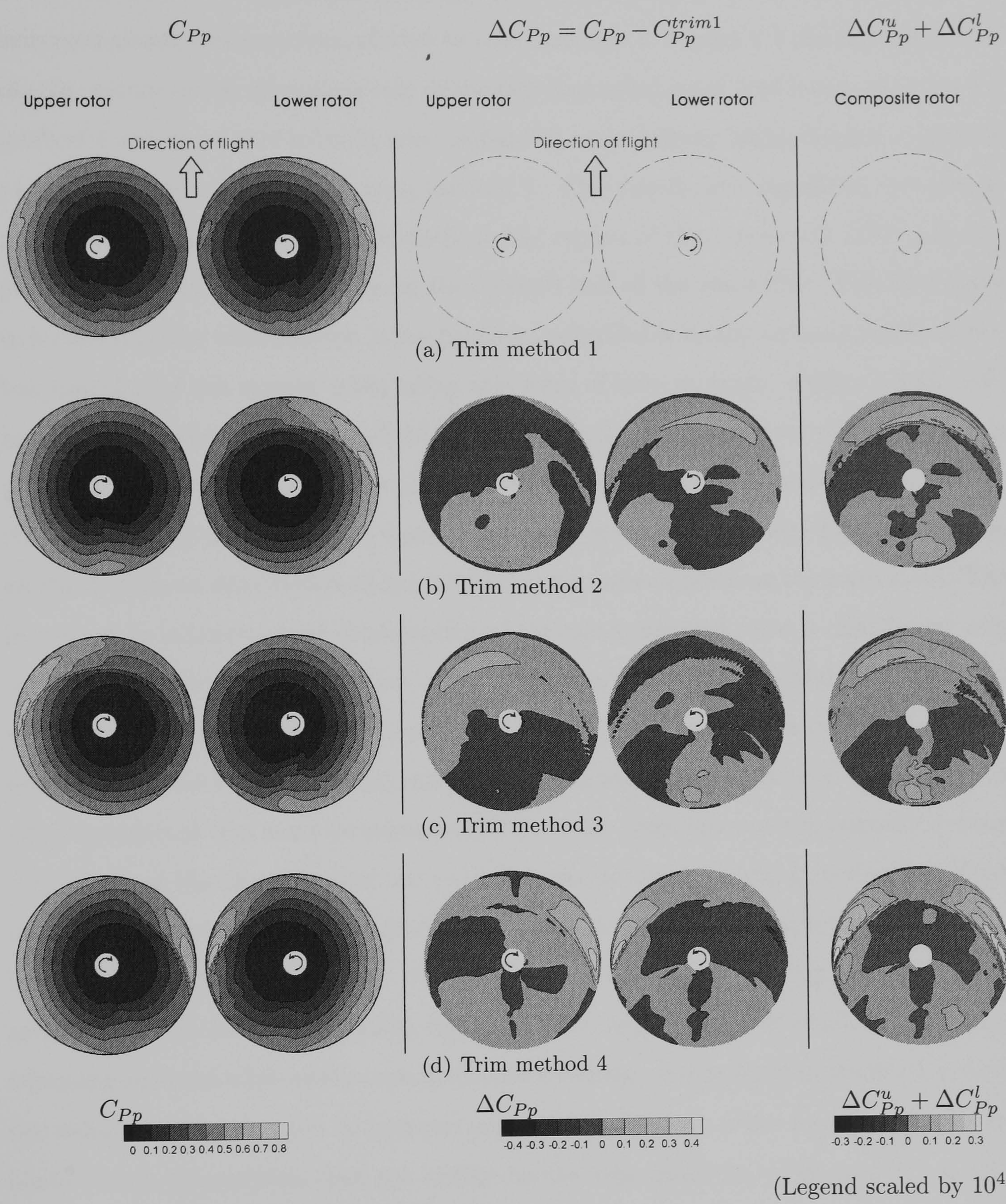


Figure 4.5: *Distribution of profile power consumption on the upper and lower rotors of the rigid coaxial system at advance ratio* $\mu = 0.12$. *Trim methods 1 to 4 compared.*

Figure 4.2 shows that both trim strategies 2 and 3, where only one of the two rotors is used to trim the rolling and pitching moments generated by the system, result in increased power consumption relative to trim strategy 1. Figure 4.3 shows clearly that the tip regions of the advancing side of the non-controlled rotor (the lower rotor in trim method 2 and the upper rotor in trim method 3) are relatively highly loaded compared to when the rotor is trimmed using method 1. This results in a significant penalty in profile power consumption, particularly in the region of the intra-rotor BVI that is a prominent feature of the loading on the forward half of the rotor disc. This increment in localised power consumption is the principal contributor to the elevated profile power consumption of the system when using this form of trim strategy. Figure 4.2 though, shows that, of the two very similar trim strategies 2 and 3, a greater power penalty is paid when the lower rotor alone is used to trim the overall moments acting on the system (trim method 3) than when the upper rotor (trim method 2) is used. This is primarily an effect of the re-distribution of the induced power consumption on the rotor discs. The increment in induced power consumption of the non-controlled rotor is distributed very similarly in both cases; alleviation of the requirement to trim the moments produced by the rotor results in a reduction in induced power consumption over a significant proportion of both the front and rear of the rotor but also results in a strong nose-up pitching moment that must be counteracted by cyclic pitch input to the controlled rotor. The effects of this control input are evident in the increased loading on the rear of the rotor disc and an associated longitudinal gradient in induced power consumption. The lower rotor operates in the wake of the upper rotor, however, and the less favourable aerodynamic environment in which the lower rotor is required to produce a restorative trimming moment when using trim method 3 is evident, particularly in Figure 4.4, from the enhanced consumption of induced power in the region of the series of inter-rotor blade vortex interactions that are visible on the rear quadrant of its advancing side. The superposition of increased loading, as a result of the imposition of trim conditions, onto precisely the same region of the disc where the loading is already locally elevated by the action of BVIs appears to be the prime contributor to the enhanced induced power consumption associated with this type of trim strategy.

A similar effect is seen with trim method 4. This method, where the rotors are trimmed individually to yield zero moment, results in the most extreme power penalty

of all the strategies that were tested. This trim strategy effectively negates the advantage of the rigid coaxial rotor in providing an inherent load-balancing mechanism between the two rotors (as is exploited in trim method 1). Given the aerodynamic similarities between the two types of rotor system when trim method 4 is employed, Figure 4.3 not unexpectedly shows the loading distribution on both discs of the rigid rotor to bear a close qualitative resemblance to that found on the rotors of an articulated coaxial system. The tips of the blades on the retreating sides of both rotor discs are highly loaded to counteract the effects of the load deficit on the inboard sections of the retreating side on the lateral moments that are generated by the rotor. On the other hand, the loading distribution on the advancing sides of both rotors shows a characteristically more benign variation with radius. Both rotors thus exhibit significantly elevated profile power consumption in the region of the prominent intra-rotor BVI on the forward half of the retreating side of the rotor disc; this feature is the primary contributor to the significantly elevated profile power consumption of the coaxial system when using this trim strategy.

Because of the inherent rigidity of the system, the lateral moments that are produced individually by the loading distributions on each of the two rotors cancel to some extent when the same cyclic inputs are made to both rotors (as with trim method 1). This results in the overall lateral moment on the system being naturally rather small. Hence only a marginal power overhead is incurred by the additional cyclic input that is required to drive the system away from its natural aerodynamic state in order to achieve overall trim of the system. When each rotor is individually trimmed to zero lateral moment, however, as with trim method 4, significant cyclic control input is required to modify the lateral gradient of loading from its natural state in order to balance the system. Associated with this control-induced increment in loading is a similar increment in the lateral gradient of the localised induced power consumption on the rotor. This can be seen quite clearly in Figure 4.4. Interactions between individual tip vortices and the highly-loaded sections of the blades, particularly on the retreating side, result in a series of localised elevations in the induced power consumption of the rotors, however. These combine to give the overall increase in induced power consumption of the system that was observed when using this particular trim strategy.

4.3.1 The Importance of Accurate Trim

In the following sections of this chapter, the performance of rotors with different hub stiffness are compared at various flight speeds when trimmed using ostensibly the same strategy. This section serves simply to show how carefully the trim conditions need to be applied to the system to yield comparable results.

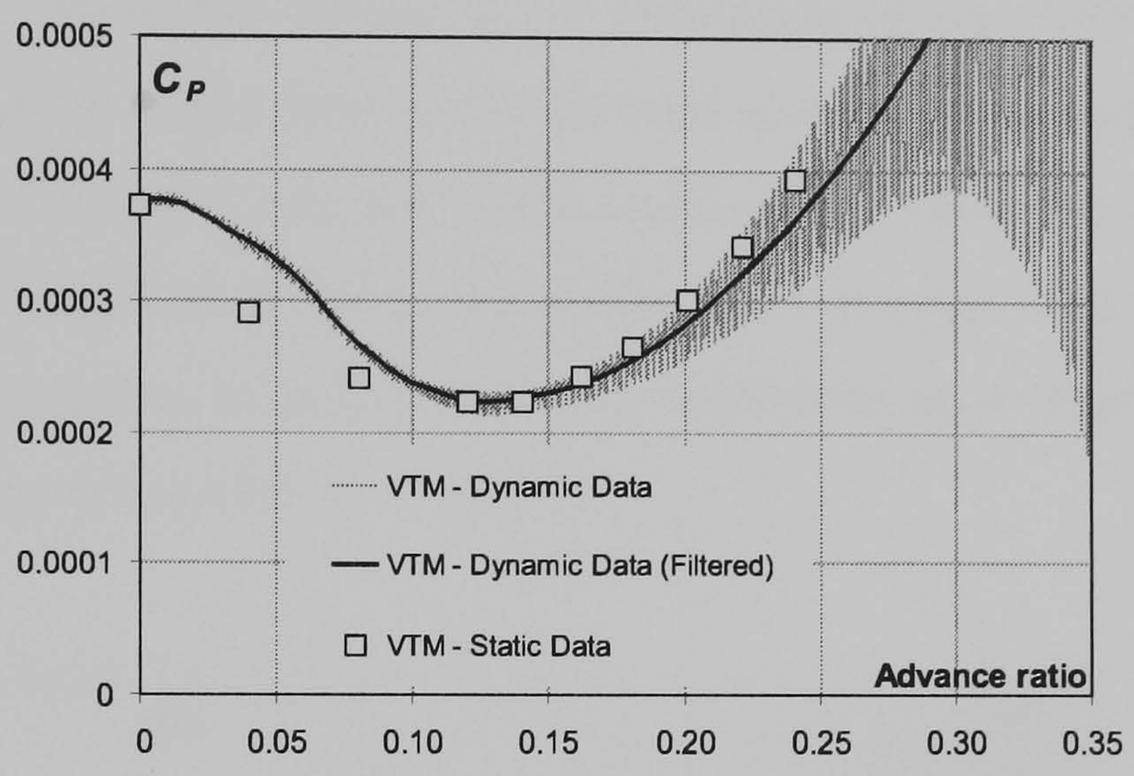


Figure 4.6: *Total power consumed in forward flight. Static VTM computations for Harrington's rotor in steady level flight compared with VTM computation of accelerated level flight.*

In Figure 4.6, the simulations of the original teetering configuration in steady forward flight, in other words with the advance ratio of the rotor fixed at a given value for each simulated case, is presented together with data that were obtained when the same rotor was accelerated through the range of advance ratios of interest during the course of a single simulation. Significant gains in computational efficiency can be obtained using this procedure, and the data so obtained are generally very close to the data obtained from simulations under quasi-steady conditions as long as the acceleration of the rotor is kept small. Comparison of simulated power data obtained under accelerated conditions, filtered to remove all fluctuations at greater than blade-passing frequency (the dark curve) with equivalent quasi-static data reveals this indeed to be the case except in the pre-transitional regime ($\mu < 0.1$) where the power consumed under accelerated conditions is significantly higher than that obtained under quasi-static conditions. It is known that in the pre-transitional regime the structure of the wake swaps intermittently

and irregularly between its hover-like tubular geometry and the flattened aeroplane-like geometry that is characteristic of higher advance ratios (see Section 3.4.2). Even very small acceleration applied to the system appears to suppress the effects of the fluid dynamic instability that drives this intermittency, causing the wake to retain its pre-transitional form to higher advance ratios and the power consumption to remain at the elevated levels associated with low-speed flight. In addition, the simulations of the accelerated system reveal the change in the amplitude of the vibratory component of the power consumption of the rotor as the forward speed of the system is increased (the light grey curve). The rapid increase in the amplitude of these fluctuations beyond an advance ratio of about 0.25 is indicative of the onset of rotor stall. The advantage of the accelerated simulation is in that the trim conditions at a broad range of forward speeds can be compared easily.

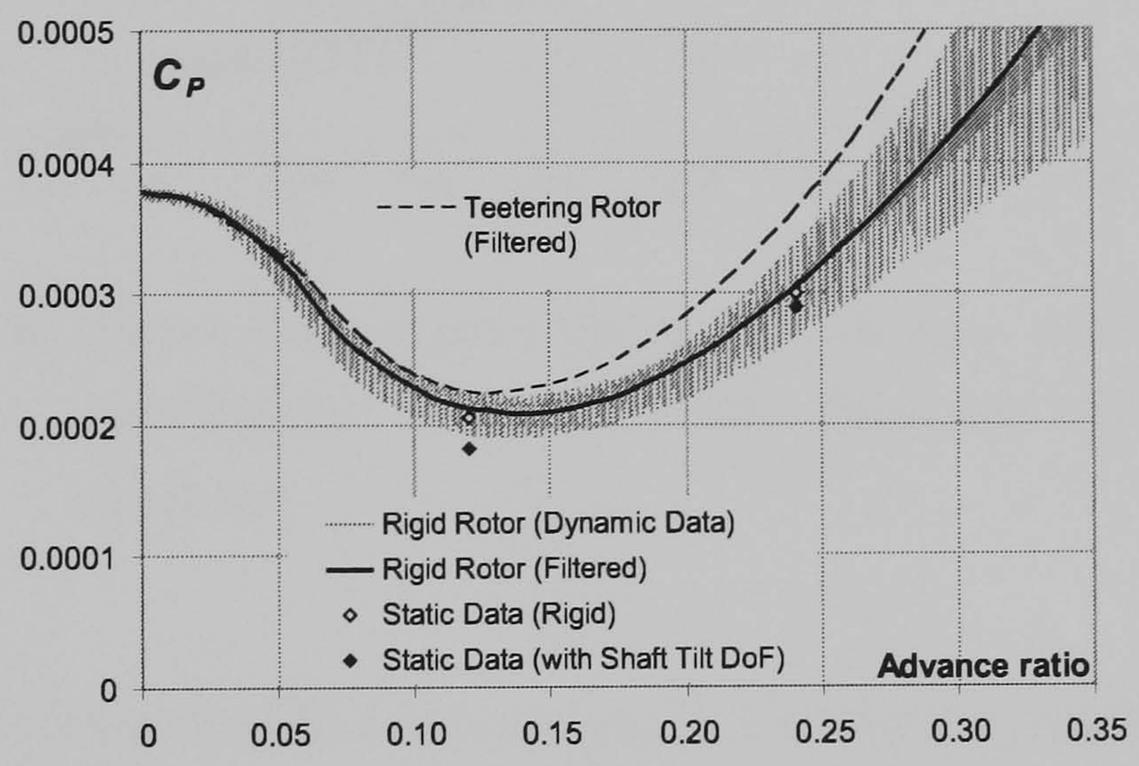


Figure 4.7: *Total power consumed by the coaxial system in forward flight. Rigid and teetering rotors compared.*

Figure 4.7 shows the same predicted variation of power with forward speed for Harrington's original teetering rotor as was presented in Figure 4.6. Similar data is presented for simulations of the rigid equivalent of Harrington's rotor but where, since cyclic pitch has only an indirect effect on the forward force produced by the system, the rotor is flown simply at the same thrust and shaft tilt as measured during Dingeldein's experiment (as well as to net zero pitching and rolling moment using trim method 1). Data from both quasi-static and accelerated simulations is presented for the second sys-

tem; negligible difference between the results of the two types of simulation is apparent. Figure 4.7 reveals a major difference between the power required by the teetering and rigid systems, however, and it is tempting to ascribe the favourable performance of the rigid rotor solely to its dynamic characteristics.

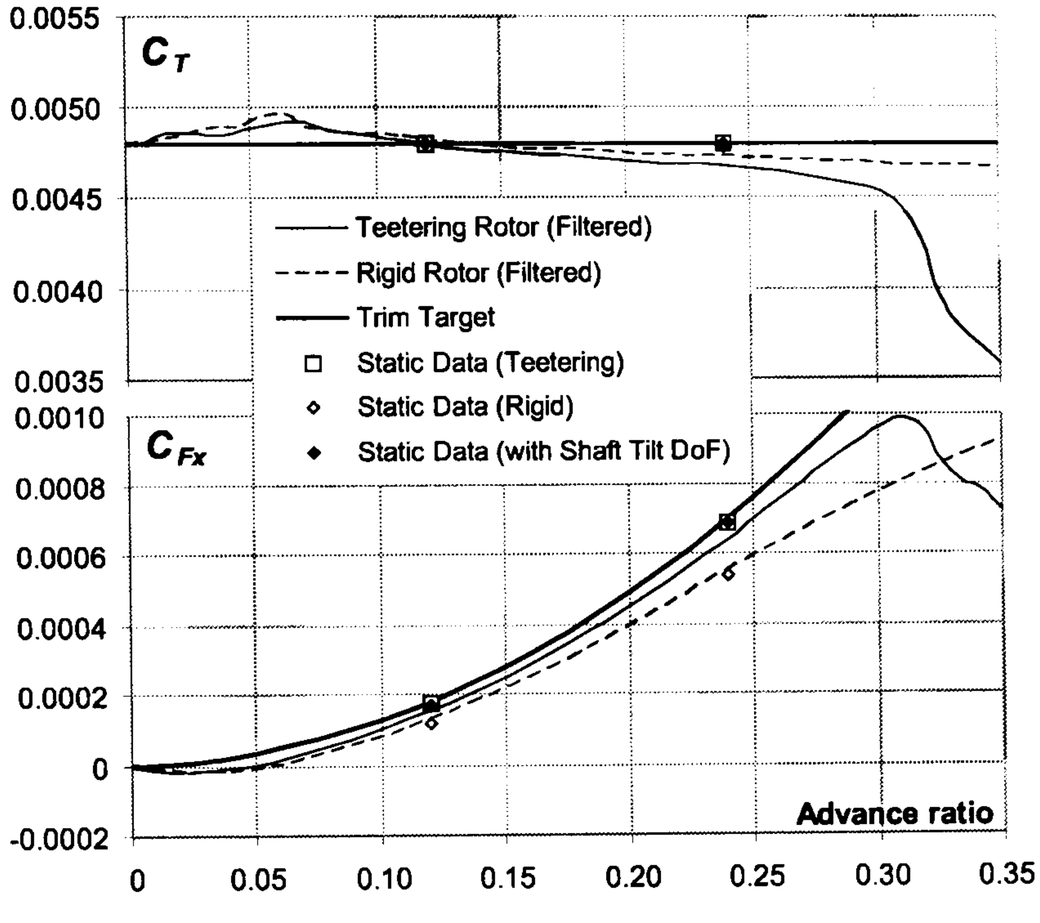


Figure 4.8: *Thrust and propulsive forces, C_T and C_{Fx}, produced by the coaxial system in forward flight. Rigid and teetering rotors compared.*

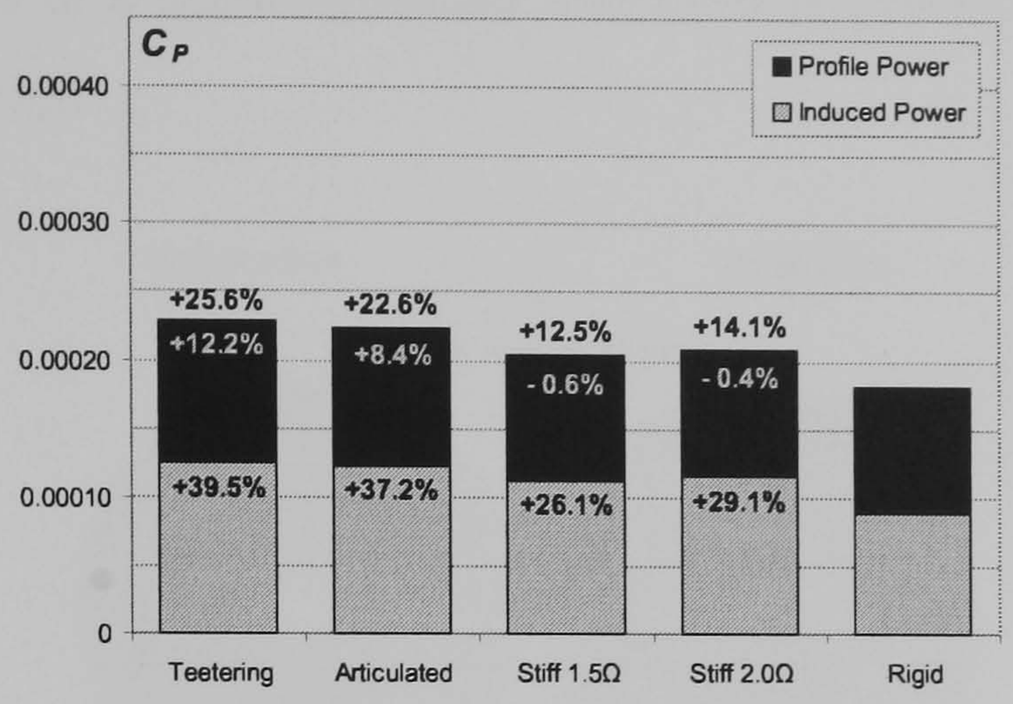
Figure 4.8 shows that the two rotors are not in directly comparable flight conditions, however. The teetering rotor follows closely the specified trim targets for thrust and forward force up to an advance ratio of approximately 0.25 (after which rotor stall causes the thrust produced by the system to diverge from the trim target despite corrective collective pitch input). Even though the thrust produced by the rigid rotor matches closely the trim target throughout the range of advance ratios that was simulated, the absence of disc tilt as a degree of freedom causes the system to fall short of generating the required forward force when flown simply at the same shaft tilt as the teetering rotor. Hence some suspicion must be entertained that the advantageous characteristics of the rigid rotor that are revealed in Figure 4.7 should be ascribed, at least partially, to the reduced parasite power consumption that results simply from the rotor being inherently incapable of meeting the required trim targets on the forces produced by

the system. The results of a second series of quasi-static simulations of the rigid rotor, where the prescribed conditions on the thrust and forward force are indeed satisfied by suitable collective pitch input and shaft tilt, are also shown in Figure 4.7. These results simply add further confusion to the argument by suggesting that the favourable characteristics of the rigid rotor might extend to lower advance ratios than was indicated by the simulations where the forward force was not correctly matched! This analysis serves to show how, when comparing the performance of any two given rotor systems, very misleading results can be obtained if the two systems are not flown at precisely equivalent flight conditions.

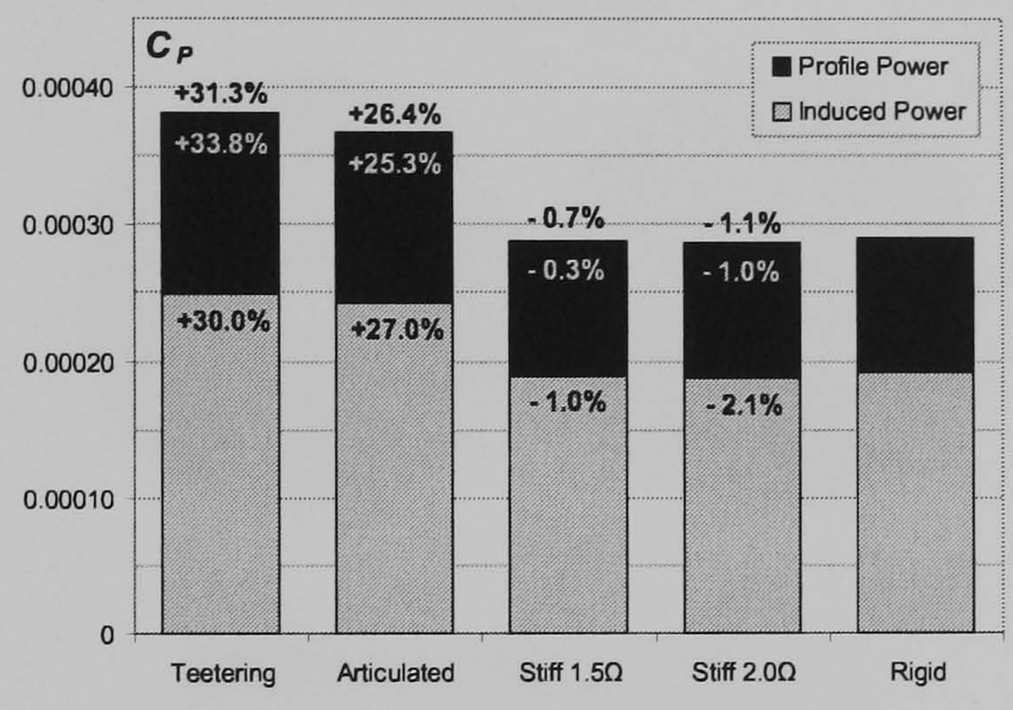
4.4 The Effect of Stiffness on Performance

Figure 4.9 compares the power consumption of coaxial rotors with various degrees of flapwise stiffness at three different forward flight speeds. All rotors were trimmed to the same thrust and forward force and, in the case of the stiffened rotors, overall moment using trim method 1. The results for the low and intermediate flight speeds ($\mu = 0.12$ and $\mu = 0.24$) are directly comparable: in both these cases the forward force was trimmed to counteract directly the representative drag of the fuselage. The high-speed case ($\mu = 0.36$) is somewhat different, however. At this forward speed none of the rotors was able to produce the required propulsive force, so the presence of an auxiliary propulsive system that was capable of counteracting the fuselage drag was assumed. Even so, at this advance ratio, the onset of rotor stall made it impossible to trim the rotors with articulated and teetering hubs — only the stiffened systems could be driven into a fully consistent trim state using the collective and cyclic pitch inputs.

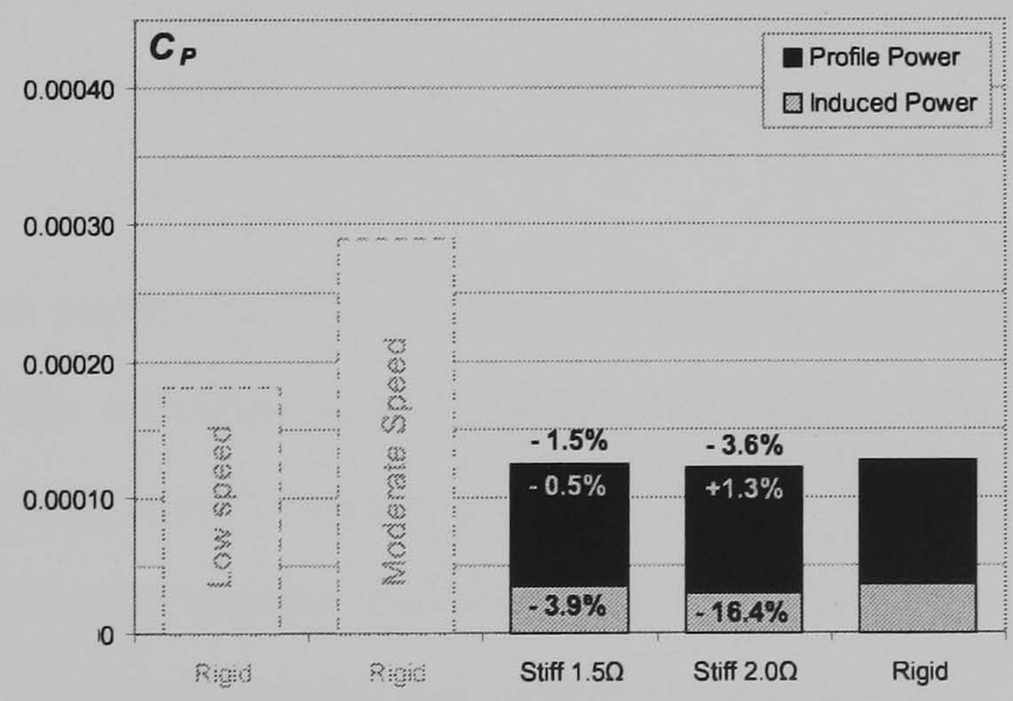
Figure 4.9 shows the rotors with stiffened hubs to require consistently less power in forward flight than the articulated or teetering systems, although the trend with decreasing hub stiffness is not entirely consistent between flight speeds. At the higher flight speeds, the power consumption of the rotor is considerably less sensitive to hub stiffness than at the lowest advance ratio that was tested — certainly it appears that the benefits of finite but large flap stiffness are felt most strongly as the forward speed of the system is increased. Even at low forward speed though the stiffened rotors consume considerably less power than the equivalent articulated system, but, interestingly, con-



(a) Low speed: $\mu = 0.12$



(b) Moderate speed: $\mu = 0.24$



(c) High speed: $\mu = 0.36$

Figure 4.9: *The effect of rotor stiffness on overall power consumption ($C_T = 0.0048$, various flight speeds). Percentage figures indicate relative increase or decrease with respect to the rigid rotor.*

straining the relative flapping of the two blades by adopting a teetering configuration for each rotor results in a not insignificant increment in power consumption over the freely articulated design.

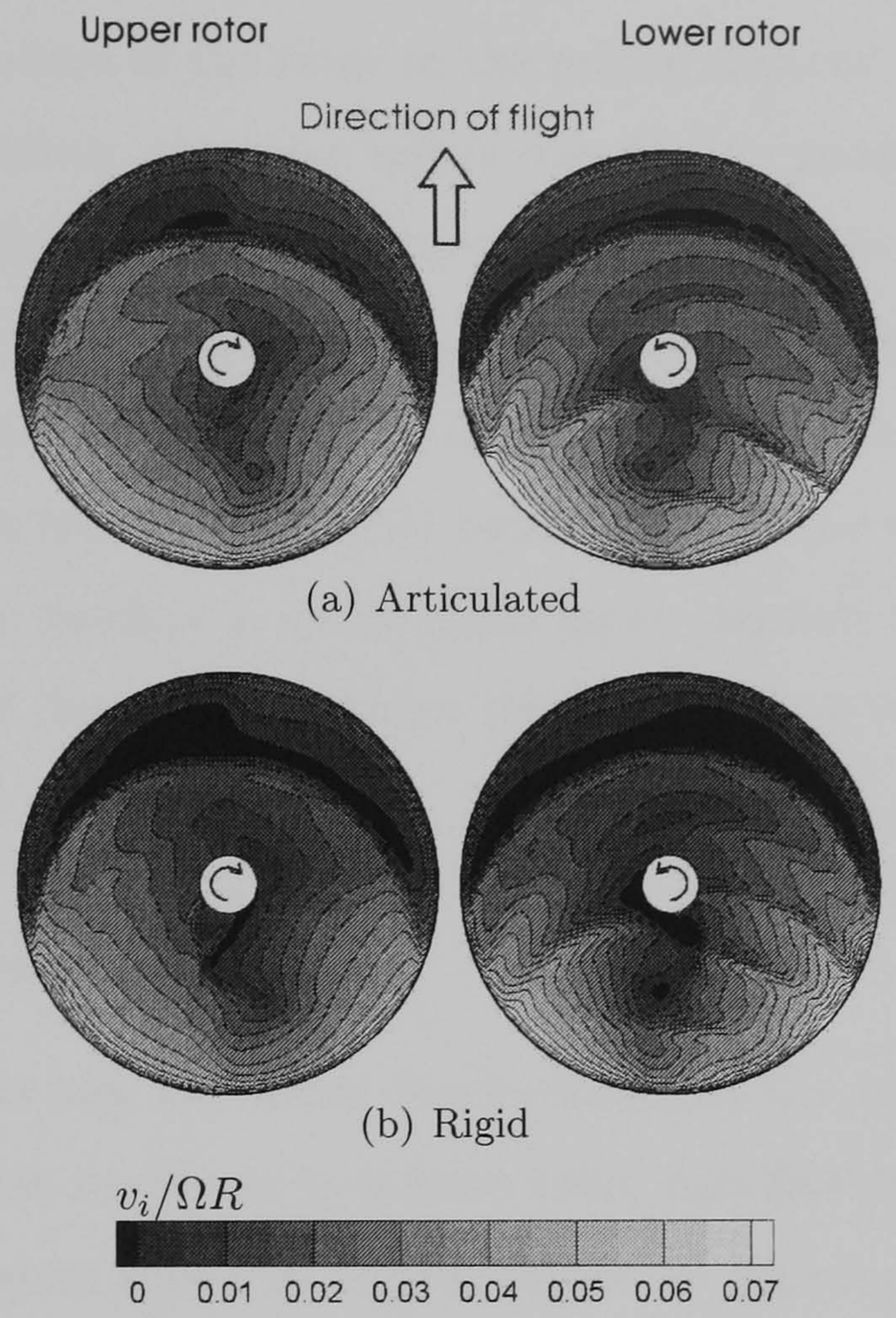


Figure 4.10: *Inflow distribution at advance ratio* $\mu = 0.12$, $C_T = 0.0048$. *Articulated and rigid rotors compared.*

Figure 4.10, which shows the inflow distributions that are experienced by the upper and lower rotors of the articulated and completely rigid configurations, is the key to understanding the aerodynamic behaviour of the rotors. The figure shows that the two types of rotor generate very similar distributions of inflow when flown under equivalent trim conditions. Although additional fine detail is superimposed by the action of intra-rotor BVIs on both rotors and inter-rotor BVIs on the lower rotor, the rotors are exposed essentially to a weak lateral gradient of inflow together with a comparatively stronger longitudinal gradient that results in significantly higher inflow at the rear of the rotor disc than at the front. This gradient would produce a significant nose-up pitching moment on the rigid rotor were it not counteracted by cyclic pitch input. Since the

upper and lower rotors rotate in opposite directions, the rolling moments produced by the two rotors are in opposition. The stiffness of the rotor hubs causes the contribution of each individual rotor to the overall rolling moment on the vehicle to cancel internally within the system, and this reduces, to a significant extent, the need for cyclic control to trim out the contribution of the rotor to the rolling moment on the vehicle. On the articulated system, however, the same inflow distribution produces significant lateral flapping of the rotors, which, because the rotors rotate in opposite directions, reduces the separation between the upper and lower discs on the left hand side, at least for systems with rotor sense of rotation as simulated here. This dynamic cannot be controlled because of the coupling between the cyclic pitch inputs to the upper and lower rotors that is inherent in trim method 1; cyclic pitch input can only be used to control the longitudinal flapping of the rotor and hence the forward force that is produced by the system.

4.4.1 Rotor Power Consumption

Figures 4.11 – 4.16 show how the inflow distribution, and the cyclic control inputs that are required to overcome its effects to achieve trim, manifest in the changes in power consumption of the system shown in Figure 4.9 as the flapping stiffness of the rotors is varied. The plots are presented in the same format as Figures 4.4 and 4.5. For the stiffened systems, significant cosine cyclic pitch input is required to generate the increased loading at the rear of both the upper and lower rotor discs that is required to overcome the inflow-induced nose-up pitching moment on the system. Treating the power consumption of the rigid rotor as the baseline case, the loading changes associated with this control input manifest as a very obvious longitudinal gradient in the induced power distribution on the system that becomes more apparent as the induced power consumption over almost the entire rear half of both upper and lower rotors increases as the stiffness of the system is reduced.

All the rotors with finite stiffness tested in this study lie in the regime where the phase shift between cyclic pitch input and the moment (or flapping) produced on the system is very small. In contrast, the very low stiffness of the articulated rotor results in a phase shift of the rotor flapping response to cyclic control input that requires significant sine cyclic to overcome the tendency of the rotor discs to flap backwards

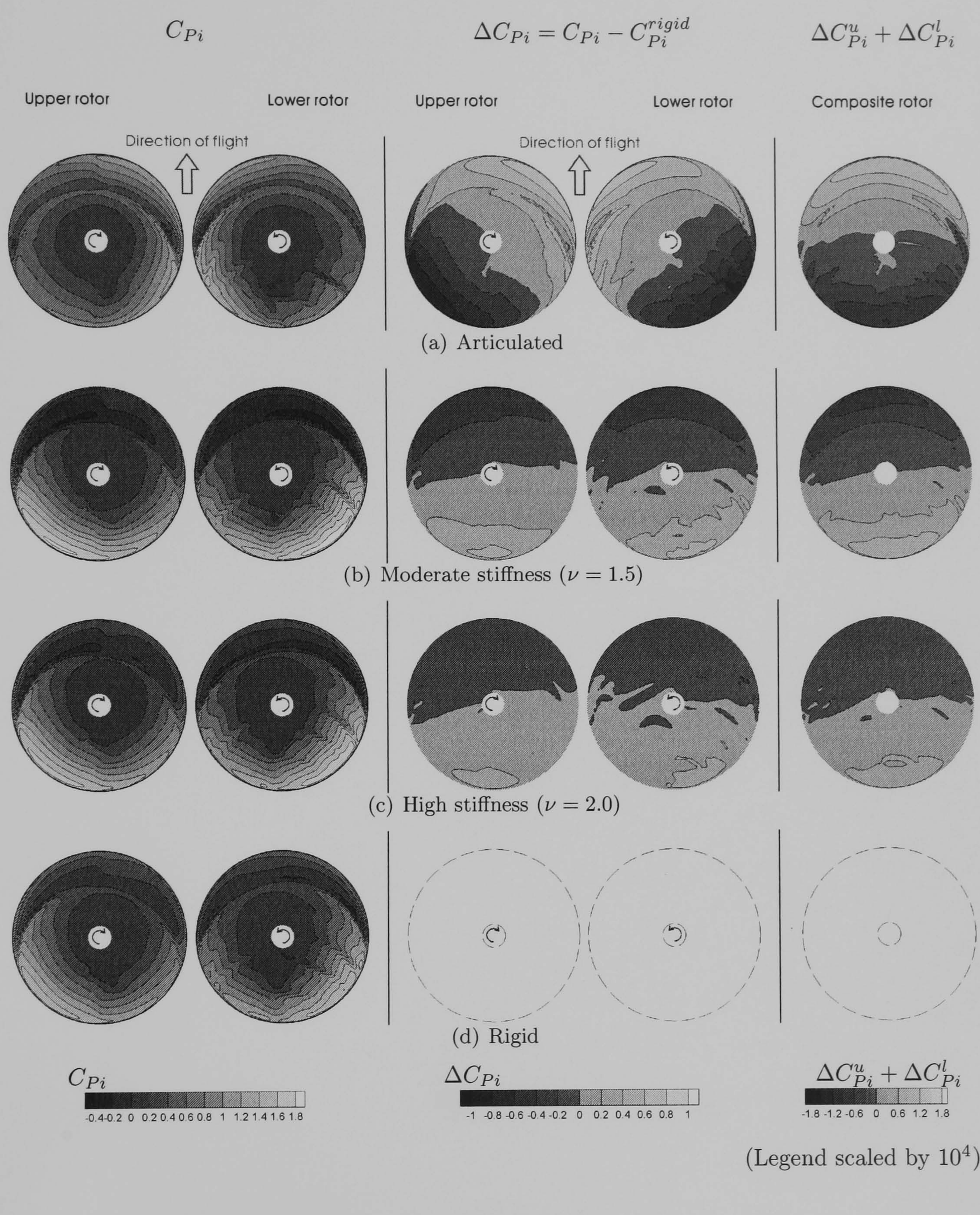


Figure 4.11: *Effect of rotor stiffness on the distribution of induced power consumption on the upper and lower rotors of the coaxial system at advance ratio* $\mu = 0.12$.

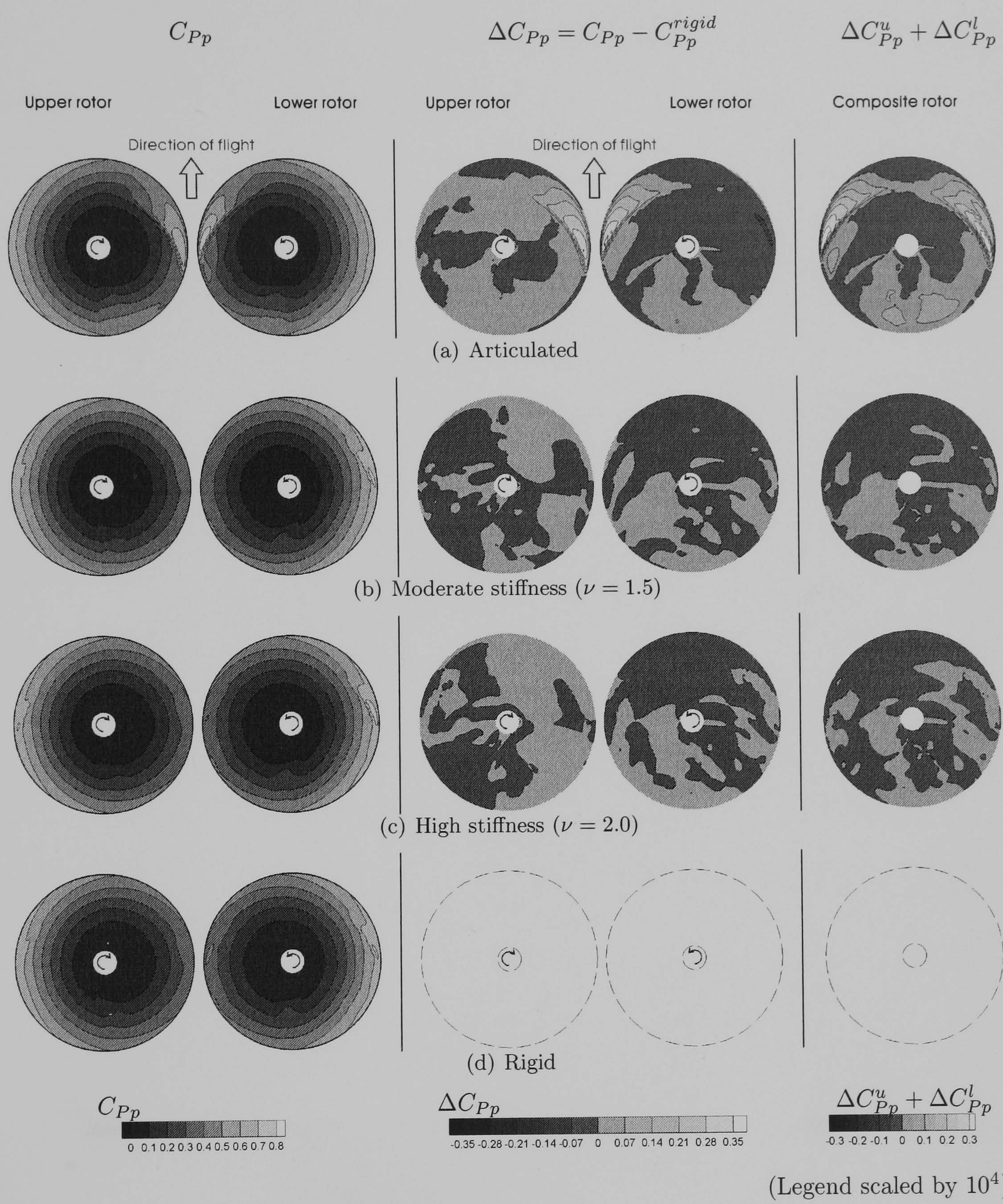


Figure 4.12: *Effect of rotor stiffness on the distribution of profile power consumption on the upper and lower rotors of the coaxial system at advance ratio* $\mu = 0.12$.

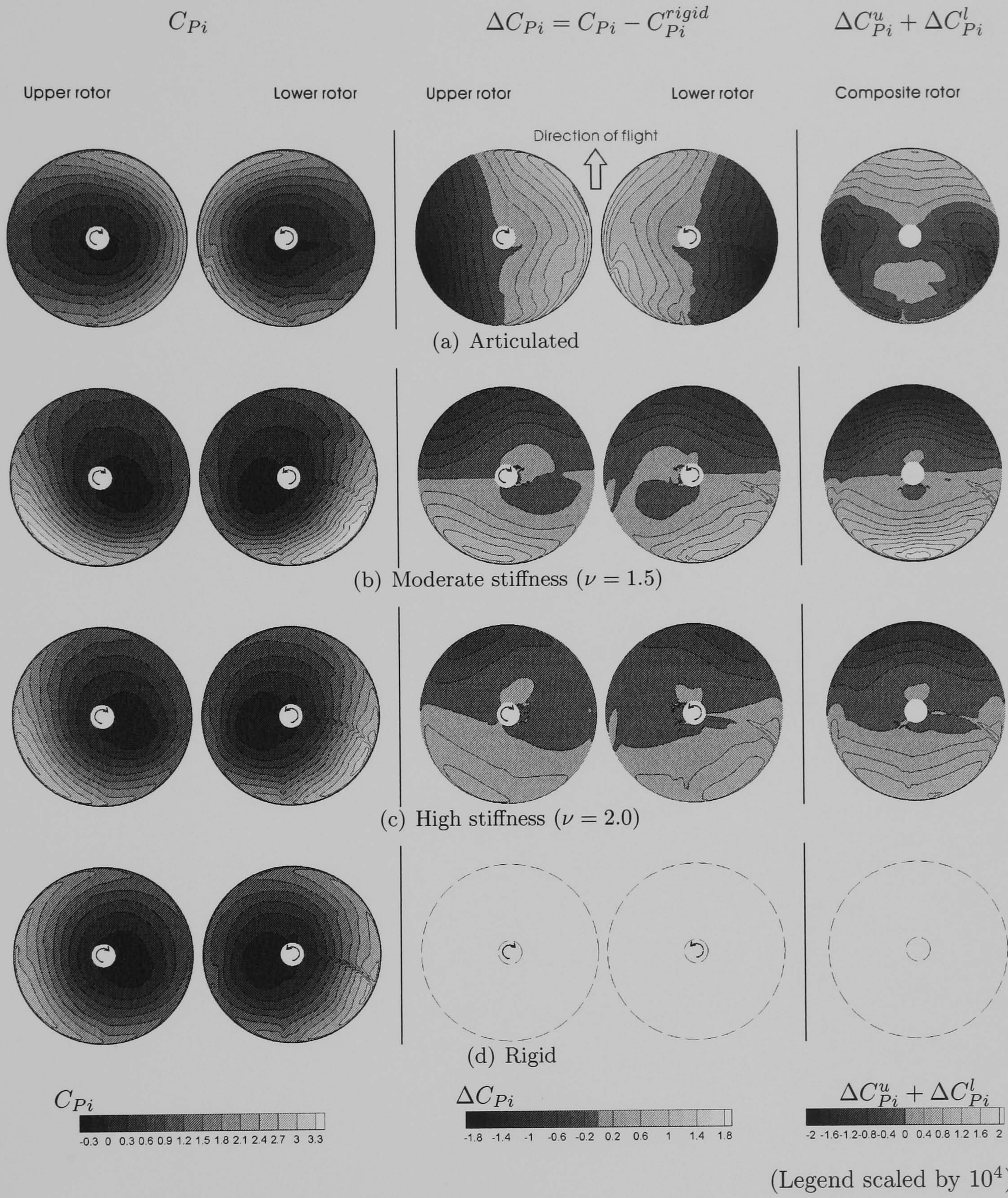


Figure 4.13: *Effect of rotor stiffness on the distribution of induced power consumption on the upper and lower rotors of the coaxial system at advance ratio* $\mu = 0.24$.

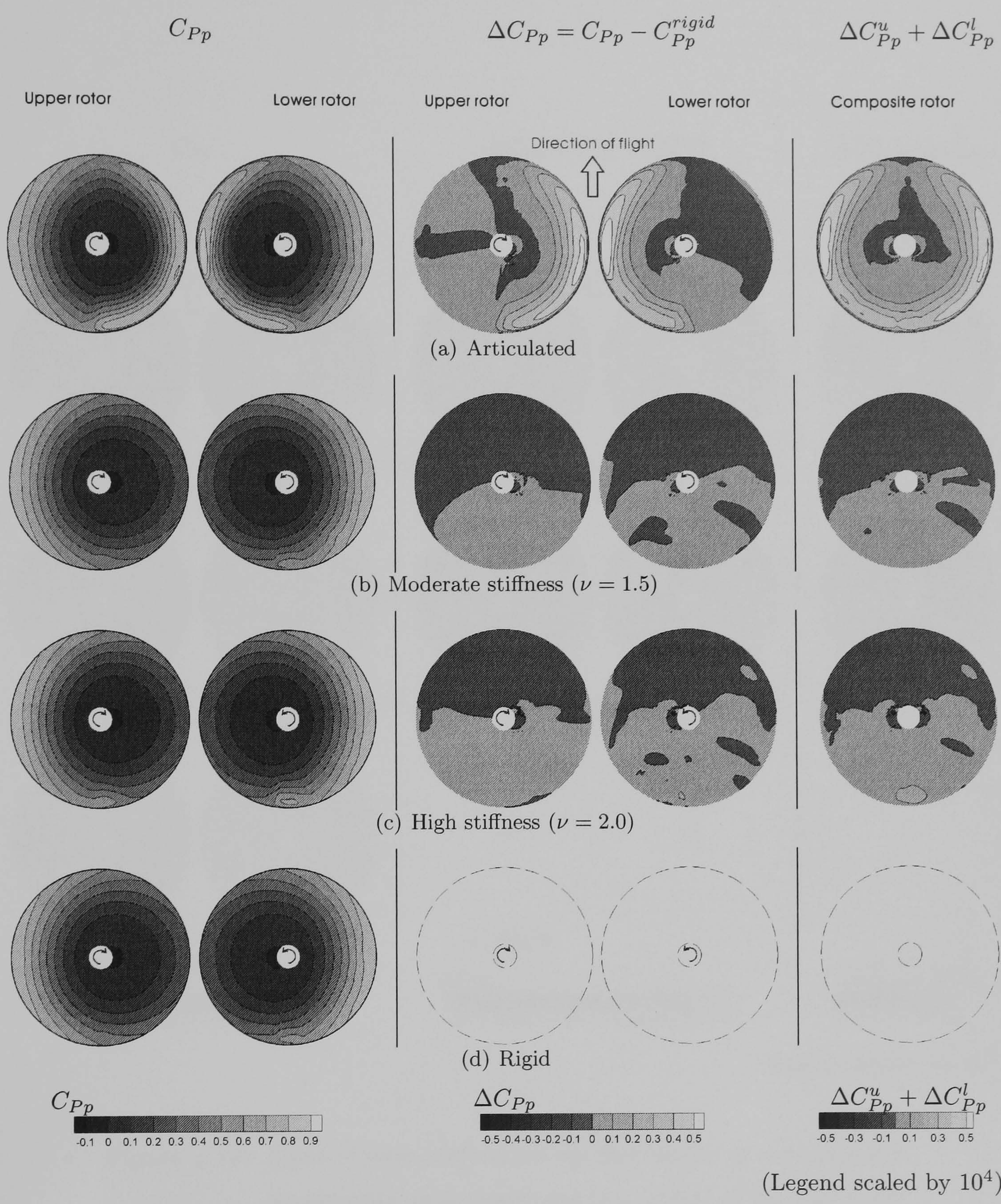


Figure 4.14: *Effect of rotor stiffness on the distribution of profile power consumption on the upper and lower rotors of the coaxial system at advance ratio* $\mu = 0.24$.

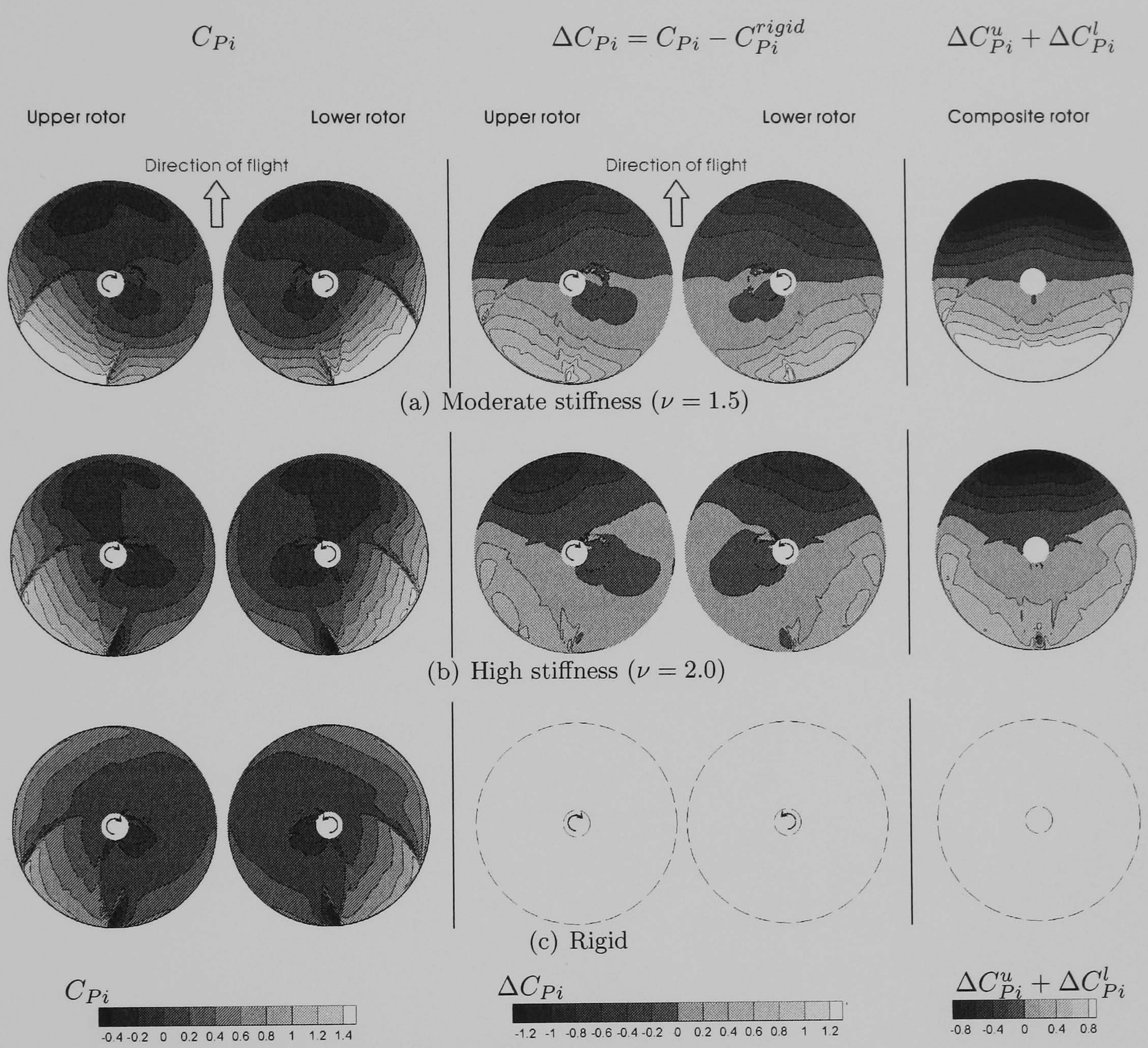
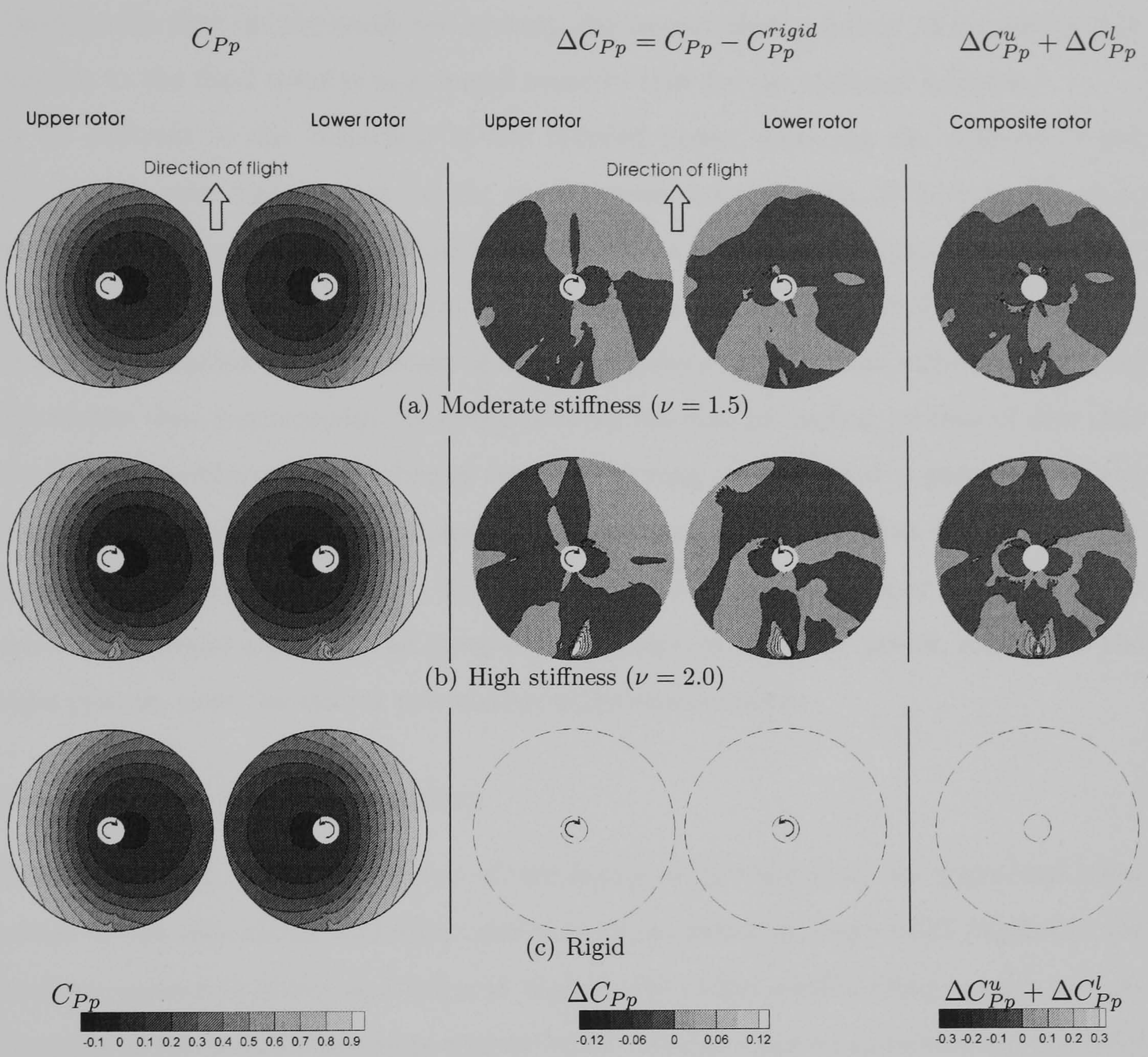


Figure 4.15: *Effect of rotor stiffness on the distribution of induced power consumption on the upper and lower rotors of the coaxial system at advance ratio* $\mu = 0.36$.



(a) Moderate stiffness ($\nu = 1.5$)

(b) High stiffness ($\nu = 2.0$)

(c) Rigid

(Legend scaled by 10^4)

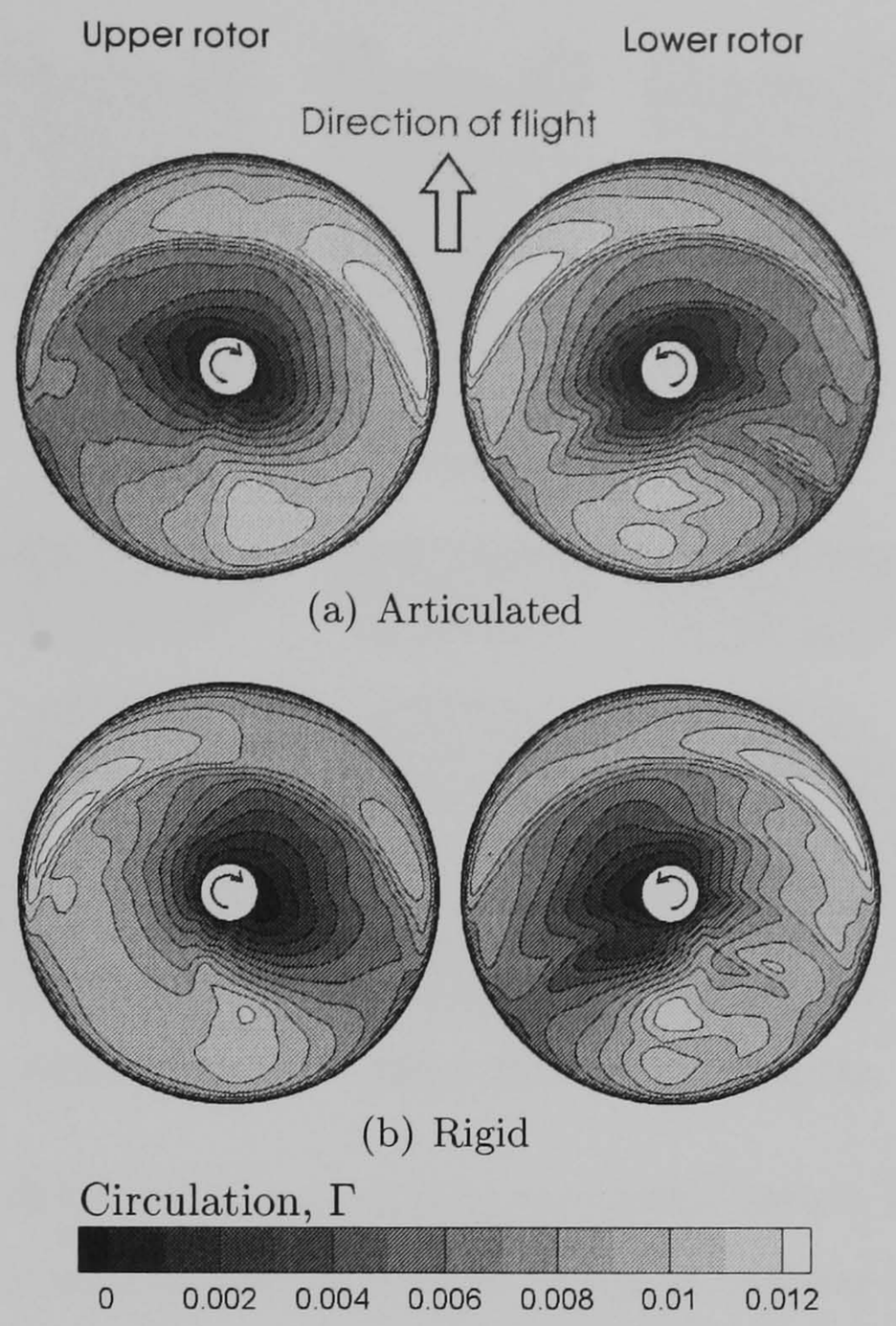
Figure 4.16: *Effect of rotor stiffness on the distribution of profile power consumption on the upper and lower rotors of the coaxial system at advance ratio* $\mu = 0.36$.

(and hence to produce an un-trimmed forward force). This control input manifests as a significant, additional, lateral component to the induced power gradient on the rotors of the articulated system. This lateral component is such that, on each individual rotor, the highest induced power consumption is shifted towards the retreating side, with the consequence that on the combined system, the longitudinal gradient of induced power relative to the rigid rotor is in reversed sense to that for the stiffened systems.

In contrast to the behaviour of the induced power, reducing the stiffness of the system has very little impact on the profile power consumption of the coaxial rotors with finite stiffness — if any trend is discernible, it follows that of the induced power. This suggests that the primary contributing mechanism to any sensitivity of the profile power consumption to the stiffness of the rotor system is simply the increase in drag on the blades that accompanies the cyclic-induced increase of loading on rear of disc that is required to overcome the inherent nose-up pitching moment that is generated by the rotor. In the case of the articulated rotor, the situation is somewhat different in that the highly loaded tip-regions on the retreating side of both the upper and lower discs contribute almost equally to an increased consumption of profile power, relative to the rigid system, near the lateral extremities of the coaxial rotor.

4.4.2 Rotor Wake Geometry

The comparison of the distribution of circulation on the blades of the upper and lower rotors of the articulated and rigid coaxial systems shown in Figure 4.17 reinforces the analysis presented above and helps to explain the rather subtle differences in the geometries of the wakes that are produced by the various rotor systems that are revealed in Figures 4.18 – 4.21. The figure highlights the intrinsic differences in the aerodynamic behaviour of articulated and very stiff rotor systems. For the trimmed articulated rotor, the highest circulation, on both upper and lower rotors, is generated on the blade tips as they traverse the retreating side of the rotor discs. For the rigid rotor, the highest circulation is again generated at the tips of the blades, but the peak values are much lower than with the articulated rotor and occur instead on the advancing sides of the rotor discs. The rate of change of circulation along the length of the blade translates directly into the strength of the vorticity that is trailed from the blades into the flow downstream of the rotor, and this in turn has direct consequences for the overall struc-



(a) Articulated

(b) Rigid

Figure 4.17: *Circulation distribution on upper and lower rotors at advance ratio $\mu = 0.12$ and thrust coefficient $C_T = 0.0048$. Articulated and rigid rotors compared.*

ture of the resultant wake of the system. Figure 4.18 compares the geometry of the wakes that are generated by the various types of rotor at low forward speed ($\mu = 0.12$) by showing the series of surfaces embedded in the flow on which the wake vorticity has some prescribed constant strength. The vortex strength has been set high enough to reveal the structure of the individual tip vortices while suppressing much of the finer structure that is associated with the dynamics of the vortex sheets that are created inboard of the blade tips. The figure shows the wakes of the articulated and rigid rotors to have a subtly different structure, especially along the lateral extremities of the wake where the individual tip vortices from the upper and lower rotors coalesce to form the concentrated, aeroplane-like 'super-vortices' that trail downstream of the system. There are noticeable differences too in the geometry of the under-side of the wake where the stronger root-vortex structures that are created by the stiffened rotors produce a distinct kink down the centreline of the wake and, indeed, a much more flattened wake

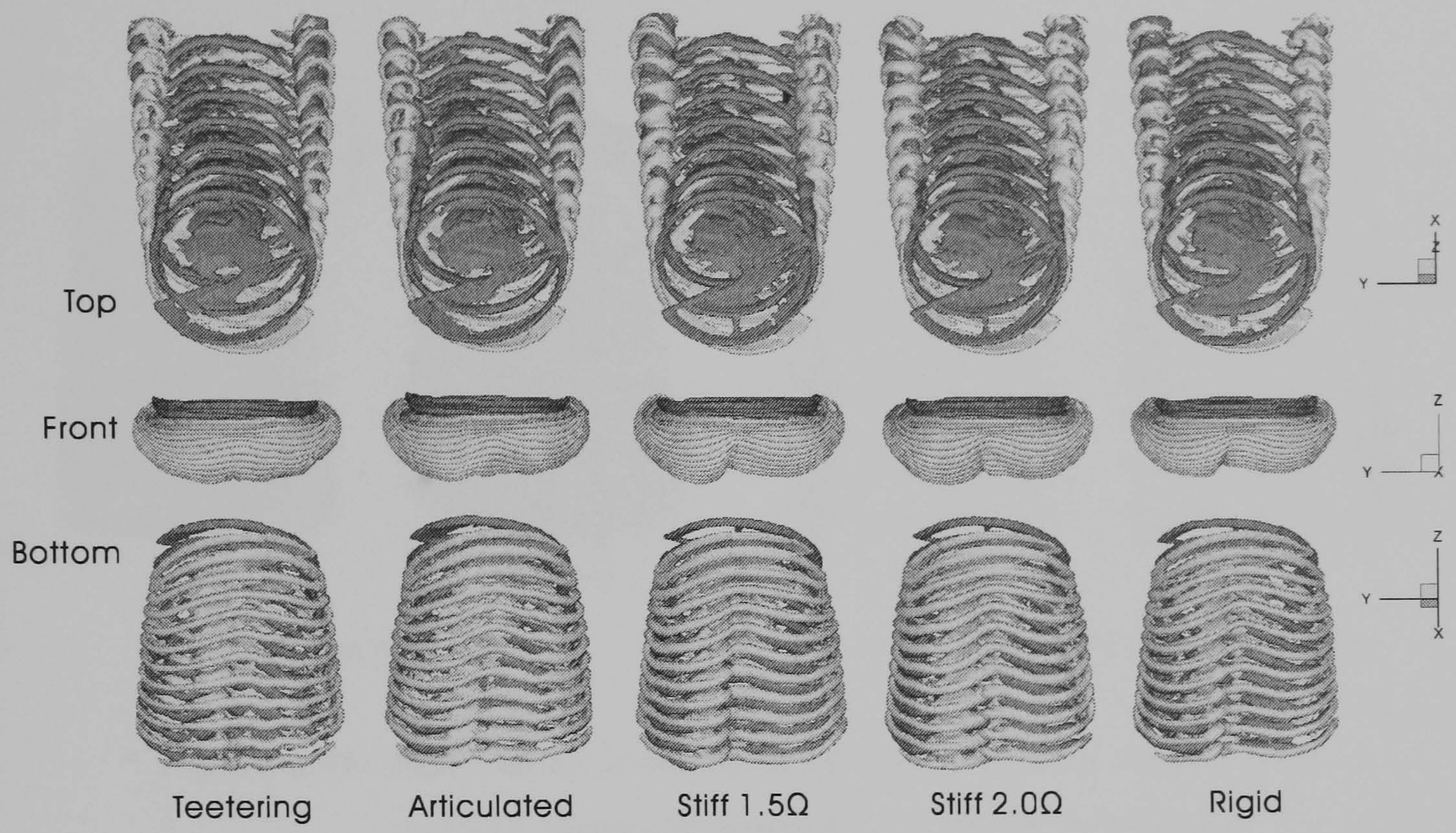
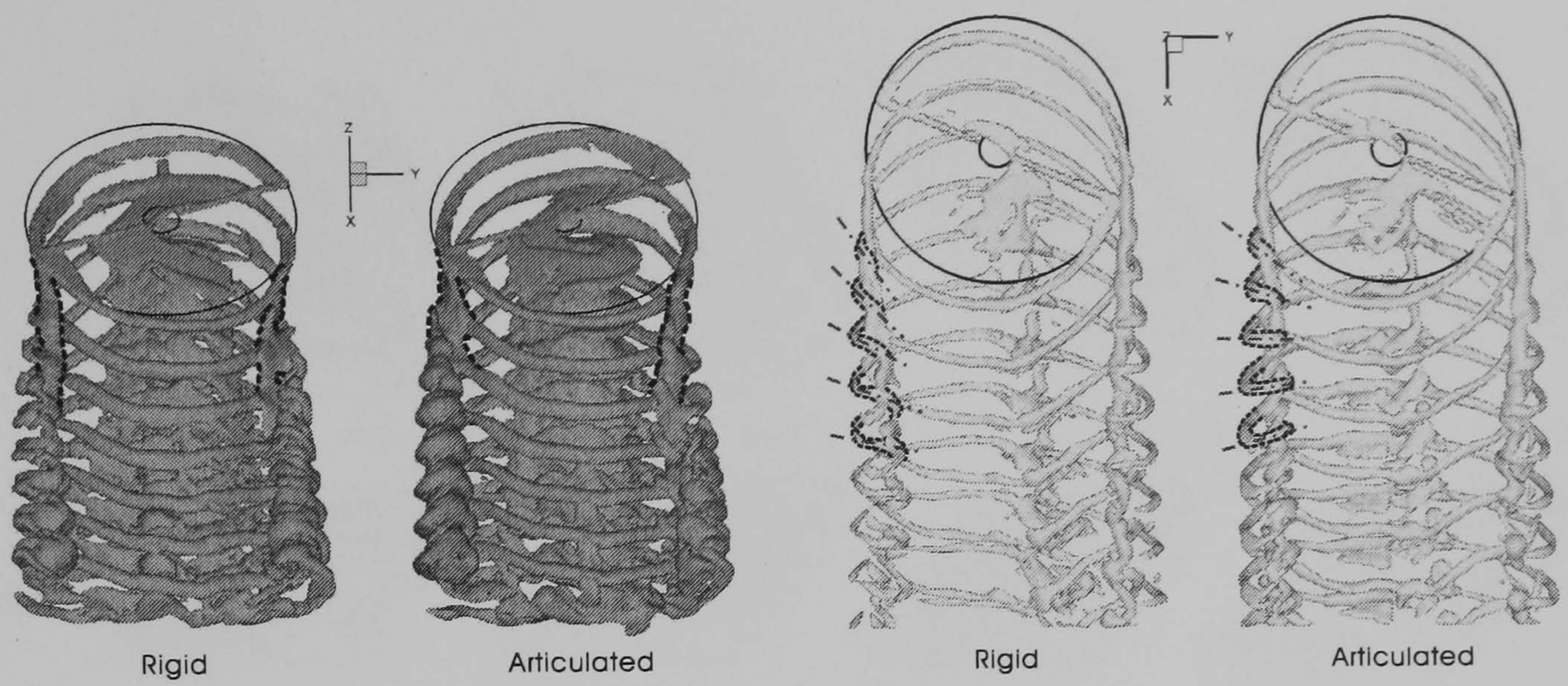


Figure 4.18: *Rotor wakes generated by the coaxial system in forward flight at advance ratio $\mu = 0.12$. (Varying stiffness including teetering configuration). The wake generated by the upper rotor is coloured a darker shade than the wake from the lower rotor.*

structure overall. This feature may have an impact on how the wakes of the two types of rotor system interact with other downstream components of the helicopter and hence perhaps on the stimulation of aerodynamically-induced vibratory loads on the airframe.

The fluid dynamic interaction that takes place during the formation of the super-vortices to either side of the main body of the wake is shown more clearly by plotting separately the components of the wake that are generated by the upper and lower rotors as in Fig 4.19. Essentially the interaction consists of two fundamental processes. The first process is one of entrainment, whereby the vorticity from one of the rotors is drawn away from the path that it might follow, were the rotor to operate in isolation, and into closer proximity to the wake of the other rotor. The second process is one of entwinement, where components of the wakes of the individual rotors co-orbit to eventually create a single, merged structure. Because of the downwards flow that is induced by the trailed wake system, the effects of entrainment are nearly always confined to the wake produced by the upper rotor as it is drawn down towards the wake of the



(a) Upper rotors

(b) Lower rotors

Figure 4.19: *Super-vortex formation on the coaxial rotor at advance ratio* $\mu = 0.12$. *Rigid and articulated configurations compared.*

lower rotor. The relative pace at which the entrainment process occurs on the left and right hand sides of both systems is consistent with the different relative strengths of the vorticity produced from the blades that can be inferred from the circulation distributions that are portrayed in Figure 4.17. The entrainment of the vorticity of the upper rotor of the articulated system into the right hand super-vortex occurs over a significantly longer distance downstream of the rotors than does the similar process that takes place on the left hand side of the system. This is consistent with the influence of the significantly stronger trailed vorticity on the left hand side of the lower rotor than the right on the process of entrainment. On the rigid system, however, the entrainment on both sides of the rotor takes place at roughly the same pace. This is consistent with the much smaller differential in trailed vortex strength between the left and right hand sides of the lower rotor of the rigid coaxial system. Comparing the structures produced during the subsequent process of entwinement shows the stronger vortex from the left hand side of the lower rotor of the articulated system to produce a far more coherent rolled-up structure with significantly reduced pitch of the individual tip vortex filaments as they orbit the core of the developing super-vortex than the equivalent structure that is associated with the weaker vortex that trails from the left hand side of the lower rotor of the rigid system.

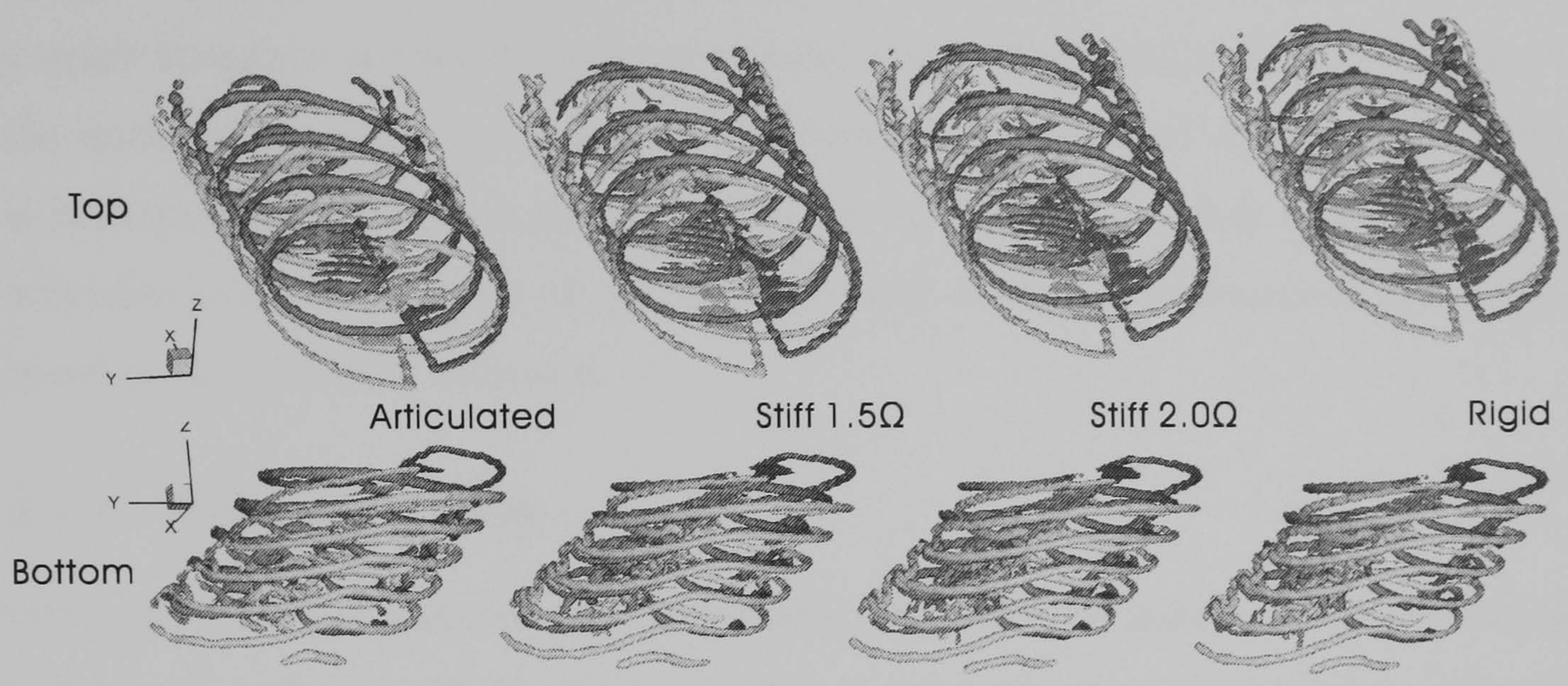


Figure 4.20: *Rotor wakes generated by the coaxial system in forward flight at advance ratio* $\mu = 0.24$. *The wake generated by the upper rotor is coloured a darker shade than the wake from the lower rotor.*

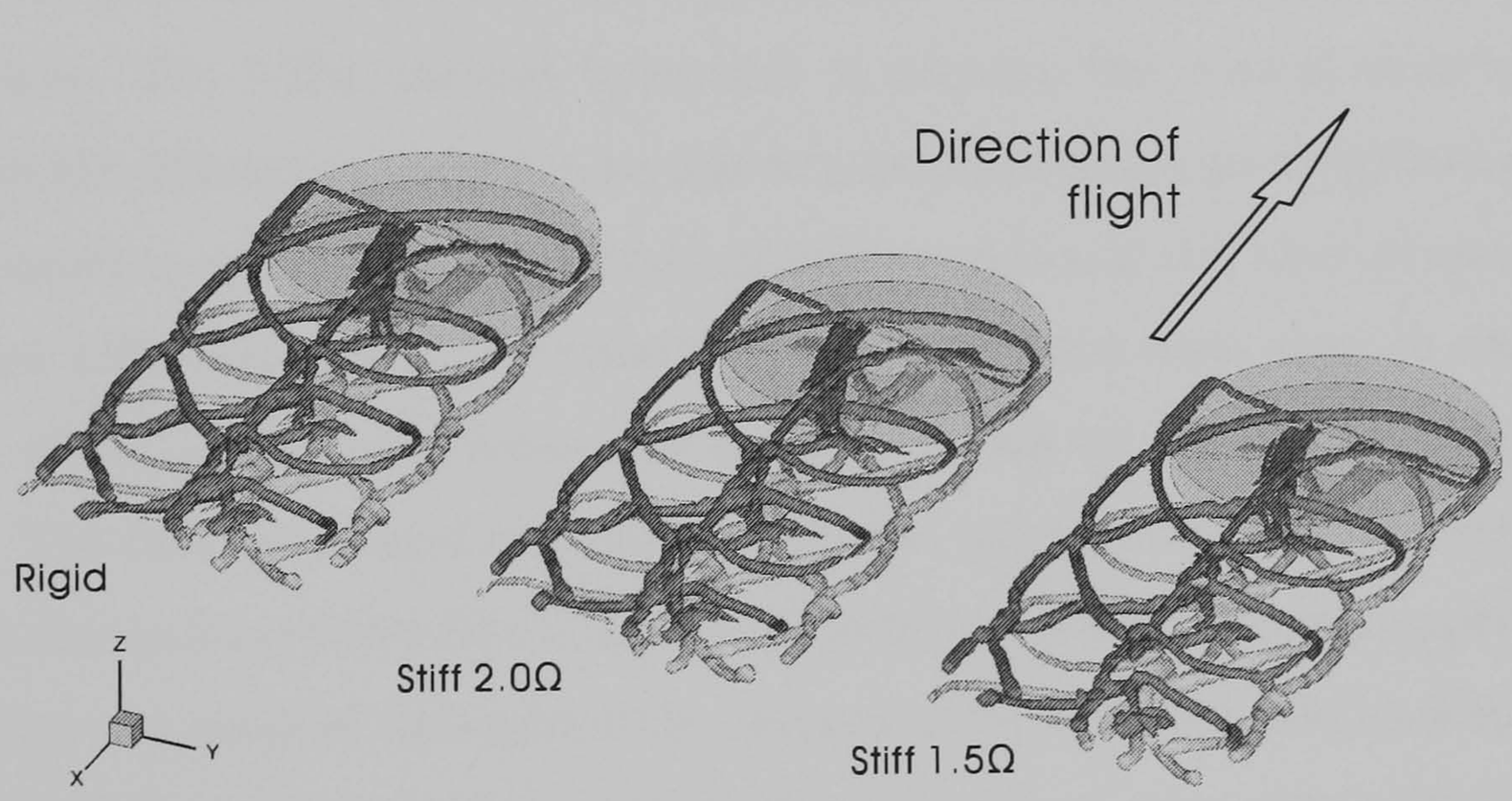


Figure 4.21: *Rotor wakes generated by the stiff coaxial system in high-speed forward flight at advance ratio* $\mu = 0.36$. *The wake generated by the upper rotor is coloured a darker shade than the wake from the lower rotor. Rotor discs plotted for clarity.*

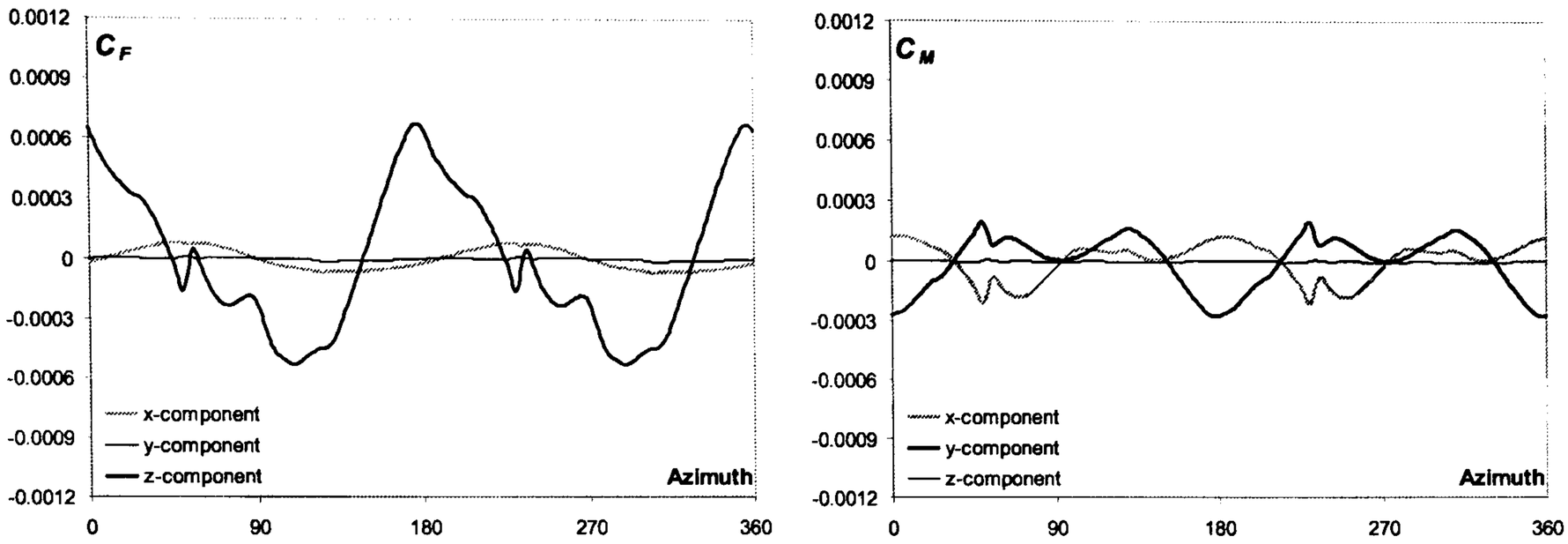
Increasing the forward speed of the system simplifies significantly the geometry of the wake that is produced by both types of rotor. Figures 4.20 and 4.21 show that, beyond an advance ratio of about 0.24, the wakes produced by the upper and lower

rotors remain essentially distinct downstream of the system, rather than merging into a single structure as they do at lower forward speed. The reduced interaction between the wakes of the upper and lower rotors of both the articulated and stiffened systems is principally due to the convective effect of the free stream that delays significant mutually-induced distortion of the wakes to much further downstream as the forward speed of the system is increased.

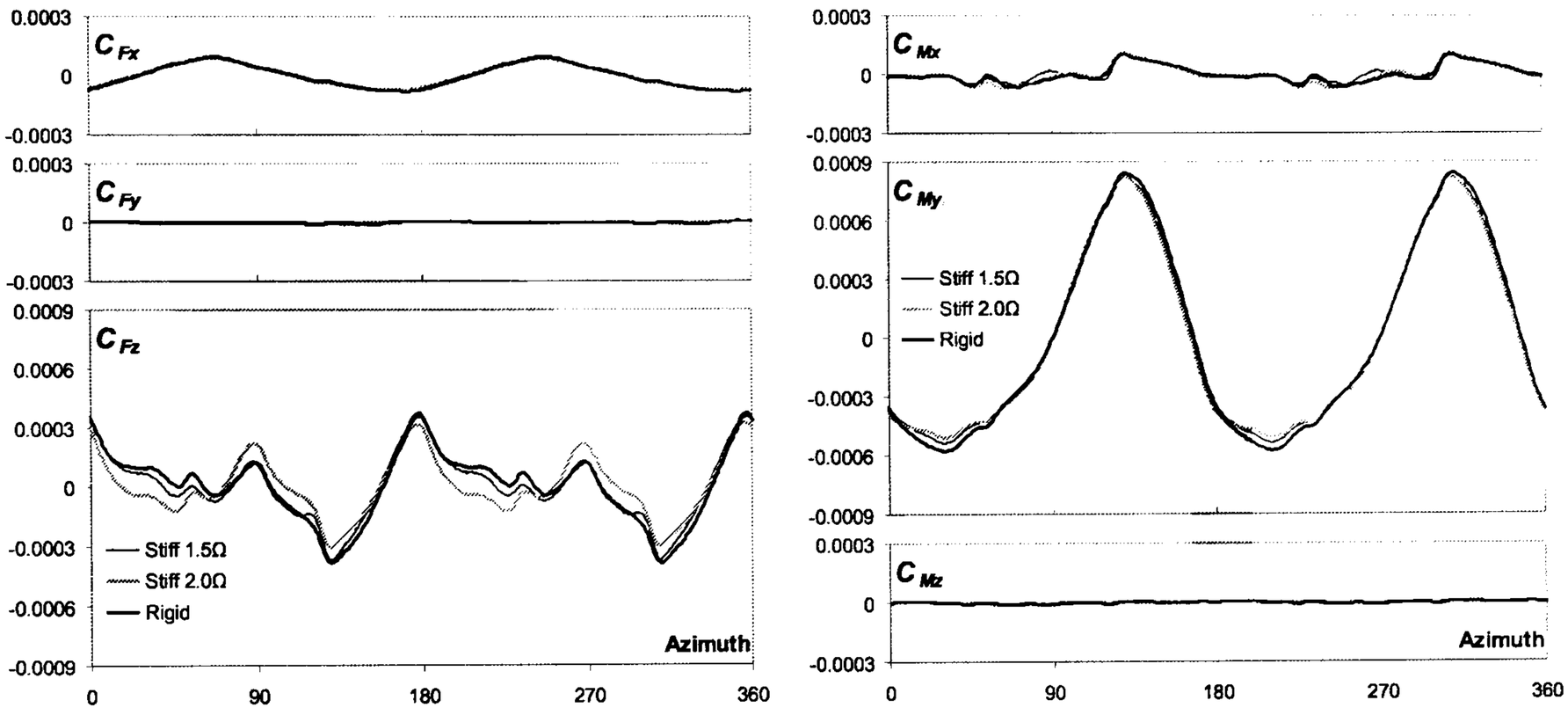
4.4.3 Rotor Vibration

Of significant practical interest is the penalty that has to be paid, in terms of increased vibrational excitation of the system, for the obvious advantages in power consumption of adopting a configuration that uses a stiff coaxial rotor system. With a conventional rotor, a significant contribution to the vibration of the system comes from the loading perturbations that are induced by the intra-rotor BVIs within the system. The behaviour of the coaxial system is complicated further by the effects of the longer-range inter-rotor BVIs that originate in the aerodynamic interference between the upper and lower rotors. The VTM, through being able to preserve the vortical structures in the wake over the distances required to be able to capture these longer-range interactions, is ideally suited to examining the vibrational characteristics of this class of rotor system.

Figure 4.22 compares the net contribution of upper and lower rotor to the six components of the aerodynamic forces and moments acting on the lower hub of the rotor system. The data are plotted as a function of time, indexed to the azimuth of the lower rotor. In interpreting these data it should be borne in mind that the assumption of rigid blades that was adopted throughout the analysis so far, although adequate for analyses of the overall loads on the system associated with issues of trim and performance, runs the risk of being taken too far when examining the high-frequency content of the loading on the system. Analysis of the vibrational characteristics of the system in terms solely of the overall aerodynamic loading is strictly only accurate for the infinitely stiff rotor system. For real systems with finite hub stiffness and flexible blades the link between aerodynamic loading and vibrational forcing of the helicopter is complicated by the dynamic characteristics of the blades themselves. To put the data in perspective, the entire aerodynamic contribution to the rolling and pitching moments C_{Mx} and C_{My} and a significant proportion of the vertical force C_{Fz} shown in Figure 4.22 to be generated



(a) Articulated rotor



(b) Stiffened rotors

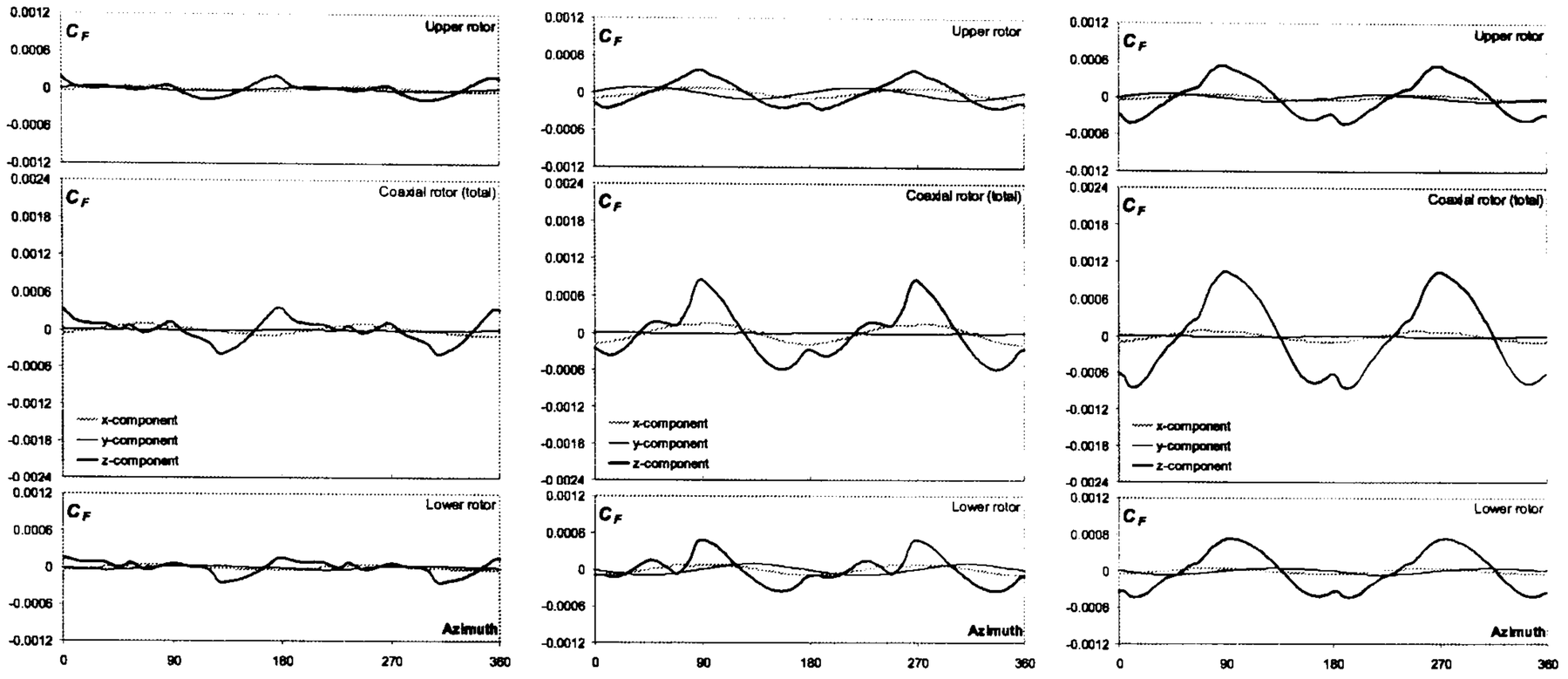
Figure 4.22: *Effect of rotor stiffness on unsteady aerodynamic forcing of the coaxial system at advance ratio* $\mu = 0.12$*, thrust coefficient* $C_T = 0.0048$*. (Mean component removed.)*

by the articulated rotor would be attenuated by blade flapping.

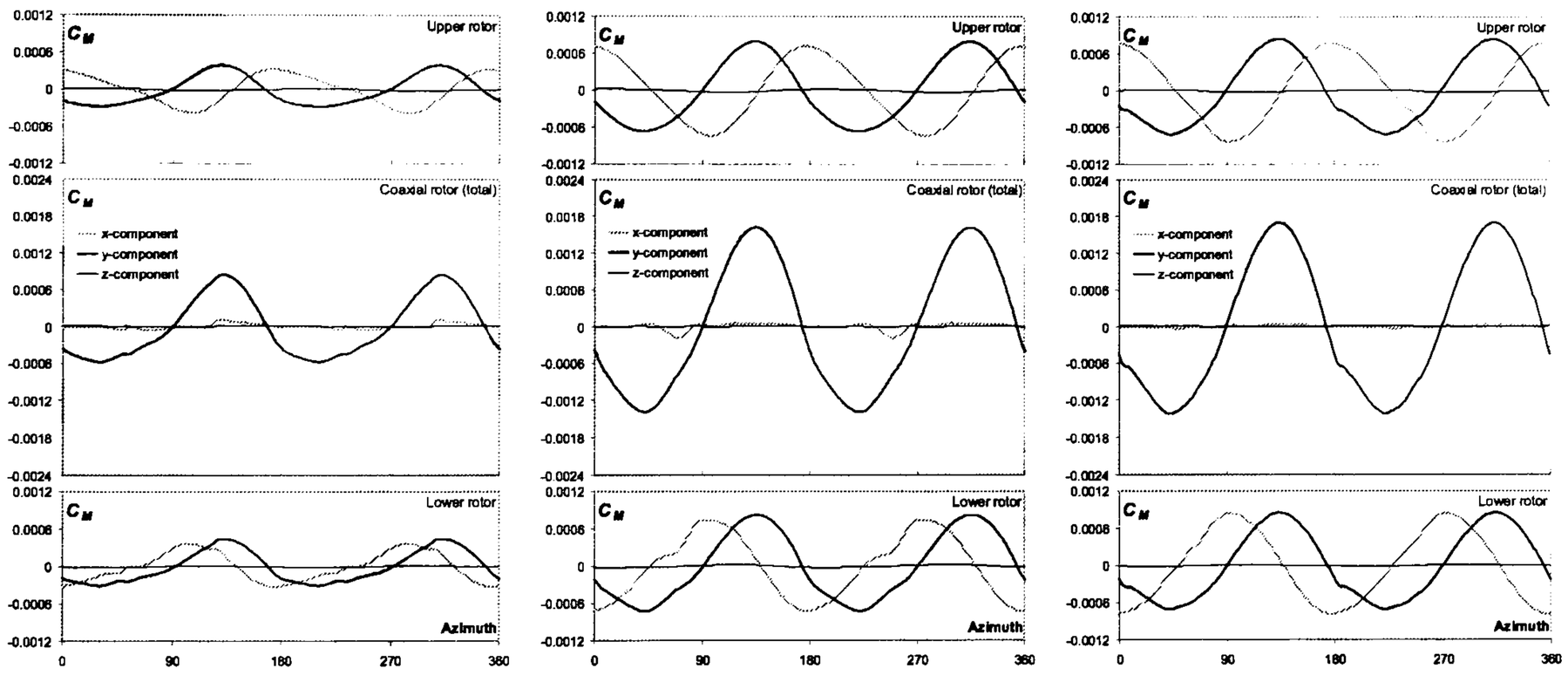
Nevertheless the results that are presented for the stiff rotors are very interesting, showing a marked insensitivity of the time-dependent component of the aerodynamic forcing of the system to the actual stiffness of the rotors. This insensitivity suggests that very stiff coaxial systems, at least those with fundamental flapping frequencies similar to those tested here, may be beyond the range where relatively simple palliative measures such as aeroelastic tailoring of the blades may have useful effect in modifying the fundamental vibrational characteristics of the system. In all cases, the vibratory

signal from the stiff coaxial rotor is dominated by a very strong two-per-revolution pitching moment together with a vertical forcing which has similar frequency (although with significant higher-frequency content too) and an amplitude of about six percent of the mean thrust generated by the rotor. The frequency and amplitude of both of these components of forcing could plausibly result in rather objectional vibrational excitation of the aircraft. The relatively small contribution to the vibrational loading on the system from the aerodynamic rolling moment C_{Mx} is a consequence of the near-cancellation of the individual contributions from the upper and lower rotors. In the absence of interaction between the rotors it might be expected that net zero rolling moment would be produced as a result of mutual cancellation of the contributions from the upper and lower rotors given suitable cyclic control inputs to the system. This symmetry is broken though by the effect on the lower rotor of aerodynamic interaction with the upper rotor. The perturbations in loading that are induced by the inter-rotor BVIs on the lower rotor manifest as a series of periodic spikes in the overall rolling moment that is produced by the system. The resulting perturbations in the rolling moment are hence expected to be affected by any changes in the character of the inter-rotor BVIs and also the locations of the blade overpassage caused by alternative phasing arrangement between the upper and lower rotors. These spikes are strongest at the intermediate forward speed but reduce in amplitude as the forward speed of the rotor is increased and the interaction between the wakes produced by the two rotors becomes less significant (see Figure 4.23). Note too that although suppression of these effects may be possible through appropriate feathering of the blades, control inputs to the rotor at higher frequency than those considered in the present study would be required.

Figure 4.23 illustrates the effects of aerodynamic interference between the rotors more clearly by showing the individual contributions from the upper and lower rotor to the aerodynamic forcing of the system for various forward speeds for the rigid rotor alone. The very obvious increase in amplitude of the 2Ω variation in pitching moment with forward speed is arrested at the highest forward speed by the effect of the auxiliary propulsor in reducing the cyclic input required to trim the rotor at this flight condition, but no such similar attenuation of the heave component of the aerodynamic forcing is apparent. At all forward speeds the contribution to the pitching moment is shared almost evenly between the upper and lower rotors. In most cases where significant



(a) $\mu = 0.12$ (b) $\mu = 0.24$ (c) $\mu = 0.36$

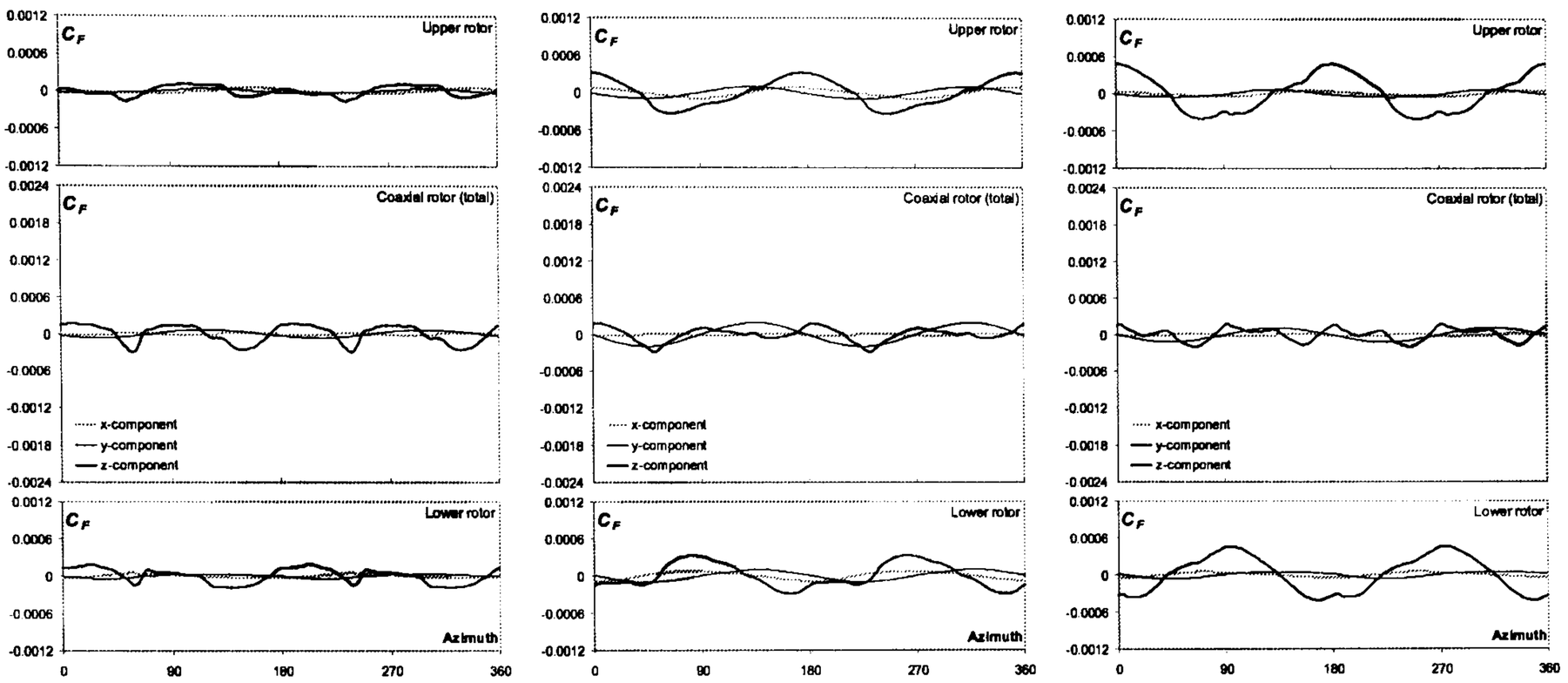


(a) $\mu = 0.12$ (b) $\mu = 0.24$ (c) $\mu = 0.36$

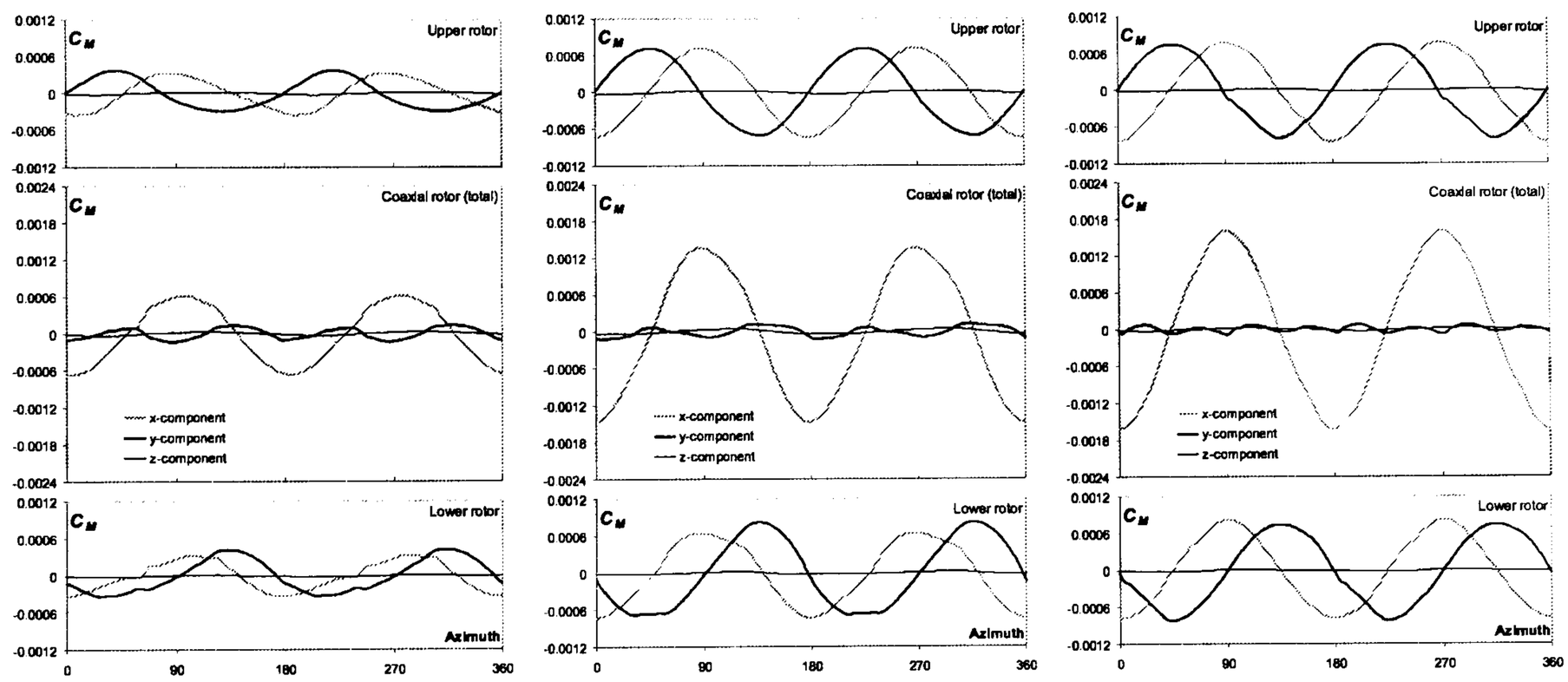
Figure 4.23: *Unsteady aerodynamic forcing of the rigid coaxial system. Contributions from upper and lower rotors to overall forcing compared at various forward speeds. (Mean component removed.)*

higher frequency content is visible in the signal it originates predominantly in the loading perturbations on the lower rotor that result from its aerodynamic interaction with the upper rotor.

Past studies have shown the relative phasing of the blades between the upper and the lower rotor to affect significantly the dynamic characteristics of the aircraft [3, 6]. For example, the high level of vibration at the fundamental blade passage frequency (primarily from the rolling moment) associated with the three-bladed XH-59A configuration was reduced significantly by shifting the location of blade overpassage from 90° to 0° [6]. It is interesting to note that a rearrangement of the relative phasing between the upper and lower rotors, such that the blade overpassage occurs at azimuths of 45°, 135°, 225°, and 315° (rather than at azimuths of 0°, 90°, 180°, and 270° as originally configured), has a clear impact on the vibratory forcing of the system. This can be seen by comparing Figures 4.23 and Figures 4.24. The comparison reveals that the large amplitude, two-per-revolution forcing in heave that results when the rotor overlap as originally configured, is attenuated by a 90° shift in phase of the upper rotor relative to the lower. This attenuation arises from the destructive interference between the individual heave forcing of the upper and the lower rotors. The high frequency components of the unsteady forcing in heave persist, though with smaller amplitude than with the original phasing of the rotors. The change in phasing of the rotors also alters the character of the forcing of the system. The longitudinal and lateral components of the aerodynamic forcing on the system appear to be interchanged as a result of the 90° shift in phase between the rotors. This effect is most clearly seen in the moments induced on the system where the large fluctuation in pitch is transformed into a similar fluctuation in roll as a result of the change in phasing. In all cases, the gross changes in the aerodynamic forcing appear to be determined primarily by the changes in relative phasing of the two-per-revolution variation in loading between the upper and lower rotors that result from the phase shift of the rotors relative to each other. Perturbations in the loading, at higher frequency than the fundamental blade passage frequency are primarily due to modification of the BVI patterns, primarily over the lower rotor that results from the phase difference of the impulsive changes in loading associated with blade overpassage. Figure 4.25 shows the effect of the alternative phasing arrangement on the pattern of BVIs on the discs of the upper and lower rotors. It is evident from this



(a) $\mu = 0.12$ (b) $\mu = 0.24$ (c) $\mu = 0.36$



(a) $\mu = 0.12$ (b) $\mu = 0.24$ (c) $\mu = 0.36$

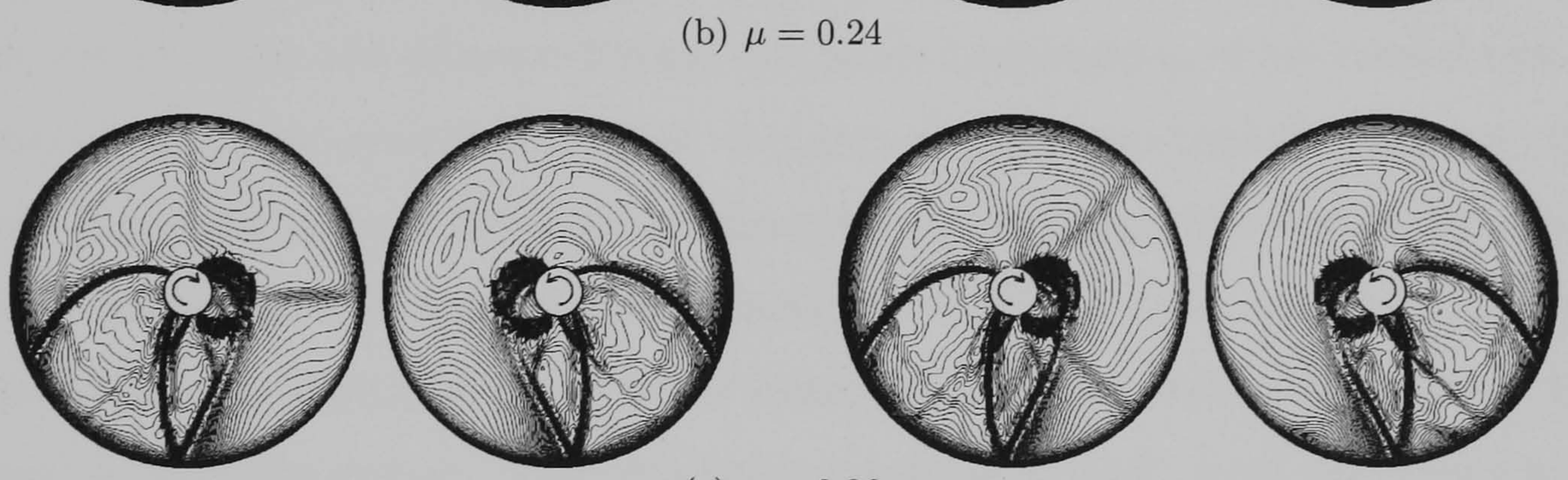
Figure 4.24: *Unsteady aerodynamic forcing of the rigid coaxial system with alternative blade phasing (90° offset compared to that from Figure 4.23). Contributions from upper and lower rotors to overall forcing compared at various forward speeds. (Mean component removed.)*



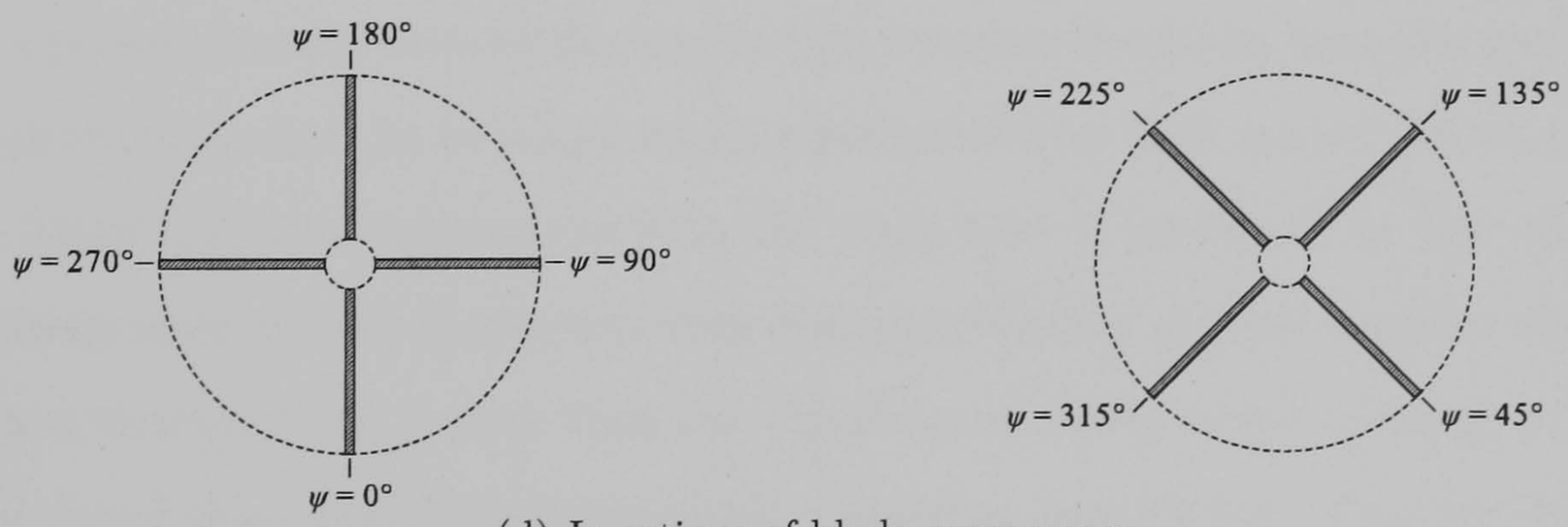
(a) $\mu = 0.12$



(b) $\mu = 0.24$



(c) $\mu = 0.36$



(d) Locations of blade overpassage

Figure 4.25: *Comparison of BVI patterns for different phasing. BVI visualised by high gradients of inflow using line contours. (Left: original phasing. Right: alternative phasing.)*

figure that the BVI pattern on the upper rotor is largely unaffected by the change in phasing of the rotors. This observation is entirely consistent with the fact that the only discernible effect on the upper rotor of the change in phasing is a change in the phasing of the weak interaction with the lower rotor that is induced by blade overpassage (see Figures 4.23 and 4.24). The BVI pattern on the lower rotor is, however, noticeably modified by the change in phasing, particularly at lower forward speeds. At the highest advance ratio, $\mu = 0.36$, the two systems with different phase arrangements share a very similar pattern of BVI features over both upper and lower rotor discs.

4.5 Summary

The impact of rotor trim strategy in conjunction with rotor hub stiffness on the performance of a coaxial rotor in forward flight is examined using the VTM. The model is able to capture the subtle effects of aerodynamic interactions between the upper and lower rotors on the aerodynamic forcing and power consumption of the coaxial system. A simplified system consisting of a pair of contra-rotating, two-bladed rotors is studied in which the dynamics of the rotor are modelled by assuming rigid blades, articulated at their roots. The effects of flapwise stiffness are accounted for using springs. The calculations show a sensitivity of the power consumption of the rotor to the method that is used to trim the system. This sensitivity results principally from the effect on the induced power consumption of the interaction between the loads that are introduced by cyclic pitch input and the localised loading perturbations that are produced, principally on the lower rotor, by interaction with the wake that is produced by the upper rotor. Simulations support the contention that the introduction of high flapwise stiffness can produce a coaxial rotor system that has significantly lower power consumption at high forward speed than more conventional rotor systems, particularly if an auxiliary device is used to alleviate the requirement for the main rotor system to produce a propulsive force component. A detailed analysis of the unsteady aerodynamic forcing of the system suggests though that an unavoidable penalty might be paid by the stiffened coaxial system in terms of enhanced noise and vibration. The role of inter-rotor blade vortex interactions in disrupting the balance in loading between upper and lower rotors at frequencies that cannot be counteracted by simple one-per-revolution control inputs is

captured in the simulations. Furthermore, altering the relative phasing arrangement between the upper and lower rotor is shown to affect significantly the characteristics of the unsteady aerodynamic forcing. While it is possible to attenuate the heave component of the vibrational forcing by altering the relative phasing of the rotors, the vibratory excitation in pitch and roll appear simply to be interchanged rather than attenuated by a 90° change in the relative phasing of the upper and lower rotors. As such, the computational model exhibits sensitivity to the same physical effects that have arisen in practical implementations of the stiffened coaxial configuration and shows promise in being able to analyse the performance and dynamics of realistic stiffened coaxial rotor configurations.

Chapter 5

Aeroacoustics of Coaxial Rotors

5.1 Introduction

Most of the existing literature has failed to provide a truly fair comparison of the relative performance of conventional and coaxial rotors. It is argued in Chapter 3 that the fairest comparison between conventional and coaxial rotors is on the basis of equal solidity, and identical overall blade number and aerodynamic properties. On this basis the coaxial rotor is shown to consume less power, mainly due to its slightly lower consumption of induced power compared to the equivalent single rotor (see Chapter 3). The advantage of the coaxial rotor system in terms of reduced power requirement was shown in Chapter 4 to be enhanced by the introduction of significant flapwise stiffness. Additionally, compared to single rotor systems, coaxial rotors with significant flapwise stiffness can operate at lower tip speeds than the equivalent articulated system, thus offering the potential to postpone the detrimental effects of compressibility on aerodynamic and acoustic performance to higher forward speeds [67].

While the aerodynamic characteristics of coaxial rotors are not as well studied as those of conventional rotors, detailed investigations of the acoustic performance of coaxial rotors are even more rare in the open literature. In the early 1980s Peterson and Mosher [67] conducted a full scale wind tunnel experiment on Sikorsky's XH-59A rotor. In this test, acoustic measurements were obtained over a range of rotor lift coefficients, advance ratios and shaft angles. The noise level of the coaxial system was shown to increase with loading on the rotor and as the shaft angle approaches zero just as observed

in the case of a typical single rotor. The microphone array used in the experiment was too sparse, however, to reveal any detail of the acoustic radiation pattern that was generated by the rotor system. Blade vortex interaction (BVI) noise was speculated to be influenced by the distribution of lift between the upper and lower rotors but unfortunately, within the scope of the experiment, no firm conclusions could be drawn on the effect of interactions between the upper and lower rotors on the resulting acoustic characteristics of the coaxial system. More recently, Boyd *et al.* [68] provided a numerical comparison between the acoustic signature of a Bö105 model rotor that was similar to the rotor used in the HART II experiments [52], and a fictitious coaxial system, consisting of two Bö105 rotors contra-rotating about the same axis. The wakes of the rotors were approximated by a system of single tip vortices. In this comparison, it was found that the coaxial system generated higher BVI noise compared to the single rotor system. It was also observed that the interference between the upper and lower rotors of the coaxial system had a significant effect on its acoustic character. Based on comparisons against experimental results from the HART II rotor test [52], it was concluded, however, that a vortex filament model may not have been accurate enough to represent the wake to the detail required for accurate acoustic predictions.

Aeroacoustics is a rapidly maturing discipline and its application to helicopter rotors is a very active field of research (refer to Ref. 50 for a review of recent accomplishments). Coaxial rotor systems generally do not seem to have been subject to detailed aeroacoustic study, however. The aim of the first part of this chapter is to compare the aeroacoustic characteristics of a coaxial rotor system with those of an aerodynamically equivalent, conventional single rotor. Since a significant part of the lower rotor of the coaxial system operates in the wake of the upper rotor, additional noise associated with the inter-rotor BVIs (which do not occur on a single rotor) can be expected, and a detailed study of these interactions and the associated noise produced by a coaxial rotor operating in forward flight is presented. The second part of the chapter investigates the effects of rotor stiffness on the acoustic characteristics of a coaxial rotor system.

5.2 Rotor Setup

The rotor configuration used in this section mimics that used by Harrington (referred to as 'rotor 1' in Ref. 11), consisting of two identical articulated two-bladed rotors that contra-rotate about the same axis. This rotor is exactly the same as that used in Chapter 3 to compare the performance of a coaxial rotor system against that of an equivalent single rotor. The observed agreement between the predicted performance of the coaxial rotor system against the well-regarded set of experimental data lends confidence in the ability of the VTM to provide the acoustic model with a reliable loading pattern on the rotors from which the sound radiation from the system can be computed with some confidence. The detailed description of the geometry is contained in Chapter 3 and hence will not be repeated here.

Unlike in the original experiments described in Refs. 11 and 12 (and also in Ref. 68), where comparisons of the performance of the coaxial rotor were made against one of its own constituting rotors, in this chapter, acoustic comparisons are made against a suitably defined single rotor with equal solidity and the same blade geometry as the coaxial rotor described in Chapter 3. This allows for an acoustic comparison between two systems in which the rotor blades operate within a comparable aerodynamic environment. For Harrington's twin coaxial system, where each rotor consists of two blades, the equivalent single rotor thus consists of four co-planar blades which are geometrically identical. To match the original experimental setup, the hubs of the coaxial rotor are modelled to have a teetering configuration while the equivalent single rotor is given a fully articulated hub. It should be noted that the loading distribution on coaxial rotors with articulated hubs, and hence their acoustic behaviour, can be significantly different to that when the rotor has some degree of hub stiffness. A discussion of the effects of hub stiffness on the acoustic properties of the coaxial system is deferred to Section 5.4. It should also be borne in mind that the acoustic effects of the tail rotor, in the case of the single rotor system, are not considered anywhere within this chapter. The acoustic characteristics of a tail rotor depend heavily on its exact geometry and position (due to the aerodynamic interaction between the wake of the main rotor and the tail rotor itself) [69]. Since the aim of this chapter is to shed light on the origins of, and the differences in, the noise generating mechanisms within the two types of main rotor systems, undue complication of the analysis from the presence of the tail rotor has been avoided

explicitly.

In all the cases considered here, the coaxial rotor system is trimmed to zero net moment in yaw using differential collective pitch input to the upper and lower rotors whilst satisfying a pre-specified thrust requirement. The cyclic pitch inputs to the upper and lower rotor are coupled so that both rotors receive the same control inputs. The coupled cyclic input is used to tilt the thrust vector forward in order to generate a propulsive force while maintaining zero lateral force on the system. Although the fuselage is not explicitly modelled, the effect of its drag on the trim state of the rotor has been accounted for. As in Chapters 3 and 4, the drag of the fuselage is represented by the drag of a flat plate with an area of 2% of the rotor disc area to follow the approach that was adopted in Dingeldein's experiment [12]. The equivalent single rotor is trimmed to the same overall forces and moments as the coaxial rotor system at the same forward speed thus yielding a fair comparison between the acoustics of the two systems.

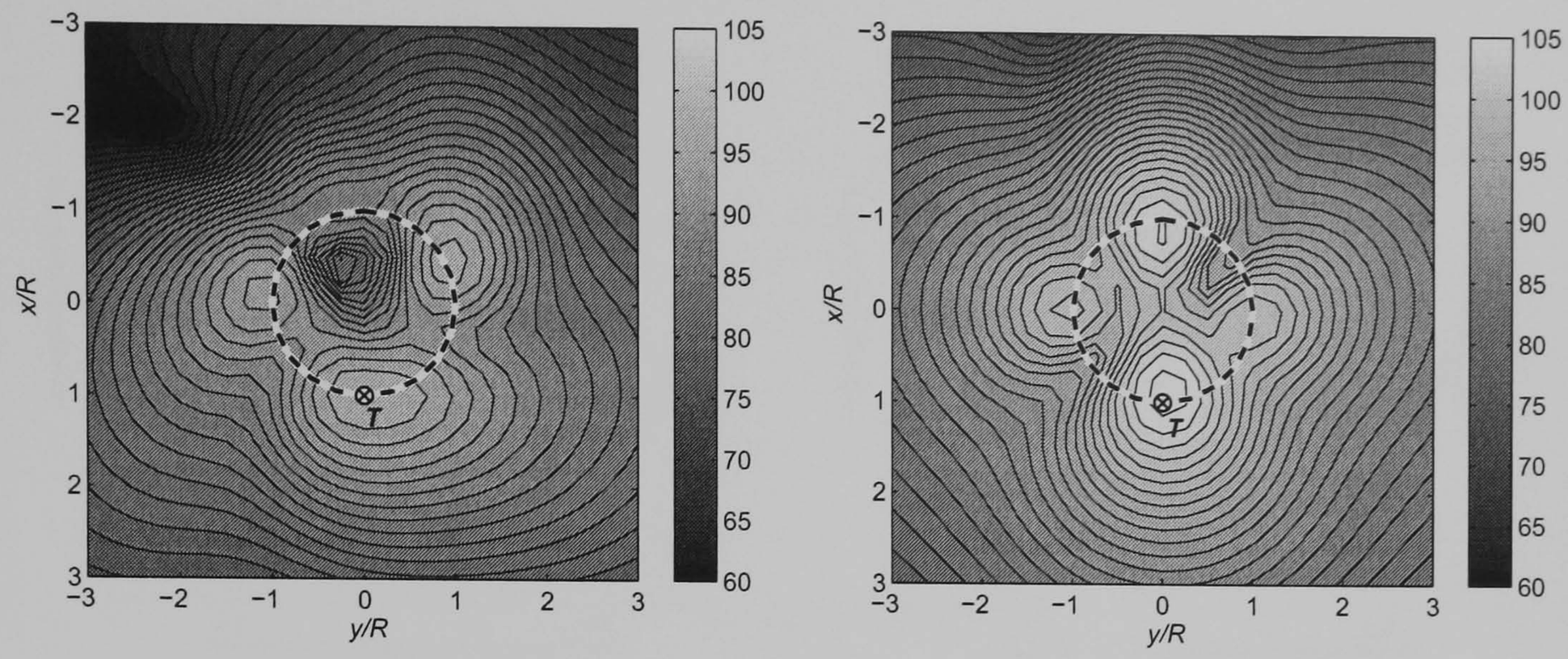
5.3 Acoustic Analysis of Conventional Coaxial Rotor

Detailed analysis of the acoustic characteristics of the coaxial rotor and the equivalent single rotor in forward flight is limited to two representative flight speeds (advance ratios of $\mu = 0.12$ and 0.24) in order simply to contrast the differences in the behaviour of the systems at low and at high advance ratios.

Table 5.1: *Summary of rotor dimensions*

Rotor radius	3.81 m
Rotor speed	37.52 rad/s
Tip Mach number	0.42

In all the analyses presented in this chapter, the acoustic sources are scaled to represent the noise generated by the specific rotor that was used by Harrington and Dingeldein in their experiments. The dimensions and relevant operating conditions of this rotor that are required to conduct this scaling are summarised in Table 5.1.



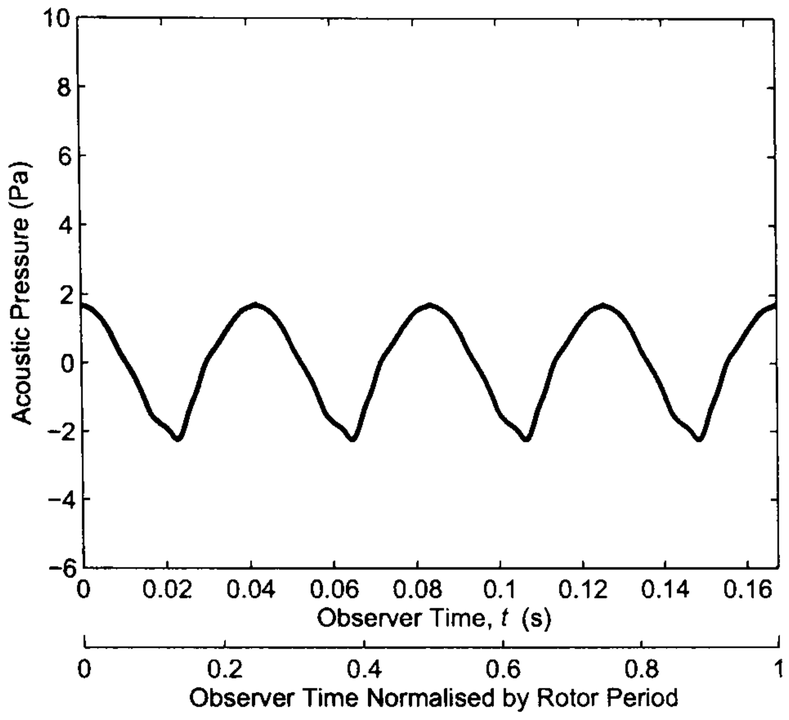
(a) Equivalent single rotor (sound pressure at 'T' is 96.3 dB)

(b) Coaxial rotor (sound pressure at 'T' is 105.7 dB)

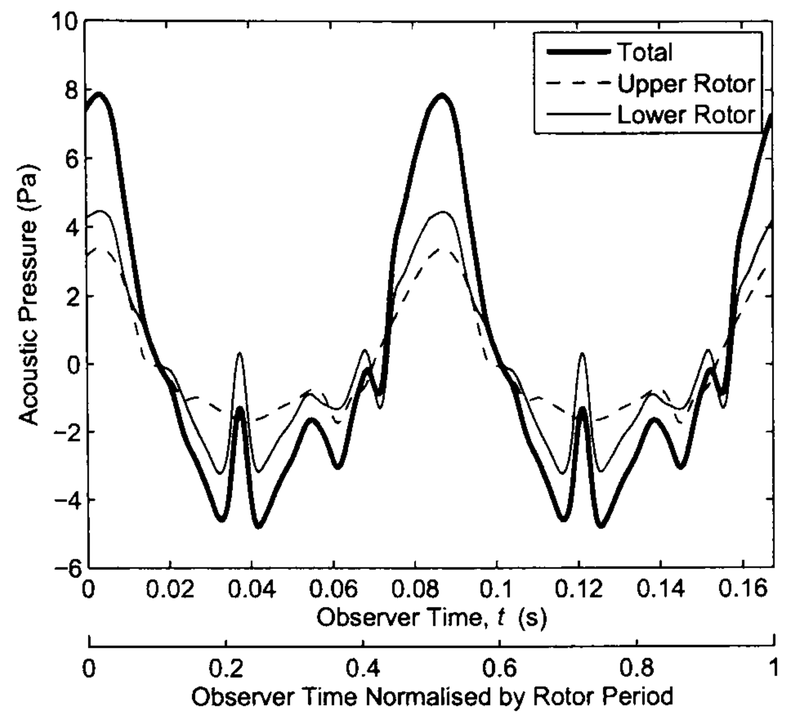
Figure 5.1: *Overall SPL in decibels in steady level flight at advance ratio* $\mu = 0.12$.

5.3.1 Overall Noise Characteristics

Figure 5.1 shows a contour plot of the overall sound pressure level (OASPL) that is produced on a horizontal observer plane located at a distance of one rotor radius below the hub by the coaxial rotor and its equivalent single rotor at an advance ratio of $\mu = 0.12$ (for the coaxial system, the observer plane is located one rotor radius below the hub of the lower rotor). The noise levels are seen to peak at a sequence of 'hot spots' that are located directly underneath the tips of the rotor discs. Figures 5.2 and 5.3 show the time history and frequency spectrum, respectively, of the acoustic pressure at the hot spot at the rear edge (at $\psi = 0°$) of each of the rotor systems. As is typical of measured acoustic data from conventional helicopters in both model and flight tests (e.g. Refs. 52 and 70), the major contribution to the noise produced by the equivalent single rotor is at very low frequencies (less than five times the blade passage frequency). At the corresponding locations of maximum noise on the observer plane, the SPL of the coaxial rotor is found to be around 10 dB higher than that of the equivalent single rotor. This trend appears to persist for all advance ratios between $\mu = 0.12$ and $\mu = 0.24$. It should be borne in mind, though, that the acoustic contribution of the tail rotor of the equivalent single rotor system is not accounted for as described earlier.

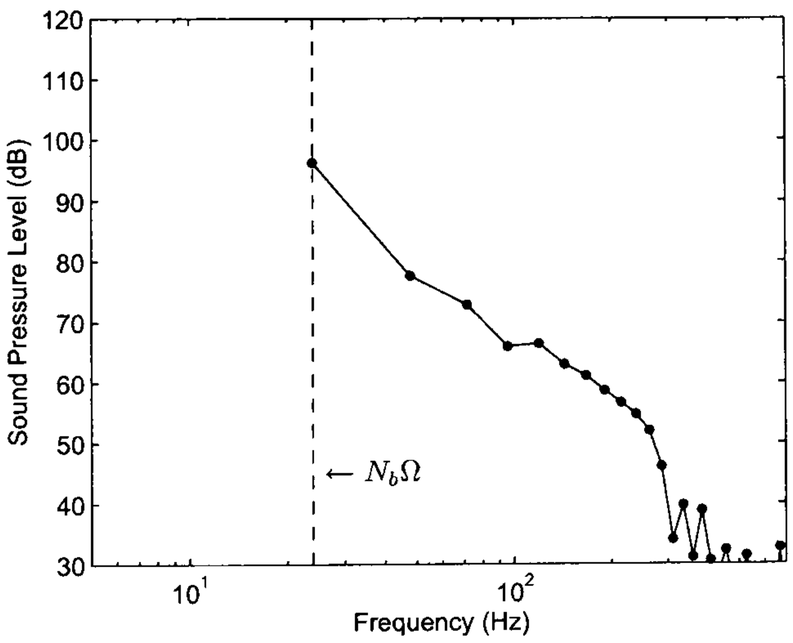


(a) Equivalent single rotor

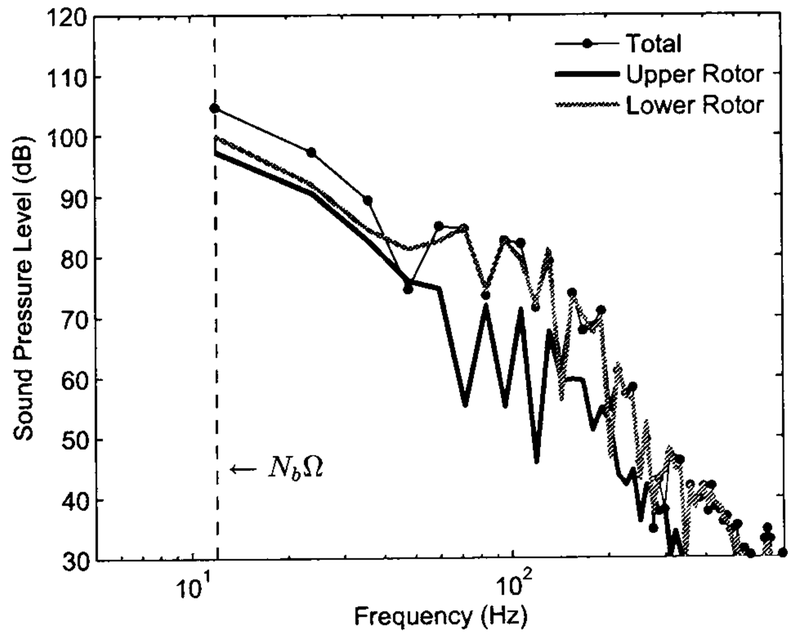


(b) Coaxial rotor

Figure 5.2: *A time history of acoustic pressure over one rotor revolution one rotor radius below the tip of the rotor disc at* $\psi = 0°$ *(labelled 'T') for advance ratio* $\mu = 0.12$.



(a) Equivalent single rotor

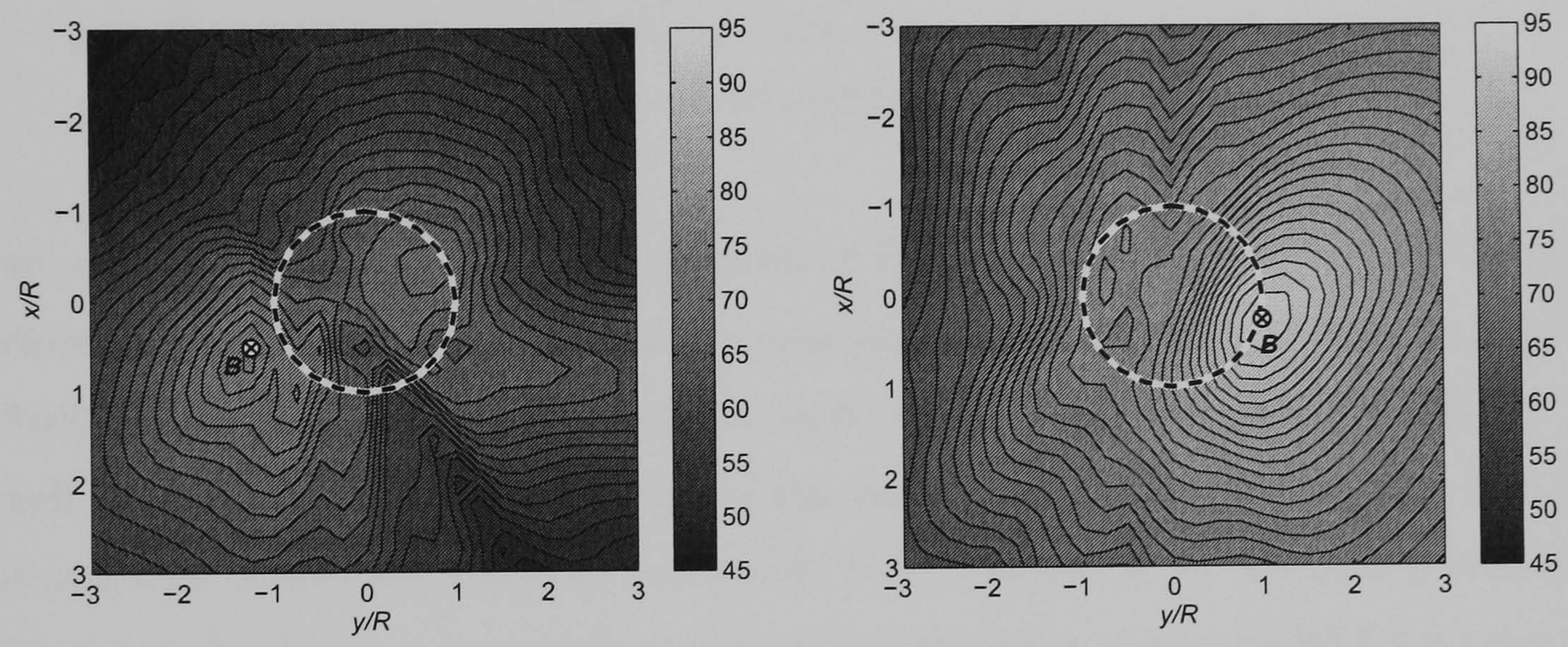


(b) Coaxial rotor

Figure 5.3: *Frequency spectrum of sound pressure level one rotor radius below the tip of the rotor disc at* $\psi = 0°$ *(labelled 'T') for advance ratio* $\mu = 0.12$. *The vertical dashed line represents the fundamental blade passage frequency.*

Figure 5.2 shows that the noise due to the lower rotor of the coaxial system is highly impulsive even at the location of maximum overall noise. Correspondingly, it is evident

from Figure 5.3 that the noise of the coaxial rotor is distributed over a much wider range of frequencies than that produced by the equivalent single rotor. Similarly though to the single rotor, the main contribution to the noise produced by the coaxial rotor is at low frequency. It is worth noting that the low frequency noise is related to the low harmonic airloads on the rotor blades. Impulsive noise that is radiated to the ground, on the other hand, is primarily caused by wake interactions. In a coaxial rotor system, interactions between the wake produced by the upper rotor and the blades of the lower rotor act as an additional source of noise that is not present in a single rotor system. Given the focus of this chapter on the acoustics of coaxial rotor systems, further discussion will concentrate on the high frequency noise that is associated with these BVIs.



(a) Equivalent single rotor (sound pressure at 'B' is 74.2 dB)

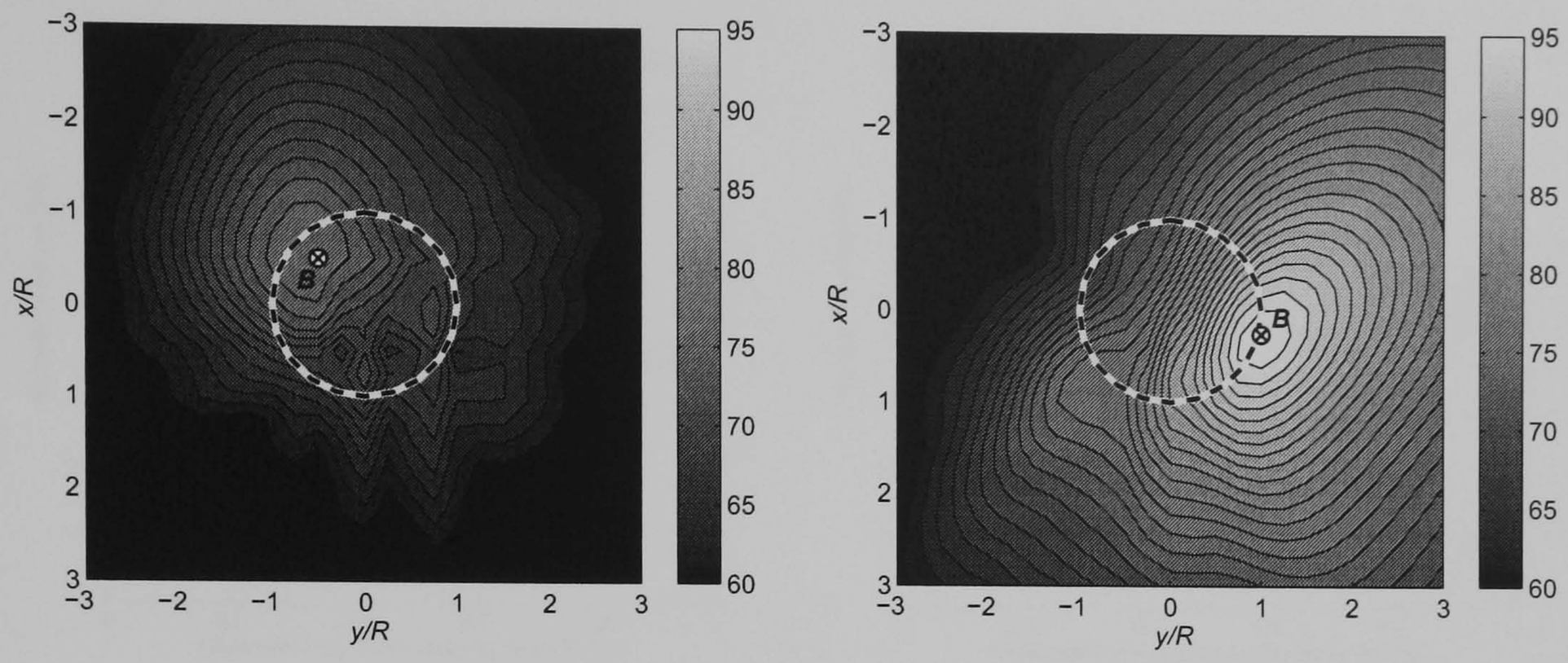
(b) Coaxial rotor (sound pressure at 'B' is 92.3 dB)

Figure 5.4: *BVI sound pressure levels (5–40N_{bt}/rev) in decibels at advance ratio $\mu = 0.12$.*

5.3.2 BVI Noise Characteristics

The contour plots presented in Figure 5.4 contrast the distribution of SPL on the observer plane in the BVI frequency range (computed by aggregating the acoustic energy in the Fourier modes ranging from $5N_{bt}$/rev to $40N_{bt}$/rev where N_{bt} is the total number of blades) for the equivalent single rotor and the coaxial rotor.

For the equivalent single rotor at an advance ratio $\mu = 0.12$, two BVI hot spots



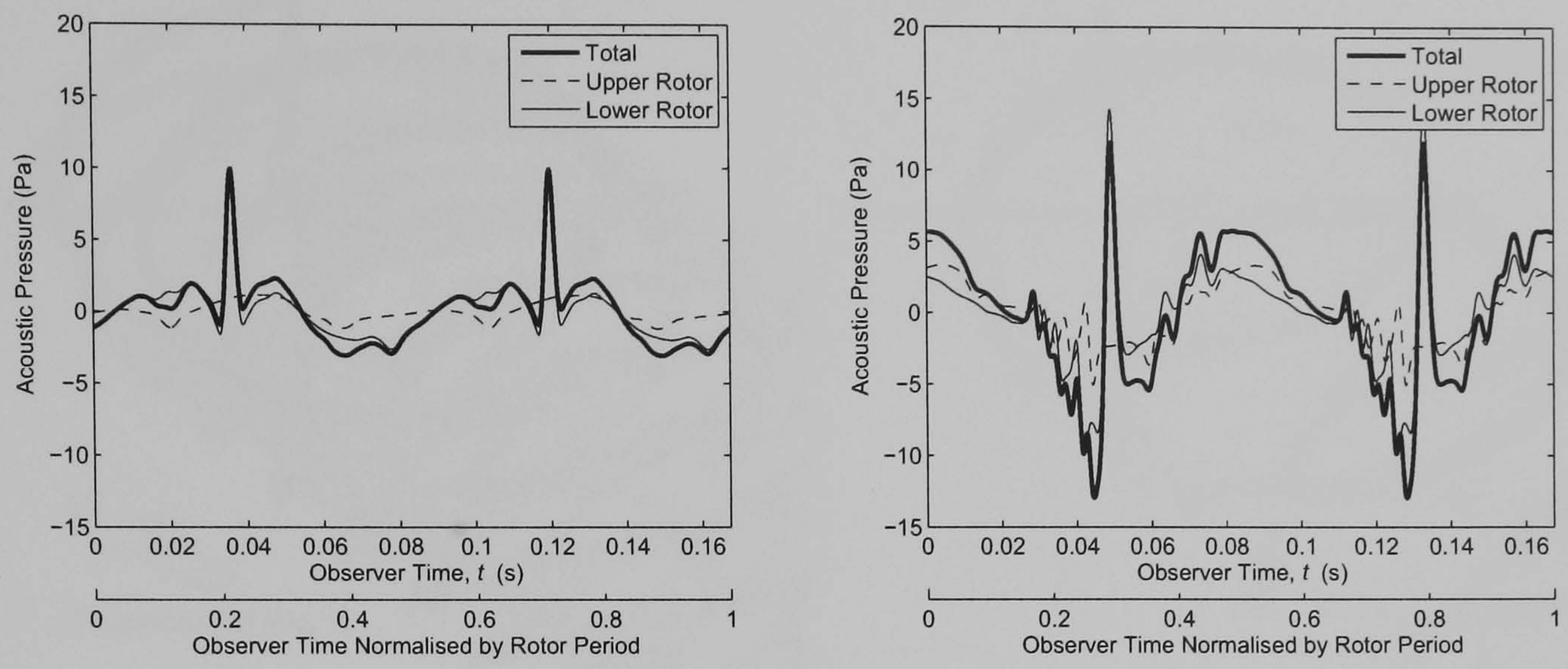
(a) Upper rotor (sound pressure at 'B' is 76.2 dB) (b) Lower rotor (sound pressure at 'B' is 92.3 dB)

Figure 5.5: *BVI sound pressure levels (5–40N_{bt}/rev) in decibels for individual rotors in coaxial configuration at advance ratio $\mu = 0.12$.*

are evident on the observer plane as shown in Figure 5.4(a). One of these is situated directly below the advancing side of the rotor and the other below the retreating side. Such a radiation pattern is typical of a single rotor in forward flight [52, 53]. It is well recognised that the dipole nature of the loading noise results in a propagation of sound that is directed primarily downwards [70]. The hot spots are thus positioned roughly beneath the corresponding positions on the rotor where the BVI sources are most intense, that is, where the combination of miss-distance and alignment of the passing vortices results in the strongest impulsive loads on the rotor blades.

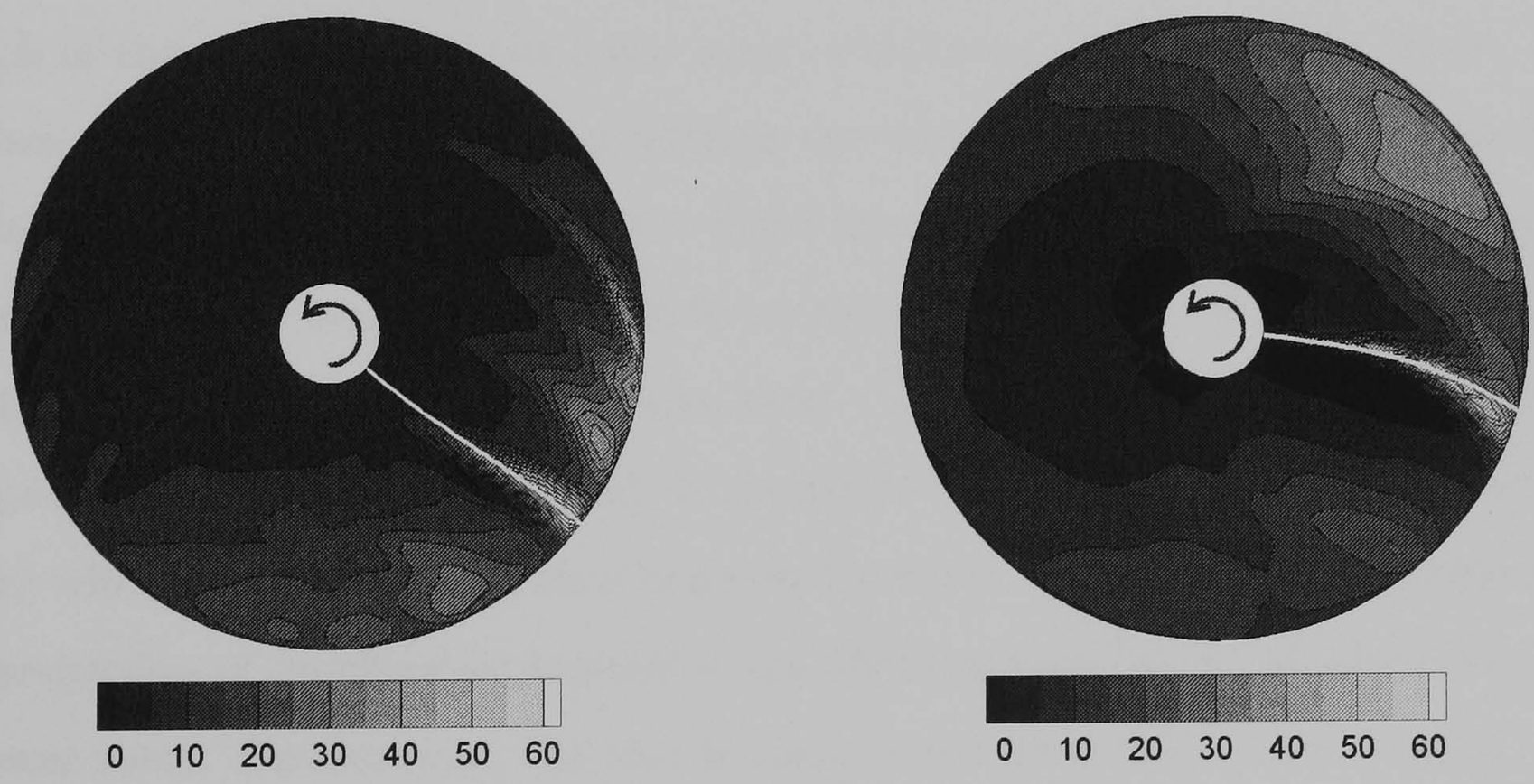
For the coaxial rotor, the highest sound pressure is concentrated under the advancing side of the lower rotor as shown in Figure 5.4(b). The sound pressure level at the hot spot (marked by ⊗ and labelled as 'B' in the figure) is appreciably higher (by 18 dB) than the highest sound pressure level generated by the equivalent single rotor at this flight condition.

Figure 5.5 shows the separate contributions from the upper and lower rotors to the noise generated by the coaxial rotor. The figure shows the lower rotor to be the dominant source of noise on the observer plane below the rotor, as might be expected from the additional wake interactions to which the lower rotor is subjected. This inference is supported by Figure 5.6 in which the time history, over one rotor revolution, of the



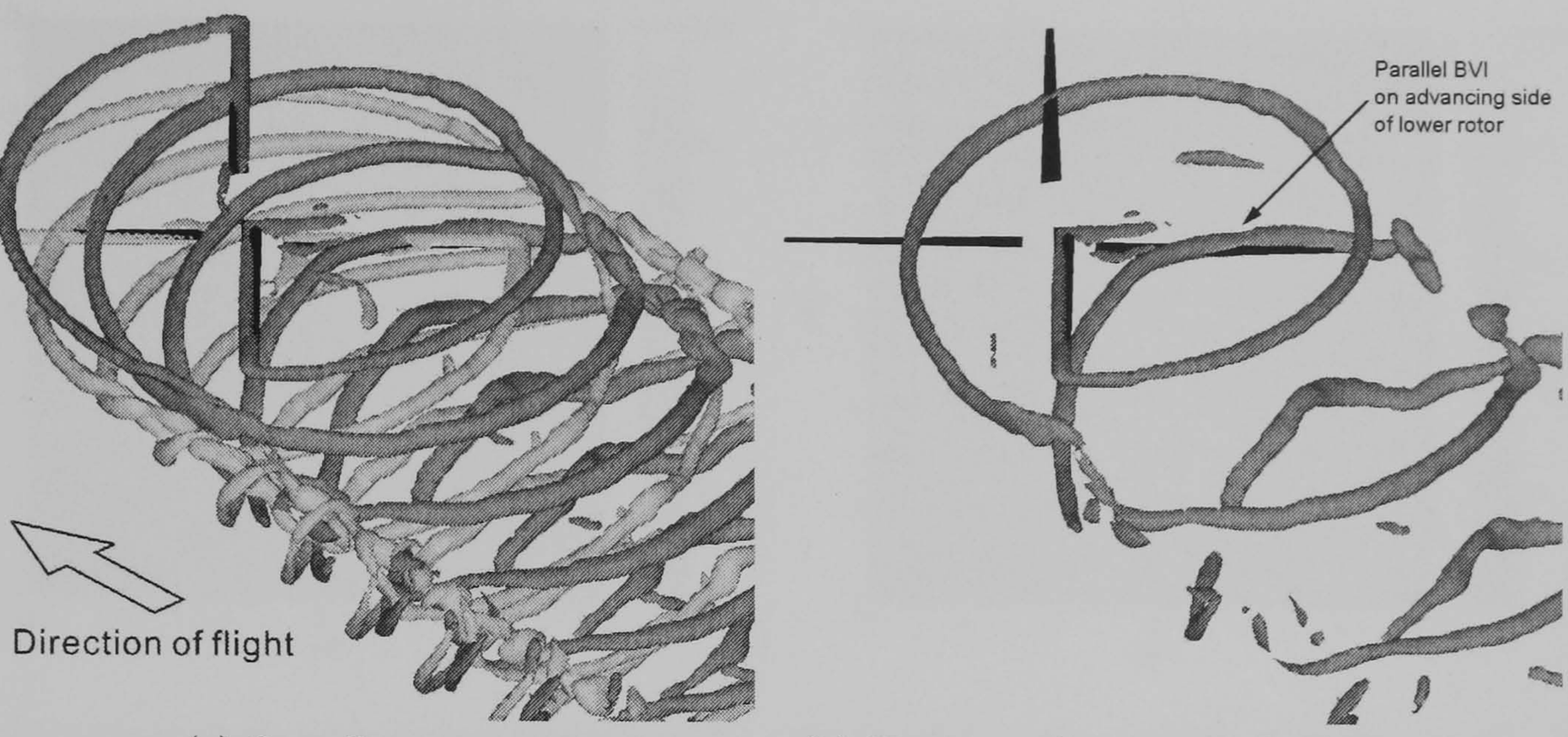
(a) $\mu = 0.12$ (b) $\mu = 0.24$

Figure 5.6: *Time history of acoustic pressure at the BVI hot spot, marked 'B' in Figures 5.4 and 5.9, for coaxial rotor.*



(a) $\mu = 0.12$ (b) $\mu = 0.24$

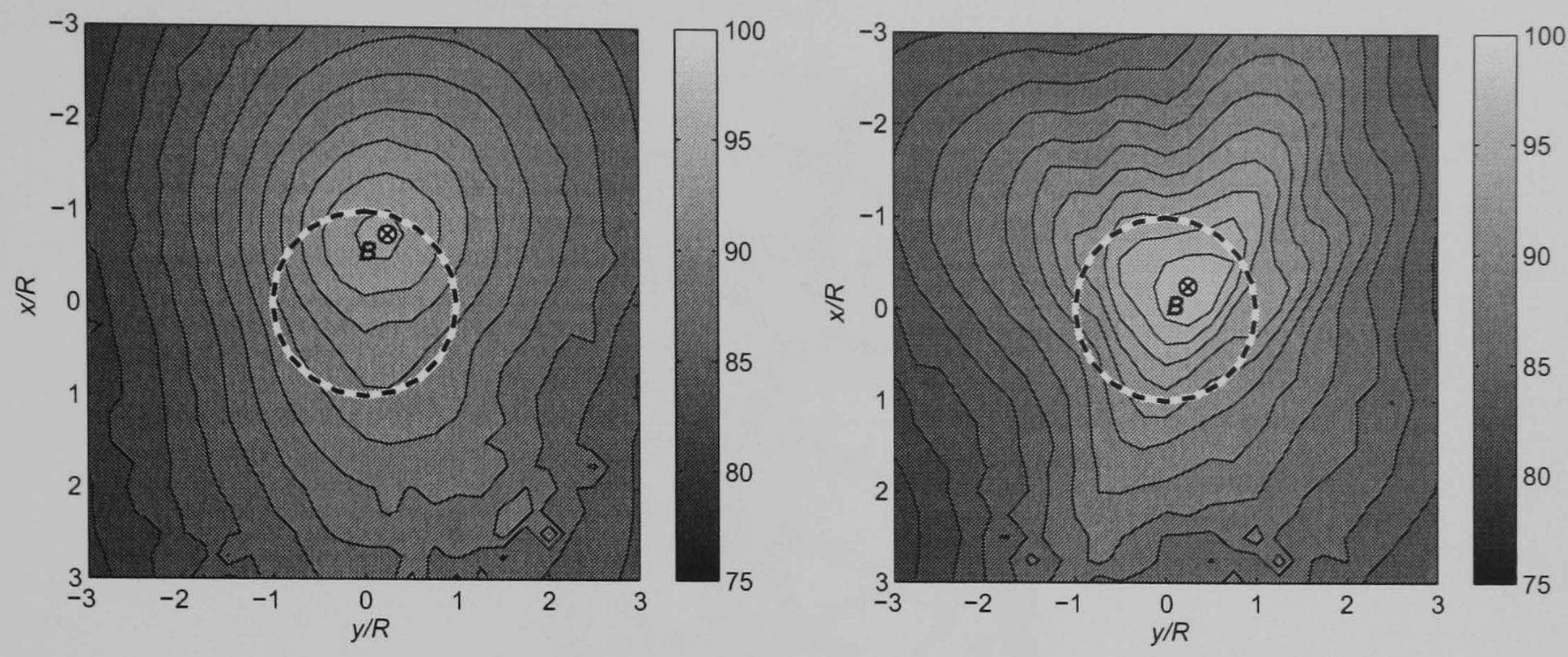
Figure 5.7: *Acoustic source density (loading noise, Pa/m^2) on lower rotor of coaxial system as evaluated at the BVI hot spot. Also shown as a white line is the locus of sources corresponding to observer time $t = 0.036$ s in (a) and $t = 0.049$ s in (b).*



(a) Overall structure (b) Tip vortex from one blade of upper rotor

Figure 5.8: *Tip vortex structure of coaxial rotor at advance ratio $\mu = 0.12$ showing inter-rotor BVI via parallel impingement.*

acoustic pressure at the hot spot on the advancing side of the lower rotor is shown. The two highly impulsive peaks in the acoustic pressure correspond to identical events on each of the two blades of the lower rotor of the coaxial system. The origin of these impulses can be understood by considering the distribution of the acoustic sources on the blade over a single revolution of the lower rotor. Figure 5.7 shows the density of the noise sources due to loading (evaluated from the loading noise term in Equation 2.50 and scaled by the local panel area) in 'source time' *i.e.* corresponding to the location of the blade when the sound was generated. It should be noted that the distribution of source density will of course differ for each observer location. The plot is thus generated from the perspective of an observer located at the BVI hot spot below the advancing side of the lower rotor. Furthermore, the plot is constructed from the sources located on only one of the blades. Also indicated in Figure 5.7, as a thick white line, is the locus of all the sources that contribute to the noise at the specific observer time corresponding to the peak in impulsive noise. For instance, the locus of sources in Figure 5.7(a) corresponds to the peak at $t = 0.036$ s in Figure 5.6(a). It is evident that the intense interaction at the azimuthal location of $\psi \approx 45°$ (corresponding to the locus of sources contributing to the noise at $t = 0.036$ s) is responsible for the impulsive noise. Figure 5.8(a) shows the overall structure of the wake at the instant at which one of the blades of the lower rotor



(a) Equivalent single rotor (sound pressure at 'B' is 94.1 dB)

(b) Coaxial rotor (sound pressure at 'B' is 97.4 dB)

Figure 5.9: *BVI sound pressure levels (5–40N_{bt}/rev) in decibels at advance ratio $\mu = 0.24$.*

is at an azimuth of $\psi = 45°$. In Figure 5.8(b) some of the detail of this plot is suppressed to show the specific inter-rotor BVI that is responsible for the impulsive noise. It is evident that during this BVI, the blade on the lower rotor passes directly through the axis of a trailing vortex from the upper rotor. Furthermore, the trailing vortex is essentially parallel to the blade span at the time of impingement, thus generating a highly impulsive incident velocity field over a significant portion of the blade span.

At higher advance ratio ($\mu = 0.24$), the character of the BVI acoustic pattern generated by the equivalent single rotor is somewhat different to that observed at lower advance ratio. The hot spot under the advancing side shifts towards the front of the rotor disc (to approximately $\psi = 170°$ as shown in Figure 5.9). The primary origin of the noise at this hot spot is an oblique blade vortex interaction as shown in Figure 5.10. Even though the BVI is not parallel, the prolonged interaction (from $\psi \approx 90°$ to 270°) generates high intensity noise. Interestingly, the figure also shows secondary trailing vortices that are generated as a result of the abrupt changes in loading along the span of the blade that are induced by the BVIs. The pattern of BVIs on the rotor disc at this advance ratio is somewhat more sparse than at lower advance ratio. Indeed, the increasing forward tilt of the rotor disc with forward speed that is required to provide

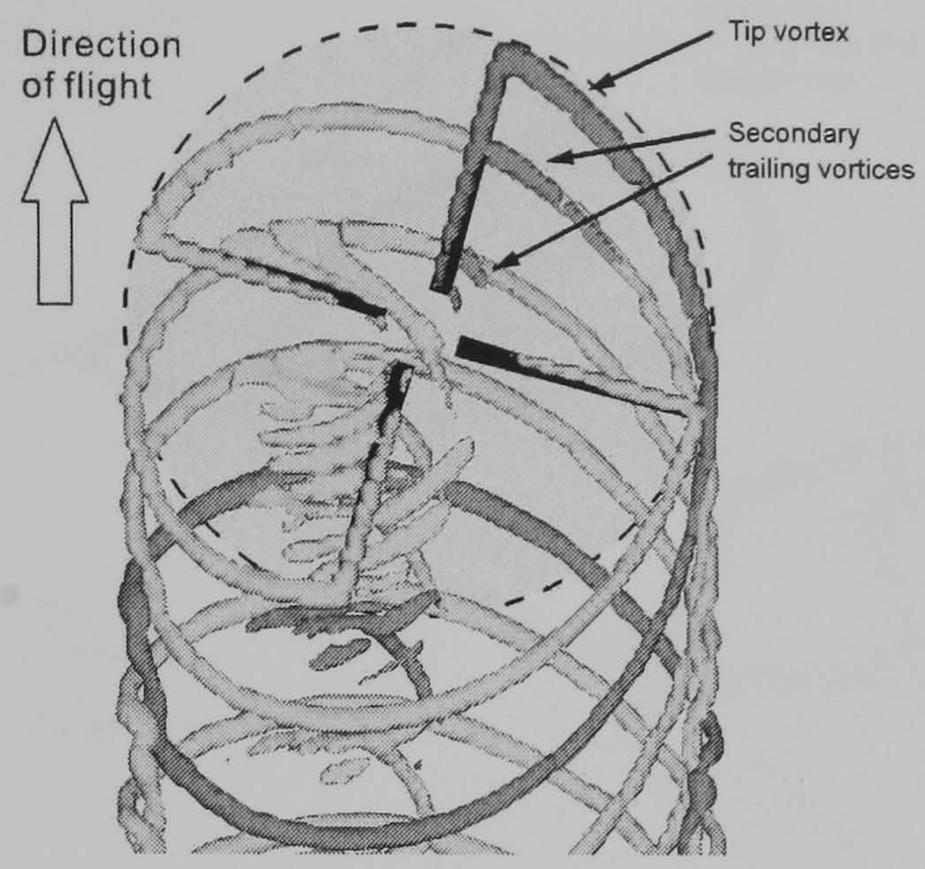


Figure 5.10: *A rotor blade of the equivalent single rotor at advance ratio* $\mu = 0.24$ *interacting with tip vortex from preceding blade at* $\psi \approx 170°$. *Trailed vorticity generated by this blade is shaded dark to highlight secondary trailing vorticity generated by this interaction.*

the propulsive component of force on the system increases the miss-distance between the wake vortices and the blades and thus acts to weaken the strength of individual BVI events.

On the other hand, the BVI induced sound pressure level on the observer plane for the coaxial rotor has the same qualitative pattern at high advance ratio as observed at lower forward flight speed. The location of the hot spot moves further inboard as shown in Figure 5.9(b), but the highly impulsive peaks in the time history of the acoustic pressure seen for $\mu = 0.12$ persist at $\mu = 0.24$ (see Figure 5.6). The amplitude of the peaks in the acoustic pressure at high forward speed are significantly larger and occur slightly later than at low forward speed, however. The high intensity BVI that is evident at an observer time of $t = 0.049$ s corresponds to the source time indicated by the white line (at roughly $\psi = 80°$) on the plot of decomposed noise sources due to loading shown in Figure 5.7(b). The impulsive noise field appears to be dominated by a BVI event that occurs as one of the rotor blades approaches the azimuth at which it experiences maximum incident velocity. Figure 5.11 captures the wake structure at the instant when one of the blades of the lower rotor is at an azimuth of $\psi = 80°$. The

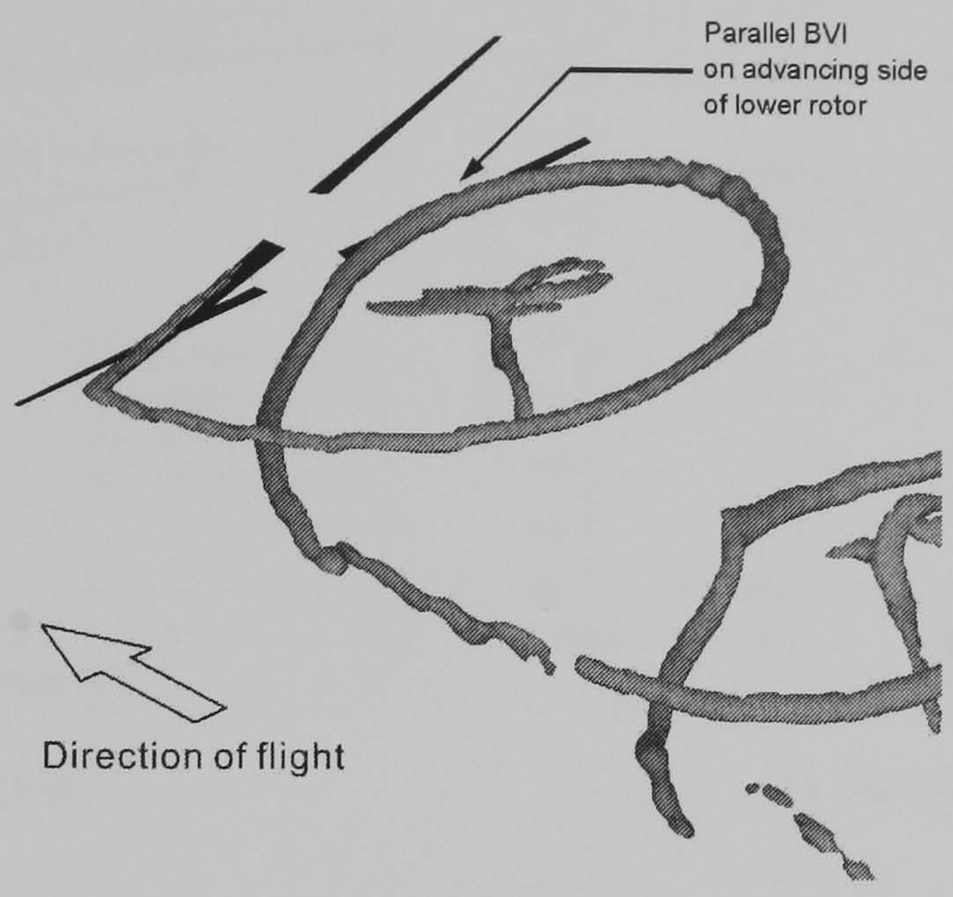


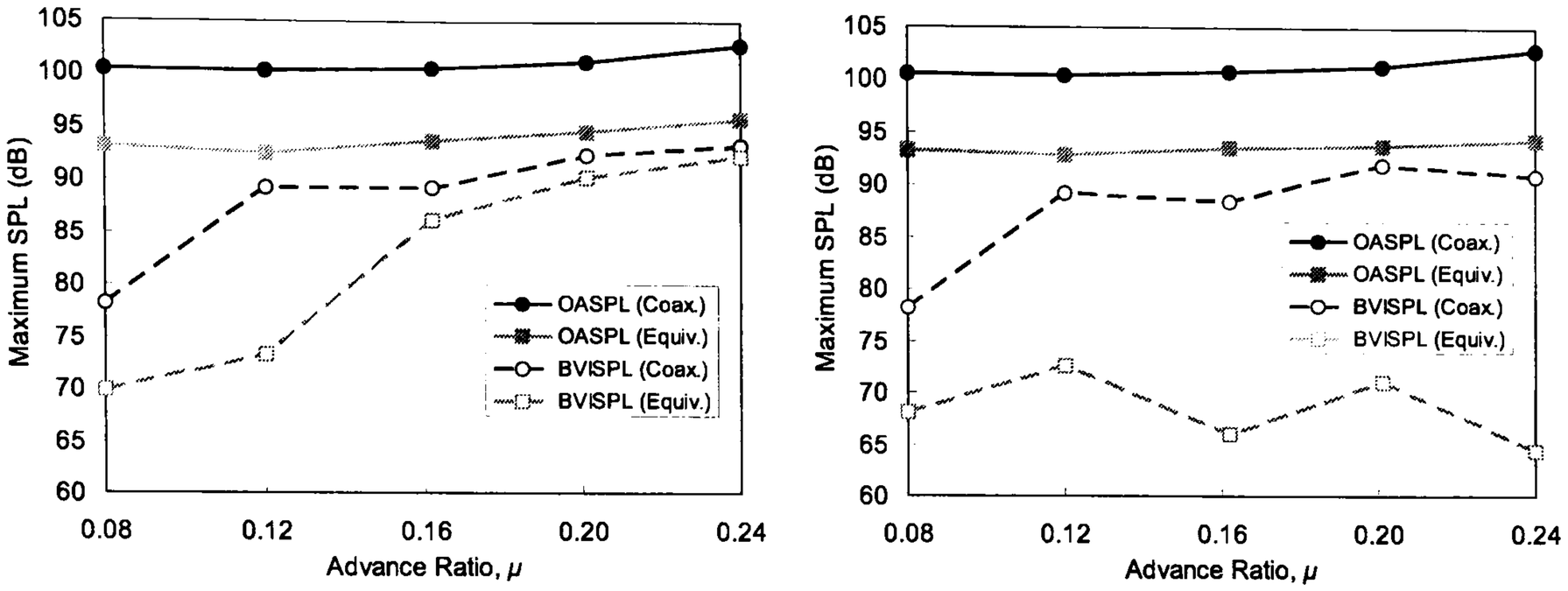
Figure 5.11: *Parallel inter-rotor BVI where the tip vortex structure from upper rotor of coaxial system impinges on advancing blade of lower rotor at* $\mu = 0.24$.

figure shows the blade to interact strongly with a tip vortex that is generated from the upper rotor. As at lower forward speed, the axis of the interacting vortex lies almost parallel to the blade, resulting in a highly impulsive change in loading along its span and significant acoustic radiation.

Even though the intensity of the BVIs on the equivalent single rotor reduces with forward speed, the BVI sound pressure level on the observer plane one radius below the rotor is significantly higher for *both* rotors at $\mu = 0.24$ than at $\mu = 0.12$. This seeming anomaly in the case of the equivalent rotor is a result of the dominance of the near field contribution to the loading noise (the second term of Equation 2.50 in Chapter 2). Furthermore, the noise from the equivalent single rotor is less impulsive when compared to the coaxial rotor.

5.3.3 Far-Field Noise

In the following discussion, sound pressure levels on a hemispherical observer surface of radius $2R$, centred at the rotor hub (in the case of the coaxial rotor, at the hub of the lower rotor) are considered. This representation of the acoustic field generated by the rotor is useful for purposes of interpreting far-field acoustics as the surface can roughly



(a) Total Noise

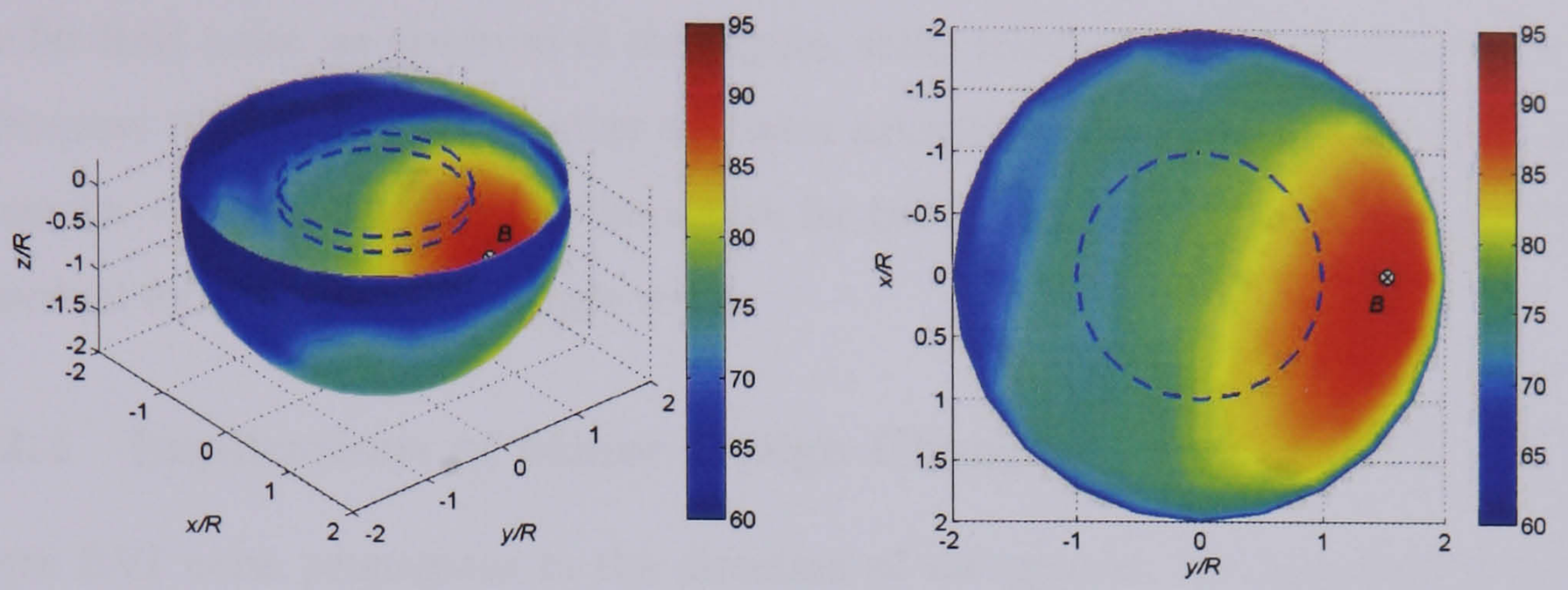
(b) Loading Noise

Figure 5.12: *Maximum OASPL and BVISPL in decibels at $M_{tip} = 0.42$ on a hemispherical observer surface of radius $2R$, centred on the rotor hub.*

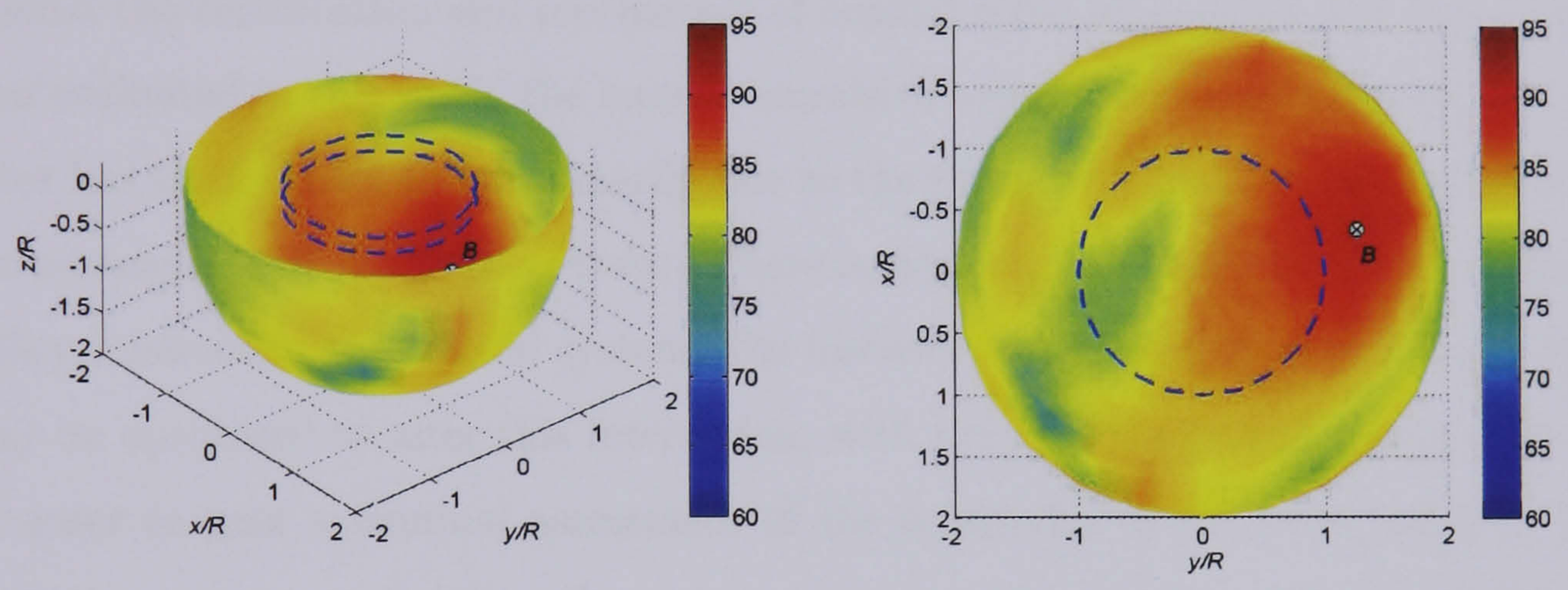
be considered as a hemispherical source of sound with the same acoustic properties as the rotor at its centre. Figure 5.12(a) shows the maximum overall SPL (OASPL) on the hemisphere over a range of forward speeds. For both the coaxial system and the equivalent single rotor, the rate of increase of the OASPL with flight speed is roughly similar although the coaxial rotor is consistently noisier by approximately 8 dB.

For the equivalent single rotor, the contribution of the BVISPL to the overall SPL increases significantly as the advance ratio is increased from $\mu = 0.12$ to 0.16 as shown in Figure 5.12(a). On the other hand, Figure 5.12(b) shows the loading-induced component of noise in the BVI range to reduce with increasing flight speed. This trend arises from the increased disc tilt that is required to generate the propulsive force at higher speeds as described in the previous section. The increase in the impulsive noise in the BVI range of frequencies in Figure 5.12(a) for the equivalent single rotor is thus due to intensification of thickness noise at higher flight speeds.

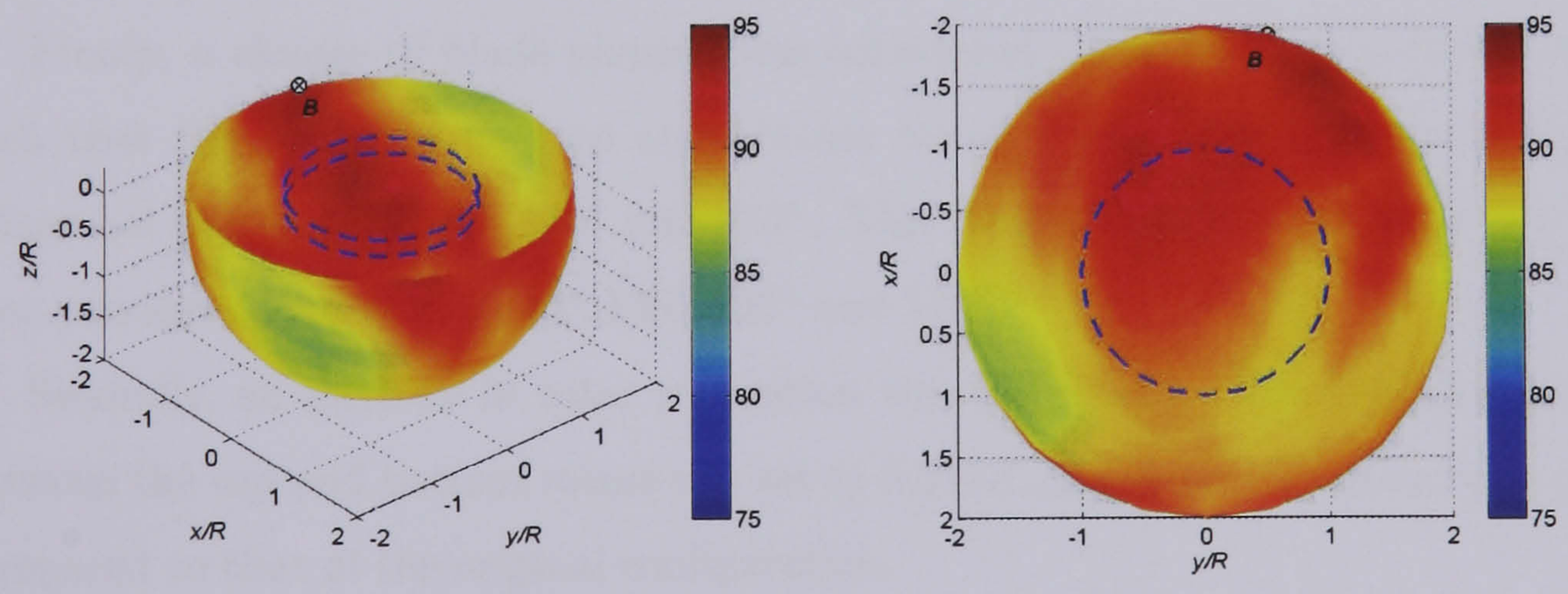
As explained in the previous section, for the coaxial system, the inter-rotor BVIs are intensified as the forward speed is increased. Indeed, Figure 5.12(b) shows the increasing loading noise within the BVI frequency range as flight speed is increased. Figure 5.13 shows the associated contours of SPL mapped on to the hemispherical observer surface at various forward speeds for the coaxial rotor. Note that in this case, the hemispherical



(a) $\mu = 0.12$ (sound pressure at 'B' is 89.2 dB)



(b) $\mu = 0.16$ (sound pressure at 'B' is 89.3 dB)



(c) $\mu = 0.24$ (sound pressure at 'B' is 93.3 dB)

Figure 5.13: *BVISPL in decibels for coaxial rotor on a hemispherical surface of radius $2R$ centered on the hub of the lower rotor. (Left: isometric view. Right: top view.)*

surface extends above the level of the lower rotor hub by $0.2R$ to capture the in-plane propagation of noise from this rotor as the forward speed is increased. The directivity of the far-field noise, as observed in this figure, shifts towards the front of the rotor. This is because the primary BVI occurs at a later azimuth as the speed of flight is increased. A similar trend in directivity of impulsive far-field noise, though at a reduced SPL, was observed for the equivalent single rotor.

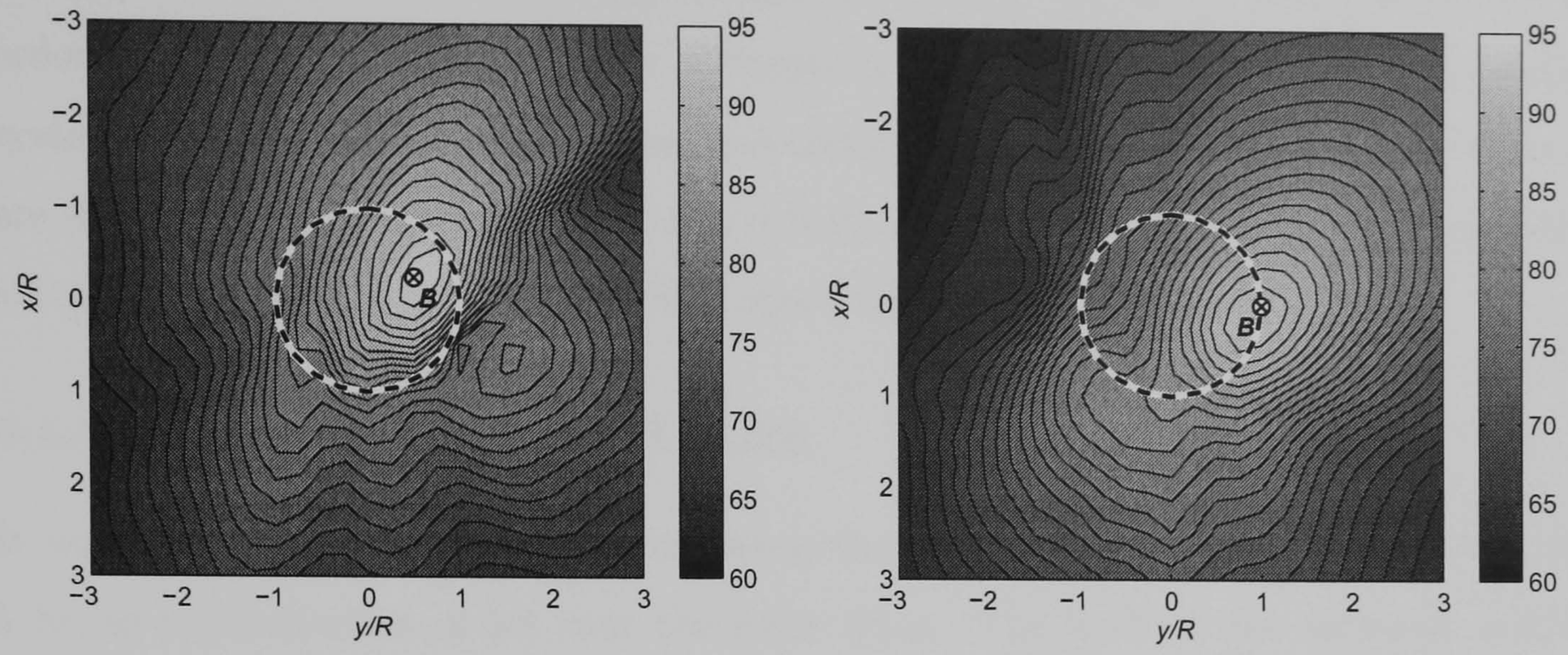
5.3.4 Implications of Minor Design Changes

Since BVI noise propagates in the direction of the ground, the high BVI noise levels generated by the coaxial system in comparison to the equivalent single rotor may work against the certification and routine use of coaxial rotor helicopters. For the configuration evaluated in this work, the intense impulsive noise that is generated by the coaxial rotor has been shown to be primarily due to the inter-rotor blade vortex interaction on the advancing side of the lower rotor. There is, however, a certain amount of design flexibility inherent in the coaxial system. For instance, rotor separation and blade phasing may be optimised to alter this interaction, with the aim of alleviating impulsive noise. In order to gain a nominal assessment of the sensitivity of the noise radiated by the coaxial system to such design changes, two representative configurational modifications to the original coaxial system were performed.

Firstly, a change of blade phasing was considered. The original configuration was such that the blades of the top and bottom rotors were aligned with each other at azimuthal angles of $0°, 90°, 180°$ and $270°$. This phasing was altered, such that blade over-passage was shifted to $45°, 135°, 225°$ and $315°$.

Secondly, an increase in rotor separation was considered. The vertical separation between the top and bottom rotors was set to $0.247R$, amounting to an increase of 30% compared to that of the original configuration.

Figure 5.14 shows the effect of these design changes on the BVI sound pressure levels (at $\mu = 0.12$) on a horizontal plane one rotor radius below the hub of the lower rotor. This figure should be compared to Figure 5.4(b). The change in rotor phasing does not affect the maximum BVI sound pressure level significantly and appears simply to shift the location of the BVI hot spot to be further inboard. The direction of propagation of the BVI noise has also shifted towards the fore of the rotor disc. These observations



(a) Effect of rotor phasing (sound pressure at 'B' is 93.8 dB)

(b) Effect of increased rotor separation (sound pressure at 'B' is 91.2 dB)

Figure 5.14: *BVI sound pressure levels (5–40N_{bt}/rev) in decibels for coaxial rotor with design changes at advance ratio $\mu = 0.12$.*

suggest that, while the intensity of the BVI noise produced by the coaxial system may not be sensitive to rotor phasing, there may be limited scope to modify the directivity of the BVI noise. Although the results are not shown here, the overall noise levels were found to be unaffected by rotor phasing. The four OASPL hot spots, however, were found to be 45° out of phase with those shown in Figure 5.1(b). The increased rotor separation caused a decrease of 2 dB in the maximum BVI sound pressure level. It should be borne in mind though that there is a drag penalty that is associated with the increased mast height which may offset the benefits in terms of a reduction in noise levels.

5.4 Effect of Rotor Stiffness on Acoustic Characteristics

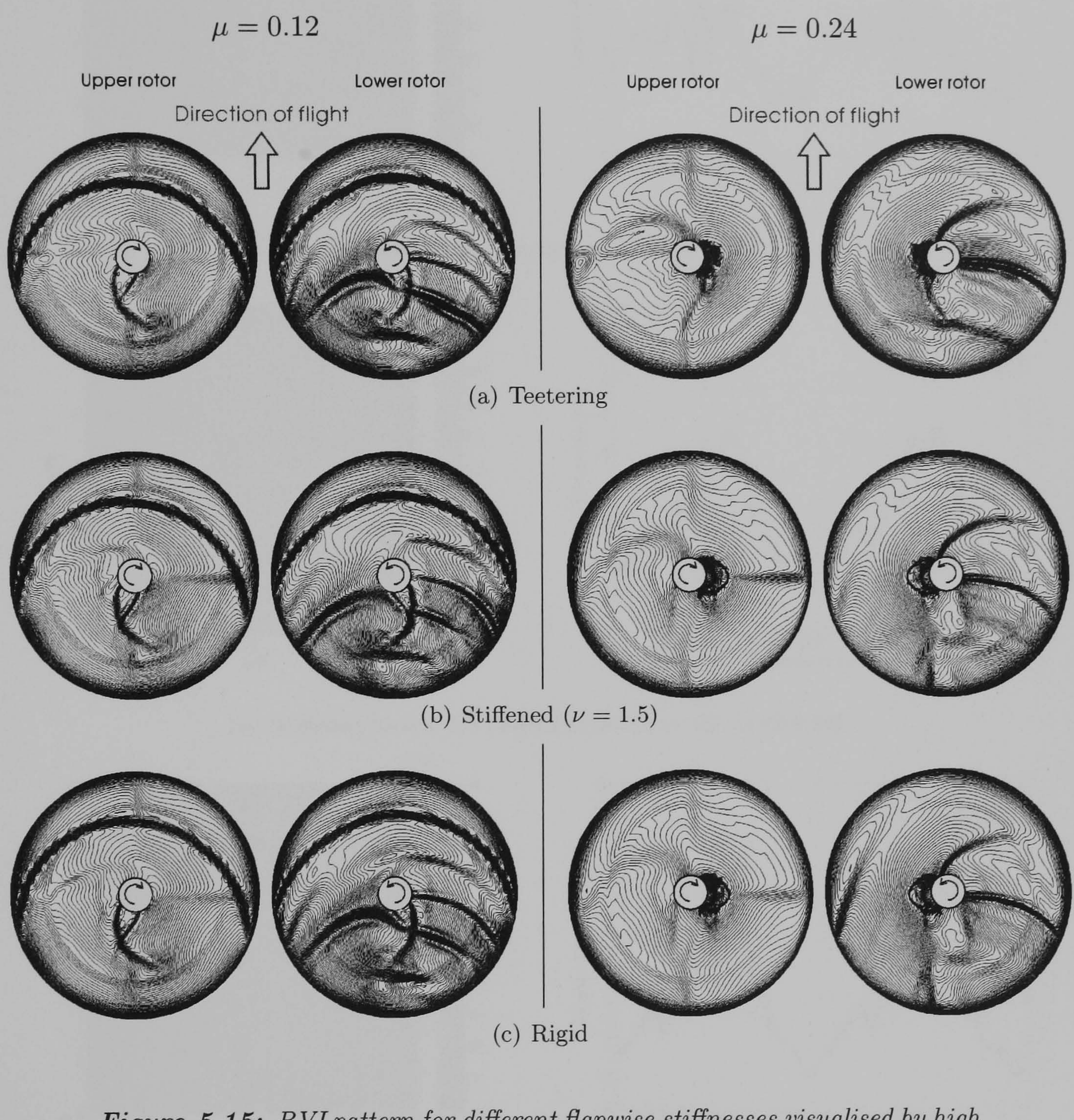
The effect of increased hub stiffness on the acoustic characteristics of the coaxial rotor has also been investigated. The first case to be considered is that of the stiffened system with a flap spring of finite value such that the non-dimensional natural frequency of the first flapping mode is $\nu = 1.5\Omega$. The second case to be considered is that of the completely rigid system with infinite flapwise stiffness. The acoustic characteristics of the two coaxial rotor configurations, with different degrees of flapwise stiffness, are

compared to those of the teetering configuration described in the previous section in order to expose the effects of rotor stiffness on the acoustic behaviour of the coaxial system. To be consistent with the previous section, the acoustic properties of the system are analysed only at advance ratios of $\mu = 0.12$ and 0.24 to yield an appreciation of the acoustic characteristics at low and high speed flight.

5.4.1 Consequences for BVI Noise

It was shown in Chapter 4 that stiffening the hub of a coaxial system allowed for a broad redistribution of lift over the rotor discs. The load on the stiffened system is redistributed laterally such that the advancing blades carry higher lift (and vice versa for the retreating blades) than when the hubs of the rotors are articulated. As a consequence, the strengths of the trailed tip vortices are modified and this results in a subtly different wake structure to that of a conventionally articulated system. The change in the strength of the vortices is not severe enough to distort the wake to the extent that the positions of the BVI on the rotor disc are affected significantly. This notion is supported by the comparison of the BVI patterns for the rotor with various stiffnesses shown in Figure 5.15. In this figure, the positions of the BVI events in both low and high speed flight are seen to be largely independent of the flapwise stiffness of the blades of the rotors. More importantly, though, the strengths of these BVIs, particularly of the inter-rotor BVIs on the advancing side of the lower rotor, can be seen to be modified as a result of the lateral redistribution of loading across the rotor disc. The strengths and the impulsive nature of these interactions govern the amplitude of the acoustic pressure pulses, via the time rate of change in blade loading (see Equation 2.50 in Chapter 2), and thus affect significantly the acoustic signature of the rotor system.

Figure 5.16 shows a series of comparisons of BVI sound pressure on the horizontal observer plane and also the time history of the acoustic pressure at the BVI hot spots for the coaxial rotors of various stiffnesses at advance ratio of $\mu = 0.12$. It should be noted that, for both the stiffened and rigid coaxial rotors, the distribution of acoustic sound pressure on the plane below the rotor contains two localised peaks (or acoustic hot spots) in the observer plane, one directly below the advancing side of the lower rotor and the other below the rear of the disc. Interestingly, the hot spot below the advancing side of the lower rotor coincides with the only distinct peak in the acoustic signature of

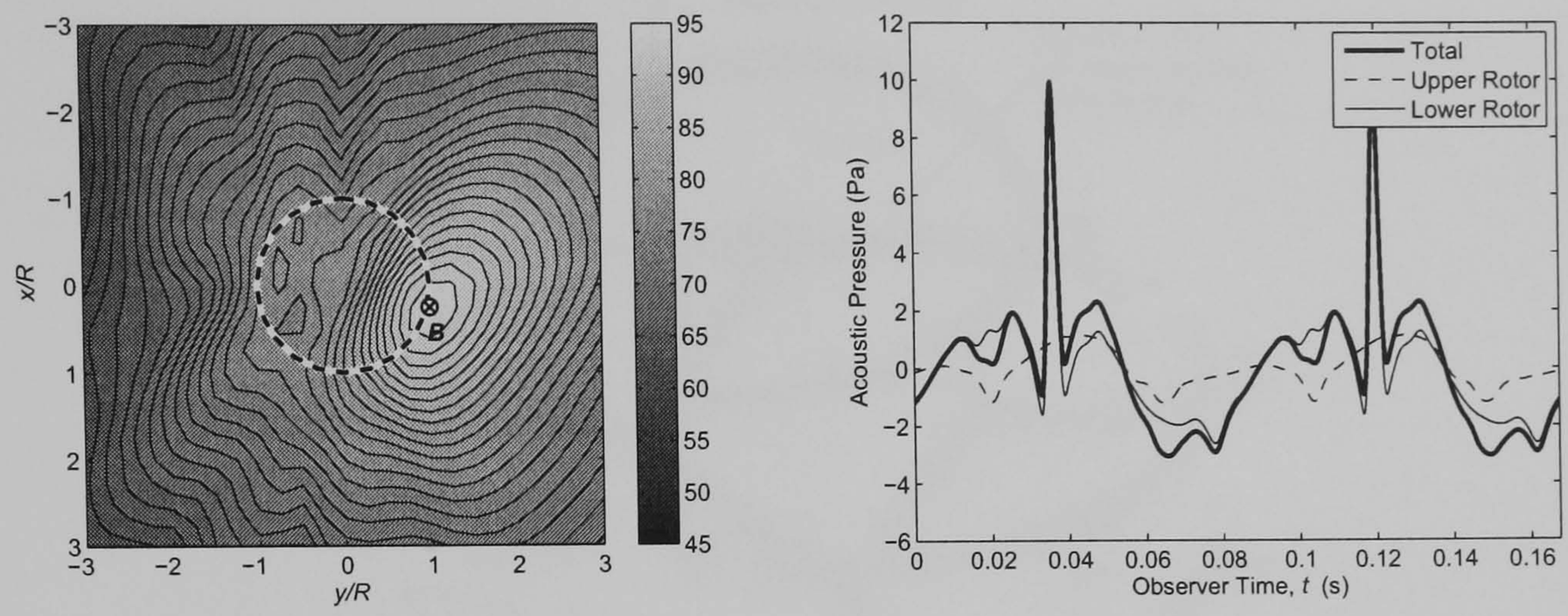


(a) Teetering

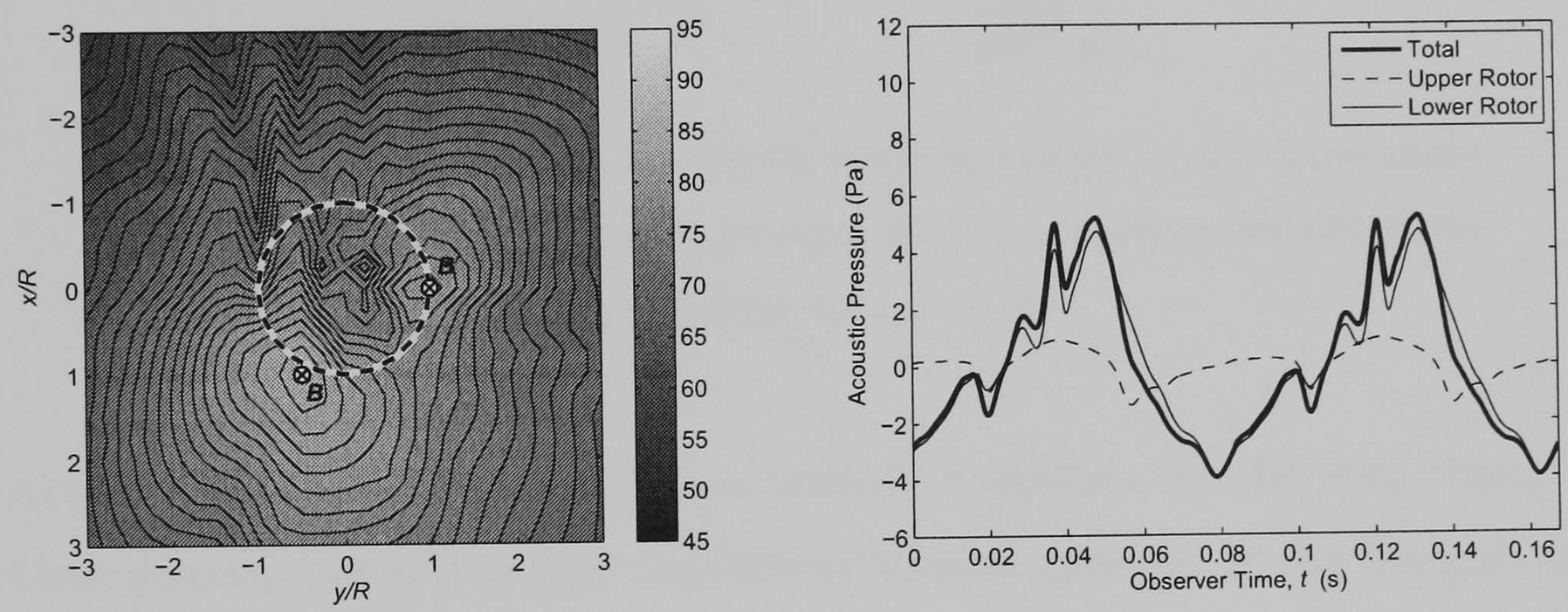
(b) Stiffened ($\nu = 1.5$)

(c) Rigid

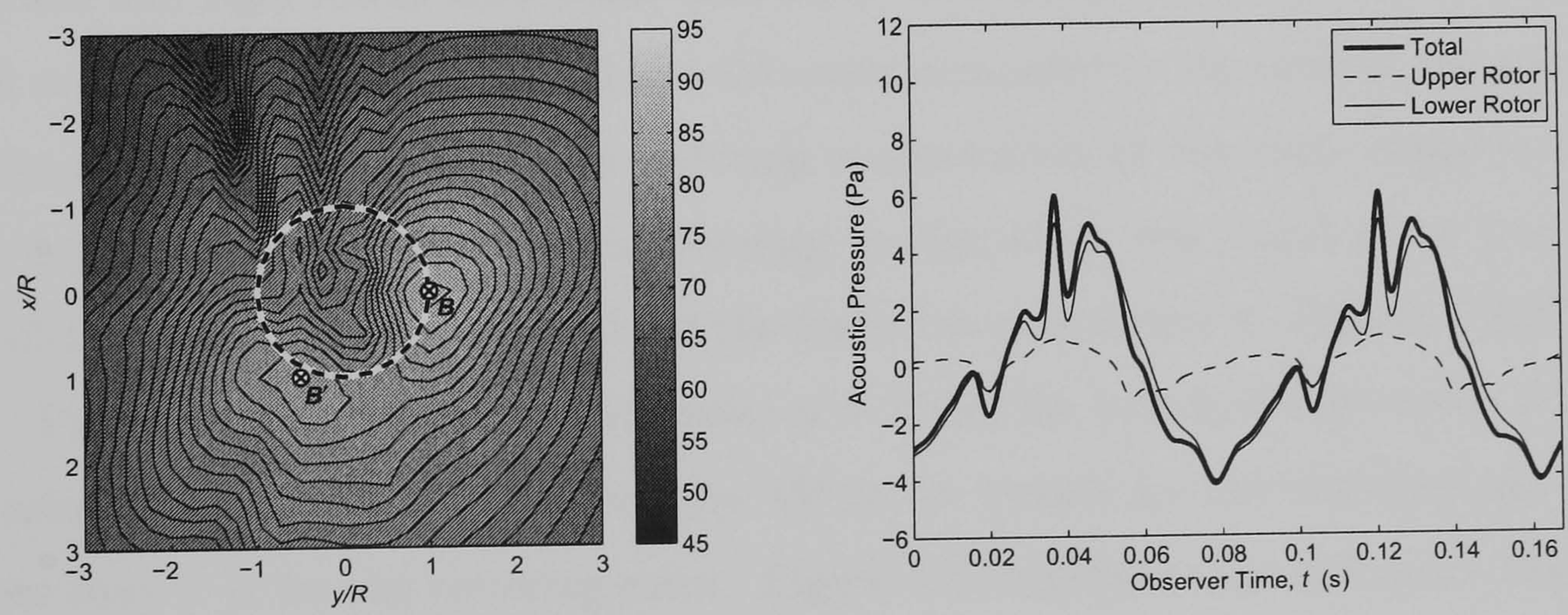
Figure 5.15: *BVI pattern for different flapwise stiffnesses visualised by high gradients of inflow using line contours at advance ratios* $\mu = 0.12$ *(left) and* $\mu = 0.24$ *(right).*



(a) Teetering (sound pressure at 'B' is 92.3 dB)



(b) Stiffened to $\nu = 1.5$ (sound pressure at 'B′' is 80.9 dB)



(c) Rigid (sound pressure at 'B' is 84.3 dB)

Figure 5.16: *BVI sound pressure levels (5–40N_{bt}/rev) in decibels (left) and time history of acoustic pressure over one rotor revolution (right) at BVI hot spot on the advancing side of the lower rotor for advance ratio* $\mu = 0.12$.

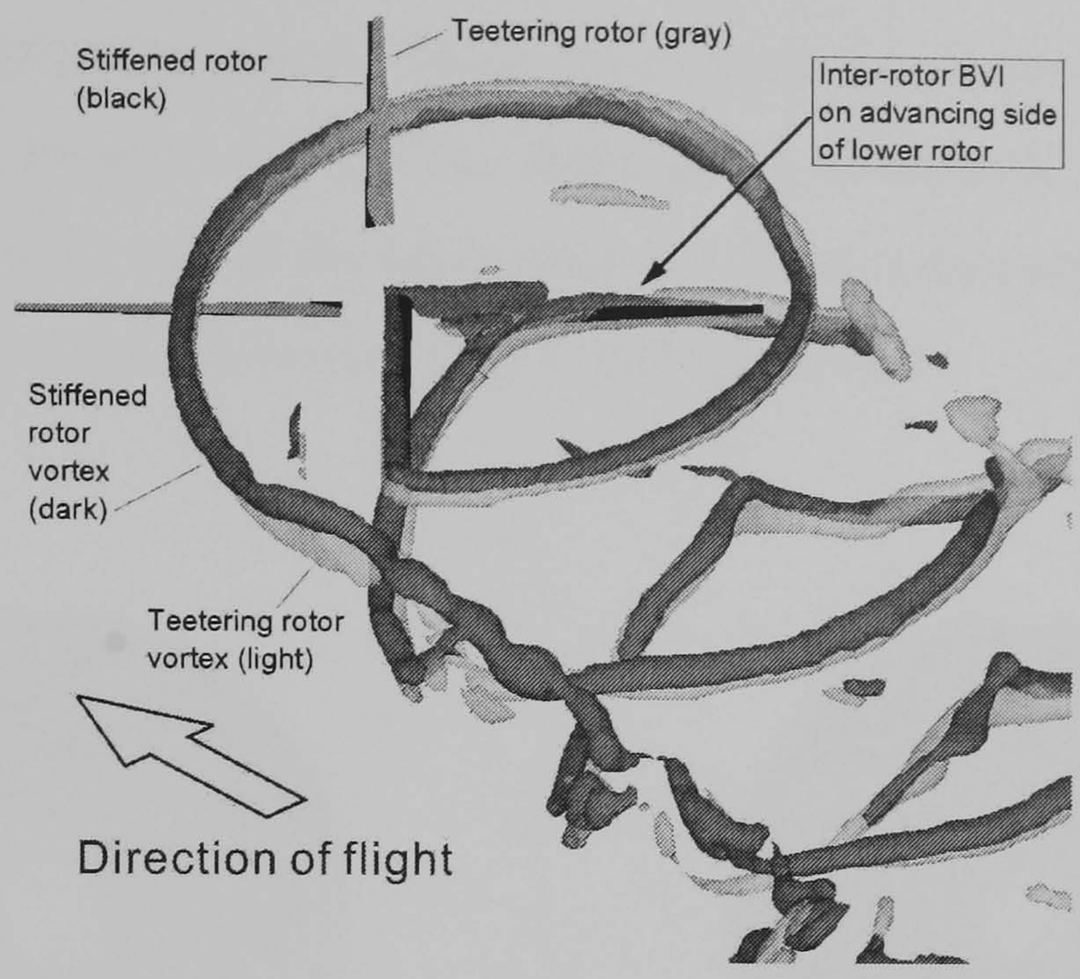
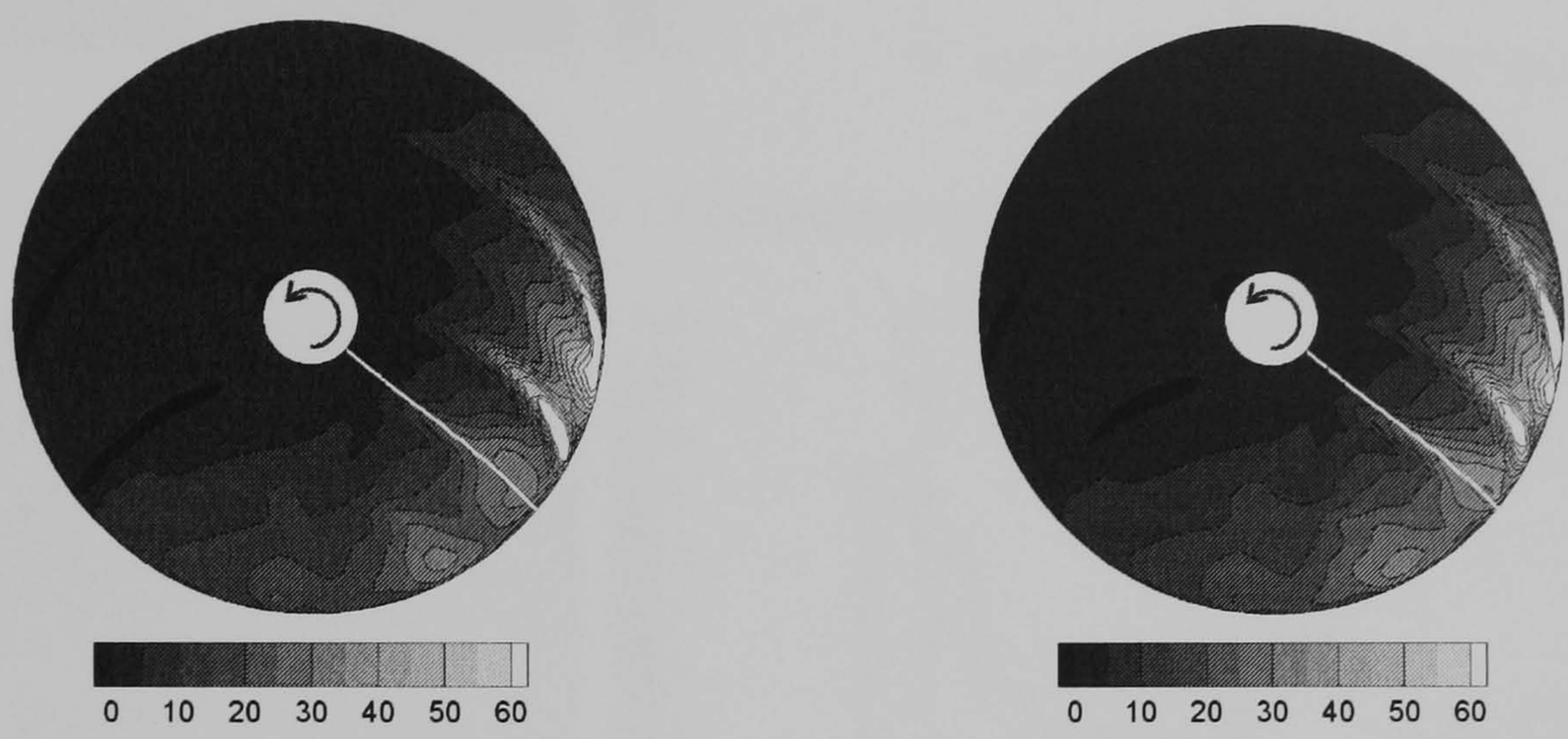


Figure 5.17: *Comparison between the teetering and stiffened configurations of the principal inter-rotor BVI on the advancing side of the lower rotor at advance ratio* $\mu = 0.12$.

the conventional coaxial rotor suggesting possibly a common aerodynamic origin.

Close examination of the time histories of acoustic pressure at the hot spot below the advancing side of the lower rotor, as shown in Figure 5.16, reveals that both the stiffened and rigid rotors have peaks that occur at observer time of $t = 0.036$ s, albeit with much reduced amplitude and impulsiveness compared to the peak in the acoustic pressure that is generated by the teetering configuration at the same observer time. The highly impulsive peak for the teetering configuration was found to be due to a parallel BVI on the advancing side of the lower rotor as shown in Figures 5.7(a) and 5.8. Figure 5.15 shows, at advance ratio $\mu = 0.12$, the principal inter-rotor BVI at an azimuthal location of approximately 45° to be weaker for the stiffened and rigid rotors than it is for the teetering rotor. Figure 5.17 highlights the difference between the teetering and stiffened configurations in the geometry of this particular inter-rotor BVI. The effect of the weakening of this BVI is clearly seen in the distribution of acoustic sources on the lower rotors of both the stiffened and rigid systems, as shown in Figure 5.18, where the sharp peak that was present in the teetering case (Figure 5.7(a)) is no longer visible. Instead, the region of high acoustic source density is shifted outboard towards the tip region of the advancing side of the lower rotor (for both the stiffened and

rigid rotors) as a result of the increased loading in this region compared to the teetering rotor (see Figure 4.17 in Chapter 4). These observations reveal that the focusing of the distributed acoustic pressure to form the sharp peaks in acoustic pressure at the hot spot below the advancing side of the lower rotor is a direct consequence of the impulsive nature of the blade vortex interaction that is highlighted here.

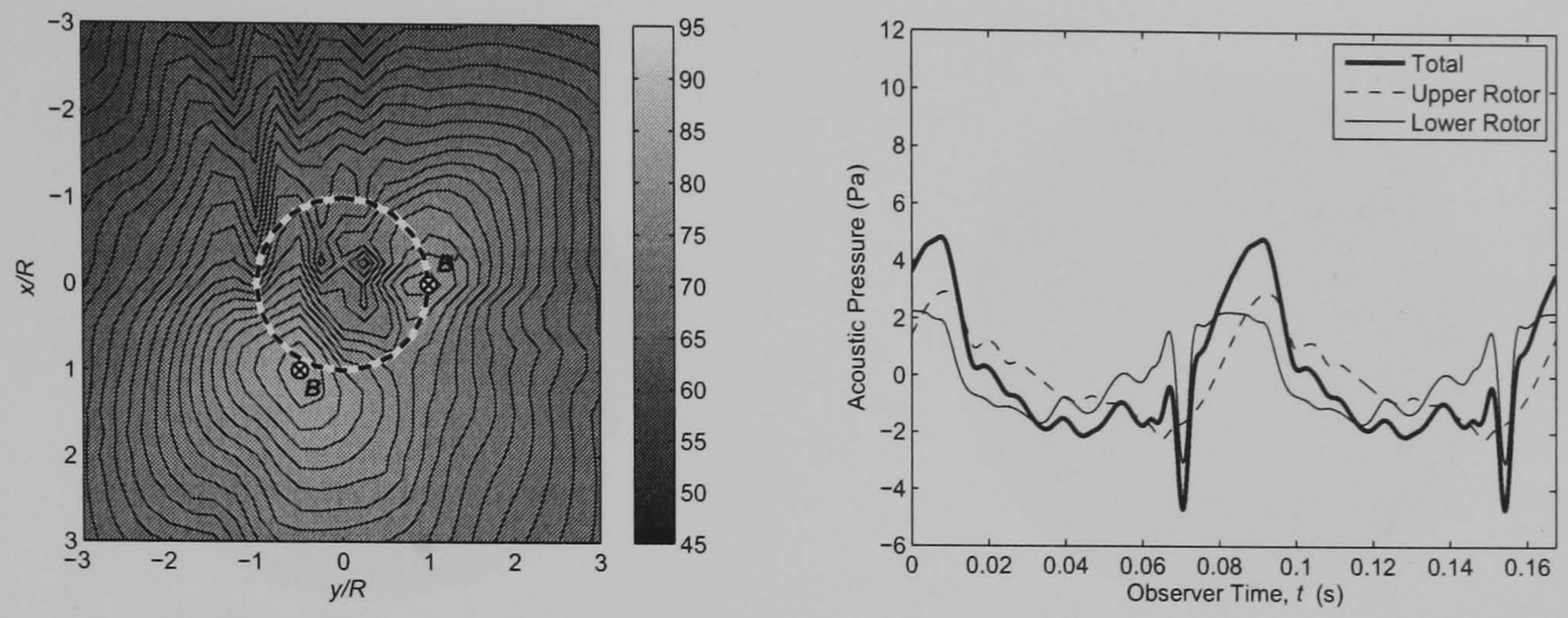


(a) Stiffened ($\nu = 1.5$)

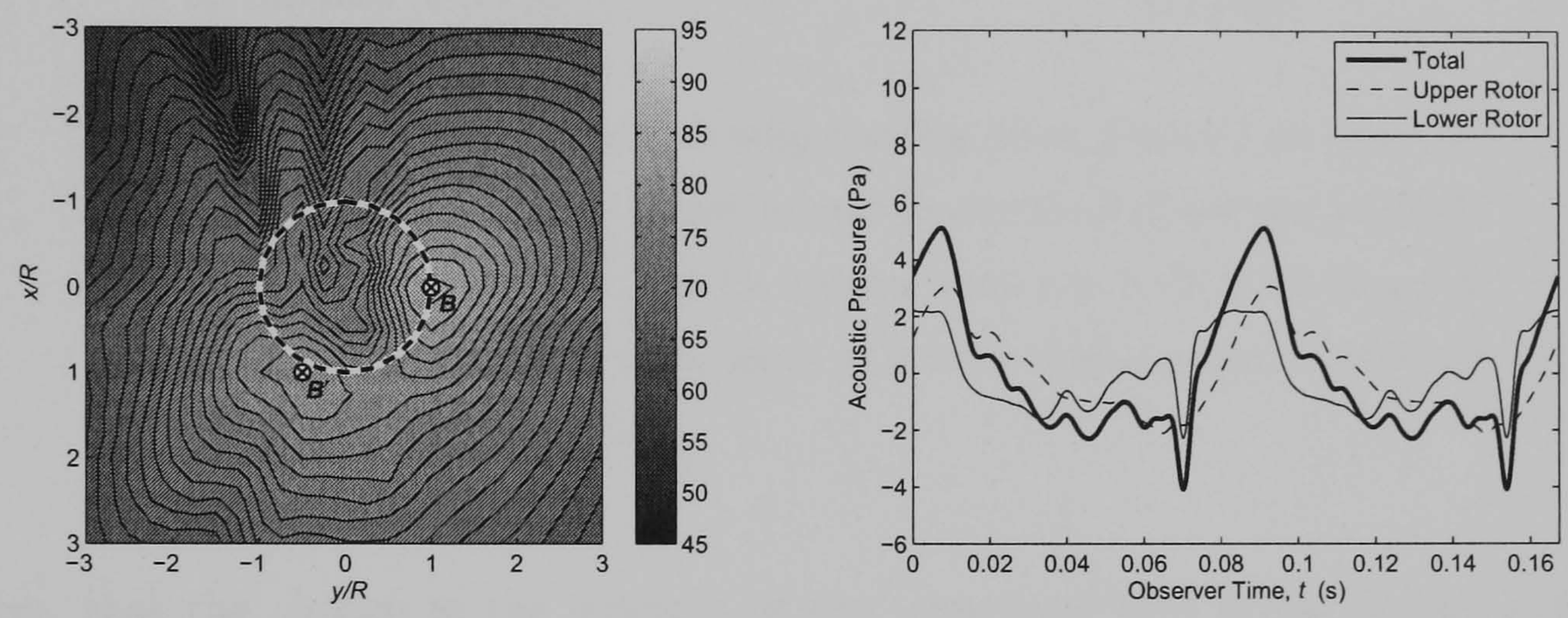
(b) Rigid

Figure 5.18: *Acoustic source density (loading noise, Pa/m^2) on lower rotor of coaxial system as evaluated at the BVI hot spot directly below advancing side of lower rotor for advance ratio $\mu = 0.12$. Also shown as a white line is the locus of sources corresponding to observer time $t = 0.037$ s.*

The secondary hot spot which occurs below the rear of the disc, again for both the stiffened and rigid rotors (see Figure 5.16), originates from the BVI on the retreating side of the lower rotor. In contrast to the weakening of the inter-rotor BVI on the advancing side of the lower rotor, the upper rotor blade of the stiffened system trails an intensified tip vortex as it advances into the freestream (see Figure 4.17, Chapter 4). As this vortex passes the retreating blade of the lower rotor, it yields an intensified inter-rotor BVI in this region compared to the situation with the teetering configuration. The time histories of the acoustic pressure shown in Figure 5.19 reveal the peaks associated with this interaction, culminating in the hot spot below the rear of the disc, to occur at an observer time of $t = 0.070$ s (or 0.154 s) for both the stiffened and rigid rotors. It is



(a) Stiffened to $\nu = 1.5$ (sound pressure at 'B' is 84.9 dB)

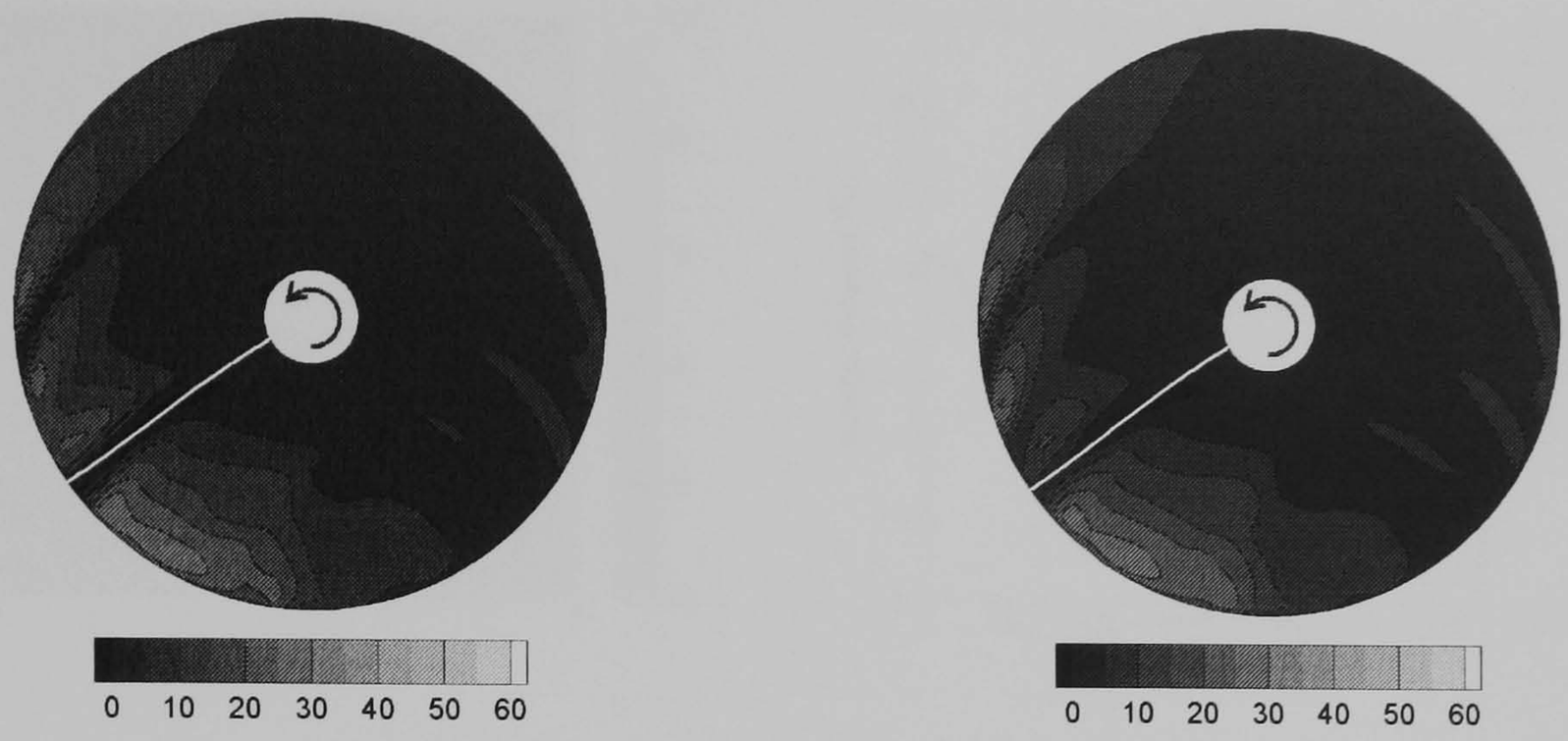


(b) Rigid (sound pressure at 'B′' is 80.0 dB)

Figure 5.19: *Time history of acoustic pressure over one rotor revolution at BVI hot spot below the rear of the rotor disc for advance ratio* $\mu = 0.12$.

clear from this figure that the pressure pulse due to the inter-rotor BVI on the retreating side is more impulsive in character for the stiffened rotor than it is for the rigid rotor. This observation is supported by the observed distribution of acoustic sources shown in Figure 5.20 where the stiffened rotor can be seen to yield a higher spatial gradient of source density near the BVI on the retreating side of the lower rotor than with the rigid rotor.

It is interesting to note, though, that the relative impulsiveness, and hence the resulting maximum sound pressure level, of the two hot spots appears to differ between the stiffened and rigid rotors. One may expect, according to the observations presented

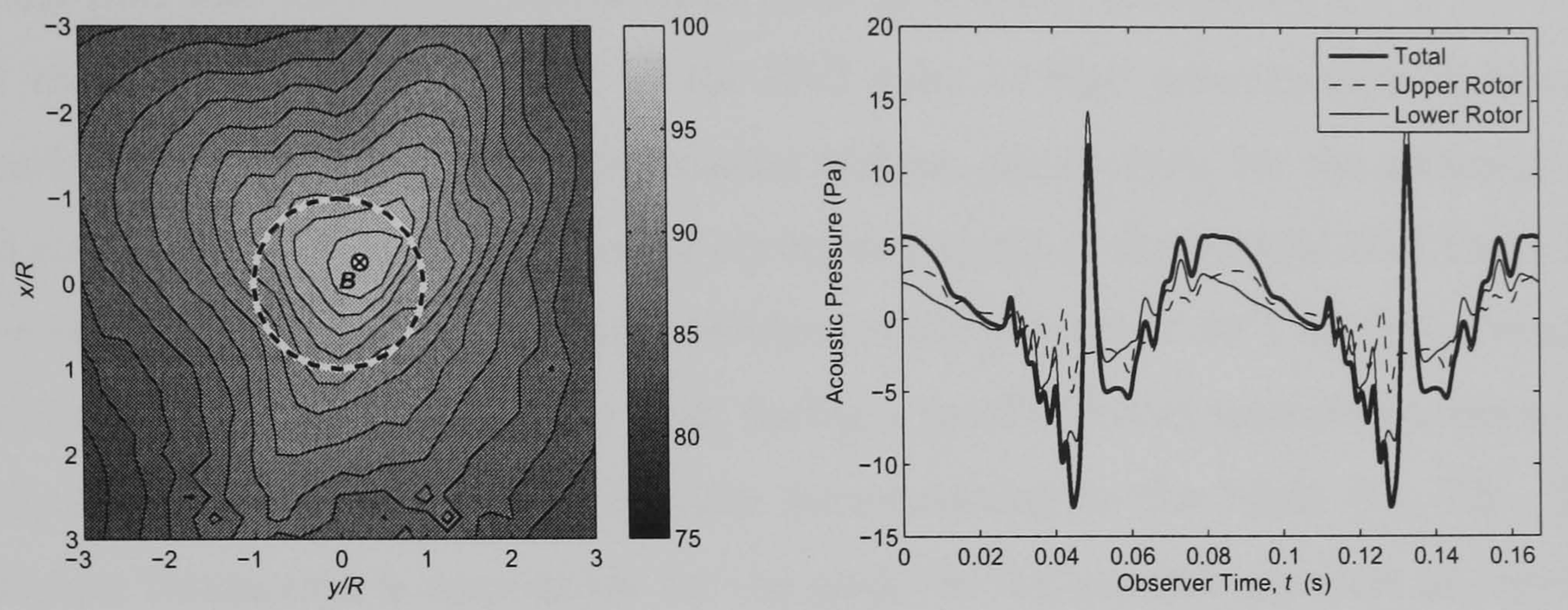


(a) Stiffened ($\nu = 1.5$) (b) Rigid

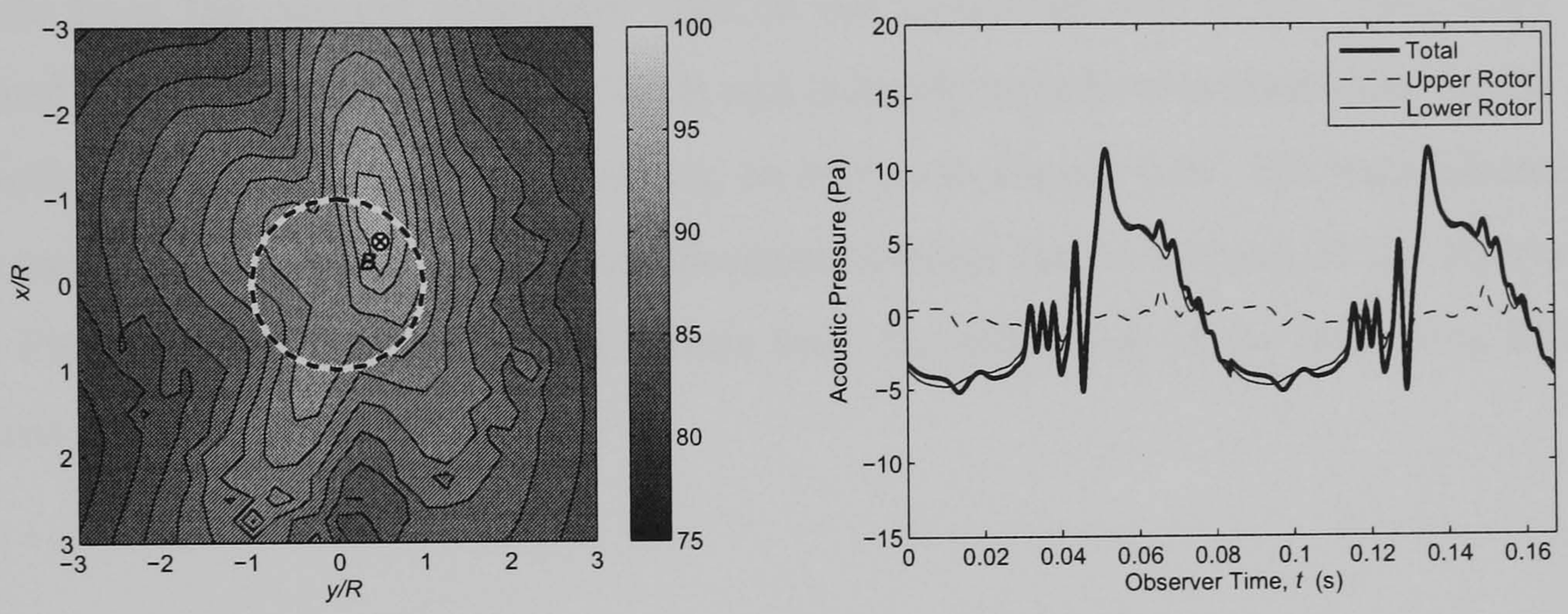
Figure 5.20: *Acoustic source density (loading noise, Pa/m^2) on lower rotor of coaxial system as evaluated at the BVI hot spot below the rear of rotor disc for advance ratio $\mu = 0.12$. Also shown as a white line is the locus of sources corresponding to observer time $t = 0.154$ s.*

above, that the change in the strength of the inter-rotor BVI would be the greatest in the limiting case of infinite stiffness, thus yielding the greatest reduction in acoustic pressure on the advancing side and similarly the greatest amplification on the retreating side of the lower rotor. In that respect, the trends observed above may seem somewhat counter-intuitive. It should be borne in mind though that the strength of a BVI event, and thus the amplitude of the associated acoustic radiation of the rotor system, is not dependent solely on the strength of the vortex that interacts with the blade but is also sensitive to subtle variations in the relative orientation and distance between the vortex and the blade. While the assumption of infinite stiffness appears to yield a reasonable representation of the level of stiffness that is practically achievable, the results presented here suggest that the incorporation of the blade dynamics, including the structural deformation of the blades, might be warranted in any detailed study of a real system in order to capture accurately these secondary effects before any concrete conclusions regarding its acoustic performance are drawn.

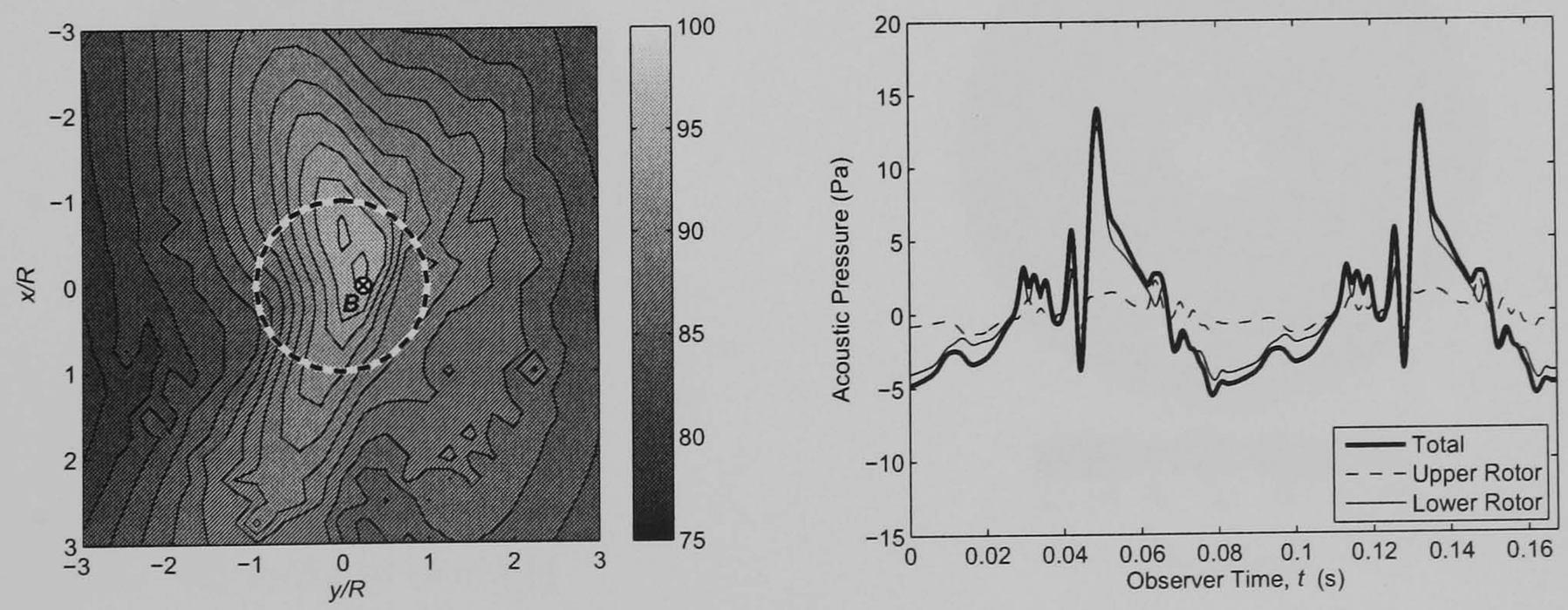
At high advance ratio ($\mu = 0.24$), the reduction in BVI noise associated with an



(a) Teetering (sound pressure at 'B' is 97.4 dB)



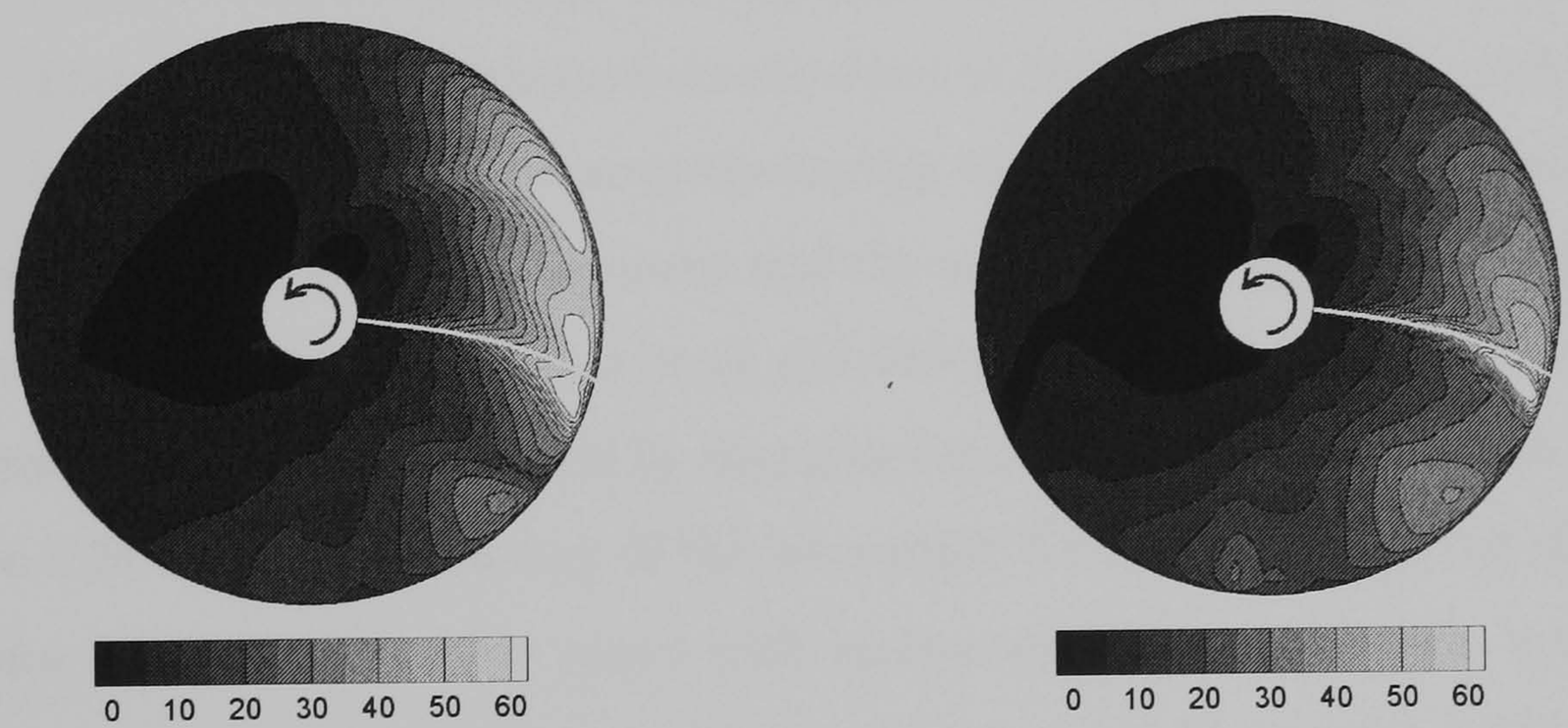
(b) Stiffened to $\nu = 1.5$ (sound pressure at 'B' is 94.5 dB)



(c) Rigid (sound pressure at 'B' is 95.4 dB)

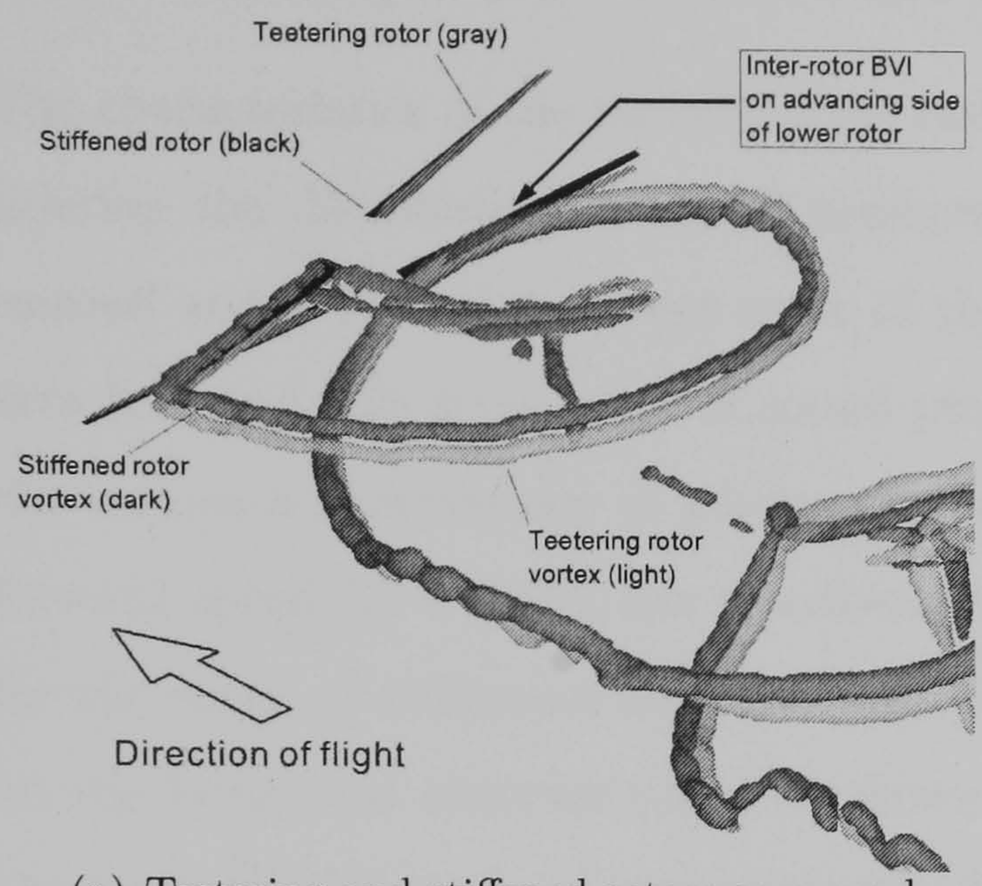
Figure 5.21: *BVI sound pressure levels (5–40N_{bt}/rev) in decibels (left) and time history of acoustic pressure over one rotor revolution at BVI hot spot marked 'B' (right) for advance ratio $\mu = 0.24$.*

increase in rotor stiffness is relatively limited (about 2–3 dB) compared to the reduction of 8 dB that was observed at low advance ratio ($\mu = 0.12$). In Figure 5.21, it is evident that the direction of propagation of the BVI noise at high advance ratio is focused towards the fore and the aft of the coaxial system, particularly for the stiffened and rigid rotors. This longitudinal focusing occurs as a result of the parallel BVI that takes place close to the point of maximum incident velocity (at $\psi = 90°$) on the advancing side of the lower rotor and the fact that, during a parallel vortex interaction, the sound wavelets are highly focused in directions perpendicular to the blade [71, 72]. This particular interaction is responsible for the peaks in the acoustic pressure at observer time $t = 0.049$ s, as shown in Figure 5.21. For the teetering configuration, a similar peak results from the parallel inter-rotor BVI on the advancing side of the lower rotor (see Figures 5.7(b) and 5.11 in Section 5.3.2) and is highly impulsive in character. In the case of both the stiffened and rigid systems, as shown in Figure 5.21, the impulsiveness of this particular inter-rotor BVI is ameliorated through the weakening of the interaction (see Figures 5.7(b) and 5.22) that results from the offloading of the retreating sides of the rotors.

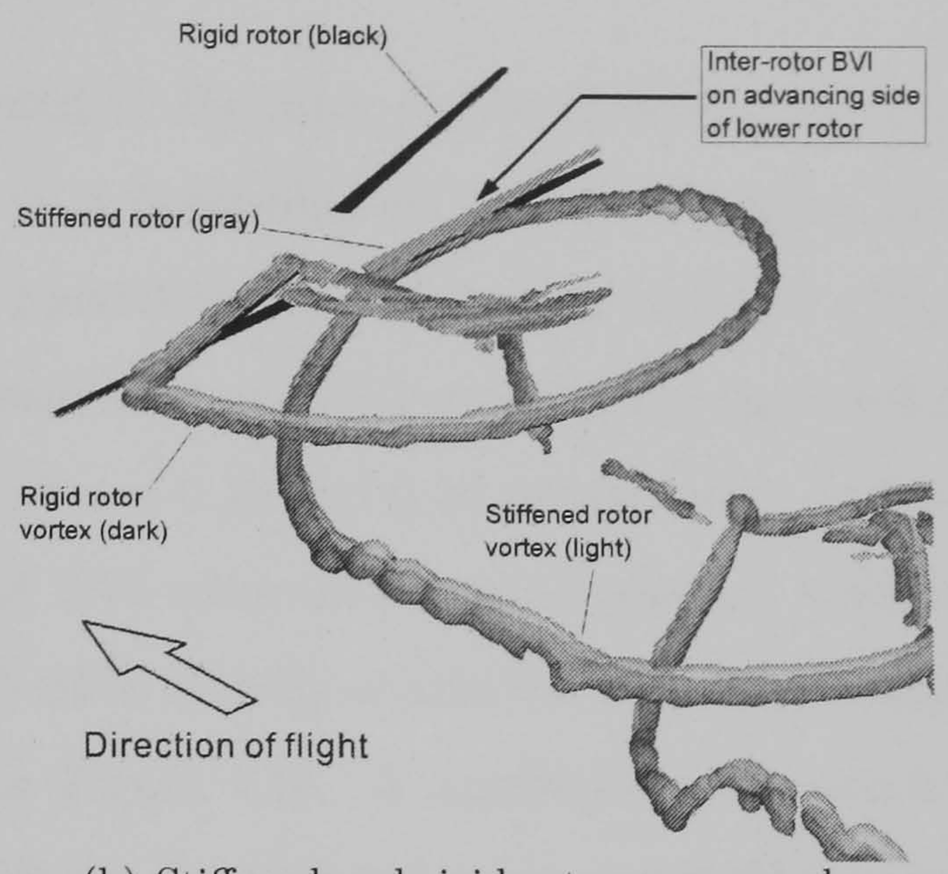


(a) Stiffened ($\nu = 1.5$) (b) Rigid

Figure 5.22: *Acoustic source density (loading noise, Pa/m^2) on lower rotor of coaxial system as evaluated at the BVI hot spot for advance ratio $\mu = 0.24$. Also shown as a white line is the locus of sources corresponding to observer time $t = 0.051$ s in (a) and $t = 0.049$ s in (b).*



(a) Teetering and stiffened rotors compared



(b) Stiffened and rigid rotors compared

Figure 5.23: *Comparison of the principal inter-rotor BVI on the advancing side of the lower rotor between the configurations with various stiffnesses at advance ratio* $\mu = 0.24$.

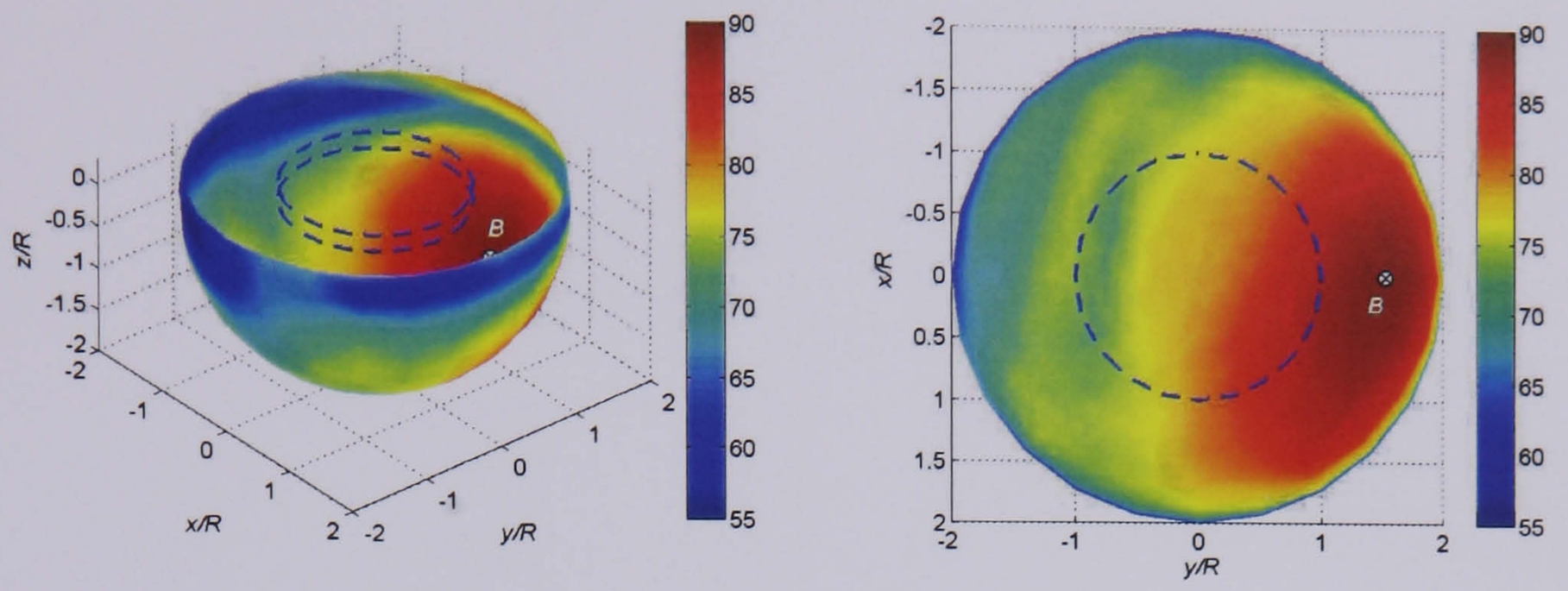
The subtle differences in the exact location of the hot spots and in the direction of propagation of the BVI noise observed at this speed for the various rotor systems can be attributed to the differences in the relative orientation of the blades and the interacting vortices. These differences originate from the effect of flapwise stiffness in modifying the dynamic behaviour of the blades notwithstanding the imposed trim conditions on the rotor system. As a result, the alignment and the miss-distance of the rotor blade with respect to the oncoming vortex, and hence the direction of the noise propagation due to this interaction, are subtly modified by changing the rotor stiffness. This effect is shown in Figure 5.23 where the geometry of the inter-rotor BVI on the advancing side of the lower rotor is compared for the rotors with various stiffnesses. Although, admittedly, the assumption of infinite stiffness may be inadequate to yield an exact representation of a coaxial system with a practical level of flapwise stiffness, the analysis presented here does lend a useful insight into the aerodynamic and acoustic behaviour of coaxial rotor systems with stiffness comparable to current designs.

5.4.2 Consequences for Far-Field Noise

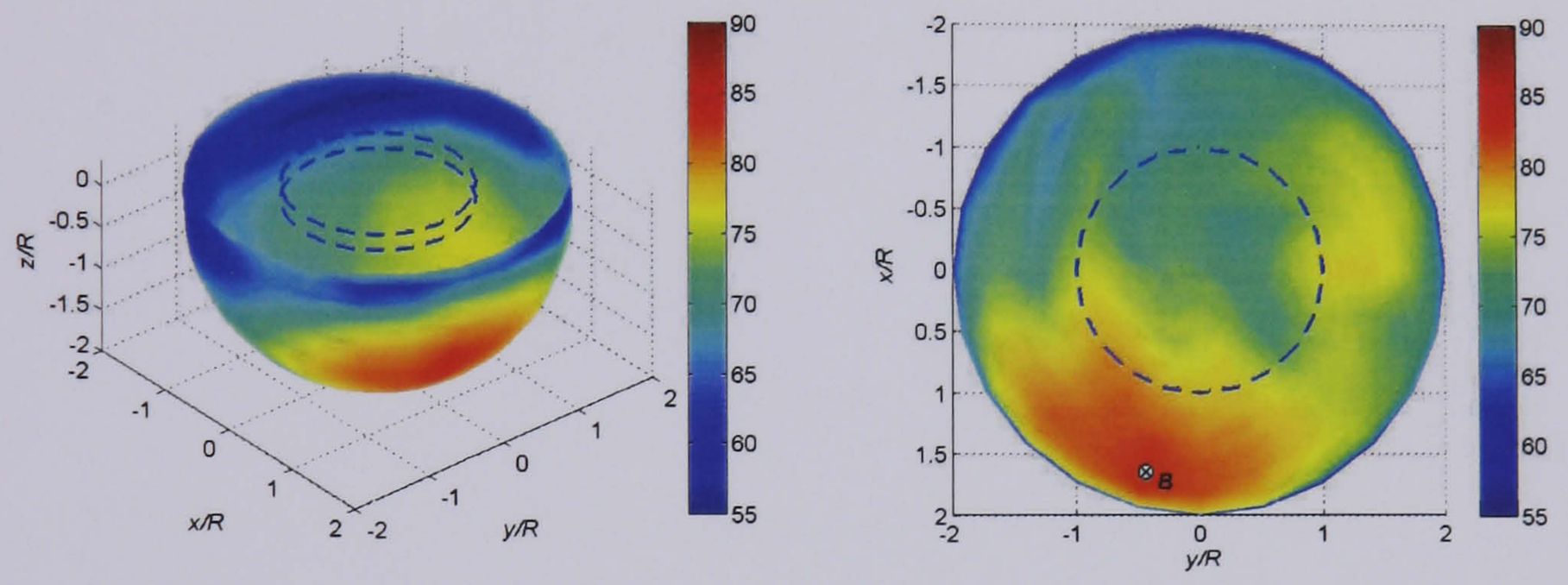
The characteristics of the far-field noise radiated by the rotor can be examined by considering the distribution of sound pressure on a hemispherical surface of radius $2R$, centred at the hub of the lower rotor of the coaxial system (as in Section 5.3.3). Figures 5.24 and 5.25 show maps of sound pressure level on this hemispherical surface for the various hub stiffnesses at advance ratios of $\mu = 0.12$ and 0.24 respectively. At low forward speed ($\mu = 0.12$), the distribution of BVI noise on the hemispherical surface for the range of stiffnesses shown in Figure 5.24 is entirely consistent with that found on the horizontal observer plane as shown in Figure 5.16. A significant reduction in the far-field BVI noise (of approximately 7 dB for the stiffened rotor and 8 dB for the rigid rotor) compared to that of the teetering configuration is also consistent with the distribution of sound pressure level on the horizontal observer plane as described earlier.

Interpretation of the far-field noise for the high speed case requires more care as the contribution from thickness noise becomes more significant with increased flight speed as a result of Doppler amplification. This is shown clearly in Figure 5.26 where, at high speed ($\mu = 0.24$), a significant difference between the total BVI noise and the component due to loading is apparent. At low speed ($\mu = 0.12$), however, there is no notable difference between the total BVI noise and the loading noise. Indeed, when the thickness component of noise is included in the analysis at high speed, the points at which the BVI sound pressure level is maximal are shifted to lie within the plane of the rotor. Figure 5.25 shows only the loading component of the BVI sound pressure level on the hemispherical surface in order to allow unbiased representation of the BVI noise characteristics in the far-field. The change in the directivity of the BVI noise towards the front left of the rotor is consistent with the change in the directivity observed on the horizontal observer plane as shown in Figure 5.16.

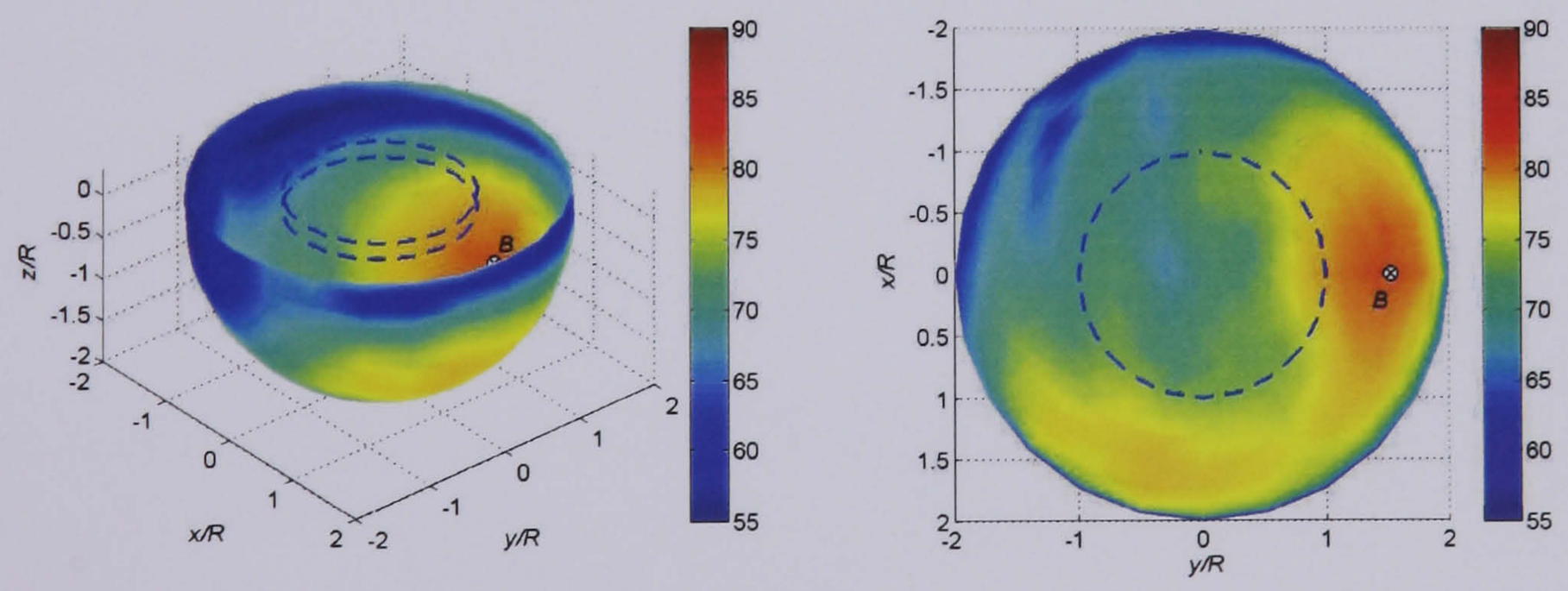
The maximum overall sound pressure level on the hemispherical surface, at both $\mu = 0.12$ and $\mu = 0.24$, does not appear to be affected significantly by the introduction of stiffness into the rotor system (see Figure 5.26). This suggests that, despite the significant reduction in the BVI noise that is achieved by increasing the rotor stiffness, the significance of the low harmonic noise increases also, thus offsetting to a certain extent the benefits of stiffening in terms of overall sound pressure level. The results presented above suggest, however, that the intensity and directivity of the noise pro-



(a) Teetering (sound pressure at 'B' is 89.2 dB)

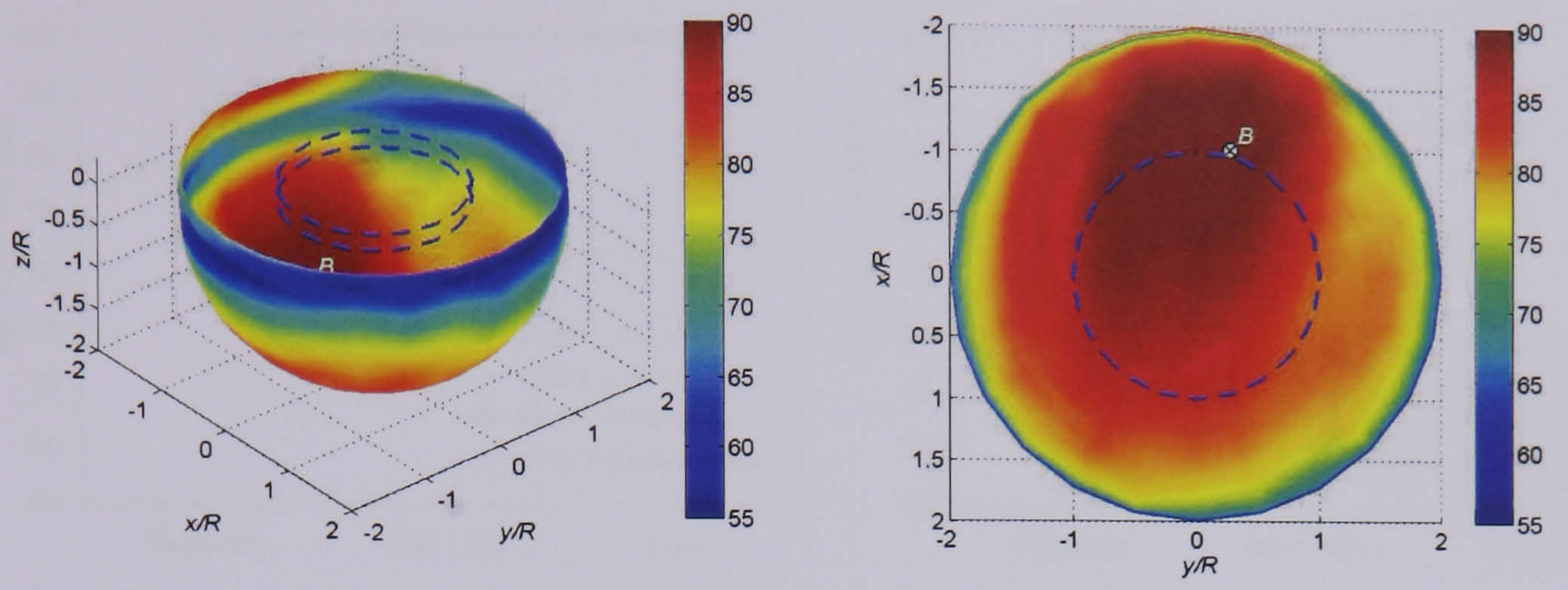


(b) Stiffened to $\nu = 1.5$ (sound pressure at 'B' is 82.3 dB)

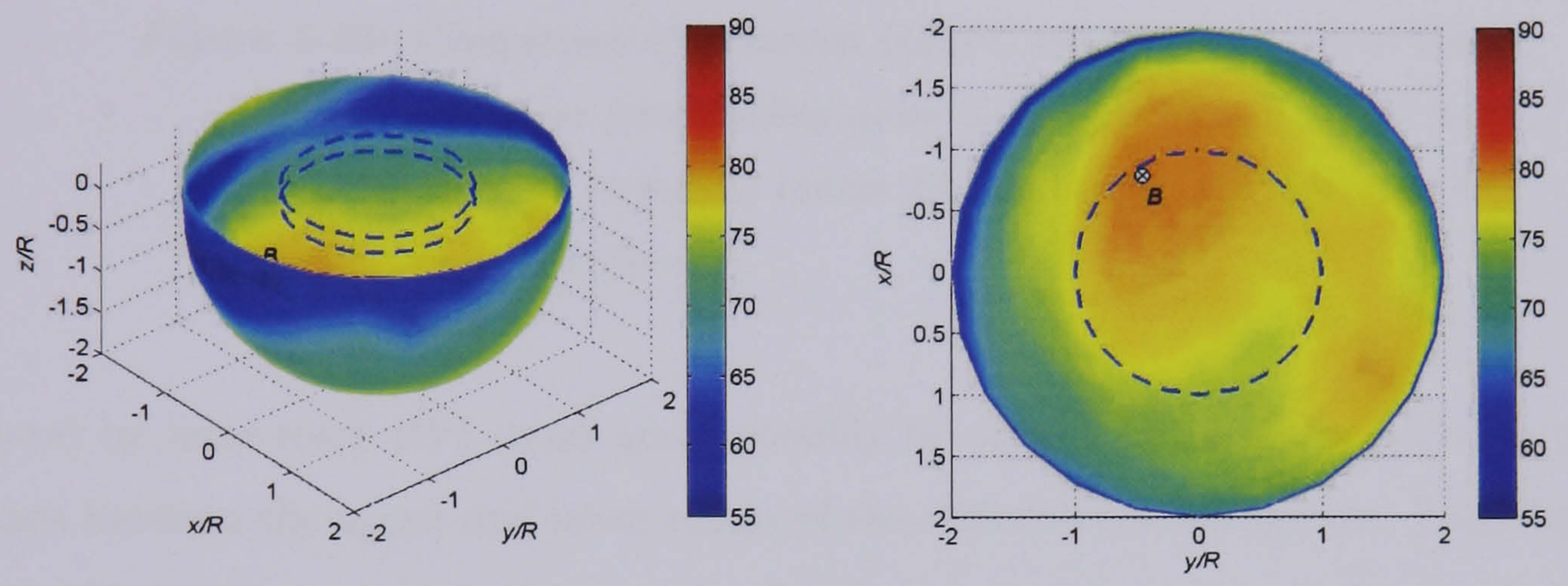


(c) Rigid (sound pressure at 'B' is 81.3 dB)

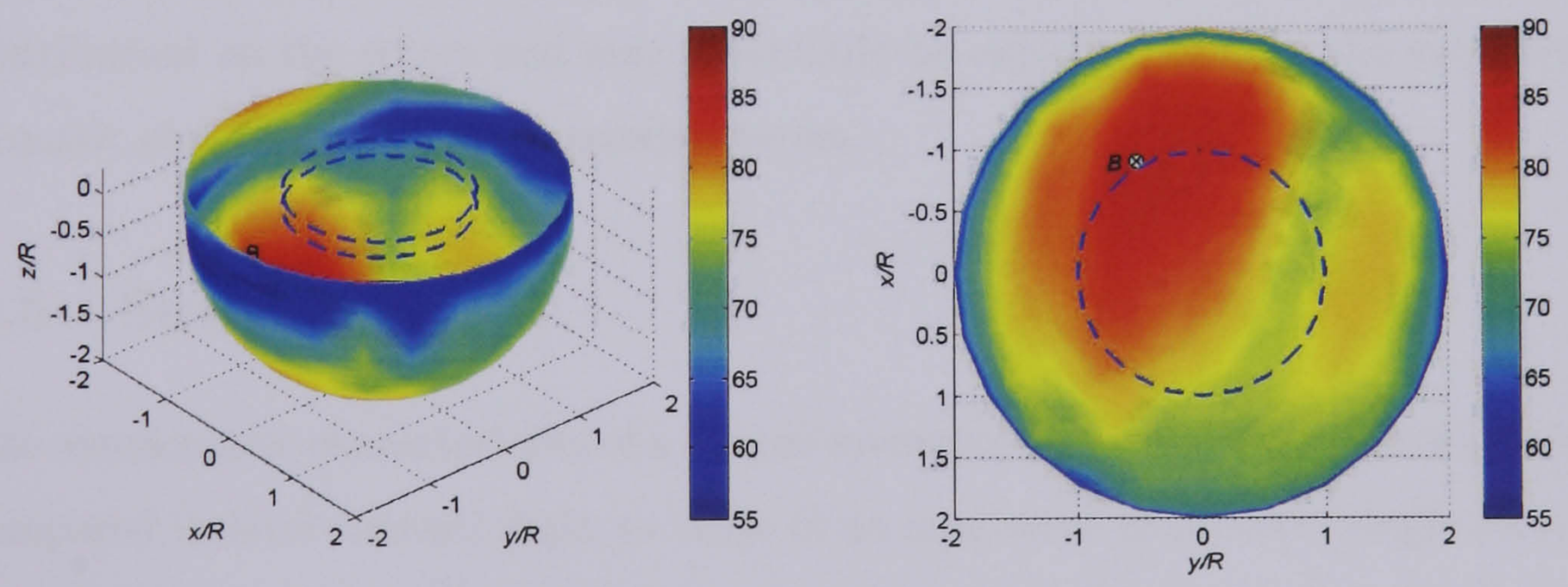
Figure 5.24: *BVISPL in decibels for various stiffnesses of coaxial rotor system on a hemispherical surface of radius $2R$ centred on the hub of the lower rotor at advance ratio $\mu = 0.12$. (Left: isometric view. Right: top view.)*



(a) Teetering (sound pressure at 'B' is 91.0 dB)

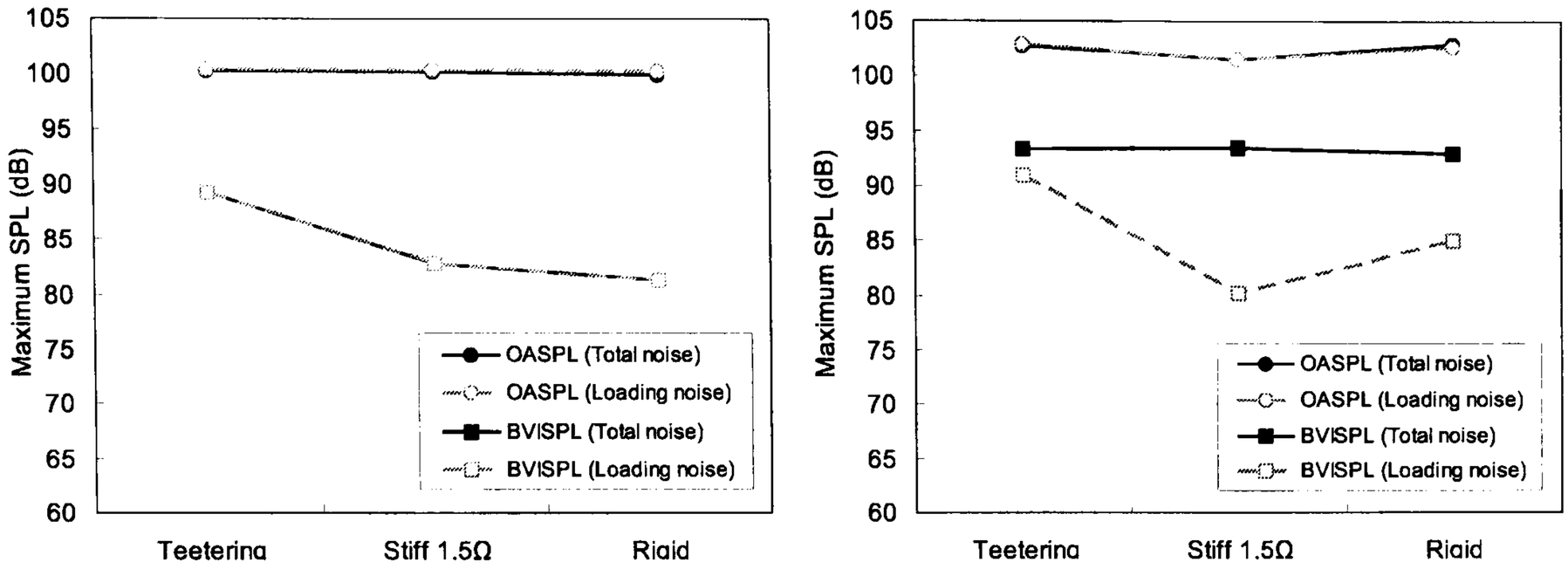


(b) Stiffened to $\nu = 1.5$ (sound pressure at 'B' is 80.2 dB)



(c) Rigid (sound pressure at 'B' is 85.0 dB)

Figure 5.25: *Loading noise BVISPL in decibels for various stiffnesses of coaxial rotor system on a hemispherical surface of radius* $2R$ *centred on the hub of the lower rotor at advance ratio* $\mu = 0.24$. *(Left: isometric view. Right: top view.)*



(a) $\mu = 0.12$ (b) $\mu = 0.24$

Figure 5.26: *Comparison of maximum OASPL and BVISPL of total noise and those from loading noise in decibels on a hemispherical observer surface of radius $2R$, centred on the rotor hub for various stiffnesses.*

duced by inter-rotor BVI could quite possibly be altered by careful scheduling of the loads between the upper and lower rotors of the stiffened coaxial system. Furthermore, individual rotor control in the context of stiffened coaxial systems, for example by using differential cyclic pitch inputs, offers significant flexibility in controlling the load distribution on the rotors and may potentially be exploited to alter the low harmonic acoustic characteristics of the coaxial system.

5.5 Summary

The aeroacoustic characteristics of a coaxial system consisting of two teetering rotors are compared in level forward flight to those of an equivalent articulated single rotor with the same solidity. The effects of introducing hub stiffness into the system on the acoustic characteristics of the coaxial rotor are also investigated. A lifting-line representation of the blade aerodynamics within the VTM is used to simulate the aerodynamics of the rotor systems. The acoustic field is determined using the Ffowcs Williams-Hawkings equation implemented using the Farassat-1A formulation. Acoustic analysis shows that the principal contribution to the noise radiated by both the coaxial and the equivalent single rotor systems is at the fundamental blade passage frequency, but that the coaxial

rotor generates higher sound pressure levels (by 10 dB for the evaluated configurations) than the equivalent single rotor at all flight speeds. The sources of BVI noise are investigated and the principal BVI events are identified. For the coaxial rotor, the most intense impulsive noise is seen to be generated by the inter-rotor BVI on the advancing side of the lower rotor. The impulsive noise that is generated by blade vortex interactions on the equivalent single rotor reduces in amplitude as the strength of the BVI events on the rotor decreases with forward speed. Conversely, the BVI noise of the coaxial rotor intensifies with increasing flight speed due to the increasing strength of the interaction between the wake of the upper rotor and the blades of the lower rotor. The impulsive noise due to BVI events for the coaxial rotor is found to be higher by 15–25 dB compared to the equivalent single rotor. The overall and impulsive noise characteristics of the coaxial system are found to be weakly sensitive to changes in rotor separation and to the relative phasing of the rotors.

Increasing the rotor stiffness alters the strengths of the blade vortex interactions, particularly those between the upper and lower rotors of the system, and this affects significantly the intensity and directivity of the BVI noise produced by the system. The flapwise stiffness of the hubs of the coaxial system acts to re-distribute the spanwise loading on the rotors in forward flight, thus weakening the tip vortex that is trailed on the retreating side of the upper rotor. This vortex subsequently passes the advancing blade on the lower rotor but results in a relatively weak interaction compared to the same BVI event for the original teetering rotor, which is highly impulsive in nature. Conversely, the retreating side of the lower rotor experiences a strengthened BVI event at low advance ratio. Despite a significant reduction in BVI noise of about 8 dB, the maximum overall sound pressure level in the far-field is largely unaffected by the introduction of rotor stiffness. The results presented here highlight the sensitivity of the BVI noise characteristics to the flapwise stiffness of the coaxial system. This sensitivity may potentially be exploited to reduce the acoustic signature of stiffened coaxial systems.

Chapter 6

Compound Coaxial Helicopter

6.1 Introduction

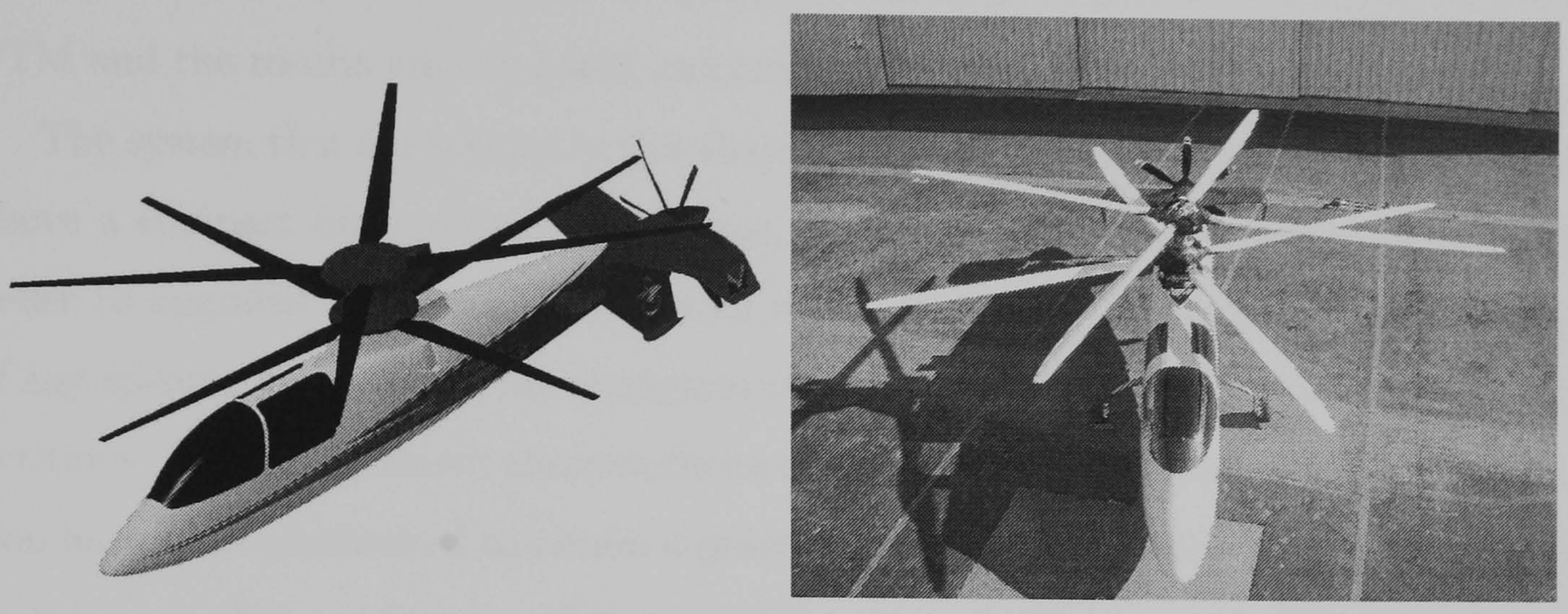
Recent design studies have revisited the twin contra-rotating coaxial rotor system as a potential solution to emerging requirements for a heavy-lift helicopter that can achieve much higher forward speed than has traditionally been possible with single-rotor platforms [7].

Most helicopters rely on forward tilt of the rotor to produce the force required to propel the system through the air. With a conventional rotor system with an articulated hub (or a hingeless hub but with low flapwise stiffness) the maximum performance of the system in forward flight is often limited by the high lift coefficients that are required on the retreating side of the rotor disc in order to overcome the natural tendency of the rotor to flap backwards. The same limitation applies to conventional coaxial rotors where the hubs of the individual rotors are articulated. Unique to a coaxial configuration, though, is the prospect of introducing significant flapwise stiffness into the system in order to relieve the retreating blade from the requirement to operate at high lift coefficients. The presence of flapwise stiffness alters the phase relationship between blade flapping and the applied aerodynamic load such that the natural response of a stiffened rotor in forward flight is no longer to flap backwards but instead to produce a rolling moment about its hub. The contributions to the rolling moment from two contra-rotating rotors can be made to cancel naturally, however, and this allows the retreating sides of the rotors to be flown at relatively benign average lift coefficients compared to those associated with

a conventional rotor. The premise is that such rotors can thus be flown at much higher advance ratios than traditional single main rotor systems before the aerodynamics of the retreating blades pose a serious limit to the performance of the system. This is essentially the design philosophy of the Advancing Blade Concept (ABC) rotor system developed by Sikorsky Aircraft Corporation and implemented on the prototype XH-59A aircraft in the 1970s (see Refs. 6 and 73 for a detailed overview of the development of this helicopter).

The equivalent argument in terms of speed rather than advance ratio is weakened somewhat by the fact that compressibility on the advancing side of the rotor at high forward speed poses as great an impediment to the performance of a stiffened coaxial rotor as it does to a conventional system. This is particularly so if the rotors are highly loaded, for instance through being required to produce a significant proportion of the propulsive force required by the aircraft. The effects of compressibility can be ameliorated and delayed to higher forward speed however if the main rotor system can be off-loaded by a suitable means of lift or thrust augmentation. This can be done by the addition of wings or an auxiliary propulsion system, for instance, and by allowing the main rotor to operate at a reduced rotational speed [74]. For this reason, the thrust compounded, stiffened coaxial rotor is considered to be a very strong contender to form the basis of a new generation of heavy-lift, high-speed rotorcraft. The XH-59A itself used a pair of turbojets to augment the thrust produced by the main rotor (see Figure 4.1 in Chapter 4), but despite the considerable effort that was put into testing scaled models and prototype aircraft, this design did not reach production. The stiffened coaxial rotor concept has been revived more recently though, aided by recent advancements in composite material technology and vibration suppression techniques, in the development of Sikorsky's X2 technology demonstrator. As shown in Figure 6.1, taken from Ref. 7, this helicopter uses a tail-mounted pusher propeller to augment the propulsive force that is provided by its ABC-type coaxial main rotor.

This particular configuration, although showing significant promise as a viable technological solution to operational requirements for increased helicopter forward speed, manoeuvrability and load-carrying ability, is inherently very complex from an aerodynamic point of view. Under certain flight conditions, the performance and flight mechanics of such a configuration are likely to be influenced very strongly by aerodynamic



(a) Schematic

(b) Prototype aircraft

Figure 6.1: *Sikorsky's X2 technology demonstrator. (Images courtesy of Ashish Bagai, Sikorsky Aircraft Corporation.)*

interactions between the various components of the helicopter. In order to maximise the efficiency and potential of this type of aircraft, a thorough understanding of the nature and form of the aerodynamic interactions that occur within the system, as well as an appreciation of the flight conditions under which such interactions might pose the greatest challenges to the operation and control of the vehicle, is essential [74].

For many years, the aim of the developers of computational tools for the analysis of rotorcraft has been to develop a method that can be used very early in the design process to inform the designers of such aircraft of the potential aerodynamic problems that might arise from injudicious juxtaposition of the various elements of their proposed configuration. The ideal has always been for this information to become available to the designers well before any such problems might manifest on the prototype or production vehicle [75]. Unfortunately, the historical record shows past efforts in this regard to have met with limited success [76, 77, 78, 79, 80, 81].

The aim of this chapter is thus to demonstrate some progress in the computational modelling of helicopter interactional aerodynamics, and to suggest perhaps that the state of the art of computational helicopter aerodynamic predictions is advancing to a stage where some insight into the detailed features of aerodynamic interactions in a system as aerodynamically complex as a propeller-augmented hingeless coaxial helicopter can be obtained. To this end, computational predictions of the aerodynamics

and acoustics of a generic, thrust-compounded coaxial helicopter are obtained using the VTM and the results are compared and contrasted at various forward flight speeds.

The system that is analysed in this chapter has a stiff coaxial rotor system, mounted above a compact but streamlined fuselage, together with a rear-mounted pusher propeller to augment the thrust of the main rotor. Instead of focusing on the properties of any specific, real vehicle, the configuration that is analysed in this chapter is entirely fictitious. Various pertinent characteristics of the thrust-compounded coaxial configuration have been synthesised to obtain a generic representation of this class of helicopters, in the hope that predictions of the aerodynamic environment of the generic configuration might shed some light on the behaviour of this class of helicopters as a whole. Nevertheless, many of the properties of the various components of the generic system have been simplified considerably from those of any real design, and it should be borne in mind that it is highly likely that most of the various aerodynamic pathologies that appear to be attributed to this configuration by this study could be ameliorated fairly easily through sensible engineering design or simple geometric modification.

6.2 Description of Simulated Configuration

This chapter analyses the aerodynamic interaction between the components of a generic helicopter configuration that comprises a stiffened twin coaxial rotor system together with an auxiliary tail propeller, or 'propulsor,' to augment the propulsive thrust that is produced by the main rotor system (see Figure 6.2). Each of the components of this configuration is described in detail below. Although the inspiration for much of the geometry of the configuration is derived from helicopters such as the XH-59A and X2, it should be borne in mind throughout that significant simplifications have been introduced in many instances in order to allow the results presented in this chapter to represent more straightforwardly the generic characteristics of such a configuration rather than the specifics of any one particular aircraft.

6.2.1 Main Rotor System

The main rotor system modelled in this study follows closely that of the XH-59A's ABC rotor in terms of its geometry. Two counter-rotating, three-bladed rotors are sep-

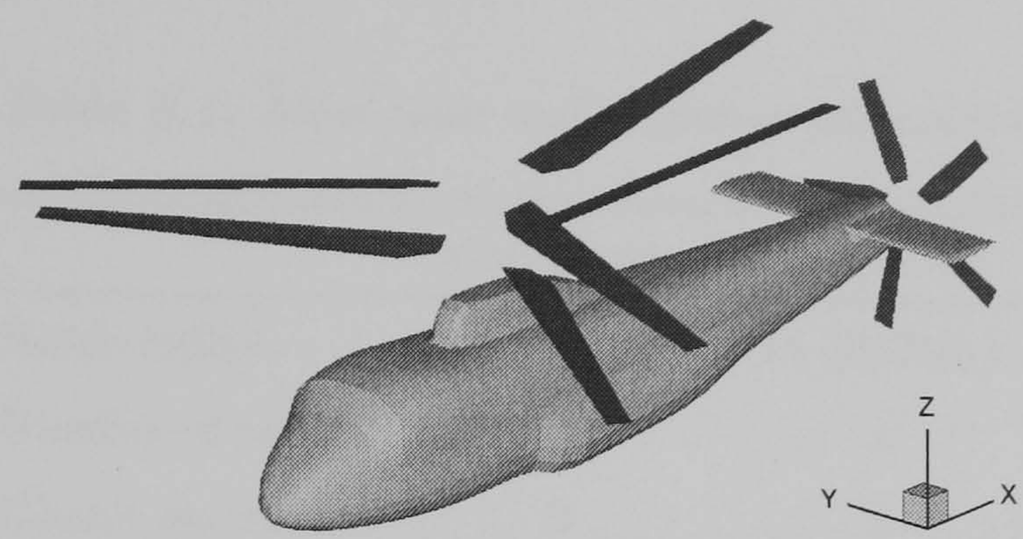


Figure 6.2: *Generic thrust-compounded hingeless coaxial configuration.*

arated axially by a distance of $0.139R$. The blades of both rotors are tapered linearly in planform and have $-10°$ of non-linear twist. For simplicity, however, a constant airfoil section, NACA 23012, is used along the entire span of the rotor blades. In reality, the blades of ABC-type rotors feature a rather more complex spanwise variation of aerofoil section and twist than that modelled here [7, 82]. While the use of constant blade sections yields a rather crude representation of the sophisticated design of real ABC-type rotor blades, the broad characteristics of the resulting wake structure, and hence the aerodynamic interference between the main rotor system and the other lifting devices in the configuration, should nevertheless be sufficiently representative of a realistic full-scale vehicle of this type. The geometric properties of the main rotor system are summarised in Table 6.1.

In all simulations presented in this chapter, the flapwise stiffness of the main rotor of the system is approximated by assuming the rotor blades and their attachments to the rotor hub to be completely rigid. This simplification may appear to be rather crude, and of course the flap-lag dynamics of the blades is suppressed entirely using this approach. Nevertheless, it was shown in Chapter 4 that the loading on the rotors and the resultant wake geometry of such a system are very similar to that of rotors with the high level of flapwise stiffness that are characteristic of the coaxial rotors of ABC-type systems [64, 63]. Thus, as far as the effects of aerodynamic interference are concerned, the simplified rigid rotor model is expected to provide a very close representation of the aerodynamic environment that is generated by practical semi-rigid coaxial rotor systems.

The twin rotors of the coaxial system are arranged so that the upper rotor rotates

Table 6.1: *Main rotor and propulsor geometries*

	Main Rotor	Propulsor
Rotor radius	R_c (5.5m)	R_t $(0.28R_c)$
Number of rotors	2	1
Blades per rotor	3	5
Rotor separation	$0.139R_c$	–
Root cutout	$0.12R_c$	$0.20R_t$
Solidity	0.127	0.222
Twist	$-10.0°$	$-30.0°$
Chord	Tapered (2:1)	$0.18R_t$
Aerofoil sections	NACA 23012	NACA 0012

anticlockwise and the lower rotor rotates clockwise when viewed from above. The rotors have been arranged to overlap when blades from both the upper and the lower rotors pass directly over the centreline of the rear fuselage. For simplicity, the hub of the rotor is not modelled in the simulations, but it should be realised that the omission of this feature of the system will have some effect on the physical plausibility of the predicted structure of the wake immediately downstream of the rotor shaft.

6.2.2 Auxiliary Propulsor

A five-bladed propeller is used to represent an auxiliary thrust-producing device mounted in pusher configuration to the rear of the fuselage. The blades of this propulsor feature a tapered root end, $-30°$ of linear twist, and a NACA 0012 sectional profile. The propulsor is mounted so that its rotational axis is aligned with the longitudinal axis of the aircraft. The radius of the propulsor is $0.28R_c$ and the rotational speed is fixed at 4.25 times that of the main rotor. The tip speed of the propulsor is thus 19% greater than that of the main rotor. The direction of rotation of the propulsor is clockwise when seen from the rear of the aircraft.

The pitch angle of all the blades of the propulsor is adjusted simultaneously to produce the desired level of thrust in much the same manner as the collective pitch control affects the feathering of the blades of the main rotors. The blades of the propulsor and

their attachments to their hub are otherwise assumed to be rigid. Note that, as with the main rotor system, the hub of the rotor itself is not modelled. A summary of the geometry of the propulsor is given in Table 6.1.

Table 6.2: *Fuselage geometry*

Fuselage length ($2l$)	$2.04R_c$
Tailplane :	
Aerofoil section	NACA 0012
Span	$0.667l$
Chord	$0.167l$
Hub x,y,z coordinates:	
Main rotor (lower)	$0.765l$, $0.000l$, $0.386l$
Main rotor (upper)	$0.765l$, $0.000l$, $0.522l$
Propulsor	$2.079l$, $0.000l$, $0.111l$
(relative to fuselage nose)	

6.2.3 Fuselage Geometry

The modelled configuration includes a fuselage as shown in Figure 6.2. The geometry of the fuselage is entirely fictitious but was selected to be representative of the compact but streamlined configuration of modern high-performance helicopters. The fuselage features a large horizontal tail surface to represent current design practice, and to allow the effects of aerodynamic interactions that might arise as a consequence of the rotorcraft featuring a lifting empennage arrangement to appear in the simulations. Indeed, the aerodynamic interaction between the wake from the main rotor and the empennage has been documented as being responsible for a number of unexpected flight mechanic issues in modern helicopters (e.g. Refs. 76–81). The tail surface is untwisted and has a rectangular planform, and the Kutta condition is satisfied along its entire trailing edge. This allows it to act as a lifting surface and to produce a representative wake structure. Other relevant properties of the fuselage are summarised in Table 6.2.

6.2.4 Trim Methodology

The self-induced aerodynamic environment of the helicopter is strongly influenced by the method that is used to trim the rotorcraft. The compounded coaxial configuration in particular has several redundant degrees of freedom that can be used in various ways to produce overall force and moment balance within the system. For this reason, the method used to trim the simulated vehicle is set out below.

For present purposes the system is assumed to be in trim when there is zero net moment about the base of the main rotor mast and simultaneously the propulsive force matches the drag on the vehicle and the weight of the aircraft is balanced by the vertical component of the force produced by the rotors. Given the xyz-coordinate system shown in Figure 2.12 (Section 2.7, Chapter 2), this trim state is imposed on the system by defining the array

$$F^* = [-C_D, 0, C_W, 0, 0, 0] \tag{6.1}$$

of prescribed target loads on the vehicle. Given control inputs $\theta^u = [\theta_0^u, \theta_{1s}^u, \theta_{1c}^u]$ and $\theta^l = [\theta_0^l, \theta_{1s}^l, \theta_{1c}^l]$ to the upper and lower rotors respectively, and $\theta^t = [\theta_0^t]$ to the propulsor, the trim algorithm for the compound coaxial helicopter can be written as

$$\left[\dot{\theta}^u(t), \dot{\theta}^l(t), \dot{\theta}^t(t) \right] = K \ (F^* - F(t)) \tag{6.2}$$

where K is a 7×6 coupling matrix that prescribes the rate at which each of the controls should respond to any discrepancy between F^* and F. The dynamic nature of this approach requires the system to be considered to be in trim only when $\overline{F} = F^*$, where $\overline{F}$ is the long-term average of $F(t)$, but no further assumptions regarding the frequency content of the loading on the system are required to establish a steady-state operating condition. The approach is thus ideal for the analysis of flight cases where aerodynamic interactions between the various components of the system might not necessarily result in periodic long-term behaviour of the loads on the vehicle. For brevity, a detailed account of the construction of the coupling matrix K is omitted here as the process is identical to that described in Section 4.2.2 of Chapter 4 except for the addition of the propulsor pitch control.

In all simulations presented in this chapter, the collective pitch inputs to both upper and lower rotors are varied together to alter the total thrust produced by the system while differential collective pitch input to the upper and lower rotors is used to maintain

Table 6.3: *Simulated flight conditions and corresponding trim targets*

Speed	Weight	Drag	Shaft tilt
μ	C_W	C_D	α_s
0.05	0.012	0.00008	0°
0.10	0.012	0.00032	0°
0.15	0.012	0.00072	4°
0.30	0.012	0.00288	4°

zero net yawing moment on the system. The XH-59A employed differential cyclic pitch input to optimise the performance of the rotor [6, 63, 66, 59], but in the present analysis this complication is avoided and the same cyclic pitch inputs are applied simultaneously to both upper and lower rotors to generate the required rolling and pitching moments on the system.

The rigidity of the main rotor system limits the ability of the cyclic pitch controls to tilt the tip path plane relative to the rotor shaft in order to produce a propulsive thrust component to the system, but the high control power of the stiffened rotors allows very direct control of the pitch attitude of the aircraft and hence the disc tilt with respect to the flightpath. The balance of propulsive force between the main rotor system and propulsor that is required to maintain a given forward flight speed is thus largely controlled by the pitch moment that is demanded from the main rotor system. Representation of this characteristic of the helicopter needs to be approached with some care since the rigid-body dynamics of the fuselage is not modelled directly. The approach taken was to assume that, at very low forward speed, just sufficient pitching moment is demanded from the main rotor to maintain its tip path plane parallel to the flightpath, but, beyond an advance ratio of 0.10, additional pitching moment is demanded from the main rotor to force its tip path plane to incline 4° forward, thereby allowing the main rotor to contribute partially to the forward thrust that is required to maintain the forward speed of the helicopter. Any deficit in the propulsive force that is generated by the main rotor is then provided by the tail propulsor by suitable variation of its own collective pitch.

The required propulsive force is calculated by assuming the parasite drag of the

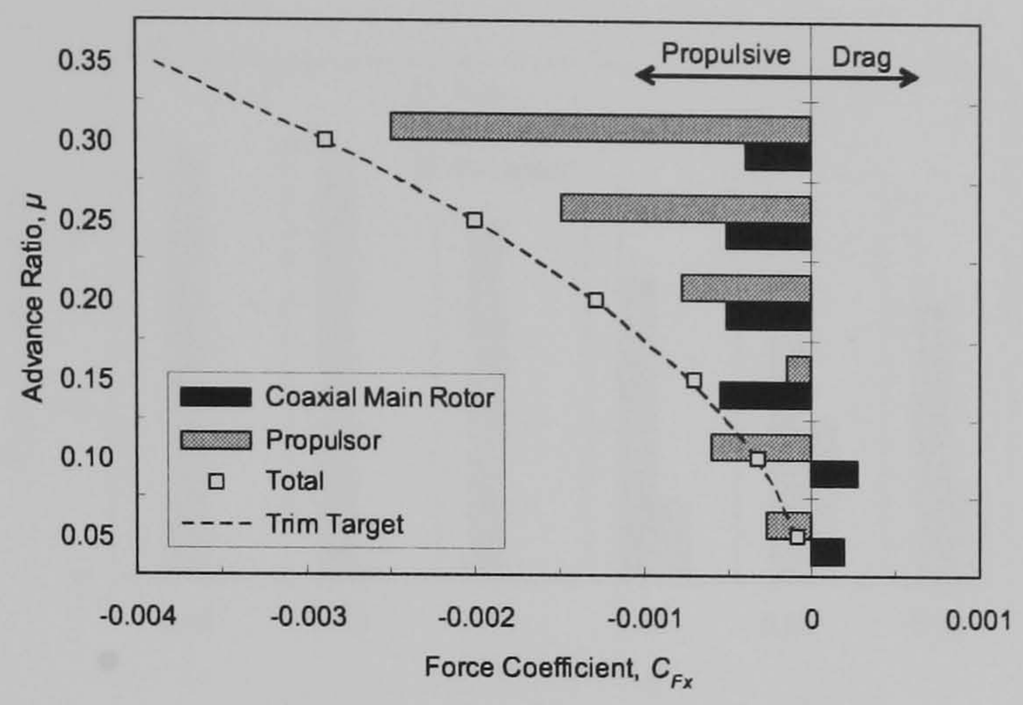


Figure 6.3: *Partition of the propulsive force between the main rotor and propulsor as a function of forward speed.*

system to be represented by an equivalent flat plate with $1/25^{th}$ of the main rotor disc area. This yields a quadratic variation of the required propulsive force with forward speed that is comparable, in non-dimensional terms, to that of the XH-59A [83]. The weight of the aircraft was assumed to be balanced throughout by a vertical component to the thrust coefficient that is produced by the system of 0.012, this again being representative of an aircraft of the size of the XH-59A. The range of forward speeds for which calculations were performed, and the corresponding trim targets for the simulations are summarised in Table 6.3.

6.3 Aircraft Performance

Figure 6.3 shows the variation with forward flight speed of the propulsive force that is required to overcome the drag of the aircraft given the model described above. At low forward speed, the absence of any forward tilt of the main rotor causes it to generate an in-plane component of force that has to be counteracted by the propulsor in order to produce the requisite propulsive force on the configuration. This is certainly non-optimal and results in a higher consumption of power at low forward speed than is necessary, as is shown in Figure 6.4 where the overall power consumption of the system is plotted as a function of advance ratio. It is likely though that this flaw could be corrected through a more refined scheduling of the shaft tilt with forward speed than that adopted here. Indeed, the forward tilt of the rotor shaft that is scheduled at

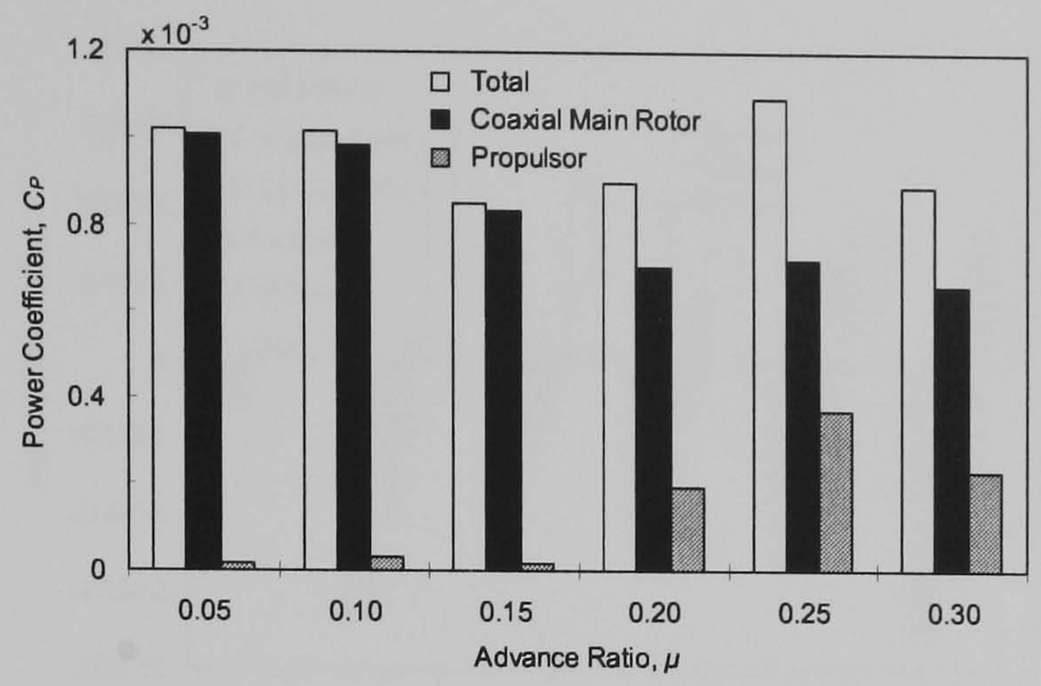


Figure 6.4: *Partition between the main rotor and propulsor of the power required by the vehicle as a function of forward speed.*

advance ratios greater than 0.10 allows the main rotor to contribute to the propulsive force that is required to overcome the drag of the system, and translates into a marked reduction in the power that is consumed by the main rotor at higher forward speed, as shown in Figure 6.4. This observation needs to be placed in context, though. By partitioning the power consumption into the individual contributions from the main rotor and propulsor, Figure 6.4 also reveals that, although the power consumed by the main rotor can be reduced quite considerably by unloading the system in favour of the propulsor, this advantage can be outweighed by the power requirements of the propulsor itself at high forward flight speeds.

Finally, Figure 6.5 shows the partition of the pitching moment into the individual contributions that are generated by the main rotor system, the propulsor and the horizontal tailplane in order to maintain the aircaft in trim at the various forward speeds that were simulated. The origin of the very large contribution to the overall pitching moment from the tailplane, particularly at low forward speeds, will be discussed later in this chapter. The contribution of the tailplane translates into a significant variation with forward speed in the pitching moment that must be commanded by cyclic input into the main rotor system in order to maintain overall zero pitching moment on the configuration and hence the aircraft in trim. The requirement on the main rotor to produce this moment will be shown shortly to result in a significant elevation in the loading on the rear of both the upper and lower rotors of the coaxial system, particularly at low

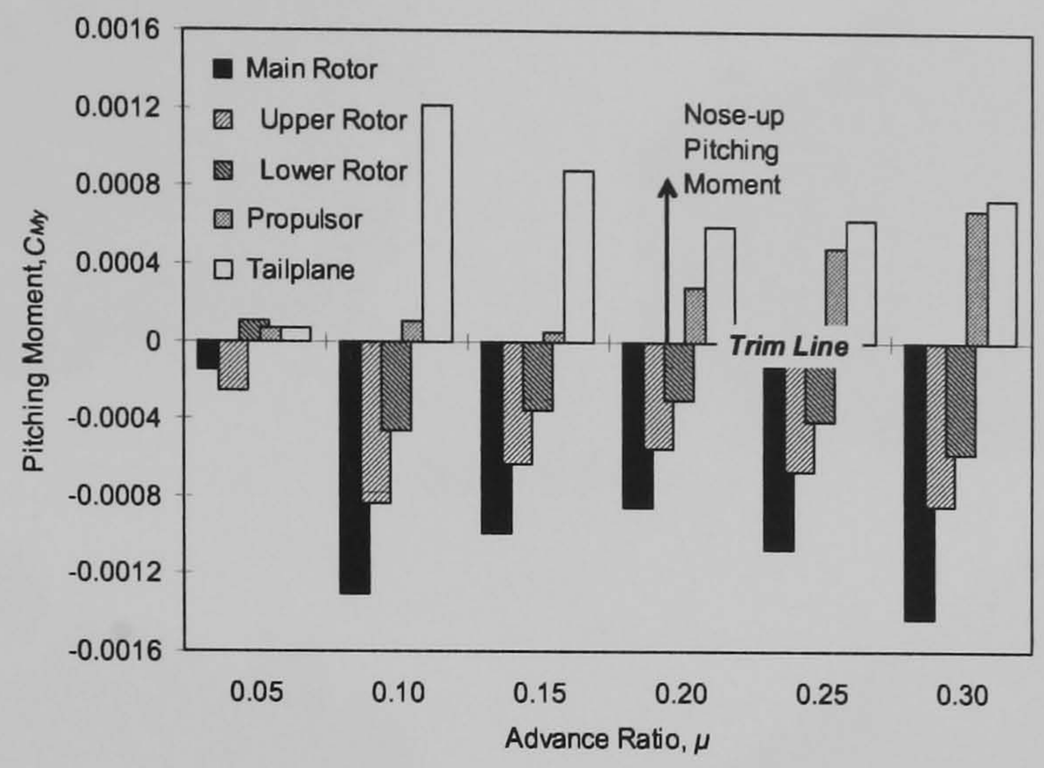


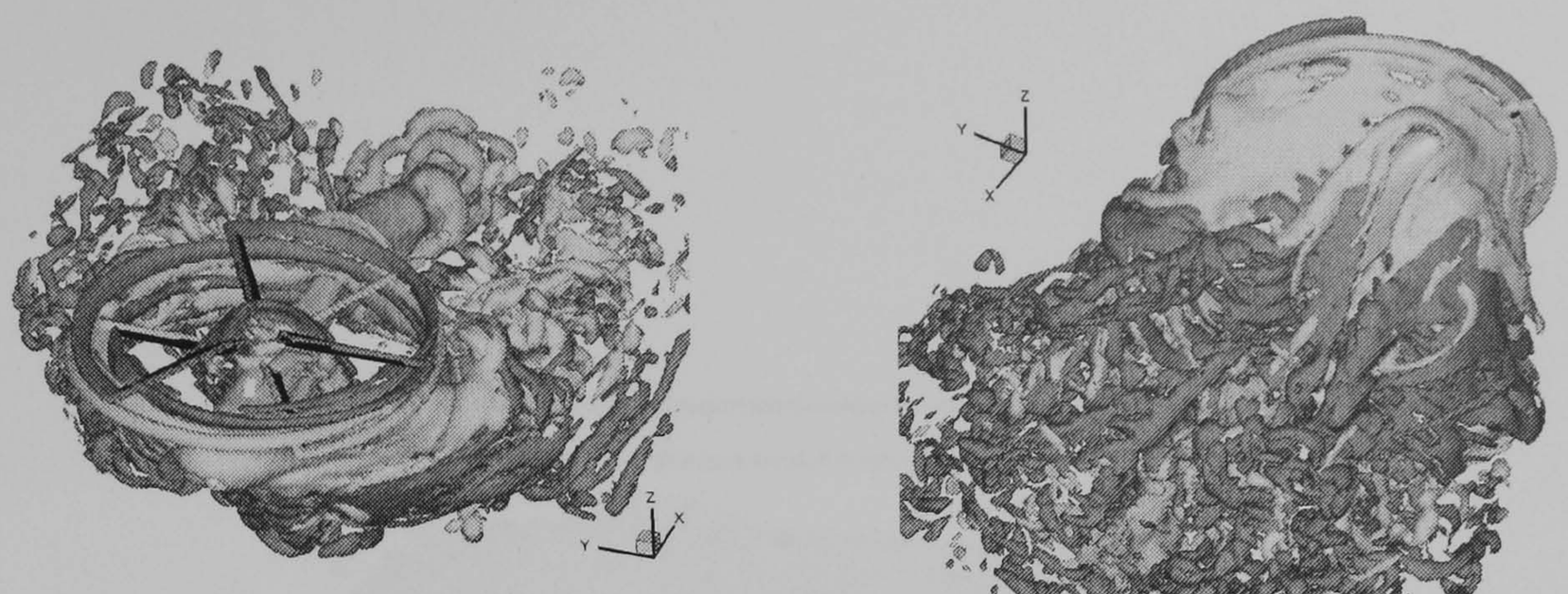
Figure 6.5: *Partition between the main rotor, propulsor and tailplane of the pitching moment required to trim the vehicle as a function of forward speed.*

forward speed, that has interesting consequences particularly for the vibration and the acoustic radiation that is produced by the configuration.

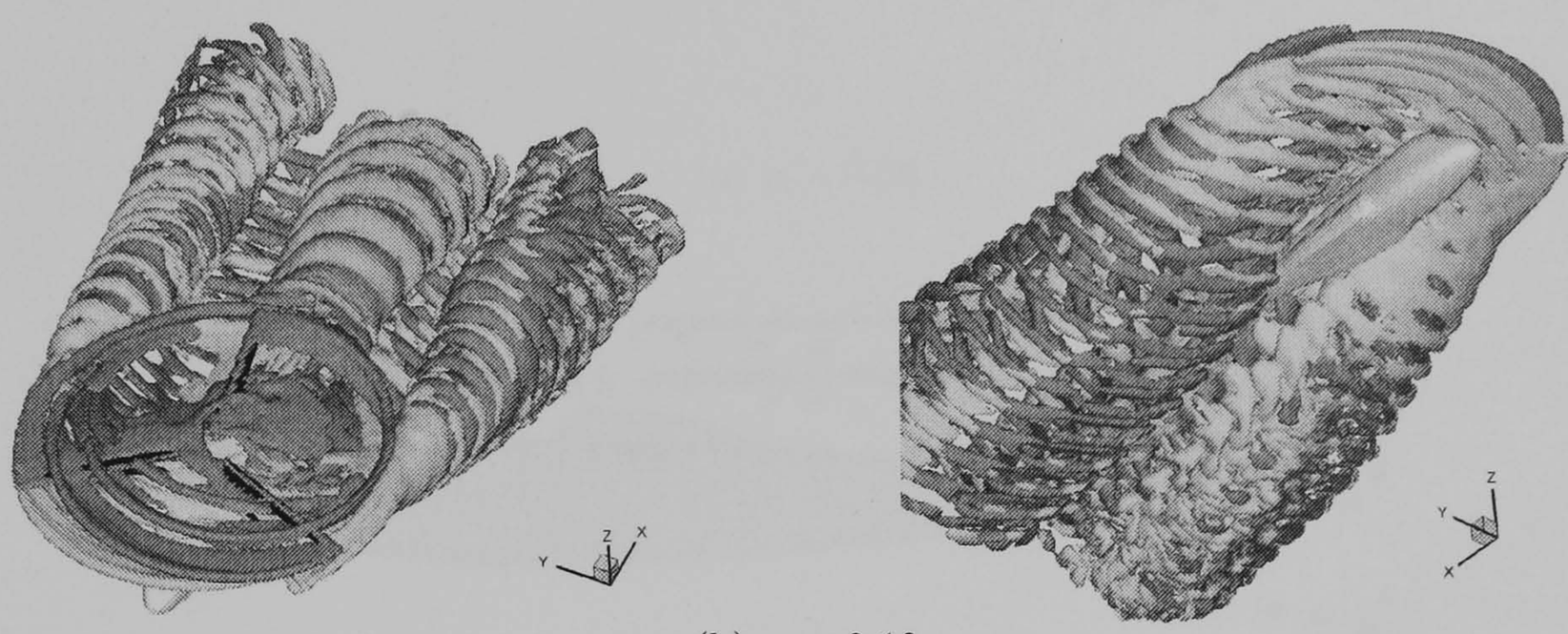
6.4 Wake Structure

Figure 6.6 shows a series of snapshots of the structure of the wake that is generated by the helicopter at each of the advance ratios that was simulated. In each plot, a set of iso-surfaces is presented on which the vorticity in the flow around the vehicle has constant magnitude. The wakes that are generated by each of the main rotors, the tail propulsor and the horizontal tail surface are coloured separately in various shades of grey. To aid in the interpretation of these figures, Figure 6.7 reveals the relative extent of the wake envelope that is associated with each rotor by plotting the trajectories of their tip vortices as they intersect the plane of lateral symmetry of the fuselage.

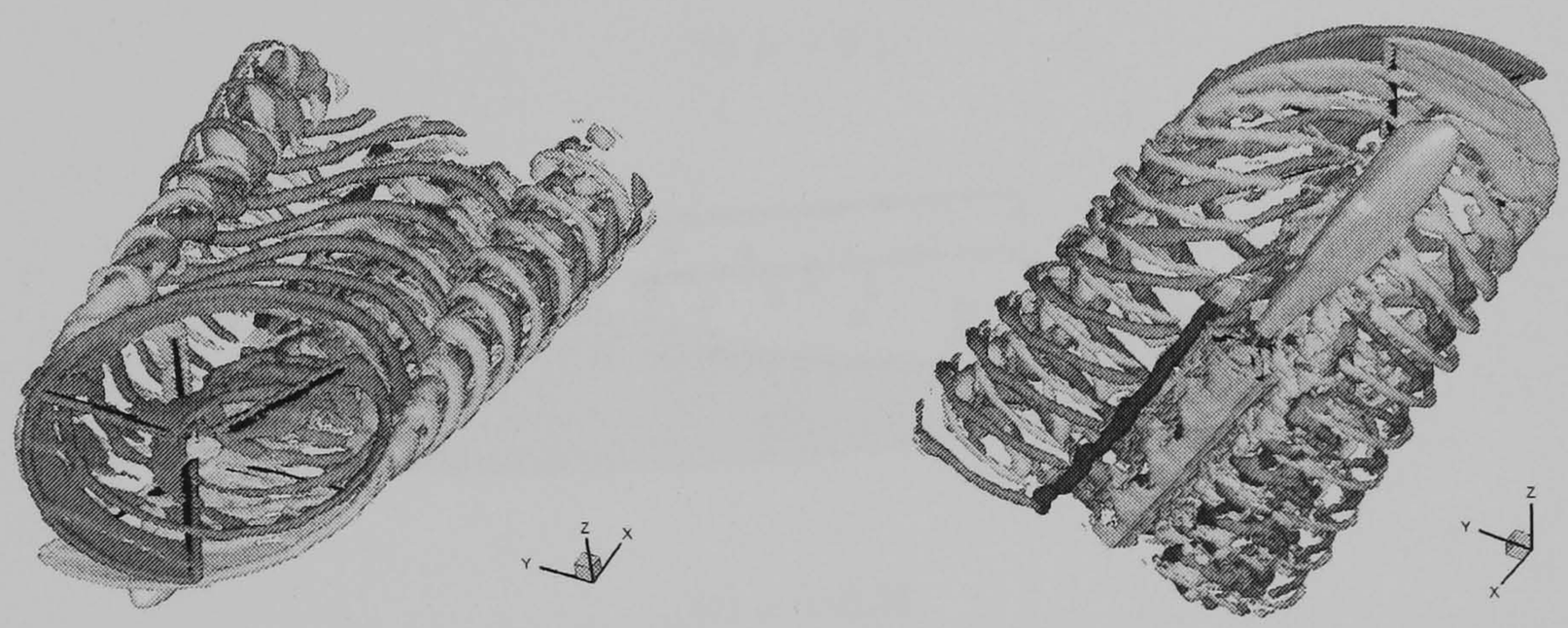
Figures 6.6(a) and 6.7(a) show the wake of the helicopter when operating at an advance ratio $\mu = 0.05$. At this forward speed, the wake of the main rotor system is in a transitional state between the cylindrical, hover-like form that it would adopt at lower advance ratios and the flattened, aeroplane-like form that is characteristic of the system at higher advance ratios. The precursors of the rolled up super-vortices that form at the sides of the wake at higher advance ratios are clearly evident, but at this forward speed



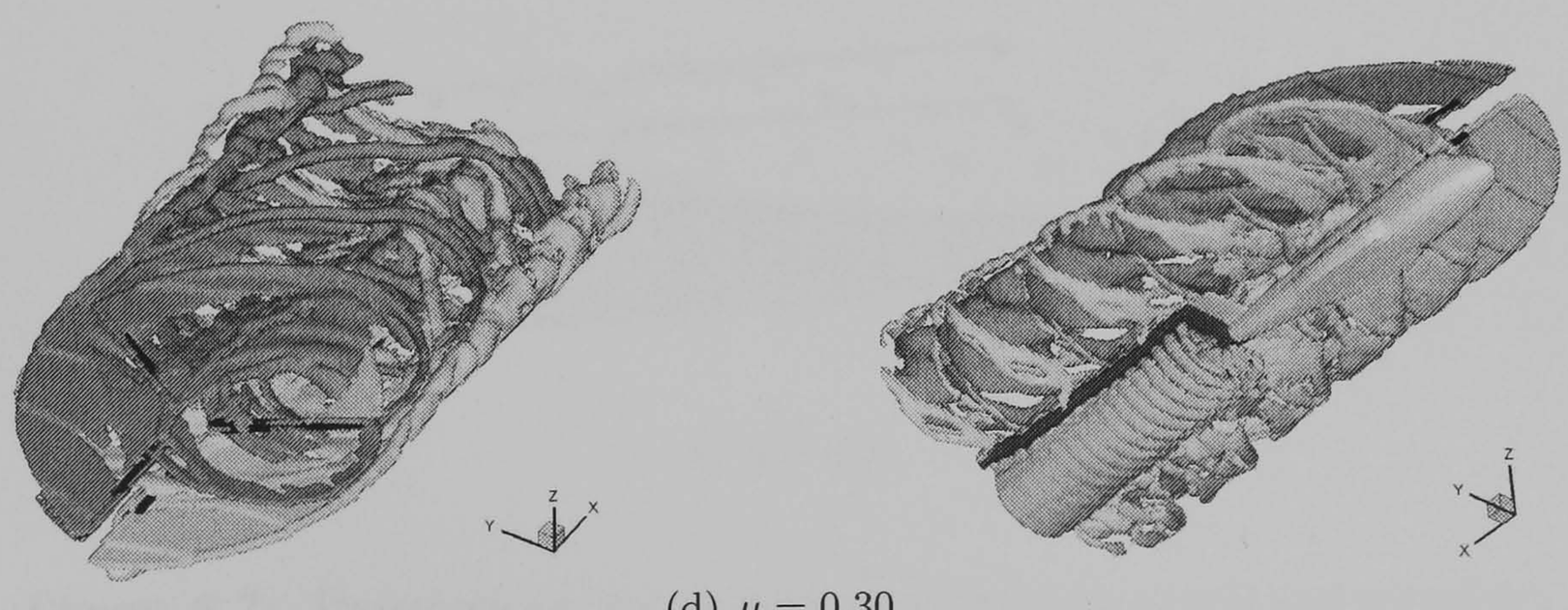
(a) $\mu = 0.05$



(b) $\mu = 0.10$

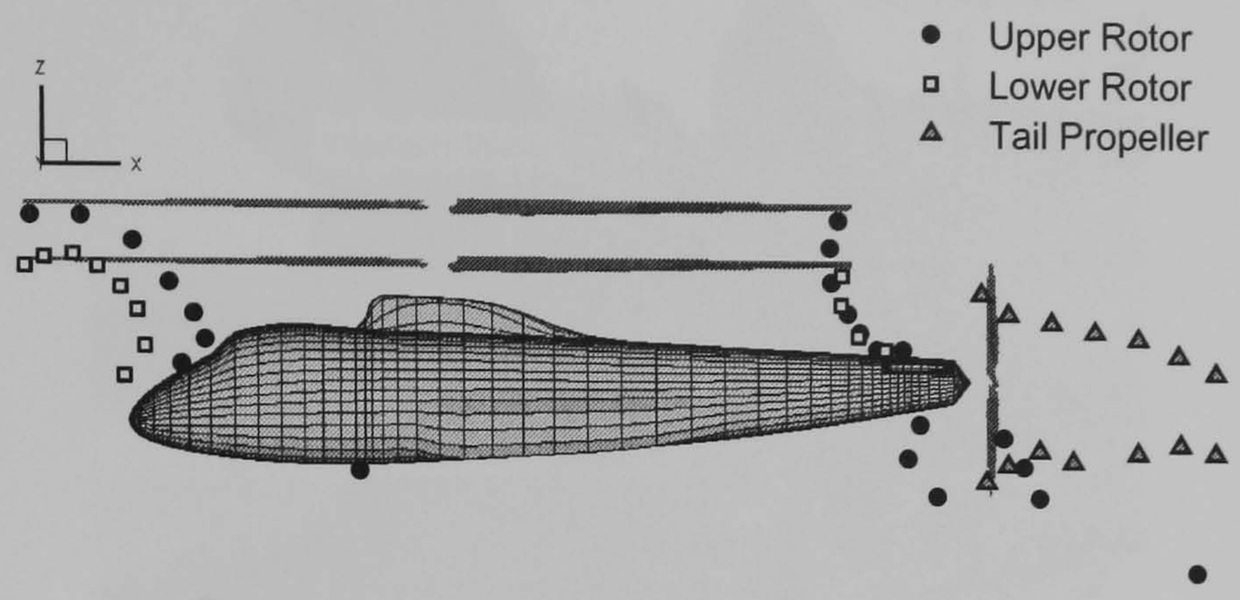


(c) $\mu = 0.15$

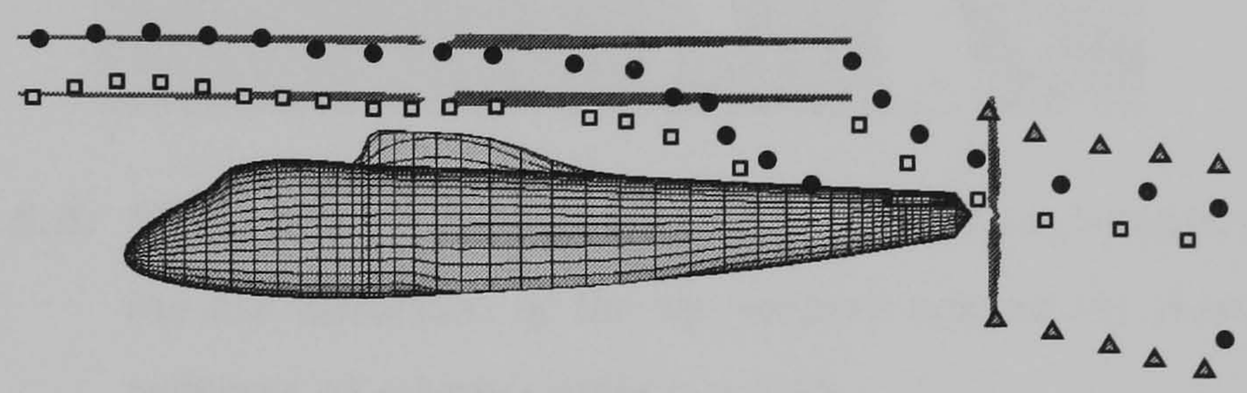


(d) $\mu = 0.30$

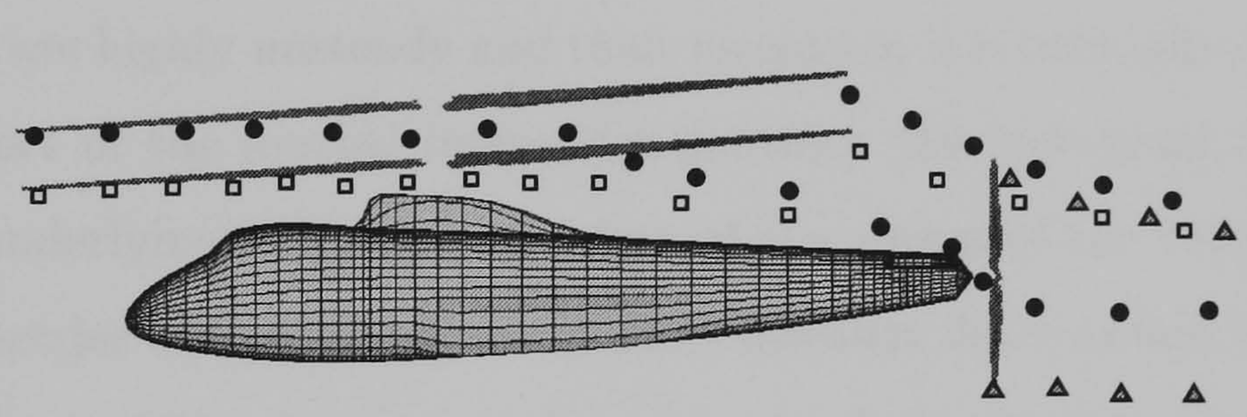
Figure 6.6: *Visualisation of the wake structure of the full configuration in steady forward flight at various advance ratios. Wakes from the different elements of the configuration coloured in separate shades of grey. (Left: top view. Right: bottom view.)*



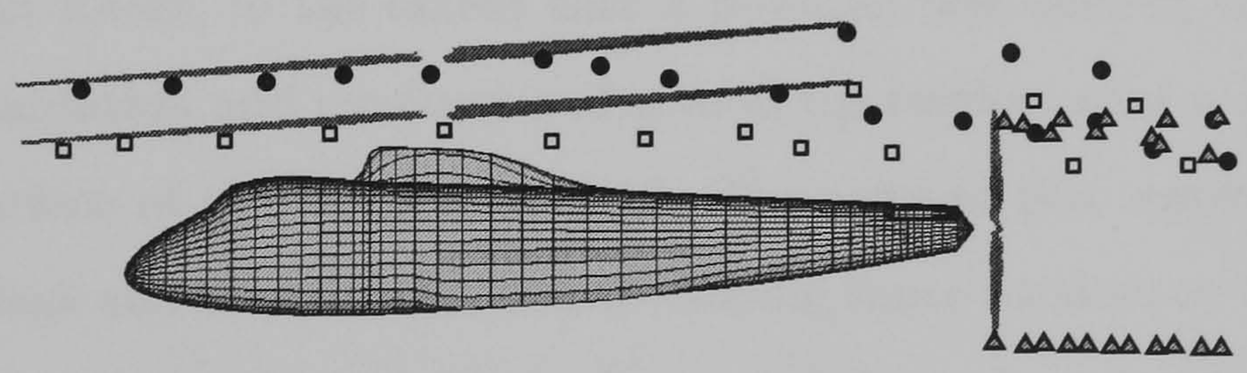
(a) $\mu = 0.05$



(b) $\mu = 0.10$



(c) $\mu = 0.15$



(d) $\mu = 0.30$

Figure 6.7: *Trajectories of the tip vortices of the main rotors and propulsor. (Each plot is a composite showing the points of intersection of individual vortices with the longitudinal plane through the fuselage centreline at various times during a single main rotor revolution.)*

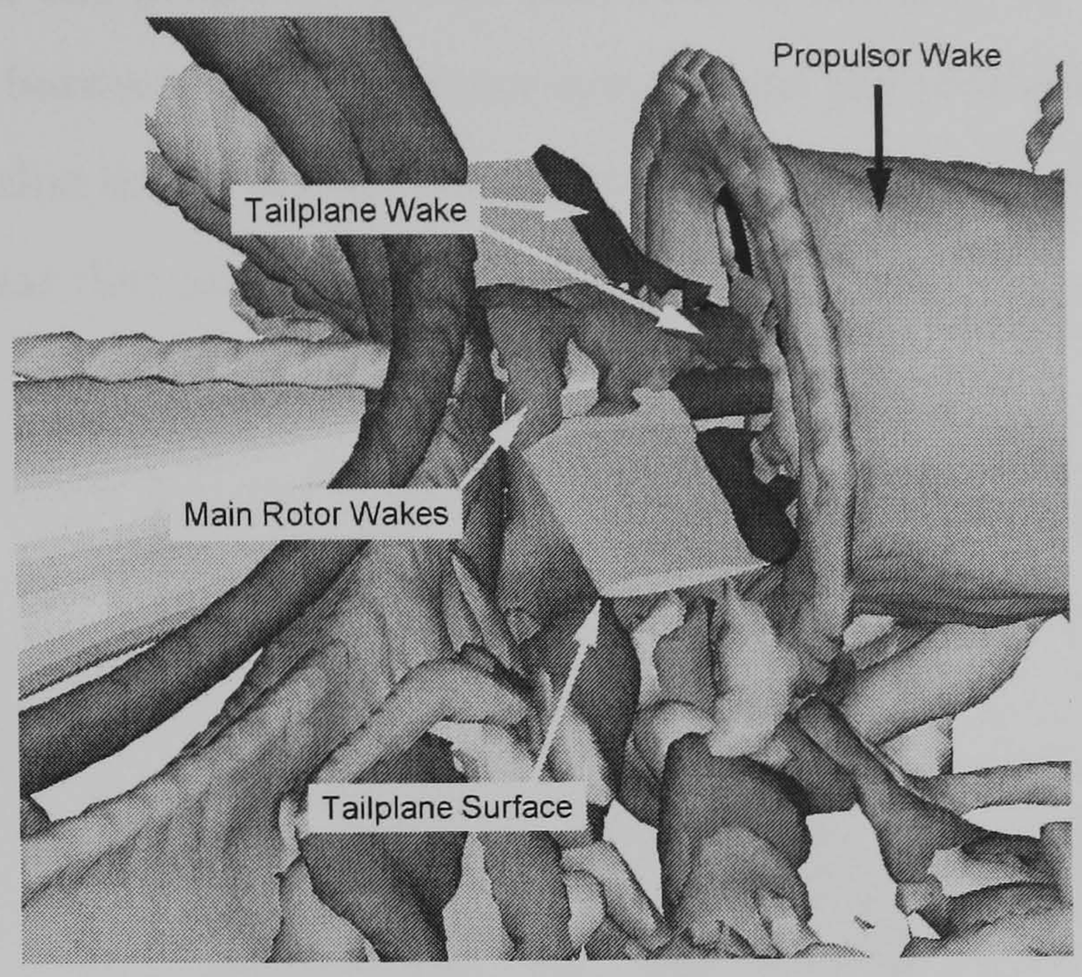


Figure 6.8: *Visualisation of the wake structure of the configuration, showing the distortion of the tip vortices around the fuselage and tailplane at advance ratio* $\mu = 0.05$.

these structures are highly unsteady and their formation is continually disrupted by the destabilising effect of the mutual interaction between the individual tip vortices that constitute the underlying helicoidal structure of the wakes of the rotors. This results in significant disorder in the wake a fairly short distance downstream of the tail as the products of this instability interact to form progressively smaller coherent structures. The view from below shows the very strong influence of the fuselage in displacing the wake of the main rotors, to the extent that a powerful bow-shaped vortex forms as a result of the retardation and confluence of several tip vortices near a stagnation point on the upper surface of the forward fuselage. The arms of this vortex trail down the sides of the fuselage and interact with the developing super-vortices on both sides of the aircraft. Figure 6.8 shows the wake from the rear of the main rotors to impinge on the fuselage just slightly forward of the tailplane. The marked downwards trajectory of the wake from the main rotor results in very little direct interaction between the main rotor and the propulsor; although some vorticity is indeed ingested into the bottom of the propulsor disc, and some also rolls backwards along the top surface of the fuselage to interact with the tailplane, most of the vorticity created by the main rotors can be seen to pass below the propulsor at this forward speed. The very obvious skewing of the wake

seen in Figure 6.9 of the propulsor to the port side of the aircraft suggests a powerful indirect interaction between the main rotor system and the propulsor, although part of this effect might be due to the almost complete entrainment of the wake of the tailplane through the propulsor disc at this forward flight speed.

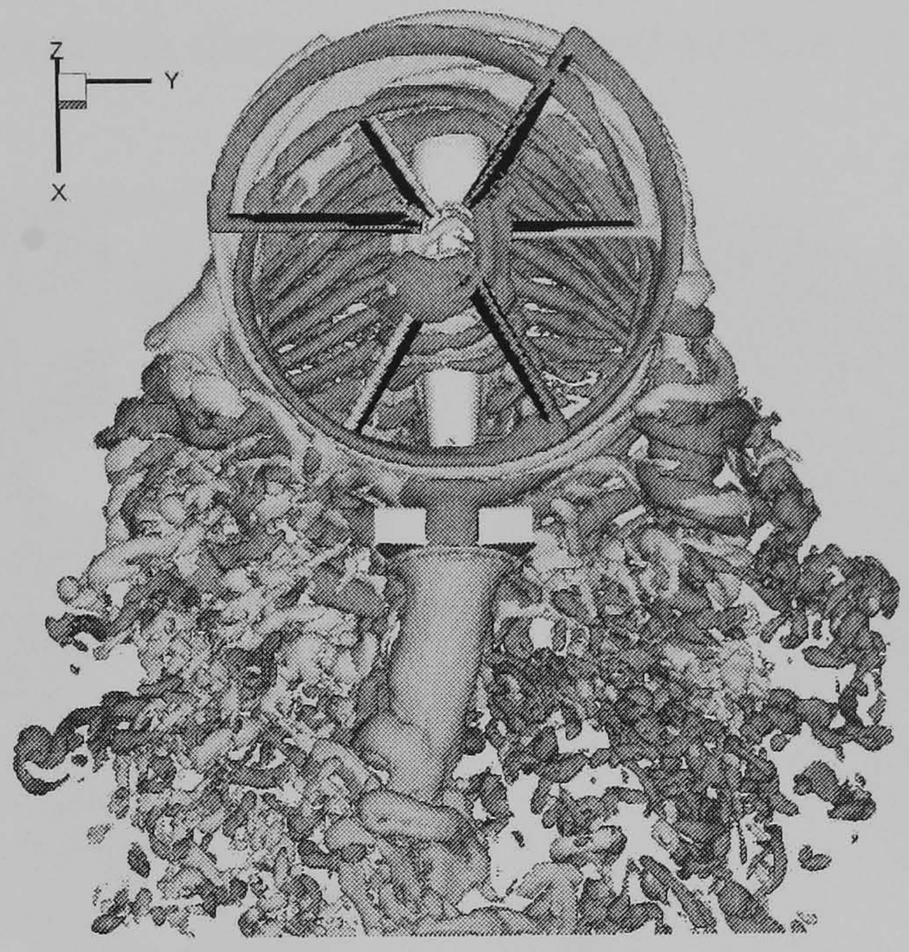


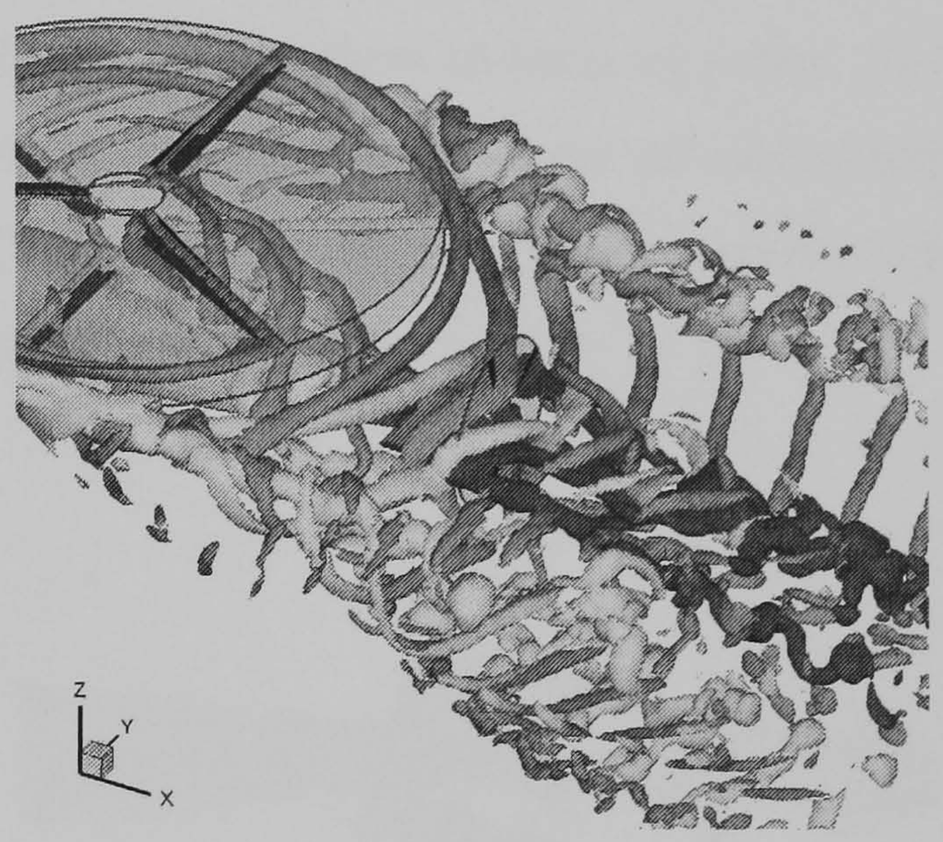
Figure 6.9: *Visualisation of the wake structure of the configuration: view from above at advance ratio $\mu = 0.05$ showing the incipient formation of super-vortices in the wake of the main rotor and the interaction-induced skewing of the propulsor wake.*

Figures 6.6(b) and 6.7(b) show the wake of the helicopter when operating at a slightly higher advance ratio ($\mu = 0.10$). At this forward speed, the individual tip vortices from the blades of the main rotors interleave and co-orbit to form a pair of highly-structured super-vortices along both sides of the wake. As at the lower flight speed, the wake from the tailplane is again entrained almost completely into the propulsor; the presence of the two powerful, counter-rotating vortices from the tips of the tailplane at this forward flight speed results in significant flattening of the wake tube of the propulsor a short distance downstream of the aircraft. The indirect interaction between the propulsor and the main rotor results in a strong modulation of the vorticity in the wake tube of the propulsor to form a series of toroidal structures that have a characteristic wavelength that is very similar to the spacing between the individual tip vortices from the main rotor system. This modulation is most likely enhanced by the rather obvious and very direct

impingement of tip vortices from the main rotor system on the tail of the configuration at this flight speed. Indeed, Figure 6.10(a) shows a succession of tip vortices from the main rotor to pass very closely over the upper surface of the tailplane, subsequently to be ingested directly into the upper half of the propulsor (see Figure 6.10(b)). The effect of this powerful interaction between the main rotor and the tail of the configuration on the loading on the helicopter is discussed in the next section of this chapter.



(a) Close-passage and impingement of the tip vortices from the main rotors on the upper surface of the tailplane. (Tailplane wake not visualised for clarity.)

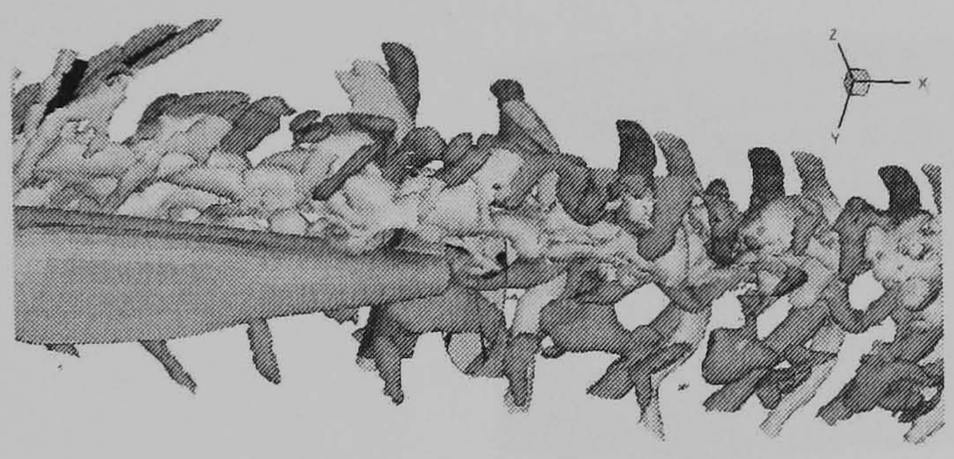


(b) Ingestion of the main rotor vortices through the propulsor showing subsequent distortion due to interaction with propulsor and tailplane wake

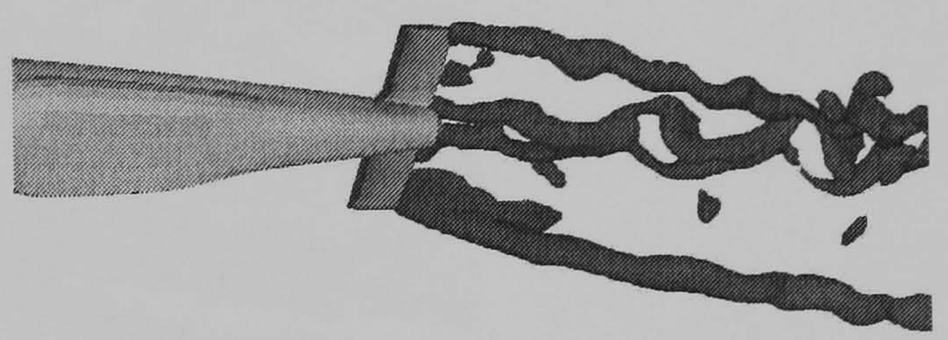
Figure 6.10: *Visualisation of the wake structure of the configuration, showing the distortion of the flow around the tail at advance ratio* $\mu = 0.10$. *(Propulsor wake not visualised for clarity.)*

Figures 6.6(c) and 6.7(c) show the wake of the system when flying through the air at advance ratio $\mu = 0.15$. At slower flight speeds the root vortex system that is generated by the main rotors is helicoidal in structure and is only moderately skewed. Interaction of this vortex system with the other components of the configuration is thus generally limited to a direct impingement on the fuselage, well forward of the tailplane (as shown in Figure 6.10), in such a way that the individual vortices encounter the fuselage at such a steep angle that they do not tend to propagate far along the length of the body before being swept away into the flow below the helicopter. At low forward flight speed the root vortex system thus does not tend to interact with the tailplane.

Figure 6.11(a) shows the root vortex system that is generated by the main rotors at higher advance ratio to roll up into a pair of concentrated structures that trail down the sides of the fuselage. At $\mu = 0.15$ these structures are biased strongly towards the port side of the fuselage. As shown in Figure 6.11(b), the port-side vortex interacts very strongly with the tailplane, producing a corkscrew-like perturbation to the trailing vortex that is produced by the port side of this surface. Further downstream, the root vortex structure causes significant disruption to the structure of the wake tube of the propulsor, forcing it to roll up along its port edge and to skew to such an extent that the trailing vortex from the starboard tip of the tailplane is no longer entrained into the wake of the propulsor but instead is able to convect without significant interference into the flow downstream of the helicopter (see Figure 6.6(c)).



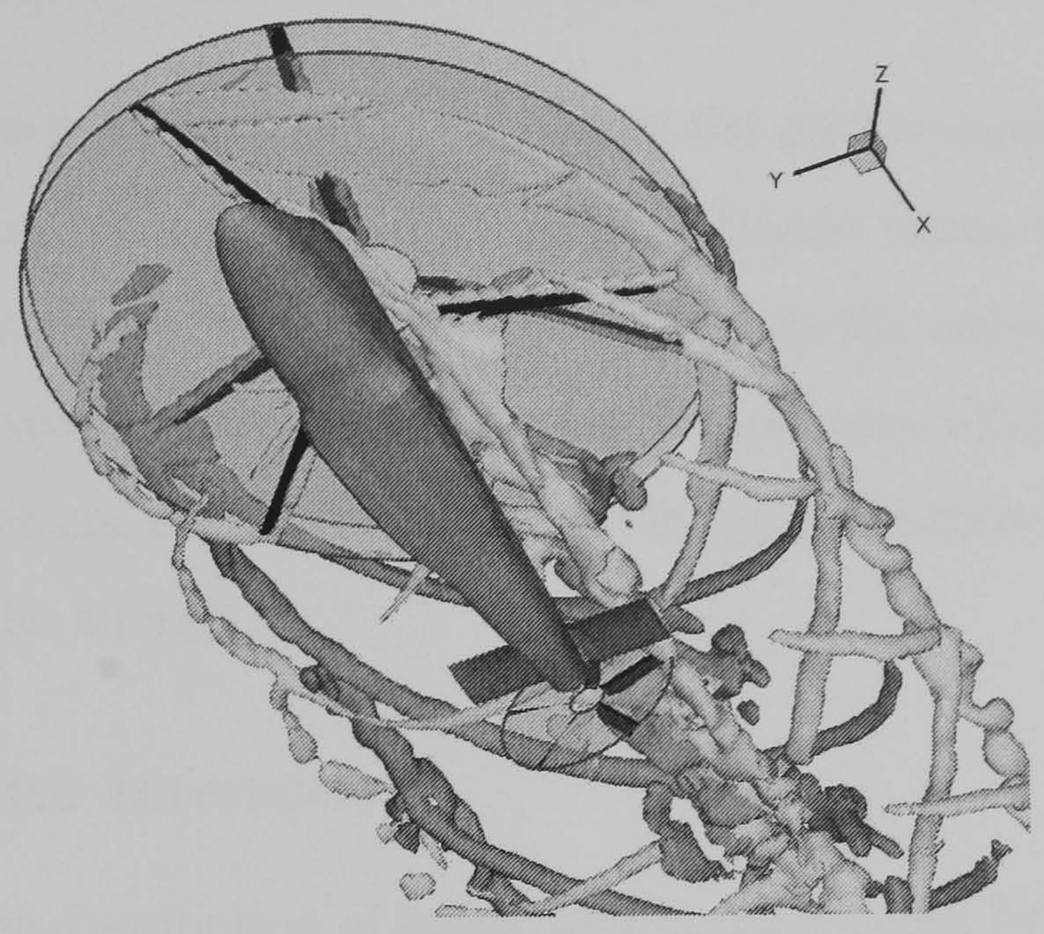
(a) View showing the formation of a concentrated root vortex structure from the main rotor and its subsequent impingement on the tailplane



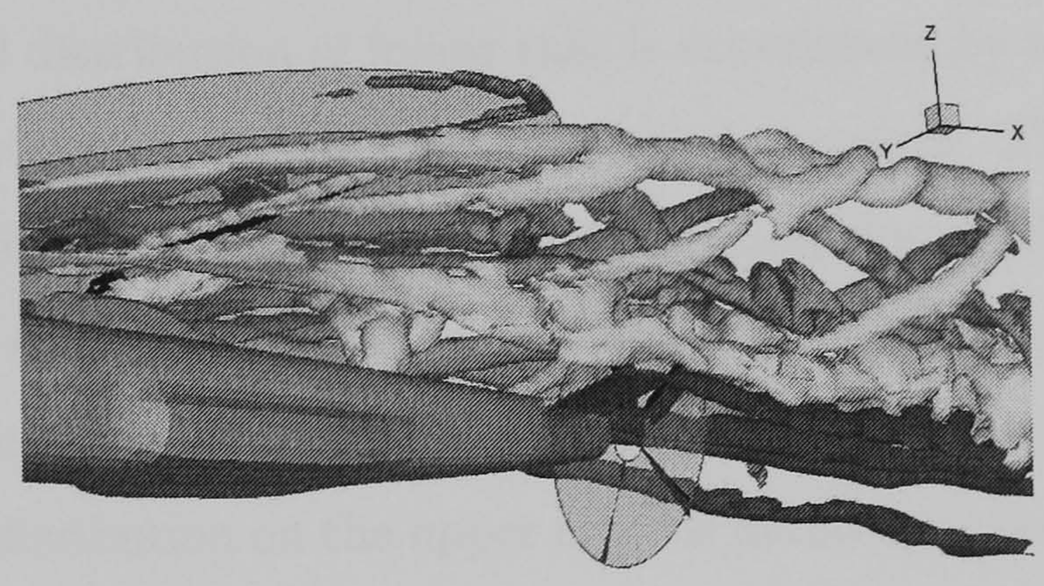
(b) View showing the distortion of the tailplane wake under the influence of the main rotor root vortices and the propulsor

Figure 6.11: *Visualisation of the wake structure of the configuration, showing the distortion of the flow around the tail at advance ratio $\mu = 0.15$. View from below the port side of the aircraft. (Propulsor wake not visualised for clarity.)*

As the advance ratio of the system is increased, the effect of the main rotor wake in modulating the structure of the wake produced by the propulsor steadily decreases, to the extent that at the highest advance ratio that was simulated ($\mu = 0.30$) this effect is almost entirely absent, as can be inferred from the very orderly, helical structure of the wake produced by the propulsor that is shown in Figure 6.6(d). Similarly, the amount of vorticity from the main rotor system that is entrained directly through the propulsor disc decreases significantly as the rearwards skew of the wake of the main rotor increases



(a) View from below the aircraft (Tailplane wake not visualised for clarity)



(b) View from below the port side of the aircraft

Figure 6.12: *Visualisation of the wake structure of the configuration, showing the close passage of the root vortex from the lower rotor over the empennage at advance ratio* $\mu = 0.30$. *(Propulsor wake not visualised for clarity.)*

with forward speed of the aircraft. This can be seen by comparing Figure 6.11(a), which shows a significant proportion of the vorticity that is produced from the tips of the main rotor to be entrained into the upper half of the propulsor at an advance ratio of 0.15 (see also Figure 6.7(c)), with Figure 6.12 which shows minimal such entrainment at an advance ratio of 0.30 (see also Figure 6.7(d)).

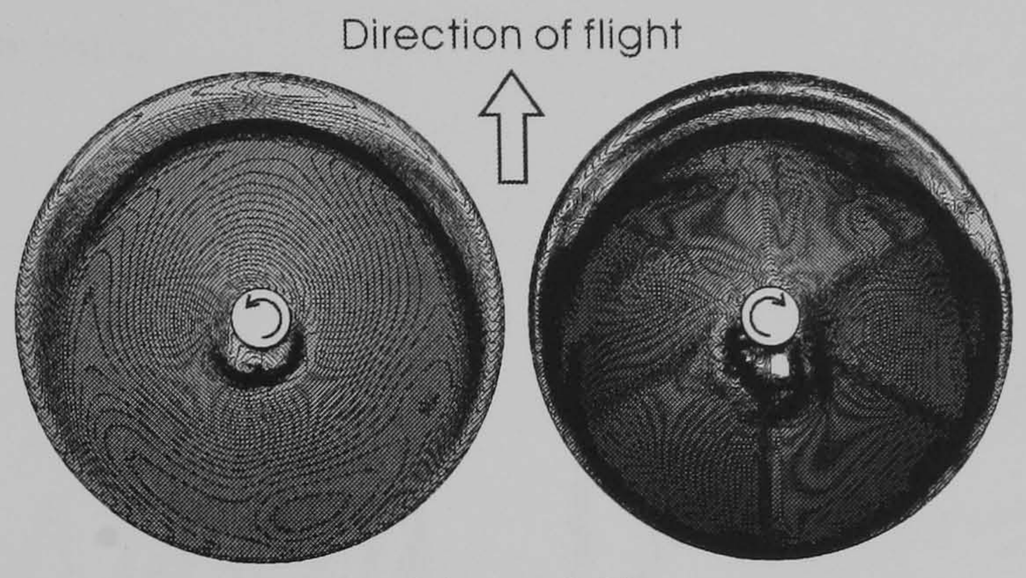
6.5 Aerodynamic Interaction Between Sub-components

This section examines in more detail the effects of the aerodynamic interactions on the loads produced within the system at the various advance ratios discussed in the previous sections. In particular, the analysis is focused on the aerodynamic interactions between the main coaxial system and the other components where the interaction involves direct impingement of the wake produced by the main rotor system on the other sub-components of the aircraft.

6.5.1 Rotor-Rotor Interaction

Figure 6.13 shows the distribution of inflow that is experienced by the upper and lower rotors of the coaxial system at each advance ratio that was simulated. Each individual plot shows the radial distribution of inflow that is experienced by a single blade, during a single rotor revolution, as a polar function of blade azimuth. The higher the inflow, the darker the shading of the plot. At all advance ratios, the aerodynamic environment of the lower rotor is strongly modified by interaction with the wake of the upper rotor, whereas the influence of the lower rotor on the upper is far less marked. A series of sharp ridges in the inflow disribution on the upper rotor is induced by the close passage of the tip vortices that trail from the blades of the same rotor; similar features can be seen in the inflow distribution on the lower rotor, but these are interleaved with additional ridges that are induced by the close passage of tip vortices that are generated by the blades of the upper rotor. Some disruption to the inflow distribution is also visible at the rear, particularly of the lower rotor, at all forward speeds. This is due to the root vortex system that is generated by the blades of the rotors; as shown in Figure 6.6, the presence of the fuselage immediately below the main rotor system forces these vortices to remain very close to the plane of the lower rotor for a considerable distance aft of the rotor shaft.

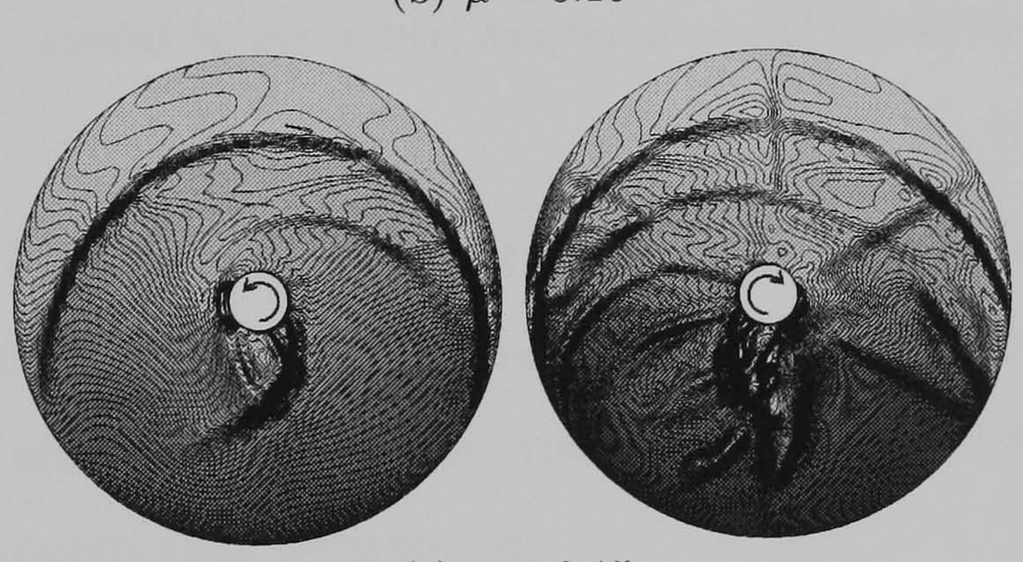
The effects of the passage of the individual blades of the top rotor over those of the lower rotor are clearly evident as a set of six radial ridges in the inflow experienced by the lower rotor; similar features are almost entirely absent from the inflow distribution on the upper rotor. At the lowest advance ratio a significant proportion of the lower rotor lies within the downwash field that is generated by the upper rotor, but as the



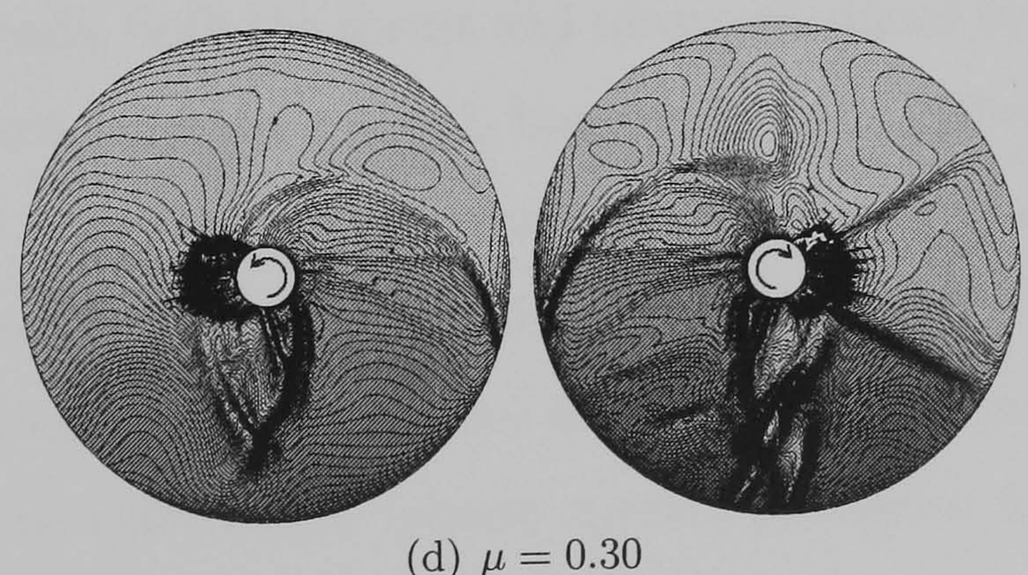
(a) $\mu = 0.05$



(b) $\mu = 0.10$



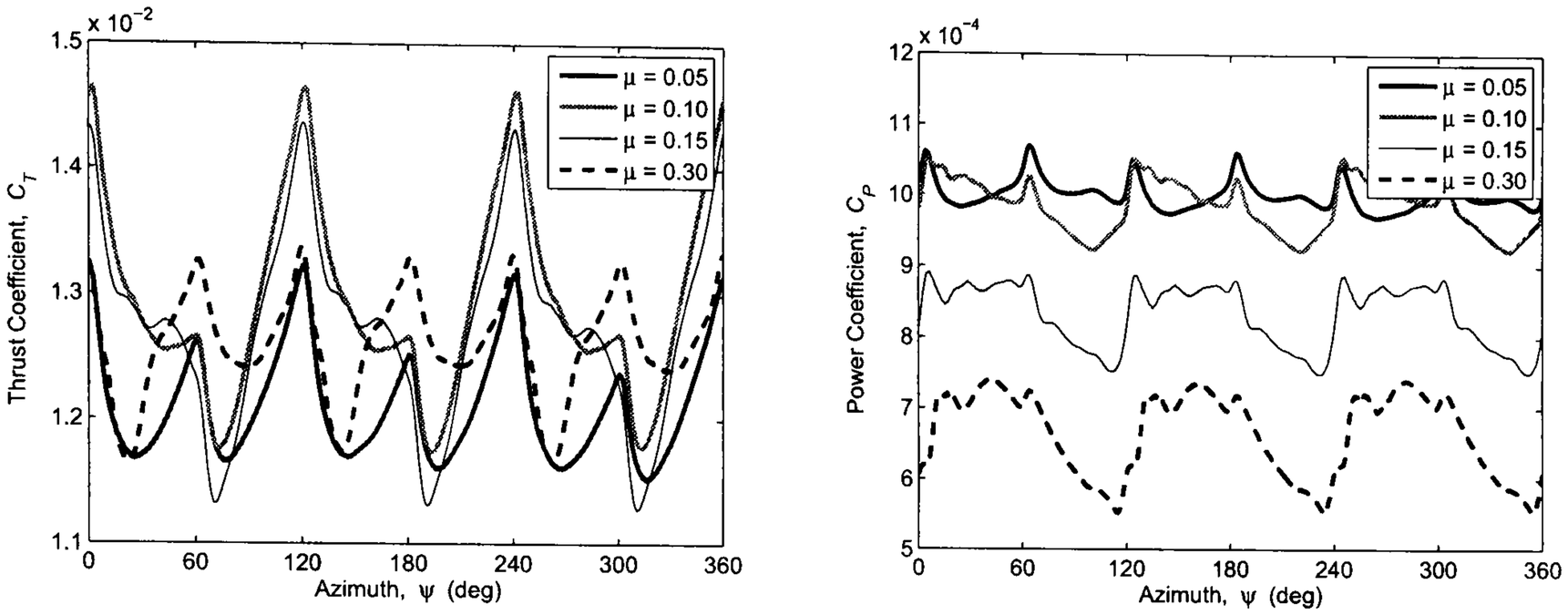
(c) $\mu = 0.15$



(d) $\mu = 0.30$

Figure 6.13: *Inflow distribution over the main rotor discs, showing the strong interaction between the upper and lower rotors at all forward speeds. (Left: upper rotor. Right: lower rotor.)*

forward speed of the system is increased, this region of maximum interaction between the rotors moves aftwards on the lower rotor in response to the rearwards skewing of the wake of the upper rotor.



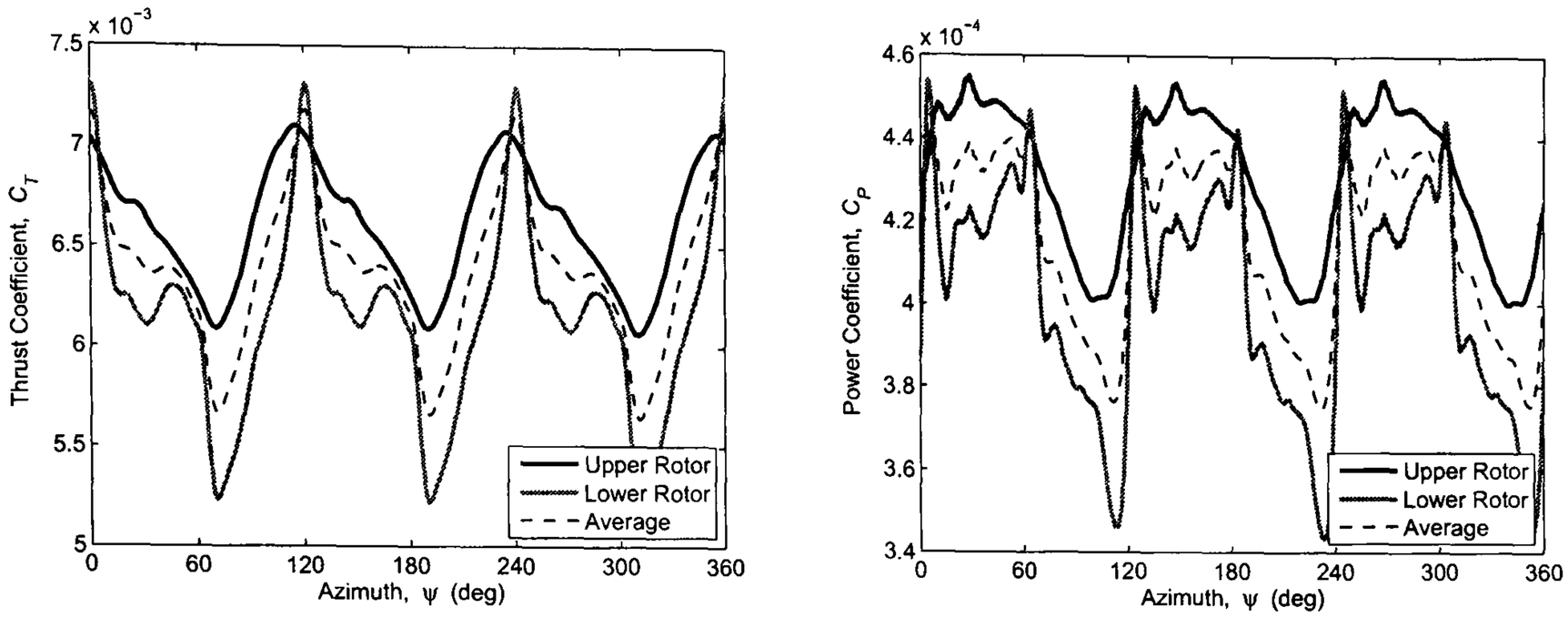
(a) Total thrust coefficient

(b) Total power coefficient

Figure 6.14: *Temporal variation in the thrust produced and power consumed by the coaxial system over one revolution.*

Figures 6.14 and 6.15 show the effect of the interactions between the two rotors on the loading produced on the main rotor system. Figure 6.14 shows the variation of thrust and power produced by the coaxial rotor over a single rotor revolution at each of the various flight speeds that were tested.

At all forward speeds, both the thrust and torque produced by the main rotor show significant unsteadiness, principally at $3\Omega_c$ but also with a significant $6\Omega_c$ contribution. Although it is likely that the fuselage vibration modes in a practical system will be tuned away from these fundamental rotor frequencies, the amplitude of the excitation as predicted here, especially for advance ratios in the transitional range between $\mu = 0.10$ and $\mu = 0.15$, may be sufficient to require specific provisions for attenuation within the drive train and rotor mounting system. To reveal the origins of the excitation, Figure 6.15 shows the variation of thrust and power produced by the coaxial system, decomposed into the individual contributions from the upper and lower rotors. The figure shows the situation at an advance ratio $\mu = 0.15$ where arguably the interaction between the upper and lower rotors is at its strongest. The curves marked 'average' represent half the total thrust or torque produced by the system and are included



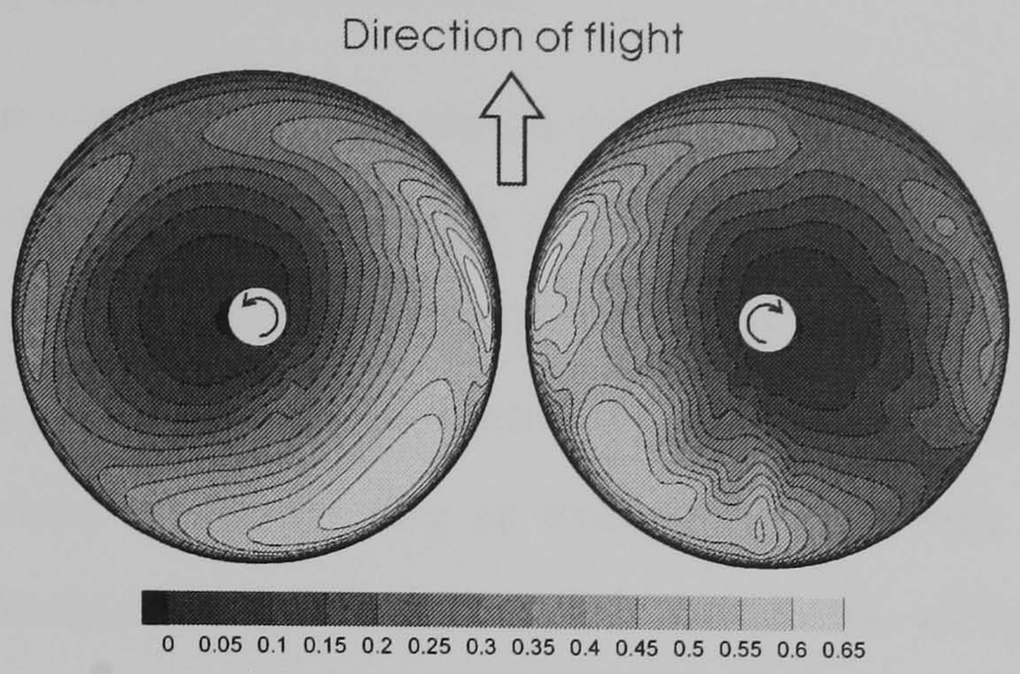
(a) Thrust coefficient

(b) Power coefficient

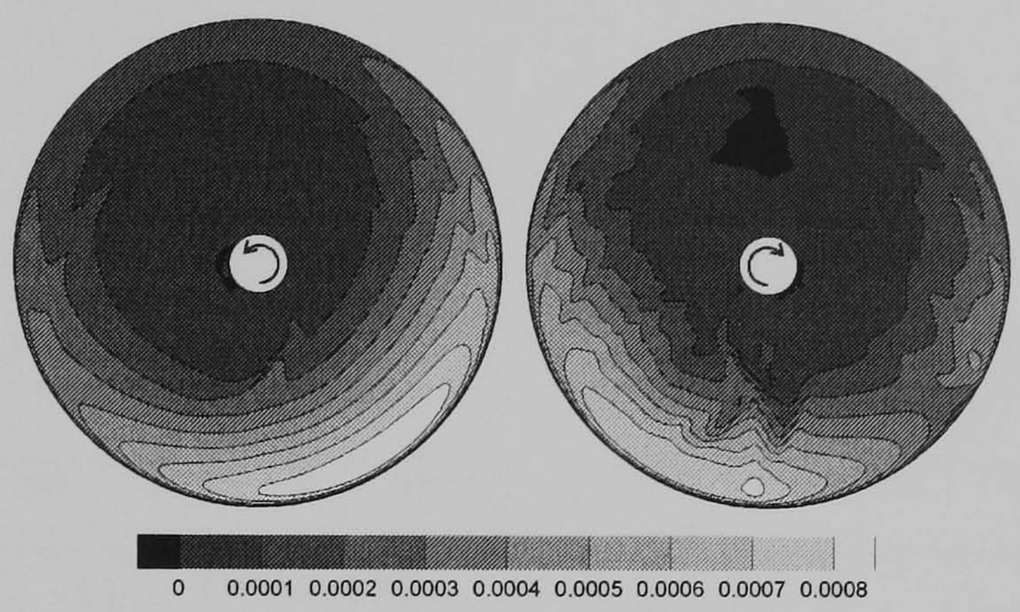
Figure 6.15: *Temporal variation in the thrust produced and power consumed by the upper and lower rotors of the coaxial system over one revolution at advance ratio* $\mu = 0.15$.

to show how the contributions from the individual rotors combine to give the overall characteristic of the main rotor system.

To achieve yaw moment equilibrium on the aircraft at this advance ratio, the upper rotor is driven by the trim routine to generate more power in the mean than the lower rotor; this effect manifests also in a difference in the mean thrust produced by the two rotors. In the context of the vibrational content of the loading on the system, Figure 6.14 shows the lower rotor to be the primary source of the $6\Omega_c$ excitation of the system. The phasing of the $6\Omega_c$ load on the rotor and the observation that this component of the load persists so strongly to higher advance ratios — where direct aerodynamic interaction between the rotors is significantly ameliorated by the rearwards sweep of their wakes — is consistent with its origin being in the overpassage-type interference with the blades of the upper rotor that appeared in Figure 6.13 as the set of radial ridges in the inflow distribution on the lower rotor. The $3\Omega_c$ component of the forcing of both the thrust and the torque is almost equally shared between the upper and lower rotors, and arises in the fundamental aerodynamic behaviour of the very stiff rotors from which the coaxial main rotor system is constructed. Figure 6.16 shows the radial variation of loading and power consumption on the blades of upper and lower rotor as a function of azimuth with the helicopter trimmed into forward flight at $\mu = 0.15$. The phasing of the $3\Omega_c$



(a) Blade loading coefficient



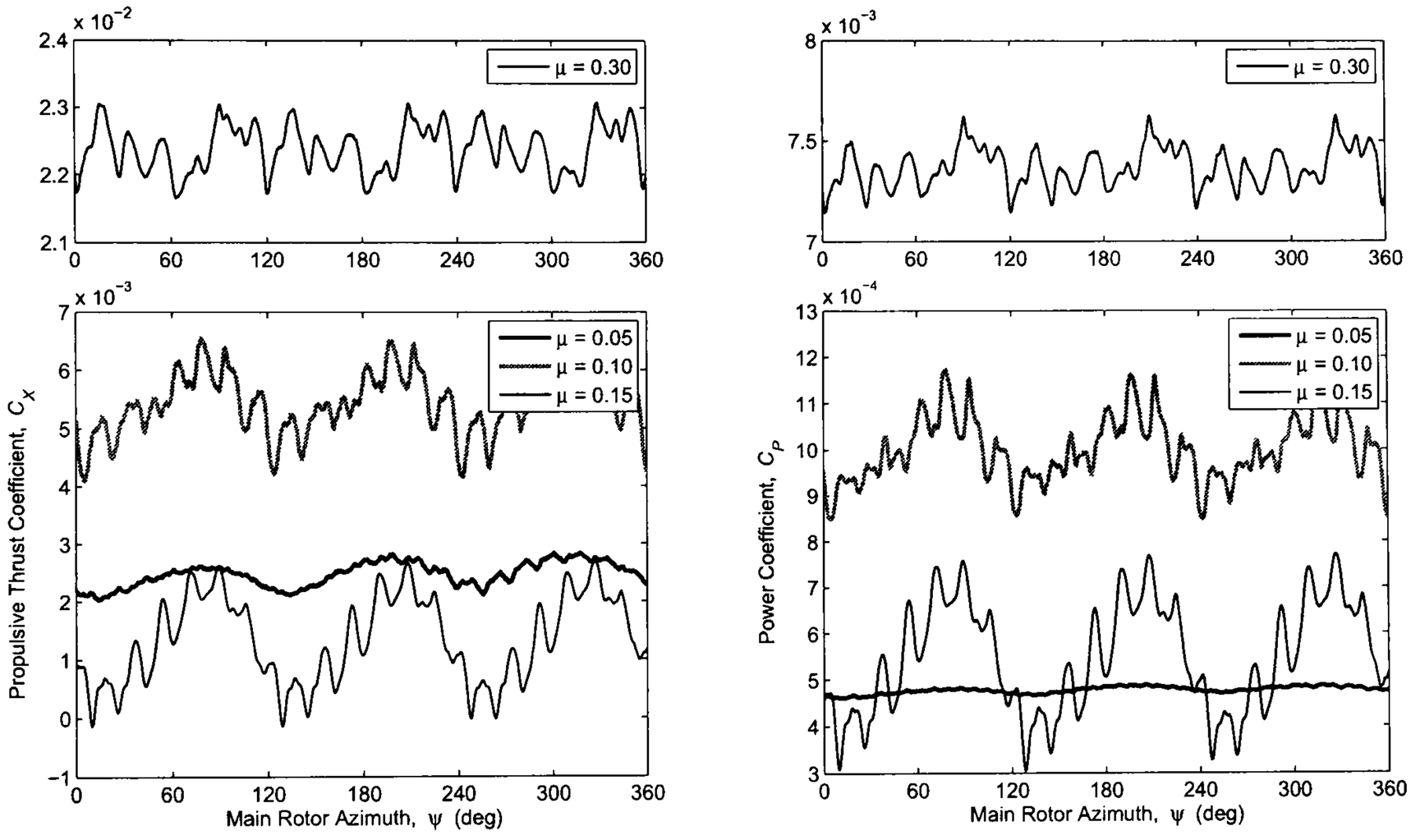
(b) Power coefficient

Figure 6.16: *Distribution of blade loading and power consumption over the upper and lower rotors of the coaxial system at advance ratio* $\mu = 0.15$. *(Left: upper rotor. Right: lower rotor.)*

variation in the thrust and the torque produced by the main rotor system is entirely consistent with the localisation of the peaks of maximum loading produced by both rotors to the rear quadrant of their respective advancing sides. During the XH-59A development programme, significant success in reducing overall vibration of the system was achieved by using differential cyclic input to the upper and lower rotors to change the load distribution on the rotors, and hence the relative phasing of the $3\Omega_c$ vibrational component of their thrust and torque, in order to avoid the constructive interference between the loading signals from the upper and lower rotors that is shown in this study [6, 59, 66, 83].

6.5.2 Rotor-Propulsor Interaction

Figure 6.17 shows the variation of the thrust produced by the propulsor, over a single revolution of the main rotor system, with the system trimmed into forward flight at the various advance ratios that were simulated. This figure reveals that the loading produced on the propulsor is also highly unsteady at all but the highest forward speeds. A strong $3\Omega_c$ component to the loading as well as a component at the blade-passage frequency of the propulsor is clearly discernible at all the advance ratios that were simulated.

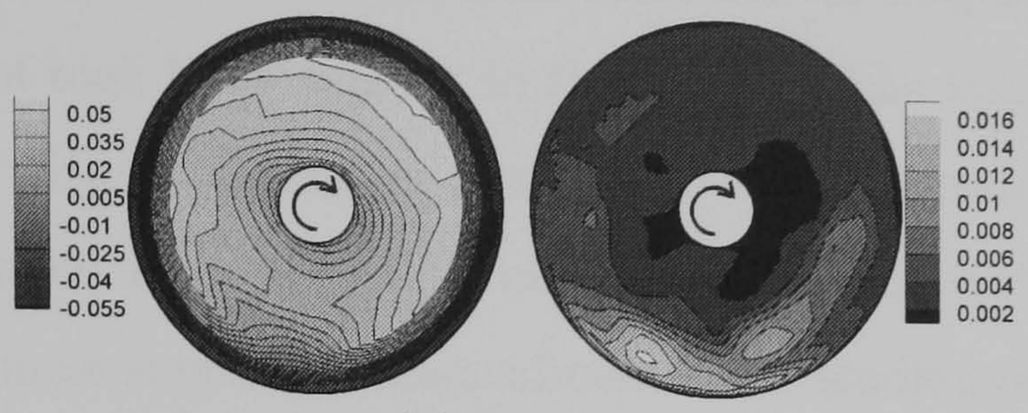


(a) Thrust generated by propulsor

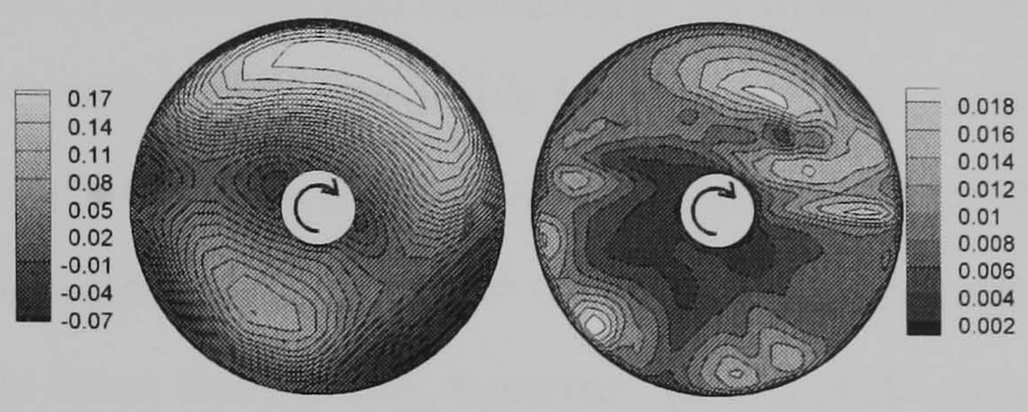
(b) Power required by propulsor

Figure 6.17: *Temporal variation in propulsor thrust and power over one main rotor revolution.*

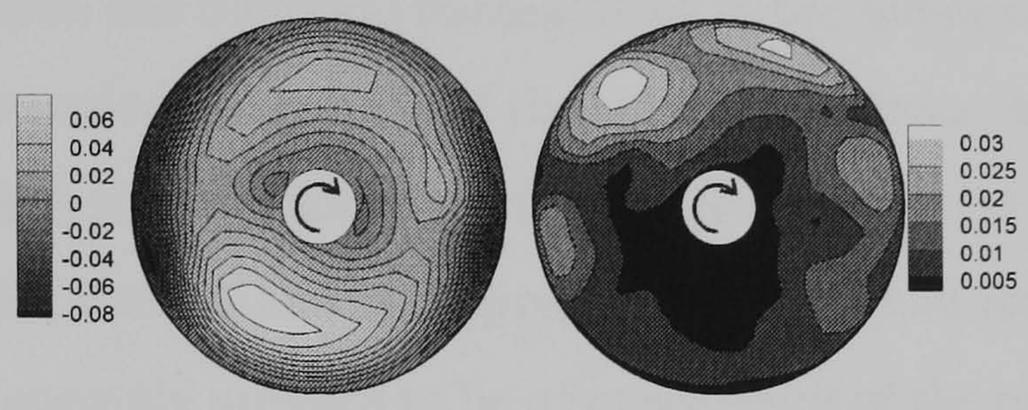
Figure 6.18 shows the distribution of load on the propulsor disc at each of the advance ratios that were simulated. Each individual plot shows the radial distribution of load that is experienced by a single blade of the propulsor, during a single rotor revolution, as a polar function of blade azimuth. The blade loading has been decomposed into a mean component and a superimposed RMS fluctuation to allow the origins of the unsteadiness in the loading on the system to be identified. Given its design, the propulsor would



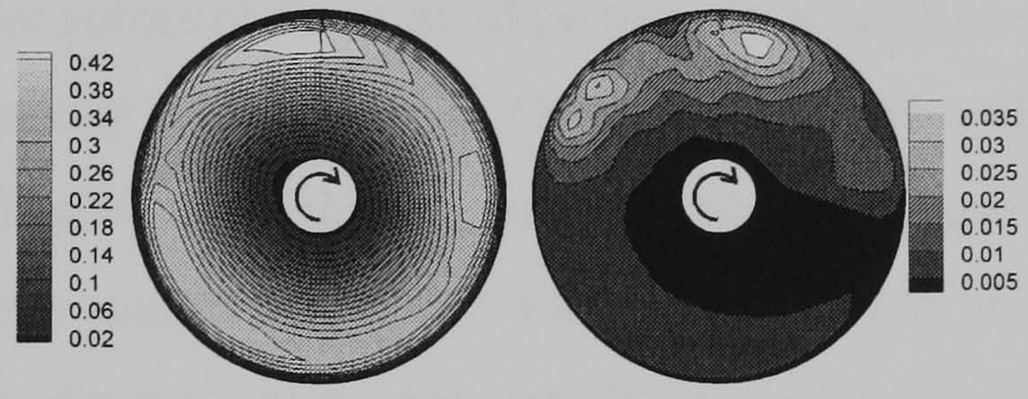
(a) $\mu = 0.05$



(b) $\mu = 0.10$



(c) $\mu = 0.15$



(d) $\mu = 0.30$

Figure 6.18: *Distribution of the blade loading coefficient over the propulsor disc, as seen from behind the helicopter. (Left: mean loading. Right: RMS fluctuation in loading.) Note that different scales are used in each plot.*

produce its best performance if it were to operate in similar fashion to a propeller in free air, in other words, if it were to be exposed to a steady, axially-symmetric onset flow. The loading that is produced on the propulsor suggests that the onset flow experienced by this rotor is far from this ideal, however, except perhaps at the highest forward flight speed that was simulated. Indeed, Figure 6.18 reveals the significant non-uniformity in the loading on the propulsor, at all forward flight speeds, that is induced by its aerodynamic interaction with the main rotor system and tailplane. The effects of the

direct impingement of the wakes from the main rotor and the tailplane are clearly evident as localised patches of high RMS content to the loading. The location of these patches is entirely consistent with the dynamics of the wake that is revealed in Fig 6.6 and 6.7; as the wake of the main rotor skews increasingly rearwards with increasing advance ratio, the patches of most significant unsteadiness in the loading on the propulsor track upwards across its face. The azimuthal inhomogeneity in the loading experienced by the blades as they rotate is primarily responsible for the fluctuations in the thrust produced by the propulsor at and above its blade-passage frequency. The $3\Omega_c$ component of the thrust produced by the propulsor is below the rotational frequency of the device and hence cannot originate from this source, however. In fact, this component of the loading must result directly from the temporal unsteadiness in the inflow through the propulsor that is caused by the periodic ingestion of the tip vortices from the main rotor.

It may well be asked why the dominant frequency of excitation of the load produced by the propulsor is $3\Omega_c$ rather than $6\Omega_c$, given that the coaxial main rotor contains six blades in total. This anomaly appears to be a consequence of the phasing of the rotation of the upper and lower rotors of the coaxial system. It is suggested above that the root cause of the low-frequency unsteadiness in the propulsor load is the entrainment of the tip vortices that the blades of the upper and lower rotors produce from the rear of their respective discs. In the configuration that was simulated, the blades of the upper and lower rotors pass directly over each other at the rear of the fuselage, with the result that the tip vortices from the two systems are laid down almost simultaneously into the flow at the rear of rotor. Except at the lowest forward speeds, where the downwards trajectory of the wake and the separation between the rotor discs causes the tip vortices to remain as relatively distinct structures, the vortices from the upper and lower rotors interact behind the rotor to behave effectively as a single coherent structure by the time that they interact with the propulsor. This process can be seen by careful examination of Figure 6.10 and has the consequence that the inflow through the propulsor, and hence the loading, fluctuates at the lower than expected frequency.

Most interestingly, Figure 6.17 illustrates well the difficulties that might be encountered with the pusher-propulsor configuration in properly scheduling the division of loading between the main rotor system and the propulsor. Figure 6.3 shows that, at an advance ratio $\mu = 0.15$, the propulsor is required to produce very little thrust —

the scheduling of the rotor tilt has resulted in most of the propulsive requirement being transferred to the main rotor. Figure 6.17 shows the resultant $3\Omega_c$ fluctuation in the propulsor loading to be almost as large as the required mean thrust from the propulsor. The propulsor thus acts as a powerful source of dynamic excitation of the helicopter without much beneficial effect on the performance of the vehicle. This case is extreme, but given that the main rotor wake ceases to impinge on the propulsor only at relatively high advance ratio, there is the possibility that similar dynamic excitation might be a feature of the configuration over a relatively broad range of forward speeds — at least, given the data presented in Figure 6.17, over the transitional range of advance ratios from $\mu = 0.10$ to 0.15. Certainly a tail-mounted propulsor that is left to rotate at or near its operating speed without producing any useful thrust does not appear to yield an ideal design solution, and the device may well do simply to be stopped and its blades feathered until high enough forward flight speed is attained for it to be clear of the main rotor wake.

6.5.3 Rotor-Tailplane Interaction

The close passage of the main rotor tip vortices over the empennage also induces significant unsteadiness in the pressure distribution on the horizontal tailplane. Figure 6.19 compares the pressure coefficient $C_P{}' = 100(p - p_\infty)/(\frac{1}{2}\rho(\Omega R)^2)$ at the centre of area of the upper surfaces of the port and starboard sides of the tailplane, at advance ratio $\mu = 0.10$, by plotting its variation over a single main rotor revolution. The amplitude of the pressure fluctuations on the port and starboard sides of the tailplane are similar in magnitude but the $3\Omega_c$ pressure peaks on the port and starboard sides are offset in phase by approximately 30° of a main rotor revolution. At this advance ratio, the tip vortex from the upper rotor passes closest to the port side of the tailplane, and the tip vortex from the lower rotor passes closest to the starboard side of the tailplane as shown in Figure 6.10. The observed phase offset is a result of the slightly different times of arrival at the tailplane of the vortices from the upper and lower rotors at this low forward speed.

At $\mu = 0.15$, the effect of the root vortices from the main rotors in skewing the flow near the empennage can be seen quite strongly in the loading distribution on the tailplane. Figure 6.20 again compares the pressure coefficient at the centre of area of the

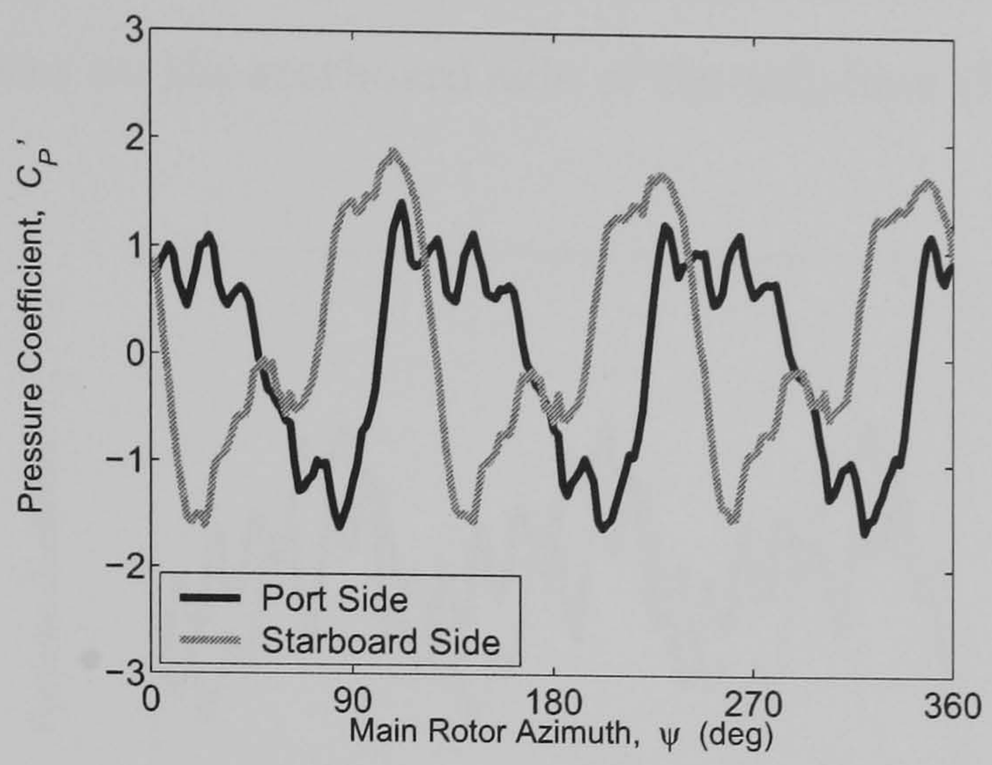


Figure 6.19: *Time-dependent pressure signals on the upper surface of the tailplane at advance ratio* $\mu = 0.10$. *(Mean removed.)*

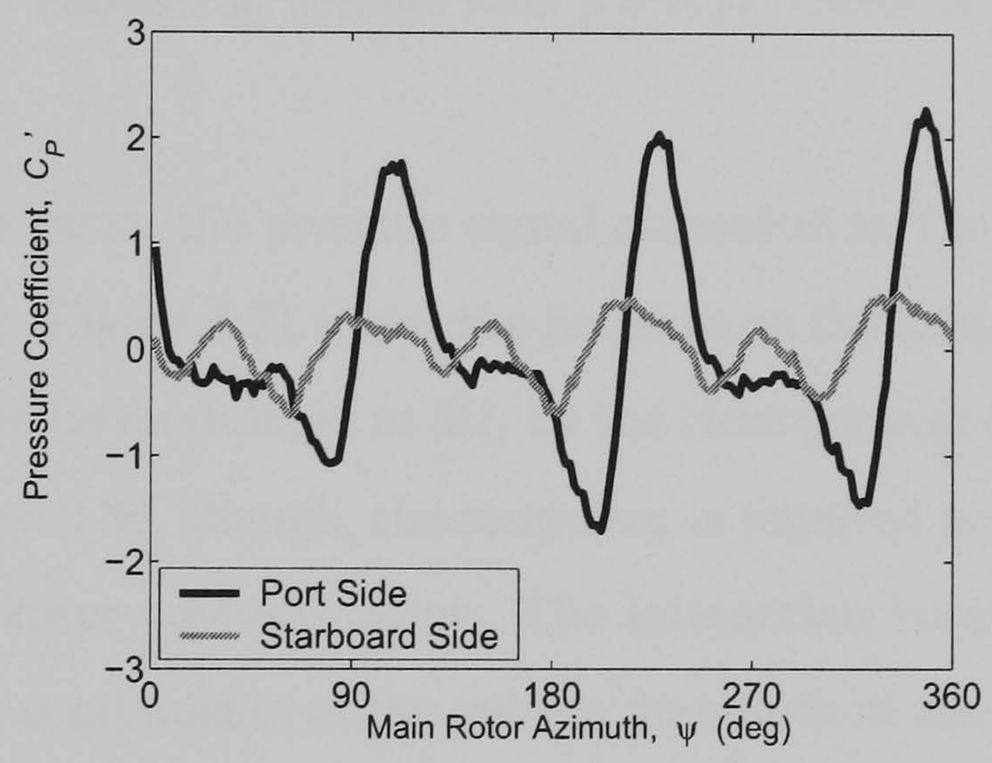


Figure 6.20: *Time-dependent pressure signals on the upper surface of the tailplane at advance ratio* $\mu = 0.15$. *(Mean removed.)*

upper surfaces of the port and starboard sides of the tailplane by plotting its variation over a single main rotor revolution. As at the lower advance ratio, the pressure on both the port and starboard sides of the tailplane is characterised by a marked fluctuation at the blade-passage frequency of the main rotor. The shape of the pressure signal at this location is reminiscent of those generated by the 'type 2' close wake-surface interactions that are described by Leishman [84]. The pressure signals that result from this type of interaction are very sensitive to the location of the vortices relative to the surface, and, indeed, the asymmetry in the amplitude of the pressure fluctuations on either side

of the tailplane is suggestive of a greater miss-distance between the tailplane and the interfering wake vortices on the starboard side of the tailplane than on the port.

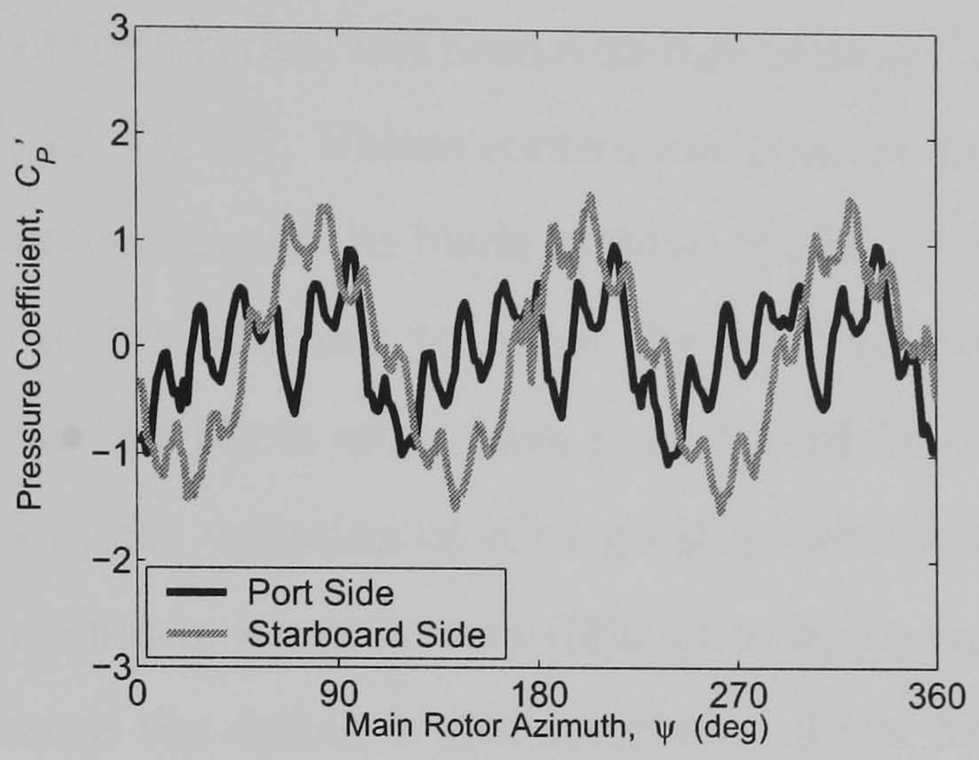


Figure 6.21: *Time-dependent pressure signals on the upper surface of the tailplane at advance ratio* $\mu = 0.30$. *(Mean removed.)*

At higher advance ratio, the pressure signal measured on the tailplane changes significantly in character. Figure 6.21 shows the pressure on the tailplane at $\mu = 0.30$, as at lower forward speed, to be modulated at $3\Omega_c$ by the close passage of the tip vortices from the main rotor. At $\mu = 0.30$, though, the propulsor is required to generate considerably more thrust than at lower advance ratios. The interaction between the highly-loaded propulsor and nearby components of the vehicle manifests in the pressure measured on the tailplane as a high-frequency fluctuation at the propulsor's blade-passage frequency. On some fixed-wing aircraft with pusher propellers the fatigue life of any aerodynamic surfaces that are exposed to such an interaction can be reduced significantly, but it is also known that the actual magnitude of the interaction is very sensitive to the relative position of the propeller and the affected aerodynamic surface and thus is amenable to reduction through careful design.

These localised pressure fluctuations integrate to produce a periodic forcing of about five percent of the time-averaged loading on the tailplane at all of the forward speeds that were simulated. The principally $3\Omega_c$ character of the unsteady forcing of the tailplane may contribute to the vibration of the empennage of the vehicle. In strong contrast, Figure 6.5 shows the integrated effect of the pressures to result in very large changes with forward speed in the steady nose-up moment that is produced by the tailplane. This

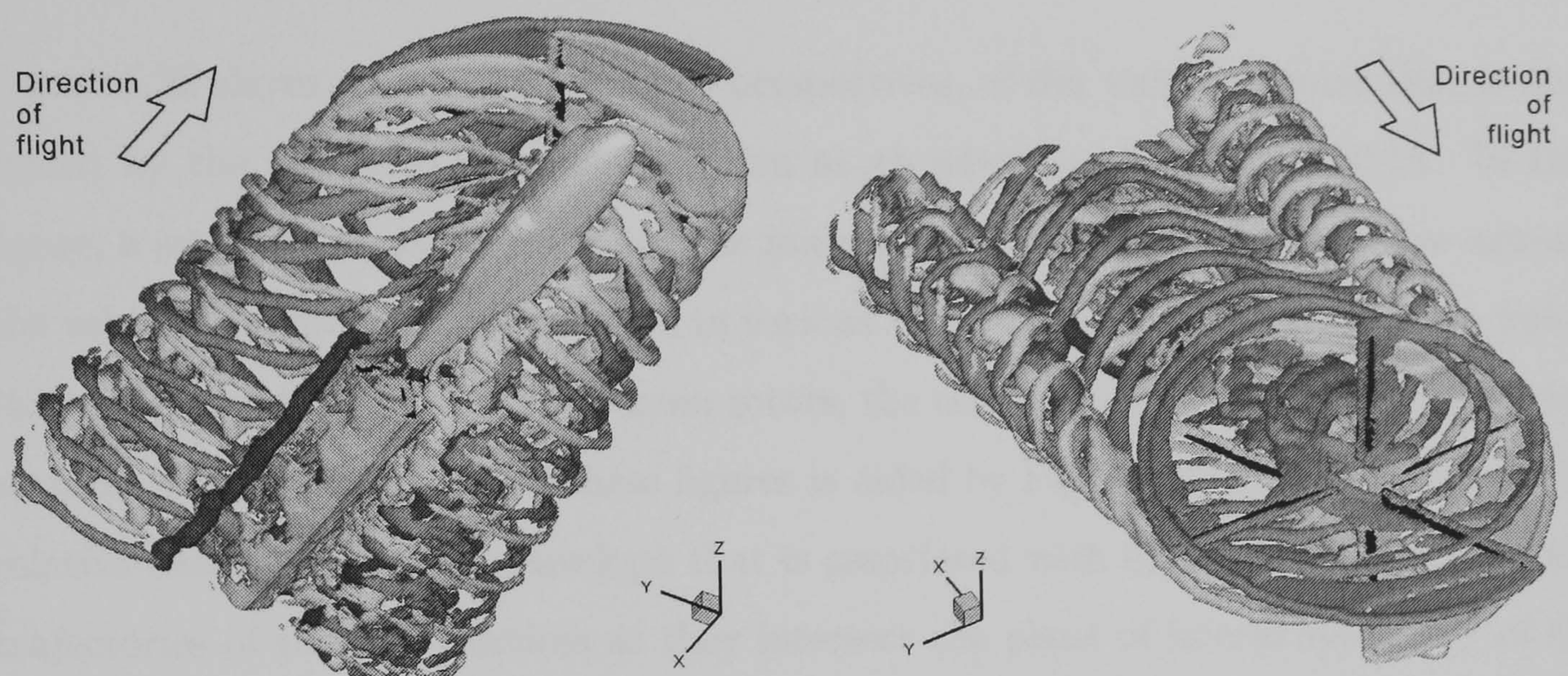
is particularly so as the aircraft passes through the range of advance ratios between 0.05 to 0.15, where Figure 6.7 shows the wake of the main rotor to impinge directly on the tailplane. This particular pathology, known as 'pitch up' when coupled to the longitudinal dynamics of the aircraft, has been a feature of many helicopters during their development stage [76, 77, 78, 80]. Unless control margins are particularly narrow (for instance to prohibit overstressing of the blade system) the control power of the stiffened coaxial rotor is likely to be sufficient to allow the pilot to fly the aircraft through the affected speed range, but pilots often have poor regard for the strong nonlinearity that this effect induces in the variation of stick position with forward speed. As many historical examples have shown, it can be very difficult to find a position for the tailplane which allows it to enhance the dynamic characteristics of the helicopter in high speed flight while avoiding the dynamic side-effects that are induced by interaction with the wake of the main rotor at low forward speed.

6.6 Interdependencies in the Interactional Aerodynamics

6.6.1 Flight Condition of Interest

The present section aims to investigate further the origins of the aerodynamic characteristics of the helicopter configuration that was studied in the previous sections. In particular, the aim of this part of the chapter is to shed light on how the performance of the sub-components of the system in isolation are modified by aerodynamic interaction with the other sub-components of the system once integrated into the configuration of the helicopter. In this vein, the aerodynamic characteristics of several different combinations of the main rotor system, fuselage, and propulsor are contrasted in order to reveal the processes through which their aerodynamic interaction influences the aerodynamic and acoustic character of the overall helicopter system.

In Sections 6.3, 6.4, and 6.5, the aerodynamic performance of the generic compounded hingeless coaxial configuration was analysed at various forward flight speeds, and the various aerodynamic interactions that manifested at different advance ratios were described in detail. Of the various forward speeds simulated in the earlier sections, the broadest and most interesting range of interactions between the various components of the system were encountered at the relatively moderate advance ratio of $\mu = 0.15$.



(a) Bottom view

(b) Top view

Figure 6.22: *Visualisation of the wake structure of the full configuration in steady forward flight at advance ratio* $\mu = 0.15$. *(Wakes from the different elements of the configuration coloured in separate shades of grey.)*

The present section concentrates solely on the aerodynamic interference between the various components of the compounded hingeless coaxial helicopter at this forward flight speed, and attempts to analyse in detail the influence of each component on the aerodynamic characteristics of the remainder of the configuration.

To allow valid comparison between the performance of the entire configuration and that of its various components in isolation, and hence to expose the effects of aerodynamic interaction on the performance of the system, care must be taken to match as closely as possible the operating conditions of the various systems being compared. Calculations of the performance of the rotor system with the fuselage absent were thus conducted with the rotor system trimmed to the same overall conditions on weight, drag and moment as for the full configuration. Calculations of the performance of the isolated propulsor were conducted with this device trimmed to produce the same propulsive thrust as when integrated into the full configuration.

6.6.2 Categorisation of Interactions

Figure 6.22 shows snapshots, from two perspectives, of the wake structure that is generated by the full helicopter configuration at an advance ratio of $\mu = 0.15$. In this figure, a set of iso-surfaces, on which the magnitude of the vorticity in the flow around the vehicle is constant, are presented in various shades of grey to distinguish the wakes that are generated by each of the main rotors, the tail propulsor and the horizontal tail surface. The interpretation of these figures is aided by Figure 6.7(c), which reveals the relative extent of the wake envelope that is associated with each rotor by plotting the trajectories of their tip vortices as they intersect the plane of lateral symmetry of the fuselage.

Figures 6.22 and 6.7(c) illustrate the complex nature of the interaction between the lifting components of the compounded coaxial helicopter and their wakes at this advance ratio. Careful study of these images supports the notion that the aerodynamic interference between the various components of the system can be characterised in terms of two rather different possible modes of interaction. The first, rather obvious 'direct' mode involves the direct impingement of the wake of one of the components of the system on the other. The aerodynamic environment experienced by the affected component, and hence its loading, is usually modified very strongly and directly during this mode of interaction. Interaction between the wake of one of the components of the configuration and the wake of another component can result in a second 'indirect' mode of interaction, however. In this mode, the distortion of the wake of the component that is induced by the interaction usually feeds back into its aerodynamic loading in a manner that is more subtle, and often far more obscure, than during a direct interaction. Both modes of interaction have a profound influence on the aerodynamic characteristics of the helicopter configuration examined in this study.

Figure 6.23, adapted from the influential work of Sheridan and Smith [75], summarises the range of interactions that are possible between the various components of the system. Sheridan's network-type analysis and associated reductive approach has proved to be a very instructive means of classifying the multitude of aerodynamic interactions that can be present within the rotary-winged system and is used here to help differentiate between the various sources of aerodynamic interaction that are present within the aerodynamic environment of the compounded coaxial helicopter.

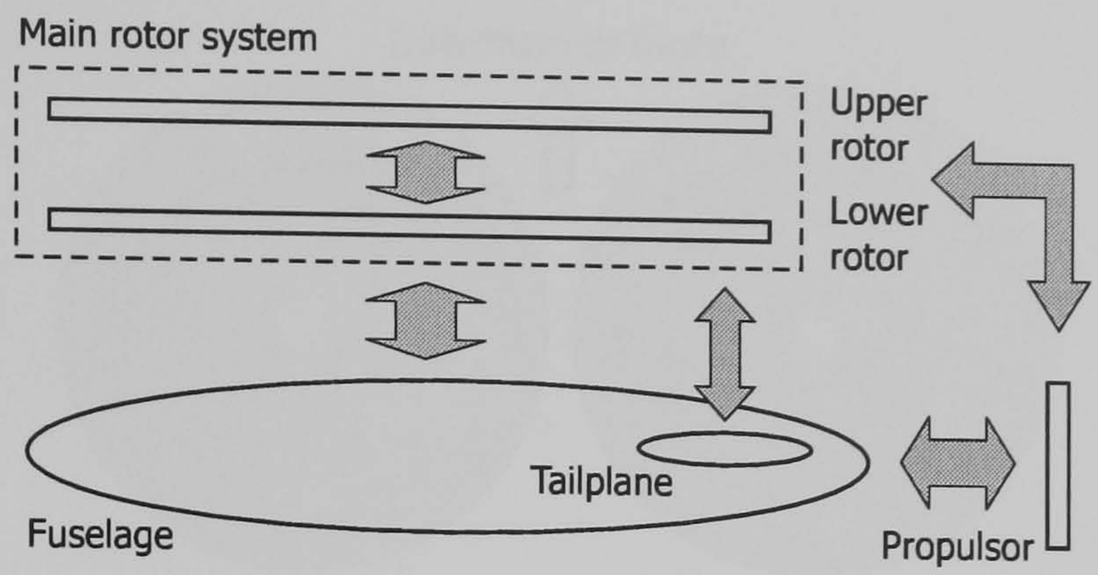
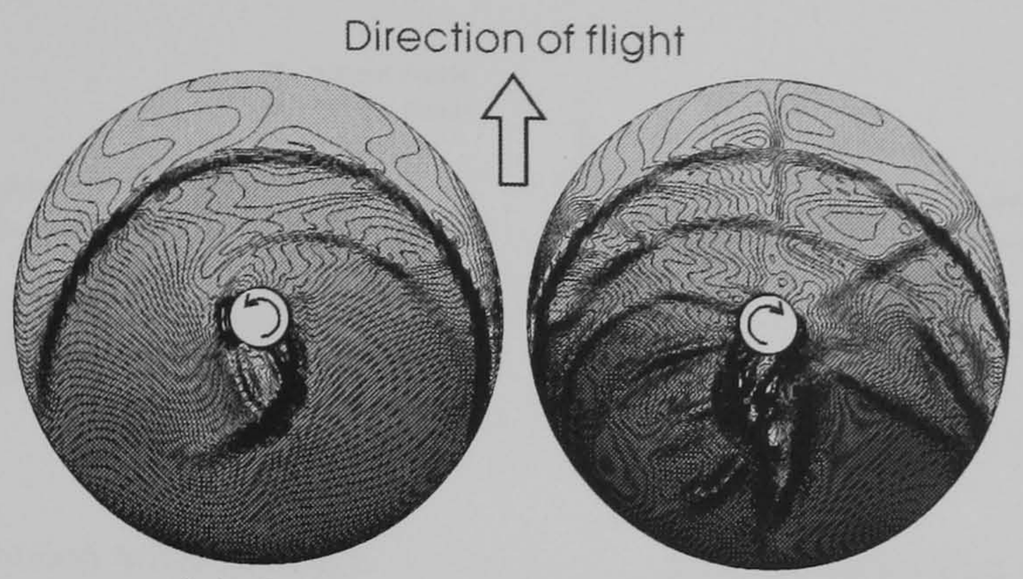


Figure 6.23: *Schematic summarising the various aerodynamic interactions between the various components of the simulated configuration. (Interactions represented by arrows.)*

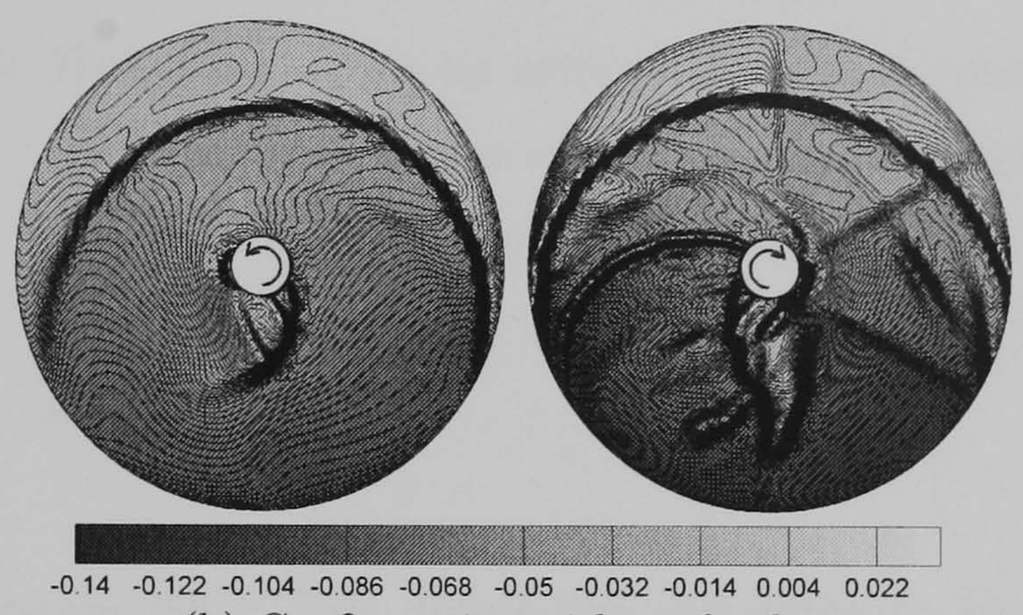
6.6.3 Main Coaxial Rotor

The aerodynamic environment of the main rotor is strongly influenced by an indirect interaction with the fuselage that results in a significant upwards displacement of its wake. The pitching moment and download on the tailplane as a result of the direct interaction of this surface with the wake of the main rotor also feeds back through the trim conditions on the aircraft to modify very strongly the loading distribution on the main rotor system.

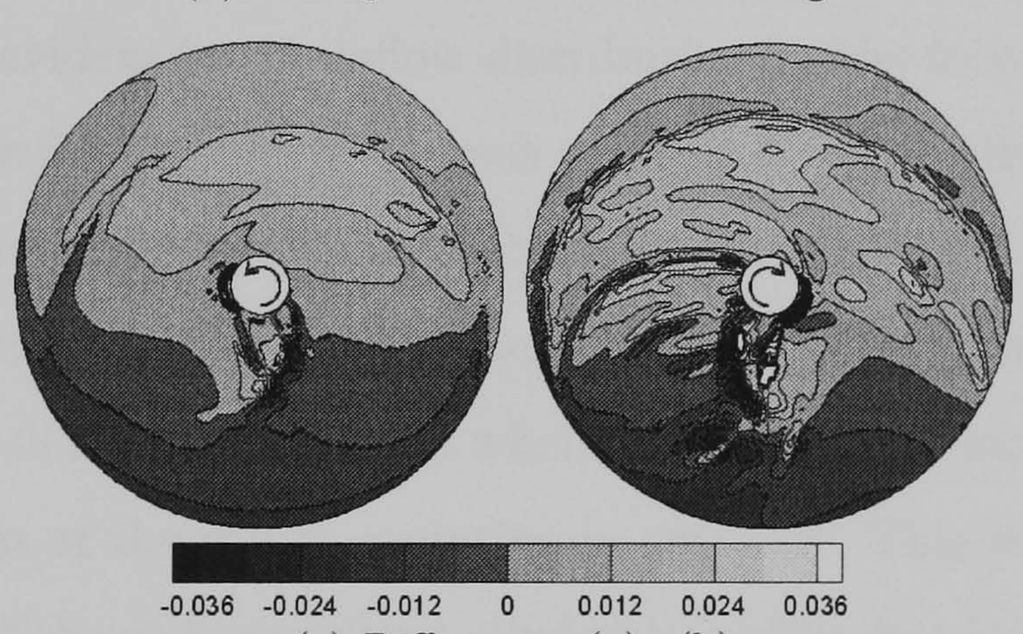
Figure 6.24(a) shows the distribution of inflow over the upper and lower rotors of the main rotor system of the full configuration. The inflow pattern is characterised by a strong longitudinal gradient, associated primarily with the skew, in the mean, of the vortex tube comprising the rotor wake. The distribution of inflow over the rotor discs is dissected by a series of ridges corresponding to the positions of various localised interactions between the blades of the rotors and their tip vortices. On the upper rotor, these interactions result primarily from interactions between the blades and the tip vortices from blades on the same rotor, whereas on the lower rotor a sequence of additional inter-rotor interactions are also present. Figure 6.24(b) shows the equivalent inflow distribution in the absence of the fuselage, and Figure 6.24(c) shows the difference between the inflow through the rotor with and without the fuselage present and reveals very clearly the effect of interaction with the fuselage on the aerodynamic environment of the main rotor system. Three primary effects are apparent. Firstly the strengths of some of the localised blade vortex interactions are modified, with the major effect being



(a) Full configuration with fuselage



(b) Configuration without fuselage

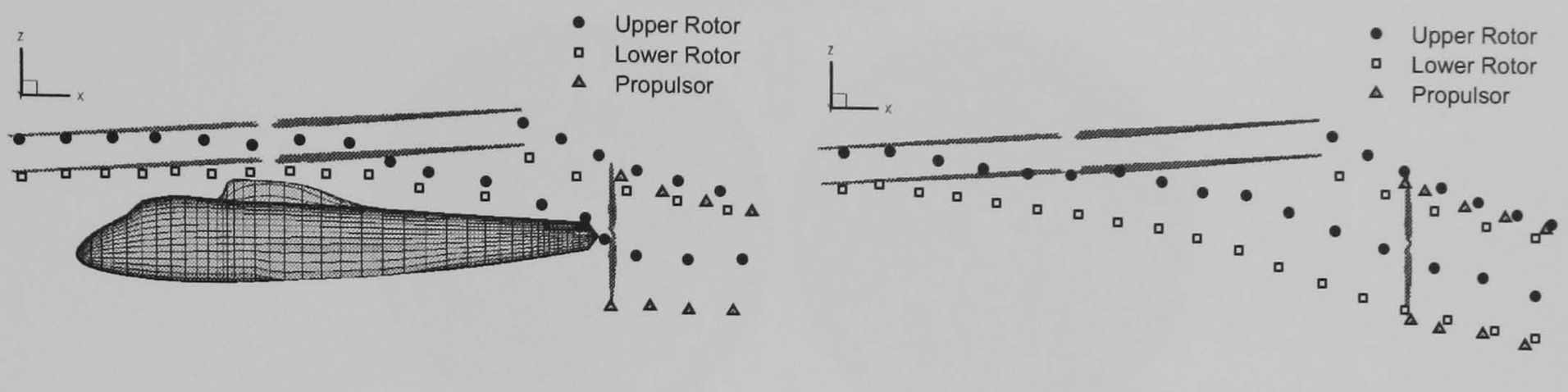


(c) Difference: (a)−(b)

Figure 6.24: *Distribution of inflow, $-v_i/R_c\Omega_c$, over the main rotor discs, showing the strong interaction between the upper and lower rotors at advance ratio $\mu = 0.15$. (Left: upper rotor. Right: lower rotor.)*

evident on the lower rotor. The shift in the pattern of localised interactions is entirely consistent with the deflection of the wake of both the upper and lower rotors that is evident in Figure 6.25. In this figure, the marked influence of the fuselage in modifying the trajectory of the vortices from the main rotor is clearly visible.

Secondly, the displacement of the free-stream by the fuselage is also responsible for a weak upflow inboard on the forward half of the lower rotor and a similar downflow

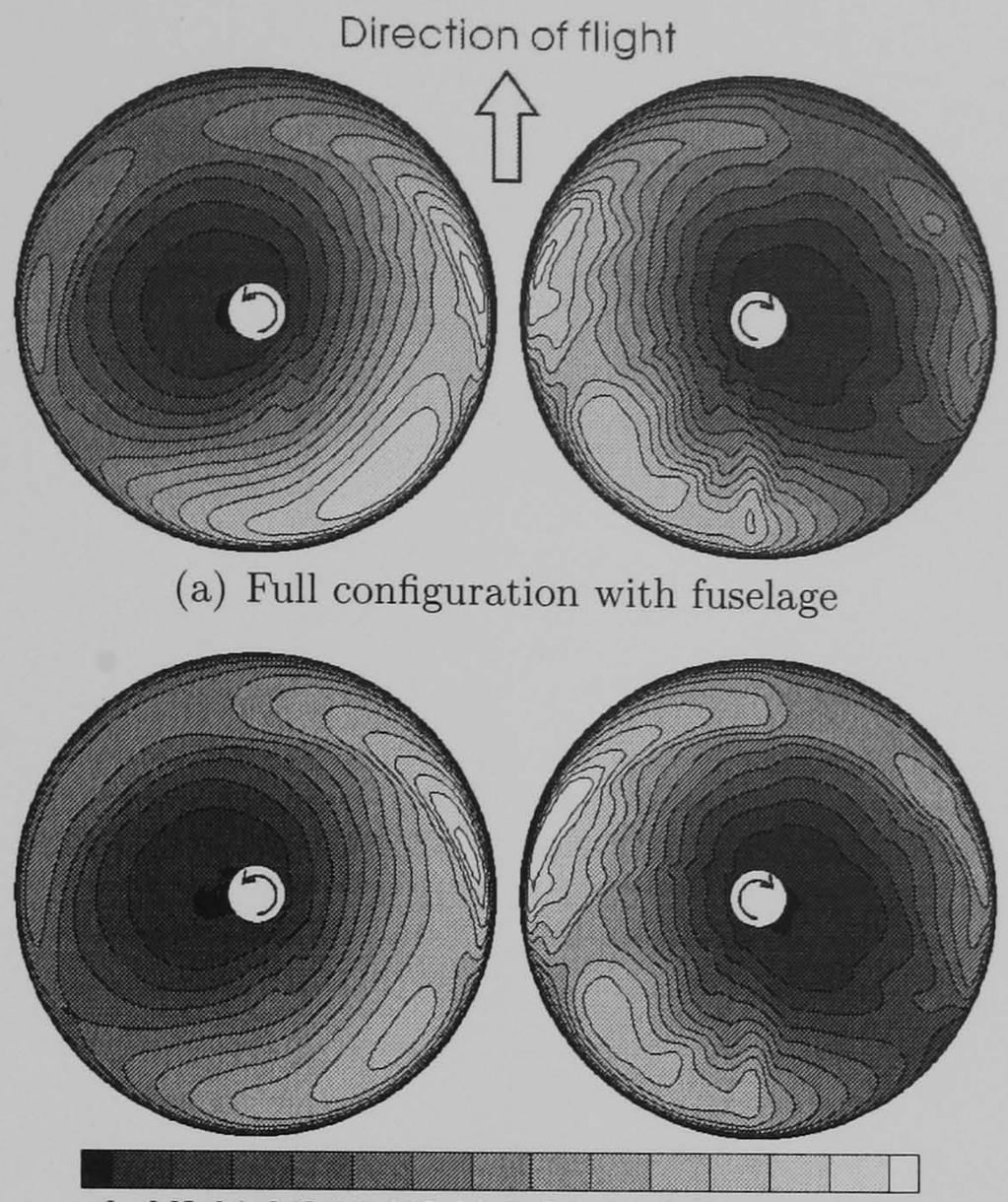


(a) Full configuration with fuselage (b) Configuration without fuselage

Figure 6.25: *Trajectories of the tip vortices of the main rotors and propulsor at advance ratio $\mu = 0.15$ showing the points of intersection of individual vortices with the longitudinal plane through the fuselage centreline at various times during a single main rotor revolution.*

on the rear of the system [55]. This dipole-like distortion to the velocity field of the rotor is particularly evident in the inflow distribution on the forward part of the lower rotor shown in Figure 6.24(c); the downwash on the rear of the discs is obscured by the complex pattern of interleaving ridges that result from localised interactions between the blades and the vortices trailed from their roots. Finally, a strong difference in the longitudinal gradient of inflow is apparent when the distribution for the full configuration is compared with that of the rotors operating in isolation. This is not due primarily to the gross distortion of the wake structure alluded to earlier, but is a more direct effect of the strong nose-up pitching moment on the system that is induced by the impingement of the wake of the main rotor on the tailplane.

To expose this effect more clearly, Figure 6.26 shows the associated distribution of blade loading on the upper and lower rotors of the main rotor system. The concentration of blade loading at the tips of the blades on the advancing sides of both rotors is characteristic of a very stiff coaxial rotor system. Figure 6.26(c), showing the difference in loading distribution on the rotors with and without the fuselage present, reveals an additional strong concentration of loading at the rear of the rotor of the full configuration. This concentration is almost entirely due to the longitudinal cyclic input that is required to produce a nose-down pitching moment to counteract the effect of the tailplane. This re-distribution of loading in order to satisfy overall trim of the aircraft



(a) Full configuration with fuselage

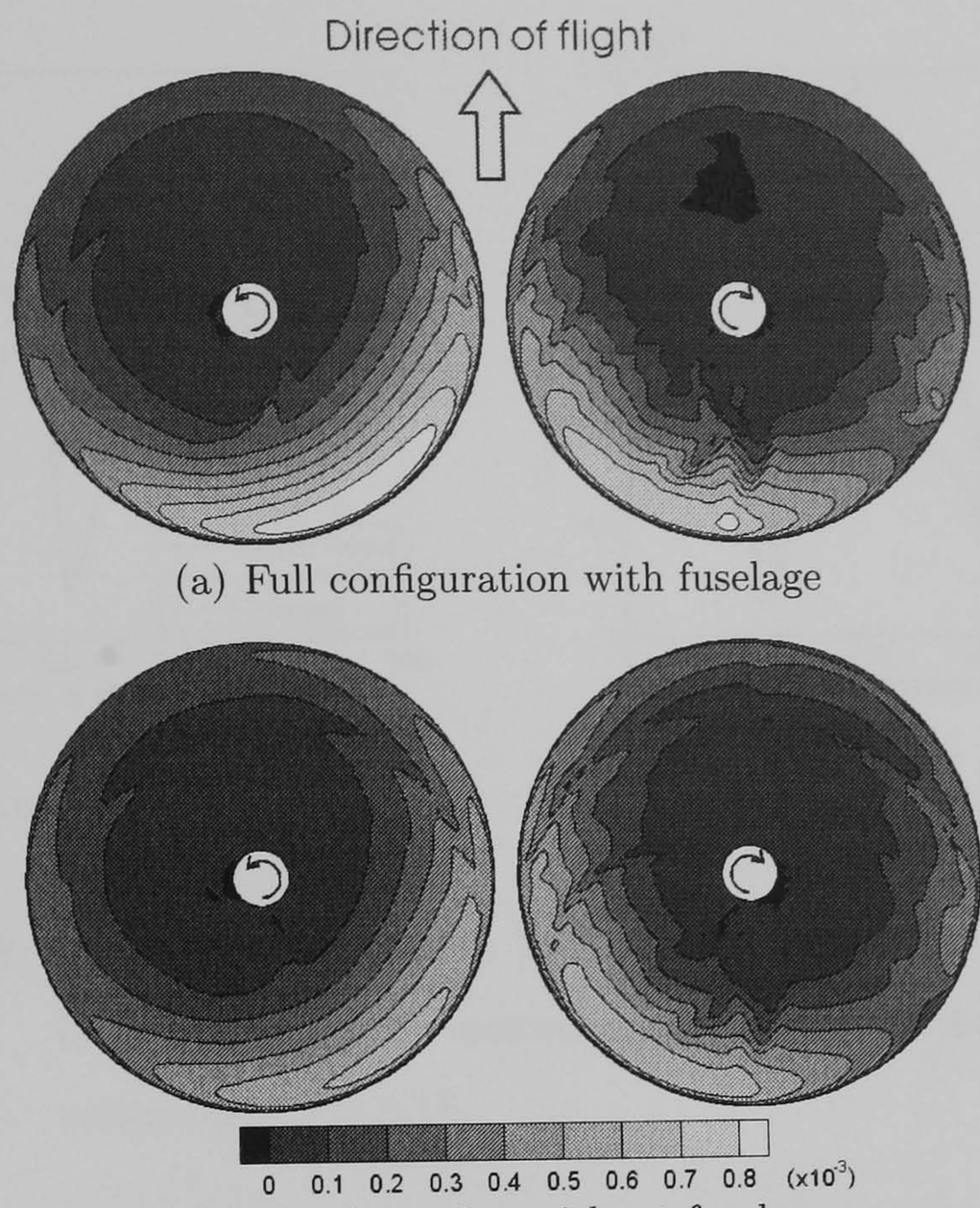
(b) Configuration without fuselage

(c) Difference: (a)−(b)

Figure 6.26: *Distribution of blade loading over the main rotor discs at advance ratio* $\mu = 0.15$. *(Left: upper rotor. Right: lower rotor.)*

has a clear impact on the power required by the main rotor system, as can be seen in Figure 6.27 where a significant increase in the power consumed by the system when operated as part of the configuration rather than in isolation can be correlated with the concentration in loading at the rear of the rotor discs.

Figures 6.28 and 6.29 show the variation, over a single rotor revolution, of the thrust generated, and power consumed, by the upper and lower rotors of the main rotor system. The characteristic three-per-revolution variation of the thrust and power is a



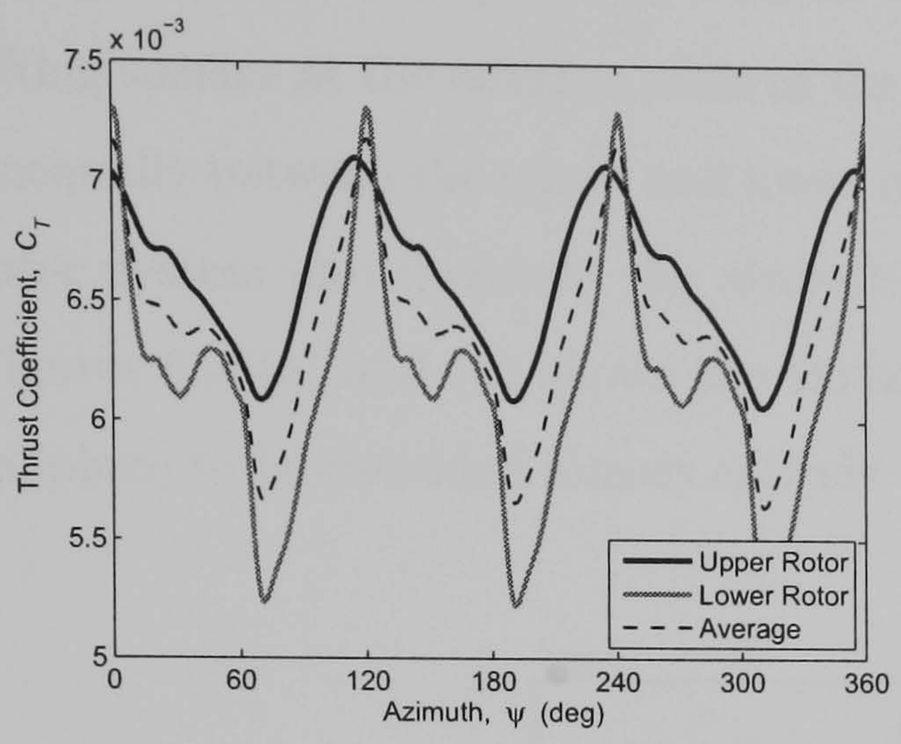
(a) Full configuration with fuselage

(b) Configuration without fuselage

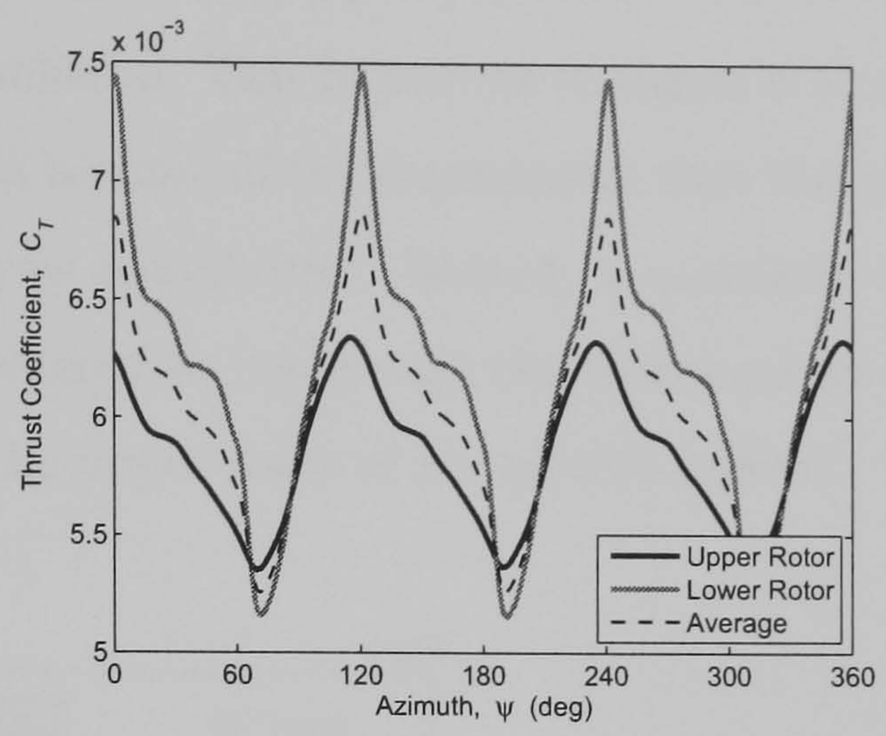
(c) Difference: (a)−(b)

Figure 6.27: *Distribution of power coefficient over the main rotor discs at advance ratio* $\mu = 0.15$. *(Left: upper rotor. Right: lower rotor.)*

basic consequence of the aerodynamics of stiff rotor systems. The six-per-revolution variation in thrust and power that is generated predominantly by the lower rotor is an effect of the aerodynamic interference between the blades of the two rotors as they pass by each other. These interactions are also visible as the sequence of radial ridges in the inflow distributions shown in Figure 6.24. Comparison of parts (a) and (b) of Figures 6.28 and 6.29 show that these vibratory characteristics of the main rotor are

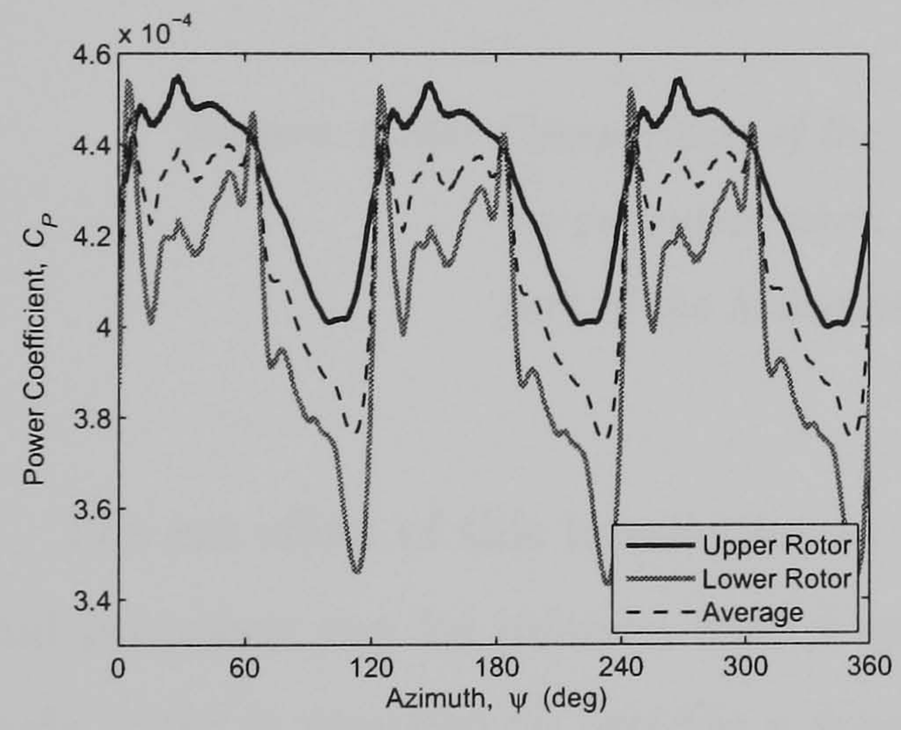


(a) Full configuration with fuselage

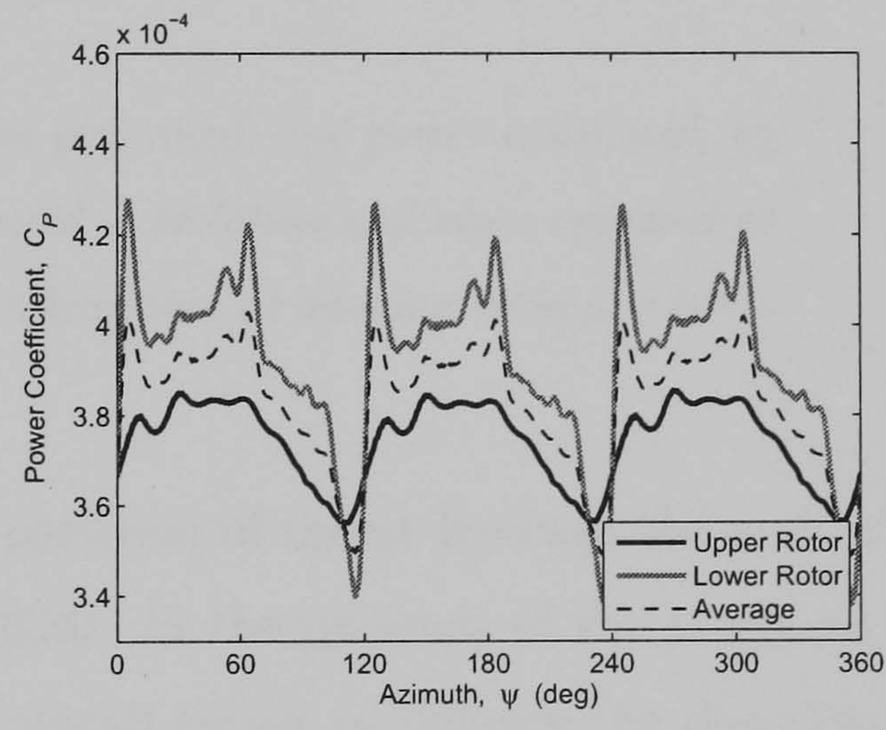


(b) Configuration without fuselage

Figure 6.28: *Temporal variation in the thrust produced by the upper and lower rotors of the coaxial system over one revolution at advance ratio* $\mu = 0.15$.



(a) Full configuration with fuselage



(b) Configuration without fuselage

Figure 6.29: *Temporal variation in the power consumed by the upper and lower rotors of the coaxial system over one revolution at advance ratio* $\mu = 0.15$.

modified in amplitude, but not significantly in character, by integration of the rotor system into the helicopter configuration.

When installed as part of the complete helicopter configuration, however, the main rotor is required to generate sufficient additional thrust to overcome the download that

it induces on the tailplane as a result of the direct impingement of its wake on this lifting surface at the advance ratio of the simulation. This increment in thrust is shared unequally between the upper and lower rotors because of the requirement that the main rotor system also maintain the aircraft in yaw equilibrium. Indeed, a comparison of Figures 6.28(a) and (b) shows the thrust required to counteract the download on the tailplane to be provided almost entirely by the upper rotor of the coaxial system.

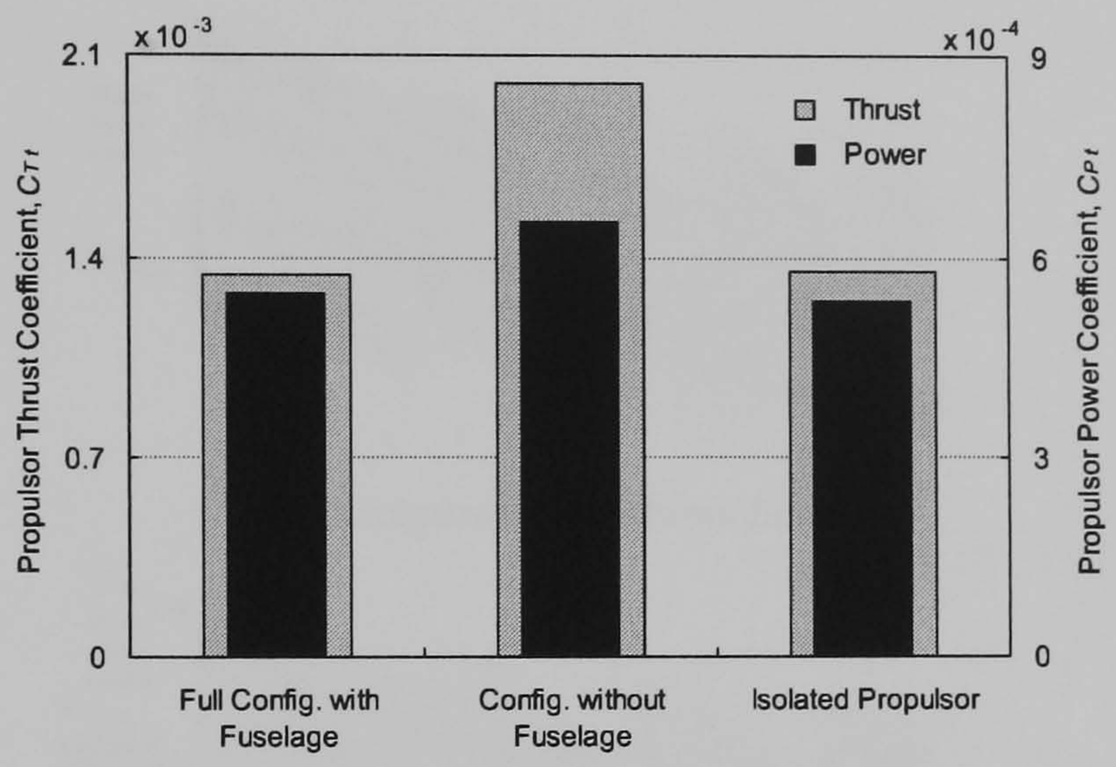
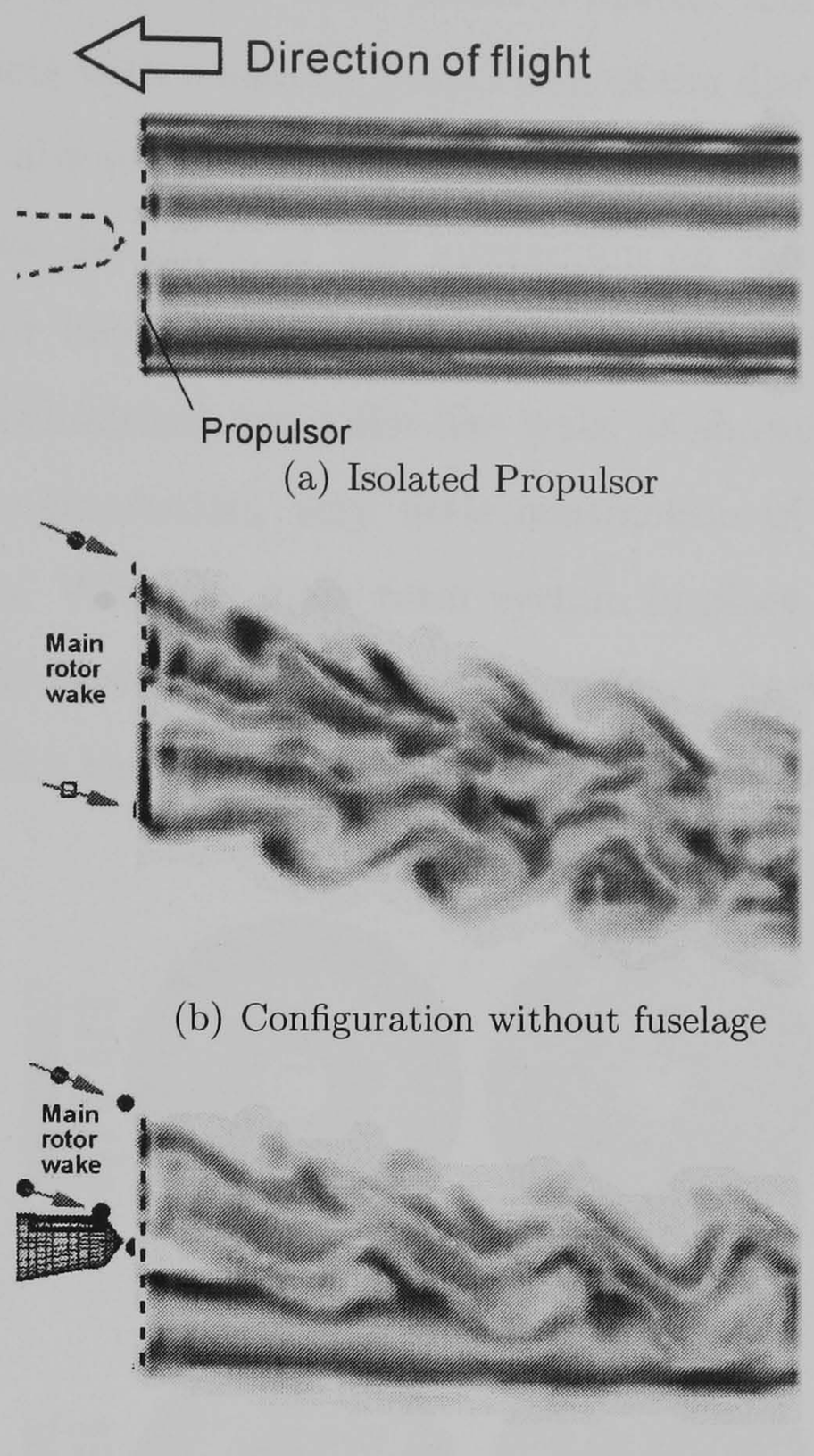


Figure 6.30: *Comparison of the thrust generated, and power consumed, by the propulsor when operated in isolation and when operated as part of the helicopter configuration at advance ratio* $\mu = 0.15$.

The net effect of this interaction on the partition of thrust between the main rotor and propulsor can be inferred from Figure 6.30. In the presence of the tailplane, the main rotor is required to provide a greater overall thrust to balance the download on the tailplane. A larger propulsive component to the rotor thrust thus results from the forward tilt of the main rotor. The procedure used to trim the aircraft translates this increment in propulsive force from the main rotor into a reduction in the propulsive force required from the propulsor and hence, quite surprisingly, into a fairly significant reduction in the power required by the propulsor when the rotor systems are integrated into the full configuration. This example illustrates the extreme care with which the scheduling of the propulsor in relation to the main rotor needs to be approached in such a configuration.



(a) Isolated Propulsor

(b) Configuration without fuselage

(c) Full configuration with fuselage

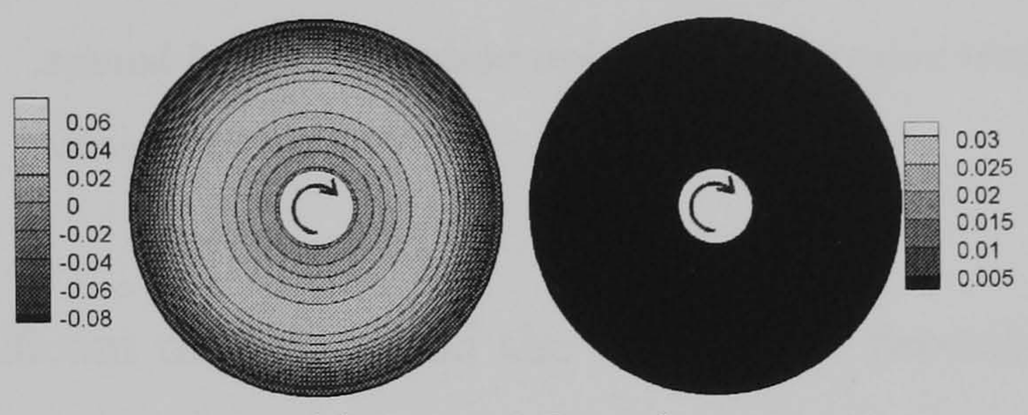
Figure 6.31: *Comparison of propulsor wake geometry, when operated in isolation and when operated as part of the helicopter configuration at advance ratio* $\mu = 0.15$*, visualised as contours of vorticity magnitude on a vertical plane through the centreline of the fuselage.*

6.6.4 Propulsor

Figure 6.25 shows the very strong direct interaction that exists between the main rotor and the propulsor. The important role of the fuselage in modifying the form of this interaction is clearly evident by comparing Figures 6.25(a) and (b). With the fuselage absent, the propulsor is entirely enveloped within the main rotor wake at the advance ratio of the simulations. As shown in Figure 6.25(a), the fuselage and tailplane distort the trajectories of the individual vortices from the main rotor as they are swept back

into the flow behind the system. This yields a flatter, more vertically-compact wake structure that interacts with a smaller proportion of the disc area of the propulsor than when the fuselage is absent.

Figure 6.31 shows the effect of this interaction on the resultant structure of the wake of the propulsor itself. When operated in isolation, the propulsor generates, as expected, a steady, cylindrical, propeller-like wake as shown in Figure 6.31(a). At the advance ratio of the simulation, very little contraction of the wake is evident as it convects downstream. With the main rotor system in place, the wake of the propulsor is skewed significantly downwards due to the downwash from the main rotor, as shown in Figure 6.31(b). With the fuselage present, the lower half of the wake of the propulsor

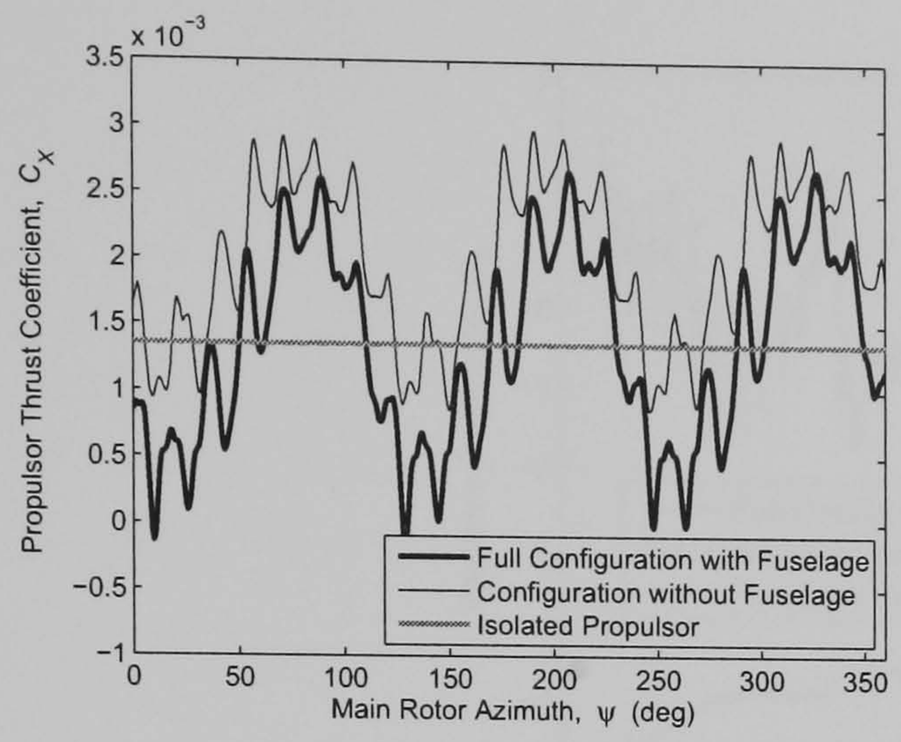


(a) Isolated Propulsor

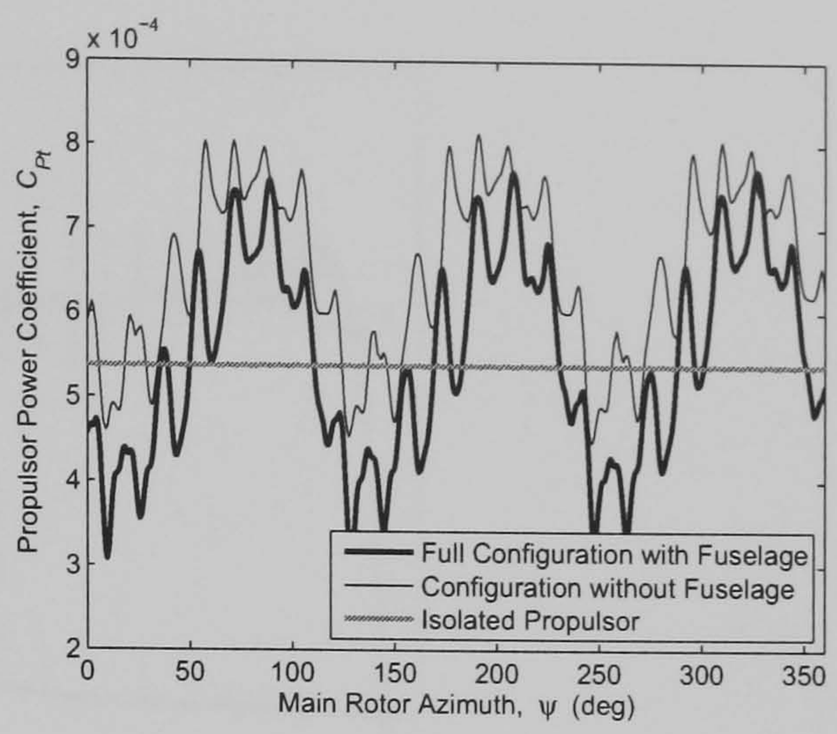
(b) Configuration without fuselage

(c) Full configuration with fuselage

Figure 6.32: *Distribution of blade loading coefficient over the propulsor disc, as seen from behind the helicopter at advance ratio* $\mu = 0.15$. *(Left: mean loading. Right: RMS fluctuation in loading.) Note that different scales are used for the mean and RMS loading.*



(a) Thrust coefficient



(b) Power coefficient

Figure 6.33: *Temporal variation in the thrust produced and power consumed by the propulsor over one main rotor revolution at advance ratio* $\mu = 0.15$.

is shielded from significant distortion and the wake of the propulsor adopts the rather unusual, asymmetric configuration shown in Figure 6.31(c).

Figure 6.32 shows the distribution of loading on the propulsor disc after decomposition into mean and fluctuating (root-mean-square) components. By comparing Figures 6.25 and 6.18, it can be seen that the locations of maximum unsteadiness in the loading on the propulsor disc correlate directly to the regions where the vortices from the main rotor pass directly through the plane of the propulsor disc. The variation in propulsive force generated by the propulsor over a single main rotor revolution is shown in Figure 6.33. As expected, the loading on the isolated propulsor is entirely steady. A modulation of the propulsor thrust at the main rotor blade-passage frequency is clearly apparent when the propulsor is operated in the presence of the main rotor system. This modulation is a direct consequence of a fairly gross variation in the aerodynamic environment of the propulsor that is caused by the fluctuating velocity field associated with the passage of the train of individual main rotor vortices through the propulsor disc. Why this modulation occurs at the main rotor blade passage frequency and not, as might be expected, at twice this frequency (given the total number of blades present on the main rotor) was explained in Section 6.5.2 in terms of a spatial and temporal coherence between the vortical structures that are produced in the wakes of the upper

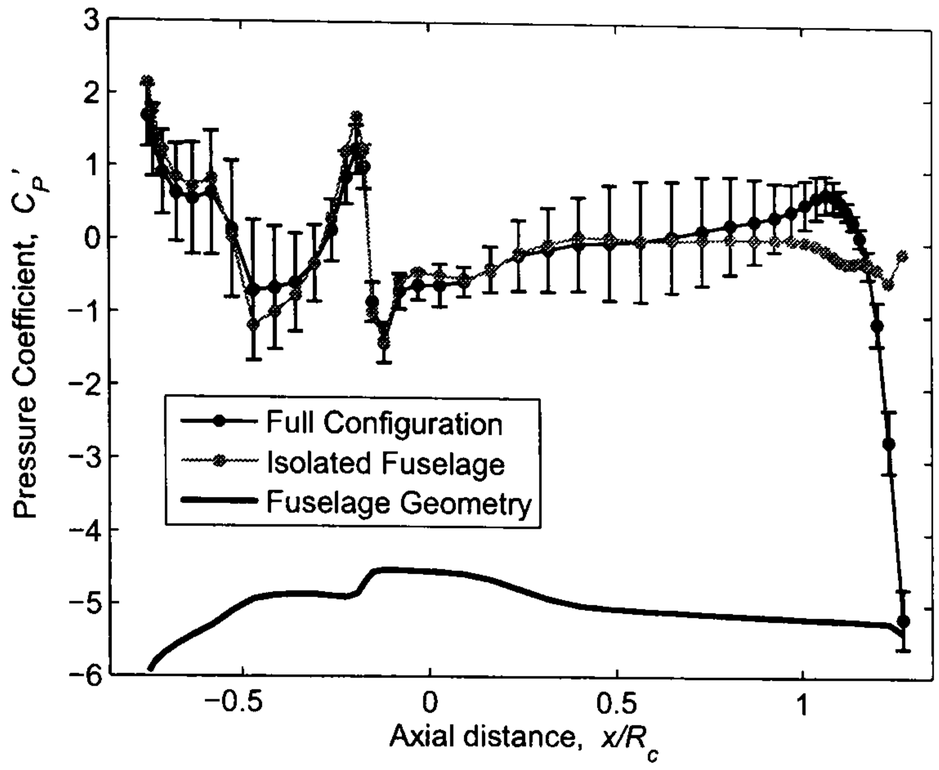


Figure 6.34: *Pressure variation along the top centreline of the fuselage at advance ratio* $\mu = 0.15$. *(Mean signal represented by curves, root-mean-square amplitude of fluctuating signal represented by error bars.)*

and lower rotors. This coherence results from the particular choice of phasing between the upper and lower rotors, but could quite feasibly be absent if the phasing were to be changed. A significant contribution to the unsteadiness in the loading on the propulsor at its own blade passage frequency arises only in the presence of the main rotor. This component of the unsteadiness in the loading on the propulsor is primarily an inherent characteristic of the aerodynamics of the rotor when operated in the skewed onset flow that is induced by the main rotor, but an additional contribution at blade-passage and higher frequency undoubtedly arises from smaller-scale, chopping-type interactions between the individual blades of the propulsor and the main rotor vortices.

6.6.5 Fuselage

The variation of the pressure coefficient along the top centreline of the fuselage is shown in Figure 6.34. In this figure, the pressure distribution along the fuselage of the full configuration is compared with that along the isolated fuselage when flying at the same forward speed (at $\mu = 0.15$). Comparing Figure 6.34 with Figure 6.7(c), it is evident that the effects of the main rotor and its wake on the mean component of pressure on the fuselage is most pronounced at the rear of the fuselage where the wake vortices pass

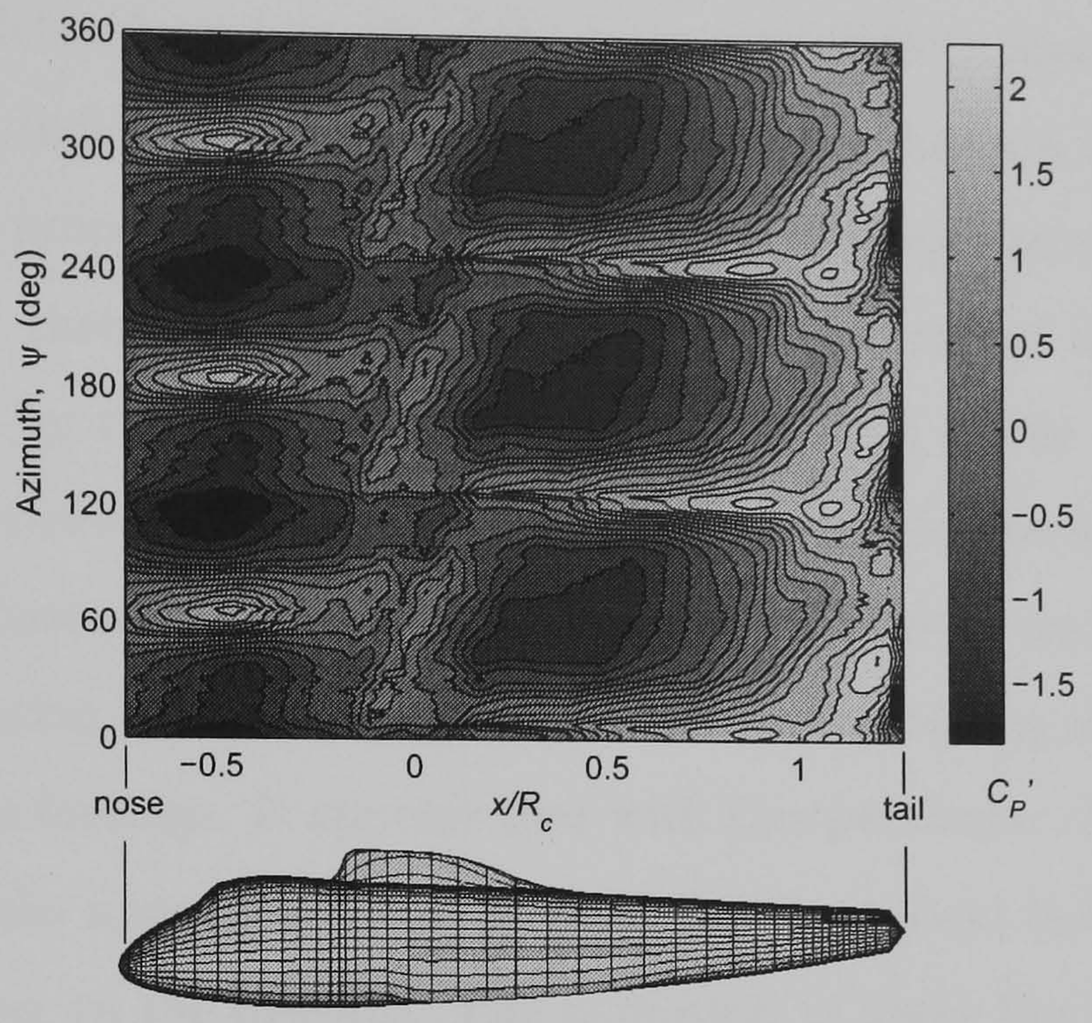


Figure 6.35: *Pressure distribution along the top centreline of the fuselage as a function of time (main rotor azimuth) at advance ratio* $\mu = 0.15$. *Mean component of signal removed.*

very close to the surface of the fuselage. The limited extent of this direct interaction is a consequence of the particular advance ratio of the simulated case presented here. For similar reasons, the propulsor has minimal effect on the pressure distribution on the fuselage. At lower forward speed, where the wake of the main rotor impinges on a much larger proportion of the fuselage, the effect of the main rotor in producing a significant download on the fuselage is much more pronounced, however.

The most pronounced effect of the main rotor system on the fuselage at the advance ratio of the case presented here is to introduce significant unsteadiness into the aerodynamic loading on the fuselage. The vertical bars in Figure 6.34 represent the root-mean-square amplitude of the fluctuations in pressure along the top centreline of the fuselage. The greatest fluctuations are experienced on those parts of the fuselage that lie directly below the main rotor blades. To reveal the origins of the pressure fluctuations in more detail, Figure 6.35 shows the pressure along the top centreline of the fuselage, plotted as a function of main rotor azimuth (in other words, as a function of time). The plot shows two distinct types of feature. The most obvious features in this diagram are the horizontal ridges of elevated pressure that extend from the nose of

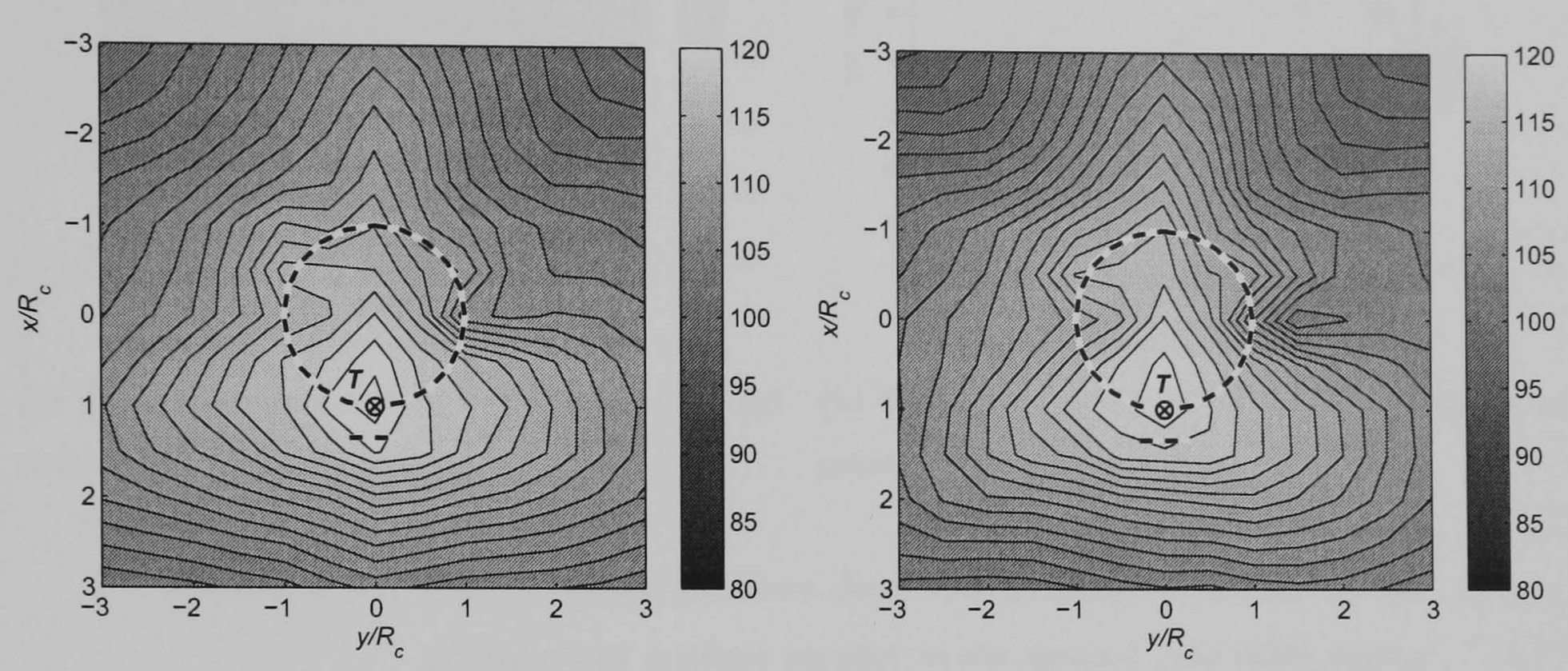
the helicopter to just short of the hub of the main rotor (at $x/R_c = 0$), then continue, after a short time delay, from just aft of the main rotor hub to near the tail. The form of these features is indicative of a series of disturbances that are felt instantaneously along a significant proportion of the fuselage. The three-per-revolution character of these features, and their phasing between the front and rear of the fuselage, reveals them to be caused by the direct passage over the fuselage of the blades of the main rotor. The three-per-revolution rather than six-per-revolution character of these disturbances is again a consequence of the rotor phasing — the upper and lower rotors of the simulated configuration were arranged to overlap with the blades aligned with the longitudinal axis of the fuselage. It appears that with this particular choice of phasing the disturbances from the upper and lower rotors combine to yield the strongest effect on the unsteady loading on the fuselage. The amplitude of these blade overpressure-type events could quite feasibly be altered though by modifying the phasing of the upper and lower rotors, but not without consequence for the unsteadiness in the loading on the propulsor alluded to earlier, and possibly also for the acoustic signature of the system as described later in this chapter.

The secondary, diagonal features in this form of presentation of pressure data are characteristic of pressure disturbances that are induced by the convection along the length of the fuselage of vortical structures within the flow. Comparison of Figures 6.22(b) and 6.35 shows these disturbances to be associated primarily with the passage of the root vortices (for $-0.1 < x/R_c < 0.3$) and the tip vortices (for $1.0 < x/R_c < 1.3$) from the main rotor in close proximity to the surface of the fuselage.

6.7 Interactional Aeroacoustics

This final section of the chapter considers the effect of the aerodynamic interactions between the various components of the system on the noise produced by the thrust-compounded hingeless coaxial configuration. The radiated acoustic field of the vehicle is computed using the Farassat-1A formulation of the Ffowcs Williams-Hawking equations [51] (see Section 2.8, Chapter 2). Noise due to quadrupole terms is neglected in the present work as is any acoustic radiation or reflection from the fuselage. In the interests of brevity, data for only one observer plane, located one rotor radius below the hub of

the lower main rotor, is presented here. The acoustic sources are scaled to represent the noise that is generated by an aircraft with a main rotor radius of 5.5 m, a main rotor speed of 345 rpm and an all-up weight of 5562 kg and thus to be representative of a helicopter of the size and weight of the XH-59A [85].

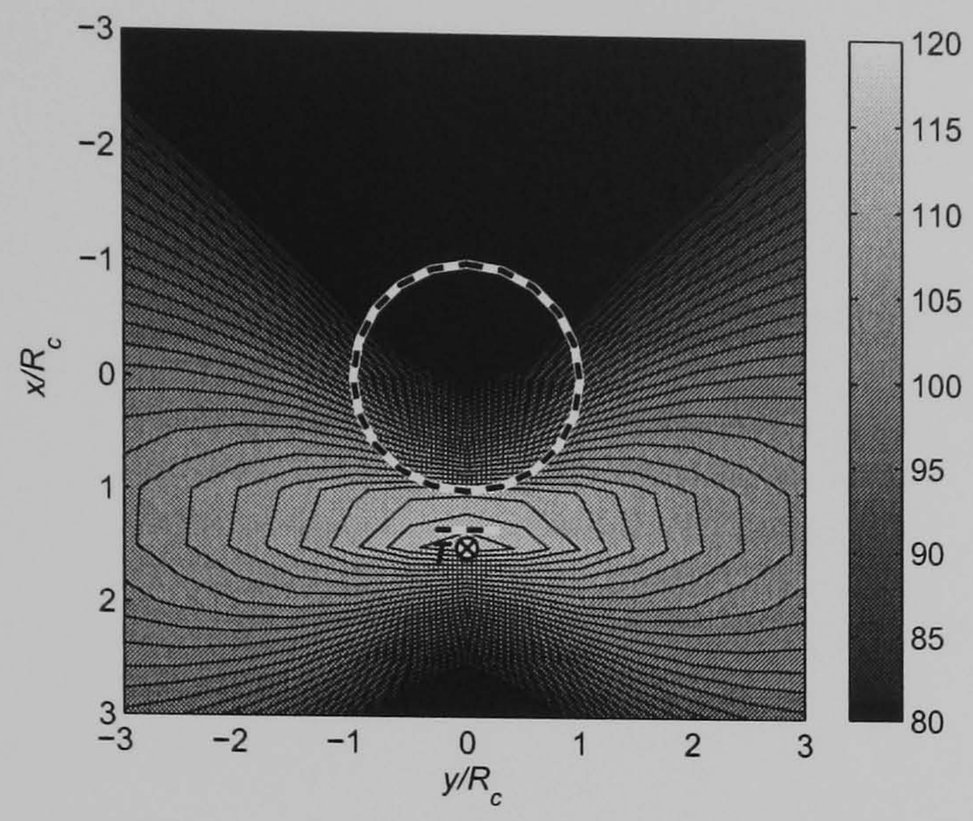


(a) Full configuration with fuselage (sound pressure at 'T' is 120.7 dB)

(b) Configuration without fuselage (sound pressure at 'T' is 114.7 dB)

Figure 6.36: *Overall sound pressure level (in decibels) produced by the main rotor and propulsor on a plane parallel to the ground, one rotor radius below the hub of the lower main rotor at advance ratio $\mu = 0.15$. (Rotor positions marked by dashed lines.)*

Figure 6.36 shows contours of overall sound pressure on the observer plane below the helicopter, and reveals that the dominant contribution to the noise produced by the system on this plane is from the propulsor. The thickness noise produced by the propulsor is particularly significant because of the rotor's relatively high tip Mach number ($M = 0.7$ assuming sea-level conditions). Figure 6.37(a) shows the contribution to the noise on the observer plane from the propulsor in isolation, and illustrates how its noise radiates directly outwards within its tip-path plane to produce a narrow band of extremely high acoustic pressure on the observer plane. The maximum sound pressure level produced by the propulsor on the observer plane is estimated to be approximately 115 dB. It should be noted though that the design of the blades of the simulated propulsor is exceptionally simple and that, in practice, the acoustic signature of this device



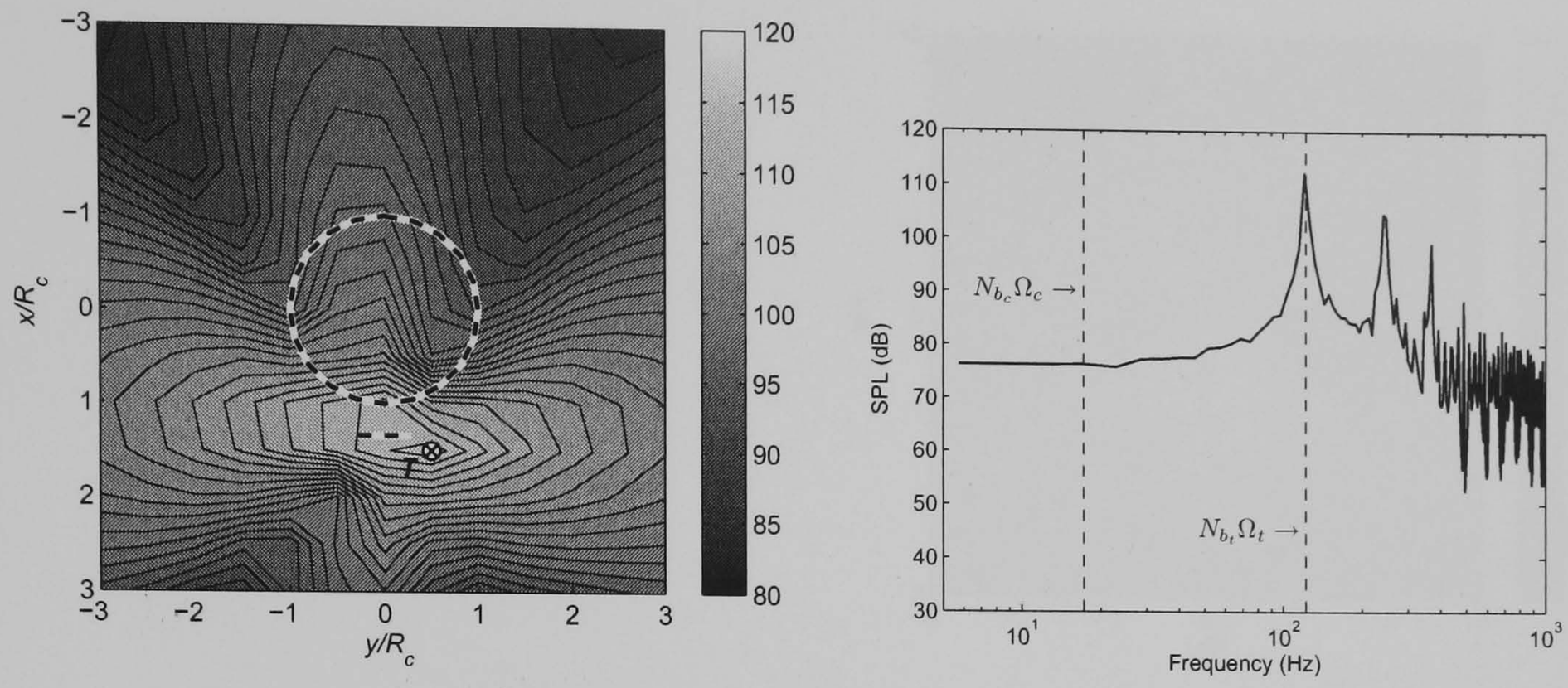
(a) Total noise produced by the propulsor (sound pressure at 'T' is 114.9 dB)

(b) Frequency spectrum of acoustic pressure at point 'T' in figure at left

Figure 6.37: *Overall sound pressure level (in decibels) produced by the propulsor on a plane parallel to the ground, one rotor radius below the hub of the lower main rotor when operated in isolation at advance ratio $\mu = 0.15$. (Rotor positions marked by dashed lines.)*

could quite feasibly be ameliorated by the introduction of tip sweep or by more appropriate aerofoil selection. As shown in Figure 6.37(b), the noise from the propulsor, as might be expected from the observations made above, is concentrated at its blade passage frequency and integer multiples thereof [86]. When integrated into the full configuration, the noise produced by the propulsor on the observer plane is distorted quite significantly by the loading perturbations that are induced by its interaction with the main rotor. Comparing Figures 6.37 and 6.38, it can be seen that these aerodynamic interactions cause a significant proportion of the acoustic radiation from the propulsor to be directed forward along the longitudinal axis of the aircraft.

The aerodynamic interactions within the system also have a significant effect on the noise that is produced by the main rotor. Figure 6.39 shows the contribution of the main rotor system to the sound pressure level on the observer plane below the helicopter. In the absence of the aerodynamic influence of the fuselage, the position of maximum sound intensity (marked 'T' in the diagram) is located significantly further forward below the rotor in comparison to its position on the full configuration. This

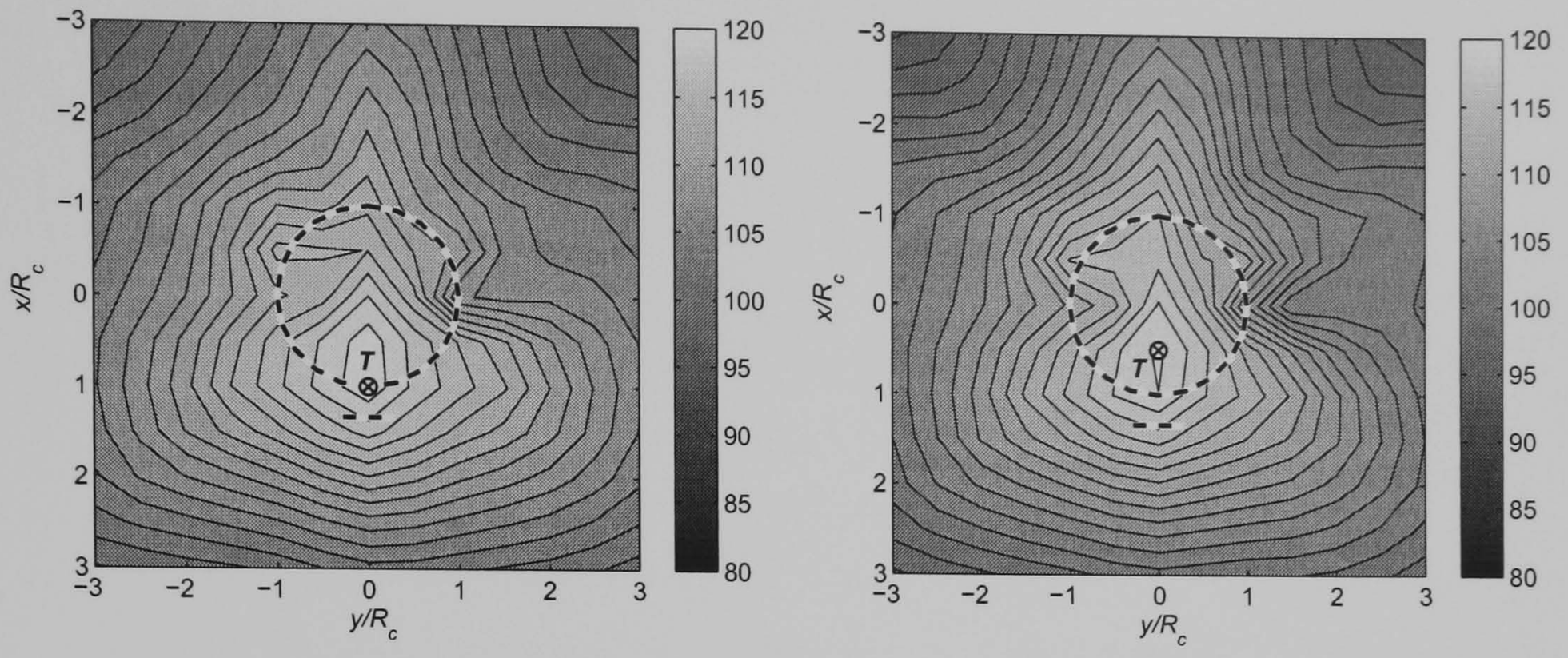


(a) Total noise produced by the propulsor (sound pressure at 'T' is 114.7 dB)

(b) Frequency spectrum of acoustic pressure at point 'T' in figure at left

Figure 6.38: *Contribution from the propulsor to the sound pressure level (in decibels) produced by the full helicopter configuration on a plane parallel to the ground, one rotor radius below the hub of the lower main rotor at advance ratio $\mu = 0.15$. (Rotor positions marked by dashed lines.)*

is consistent with the shift in loading on the rotor, described earlier, that is required to trim the pitching moment on the aircraft that is induced by the impingement of the wake of the main rotor on the tailplane. The maximum sound pressure produced by the main rotor is about 119 dB, and is about 1 dB higher for the full configuration than when the fuselage is absent. Figure 6.40 shows the same data as presented in Figure 6.39, filtered to contain only those harmonics between 5 to 40 times the main rotor blade-passage frequency and hence to expose the component of noise that can be associated directly with the blade vortex interactions (BVIs) that are responsible for the well-defined, ridge-like perturbations in the inflow distribution through the main rotor shown in Figure 6.24. Comparison of Figures 6.40(a) and (b), which contrast the BVI-related acoustic signature of the aircraft with and without the tailplane (and fuselage) present, shows the extent of the region of maximum BVI sound intensity to be quite significantly altered in the presence of the fuselage. This observation serves to indicate that the primary reason for the concentration of BVI-related sound below the left rear of the main rotor system is the concentration in loading on the rear of the disc



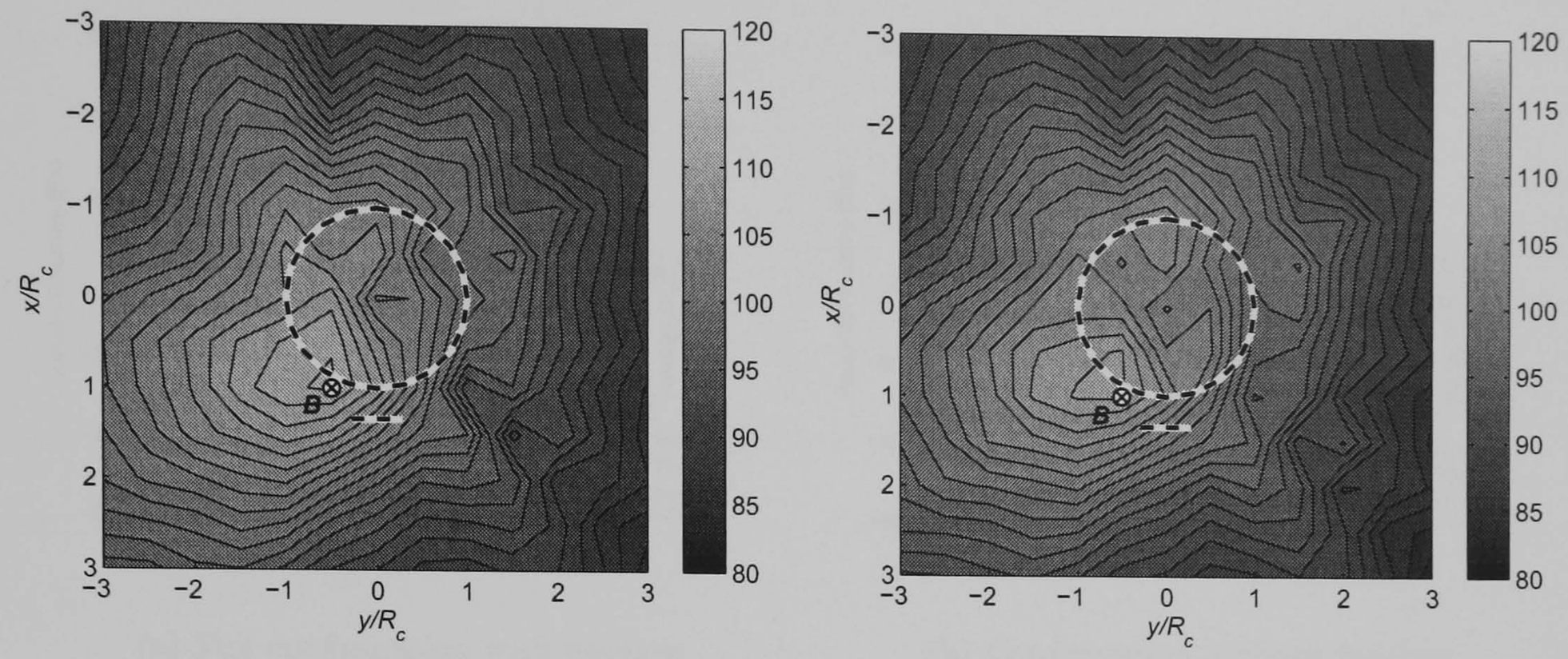
(a) Full configuration with fuselage (sound pressure at 'T' is 119.7 dB)

(b) Configuration without fuselage (sound pressure at 'T' is 119.0 dB)

Figure 6.39: *Contribution from the main rotor to the sound pressure level (in decibels) produced by the helicopter configuration on a plane parallel to the ground, one rotor radius below the hub of the lower main rotor at advance ratio* $\mu = 0.15$. *(Rotor positions marked by dashed lines.)*

in response to the requirement to trim the moment from the tailplane. A change in maximum BVI-related sound pressure at the location of maximum sound pressure level (marked 'B' in the diagrams) from 108 dB with the fuselage absent to about 110 dB for the full configuration is most likely a response to the subtle changes in the strength and position of individual BVIs that was referred to in connection with Figure 6.24 and that was attributed to the distortion of the trajectory of the wake of the main rotor by the fuselage.

The dominant influence of the propulsor runs the risk of obscuring the rather subtle effect of the interactions within the system on the acoustic signature of the entire aircraft. It should be borne in mind that the acoustic influence of the propulsor is spatially rather confined, and indeed, away from the disc-plane of the propulsor, the acoustic signature of the vehicle consists of a more balanced combination of acoustic contributions from the propulsor and main rotor. Figure 6.41, for instance, shows the history, over a single main rotor revolution, of the acoustic pressure at the points marked 'T' in the plots of overall sound pressure level on the observer plane below the helicopter shown

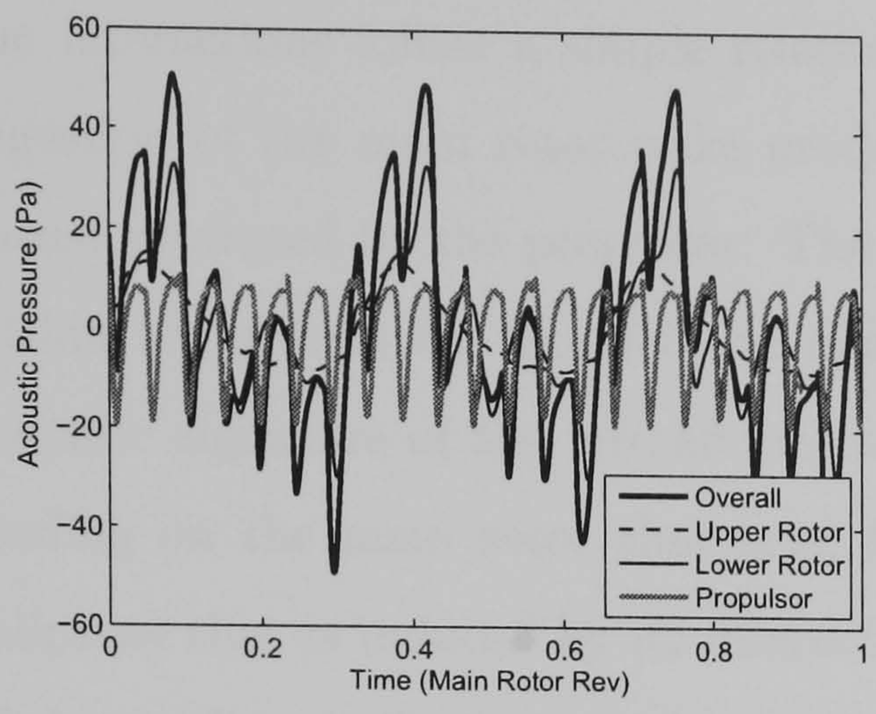


(a) Full configuration with fuselage (sound pressure at 'B' is 110.2 dB)

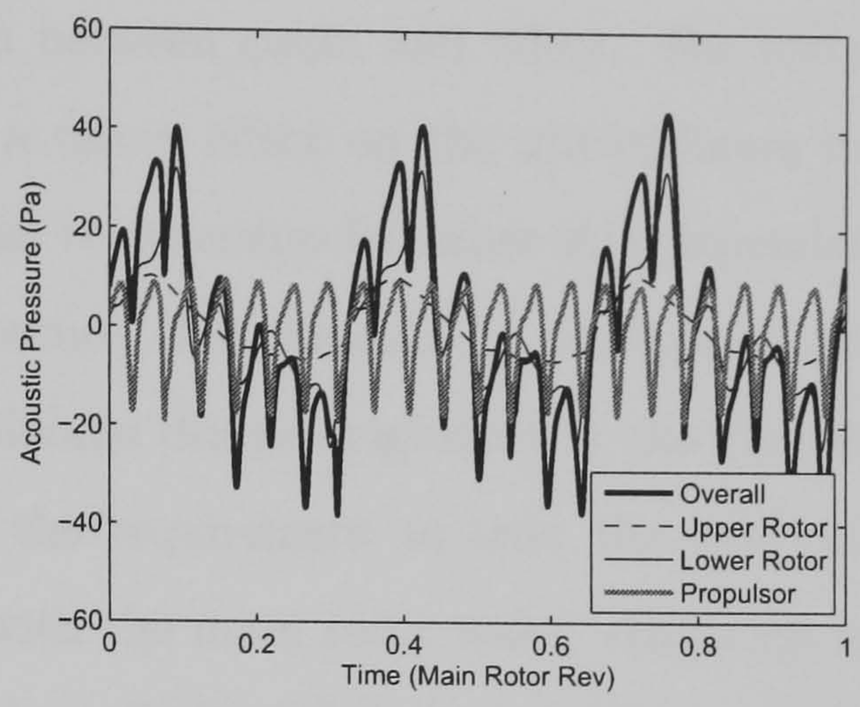
(b) Configuration without fuselage (sound pressure at 'B' is 107.7 dB)

Figure 6.40: *Contribution from the main rotor to the sound pressure level (in decibels) in the BVI frequency range produced by the helicopter configuration on a plane parallel to the ground, one rotor radius below the hub of the lower main rotor at advance ratio $\mu = 0.15$. (Rotor positions marked by dashed lines.)*

in Figure 6.36. This figure reveals the rather different character of the acoustic contribution from upper and lower rotors of the coaxial system — the contribution from the upper rotor is essentially at its blade-passage frequency and lacks the higher-harmonic content that arises on the lower rotor as a result of its loading being more strongly influenced by localised blade vortex interactions. At this observer location, the acoustic contribution from the propulsor is primarily at its blade passage frequency, but has a clearly observable, additional component that appears to be aperiodic and that arises from its interaction with the wake from the main rotor. The influence of the interaction between the main rotor, fuselage and tailplane, through the mechanisms described earlier, in increasing the peak-to-peak acoustic signal from the system by approximately 10 Pa (which translates to about 6 dB difference) is also more clearly apparent in this rendition of the data than perhaps in the maps of overall sound pressure level presented above.



(a) Full configuration with fuselage



(b) Configuration without fuselage

Figure 6.41: *Time-history of acoustic pressure at the locations of maximum sound pressure level, marked 'T' in Figure 6.36.*

6.8 Summary

The aerodynamic and acoustic characteristics of a generic hingeless coaxial helicopter with a tail-mounted propulsor and stabiliser have been simulated using the VTM. This has been done to investigate the ability of models of this type to capture the aerodynamic interactions that are generated between the various components of realistic, complex helicopter configurations. Simulations reveal the aerodynamic environment of the coaxial main rotor of the configuration to be dominated by internal interactions that lead to high vibration and noise. The wake of the main rotor is predicted to interact strongly with the tailplane, particularly at low forward speed, to produce a strong nose-up pitching moment that must be countered by significant longitudinal cyclic input to the main rotor. The wake from the main rotor is ingested directly into the tail propulsor over a broad range of forward speeds, where it produces significant vibratory excitation of the system as well as broadband noise. The numerical calculations also suggest the possibility that poor scheduling of the partition of the propulsive force between the main rotor and propulsor as a function of forward speed may yield a situation where the propulsor produces little thrust but high vibration as a result of this interaction.

By comparing the aerodynamics of the full configuration of the helicopter to the aerodynamics of various combinations of its sub-components, the influence of these

aerodynamic interactions on the behaviour of the system can be isolated. Many of the interactions follow a simple relationship between cause and effect. For instance, ingestion of the main rotor wake produces a direct effect on the unsteadiness in the thrust produced by the propulsor. The causal relationship for other interdependencies within the system are found to be more obscure. For instance, a dependence of the acoustic signature of the aircraft on the tailplane design originates in the changes in loading on the main rotor that arise from the requirement to trim the load on the tailplane that is induced by its interaction with the main rotor wake. Although many of the predicted effects might be ameliorated or eliminated entirely by more careful or considered design, the model captures many of the aerodynamic interactions, and the resultant effects on the loading on the system, that might be expected to characterise the dynamics of such a vehicle.

The traditional approach to the analysis of interactional effects on the performance of the helicopter relies on characterising the system in terms of a network of possible interactions between the separate components of its configuration. This approach, although conceptually appealing, may obscure the closed-loop nature of some of the aerodynamic interactions within the helicopter system. It is suggested that modern numerical simulation techniques may be ready to supplant any overt reliance on this reductionist type approach and hence may help to forestall future repetition of the long history of unforeseen, interaction-induced dynamic problems that have arisen in various new helicopter designs.

Chapter 7

Conclusions

Helicopters that use a twin counter-rotating coaxial main rotor system have recently generated renewed interest as a potential solution to future requirements for an efficient heavy-lift machine that is also capable of much higher forward flight speeds than conventional rotary-winged vehicles have traditionally been able to achieve. The aim of the research presented in this dissertation is to further the current understanding of the aerodynamic characteristics of coaxial rotors using high-resolution wake modelling to capture the flow physics associated with such rotor systems. In this vein, the Vorticity Transport Model (VTM), developed by Brown, is used to simulate the aerodynamics of various coaxial rotor systems ranging from an isolated rotor system to a complete aircraft.

The relative merit of a twin coaxial rotor over a conventional single rotor in terms of efficiency and performance has long been a point of contention. Comparisons made in the existing literature have often failed to account correctly for the essential differences in the configurations of the two types of rotor and thus on occasion have drawn seemingly conflicting conclusions [1]. Numerical results from the VTM have been used to establish a rational approach to a like-for-like comparison of performance between coaxial and conventional single rotor systems. It should be borne in mind, however, when extrapolating isolated rotor data to full helicopter systems, that the comparisons of performance can be skewed by the additional 5–10% of the main rotor power that is required by the tail rotor of the single rotor platform to trim the yaw moment in the system [55]. This torque compensation is provided inherently within the coaxial system.

The numerical results obtained by replicating Harrington's experiment [11] have been used to highlight the potential for misrepresentation of the relative merit of the coaxial rotor when compared to a rotor of more conventional configuration. In the experiment, the performance of one of the constituent rotors of the coaxial system was compared to the performance of the entire coaxial system. Because of its lower solidity, the single rotor is inherently limited in thrust-generating capability by blade stall, and hence, even when the numerical results are normalised by solidity, the comparison of the performance of the two systems is misleading. It was proposed that the equivalent, conventional single rotor should thus have the same total number of blades as the coaxial system and that the blades of the two systems should be geometrically identical. As the two rotor systems then have the same solidity, the lifting potential of the two systems is matched. In other words, blade stall cannot obscure the comparison between the two systems and the blades also operate in a comparable aerodynamic environment. This definition is shown to yield a fair like-for-like comparison between the two disparate systems. The differences in the performance of the two systems, when defined to be equivalent in this way, are then induced solely by the fundamental difference in the way that the wakes of the two types of rotor interact with the blades. It is expected that a similar approach might be adopted for comparisons of the relative performance between other dual rotor configurations and a suitably defined equivalent single rotor in order to highlight their aerodynamic differences.

The performance of a coaxial rotor in hover, in steady forward flight, and in a level, coordinated turn has been contrasted with that of an equivalent, conventional rotor with the same overall solidity, number of blades and blade aerodynamic properties. Simulations using the VTM have allowed differences in the performance of the two systems (without undue complication from fuselage and tail rotor effects) to be investigated in terms of the profile, induced and parasite contributions to the overall power consumed by the rotors, and for these differences to be traced to differences in the structure of the wakes of the two systems. Comparison of numerical predictions against experimental data has shown that the overall power consumption is particularly sensitive to the model that is used to represent the drag polar for the blade aerofoil sections, and possibly thus to the precise operating conditions of the rotor blade. However, some degree of absolute quantification does appear to be justified when this variability in profile drag, hence

profile power, is removed to reveal the induced component of the power consumption.

In hover, the coaxial system was shown to consume less induced power than the equivalent conventional system. The wake of the coaxial system in hover is dominated, close to the rotors, by the behaviour of the individual tip vortices from the two rotors as they convect along the surface of two roughly concentric, but distinct, wake tubes. The axial convection rate of the tip vortices, particularly those from the upper rotor, is significantly greater than for the tip vortices of the same rotor operating in isolation. The resultant weakening of the blade-wake interaction yields a significantly reduced induced power consumption on the outer parts of the upper rotor that translates into the observed benefit in terms of the overall induced power required by the coaxial system.

In steady, forward flight, the coaxial rotor again shows a distinct induced power advantage over its equivalent, conventional system at transitional and low advance ratios, but at high advance ratio there is very little difference between the performance of the two systems. At a thrust coefficient of 0.0048, the maximum forward flight speed of the systems that were simulated was limited to an advance ratio of about 0.28 by stall on the retreating side of the rotors. The rather limited maximum performance of the two systems was most likely related to the low solidity of the rotors that were simulated. With the coaxial system, the near-simultaneous stall on the retreating sides of both top and bottom rotors leads to backwards flapping of both discs, although blade strike occurs at the back of the system because the upper rotor stalls more severely than the lower.

The structure of the wake generated by the coaxial and conventional systems is superficially similar at all advance ratios, and shows a transition from a tube-like geometry at low advance ratio to a flattened, aeroplane-like form at high forward speed. The formation of the wake of the coaxial rotor at post-transitional advance ratio involves an intricate process whereby the vortices from both upper and lower rotors wind around each other to create a single, merged pair of super-vortices downstream of the rotor. The loading on the lower rotor is strongly influenced by interaction with the wake from the upper rotor, and there is also evidence on both rotors of intra-rotor wake interaction especially at low advance ratio. In comparison, the inflow distribution on the conventional rotor, since the inter-rotor blade-vortex interactions are absent, is very

much simpler in structure.

Simulations of a wind-up turn at constant advance ratio again show the coaxial rotor to possess a distinct advantage over the conventional system — a reduction in power of about 8% for load factors between 1.0 and 1.7 is observed at an advance ratio of 0.12 and a thrust coefficient of 0.0048. As in forward flight, the improved performance of the coaxial rotor results completely from a reduction in the induced power required by the system relative to the conventional rotor. This advantage is offset to a certain degree by the enhanced vibration of the coaxial system during the turn compared to the conventional system. As in steady level flight, the turn performance is limited by stall and, in the coaxial system, by subsequent blade strike, at a load factor of about 1.7 for the low-solidity rotors that were used in this study. The inflow distribution on the rotors is subtly different to that in steady, level flight, and a progressive rearwards shift in the positions of the interactions between the blades and their vortices with increasing load factor appears to be induced principally by the effects of the curvature of the trajectory on the geometry of the wake. Results for the simulated wind-up turn are demonstrated to be very similar to those for steady turns at the same load factor, and right-hand turns (given that the conventional rotor, and the bottom rotor of the coaxial system, rotate in counterclockwise sense when viewed from above) appear to require marginally (1–2%) more power than left hand turns (the asymmetry is less marked for the coaxial system than for the equivalent, conventional rotor).

The observed differences in induced power required by the coaxial system and the equivalent, conventional rotor originate in subtle differences in the loading distribution on the two systems that are primarily associated with the pattern of blade-vortex interactions on the rotors. The beneficial properties of the coaxial rotor in forward flight and in steady turns appears to be a consequence of the somewhat greater lateral symmetry of its loading compared to the conventional system. This symmetry allows the coaxial configuration to avoid, to a small extent, the drag penalty associated with the high loading on the retreating side of the conventional rotor. It is important, though, to acknowledge the subtlety of the effects that lead to the reduced induced power requirement of the coaxial system. The computations suggest that the benefits of the coaxial system do not come about merely through a broad redistribution in the loading on the system, as might be captured by a very simple model for rotor performance in

which the presence of localised blade-vortex interactions is wholly neglected (e.g. blade element – momentum theory), but rather through the effect this shift in loading has in modifying the character and strength of the localised interaction between the developing super-vortices and the highly-loaded blade-tip regions of the rotors. Reliable prediction of these effects is well beyond the scope of simple models and is absolutely dependent on accurate prediction of the detailed structure of the rotor wake.

The effects of hub stiffness on the natural frequency of blade flapping were introduced into the simulations by modelling the blades of the rotors as being completely rigid and applying springs across the flapping hinges of articulated rotor hubs. The number of control degrees of freedom inherent in the coaxial system allows four different strategies to be adopted if the system is to be trimmed to a prescribed aircraft weight and propulsive force component while producing zero net moment. The most practical approach is to couple the cyclic controls to the upper and lower rotors so that the same control inputs are made to both systems. Alternatively, it is possible to fix the cyclic controls of one of the rotors and to use the other alone to cancel the pitching and rolling moments produced by the system. Finally, each rotor can be trimmed to produce zero pitching and rolling moment independently. Of these strategies, coupling the cyclic controls and using both rotors to produce the necessary pitching and rolling moments on the system requires the least power. This appears to be because, using this technique, the elevated loads that are introduced into the rotor system by the controls interfere the least with the established pattern of blade vortex interactions (BVI) on the rotor discs and thus produce the smallest overall increment in induced power consumption.

Introduction of flapping stiffness into the system has a marked effect on the power consumption of the coaxial rotor in forward flight. Calculations suggest that the equivalent articulated system has a power requirement that is over twenty percent greater than that of the rigid system when trimmed to an equivalent flight condition. Most of this enhanced power requirement can be attributed to a large increase in the induced power of the system when the blades of the rotors are allowed to flap freely. Most of the advantage of the rigid configuration is retained if the stiffness of the rotors is reduced to practical levels, but the performance of the system with finite stiffness deteriorates quite significantly as the forward speed of the system is reduced. In high-speed forward

flight, significant further power savings can be achieved, at least in principle, if an auxiliary device is used to alleviate the requirement for the main rotor system to produce a propulsive force component, and, indeed, such an arrangement might be necessary to prevent rotor performance being limited by aerodynamic stall.

Simulations suggest that the unsteady aerodynamic forcing of very stiff rotor systems is relatively insensitive to the actual flapwise stiffness of the system. This implies that simple palliative measures, such as structural tailoring, may have little effect in being able to modify the inherent vibrational characteristics of stiff coaxial rotor systems. The principal effect of the aerodynamic forcing of very stiff coaxial systems is to produce an excitation of the system, primarily at the fundamental blade passing frequency, in both pitch and heave, but aerodynamic interference between the rotors may introduce a small component of roll excitation into the vibration of the rotor. The characteristics of the vibratory forcing are also shown to be affected directly by the relative phasing of blade azimuth between the upper and lower rotor. By rearranging the phasing so that blade overpassage occurs at 45° out of phase from the original arrangement (such that the locations of the overpassage are modified from $\psi = 0°, 90°, 180°, 270°$ to $\psi = 45°, 135°, 225°, 315°$), the heave component of the vibratory excitation is attenuated but the forcing character in pitch and roll are essentially interchanged as a consequence. Changes in forcing character such as this may ultimately influence the dynamic behaviour of the overall aircraft but, of course, accurate representation requires a fuselage as well as the vibratory loads transmitted to the fuselage to be accounted for and these were not addressed in the present work.

The numerical results presented lend strong support to the existing contention that the introduction of flapwise stiffness can lead to a coaxial rotor system that possesses clear advantages in performance over the corresponding articulated system, and hence, by comparison against the results of previous studies, over the equivalent, conventional, planar rotor system. The results also lend some support, though, to the contention that the advantages of the coaxial rotor configuration in terms of overall performance may need to be offset against fundamentally unavoidable penalties in terms of the vibration, and thus, possibly, the noise that is produced by the lower rotor as a result of its aerodynamic interference with the wake that is produced by the upper rotor. It seems risky to jump to such overarching conclusions in the absence of the further

insight that could be gleaned from simulations of rotor systems that are more physically representative of full-scale practice than those tested here, however.

The aeroacoustic characteristics of a hinged coaxial rotor in forward flight, computed using Farassat-1A formulation of the Ffowcs Williams-Hawkings equation coupled to the VTM, are compared to those of a suitably defined aerodynamically equivalent single rotor. In all cases, the rotors were assumed to be carrying a weight of 5483 N and to have a tip speed of 143.0 m/s (corresponding to $C_T = 0.0048$ and $M_{tip} = 0.42$ respectively) and thus to be representative of Harrington's rotor in Dingeldein's forward flight experiment. In the intermediate far-field (less than two rotor radii from the rotor disc), the main contribution to the noise generated by both the coaxial and the equivalent single rotor systems is at the fundamental blade passage frequency. The coaxial rotor examined is this study is consistently noisier than the equivalent single rotor by approximately 10 dB. As expected, the noise generated by the coaxial rotor examined in this study is highly impulsive, principally as a result of inter-rotor blade-wake interactions on the lower rotor. It should be borne in mind, though, that a real conventional single rotor system will have an added acoustic contribution from the tail rotor that is required for torque balance. The acoustic characteristics of a tail rotor are highly sensitive to the rotor's exact configuration as well as to the details of its interaction with the wake of the main rotor. Although a comparison between any real systems would certainly warrant inclusion of the effects of the tail rotor, given the focus on the coaxial rotor configuration in this dissertation, any undue complication to the comparison is avoided by simply ignoring the effects of tail rotor in the case of the equivalent single rotor.

The BVI loading noise for the equivalent single rotor reduces with increasing forward speed as the disc tilt required to provide the propulsive force component to the system acts to increase the miss distance between the blades and their trailed vortices and thus to reduce the strength of individual BVI events. The BVI noise of the coaxial rotor is intensified with increasing forward speed due to the increasing strength of the interaction between the tip vortices from the upper rotor and the blades on the advancing side of the lower rotor. The impulsive noise due to BVI, as measured on a hemispherical surface that is located two rotor radii from the rotor hub, is about 20–35 dB higher for the coaxial rotor than for the equivalent single rotor, depending on the forward speed of the

rotor.

The higher BVI noise of helicopters with coaxial rotors may ultimately hinder their routine use in civilian and military applications. It may be possible to optimise the design of the rotor to mitigate the noise levels, however. A change of blade phasing between the upper and lower rotors had a marginal effect on the noise characteristics of the coaxial system. An increase of 30% in the separation distance between the upper and lower rotors resulted in a decrease of 2 dB in the maximum BVI sound pressure level. The weight, drag and structural dynamic penalties of the elongated mast may not be justified for such a marginal reduction in noise levels, however.

The introduction of significant flapwise stiffness into the coaxial system results in a marked reduction in the BVI noise that is produced by the system. This is a direct result of a re-distribution in loading, in which the principal inter-rotor BVIs, as identified for the conventionally articulated coaxial system, are weakened. This weakening occurs simply because the strength of the tip vortex trailed from the retreating blade of the upper rotor is reduced as the blade is offloaded. The relative orientation and the distance between the interacting blade and the vortex also appear to change subtly the direction of propagation of the BVI noise. While the rigid rotor assumption yields a reasonable representation of the overall aeroacoustic characteristics of the relatively generic coaxial rotor modelled in this study in terms of maximum sound pressure levels and noise directivity, as well as performance, direct comparison of real helicopter configurations may warrant an incorporation of structural dynamic model to account for the flexure of the rotor blades. Most importantly, though, the sensitivity of the amplitude and the direction of the BVI noise to rotor stiffness, arising from the re-distributed loading, suggests that it may be possible to alter these characteristics quite considerably by careful scheduling of the loads between the two rotors of the system.

Finally, the aerodynamic and acoustic characteristics of a generic, thrust-compounded coaxial helicopter have been simulated. The configuration that has been studied comprises a stiff coaxial main rotor system consisting of two, counter-rotating, three-bladed rotors. An auxiliary propulsor is mounted in pusher configuration at the rear of the fuselage, which features a horizontal tailplane mounted just forward of the propulsor. The various aerodynamic interactions that are predicted to arise within the system over a range of forward speeds have been analysed in detail, the aim of the work being to

show that modern computational techniques are advancing to a state where they can be used at an early stage in the design process to provide useful insight into the likely aeromechanical behaviour of realistic helicopter configurations.

The aerodynamic environment of the configuration that was studied is characterised by very strong aerodynamic interactions between its various components. The aerodynamic environment of the main rotors of the system is dominated by the direct impingement of the wake from the upper rotor onto the blades of the lower rotor, and the thrust and torque produced by the system are highly unsteady — particularly at low forward speed. The fluctuations in the loading on the coaxial system occur at the fundamental blade-passage frequency and are particularly strong as a result of the phase relationship between the signals from the upper and lower rotors, and also at twice the blade-passage frequency as a result of the loading fluctuations that are induced on the system as a result of direct blade overpassage. The results support the rationale behind previous studies that have suggested that the vibration that is produced by stiffened coaxial systems can be ameliorated by applying differential cyclic inputs to the upper and lower rotors or by modifying the phasing of the rotation of the upper rotor with respect to the lower.

The wake of the main rotor sweeps over the fuselage and tailplane at low forward speed, inducing a significant nose-up pitching moment on the tailplane that must be counteracted by longitudinal cyclic input to the main rotor. This pitch-up characteristic has been encountered during the development of several helicopters and has proved on occasion to be very troublesome to eradicate. Over a broad range of forward flight speeds, the wake from the main rotor is ingested directly into the propulsor, where it induces strong fluctuations in the loading produced by this rotor. These fluctuations occur at both the blade-passage frequency of the main rotor and of the propulsor, and are likely to excite significant vibration of the aircraft. The unsteady loading on the propulsor is intimately related to the passage of main rotor vortices such that the exact configuration of the main coaxial rotor, such as the number of blades and relative phasing, is expected to play a significant role in characterising the unsteady behaviour of the propulsor. The results suggest that this interaction, together with poor scheduling of the partition of the propulsive thrust between the main rotor and a rear-mounted propulsor with forward speed can lead to a distinctly non-optimal situation

where the propulsor produces significant vibratory excitation of the system but little useful contribution to its propulsion. The propulsor induces significant vibratory forcing on the tailplane at high forward speed. This forcing is at the fundamental blade-passage frequency of the propulsor, and suggests that the tailplane position in any vehicle where the lifting surface and propulsor are as closely coupled as in the present configuration may have to be considered carefully to avoid shortening the fatigue life of the tailplane. Nevertheless, the unsteady forcing of the tailplane is dominated by interactions with the wake from the main rotor — the fluctuations at the fundamental blade passage frequency of the main rotor that are observed in the pressure distribution on the tailplane are characteristic of the close passage of individual vortices over its surface.

The acoustic data on a plane below the system at one particular flight condition has been presented to suggest that the overall noise produced by the system, at least in slow forward flight, is significantly higher than that produced by similar conventional helicopters in the same weight class. The major contribution to the BVI noise comes from the lower rotor because of strong aerodynamic interaction with the upper rotor. The propulsor contributes significant noise over a broad frequency spectrum. At the flight condition that was considered, much of this noise is induced by interactions between the blades of the propulsor and the wake of the main rotor and tailplane.

The numerical calculations were thus able to reveal many of the aerodynamic interactions that might be expected to arise in a configuration as aerodynamically complex as the generic thrust-augmented coaxial helicopter that formed the basis of this study. Of course the exact form, and particularly the effect on the loading produced on the system, of these interactions may vary depending on the specifics of the configuration. Indeed, more careful or considered design may be capable of eliminating entirely some of the effects that were highlighted in this study.

By comparing the aerodynamics of the full configuration of the helicopter to the aerodynamics of various combinations of its sub-components, the influence of the various aerodynamic interactions within the system on its behaviour could be isolated. The traditional approach to the analysis of interactional effects on the performance of a helicopter relies on an initial characterisation of the system in terms of a network of possible interactions between the separate components of its configuration [75]. Thus, within the configuration that was studied, it is possible to identify the effect of the main

rotor on the fuselage and propulsor, the distortion of the wake of the main rotor that is caused by the presence of the fuselage, and so on. Many of the interactions that were exposed within the aerodynamics of the configuration exhibited a relatively linear relationship between cause and effect and hence would be amenable to the reductionist approach described above. For instance, the distortion of the wake of the main rotor by the fuselage has a marked effect on the loading generated by the propulsor, but the effect on the propulsor is prevented from feeding back into the performance of the main rotor. This is because of the isolation that is provided by the particular method that is used to trim the vehicle, and also by the inherent directionality of the interaction that results from its physics being dominated by the convection of the wakes of the two systems into the flow behind the vehicle.

Several of the interactions that have been observed for this helicopter configuration exhibit a less direct relationship between cause and effect, however. These interactions are characterised by strong feedback or closed-loop type behaviour, in certain cases through a path which remains relatively obscure and hidden within the network of interactions that form the basis of the traditional reductionist type approach. For instance, the load that is induced on the tailplane by the direct impingement of the wake of the main rotor requires, through the requirement for overall trim of the forces and moments on the aircraft, a compensatory change in the loading distribution on the main rotor itself, which then modifies the strength of its wake and hence in circular fashion, the loading on the tailplane itself. Without this understanding of the strong mutual coupling between the performance of the tailplane and the main rotor, the observed dependence of the acoustic radiation of the aircraft on the presence or not of the tailplane (or, in practical terms, more likely on its design and positioning) may appear to the analyst as a very obscure and possibly even unfathomable interdependence within the system.

Thus, although the reductionist, network-based approach to classifying the interactions present within the system is conceptually appealing and simple, it must be realised that the possible presence of feedback loops deep within the interactional aerodynamics, such as the one described above, may cause the approach to miss, obscure or hide the presence of interactions between some of the various sub-components of the system. The analysis presented in Chapter 6 warns against an overly literal application of this

reductive, building-block type approach to the categorisation of the interactions that are present within the system.

The research contained in this dissertation demonstrates that the current state of the art in computational modelling of helicopter aerodynamics has progressed in recent years to the point where the interactive aerodynamic flow field associated with a coaxial rotor system, and hence its performance, can be captured accurately. This assertion is extended further to apply to a compounded coaxial helicopter with a configuration that is similar to one of the complex designs that is currently being considered as a possible future high-performance rotorcraft. Many of the interactions highlighted in this dissertation result principally from subtle differences in the character and strength of localised aerodynamic interactions. Reliable prediction of these effects is well beyond the scope of simple models. This bodes well for the assertion that modern computational techniques, such as those embodied within the VTM, may be in a position to help forestall future repetition of the long history of unforeseen, interaction-induced problems that have arisen during the development of many of the helicopter designs that are currently in service.

References

[1] Coleman, C.P., "A Survey of Theoretical and Experimental Coaxial Rotor Aerodynamic Research," NASA TP-3675, March 1997.

[2] Gordon, Y., Komissarov, D., *Kamov -27/-32 Family*, Red Star Volume 29, Midland Publishing, UK, 2006.

[3] Anikin, V.A., "Aerodynamic Feature of a Coaxial Rotor Helicopter," Paper No. 66, 17th European Rotorcraft Forum, Berlin, Germany, 24–27 September 1991, pp. 533–551.

[4] Muren, P., "Passively Stable Rotor System for Indoor Hovering UAS," AHS/AIAA/RAeS/SAE 9th International Powered Lift Conference, London, UK, 22–24 July 2008.

[5] Cheney, M.C., Jr., "The ABC Helicopter," *Journal of the American Helicopter Society*, Vol. 14, No. 4, October 1969, pp. 10–19.

[6] Burgess, R.K., "The ABC™Rotor — A Historical Perspective," American Helicopter Society 60th Annual Forum, Baltimore, MD, 7–10 June 2004.

[7] Bagai, A., "Aerodynamic Design of the Sikorsky X2 Technology Demonstrator™ Main Rotor Blade," American Helicopter Society 64th Annual Forum, Montréal, Canada, 29 April–1 May 2008.

[8] Saito, S., Azuma, A., "A Numerical Approach to Co-axial Rotor Aerodynamics," Paper No. 42, 7th European Rotorcraft and Powered Lift Aircraft Forum, Garmisch-Partenkirchen, Germany, 8–11 September 1981.

[9] Andrew, M.J., "Coaxial Rotor Aerodynamics in Hover," *Vertica*, Vol. 5, 1981, pp. 163–172.

[10] Zimmer, H., "The Aerodynamic Calculation of Counter Rotating Coaxial Rotors," Paper No. 27, 11th European Rotorcraft Forum, London, UK, 10–13 September 1985.

[11] Harrington, R.D., "Full-Scale-Tunnel Investigation of the Static-Thrust Performance of a Coaxial Helicopter Rotor," NACA TN-2318, March 1951.

[12] Dingeldein, R.C., "Wind-Tunnel Studies of the Performance of Multirotor Configurations," NACA TN-3236, August 1954.

[13] Leishman, J.G., Syal, M., "Figure of Merit Definition for Coaxial Rotors," *Journal of the American Helicopter Society*, Vol. 53, No. 3, July 2008, pp. 290–300.

[14] Caradonna, F.X., "Developments and Challenges in Rotorcraft Aerodynamics," 38th AIAA Aerospace Sciences Meeting and Exhibit, AIAA 2000-0109, Reno, NV, 10–13 January 2000.

[15] Caradonna, F.X., "The Role of CFD in the Development of Rotorcraft Analyses — observations on accomplishments and difficulties, using the hover problem as an example," 2nd International Basic Research Conference on Rotorcraft Technology, Nanjing, China, 7–9 November 2005.

[16] Datta, A., Nixon, M., Chopra, I., "Review of Rotor Loads Prediction with the Emergence of Rotorcraft CFD," *Journal of the American Helicopter Society*, Vol. 52, No. 4, October 2007, pp. 287–317.

[17] Whitehouse, G.R., Boschitsch, A.H., Quackenbush, T.R., Wachspress, D.A., Brown, R.E., "Novel Eulerian Vorticity Transport Wake Module for Rotorcraft Flow Analysis," American Helicopter Society 64th Annual Forum Proceedings, Montréal, Canada, 29 April–1 May 2008.

[18] Kim, H.W., Brown, R.E., "Coaxial Rotor Performance and Wake Dynamics in Steady and Manoeuvring Flight," American Helicopter Society 62nd Annual Forum Proceedings, Phoenix, AZ, 9–10 May 2006.

[19] Kim, H.W., Brown, R.E., "A Rational Approach to Comparing the Performance of Coaxial and Conventional Rotors," *Journal of the American Helicopter Society*, accepted with revision, 2007.

[20] Kim, H.W., Brown, R.E., "A Comparison of Coaxial and Conventional Rotor Performance," *Journal of the American Helicopter Society*, accepted with revision, 2007.

[21] Kim, H.W., Duraisamy, K., Brown, R.E., "Aeroacoustics of a Coaxial Rotor in Level Flight," American Helicopter Society 64th Annual Forum Proceedings, Montréal, Canada, 29 April–1 May 2008.

[22] Kim, H.W., Brown, R.E., "Impact of Trim Strategy and Rotor Stiffness on Coaxial Rotor Performance," 1st AHS/KSASS International Forum on Rotorcraft Multidisciplinary Technology, Seoul, Korea, 15–17 October 2007.

[23] Kim, H.W., Kenyon, A.R., Duraisamy, K., Brown, R.E., "Interactional Aerodynamics and Acoustics of a Propeller-Augmented Compound Coaxial Helicopter," American Helicopter Society Aeromechanics Specialists' Meeting, San Francisco, CA, 23–25 January 2008.

[24] Kim, H.W., Kenyon, A.R., Duraisamy, K., Brown, R.E., "Interactional Aerodynamics and Acoustics of a Hingeless Coaxial Helicopter with an Auxiliary Propeller in Forward Flight," AHS/AIAA/RAeS/SAE 9th International Powered Lift Conference, London, UK, 22–24 July 2008.

[25] Kim, H.W., Kenyon, A.R., Duraisamy, K., Brown, R.E., "Interactional Aerodynamics and Acoustics of a Hingeless Coaxial Helicopter with an Auxiliary Propeller in Forward Flight," *Aeronautical Journal*, accepted with revision, 2008.

[26] Leishman, J.G., *The Helicopter — Thinking Forward, Looking Back*, College Park Press, Maryland, USA, 2007.

[27] Kim, H.W., Brown, R.E., "Modelling the Aerodynamics of Coaxial Helicopters — from an Isolated Rotor to a Complete Aircraft," Proceedings of the EU-Korea Conference on Science and Technology, Heidelberg, Germany, 28–31 August 2008.

[28] Brown, R.E., "Rotor Wake Modeling for Flight Dynamic Simulation of Helicopters," *AIAA Journal*, Vol. 38, No. 1, January 2000, pp. 57–63.

[29] Brown, R.E., Line, A.J., "Efficient High-Resolution Wake Modeling Using the Vorticity Transport Equation," *AIAA Journal*, Vol. 43, No. 7, April 2005, pp. 1434–1443.

[30] Brown, R.E., Houston, S.S., "Comparison of Induced Velocity Models for Helicopter Flight Mechanics," *AIAA Journal of Aircraft*, Vol. 37, No. 4, July 2000, pp. 623–629.

[31] Ahlin, G.A., Brown, R.E., "Investigating the Physics of Rotor Vortex-Ring State using the Vorticity Transport Model," Paper 89, 31st European Rotorcraft Forum, Florence, Italy, 13–15 September 2005.

[32] Ahlin, G.A., Brown, R.E., "The Vortex Dynamics of the Rotor Vortex Ring Phenomenon," American Helicopter Society 63rd Annual Forum Proceedings, Virginia Beach, VA, 1–3 May, 2007.

[33] Whitehouse, G.R., Brown, R.E., "Modeling the Mutual Distortions of Interacting Helicopter and Aircraft Wakes," *Journal of Aircraft*, Vol. 40, No. 3, May 2003. pp. 440–449.

[34] Whitehouse, G.R., Brown, R.E., "Modelling a Helicopter Rotor's Response to Wake Encounters," *Aeronautical Journal*, Vol. 108, No. 1079, January 2004, pp. 15–26.

[35] Brown, R.E., Whitehouse, G.R., "Modeling Rotor Wakes in Ground Effect," *Journal of the American Helicopter Society*, Vol. 49, No. 3, July 2004, pp. 238–249.

[36] Phillips, C., Brown, R.E., "Eulerian Simulation of the Fluid Dynamics of Helicopter Brownout," American Helicopter Society 64th Annual Forum Proceedings, Montréal, Canada, 29 April–1 May 2008.

[37] Toro, E.F., "A Weighted Average Flux Method for Hyperbolic Conservation Laws," *Proceedings of the Royal Society of London. Series A, Mathematical and Physical Sciences*, Vol. 423, No. 1864, 1989, pp. 401–418.

[38] Brown, R.E., "Numerical Solution to the Two-Dimensional Navier-Stokes Equations Using Viscous-Convective Operator Splitting," *M.Sc. Thesis*, College of Aeronautics, Cranfield Institute of Technology, 1990.

[39] Harlow, F.H., Welsh, J.E., "Numerical Calculation of Time Dependent Viscous Incompressible Flow with Free Surface," *Phyics of Fluid*, Vol. 8, 1965, pp. 2182–2189.

[40] Toro, E.F., "Some Aspects of Shock Capturing Methods for Gas Dynamics," College of Aeronautics Report No. 9112, Cranfield Institute of Technology, June 1991.

[41] Strang, G., "On the Construction and Comparison of Finite Difference Schemes," *SIAM Journal on Numerical Analysis*, Vol. 5, No. 3, September 1968, pp. 506–517

[42] Weissinger, J., "The Lift Distribution of Swept-Back Wings," NACA TM 1120, March 1947

[43] Beddoes, T.S., "A Synthesis of Unsteady Aerodynamic Effects Including Stall Hysteresis," *Vertica*, Vol. 1, 1976, pp. 113–123.

[44] Beddoes, T.S., "Representation of Airfoil Behaviour," *Vertica*, Vol. 7, No. 2, 1983, pp. 183–197.

[45] Beddoes, T.S., "Practical Computation of Unsteady Lift," *Vertica*, Vol. 8, No. 1, 1984, pp. 55–71.

[46] Gross, D.W., Harris, F.D., "Prediction of In-Flight Stalled Airloads from Oscillating Airfoil Data," American Helicopter Society 25th Annual National Forum, Washington, D.C., 14–16 May 1969

[47] Gormont, R.E., "A Mathematical Model of Unsteady Aerodynamics and Radial Flow for Application to Helicopter Rotors," USAAVLABS TR 72-67

[48] Ffowcs Williams, J.E., Hawkings, D.L. "Sound Generation by Turbulence and Surfaces in Arbitrary Motion," *Philosophical Transactions of the Royal Society of London. Series A, Mathematical and Physical Sciences*, Vol. 264, No. 1151, May 1969, pp. 321–342.

[49] Schmitz, F., Yu, Y., "Theoretical Modeling of High-Speed Helicopter Impulsive Noise," *Journal of the American Helicopter Society*, Vol.23, No.1, 1979.

[50] Brentner, K., Farassat, F., "Modeling Aerodynamically Generated Sound of Helicopter Rotors," *Progress in Aerospace Sciences*, Vol. 39, 2003.

[51] Farassat, F., Succi, G.P., "A Review of Propeller Discrete Frequency Noise Prediction Technology with Emphasis on Two Current Methods for Time Domain Calculations," *Journal of Sound and Vibration*, Vol. 71, No. 3, 1980, pp. 399–419.

[52] van der Wall, B.G., Junker, B., Burley, C.L., Brooks, T.F., Yu, Y.H., Tung, C., Raffel, M., Richard, H., Wagner, W., Mercker, E., Pengel, K., Holthusen, H., Beaumier, P., Delrieux, Y., "The HART II Test in the LLF of the DNW—a Major Step towards Rotor Wake Understanding," *28th European Rotorcraft Forum*, Bristol, UK, 17–20 September 2002.

[53] Kelly, M.E., Duraisamy, K., Brown, R.E., "Blade Vortex Interaction and Airload Prediction using the Vorticity Transport Model," American Helicopter Society Specialists' Conference on Aeromechanics, San Francisco, CA, 23–25 January 2008.

[54] Kenyon, A.R., Brown, R.E., "Wake Dynamics and Rotor-Fuselage Aerodynamic Interactions," American Helicopter Society 63rd Annual Forum Proceedings, Virginia Beach, VA, 1–3 May 2007.

[55] Leishman, J.G., *Principles of Helicopter Aerodynamics, Second Edition*, Cambridge University Press, Cambridge, UK, 2006.

[56] Lakshminarayan, V.K., Duraisamy, K., Baeder, J.D., "Computational Investigation of Coaxial Rotor Aerodynamics in Hover," American Helicopter Society 63rd Annual Forum Proceedings, Virginia Beach, VA, 1–3 May 2007.

[57] Lakshminarayan, V.K., Baeder, J.D., "High Resolution Computational Investigation of Trimmed Coaxial Rotor Aerodynamics in Hover," American Helicopter Society Aeromechanics Specialists' Meeting, San Francisco, CA, 23–25 January 2008.

[58] Landgrebe, A.J., "The Wake Geometry of a Hovering Helicopter Rotor and Its Influence on Rotor Performance," *Journal of the American Helicopter Society*, Vol. 17, No. 4, October 1972, pp. 2–15.

[59] Paglino, V.M., "Forward Flight Performance of a Coaxial Rigid Rotor," American Helicopter Society 27th Annual National V/STOL Forum, Washington, D.C., May 1971.

[60] Bhagwat, M.J., Leishman, J.G., "On the Aerodynamic Stability of Helicopter Rotor Wakes," American Helicopter Society 56th Annual Forum Proceedings, Virginia Beach, VA, 2–4 May 2000.

[61] Newman, S., Brown, R., Perry, J., Lewis, S., Orchard, M., Modha, A., "Predicting the Onset of Wake Breakdown for Rotors in Descending Flight," *Journal of the American Helicopter Society*, Vol. 48, No. 1, January 2003, pp. 28–38.

[62] Bourtsev, B.N., Selemenev, S.V., "Blade Flap Motion and Lower-to-Upper Rotor Blade Tips Clearances of Helicopters," *Journal of the American Helicopter Society*, Vol.41, No.1, January 1996, pp.37–51.

[63] Burgess, R.K., "Development of the ABC Rotor," *American Helicopter Society 27th Annual Forum*, Washington, D.C., May 1971.

[64] Ruddell, A.J., "Advancing Blade Concept (ABC™) Development," *American Helicopter Society 32nd Annual Forum*, Washington, D.C., 10–12 May 1976.

[65] Johnson, W., *Helicopter Theory*, Dover Publications, New York, 1994.

[66] Halley, D.H., "ABC Helicopter Stability, Control, and Vibration Evaluation on the Princeton Dynamic Model Track," *American Helicopter Society 29th Annual Forum*, Washington, D.C., May 1973.

[67] Peterson, R.L., Mosher, M., "Acoustic Measurements of a Full-Scale, Coaxial, Hingeless Rotor Helicopter," NASA TM-84349, June 1983.

[68] Boyd, Jr., D.D., Burley, C.L., Conner, D.A., "Acoustic Predictions of Manned and Unmanned Rotorcraft Using the Comprehensive Analytical Rotorcraft Model for Acoustics (CARMA) Code System," *American Helicopter Society International Specialists' Meeting on Unmanned Rotorcraft*, Phoenix, AZ, 18–20 January 2005.

[69] Yin, J.P., Ahmed, S.R., "Helicopter Main-Rotor/Tail-Rotor Interaction," *Journal of the American Helicopter Society*, Vol. 45, No. 4, October 2000, pp. 293–302.

[70] Schmitz, F.H., "Aeroacoustics of Flight Vehicles: Theory and Practice," NASA Reference Publication 1258, Vol. 1, Chapter 2, August 1991, pp. 65–149.

[71] Kitaplioglu, C., Caradonna, F.X., " A Study of Blade-Vortex Interaction Aeroacoustics Utilizing an Independently Generated Vortex," AGARD Fluid Dynamics Panel Symposium on Aerodynamics and Aeroacoustics of Rotorcraft, Berlin, 10–14 October 1994.

[72] Leishman, J.G., "Sound Directivity generated by Helicopter Rotors using Wave Tracing Concepts," *Journal of Sound and Vibration*, Vol. 221, No. 3, 1999, pp. 415–441.

[73] Linden, A.W., Ruddell, A.J., "An ABC Status Report," *American Helicopter Society 37th Annual Forum*, New Orleans, LA, 17–20 May 1981.

[74] Orchard, M., Newman, S., "The fundamental configuration and design of the compound helicopter," *Proceedings of Institution of Mechanical Engineers Vol. 217 Part G: Journal of Aerospace Engineering*, G01702, October 2003, pp. 297–315.

[75] Sheridan, P.F., Smith, R.P., "Interactional Aerodynamics — A New Challenge to Helicopter Technology," *Journal of the American Helicopter Society*, January 1980, pp. 3–21.

[76] Cooper, D.E., "YUH-60A Stability and Control," *Journal of the American Helicopter Society*, Vol. 23, No. 3, 1978, pp. 2–9.

[77] Prouty, R.W., Amer, K.B.,"The YAH-64 Empennage and Tail Rotor — A Technical History," *American Helicopter Society 38th Annual Forum Proceedings*, Anaheim, CA, 4–7 May 1982, pp. 247–261.

[78] Main, B.J., Mussi, F., "EH101 — Development Status Report," *Proceedings of the 16th European Rotorcraft Forum*, Glasgow, UK, 18–20 September 1990, pp. III.2.1.1–12.

[79] Cassier, A., Weneckers, R., Pouradier, J., "Aerodynamic Development of the Tiger Helicopter," *Proceedings of the American Helicopter Society 50th Annual Forum*, Washington, DC, 11–13 May 1994.

[80] Eglin, P., "Aerodynamic Design of the NH90 Helicopter Stabilizer," *Proceedings of the 23rd European Rotorcraft Forum*, Dresden, Germany, 16–18 September 1997, pp. 68.1–10.

[81] Frederickson, K.C., Lamb, J.R., "Experimental Investigation of Main Rotor Wake Induced Empennage Vibratory Airloads for the RAH-66 Comanche Helicopter," *Proceedings of the American Helicopter Society 49th Annual Forum*, St. Louis, MO, 19–21 May 1993, pp. 1029–1039.

[82] Phelps, A.E., Mineck, R.E., "Aerodynamic Characteristics of a Counter-Rotating, Coaxial, Hingeless Rotor Helicopter Model With Auxiliary Propulsion," NASA TM-78705, May 1978.

[83] Paglino, V.M., Beno, E.A., "Full-Scale Wind-Tunnel Investigation of the Advancing Blade Concept Rotor System," USAAMRDL TR 71-25, August 1971

[84] Bi, N.P., Leishman, J.G., "Analysis of Unsteady Pressures Induced on a Body by a Rotor," *Journal of Aircraft*, Vol. 28, No. 11, 1991, pp. 756–767.

[85] Felker III, F.F., "Performance and Loads Data from a Wind Tunnel Test of a Full-Scale, Coaxial, Hingeless Rotor Helicopter," NASA TM 81329/USAARADCOM TR 81-A-27, October 1981

[86] Magliozzi, B., Hanson, D.B., Amiet, R.K., "Aeroacoustics of Flight Vehicles: Theory and Practice," NASA Reference Publication 1258, Vol. 1, Chapter 1, August 1991, pp. 1–64.